Universidad Autónoma de Madrid

Theoretical study of vibrationally resolved photoionization of diatomic and polyatomic molecules

Etienne Plésiat

Supervised by
Fernando Martín

2012

Je dédie ce mémoire à mes parents
et à mon frère.

Acknowledgement

I would like to thank:

- my thesis supervisor Fernando Martín, for his perceptive direction
- my collaborator Piero Decleva, for his constant help
- my colleagues Jhon Fredy Pérez-Torres, Alicia Palacios Cañas, Luca Argenti for their helpful advices and corrections
- my former professors in France, Paul-Antoine Hervieux and Giovanni Manfredi, for helping me to find a PhD scholarship in Spain
- my "cousin" Audrey, for designing the cover of this book
- my family and my friends Baptiste, Tanya, Chloe and Silvia for their moral support
- my colleagues Daniele, Ane, Thiago, Felipe, Sergio, Alberto G., Lara, Darek, Alberto S. and Chiara for all the good moments at work
- the people of the "12"
- my grand-father, for always supporting me.

Contents

Introduction

Spectroscopy refers generally to an ensemble of techniques that permit to measure the interaction of electromagnetic radiation with matter[1]. The name reflects the typical spectral distribution of the measured data which are usually presented as a plot of the response of interest versus the energy, frequency, or wavelength of the radiation. According to this definition, the history of spectroscopy started with the discovery of the white light spectrum by Isaac Newton in 1666. This discovery was the starting point of an increasing scientific effort to characterize the light and its interaction with matter. These studies must be seen in the context of the debate generated by the different scientific positions of Isaac Newton and Christiaan Huygens concerning the nature of light and which animated the scientific community for more than 250 years. Indeed, until the advent of quantum mechanics, which stated the principle of complementary for the light (and more generally for matter), the works were devoted to determined if light is a wave (as suggested by Huygens) or made of particles (as claimed by Newton). This scientific effort led to the development of many spectroscopes and some famous experiments such as the Young's double-slit experiment in 1801. As shown in the spectroscopic timeline (see Figure 1), many great scientific names are associated with the evolution of this discipline. It can be seen that the invention of new spectroscopic techniques accompanied the development of quantum mechanics: from the Max Planck's blackbody radiation to the Niels Bohr's atomic model and the photoelectric effect. Since then, the spectroscope became an essential tool in physical and analytical chemistry because interpretation of the spectra provides fundamental informations on matter such as the electronic configuration, the chemical bonding and the mechanisms of chemical reaction. When applied to sample in gas phase, spectroscopy permits to study the photoionization of atoms and molecules. Photoionization is a process in which the matter interacting with an electromagnetic radiation emits one or several electrons by absorption of one or several photons. The analysis of the spectra corresponding to the emitted electrons (photoelectrons) gives a rich information on the process and on the targets.

[1] Although it does not involve a similar interaction, mass spectrometry is commonly associated to a spectroscopic technique.

Figure 1: Timeline of the most important inventions, experiments and theories that contribute to spectroscopy.

Until the middle of the twentieth century, the light sources used in the spectroscopic experiments were rather rudimentary: poor coherence, low intensity, small energy range, etc. And then there was the light... In 1947, Frank Elder, Anatole Gurewitsch, Robert Langmuir and Herb Pollock observed the first synchrotron radiation in the General Electric synchrotron (USA). This observation and the identification of the first non thermal synchrotron radiation from astronomical sources by Hannes Olof Gösta Alfvén in 1950 confirmed the prediction made few years before by Julian Schwinger in his theory of radiation from accelerated relativistic electrons. As for the invention of the laser, a few years later in 1960, the discovery of this new radiation source permitted to elaborate new analytical techniques which benefit different scientific areas: chemistry, physics, materials, biology, medicine, environment, astrophysics. The development and the improvement of synchrotron radiation sources all over the world in the last 50 years constitutes a considerable progress in spectroscopy.

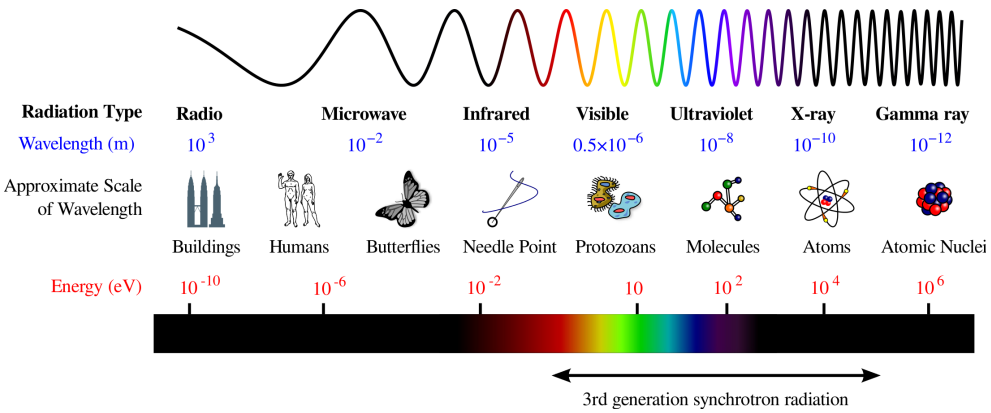

Figure 2: Electromagnetic spectrum.

The synchrotron light sources make use of the property of the charged particles to emit electromagnetic radiation when accelerated. The so-called "synchrotron radiation" is generated by accelerating radially ultra-relativistic charged particles through magnetic fields which are synchronized with the kinetic energy of the particle beam. This radiation has a characteristic polarization and the generated frequencies cover a wide range of the electromagnetic spectrum (see Figure 2).

As illustrated in Figure 3, a synchrotron light source is a combination of different devices, and more particularly of three accelerators: the linac, the booster and the storage ring. The principle is the following: a thin beam of electrons is emitted and accelerated in a linear accelerator (the linac) until reaching velocities close to the speed of light. The electrons are then directed in a synchrotron accelerator, also called "booster" and are accelerated radially

until reaching a nominal energy value. Then the electron beam is injected into the storage ring where bending magnets located at the end of each straight section permit to curve its trajectory. The electromagnetic radiation is emitted in a narrow cone in the forward direction, at a tangent to the electron's orbit. This radiation is collected in experimental facilities called beamlines where the beam is filtered and directed on the samples to be studied. In the new generation of synchrotrons (the third), the storage ring incorporate insertion devices composed of wigglers (or wavers) which are arrays of closely spaced vertically oriented dipole magnets of alternating polarity. The electron beam propagating in the wiggler oscillates in the horizontal plane and emit radiation cones at each bend of the trajectory. The constructive interference of these radiations give rise to a very bright and energetic light.

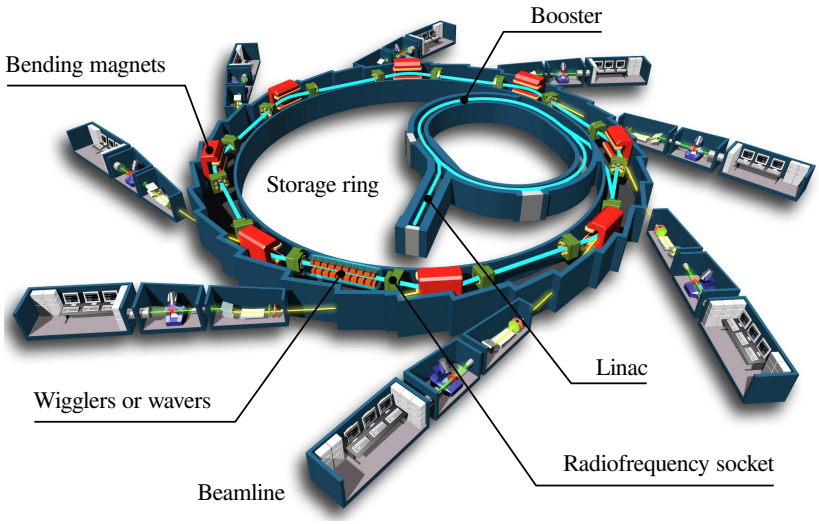

Figure 3: Schematic illustration of a synchrotron light source.

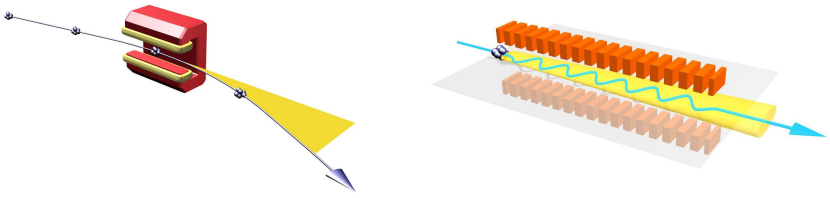

(a) Bending magnet (b) Wiggler

Figure 4

The synchrotron radiation is notable for its:

- High brightness and high intensity: synchrotron light is hundreds of thousands of times more intense than light from conventional x-ray tubes
- High level of polarization: synchrotron radiation is highly polarized (linearly, elliptically or circularly)
- Tunability: the radiation can be selected in wavelength by monochromatization
- Broad spectrum: synchrotron light is emitted with energies ranging from infrared light to hard X-rays
- High collimation: the generated photon beam has a small divergence and a small size source
- Short pulses light emission: the pulse duration is typically less than 10^{-9}s, enabling time-resolved studies

As in a circular particle accelerator, the maximum energy available is limited by the maximum strength of the magnetic fields and the minimum radius of the particle path. Then, the available frequency range is related to the size of the ring. As an example, in the "Soleil" synchrotron light source (France, 2006), electrons are accelerated up to a nominal energy of 2.75 GeV and spin in a storage ring of 354 m in circumference. The resulting radiation ranges from infrared (1 eV) to hard X-rays (50 keV) and the use of wigglers permit to obtain a brilliance of 10^{20} B.U.[2] (10000 times the brilliance of the sunlight). The nominal energy and the circumference of the "Spring-8" synchrotron light source (Japan, 1997) are respectively 8 GeV and 1436 m. The resulting radiation ranges from soft X-rays (100 eV) to hard X-rays (300 keV) for an equivalent brilliance of 10^{20} B.U..

These values represent the maximal capacities of the synchrotron light sources. In practice, each beamline covers a reduced energy domain with different beam intensities. As an example, the "Pleiades" beamline in Soleil covers the energy domain ranging from 10 eV to 1 keV for a flux of photons on sample between 10^7 and 10^{10} photons.s^{-1} in a beam size of few mm^2. These characteristics are adapted to the study of single photoionization processes since multi-photon ionizations are very unlikely at this intensity.

The development of third-generation synchrotron radiation sources in combination with the improvement of the detection techniques made possible to study very fine structures in the spectra at high photon energies. It gave access to the vibrational structure (few hundreds of meV) [157], to the measurement

[2]The brilliance is defined as the number of photons N_γ emitted per second, per unit source size, per solid angle and per photon energy bandwidth Γ: 1BU=N_γ.s^{-1}.mm^{-2}.mrad^{-2}.(0.1%Γ)$^{-1}$.

of the intrinsic line shapes and to the resolution of closed states such as the core orbitals of N_2 (less than 100 meV) [311]. The analysis of the vibrational spectra provides many informations among which the electronic configuration, the electrostatic potential, the geometry change upon ionization, the nature of the bonds (bonding, non-bonding, anti-bonding). In this work, we will show that this technique can also be used to obtain structural information.

Probing with diffraction the structure of matter at the atomic scale requires the use of light or particle beams with wavelengths of the order of the characteristic interatomic distances. Due to their short wavelength, X-rays and few-hundred-eV electron beams are thus the ideal sources. For example, they can efficiently diffract at crystals, exactly as normal waves do when they strike a diffraction grating. From the observed diffraction patterns, one can then deduce quantitative structural information such as lattice constants and symmetry [15]. When used with ultrahigh time resolution, they even allow one to map structural changes as those occurring in phase transitions [106]. X-rays can also efficiently ionize the inner shells of the atomic or molecular constituents, thus producing electrons that scatter coherently (i.e., diffract) within the surroundings of the ionized atom or molecule. The NEXAFS (near-edge X-ray absorption fine structure) or EXAFS (extended X-ray absorption fine structure) techniques are based on this principle [324]. The fingerprints of this coherent electron scattering in the measured spectra provides valuable information about the local electronic structure and coordination geometries. Thus, photoelectron diffraction is used extensively in solid state [50] and surface physics [162] to obtain structural information in crystals as well as in bulk amorphous materials.

When these techniques are applied to gases at low pressure to determine, e.g., the structure of an isolated molecule, one has to face a severe disadvantage: the extremely low density of the medium in comparison with that of bulk materials, which, in some cases, prevents one from observing any diffraction at all. Diffraction is clearly observed in the condensed phase because the relatively low number of photoelectrons generated by standard X-ray sources is amply compensated by the large number of atoms present in the solid or liquid sample (which is of the order of Avogadro's number, i.e., $\sim 10^{23}$). In the case of low density media, a possible solution is to increase the intensity of the light source, so that either more X-rays are efficiently diffracted or the outgoing flux of diffracted photoelectrons is larger. Thus, high intensity, X-ray free electron lasers (XFEL) have been recently proposed as the ideal tool for measurements on isolated species [62]. For example, they have already provided evidence of X-ray diffraction by single nanocrystals of large membrane protein complexes [54] and by a single virus particle [331]. Photoelectrons arising from XFEL irradiation of low-pressure gases have also been suggested as a way to perform time-resolved imaging of molecular structure (i.e., the

"molecular movie") by using so-called photoelectron holography [202], which in some way reminds us the EXAFS spectroscopy. This success is limited, however, by the complexity, large size (up to 4-5 km) and high cost of XFEL single-user facilities. For this reason, it is worth exploring more handy alternatives, as those provided by third-generation synchrotron radiation sources in combination with high kinetic energy resolution detection techniques.

In this quest, theoretical calculations are particularly useful since they help to resolve the experimental features as it gives a better understanding of the mechanisms involved in the photoionization process. However, the process is not simple to treat theoretically, mostly because it requires an accurate description of the continuum wavefunctions which do not decay exponentially at large distances (as bound states do). Thus, for many years, theoretical calculations were performed in the fixed nuclei approximation which assume that the nuclei are fixed at their equilibrium positions. Obviously, this assumption is no longer valid to resolve the vibrational spectra. In this case, one must also calculate the electronic wavefunctions outside the equilibrium positions, since the nuclei move in the potential created by the electrons. This makes calculations significantly more expensive, since the electronic structure must be determined for many molecular geometries, including the equilibrium one used in the fixed-nuclei approximation. High accurate method including the nuclear motion and using a B-spline basis set have been applied successfully to H_2, H_2^+ and D_2 [118, 181], also in the time domain [243, 321]. Unfortunately, such method cannot be used to treat molecules with more than two electrons. The general case requires to elaborate more flexible methods, based on different approximations. Among all the reported existent numerical methods[3], very few have been implemented to treat the nuclear motion. Most of the recent theoretical results published on the topic have been obtained by Cherepkov *et al.* by using the RPA method applied to diatomic molecules such as N_2 [340, 226, 339] and CO [1, 338, 335, 178, 2, 336]. Theoretical studies resolving the vibrational spectra of polyatomic molecules are rare because it requires to deal with few tens of electrons and various normal modes of vibration. Most of the vibrational spectra of polyatomic molecules have been calculated by Lucchese *et al.*: N_2O [233], SiF_4 [259], CF_4 [171], [229] and C_6F_6 [229]. Moreover, almost none of the existent methods have been used to explore the photoelectron spectra in the high energy region because it requires a very accurate (and then expensive) description of the high oscillating continuum wavefunctions.

[3]The Continuum Multiple Scattering Method (CMSM), the Stieltjes-Tchebycheff moment theory (STMT), the Kohn variational principle Lobatto technique (LDKL), the Multichannel Quantum-Defect Theory (MQDT), the Many-Body Perturbation Theory (MBPT), the Random Phase Approximation (RPA), the Schwinger variational method and the R-matrix method.

The present work started in this experimental and theoretical context. It aims to study theoretically the vibrationally resolved photoelectron spectra of diatomic and polyatomic molecules in the high energy region. The method presented here is based on the Born-Oppenheimer approximation which permits to treat separately electronic and nuclear degrees of freedom. The electronic structure is calculated using the so-called multicenter B-spline static-exchange DFT method developed during the last 15 years by Decleva *et al.* [357, 359, 14, 394]. As the name suggests, it makes use of the DFT formalism and B-spline basis sets. The method has been originally used in the fixed-nuclei approximation and proved to describe accurately the photoionization process in many molecular systems: H_2 [41], N_2 [357, 359], CO [360], Cl_2 [394], HF, CO_2, NH_3, H_2O, CH_4 [361], PH_3 [359], BF_3 [258], C_2H_2 [130], CF_4 [395, 131, 80], SF_6 [364, 365, 390], C_6H_6 [415], $(CH_3)_3N$ [357], uracil [393], fullerene [81]. In this work, the multicenter B-spline static-exchange DFT method has been extended to the calculation of the electronic dipole couplings in a grid of molecular geometries ; within the Born-Oppenheimer approximation, we have then involved the vibrational motion by solving the Schrödinger equation in a B-spline basis set.

In the first part of the present manuscript we will explain the theory that supports the multicenter B-spline static-exchange DFT method. We will start reminding in Chapter 1 the basic concepts leading to the general formulation of the single photoionization cross section. After introducing the Born-Oppenheimer approximation, we will detail the different methods that permit to calculate the electronic structure (Chapter 2) and vibrational structure (Chapter 3). A particular attention will be paid to the DFT formalism, to the characteristics of the B-spline functions and to the treatment of the continuum in the framework of the multicenter B-spline static-exchange DFT method. Chapter 4 will be devoted to the development of the fully differential vibrationally resolved cross section formula. In the second part of this manuscript, we will present most of the results obtained during the PhD thesis by using the present method. The results are divided in two chapters: one corresponding to diatomic molecules (H_2, N_2 and CO) and one to polyatomic molecules (C_2H_2, CH_4, CF_4, BF_3 and SF_6). Chapter 5 will show a systematic comparison between the results obtained with the multicenter B-spline static-exchange DFT method and published experimental and theoretical data for inner and valence shell photoionization. After discussing the efficiency of the present method, we will use it to interpret features appearing in new experimental measurements. Chapter 6 will be devoted to the study of inner shell photoionization of C_2H_2, CH_4, CF_4 and BF_3 and to the valence shell photoionization of SF_6. In all theses cases, the results obtained with the multicenter B-spline static-exchange DFT method will be compared to new experimental measurements. These are the first results ever obtained for vibrationally resolved cross sections of polyatomic molecules at high photoelectron energies.

For most of the molecules studied in this work, a simpler model, which permits to understand the fundamental mechanisms of the different processes, will be proposed.

Part I

Theory

1. General theory

1.1 The photoionization process

Photoionization process consists in the promotion of a bound electron to a scattering state (see Figure 1.1). Epitomized by the Rutherford's discovery, scattering is one of the most important experimental technique to investigate matter at the microscopic level. The results of such experiments are usually expressed in terms of cross section which is the quantity used to measure the probability of a certain collision event.

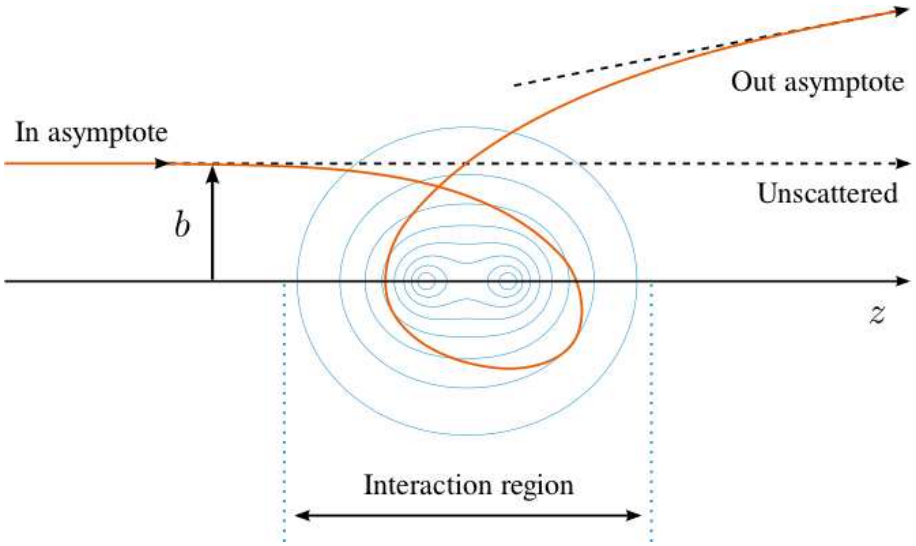

Figure 1.1: Schematic illustration of the scattering of the photoelectron by the molecular electrostatic potential in a classical picture. Orange trajectory corresponds to the scattering path of the electron and dashed black lines to the asymptotic limits of this trajectory. b is the impact parameter.

For the sake of clarity, let's consider first the scattering process in a classical picture. Looking at Figure 1.1, we understand that measuring the scattering of one particle will give information on how its momentum changed after the interaction. But the microscopic details of the event is experimentally

inaccessible. If now, and as shown in Figure 1.2, we are able to reproduce this experiment with many particle of same initial momentum $\mathbf{k}_0$ but random impact parameters, we can access to some statistical information of the event.

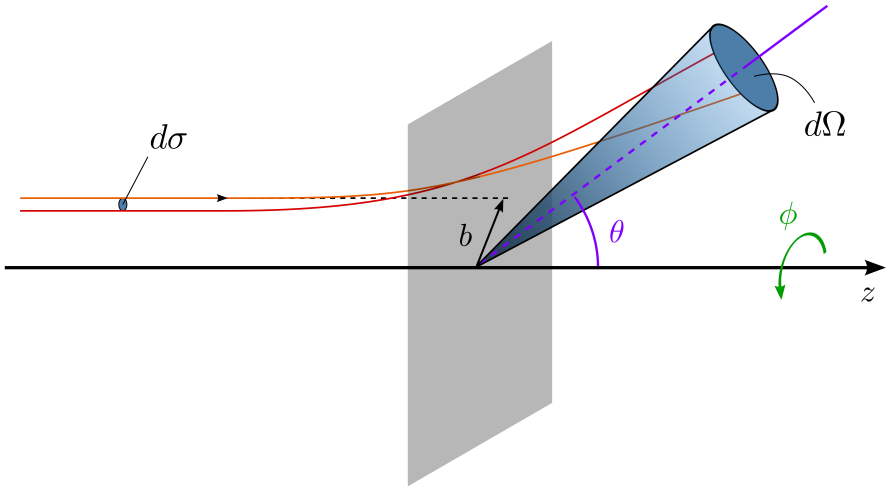

Figure 1.2: Schematic illustration of the scattering process. b is the impact parameter, contained in the plane perpendicular to the particles flux. $d\sigma$ is the area crossed by the particles scattered into the solid angle $d\Omega$. The differential cross section is equal to the ratio of these two quantities.

We consider a beam of particles weak enough that the incident particles do not interact one with another. The number of scattered particles N_{sc} in a given solid angle $d\Omega$ is related to the the number of incident particles N_0 crossing the section area $d\sigma$ perpendicular to $\mathbf{k}_0$:

$$N_{sc}\left(d\Omega\right) = \frac{N_0}{d\sigma}\sigma\left(d\Omega\right) \tag{1.1}$$

and for a solid angle small enough:

$$\sigma\left(d\Omega\right) = \frac{d\sigma\left(d\Omega\right)}{d\Omega}d\Omega \tag{1.2}$$

where $d\sigma\left(d\Omega\right)/d\Omega$ is the differential cross section and is the most detailed information that can be observed in scattering experiments.

For a single photoionization event, this quantity is independent of the incident flux. Then the cross section is interpreted as the transition probability per unit of time, per unit target scatterer and per unit flux of the incident particles with respect to the target. Considering a laser beam emitting a flux F of photon per unity of time and area, and a transition probability per unity

of interaction time Γ of the electron from an initial electronic state $|n\rangle$ to another one $|m\rangle$, then the cross section is given by:

$$\sigma = \frac{\Gamma}{F} \tag{1.3}$$

1.1.1 Transition probability

The cross section is the transition probability independently of the characteristics of the laser beam. We want to find the general expression of the single photoionization cross section, but to do so, we have to evaluate first the transition probability.

We consider the general case of an electromagnetic field, propagating as a plane wave with a wave vector $\mathbf{k}$ and interacting with an atom or a molecule. The time dependent Schrödinger equation is:

$$i\hbar\frac{\partial\Psi(\mathbf{r},t)}{\partial t} = \left[\hat{H}^{(0)}(\mathbf{r}) + \hat{V}(\mathbf{r},t)\right]\Psi(\mathbf{r},t) \tag{1.4}$$

where $\mathbf{r}$ gather the electronic and nuclear coordinates, $\hat{H}^{(0)}(\mathbf{r})$ is the Hamiltonian operator of an isolated atom or molecule and $\hat{V}(\mathbf{r},t)$ is the interaction Hamiltonian operator of the molecule with the radiation.

The time dependent wavefunction can be expanded over all the stationary states:

$$\Psi(\mathbf{r},t) = \sum_k c_k(t)e^{-\frac{i}{\hbar}E_k^{(0)}t}\psi_k^{(0)}(\mathbf{r}) \tag{1.5}$$

where $E_k^{(0)}$ is the eigenvalue from the time independent Schrödinger equation (TISE) for a given stationary state k, and $c_k(t)$ the corresponding coefficients depending on time.

Introducing (1.5) into (1.4), we end up with:

$$\begin{aligned} i\hbar\sum_k \frac{dc_k(t)}{dt}e^{-\frac{i}{\hbar}E_k^{(0)}t}\psi_k^{(0)}(\mathbf{r}) \quad &+ \quad \sum_k c_k(t)E_k^{(0)}e^{-\frac{i}{\hbar}E_k^{(0)}t}\psi_k^{(0)}(\mathbf{r}) = \\ \sum_k c_k(t)E_k^{(0)}e^{-\frac{i}{\hbar}E_k^{(0)}t}\psi_k^{(0)}(\mathbf{r}) \quad &+ \quad \sum_k c_k(t)\hat{V}(\mathbf{r},t)e^{-\frac{i}{\hbar}E_k^{(0)}t}\psi_k^{(0)}(\mathbf{r}) \end{aligned} \tag{1.6}$$

and obtain:

$$i\hbar\sum_k \frac{dc_k(t)}{dt}e^{-\frac{i}{\hbar}E_k^{(0)}t}\psi_k^{(0)}(\mathbf{r}) = \sum_k c_k(t)\hat{V}(\mathbf{r},t)e^{-\frac{i}{\hbar}E_k^{(0)}t}\psi_k^{(0)}(\mathbf{r}) \tag{1.7}$$

Projecting onto the ground state $\psi_m^{(0)^*}(\mathbf{r})$, we have:

$$\begin{aligned} & i\hbar \sum_k \frac{dc_k(t)}{dt} e^{-\frac{i}{\hbar}E_k^{(0)}t} \overbrace{\int \psi_m^{(0)^*}(\mathbf{r})\psi_k^{(0)}(\mathbf{r})d\tau}^{\delta_{mk}} \\ = & \sum_k c_k(t) e^{-\frac{i}{\hbar}E_k^{(0)}t} \underbrace{\int \psi_m^{(0)^*}(\mathbf{r})\hat{V}(\mathbf{r},t)\psi_k^{(0)}(\mathbf{r})d\tau}_{\left\langle \psi_m^{(0)} \middle| \hat{V}(\mathbf{r},t) \middle| \psi_k^{(0)} \right\rangle} \end{aligned} \tag{1.8}$$

where we made use of the Kronecker function properties to express the orthonormality of the eigenfunctions:

$$\delta_{mk} = \begin{cases} 1 & \text{if } m = k \\ 0 & \text{if } m \neq k \end{cases} \tag{1.9}$$

We finally obtain the equation for the evolution of the $c_m(t)$ coefficients:

$$i\hbar \frac{dc_m(t)}{dt} = \sum_k c_k(t) e^{i\omega_{mk}t} \left\langle \psi_m^{(0)} \middle| \hat{V}(\mathbf{r},t) \middle| \psi_k^{(0)} \right\rangle \qquad m = 1, 2, 3, \ldots \tag{1.10}$$

with:

$$\omega_{mk} = \frac{E_m^{(0)} - E_k^{(0)}}{\hbar} \tag{1.11}$$

In order to solve Equation (1.10), we work in the perturbative regime, i.e., we assume that the radiation-molecule interaction term is a small perturbation to the system. In other words, we suppose the interaction of weak intensity.

We define $t = 0$ as the time reference for the beginning of the field interaction. For $t < 0$, we find the system in a particular stationary state $\psi_n^{(0)}$. Then, we surely have:

$$c_n(t) = 1 \tag{1.12}$$

$$c_k(t) = 0 \qquad k \neq n \tag{1.13}$$

In the weak field limit, the coefficients hardly vary as a function of time and the coefficients $c_n(t)$ at $t = dt$ can be approximated by their initial values:

$$\frac{dc_m(t)}{dt} \simeq -\frac{i}{\hbar} e^{i\omega_{mn}t} \left\langle \psi_m^{(0)} \middle| \hat{V}(\mathbf{r},t) \middle| \psi_k^{(0)} \right\rangle \tag{1.14}$$

and:

$$c_m(t) = \delta_{mn} - \frac{i}{\hbar} \int_0^t e^{i\omega_{mn}t'} \left\langle \psi_m^{(0)} \middle| \hat{V}(\mathbf{r},t') \middle| \psi_k^{(0)} \right\rangle dt \tag{1.15}$$

which corresponds to a perturbative treatment of first order.

Since we are considering the case where the final state is different from the initial one (i.e. $m \neq n$), the previous equation can be reduced to:

$$c_m(t) = -\frac{i}{\hbar}\int_0^t e^{i\omega_{mn}t'} \left\langle \psi_m^{(0)} \left| \hat{V}(\mathbf{r},t') \right| \psi_k^{(0)} \right\rangle dt \tag{1.16}$$

and the transition probability from $|n\rangle$ to $|m\rangle$ is given by the square module of the coefficient:

$$P_{n\to m} = |c_m(t)|^2 = \frac{1}{\hbar^2}\left| \int_0^t e^{i\omega_{mn}t'} \left\langle \psi_m^{(0)} \left| \hat{V}(\mathbf{r},t') \right| \psi_n^{(0)} \right\rangle dt \right|^2 \tag{1.17}$$

In order to calculate the transition probability, we have to specify the interaction Hamiltonian $\hat{V}(\mathbf{r},t')$. To do so, we introduce the mathematical formulation of the electromagnetic field, assuming a plane wave propagating in $\mathbf{e}_z$ direction with a wave vector $\mathbf{k}$ and polarized along $\mathbf{e}_x$. The electric ($\mathbf{E}$) and magnetic ($\mathbf{B}$) fields thus can be written as:

$$\mathbf{E}(t) = E_0 \cos(\omega t - kz)\mathbf{e}_x \tag{1.18}$$

$$\mathbf{B}(t) = B_0 \cos(\omega t - kz)\mathbf{e}_y \tag{1.19}$$

where E_0 and B_0 are the corresponding amplitudes.

The radiation-matter interaction is completely defined by the interaction between those fields and the charged particles of the atom or the molecule. For the hydrogen atom in its ground state, it is well-known that the electric interaction is much higher than the magnetic one (by a factor of 137 approximately). Then, it is convenient to make a second approximation by neglecting the magnetic field.

Usually, electronic transitions for atoms and molecules happen when light has a wavelength belonging to the visible-UV range ($\lambda \approx 10^3$Å). Whereas, the typical atom diameter d is about 1 Å. Therefore:

$$\lambda \gg d \qquad \text{and} \qquad kz = \frac{2\pi}{\lambda} \ll 1 \tag{1.20}$$

According to Equation (1.20), it is reasonable to neglect the spatial dependence of the electric field and reduce the interacting electromagnetic field expression to:

$$\mathbf{E}(t) \simeq E_0 \cos(\omega t)\mathbf{e}_x \tag{1.21}$$

This approximation, known as the *dipole approximation*, assumes that the spatial variation of the electric field is weak compared to the size of the system and that the atom or molecule only "feels" the temporal evolution of $\mathbf{E}(t)$ (see Figure 1.3).

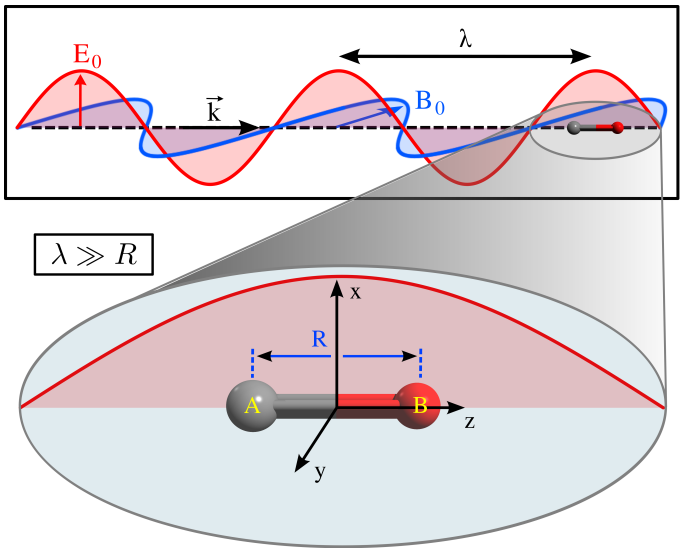

Figure 1.3: Schematic representation of the Electromagnetic field-molecule interaction

By analogy with the classical definition of the potential energy of interaction between charged particles and electric field, one can express $\hat{V}(\mathbf{r}, t')$ as a function of the electric field (in the length gauge) as:

$$\begin{aligned} \hat{V}(\mathbf{r}, t') &= e^{iH^{(0)}t/\hbar} \left[\boldsymbol{d} \cdot \mathbf{E}(t)\right] e^{-iH^{(0)}t/\hbar} \\ &= \left(e^{iH^{(0)}t/\hbar} \left[\boldsymbol{d} \cdot \mathbf{e}_x\right] e^{-iH^{(0)}t/\hbar}\right) E_0 \cos(\omega t) \\ &= \hat{d}_x \frac{E_0}{2} \left[e^{i\omega t} + e^{-i\omega t}\right] \end{aligned} \tag{1.22}$$

Inserting Equation (1.22) in (1.17), the transition probability can be written as:

$$\begin{aligned} P_{n\to m} &= \frac{|E_0|^2}{4\hbar^2} \left| \int_0^t e^{i\omega_{mn}t'} \langle \psi_m^{(0)} \left| \hat{d}_x \right| \psi_n^{(0)} \rangle \left[e^{i\omega t'} + e^{-i\omega t'}\right] dt \right|^2 \\ &= \frac{|E_0|^2}{4\hbar^2} \left| \langle \psi_m^{(0)} \left| \hat{d}_x \right| \psi_n^{(0)} \rangle \right|^2 \left| \int_0^t e^{i(\omega_{mn}+\omega)t'} + e^{i(\omega_{mn}-\omega]t'} dt \right|^2 \end{aligned} \tag{1.23}$$

Integrating over t, we finally obtain:

$$P_{n\to m} = \frac{|E_0|^2}{4\hbar^2} |T_x^{nm}|^2 \left| \underbrace{\frac{e^{i(\omega_{mn}+\omega)t} - 1}{\omega_{mn} + \omega}}_{\text{emission}} + \underbrace{\frac{e^{i(\omega_{mn}-\omega)t} - 1}{\omega_{mn} - \omega}}_{\text{absorption}} \right|^2 \tag{1.24}$$

where $T_x^{nm} = \langle \psi_m^{(0)} \left| \hat{d}_x \right| \psi_n^{(0)} \rangle$ is the transition dipole moment, that must be different from 0 to give rise to the electronic transition.

Both emission and absorption terms satisfy the Bohr conditions since the probability is maximum when:

- $\omega = \omega_{mn} \Rightarrow$ absorption of a photon whose energy equal to $E_m - E_n$
- $\omega = -\omega_{mn} \Rightarrow$ emission of a photon with an energy equal to $E_m - E_n$

In the present work, we focus on the single photoionization process, i.e. we only need to describe the absorption probability. By using the identity:

$$e^{i\alpha} - 1 = e^{i\alpha/2} \left[e^{i\alpha/2} - e^{-i\alpha/2} \right] = 2ie^{i\alpha/2} \sin \frac{\alpha}{2} \tag{1.25}$$

and removing the emission term from Equation (1.24), the absorption probability reads:

$$P_{n\to m} = \frac{|E_0|^2}{\hbar^2} |T_x^{nm}|^2 \frac{\sin^2 \left((\omega_{mn} - \omega)\, t/2 \right)}{(\omega_{mn} - \omega)^2} \tag{1.26}$$

The function $\frac{\sin^2 ((\omega_{mn}-\omega)t/2)}{(\omega_{mn}-\omega)^2}$ is maximum at $\omega = \omega_{mn}$. Its maximum value is $t^2/4$ and its bandwidth at half maximum is $4\pi/t$ (see Figure 1.4).

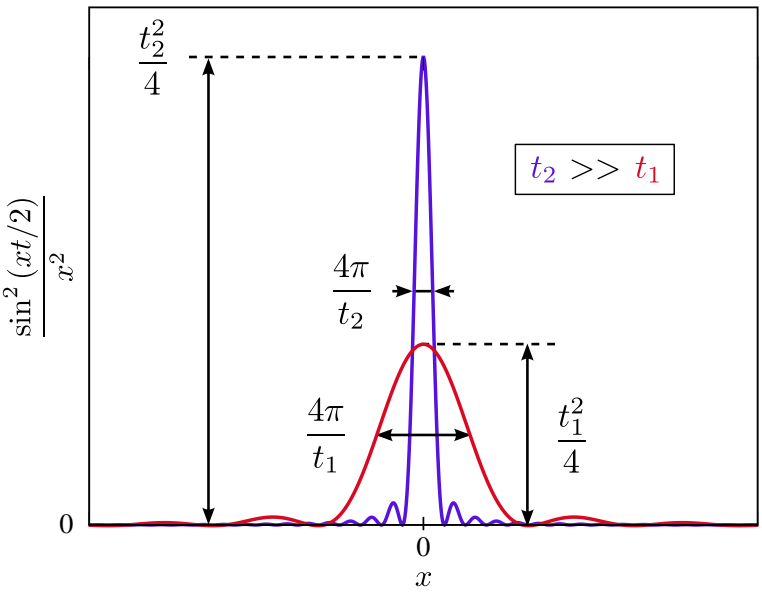

Figure 1.4: Function $\frac{\sin^2 ((\omega_{mn}-\omega)t/2)}{(\omega_{mn}-\omega)^2}$ plotted for two different times t_1 (red curve) and t_2 (violet curve).

When $t \to \infty$, the central peak of the function become higher and sharper, such as a Dirac function $\delta(\omega_{mn} - \omega)$. For large values of t:

$$\int \frac{\sin^2((\omega_{mn} - \omega)\, t/2)}{(\omega_{mn} - \omega)^2} d\omega \approx \frac{\pi t}{2} \tag{1.27}$$

Knowing that:

$$\int \delta(\omega_{mn} - \omega)\, d\omega = 1 \tag{1.28}$$

we can write:

$$\frac{\sin^2((\omega_{mn} - \omega)\, t/2)}{(\omega_{mn} - \omega)^2} \approx \frac{\pi t}{2} \delta(\omega_{mn} - \omega) \tag{1.29}$$

Therefore, the transition probability is given by:

$$P_{n\to m}(t) = \frac{|E_0|^2 \pi t}{2\hbar^2} |T_x^{nm}|^2 \delta(\omega_{mn} - \omega) \tag{1.30}$$

1.1.2 Single photoionization cross section

Going back to the definition of the cross section, now we are able to evaluate the probability transition per unit of interaction time:

$$\Gamma_{n\to m} = \frac{dP_{n\to m}(t)}{dt} \tag{1.31}$$

$$= \frac{|E_0|^2 \pi}{2\hbar^2} |T_x^{nm}|^2 \delta(\omega_{mn} - \omega) \tag{1.32}$$

Integrating over ω we obtain:

$$\Gamma_{n\to m} = \frac{|E_0|^2 \pi}{2\hbar^2} |T_x^{nm}|^2 \tag{1.33}$$

It is well-known that for a monochromatic electromagnetic field, the photon flux can be expressed as a function of the amplitude E_0 of the electric field as:

$$F = \frac{E_0^2}{8\pi} \frac{1}{\hbar\omega} c \tag{1.34}$$

Finally, using this last equation and introducing (1.34) into (1.3), we obtain the final formula for the single photoionization cross section when light is polarized linearly:

$$\sigma_{n\to m}(\omega) = \frac{4\pi^2 \omega}{\hbar c} |T_x^{nm}|^2 \tag{1.35}$$

In the case of randomly oriented molecules, the dipole operator has to be averaged over all space:

$$\langle \left| \hat{d}_x \right|^2 \rangle_\Omega = \frac{\int \left| \hat{d}_x \right|^2 d\Omega}{\int d\Omega} = \frac{\left| \hat{d} \right|^2}{3} \tag{1.36}$$

Finally, the photoionization cross section corresponding to the $n \to m$ transition is given by:

$$\sigma_{n\to m}(\omega) = \frac{4\pi^2 \omega}{3\hbar c} |T^{nm}|^2 \tag{1.37}$$

The cross section is usually expressed in cm^2 or barn b ($1b = 10^{-24} cm^2$).

1.2 The Born-Oppenheimer approximation

The Schrödinger equation of a molecular system is:

$$\hat{H}(\mathbf{r}, \mathbf{R}) \Psi(\mathbf{r}, \mathbf{R}) = E \Psi(\mathbf{r}, \mathbf{R}) \tag{1.38}$$

where the total Hamiltonian for a molecule is given in atomic units:

$$\hat{H}(\mathbf{r}, \mathbf{R}) = \hat{T}_N(\mathbf{R}) + \hat{T}_e(\mathbf{r}) + V_{eN}(\mathbf{r}, \mathbf{R}) + V_{NN}(\mathbf{R}) + V_{ee}(\mathbf{r}) \tag{1.39}$$

and:

$\hat{T}_N = -\frac{1}{2} \sum_{\alpha=1}^{M} \frac{1}{m_\alpha} \nabla_\alpha^2$ is the kinetic energy of the nuclei

$\hat{T}_e = -\frac{1}{2} \sum_{i=1}^{N} \nabla_i^2$ is the kinetic energy of the electrons

$V_{eN} = -\sum_{i=1}^{N} \sum_{\alpha=1}^{M} \frac{Z_\alpha}{|\mathbf{r}_i - \mathbf{R}_\alpha|}$ is the Coulomb attraction between electrons and nuclei

$V_{NN} = \sum_{\alpha=1}^{M} \sum_{\beta>\alpha}^{M} \frac{Z_\alpha Z_\beta}{|\mathbf{R}_\alpha - \mathbf{R}_\beta|}$ is the Coulomb repulsion between nuclei

$V_{ee} = \sum_{i=1}^{N} \sum_{j>i}^{N} \frac{1}{|\mathbf{r}_i - \mathbf{r}_j|}$ is the Coulomb repulsion between electrons

The index i and j denote the electrons, α and β the nuclei ; N is the number of electrons, M the number of nuclei and Z_α the charge of the nucleus α.

The approximation suggested by Max Born and J. Robert Oppenheimer in 1927 [34] permits to split the total wavefunction Ψ into an electronic ψ and nuclear χ part:

$$\Psi(\mathbf{r}, \mathbf{R}) = \psi(\mathbf{r}, \mathbf{R})\chi(\mathbf{R}) \tag{1.40}$$

Both wavefunctions are then eigenfunction of an electronic and nuclear Schrödinger equation respectively. The former is obtained by subtracting the nuclear kinetic energy from the total molecular Hamiltonian and is parametrically dependent of the nuclear coordinates $\mathbf{R}$:

$$\hat{H}_e(\mathbf{r}; \mathbf{R})\psi(\mathbf{r}; \mathbf{R}) = E_e(\mathbf{R})\psi(\mathbf{r}; \mathbf{R}) \tag{1.41}$$

where E_e is the electronic energy of the system.

The electrons feel the Coulomb potential due to the nuclei clamped at certain positions, which is a sensible approximation since the electrons move orders of magnitude faster than nuclei. Then, by solving the electronic Schrödinger equation varying the nuclear coordinates $\mathbf{R}$, it is possible to obtain E_e as a function of $\mathbf{R}$. This term is called potential energy surface (PES) (or potential energy curve (PEC) when it depends on a single nuclear coordinate). Calculations are made in the adiabatic theorem, i.e. assuming that the PESs obtained for small steps of $\mathbf{R}$ are continuous and correspond to unique electronic states.

In a second step, the nuclear kinetic operator is reintroduced in order to solve the nuclear Schrödinger equation:

$$\left[\hat{T}_n(\mathbf{R}) + E_e(\mathbf{R})\right] \chi(\mathbf{R}) = E\chi(\mathbf{R}) \tag{1.42}$$

where E is the total energy of the system.

It can be demonstrated that the Born-Oppenheimer approximation is valid whenever the PESs are well energetically separated:

$$E_0(\mathbf{R}) \ll E_1(\mathbf{R}) \ll E_2(\mathbf{R}) \cdots \quad \forall\, \mathbf{R} \tag{1.43}$$

Within the Born-Oppenheimer approximation, electronic and nuclear structures can then be treated separately. It is convenient for the purpose of this work because it reduces the vibronic problem into two separated calculations involving a smaller number of variables. In the following sections, we will detail the procedure which permits to obtain the nuclear and electronic structures.

2. Electronic structure

2.1 *Ab initio* methods

In this section, the basic ideas of the wavefunction methods will be introduced. A short description of the Hartree-Fock method will permit to establish the essential concepts to tackle a particular post-Hartree-Fock method: the CASSCF-MRCI. This method has been used in the present work to evaluate some of the potential energy curves. Then, a detailed description of the time independent and time dependent density functional theory will be given. In the last part of this section, characteristics of some usual basis sets and basis functions will be presented.

2.1.1 The Schrödinger equation

One of the consequence of the wave-particle duality stated by de Broglie (1924) is the formulation in 1925 of the Schrödinger equation, whose most general form is in atomic units:

$$i\frac{\partial}{\partial t}\Psi(\mathbf{r},t) = \hat{H}(\mathbf{r},t)\Psi(\mathbf{r},t) \tag{2.1}$$

The Schrödinger theory predicts that for a conservative system, standing waves (or stationary states) can arise. These states are described through the time-independent Schrödinger equation (TISE), in which the application of the Hamiltonian operator $\hat{H}(\mathbf{r})$ on $\Psi(\mathbf{r})$ gives the total energy E:

$$\hat{H}(\mathbf{r})\Psi(\mathbf{r}) = E(\mathbf{r})\Psi(\mathbf{r}) \tag{2.2}$$

It is possible to demonstrate that each state can be expanded on an finite orthonormal basis of states of the Hilbert space:

$$\Psi(\mathbf{r}) = \sum_{i=1} c_i\psi_i(\mathbf{r}) \tag{2.3}$$

where:

$$\langle\psi_i \mid \psi_j\rangle = \delta_{ij} \tag{2.4}$$

For non-relativistic particles, the total Hamiltonian operator can be written as:

$$\hat{H}(\mathbf{r}) = -\frac{1}{2}\sum_{i=1}^{N}\frac{1}{m_i}\nabla_i^2 + \hat{V}(\mathbf{r}) \tag{2.5}$$

The first term corresponds to the kinetic energy and $\hat{V}(\mathbf{r})$ to the potential created by the N particles of the system. Since the latter term depends on the coordinates of several particles and that the TISE is a second order differential equation, Equation (2.2) cannot be solved analytically for more than two particles (hydrogen-like atom systems). Then, methods based on approximations have been developed in order to tackle the many-body problem.

In atomic and molecular physics, a starting point for the resolution of the TISE is the approximation proposed in 1927 by Born and Oppenheimer: taking into account the fact that electrons move much faster than nuclei, it is reasonable to decouple their respective movements and write the wavefunction of the system as a product of the nuclear and the electronic wavefunction (see Section 1.2):

$$\Psi(\mathbf{r}, \mathbf{R}) = \psi(\mathbf{r}, \mathbf{R})\,\chi(\mathbf{R})$$

The polyelectronic wavefunction only depends parametrically on the coordinates of the nuclei $\mathbf{R}$ and both wavefunctions are eigenfunctions of a TISE. It is an important fact to note that the nuclear TISE depends explicitly on the electronic energy, i.e. the potential that the nuclei "feel" at different coordinates $\mathbf{R}$. This implies that the electronic TISE has to be solved in a first step in order to obtain the eigenvalue that will then be used to solve the nuclear TISE. In the following sections, we will detail some of the most popular quantum chemistry methods (mainly the ones used to perform the calculations presented in this work) that permits to solve the electronic TISE. A particular attention will be devoted to the description of the density functional theory (DFT), used to calculate the electronic dipole couplings, as well as some of the potential energy curves for the molecules of interests.

2.1.2 Molecular orbital theory

The Schrödinger equation is the keystone of the chemical physics because it gives access to the complete information of the system via the eigenfunctions. More than the nuclei, the electrons determine the chemical properties of interest of the system. For this reason, a constant effort has been provided in order to solve the electronic TISE.

Considering the general case of a molecule made up of M atoms and N electrons, the electronic Hamiltonian is given by:

$$\hat{H}(\mathbf{r}, \mathbf{R}) = -\frac{1}{2}\sum_{i=1}^{N}\nabla_i^2 - \sum_{i=1}^{N}\sum_{\alpha=1}^{M}\frac{Z_\alpha}{|\mathbf{r}_i - \mathbf{R}_\alpha|} + \sum_{i=1}^{N}\sum_{j>i}^{N}\frac{1}{|\mathbf{r}_i - \mathbf{r}_j|} \tag{2.6}$$

The hamiltonian can also be written under the form:

$$\hat{H}(\mathbf{r},\mathbf{R}) = \sum_{i=1}^{N} \hat{h}_i(\mathbf{r},\mathbf{R}) + \sum_{j>i}^{N} \frac{1}{|\mathbf{r}_i - \mathbf{r}_j|} \tag{2.7}$$

where the one-electron operator is defined by:

$$\hat{h}_i(\mathbf{r},\mathbf{R}) = -\frac{1}{2}\nabla_i^2 - \sum_{\alpha=1}^{M} \frac{Z_\alpha}{|\mathbf{r}_i - \mathbf{R}_\alpha|} \tag{2.8}$$

The barrier to the analytical resolution arises from the bielectronic term in Equation (2.7). A logical idea to overcome this difficulty is to approximate this part of the Hamiltonian using an effective potential. All of the methods presented here are based on such approximation and lay on the molecular orbital theory. This theory treats the electrons as moving in the whole molecule under the influence of the other particles which compose the system. Each of these electron is described by a wavefunction φ_i called molecular orbitals and which compose an orthogonal basis set for the total electronic wavefunction of the system:

$$\psi(\mathbf{r},\mathbf{R}) = \prod_{i=1}^{N} \varphi_i(\mathbf{r},\mathbf{R}) \tag{2.9}$$

where N is the number of electrons of the system. This definition, also known as the Hartree product does not satisfy the Pauli exclusion principle which edicts that since electrons are fermions, the electronic wavefunction has to be antisymmetric by exchange of two electrons. The antisymmetry requirement was carried out in 1929 by John C. Slater with the use of a determinant which guarantees the sign change of the total wavefunction when two columns are exchanged. By splitting the monoelectronic wavefunction into a spatial and spin part ($\varphi_i = \alpha\varphi_i$ and $\bar{\varphi}_i = \beta\varphi_i$), then we can write the polyelectronic wavefunction as:

$$\psi(\mathbf{r},\mathbf{R}) = \frac{1}{\sqrt{N!}} \begin{vmatrix} \varphi_1(\mathbf{r_1}) & \bar{\varphi}_1(\mathbf{r_1}) & \varphi_2(\mathbf{r_1}) & \dots & \bar{\varphi}_N(\mathbf{r_1}) \\ \varphi_1(\mathbf{r_2}) & \bar{\varphi}_1(\mathbf{r_2}) & \varphi_2(\mathbf{r_2}) & \dots & \bar{\varphi}_N(\mathbf{r_2}) \\ \vdots & \vdots & \vdots & \vdots & \vdots \\ \varphi_1(\mathbf{r_N}) & \bar{\varphi}_1(\mathbf{r_N}) & \varphi_2(\mathbf{r_N}) & \dots & \bar{\varphi}_N(\mathbf{r_N}) \end{vmatrix} \tag{2.10}$$

2.1.3 The Hartree-Fock method

The first "procedure" elaborated to handle the many-body Schrödinger equation from fundamental physical principles was developed in 1927 by Douglas R. Hartree and subsequently completed by John C. Slater and Vladimir A. Fock in 1930. Although this method was a real improvement in comparison with simpler empirical methods developed on the Bohr's model, it required

the advent of the first computers in the 1950's before starting to be efficiently implemented. In fact, due to the relatively weak computational resources available at the early years of the method, Hartree-Fock calculations were restricted for quite a long time to the study of atomic systems.

The electronic TISE (2.1.1) can be rewritten in order to obtain a simplest expression for the energy of the system:

$$E = \frac{\int \psi^* \hat{H} \psi d\tau}{\int \psi^* \psi} = \int \psi^* \hat{H} \psi d\tau \tag{2.11}$$

where we have considered ψ normalized to 1. In the Hartree-Fock approximation, the polyelectronic wavefunction ψ is defined as a single Slater determinant. The integral from Equation (2.11) can be further simplified using the Slater-Condon rules. These rules permit to reduce the integral of N-electron wavefunctions constructed as Slater determinants to sums over integrals of individual molecular orbitals. It follows that for a one-body operator, the matrix elements for two wavefunctions differing by more than two orbitals vanish. In a close-shell system, there as much electrons with spin α than electrons with spin β. In such case, assuming that an electron with spin α occupies the same spatial orbital than another electron with spin β, the energy in Equation (2.11) becomes:

$$E = 2\sum_{i=1}^{N/2} h_i + \sum_{i=1}^{N/2}\sum_{j=1}^{N/2} (2J_{ij} - K_{ij}) \tag{2.12}$$

The first term corresponds to the kinetic energy of the electrons plus their energy of interaction with the nuclei:

$$h_i = \int \varphi_i^*(\mathbf{r}_1) \left(-\frac{1}{2}\nabla_i^2 - \sum_{\alpha=1}^{M} \frac{Z_\alpha}{|\mathbf{r}_1 - \mathbf{R}_\alpha|} \right) \varphi_i(\mathbf{r}_1) d\mathbf{r}_1 \tag{2.13}$$

The second term corresponds to the energy due to the Coulomb interaction between an electron in orbital i and an electron in orbital j:

$$J_{ij} = \int \varphi_i^*(\mathbf{r}_1)\varphi_j^*(\mathbf{r}_2) \frac{1}{|\mathbf{r}_1 - \mathbf{r}_2|} \varphi_i(\mathbf{r}_1)\varphi_j(\mathbf{r}_2) d\mathbf{r}_1 d\mathbf{r}_2 \tag{2.14}$$

The third term corresponds to the exchange energy which is a pure quantum effect arising from the exchange of two electrons:

$$K_{ij} = \int \varphi_i^*(\mathbf{r}_1)\varphi_j^*(\mathbf{r}_2) \frac{1}{|\mathbf{r}_1 - \mathbf{r}_2|} \varphi_j(\mathbf{r}_1)\varphi_i(\mathbf{r}_2) d\mathbf{r}_1 d\mathbf{r}_2 \tag{2.15}$$

In "unrestricted" Hartree-Fock, for every spatial orbital $\varphi_i(\mathbf{r}_1)$, there is an equation of the form:

$$\hat{f}(1)\varphi_i(\mathbf{r}_1) = \varepsilon_i \varphi_i(\mathbf{r}_1) \tag{2.16}$$

$\hat{f}$ is the Fock operator defined as:

$$\hat{f}(1) = \hat{h}_i(1) + \sum_{j=1}^{N/2} \left(2\hat{J}_j(1) - \hat{K}_j(1) \right) \tag{2.17}$$

where:

$$\hat{h}_i(1)\varphi_i(\mathbf{r}_1) = \left(-\frac{1}{2}\nabla_1^2 - \sum_{\alpha=1}^{M} \frac{Z_\alpha}{|\mathbf{r}_1 - \mathbf{R}_\alpha|} \right) \varphi_i(\mathbf{r}_1) \tag{2.18}$$

$$\hat{J}_j(1)\varphi_i(\mathbf{r}_1) = \varphi_i(\mathbf{r}_1) \int \varphi_j^*(\mathbf{r}_2) \frac{1}{|\mathbf{r}_1 - \mathbf{r}_2|} \varphi_j(\mathbf{r}_2) d\mathbf{r}_2 \tag{2.19}$$

$$\hat{K}_j(1)\varphi_i(\mathbf{r}_1) = \varphi_j(\mathbf{r}_1) \int \varphi_j^*(\mathbf{r}_2) \frac{1}{|\mathbf{r}_1 - \mathbf{r}_2|} \varphi_i(\mathbf{r}_2) d\mathbf{r}_2 \tag{2.20}$$

The summation in Equation (2.17) define the electrostatic Hartree potential $V_H(\mathbf{r}_i)$ felt by the electron i:

$$V_H(\mathbf{r}_i) = \sum_{j=1}^{N/2} \left(2\hat{J}_j(i) - \hat{K}_j(i) \right) \tag{2.21}$$

In other words, the Hartree approximation reduces the interaction between N electrons to an interaction between each electron and a homogeneous charge distribution of the $N-1$ other electrons. Nevertheless, this mean field approximation is in many cases much too radical since it cannot take into account any electronic correlation effects.

The variational principle can be applied in order to improve systematically the value of the energy. According to this principle, any normalized trial wavefunction Ψ will have an expectation value W that is greater than or equal to the true ground state of the system E_0:

$$\langle \Psi \left| \hat{H} \right| \Psi \rangle = W \geq E_0 \tag{2.22}$$

Practically, the variational principle is implemented following the Self Consistent Field procedure (SCF): an initial guess for the wavefunction is used in order to calculate the first value of W which will then be improved iteratively varying some parameters until reaching a certain convergence. As one can see, the variational theorem implies a simple procedure to ensure that the calculated energy is correct enough. Nevertheless, one has to keep in mind that although a specific wavefunction provides a reasonable value for the energy, this doesn't mean that the same wavefunction is adapted to describe other properties of the system. The variational method can be applied to Equation (2.12) with the condition that the orbitals keep being orthonormal one to each other during the SCF procedure.

In the Hartree-Fock approximation, the energy result is affected by an error which is related to the strength of the correlation energy E_{corr} in the system:

$$E_{corr} = E_{exact} - E_{limHF} \tag{2.23}$$

where E_{exact} corresponds to the exact energy of the system and E_{limHF} to Hartree-Fock energy obtained with a complete basis set.

Such correlation energy is partly due to the electronic dynamical correlation which is characterized by the fact that the electrons are not moving independently (the motion of one affects all the others). Part of the dynamic correlation is due to the Coulomb interaction which makes the electrons repelling each others. In fact, it is said that the electron create a Coulomb hole around its position because this electrostatic repulsion ensures that no other electron will occupy the same region of the space. It has to be noticed, however, that the Coulomb interaction is not the only origin of this repulsion. Indeed, the Pauli exclusion principle implies that two fermions of same spin cannot occupy the same position simultaneously. Then, any electron create another kind of hole, called Fermi hole, which prevent the presence of another one.

When the molecular geometry is stretched, the dynamical correlation becomes less important because the distances between electrons are getting larger. However, the correlation energy increases with the stretching which suggests that it exists a non-dynamical source to the correlation energy.

Considering from one side the serious limitations of the Hartree-Fock methods and from the other side the constant progress in computing technologies, a considerable scientific effort has been dedicated to the development of enhanced *ab initio* methods: the so-called post-Hartree-Fock methods. This new generation of methods is inspired by the Hartree-Fock former one but lies on different approximations. Although there's a panel of post-Hartree-Fock methods, all of them are designed with the same ambition: recovering some of the dynamical and non-dynamical correlation that is not included in the Hartree-Fock method. In this perspective, the first logical step is to go beyond the monodeterminantal expression of the wavefunction by considering configuration of interactions.

2.1.4 Configuration interaction

It has been observed that in some cases (e.g., for degenerate states), the system is better described when the total wavefunction is expressed as a linear combination of determinants. The determinant corresponding to the ground state is given by the Hartree-Fock method. The additional determinants correspond to electronic configurations in which electrons are promoted into virtual orbitals. Such determinants represent excited states, whose contribution to the total

wavefunction of the ground state decrease with the order of excitation. The configuration interaction (CI) method exploits this idea, allowing the electrons to move more freely since they can occupy virtual orbitals. In this scheme, the total wavefunction is written:

$$\Psi = a_0\Psi_{HF} + \sum_{i}^{occ.}\sum_{r}^{vir.} a_i^r\Psi_i^r + \sum_{i<j}^{occ.}\sum_{r<s}^{vir.} a_{ij}^{rs}\Psi_{ij}^{rs} + \sum_{i<j<k}^{occ.}\sum_{r<s<t}^{vir.} a_{ijk}^{rst}\Psi_{ijk}^{rst} + \cdots \quad (2.24)$$

where i and j are the occupied MOs in the reference Hartree-Fock wavefunction, r and s the virtual MOs and where the number of index determine the number of considered excitations (for example, two excitations for Ψ_{ij}^{rs}: $i \to r$ and $j \to s$).

The CI calculation can take advantage of the symmetry properties of the system since it is known that only states of same symmetry will couple. Then, the linear combination in (2.24) can be reduced to a basis of states with the same spatial and spin symmetry, also called CSFs (configuration state functions). It can be shown very simply that, according to the Slater-Condon rules, the Hartree-Fock determinant Ψ_{HF} only couples with doubly-excited states Ψ_{ij}^{rs}, and the singly-excited states Ψ_i^r with some singly-, doubly- and triply-excited states Ψ_{ijk}^{rst}. This analysis can be extended to further orders of excitation and demonstrates that for each order of excitation, there exist determinants which couple and contribute "directly" or "indirectly" to the total energy E.

Then, for a basis of N CSFs, the full-CI solution is given by the N roots of the CI secular equation:

$$\begin{vmatrix} H_{11}-E & H_{12} & \dots & H_{1j} & \dots & H_{1N} \\ H_{21} & H_{22}-E & \dots & H_{2j} & \dots & H_{2N} \\ \vdots & \vdots & \vdots & \vdots & \vdots & \vdots \\ H_{i1} & H_{i2} & \dots & H_{ij}-E & \dots & H_{iN} \\ \vdots & \vdots & \vdots & \vdots & \vdots & \vdots \\ H_{N1} & H_{N2} & \dots & H_{Nj} & \dots & H_{NN}-E \end{vmatrix} = 0 \quad (2.25)$$

where:

$$H_{ij} = \left\langle \Psi_i \middle| \hat{H} \middle| \Psi_j \right\rangle \quad (2.26)$$

$\hat{H}$ being the Hamiltonian of the system.

The configuration interaction method does not contain approximation and exact solutions for the total wavefunction can be found if all the configurations are taking into account. Such situation is referred as a full-CI calculation. Unfortunately, it is only possible for atoms or small molecules with about a dozen

or fewer electrons because the number of determinants required in expansion grows factorially with the number of electrons and orbitals. Often, the basis of electronic configurations has to be truncated to a certain order of excitations. Such approximation is justified by observing that the Hartree-Fock determinant generally contributes for 90% to the total wavefunction and that the rest (the electronic correlation) is mainly composed by single- and double-excitations. For this reason, truncated CI's methods are a good compromise for accurate calculations on "medium" systems (such as the molecules investigated in this work), although they present the main disadvantage to be not size consistent.

2.1.5 Complete active space self consistent field method

The multiconfigurational self-consistent field (MCSCF) method is a CI method in which accurate reference electronic states[1] are generated. Multiconfigurational because it consists in expanding the total wavefunction of the system on a linear combination of CSFs (as in the CI case). Self consistent field because the orbitals are also optimized for this combination of configurations. For this reason, the method can be considered in between the CI method (where the molecular orbitals are not varied but the expansion of the wave function) and the HartreeFock method (where there is only one determinant but the molecular orbitals are varied). The SCF procedure is much complex and harder to converge than for the Hartree-Fock method. Also it is not possible to associate eigenvalues to the MCSCF orbitals. However, it is still possible to define the occupation number η as a function of the occupation numbers of the CSFs η':

$$\eta_i = \sum_j^{N_c} \eta'_{i,j} a_j^2 \tag{2.27}$$

where N_c is the number of configuration state functions and a_j their associated coefficients from the linear combination of configurations.

Because of the orthogonality of the CSFs and for a normalized MCSCF, the coefficients satisfy:

$$\sum_j^{N_c} a_j^2 = 1 \tag{2.28}$$

By including the orbital optimization in the SCF, the MCSCF allows the MOs to be partially occupied and then to describe quasi-degeneration effects which is part of the non-dynamical correlation. However, the relaxation of the MOs does not permit to recover any dynamical correlation which depend mainly on the number of CSFs included. In a more general aspect, the computational cost and accuracy of a MCSCF calculation is determined by the

[1] The Slater determinants from which the excitations are performed are called reference states or reference determinants.

choice (number and type) of the electronic configurations used in the linear expansion. This basis of configurations constitutes the *active space* and has to be defined manually for each calculation. It is the main disadvantage of the method since the choice of the active space cannot always be deduced from simple chemical considerations and often requires practical experience. A very common option is the so-called *complete active space* (CAS) which divides the included orbitals in two categories: the inactive and the active ones. The formers are fixed to a specific occupation number (0 or 2) while the actives MOs are used to generate all possible CSFs (which corresponds to a full-CI). The number N_c of singlet CSFs is given by the combination of n electrons in m orbitals:

$$N_c = \frac{m!\,(m+1)!}{\left(\frac{n}{2}\right)!\left(\frac{n}{2}+1\right)!\left(m-\frac{n}{2}\right)!\left(m-\frac{n}{2}+1\right)!} \tag{2.29}$$

Practically, this number N_c is considerably reduced by considering the molecular symmetry (see Table 2.1). The choice of the CAS depends as much on the molecule as on the phenomenon to be studied. Then, each CASSCF calculation requires a precocious parametrization otherwise fallacious results can be obtained. There are no systematic methods to detect such errors, but it exists general rules that can be used in a first step to choose the CAS:

- Each occupied orbital is generally associated with a correspondent virtual orbital and consequently n and m should not be so different
- The highest occupied orbitals and the lowest virtual orbitals are preferentially chosen
- The natural orbitals analysis from *ab initio* methods helps to select the active orbitals according to their occupation numbers (between 0.2 and 1.98)

As an example, we will present in the following the CAS that has been chosen in this work to calculate the potential energy curves of isoelectronic N_2 and CO molecules. For the ground state and homo ionized states of both molecules, we made use of a common CAS that is illustrated in Figure 2.1. As can be seen, the occupied orbitals ($1\sigma_g^2$, $1\sigma_u^2$, $2\sigma_g^2$, $2\sigma_u^2$, $1\pi_u^4$, $3\sigma_g^2$ for N_2 and $1\sigma^2$, $2\sigma^2$, $3\sigma^2$, $4\sigma^2$, $1\pi^4$, $5\sigma^2$ for CO) are obviously taken into account. In both cases, the core orbitals are not included in the optimization procedure and are "frozen" since they are well separated energetically with respect to the other orbitals and are not expected to exert a strong influence on them. Based on calculations previously reported in the literature for N_2 [17, 294] and CO [18, 113] it appears sufficient for the purpose of this work to include the two first virtual orbitals ($3\sigma_u^2$, $1\pi_g^4$ for N_2 and $6\sigma^2$, $2\pi^4$ for CO). Table 2.1 presents the number of CSFs included in the calculation of the ground states of N_2, N_2^+, CO and CO^+. The notation (n, m) denotes the span of the considered active configuration space, i.e., the n electrons in the m active orbitals.

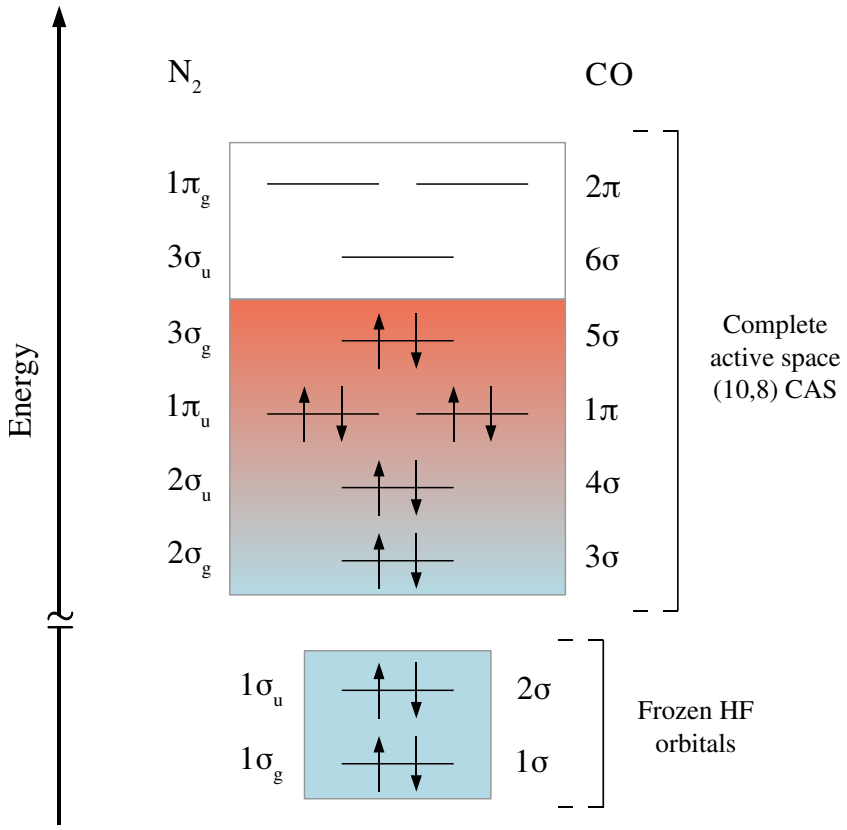

Figure 2.1: Complete active space for the present calculation of N_2 and CO

Molecule	Symmetry	CAS	N_c	CSFs
N_2	$D_{\infty h}$	(10,8)	1176	176
N_2^+	$D_{\infty h}$	(9,8)	2352	308
CO	$C_{\infty v}$	(10,8)	1176	328
CO^+	$C_{\infty v}$	(9,8)	2352	616

Table 2.1: Number of CSFs for each calculation.

The multireference configuration interaction (MRCI) is formally equivalent to the standard CI except that it makes use of a MCSCF wavefunction as reference instead of the Hartree-Fock one. Thus, a preliminary MCSCF calculation has to be performed. The CASSCF/MRCI method can then be summarized in three calculation steps:

$$\text{HF} \rightarrow \text{CASSCF} \rightarrow \text{MRCI}$$

The CASSCF step represents an additional computational effort but the

use of a better reference determinant can make the convergence faster in the MRCI. Despite of this, CASSCF/MRCI is rather expensive compared to other *ab initio* methods. Its use is limited to rather small systems and has been applied in this work only to N_2 and CO. A further limitation comes from the fact that most of the commercial programs that implement the method do not give the possibility to choose explicitly the electronic configurations to be included in the CSFs expansion. Due to this technical limitation and to the variational principle, the system will always decay in the lowest energy state of specified symmetry. Then, optimization of higher energy states of same symmetry is a nontrivial task. In the present study, only the ground states and the three first valence ionized states of N_2 and CO have been calculated. The potential energy curves for the core ionized states cannot be obtained via the CASSCF/MRCI method since a variational calculation leads inevitably to the decay of an electron from the HOMO to the singly occupied core orbital. For such electronic states, and in the case of more complex molecules (for which CASSCF/MRCI is unadapted), the potential energy curves have to be obtained using alternative methods. A way to proceed consists in fitting experimental vibrational energies in order to derive the semi-empirical analytical Morse potential (see Section 3.2). The limitation of this method is intrinsic to the Morse potential approximation since it considers only the first order anharmonic term. Also, the quality of the fitting depends mainly on the reliability of the experiment which is never easy to determine. Computational methods which are not based on the CI principle constitute also possible alternatives to the problem. It is the case of the density functional theory (DFT) which has been employed in the present work to obtain the PECs of C_2H_2 and CF_4 molecules but also to calculate the electronic dipole couplings of all of the systems. A detailed description of the DFT formalism is exposed in the following section.

2.2 Density functional theory

2.2.1 The time-independent density functional theory

The electronic density

As seen in the previous sections, *ab initio* methods use the wavefunction as a starting point to determine the properties of the system. Nevertheless, one can also wondering if it is possible to investigate the electronic structure by using a different quantity. Indeed, the computational effort of the calculation is mainly due to the fact the wavefunction depends on $3N$ variables (where N is the total number of particles of the system). The main goal of the density functional theory (DFT) is to replace the multielectronic wavefunction by a rather simple quantity: the electronic density. In this sense, the DFT formalism is a quantum reformulation of the N-body problem into a one-body problem. Because it depends only on 3 variables, the electronic density is easier to manipulate, mathematically and numerically speaking. The central idea of DFT is to consider that the electronic density can also be used to determine entirely the properties of the system. We consider a system of N electrons represented by the wavefunction $\Psi(\mathbf{r}_1, \mathbf{r}_2, \ldots, \mathbf{r}_N)$ where $\mathbf{r}_i$ corresponds to the spatial and spin coordinates of the electron i. This quantity is obtained by integrating the density function over the coordinates of all the other electrons:

$$\begin{aligned} \rho(\mathbf{r}_i) &= N \int \cdots \int \psi^*(\mathbf{r}_1, \mathbf{r}_2, \ldots, \mathbf{r}_i, \ldots, \mathbf{r}_N) \\ &\quad \times \psi(\mathbf{r}_1, \mathbf{r}_2, \ldots, \mathbf{r}_i, \ldots, \mathbf{r}_N) d\mathbf{r}_1, d\mathbf{r}_2, \ldots, d\mathbf{r}_{i-1}, d\mathbf{r}_{i+1}, \ldots, d\mathbf{r}_N \end{aligned} \tag{2.30}$$

According to the Born interpretation, this density divided by N determines the probability of finding an electron in a volume element independently of the other $N-1$ electrons. This function has notable properties[2]:

- $\rho(\mathbf{r}) \geq 0$
- $\lim_{\mathbf{r}\to\infty} \rho(\mathbf{r}) = 0$
- $\int \rho(\mathbf{r})\, d\mathbf{r} = N$

Since the Hamiltonian involves integral running over two particles, it is useful to define the second order density:

$$\begin{aligned} &\rho(\mathbf{r}_i, \mathbf{r}_j) \\ &= N(N-1) \int \cdots \int \psi^* \psi d\mathbf{r}_1, \ldots, d\mathbf{r}_{i-1}, d\mathbf{r}_{i+1}, \ldots, d\mathbf{r}_{j-1}, d\mathbf{r}_{j+1}, \ldots, d\mathbf{r}_N \end{aligned} \tag{2.31}$$

[2]Because electrons are indistinguishable: $\rho(\mathbf{r}_i) = \rho(\mathbf{r}_j) = \rho(\mathbf{r})$.

It can be demonstrated that the bielectronic density considers the Pauli exclusion principle (or *Fermi's correlation* in the DFT terminology):

$$\rho\left(\mathbf{r}_i, \mathbf{r}_i\right) = -\rho\left(\mathbf{r}_i, \mathbf{r}_i\right) = 0 \tag{2.32}$$

We have seen that post Hartree-Fock methods had to be developed in order to take into account the correlation energy that arises from the Coulomb interaction between electrons. This correlation as well as the Fermi's correlation avoids that the second order density factorizes as:

$$\rho\left(\mathbf{r}_i, \mathbf{r}_j\right) = \frac{N}{N-1}\rho\left(\mathbf{r}_i\right)\rho\left(\mathbf{r}_j\right) \tag{2.33}$$

This expression implies that electrons i and j simply do not interact one with the other. Such situation does not correspond is not physical and so that we define a function $f\left(\mathbf{r}_i, \mathbf{r}_j\right)$ that correlates both electrons:

$$\rho\left(\mathbf{r}_i, \mathbf{r}_j\right) = \rho\left(\mathbf{r}_i\right)\rho\left(\mathbf{r}_j\right)\left[1 + f\left(\mathbf{r}_i, \mathbf{r}_j\right)\right] \tag{2.34}$$

Considering the conditional probability of finding the electron j when the position of electron i is known:

$$P\left(\mathbf{r}_j|\mathbf{r}_i\right) = \frac{\rho\left(\mathbf{r}_i, \mathbf{r}_j\right)}{\rho\left(\mathbf{r}_i\right)} \tag{2.35}$$

it is possible to describe how an electron affects the behavior of another one. Then, the function h_{XC} that account for the correlation between two electrons can be evaluated by subtracting the monoelectronic density of the electron j to its conditional probability:

$$h_{XC}\left(\mathbf{r}_i, \mathbf{r}_j\right) = P\left(\mathbf{r}_j|\mathbf{r}_i\right) - \rho\left(\mathbf{r}_j\right) = \rho\left(\mathbf{r}_j\right) f\left(\mathbf{r}_i, \mathbf{r}_j\right) \tag{2.36}$$

Because the conditional probability ingrate to $N-1$ and $\rho\left(\mathbf{r}_j\right)$ to N, the integral of the correlation function over the coordinates of the electron j is:

$$\int h_{XC}\left(\mathbf{r}_i, \mathbf{r}_j\right) d\mathbf{r}_j = -1 \tag{2.37}$$

This result describes the effect of the interelectronic repulsions. In particular, the correlation function prevents an electron to be in the region where another electron "stands". This property is known as the exchange correlation hole.

The exchange correlation function can be split in two terms: the exchange function h_X which corresponds to the Fermi's hole and runs over the spins of same sign and the correlation function h_C which corresponds to the Coulomb hole and originates from the Coulomb interaction of electron:

$$h_{XC}\left(\mathbf{r}_i, \mathbf{r}_j\right) = h_X^{s_i = s_j}\left(\mathbf{r}_i, \mathbf{r}_j\right) + h_C^{s_i \neq s_j}\left(\mathbf{r}_i, \mathbf{r}_j\right) \tag{2.38}$$

The objective of DFT is to use the electronic density as the central variable from which the properties of the system will be extracted. The electronic density should then contain the essential information needed to build the Hamiltonian operator $\hat{H}$. It can be shown that the number of electrons, the position of each nucleus and their respective charge are correctly described by the electronic density. It is then reasonable to think that the electronic density contain sufficient information to define the Hamiltonian of the system and that the energy can be expressed as a function of it.

The Hohenberg-Kohn theorem

The applicability of the density to the treatment of the Schrödinger equation has been confirmed by Pierre C. Hohenberg and Walter Kohn in 1964 [163] through the formulation of two theorems:

- The ground-state energy from the Schrödinger equation is a unique functional of the electron density
- The electron density that minimizes the energy of the overall functional is the true electron density corresponding to the full solution of the Schrödinger equation.

The consequences of the Kohn and Hohenberg's statements are major: the density functional theory is formally exact and could give, in principle, the exact energy of the ground state through the variational method. By extension, any observables can also be calculated exactly from the density of the ground state, i.e. any observable is a density functional of the ground state.

The exact energy E_0 of the ground state is then a functional of the ground state density ρ_0:

$$E_0[\rho_0] = T[\rho_0] + V_{eN}[\rho_0] + V_{ee}[\rho_0] \tag{2.39}$$

In principle, from a system to another, only the term that describes the interaction between electrons and nuclei is changing.

Rewriting the equation of the energy for any density ρ and splitting the contributions of the dependent and independent terms, we obtain:

$$E[\rho] = F_{HK}[\rho] + V_{eN}[\rho] \tag{2.40}$$

where F_{HK} corresponds to the (universal) Hohenberg-Kohn functional defined as:

$$F_{HK}[\rho] = T[\rho] + V_{ee}[\rho] \tag{2.41}$$

where T is the kinetic energy:

$$T\left[\rho\left(\mathbf{r}\right)\right] = \left\langle \psi \left| -\frac{1}{2}\nabla^2 \right| \psi \right\rangle \tag{2.42}$$

V_{eN} is the attraction potential created by the nuclei:

$$V_{eN}\left[\rho\left(\mathbf{r}\right)\right] = \left\langle \psi \left| -\sum_{\alpha=1}^{M} \frac{Z_\alpha}{\left|\mathbf{r}-\mathbf{R}_\alpha\right|} \right| \psi \right\rangle = -\sum_{\alpha=1}^{M} \int \frac{Z_\alpha}{\left|\mathbf{r}-\mathbf{R}_\alpha\right|} \rho\left(\mathbf{r}_i\right) d\mathbf{r}_i \tag{2.43}$$

and where the bielectronic term V_{ee} is given by:

$$\begin{aligned} V_{ee}\left[\rho\left(\mathbf{r}\right)\right] &= \left\langle \psi \left| \sum_{i}^{N} \sum_{j>i}^{N} \frac{1}{\left|\mathbf{r}_i-\mathbf{r}_j\right|} \right| \psi \right\rangle = \frac{1}{2} \iint \frac{\rho\left(\mathbf{r}_i,\mathbf{r}_j\right)}{\left|\mathbf{r}_i-\mathbf{r}_j\right|} d\mathbf{r}_i d\mathbf{r}_j \\ &= \underbrace{\frac{1}{2} \iint \frac{\rho\left(\mathbf{r}_i\right)\rho\left(\mathbf{r}_j\right)}{\left|\mathbf{r}_i-\mathbf{r}_j\right|} d\mathbf{r}_i d\mathbf{r}_j}_{J\left[\rho\left(\mathbf{r}\right)\right]} + \underbrace{\frac{1}{2} \iint \frac{\rho\left(\mathbf{r}_i\right) h_{XC}\left(\mathbf{r}_i,\mathbf{r}_j\right)}{\left|\mathbf{r}_i-\mathbf{r}_j\right|} d\mathbf{r}_i d\mathbf{r}_j}_{E_{xc}\left[\rho\left(\mathbf{r}\right)\right]} \end{aligned} \tag{2.44}$$

The term denoted E_{xc} is called exchange-correlation energy and is unknown. It is considered as the non-classical contribution to th electron-electron interaction. As it can be seen, the second Hohenberg-Kohn theorem gives the method to obtain the energy of the system. More precisely, it shows that the variational principle applied with a self-consistent field acting on the density of the system should lead in principle the exact energy of the ground state (although it is known than DFT can lead to lower energy values). According to this theorem, DFT is in principle restricted to the calculation of properties associated with the ground state.

The Kohn-Sham approach

Although the variational method can be uses in principle to calculate these properties, its implementation in the DFT formalism is however not straightforward. In fact, many models have been developed, such as the Thomas-Fermi model and its derivatives, but they generally make drastic approximations which affect the accuracy of the calculations. In 1965 [197], Walter Kohn and Lu Jeu Sham proposed a simple and accurate approach to the problem: they suggested to introduce monoelectronic wavefunctions to the formalism. Therefore, the kinetic-energy term can be easily computed:

$$T_s\left[\rho\right] = \sum_{i}^{N} \left\langle \varphi_i \left| -\frac{1}{2}\nabla^2 \right| \varphi_i \right\rangle \tag{2.45}$$

where:

$$\rho\left(\mathbf{r}\right) = \sum_{i}^{N} \varphi_i^*\left(\mathbf{r}\right)\varphi_i\left(\mathbf{r}\right) \tag{2.46}$$

As in the Hartree-Fock approximation, the total wavefunction is expressed as a Slater determinant of N occupied orbitals $\varphi_i\left(\mathbf{r}\right)$. However, it is important

to underline that these monoelectronic wavefunctions do not correspond rigorously to the molecular orbitals and are consequently denominated Kohn-Sham orbitals. This new representation provides a determinantal wavefunction of N non-interacting electrons which evolves in an effective potential created by the rest of the electrons (as in the Hartree-Fock model) and described by the effective single-particle potential v_s. Then the Hamiltonian is written:

$$\hat{H}_s(\mathbf{r}) = \hat{T}_s + \sum_i^N v_s[\rho(\mathbf{r})] \tag{2.47}$$

where it can be seen that bielectronic terms are not included. From Equations (2.45) and (2.47), it is possible to define the one-electron Hamiltonian and then to reduce the problem to a set of N independent equations:

$$\left(-\frac{1}{2}\nabla^2 + v_s[\rho(\mathbf{r})]\right)\varphi_i(\mathbf{r}) = \epsilon_i\varphi_i(\mathbf{r}) \tag{2.48}$$

Such equation leads to an exact solution which is uniquely defined for any density but describes an independent-particle system. Returning to Equation (2.41), the Hohenberg-Kohn functional can be rewritten as:

$$F_{HK}[\rho] = T_s[\rho] + J[\rho] + E_{xc}[\rho] \tag{2.49}$$

where the exchange-correlation energy is given by:

$$E_{xc}[\rho] = T[\rho] - T_s[\rho] + V_{ee}[\rho] - J[\rho] \tag{2.50}$$

where $J[\rho]$ is the electrostatic Hartree potential and $E_{xc}[\rho]$ the exchange-correlation energy due to the interaction between the electronic cloud and the exchange correlation hole. This term accounts for the difference between the two kinetic energies and for the non-classical part of the bielectronic term. It includes all the quantum contributions to the electronic correlation but also the correction to the self-interaction (induced by $J[\rho]$) for each electron. The Euler equation then becomes:

$$\mu = v_{KS}[\rho(\mathbf{r})] + \frac{\delta T_s[\rho(\mathbf{r})]}{\delta\rho(\mathbf{r})} \tag{2.51}$$

where:

$$\begin{aligned} v_{KS}[\rho(\mathbf{r})] &= v_{eN}[\rho(\mathbf{r})] + \frac{\delta J[\rho(\mathbf{r})]}{\delta\rho(\mathbf{r})} + \frac{\delta E_{xc}[\rho(\mathbf{r})]}{\delta\rho(\mathbf{r})} \\ &= v_{eN}[\rho(\mathbf{r})] + v_H[\rho(\mathbf{r})] + v_{xc}[\rho(\mathbf{r})] \end{aligned} \tag{2.52}$$

and where the Hartree potential v_H accounts for the classical electrostatic interaction between electrons:

$$v_H[\rho(\mathbf{r})] = \int \frac{\rho(\mathbf{r}')}{|\mathbf{r}-\mathbf{r}'|} d\mathbf{r}' \tag{2.53}$$

The original idea of Kohn and Sham is in fact to consider the system as a system of non-interacting electrons moving in the external potential $v_s = v_{KS}$ defined in Equation (2.48). Then, the monoelectronic wavefunctions should satisfy the equation:

$$\left(-\frac{1}{2}\nabla^2 + v_{KS}[\rho(\mathbf{r})]\right)\varphi_i(\mathbf{r}) = \epsilon_i\varphi_i(\mathbf{r}) \tag{2.54}$$

This set of equations are known as the Kohn-Sham equations. As in the Hartree-Fock model, they can be solved self-consistently from a set of Kohn-Sham orbitals which are improved iteratively (see Figure 2.2).

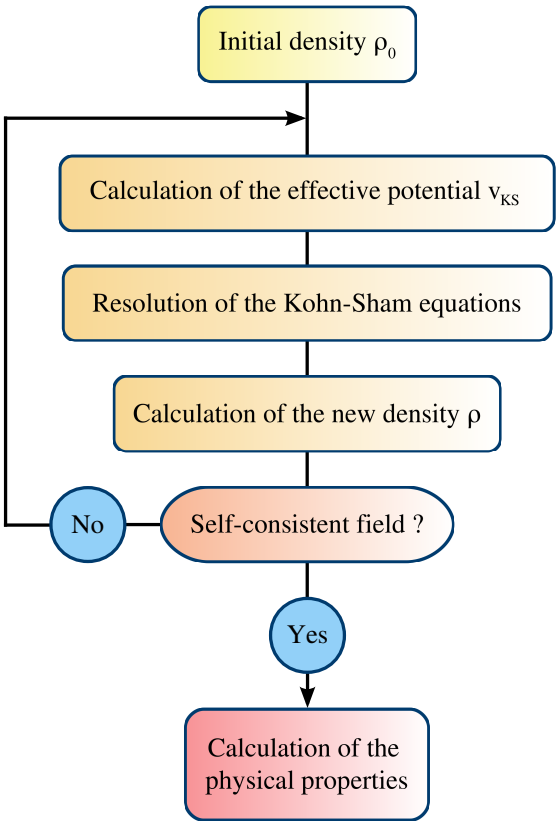

Figure 2.2: Self consistent field procedure applied to DFT.

It is important to stress that the Kohn-Sham equations are formally exact since they do not include any approximations. In principle, if the exchange-correlation functional were known, it would be possible to calculate the exact energy of the ground state. However, in practice, $v_{xc}[\rho(\mathbf{r})]$ is too complicated and has to be approximated via semi-empirical considerations. There exist a multitude of exchange-correlation functionals which have been developed from

the beginning of the DFT. It each one has been designed with the objective to improve the description of particular properties in specific systems.

2.2.2 Exchange-correlation functionals

So far, we have described an exact theory which treats rigorously the kinetic energy term and gathers the complexity of the many-particle problem (the part of the kinetic energy due to the interacting system, the non-classical electron-electron interaction and the self-interaction correction) into the exchange-correlation functional. However, implementation of the Kohn-Sham scheme requires to give a formulation to this functional. It is achieved by the development of semi-empirical algorithms based on different approximations. This particular point constitutes a peculiarity of DFT, as it rises the question of its affiliation to the *ab initio* methods category. In fact, the advantage and the disadvantage of DFT compared to standard *ab initio* methods is that it is always possible to find a better functional for a proper system, but there's no systematic way towards improve them. There exist different classes of functionals, depending on the nature of the approximation that is made. The first two important classes are the so-called local density approximation (LDA) and the generalized gradient approximation (GGA).

Local density approximation

The starting point of any approximations to the exchange-correlation functional is to consider an uniform electron gas of density ρ. This assumption implies that the electrons are moving on a positive background charge distribution which is constant everywhere and that the ensemble composed of infinite particles in an infinite volume is electrically neutral. Logically, such approximation is adapted for the description of simple metals but is expected to be inaccurate to treat atoms or molecules. For this reason, and until the advent of the generalized gradient approximation, DFT was mostly employed by solid-state physicists rather than chemists.

Defining $\varepsilon_{xc}[\rho(\mathbf{r})]$ as the exchange-correlation energy per particle, the exchange-correlation energy in the local density approximation is written:

$$E_{xc}^{LDA}[\rho(\mathbf{r})] = \int \rho(\mathbf{r})\,\varepsilon_{xc}[\rho(\mathbf{r})]d\mathbf{r} \tag{2.55}$$

and:

$$v_{xc}^{LDA}[\rho(\mathbf{r})] = \frac{\delta E_{xc}^{LDA}[\rho(\mathbf{r})]}{\delta\rho(\mathbf{r})} = \varepsilon_{xc}[\rho(\mathbf{r})] + \rho(\mathbf{r})\frac{\varepsilon_{xc}[\rho(\mathbf{r})]}{\delta\rho(\mathbf{r})} \tag{2.56}$$

Then, Kohn-Sham equations read:

$$\left(-\frac{1}{2}\nabla^2 + v_{eN}[\rho(\mathbf{r})] + v_H[\rho(\mathbf{r})] + v_{xc}^{LDA}[\rho(\mathbf{r})]\right)\varphi_i(\mathbf{r}) = \epsilon_i\varphi_i(\mathbf{r}) \tag{2.57}$$

The one-particle exchange-correlation function $\varepsilon_{xc}[\rho(\mathbf{r})]$ can be split in its two contributions:

$$\varepsilon_{xc}[\rho(\mathbf{r})] = \varepsilon_x[\rho(\mathbf{r})] + \varepsilon_c[\rho(\mathbf{r})] \tag{2.58}$$

The first term in Equation (2.58) was already derived in the late 1920's by Bloch and Dirac (see [277]):

$$\varepsilon_x[\rho(\mathbf{r})] = C_x \int \rho^{4/3}(\mathbf{r})\, d\mathbf{r} \tag{2.59}$$

with:

$$C_x = -\frac{3}{4}\left(\frac{3\rho(\mathbf{r})}{\pi}\right)^{1/3} \tag{2.60}$$

Improvement to the exchange energy is obtained by introducing a semi-empirical parameter α into the pre-factor C_x:

$$\varepsilon_{x\alpha}[\rho(\mathbf{r})] = -\frac{9}{8}\left(\frac{3}{\pi}\right)^{1/3} \alpha \int \rho^{4/3}(\mathbf{r})\, d\mathbf{r} \tag{2.61}$$

This term is known as the X_α exchange energy.

Unfortunately, no such analytical expression exist for the correlation functional. In order to give an approximated expression of $\varepsilon_c(\rho)$, various authors have developed functionals that fit the results provided by Monte-Carlo simulations of homogeneous electron gas: the Vosko-Wilk-Nusair (VWN) [417] (the most famous), the Perdew-Zunger (PZ81) [287], the Cole-Perdew (CP) [67], the Perdew-Wang (PW91) [286, 285] (the most accurate), etc.

In the local density approximation, the value of the density of the inhomogeneous system is used to calculate the exchange and correlation energy corresponding to a homogeneous system and then introduced in Equation (2.55). It is said "local" because the energies are calculated assuming that the density in the neighboring of each positions varies sufficiently smoothly to be considered constant (i.e. locally uniform). Although the local density approximation seems to be drastic, experience shows that it has a wide range of applicability and its predictions are generally comparable or even better than the Hartree-Fock ones. In the case of molecules, it has been observed that properties such as equilibrium geometries or harmonic frequencies are in good agreement with high level *ab initio* calculations [195, 386]. As we will see concretely with the calculations performed in this study, LDA is however quite inaccurate when used to obtain energetic informations (e.g., [365]). LDA is globally a good approximation since it satisfies the most essential conditions which are:

- the sum-rules
- the cusp condition
- the negativity of the exchange hole

Generalized gradient approximation

The generalized gradient approximation (GGA) is an improved version of the local density approximation. The idea is to supplement the information given by the density at each position $\rho(\mathbf{r})$ by the information given by the gradient of this density $\nabla\rho(\mathbf{r})$. Such transformation is made to account for the non-homogeneity of the true electron density. Mathematically, it is equivalent to develop the exchange-correlation functional in a Taylor series and to retain up to the first order term:

$$\begin{aligned} E_{xc}^{GEA}[\rho_\alpha(\mathbf{r}),\rho_\beta(\mathbf{r})] &= \int \rho(\mathbf{r})\,\varepsilon_{xc}[\rho_\alpha(\mathbf{r}),\rho_\beta(\mathbf{r})]d\mathbf{r} \\ &\quad + \sum_{\sigma,\sigma'}\int C_{xc}^{\sigma,\sigma'}[\rho_\alpha(\mathbf{r}),\rho_\beta(\mathbf{r})]\frac{\nabla\rho_\sigma(\mathbf{r})}{\rho_\sigma^{2/3}(\mathbf{r})}\frac{\nabla\rho_{\sigma'}(\mathbf{r})}{\rho_{\sigma'}^{2/3}(\mathbf{r})}d\mathbf{r}+\cdots \end{aligned} \tag{2.62}$$

where GEA stands for *gradient expansion approximation* and where σ and σ' are running on the spin state. Contrary to the expectations, adding this term in the Taylor series expansion of the exchange-correlation functional does not lead to any improvements, and surprisingly gives in some cases even worse results than LDA. Such failure is mainly due to the fact that the new exchange-correlation functional does not satisfy so well the most essential conditions for the exchange-correlation hole explained before. A way to overcome this problem is to force the GEA holes to respect these conditions everywhere and define exchange-correlation functionals (now called *generalized gradient approximation*) which are not completely derived from first principles but developed semi-empirically. As for the LDA, the GGA exchange-correlation functional is usually split in its two contributions:

$$E_{xc}^{GGA}[\rho(\mathbf{r})] = E_x^{GGA}[\rho(\mathbf{r})] + E_c^{GGA}[\rho(\mathbf{r})] \tag{2.63}$$

The exchange part can be rewritten as a function of the LDA one:

$$E_x^{GGA}[\rho(\mathbf{r})] = E_x^{LDA}[\rho(\mathbf{r})] - \sum_\sigma \int F(s_\sigma)\,\rho_\sigma^{4/3}(\mathbf{r})\,d\mathbf{r} \tag{2.64}$$

where F is an unknown function of the *reduced density gradient* of spin σ:

$$s_\sigma(\mathbf{r}) = \frac{|\nabla\rho_\sigma(\mathbf{r})|}{\rho_\sigma^{4/3}(\mathbf{r})} \tag{2.65}$$

$s_\sigma(\mathbf{r})$ contains the dependence on $\nabla\rho_\sigma(\mathbf{r})$ and controls the local inhomogeneity of the functional. Thus, more homogeneity will be assume for large gradients or when density is small (as for the Coulomb tail). Two classes of analytical expression have been proposed for the function F in the late 1980's.

One depends on an empirical parameter β and has been formulated by Becke in 1988 [24]:

$$F^{B88}(s_\sigma) = \frac{\beta s_\sigma^2}{1 + 6\beta s_\sigma \sinh^{-1} s_\sigma} \tag{2.66}$$

Many recent functionals such as FT97, PW91, CAM(A) and CAM(B) are based on this function. The other class corresponds to rational functions such as the one developed by Perdew in 1986 [282] and are free of empirical parameter:

$$F^{B86}(s_\sigma) = \left[1 + 1.296\left(\frac{s_\sigma}{(24\pi^2)^{1/3}}\right)^2 + 14\left(\frac{s_\sigma}{(24\pi^2)^{1/3}}\right)^4 + 0.2\left(\frac{s_\sigma}{(24\pi^2)^{1/3}}\right)^6\right]^{1/15} \tag{2.67}$$

Many semi-empirical functionals have been developed for the GGA correlation part and are generally more complex. It would be tedious trying to give here the expression of each of these functionals. For more information, we let the reader refer to the Table 2.2 which presents a summary of the common names and the proper references associated with the most popular GGA functionals.

E_x^{GGA}	B [24] PW91 [284] mPW [5] PBE [283] G96 [6] O [153]	
E_c^{GGA}	B95 [27] PW91 [285] PBE [283] P86 [282] LYP[a] [216]	

Table 2.2: The most popular GGA functionals.

[a]Contrary to all the other functionals, LYP is not based on the uniform electron gas but on the correlation energy of the hellium atom.

All the mentioned exchange functionals can be combined with any of the correlation functionals. Also, the difference in the results provided by the use of different combinations is generally qualitatively small and in practice, functionals of the same category are used together or correlation functionals are combined with the Becke exchange one (e.g., BLYP or BP86). In any case, the contribution of the exchange functional is almost always larger than the

correlation one. For this reason, a particular attention has to be devoted to the proper description of the E_x term.

Hybrid functionals

The main idea of this class of functionals is to use the exact Hartree-Fock exchange functional and mix it with different correlation functionals:

$$E_{xc} = E_x^{HF} + E_c \tag{2.68}$$

It has been observed and discussed in 1993 by Axel Becke [25, 26] that the use of several weighted exchange and correlation functionals together with the exact Hartree-Fock exchange one leads to enhanced results. By using a gradient corrected BPW91 functional and three semi-empirical parameters a, b and c, he succeed in reproduce atomization, ionization energies and proton affinities:

$$E_{xc}^{B3} = E_{xc}^{LSD} + a\left(E_{xc}^{HF} - E_x^{LSD}\right) + bE_x^B + cE_c^{PW91} \tag{2.69}$$

Along the years, many hybrid functionals have been developed and as before, it would be a very tedious task to enumerate all of them. However, it is important to mention the most popular one: B3LYP. This functional makes use of the gradient-corrected BLYP functional:

$$E_{xc}^{B3LYP} = (1-a)\,E_x^{LSD} + aE_{xc}^{HF} + bE_x^{B88} + cE_c^{LYP} + (1-c)\,E_c^{LSD} \tag{2.70}$$

The most recent hybrid functionals generally make use of less semi-empirical parameters and give very similar results to B3LYP.

Self interaction correction

So far, the use of approximated exchange-correlation functionals did not take into account an effect that introduces a small error: the electronic self interaction. This effect is clearly identified when looking to the Kohn-Sham energy expression for a one electron system:

$$E[\rho] = T_s[\rho] + J[\rho] + E_{xc}[\rho] + E_{eN}[\rho] \tag{2.71}$$

where the electrostatic repulsion term is still:

$$J[\rho] = \frac{1}{2}\iint \frac{\rho\left(\mathbf{r}_i\right)\rho\left(\mathbf{r}_j\right)}{|\mathbf{r}_i - \mathbf{r}_j|} d\mathbf{r}_i d\mathbf{r}_j \tag{2.72}$$

For a one-electron system, the term $J[\rho]$ contains an unrealistic interaction of the density with itself. The error introduced by the self-interaction can be evaluated for the above-mentioned functionals by calculating the sum $J[\rho] + E_{xc}[\rho]$. Ideally, a self-interaction free functional should satisfy $J[\rho] = -E_{xc}[\rho]$,

i.e., Equation (2.71) becomes the exact equation of an electron interacting with a nucleus. But in practice, strong discrepancies are observed (see Table 2.3) and are responsible for inaccurate energy values (as well as violation of the variational principle).

Functional	$J[\rho] + E_{xc}[\rho]$ (a.u.)	$E[\rho]$ (a.u.)
HF	0.0	-0.49999
SVWN	0.00277	-0.49639
BLYP	0.00140	-0.49789
B3LYP	-0.00281	-0.50243
BP86	-0.00074	-0.50030
BPW91	-0.00460	-0.50422
Exact	0.0	-0.5

Table 2.3: Energies obtained for the hydrogen atom by using various exchange-correlation functionals.

In 1981, Perdew and Zunger suggested a new scheme in which they derived a new set of equations on the basis of the Kohn-Sham equations but introducing a self-interaction correction (SIC). The SIC-KS equations are more complex than the standard KS ones since they involve an orbital dependent potential. For this reason, the scheme is hardly implemented in the commercial programs. This new scheme leads to significant improvement in the energetic analysis of atoms but can also be responsible for a deterioration of the results when applied to molecules. In particular, it has been pointed out that the SIC-KS scheme used to fail in the description of dissociation curve (such as H_2^+) due to a bad description of the delocalized exchange hole when $R \to \infty$.

Asymptotic behavior

For the general purpose, a good description of the Kohn-Sham orbitals around the nuclei is sufficient to provide accurate results. But the study of some particular properties (such as the electronic affinity) or systems (such as the interaction of a slow photoelectron with the residual ion) requires a better description of the potential at large distances. The correlation term in this case is not problematic since its effect is quite short-ranged. At large distances, the exchange potential should tend as:

$$\lim_{r\to\infty} V(r) = -\frac{1}{r} \tag{2.73}$$

All the above-mentioned exchange functionals rather decrease exponentially and then underestimate the attractive strength of the potential at large

distances. Although standard functionals give accurate energy results, they badly reproduce the asymptotic region.

Part of the calculations presented in this work makes use of the LB94 functional. It is a less common functional developed in 1994 by Van Leeuwen and Baerends [413] in order to describe correctly the asymptotic behavior of the exchange-correlation potential for atoms and molecules. Showing that most of the gradient-corrected potentials fail to reproduce accurately the atomic potential decay at large distances and the density cusp at the nucleus, Van Leeuwen and Baerends used the asymptotic limit of the exact Kohn-Sham potential to derive a new function F. Comparison of energies and values of the model potential at different distances for a series of atoms, showed that LB94 is much more accurate than LDA functional, specially for the energies and at large distances. However, it has been observed that the model presents some deficiencies, particularly in the atomic intershell region in which LDA excels. But for the purpose of this work whose ambition is to describe continuum states, LB94 seems to be a reasonable choice.

Usage

As seen in the previous sections, many functionals have been developed in the last few decades. Because they lie on semi-empirical considerations and have been designed to describe different theoretical aspects, these functionals have not been used for the same purposes, in the same domains and have not been employed with the same frequency among the years. Some of them became obsolete while others revealed to work well in different areas and knew a frank success. It is the case of the B3LYP hybrid functional which is nowadays broadly used in computational chemistry or the PBE for materials (see Figure 2.3). The success of these two functionals is such that nowadays the usage of the other functionals is reduced to 8% of the total.

Many studies have been carried out in order to determine the pros and cons of DFT method. Also, an abundant literature can be found where systematical comparisons with experimental data and other *ab initio* results is made. In spectroscopy, [350] shows for example that B3LYP calculations of anharmonicity and spectroscopic constants for some diatomic molecules (among them, CO and N_2) are reliables and comparable to the more expensive CCSD and CCSD(T) methods. More particularly, Decleva *et al.* have shown that LDA and LB94 functionals are well adapted for the description of continuum states [363, 362].

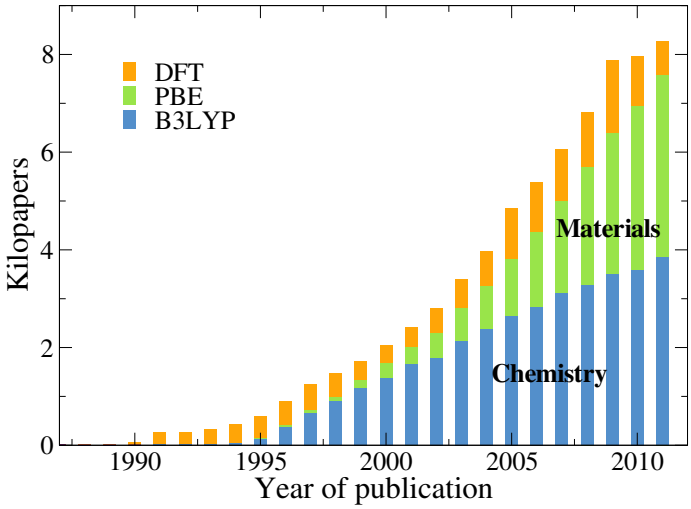

Figure 2.3: Number of papers published and containing the occurence DFT, B3LYP and PBE in the last 25 years.

2.2.3 Time-dependent density functional theory

Time-dependent density functional theory (TDDFT) can be considered as an extension of the time-independent density functional theory (TIDFT - also called DFT in the previous and following sections). It allows to go beyond the ground-state description by treating excitations and more general time-dependent phenomena. The scheme of the extended theory is general and is formulated according to two regimes:

- for a weak time-dependent potential (weak field), a linear-response of the system can be assumed and time-dependent equations can be managed at the first order of perturbation
- for a strong time-dependent potential (strong field), a full solution of the Kohn-Sham equations has to be found

Taking into account the time evolution of the system, we settle the time-dependent Schrödinger equation (TDSE):

$$i\frac{\partial}{\partial t}\Psi\left(\mathbf{r},t\right)=\hat{H}\left(\mathbf{r},t\right)\Psi\left(\mathbf{r},t\right) \tag{2.74}$$

in which the Hamiltonian reads:

$$\hat{H}\left(\mathbf{r},t\right)=-\frac{1}{2}\sum_{i=1}^{N}\nabla_i^2-\sum_{i}^{N}\sum_{\alpha=1}^{M}\frac{Z_\alpha}{|\mathbf{r}-\mathbf{R}_\alpha|}+\frac{1}{2}\sum_{i,j}^{N}\frac{1}{|\mathbf{r}_i-\mathbf{r}_j|}+v_{ext}\left(\mathbf{r},t\right) \tag{2.75}$$

The first three terms (the kinetic energy, the Coulomb attraction between the electrons and the nuclei and the Coulomb repulsion between the electrons) are time-independent. Only the last term $v_{ext}(\mathbf{r}, t)$, which corresponds to the laser field, carries the dependence in t.

In the dipole approximation, for a flux of photons dense enough to avoid quantization but with an intensity sufficiently weak to avoid relativistic effects, the laser field can be treated classically and reads in the length gauge:

$$v_{ext}(\mathbf{r}, t) = Ef(t)\sin(\omega t)\sum_{i=1}^{N}\mathbf{r}_i \cdot \alpha \tag{2.76}$$

where α stands for the polarization, ω the frequency, E the amplitude of the electric field and $f(t)$ the envelope of the laser pulse. So far, and in the conditions of an appropriate laser field, the previous equations are exact and (2.74) has been numerically solved for simple molecules such as H_2 and H_2^+. However, practical complications arise when the Schrödinger equation is applied to more complex molecular systems, as the ones of our interest. By reducing the many-body TDSE to a set of one-body Kohn-Sham equations, TDDFT propose a very convenient and elegant way to tackle this difficulty.

However, the Kohn-Sham equations as they have been derived in the time-independent regime cannot be applied directly and carelessly. In particular, the Hohenberg-Kohn theorem requires to be extended to the time-dependent regime. As seen previously, this theorem implies that the variational principle applied to the functional of the density is a valid technique for the determination of the ground-state energy. Unfortunately, this principle does not stand for time-dependent systems since energy is no more a conserved quantity. A time-dependent equivalent quantity can be found in the quantum mechanical action defined as:

$$\mathcal{A}[\psi] = \int_{t_1}^{t_2} dt \left\langle \psi(t) \left| i\frac{\partial}{\partial t} - \hat{H}(t) \right| \psi(t) \right\rangle \tag{2.77}$$

In 1984, Erich Runge and Eberhard K. U. Gross expounded a theorem which states that all observables can be derived from the density functional (as for the Hohenberg-Kohn theorem) and demonstrates[3] that the quantum mechanical action can be used in order to find the solution of Equation (2.74). The new principle does not lie in the finding of a minimum but in the searching of a stationary function ψ which satisfies $\mathcal{A}[\psi] = 0$. This technical difference and the fact that the Runge-Gross theorem can only hold for a fixed initial state makes the quantum mechanical action less useful than its time-independent counterpart.

[3]Proofs of this theorem can be found in [313].

The Runge-Gross theorem gives the procedure to obtain the observables, but, as before, it is more convenient to simplify the problem by applying the Kohn-Sham scheme to the TDSE:

$$i\hbar\frac{\partial}{\partial t}\varphi_i(\mathbf{r},t) = \left(-\frac{1}{2}\nabla^2 + v_{KS}[\rho(\mathbf{r},t)]\right)\varphi_i(\mathbf{r},t) \tag{2.78}$$

where the density of the interacting system is given by:

$$\rho(\mathbf{r},t) = \sum_i^{N_{occ}} |\varphi_i(\mathbf{r},t)|^2 \tag{2.79}$$

The Kohn-Sham potential can be decomposed as follows:

$$v_{KS}[\rho(\mathbf{r},t)] = v_{eN}[\rho(\mathbf{r},t)] + v_H[\rho(\mathbf{r},t)] + v_{xc}[\rho(\mathbf{r},t)] \tag{2.80}$$

In the time-independent regime, the exchange-correlation potential is normally related to the functional derivative of the exchange-correlation energy. Nevertheless, in order to respect the causality principle, $v_{xc}[\rho(\mathbf{r},t)]$ has to be written as a function of the exchange-correlation action functional $\mathcal{A}_{xc}$:

$$v_{xc}[\rho(\mathbf{r},t)] = \left.\frac{\delta\mathcal{A}_{xc}}{\delta\rho(\mathbf{r},\tau)}\right|_{\rho(\mathbf{r},t)} \tag{2.81}$$

where τ stands for the Keldysh pseudo-time.

The time-dependent Kohn-Sham (TDKS) equations are formally exact and the only approximations are introduced by the exchange-correlation functionals which are defined semi-empirically. Since $v_{xc}[\rho(\mathbf{r},t)]$ depends on time and on the exchange-correlation action functionals, the static approximated exchange-correlation functionals are useless and new developments have to be made in that direction. Due to the complexity and the youth of the TDDFT compared to TIDFT, there exist only few available functionals, such as the adiabatic local density approximation (ALDA) which is equivalent to the former LDA. Newer and more accurate functionals have been developed but the most commonly used is unquestionably the ALDA one. The success of this approximation probably lies in its simplicity, but above all on the fact that it can make use of the existent TIDFT functionals. Assuming that the system evolves smoothly in time (which is generally the case for weak fields), then the local approximation can be applied to the time coordinate and the exchange-correlation potential can be approximated as:

$$v_{xc}^{ALDA}[\rho(\mathbf{r},t)] = \left.v_{xc}^{LDA}(\rho)\right|_{\rho=\rho(\mathbf{r},t)} \tag{2.82}$$

Once defined the exchange-correlation functional, the TDKS equations (2.78) have to be solved by finite time steps, starting from the initial state $\varphi_i(\mathbf{r},t_0)$.

The state at t_0 is generally computed with the time-independent Kohn-Sham equations and propagated using numerical methods, such as the modified Crank-Nicholson scheme. Due to the self-consistent approach and depending on the time propagation step and delay, the full resolution of the TDKS equations can be very time-demanding. For such cases and assuming the proper conditions, it is convenient to work in the regime of the linear response theory.

The linear response theory

We assume that initially, the system is in its ground state with the static density $\rho^{(0)}(\mathbf{r})$. The unperturbed potential is composed only by the nuclear potential. At a certain time, a small time-dependent perturbation $v^{(1)}(\mathbf{r},t)$ is applied to the system and induces a change in the density. The density of the system now depends on time and can be expanded in a perturbative series. If the field is sufficiently weak, we can retain the terms of the series up to the first order (the linear term) and the density of the time-dependent system reads:

$$\rho(\mathbf{r},t) = \rho^{(0)}(\mathbf{r}) + \rho^{(1)}(\mathbf{r},t) \tag{2.83}$$

where $\rho^{(1)}(\mathbf{r},t)$ is the density deviation induces by the application of the field.

The induced density $\rho^{(1)}(\mathbf{r},t)$ is related to the density-density response functions $\chi(\mathbf{r},\mathbf{r}',t')$ through the equation:

$$\rho^{(1)}(\mathbf{r},t) = \int_{-\infty}^{t}\int \chi(\mathbf{r},\mathbf{r}',t-t')v^{(1)}\left[\rho\left(\mathbf{r}',t'\right)\right]d\mathbf{r}'dt' \tag{2.84}$$

where:

$$\chi(\mathbf{r},\mathbf{r}',t-t') = \frac{1}{i\hbar}\theta\left(t-t'\right)\left\langle\psi_0\left|\left[\hat{\rho}(\mathbf{r},t),\hat{\rho}\left(\mathbf{r}',t'\right)\right]\right|\psi_0\right\rangle \tag{2.85}$$

$\theta(t)$ being the step function, ψ_0 the exact many-particle ground state and $\hat{\rho}(\mathbf{r},t)$ the density operator defined by:

$$\hat{\rho}(\mathbf{r},t) = e^{\frac{i}{\hbar}\hat{H}t}\hat{\rho}(\mathbf{r})\,e^{-\frac{i}{\hbar}\hat{H}t} \tag{2.86}$$

For a perturbation with a fixed frequency ω, it is convenient to work in the frequency space and use the Fourier transform of the response function. Projecting on a complete set of states, the response function can be expressed in a spectral representation:

$$\begin{aligned}\chi(\mathbf{r},\mathbf{r}',\omega) &= \int e^{i\omega t}\chi(\mathbf{r},\mathbf{r}',t)dt \qquad (2.87)\\ &= \sum_i \frac{\langle\psi_0|\hat{\rho}(\mathbf{r})|\psi_i\rangle\langle\psi_i|\hat{\rho}(\mathbf{r}')|\psi_0\rangle}{\omega-(E_i-E_0)+i\eta} + \frac{\langle\psi_0|\hat{\rho}(\mathbf{r})|\psi_i\rangle\langle\psi_i|\hat{\rho}(\mathbf{r}')|\psi_0\rangle}{\omega+(E_i-E_0)+i\eta}\end{aligned}$$

where E_0 and E_i are the exact energies of the ground and excited states respectively and η is a positive infinitesimal. In principle, Equations (2.84) and (2.87) permit to determine exactly the density functional. However, it also requires to know the exact values of the wavefunctions and energies, which is impossible for a many-particle system. Such calculation can however be achieved through a self-consistent field procedure in the Kohn-Sham scheme.

Following the description of Zangwill et Soven in [444], the response potential due to a first order change in the electron density induced by the perturbation is taken into account self-consistently, giving rise to a non-interacting perturbing potential $v_{KS}^{(1)}\left[\rho\left(\mathbf{r},t\right)\right]$ that is given by:

$$v_{KS}^{(1)}\left[\rho\left(\mathbf{r},t\right)\right]=v^{(1)}\left[\rho\left(\mathbf{r},t\right)\right]+v_{H}^{(1)}\left[\rho\left(\mathbf{r},t\right)\right]+v_{xc}^{(1)}\left[\rho\left(\mathbf{r},t\right)\right] \tag{2.88}$$

where:

$$v_{H}^{(1)}\left[\rho\left(\mathbf{r},t\right)\right]=\int\frac{\rho^{(1)}\left(\mathbf{r}',t\right)}{\left|\mathbf{r}-\mathbf{r}'\right|}d\mathbf{r}' \tag{2.89}$$

and:

$$v_{xc}^{(1)}\left[\rho\left(\mathbf{r},t\right)\right]=\iint\frac{\rho^{(1)}\left(\mathbf{r}',t\right)\delta v_{xc}\left[\rho\left(\mathbf{r},t\right)\right]}{\delta\rho\left(\mathbf{r}',t'\right)}d\mathbf{r}'dt' \tag{2.90}$$

which are respectively the induced Coulomb and exchange-correlation potentials in the adiabatic local density approximation (ALDA). These quantities correspond to an additional electronic interaction due to the redistribution of the electrons through the effect of the external field.

In the frequency space, the induced density can be rewritten as a function of the non-interacting response function $\chi_{KS}(\mathbf{r},\mathbf{r}',\omega)$:

$$\begin{aligned}\rho^{(1)}\left(\mathbf{r},\omega\right) &= \int\chi(\mathbf{r},\mathbf{r}',\omega)v^{(1)}\left[\rho\left(\mathbf{r}',\omega\right)\right]d\mathbf{r}' \\ &= \int\chi_{KS}(\mathbf{r},\mathbf{r}',\omega)v_{KS}^{(1)}\left[\rho\left(\mathbf{r}',\omega\right)\right]d\mathbf{r}'\end{aligned} \tag{2.91}$$

where:

$$\chi_{KS}(\mathbf{r},\mathbf{r}',\omega)=\sum_{ij}^{\infty}\left(n_j-n_i\right)\frac{\varphi_i\left(\mathbf{r}\right)\varphi_i^*\left(\mathbf{r}'\right)\varphi_j\left(\mathbf{r}'\right)\varphi_j^*\left(\mathbf{r}\right)}{\omega-\left(\varepsilon_i-\varepsilon_j\right)+i\eta} \tag{2.92}$$

n_i and n_j correspond to the occupation numbers of the Kohn-Sham orbitals $\varphi_i\left(\mathbf{r}\right)$ and $\varphi_j\left(\mathbf{r}\right)$ with energies ε_i and ε_j. These quantities are obtained through a simple LDA calculation.

We define the time-independent kernel $K\left(\mathbf{r},\mathbf{r}'\right)$ as the sum of the Coulomb interaction and the ALDA exchange-correlation kernel:

$$K\left(\mathbf{r},\mathbf{r}'\right)=\frac{1}{|\mathbf{r}-\mathbf{r}'|}+\delta\left(\mathbf{r}-\mathbf{r}'\right)\left.\frac{\partial v_{xc}^{LDA}\left(\rho\right)}{\partial\rho}\right|_{\rho=\rho(\mathbf{r})} \tag{2.93}$$

The ALDA exchange-correlation kernel makes use of the local approximation in space and in time and contains all the complexity of the many-body interaction in the linear response approximation.

The induced density can be reformulated as:

$$\begin{aligned}\rho^{(1)}\left(\mathbf{r},\omega\right) &= \int\chi_{KS}(\mathbf{r},\mathbf{r}',\omega)v^{(1)}\left[\rho\left(\mathbf{r}',\omega\right)\right]d\mathbf{r}' \\ &\quad+\iint\chi_{KS}(\mathbf{r},\mathbf{r}',\omega)\rho^{(1)}\left(\mathbf{r}'',\omega\right)K\left(\mathbf{r}',\mathbf{r}''\right)d\mathbf{r}'d\mathbf{r}''\end{aligned} \tag{2.94}$$

Introducing the latter equation in (2.91), we obtain the expression for the exact linear density response:

$$\begin{aligned}\chi(\mathbf{r},\mathbf{r}',\omega) &= \chi_{KS}(\mathbf{r},\mathbf{r}',\omega) \\ &\quad+\iint\chi_{KS}(\mathbf{r}'',\mathbf{r}',\omega)\chi(\mathbf{r},\mathbf{r}''',\omega)K\left(\mathbf{r}''',\mathbf{r}''\right)d\mathbf{r}''d\mathbf{r}'''\end{aligned} \tag{2.95}$$

The real challenge for the TDDFT calculation in the linear response regime is to solve Equation (2.95). To do so, $\chi_{KS}(\mathbf{r},\mathbf{r}',\omega)$ has to be evaluated in a first step but the summation over the states i and j in (2.92) is slowly convergent and often requires to include many unoccupied states. Also, construction of $\chi(\mathbf{r},\mathbf{r}',\omega)$ is difficult in a three dimension grid representation. For this reason, it is convenient to use the modified Sternheimer approach (MSA) [239] since it does not require to construct explicitly the response functions in order to solve the inhomogeneous linear response equation.

At the first order perturbation theory, the TDKS Equations (2.78) read:

$$i\hbar\frac{\partial}{\partial t}\varphi_i\left(\mathbf{r},t\right)=\left(-\frac{1}{2}\nabla^2+v_{KS}^{(0)}[\rho\left(\mathbf{r}\right)]+v_{KS}^{(1)}[\rho\left(\mathbf{r},t\right)]\right)\varphi_i\left(\mathbf{r},t\right) \tag{2.96}$$

Considering the time-dependent Kohn-Sham orbitals $\varphi_i\left(\mathbf{r},t\right)$ as a sum of the static Kohn-Sham orbitals $\varphi_i^{(0)}\left(\mathbf{r}\right)$ and a small deviation $\varphi_i^{(1)}\left(\mathbf{r},t\right)$:

$$\varphi_i\left(\mathbf{r},t\right)=\left[\varphi_i^{(0)}\left(\mathbf{r}\right)+\varphi_i^{(1)}\left(\mathbf{r},t\right)\right]e^{-\frac{i}{\hbar}\varepsilon_i t} \tag{2.97}$$

from Equation (2.96), we obtain a differential equation of the deviation wavefunction:

$$i\hbar\frac{\partial}{\partial t}\varphi_i^{(1)}\left(\mathbf{r},t\right)=\left(-\frac{1}{2}\nabla^2+v_{KS}^{(0)}[\rho\left(\mathbf{r}\right)]-\varepsilon_i\right)\varphi_i^{(1)}\left(\mathbf{r},t\right)+v_{KS}^{(1)}\left[\rho\left(\mathbf{r},t\right)\right]\varphi_i^{(0)}\left(\mathbf{r}\right) \tag{2.98}$$

The external potential is real and for a fixed frequency ω it can be developed as:

$$v^{(1)}(\mathbf{r},t) = v^{(1)}(\mathbf{r},\omega)\, e^{-i\omega t} + v^{(1)*}(\mathbf{r},\omega)\, e^{i\omega t} \tag{2.99}$$

then the deviation from the TIKS orbitals can be split in a + (positive frequency) and − (negative frequency) contribution:

$$\varphi_i^{(1)}(\mathbf{r},t) = \varphi_i^{(1,+)}(\mathbf{r},\omega)\, e^{-i\omega t} + \varphi_i^{(1,-)}(\mathbf{r},\omega)\, e^{i\omega t} \tag{2.100}$$

Introducing the latter expression of $\varphi_i^{(1)}(\mathbf{r},t)$ and Equation (2.99) in (2.98) we obtain a set of two linear equations:

$$\begin{cases} \omega\varphi_i^{(1,+)}(\mathbf{r},\omega) = & \left(-\frac{1}{2}\nabla^2 + v_{KS}^{(0)}[\rho(\mathbf{r})] - \varepsilon_i\right)\varphi_i^{(1,+)}(\mathbf{r},\omega) \\ & + \left[\int K(\mathbf{r},\mathbf{r}')\,\rho^{(1)}(\mathbf{r}',\omega)\,d\mathbf{r}' + v^{(1)}(\mathbf{r},\omega)\right]\varphi_i^{(0)}(\mathbf{r}) \\ -\omega\varphi_i^{(1,-)}(\mathbf{r},\omega) = & \left(-\frac{1}{2}\nabla^2 + v_{KS}^{(0)}[\rho(\mathbf{r})] - \varepsilon_i\right)\varphi_i^{(1,-)}(\mathbf{r},\omega) \\ & + \left[\int K(\mathbf{r},\mathbf{r}')\,\rho^{(1)*}(\mathbf{r}',\omega)\,d\mathbf{r}' + v^{(1)*}(\mathbf{r},\omega)\right]\varphi_i^{(0)}(\mathbf{r}) \end{cases}$$

The deviation from the density now reads:

$$\rho^{(1)}(\mathbf{r},\omega) = \sum_i \varphi_i^{(0)*}(\mathbf{r})\,\varphi_i^{(1,+)}(\mathbf{r},\omega) + \varphi_i^{(0)}(\mathbf{r})\,\varphi_i^{(1,-)*}(\mathbf{r},\omega) \tag{2.101}$$

In the MSA formalism, the KS eigenfunctions at the first order of perturbation $\varphi_i^{(1,\pm)}$ are calculated via the inhomogeneous equation:

$$\left[\frac{1}{2}\nabla^2 - v_{KS}^{(0)}[\rho(\mathbf{r})] + \varepsilon_i \pm \omega\right]\varphi_i^{(1,\pm)}(\mathbf{r},\omega) = \hat{P}v_{KS}^{(1)}[\rho(\mathbf{r},\omega)]\,\varphi_i^{(0)}(\mathbf{r}) \tag{2.102}$$

where $\hat{P}$ is a projector operator that orthogonalizes with respect to the occupied states.

The most efficient algorithms employ $v_{KS}^{(1)}[\rho(\mathbf{r},\omega)]$ as the basic dynamical variable, thus avoiding the need of SCF iterations, which are generally unstable in complex molecules [365].

It is possible to recast Equation (2.102) into a system of linear algebraic equations of $v_{KS}^{(1)}[\rho(\mathbf{r},\omega)]$ whose matrix form reads:

$$[\mathbf{1} - \mathbf{K}\cdot\chi(\omega)]\,\mathbf{V}_{KS}^{(1)}(\omega) = \mathbf{V}^{(1)}(\omega) \tag{2.103}$$

One has to notice that, since the kernel K is energy independent, the corresponding matrix elements must be computed only once. The χ matrix

elements are energy dependent and must thus be computed at each photon energy by solving the inhomogeneous equation (2.102).

In the solution of (2.102) for $\varphi_i^{(1,-)}$ lying in the continuum, correct boundary conditions must be enforced. Finally, once V_{KS} is obtained, the cross section is calculated via transition moments that make use of V_{scf} instead of the dipole operator.

The main advantage of the TDDFT compared to TIDFT is the inclusion of electronic excitations/de-excitations. This point is clearly seen by recasting the system of linear equations (2.101) using (2.101):

$$\begin{cases} \int \left(\omega + \frac{1}{2}\nabla^2 - v_{KS}^{(0)}[\rho(\mathbf{r})] + \varepsilon_i\right) \delta\left(\mathbf{r}-\mathbf{r}'\right) \varphi_i^{(1,+)}\left(\mathbf{r}',\omega\right) d\mathbf{r}' \\ -\varphi_i^{(0)}(\mathbf{r}) \int \sum_j K\left(\mathbf{r},\mathbf{r}'\right) \varphi_j^{(0)*}\left(\mathbf{r}'\right) \varphi_j^{(1,+)}\left(\mathbf{r}',\omega\right) d\mathbf{r}' \\ -\varphi_i^{(0)}(\mathbf{r}) \int \sum_j K\left(\mathbf{r},\mathbf{r}'\right) \varphi_j^{(0)}\left(\mathbf{r}'\right) \varphi_j^{(1,-)*}\left(\mathbf{r}',\omega\right) d\mathbf{r}' = v^{(1)}(\mathbf{r},\omega)\, \varphi_i^{(0)}(\mathbf{r}) \\ \\ \int \left(-\omega + \frac{1}{2}\nabla^2 - v_{KS}^{(0)}[\rho(\mathbf{r})] + \varepsilon_i\right) \delta\left(\mathbf{r}-\mathbf{r}'\right) \varphi_i^{(1,-)}\left(\mathbf{r}',\omega\right) d\mathbf{r}' \\ -\varphi_i^{(0)}(\mathbf{r}) \int \sum_j K\left(\mathbf{r},\mathbf{r}'\right) \varphi_j^{(0)*}\left(\mathbf{r}'\right) \varphi_j^{(1,-)}\left(\mathbf{r}',\omega\right) d\mathbf{r}' \\ -\varphi_i^{(0)}(\mathbf{r}) \int \sum_j K\left(\mathbf{r},\mathbf{r}'\right) \varphi_j^{(0)}\left(\mathbf{r}'\right) \varphi_j^{(1,+)*}\left(\mathbf{r}',\omega\right) d\mathbf{r}' = v^{(1)*}(\mathbf{r},\omega)\, \varphi_i^{(0)}(\mathbf{r}) \end{cases}$$

which can be putted into a matrix form:

$$\left[\omega \begin{pmatrix} \mathbf{I} & 0 \\ 0 & -\mathbf{I} \end{pmatrix} - \begin{pmatrix} \mathbf{A} & \mathbf{B} \\ \mathbf{B}^* & \mathbf{A}^* \end{pmatrix}\right] \begin{pmatrix} \varphi^{(1,+)}(\mathbf{r}',\omega) \\ \varphi^{(1,-)*}(\mathbf{r}',\omega) \end{pmatrix} = v^{(1)}(\mathbf{r},\omega) \begin{pmatrix} \varphi_j^{(0)}(\mathbf{r}) \\ \varphi_j^{(0)*}(\mathbf{r}) \end{pmatrix} \tag{2.104}$$

where integration over $\mathbf{r}'$ is assumed and where $\mathbf{A}$ and $\mathbf{B}$ are $2N_{occ}$ matrices defined as:

$$\begin{aligned} \mathbf{A} &= \left(-\tfrac{1}{2}\nabla^2 + v_{KS}^{(0)}[\rho(\mathbf{r})] - \varepsilon_i\right) \delta(\mathbf{r}-\mathbf{r}')\, \delta_{ij} + \varphi_i^{(0)}(\mathbf{r})\, K(\mathbf{r},\mathbf{r}')\, \varphi_j^{(0)*}(\mathbf{r}') \\ \mathbf{B} &= \varphi_i^{(0)}(\mathbf{r})\, K(\mathbf{r},\mathbf{r}')\, \varphi_j^{(0)}(\mathbf{r}') \end{aligned} \tag{2.105}$$

Equation (2.104) is solved repeatedly in order to obtain $\varphi_i^{(1,+)}(\mathbf{r}',\omega)$ and $\varphi_i^{(1,-)}(\mathbf{r}',\omega)$ which are used in Equation (2.101) to compute the density deviation. The matrix form of the inhomogeneous equations shows that $\mathbf{A}$ and $\mathbf{B}$ mix different configurations involving single excitations/de-excitations.

2.3 Basis

The LCAO formalism provides an efficient technique for the self-consistent field procedure because it requires to compute all the integrals only once. This formalism is theoretically exact when a complete basis set is used in the MOs expansion. But in practice, the completeness of the standard basis are never reached because it would be necessary to expand the MO on a infinite number of basis functions. For this reason, every *ab initio* calculation contain an intrinsic error which is due to the truncation of the basis. This error can be reduced by increasing the number of basis functions but also by choosing types of functions which are adapted to the system. In this section, we will describe succinctly some common classes of basis sets and basis functions. In both cases, we will focus on the elements of interests for the present work. A particular attention will be devoted to the B-spline functions since they are particularly adapted to the treatment of continuum wavefunctions.

2.3.1 Basis sets

Minimal basis set

As the name suggests, this basis set is the minimal that can be used in a calculation. It corresponds to a number of basis functions[4] equals to the number of electrons in the system plus the ones needed to complete the valence shell. In practice, it means that atoms of the first period will require one s orbital, atoms of the second period two s and three p, atoms of the third period three s, six p and five d, etc. The basis functions typically used in such minimal basis are called STO-NG and are described in the next paragraph. This basis set requires few computational efforts but gives rather poor results because of its lack of flexibility. Minimal basis sets are generally used for very expansive calculations or to estimate the contributions of each AO to the MOs. To perform accurate calculations, and more precisely when post-HF methods are in use, it is strongly recommended to employ bigger basis sets which allow to recover some electronic correlation.

Split-valence basis set

During the bonding, each initial AO tends to extend spatially in order to overlap the most with the other AOs so as to strengthen the bond. This phenomenon cannot be represented by using a minimal basis and additional basis functions have to be introduced in the set. The molecular bond is strongly determined by the overlap of valence AOs which contribute much more than

[4] Rigorously, we should used the precise term of "contracted" functions which will be introduced in the basis functions paragraph.

core AOs. Then, a better description of the valence AOs would logically improve the description of the molecular bond. By adding few supplementary basis functions to represent the valence AOs, the expansion gets some flexibility and the electron density can be adjusted to the appropriate spatial extent. Depending on the number of supplementary basis functions, the basis sets are called valence double, triple, quadruple-zeta, etc., basis sets. Zeta here refers to the effective charge (commonly written ζ in the expression of the basis functions) and is different for core and valence orbitals: the lower ζ, the smoother will decrease the orbital and the better it will describe the valence shell.

Polarization functions

Because molecules have a lower symmetry than their constituent atoms, functions of symmetries different from those of the occupied MOs can contribute to the SCF wavefunction. In order to take into account the asymmetric distortion of the electronic cloud along the bond axis, basis functions of higher angular momentum are introduced in the basis set. The so-called polarization functions are p-orbitals for the first period atoms, d-orbitals for the second period atoms, f-orbitals for the third period atoms, etc. The use of polarization functions in the basis set is indicated by the letter P at the end of the acronym (e.g., DZP for a double-zeta polarized basis set).

Correlation-consistent basis sets

The correlation-consistent (cc) basis sets were developed by Dunning and coworkers [102] and are the state of the art for post-HF methods. They are designed to converge systematically to the complete basis set by using empirical extrapolation techniques. To each row of the periodic table corresponds a shell of appropriate functions to be added to the Hartree-Fock AOs in order to account for the correlation effects (see Figure 2.4). The adopted notation is cc-pVNZ, where p stands for "polarization" and VNZ for "valence N-zeta". For the atoms of the first and second rows, it is appropriate to use at least the cc-pVDZ which require to add one s, one p and one d function (the first shell in the figure). Larger shells of functions can be added in order to introduce more polarization functions.

Also, there exist augmented versions (aug-cc-pVNZ or avnz) which add diffuse functions to the previous basis sets. As an example, in this work, we made use of the aug-cc-pVQZ basis set to calculate the potential energy curves of N_2 and CO molecules.

2.3.2 Basis functions

The two main categories are related to the localized or delocalized nature of the functions. Functions of the former category are centered on precise

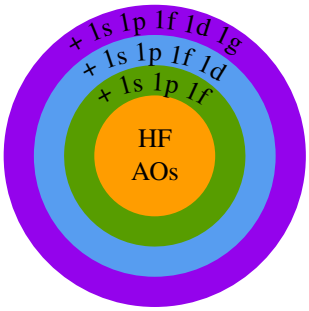

Figure 2.4: Series of supplementary functions shells in the correlation-consistent basis set.

coordinates, commonly the atoms, and for this reason, are widely employed in computational chemistry. The second category is preferentially used in solid state physics for systems with translational periodicity and will not be treated here.

Slater type orbitals

The Slater type orbitals (STOs) are based on the solutions of the Schrödinger equation for the hydrogen atom. Since the radial part of the hydrogenic functions contains nodes, positive and negative lobes, and steep variations which make the calculation very complex, Slater had the idea to keep only the exponential term, the nodal structure emerging from the expansion. The single-electron wavefunction can then be written as:

$$\phi^{STO}_{nlm\zeta}(\mathbf{r}) = R^{STO}_{n\zeta}(r)\, Y_{lm}(\theta, \phi) \tag{2.106}$$

where $R^{STO}_{n\zeta}(r)$ is the radial part, defined by:

$$R^{STO}_{n\zeta}(r) = (2\zeta)^n \sqrt{\frac{2\zeta}{(2n)!}} r^{n-1} e^{-\zeta r} \tag{2.107}$$

and $Y_{lm}(\theta, \phi)$ the spherical harmonics. n is the principal quantum number, l the azimuthal quantum number, m the magnetic quantum number and ζ the nuclear effective charge.

By their correspondence with hydrogen atomic orbitals, the STOs describe properly the electron density close to the nuclei (they satisfy the Kato's cusp condition) and the exponential decay. Also, their use in the LCAO expansion permits to describe more complex AOs in the polyelectronic atoms. Unfortunately, such basis functions involve bielectronic integrals which cannot be solved analytically for polyatomic molecules. In such cases, algorithms have

to be employed but are hardly implemented in the commercial programs and imply an additional cost of time.

Gaussian type orbitals

The most common basis functions are the Gaussian type orbitals (GTOs). They were first introduced by Frank Boys in the 1950's because of the Gaussian product theorem which avoid the problem occurring with the STOs: since the product of two gaussians with different origins can always be described by a finite sum of gaussians centered on a third point along the axis connecting them, fast analytical solutions are easily obtained, even for complex molecular systems.

The radial part of the GTOs reads:

$$R_{n\zeta}^{GTO}(r) = Ar^l e^{-\zeta r^2} \tag{2.108}$$

where A is a normalization factor.

GTOs do not describe as accurately as STOs do the probability to find an electron close to the nuclei, neither asymptotically (see Figure 2.5). However, their use is computationally cheap and a large number of GTOs can be employed, making the expansion more flexible and then the results more accurate.

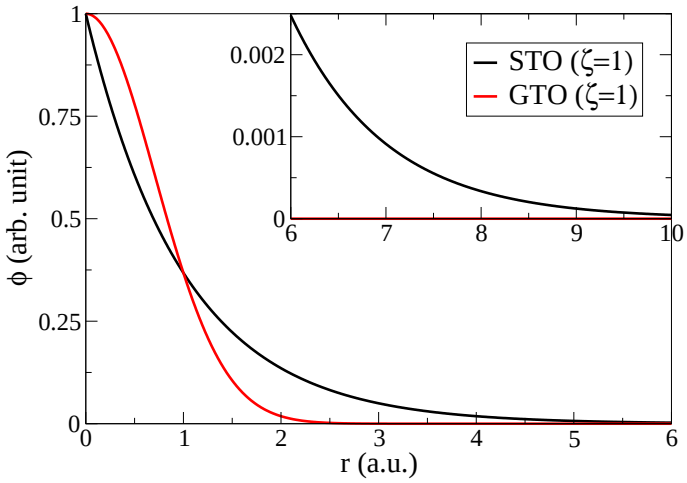

Figure 2.5: Comparison between a Slater type orbital and a Gaussian type orbital for n=1 and ζ=1.

Also, improvement to the basis set has been suggested by John Pople by expanding the STOs on a basis of GTOs. Such basis functions are referenced

as STO-NG where N stands for the number of GTOs chosen in the expansion:

$$R_{n\zeta}^{STO}(r) = \sum_{i}^{N} a_i R_{n\zeta}^{GTO}(r) \tag{2.109}$$

where a_i corresponds to the expansion coefficients or "contraction" coefficients.

By fitting the STOs with $2 \leq N \leq 6$ "primitive" gaussians, the calculation takes advantage of the efficiency of the GTOs but also of the accuracy of the STOs. It has been observed that contracting 3 gaussians (STO-3G) is sufficient in many cases.

The B-splines functions

B-splines are $\mathcal{C}^{k-2}$ piecewise polynomials with specifics properties (among many of them, a relative flexibility). For this reason, they constitute excellent basis sets and are often used to interpolate functions. B-splines have been first developed by I. J. Schoenberg in 1949 in order to approximate equidistant data using analytic functions. In the last few decades, they became a powerful tool in the framework of atomic and molecular physics. Its advent comes from the the deficiency of the standard basis functions (as STO or GTOs) to treat specific molecular problems. For instance, it has been established that the STOs are unable to describe correctly molecular bonds, excepts when including some orbital expansion factors which increase considerably the computational effort. Although the GTOs represent a real improvement and are more flexible than the STOs - overall because it is possible to include polarization or diffusion functions - they also present many limitations. The description of the continuum states, for example, is problematic since the wavefunction keeps oscillating to infinity and for this reason, is hardly reproduced using such bound-like basis sets.

B-splines are very flexible functions and produce smooth curves with continuous derivatives at every point. They are defined in a finite space (contrary to STOs or GTOs which are extended to infinity) and the grid of points can be adjusted as needed, depending on the system. Due to these two properties, it is possible to reproduce correctly the continuum wavefunctions by using a linear grid of points and a sufficient density of B-splines.

Mathematical definition In order to properly describe the B-spline functions, few mathematical definitions should be first introduced:

- The order k of the function which define the polynomial degree (maximum $k-1$):

$$p(x) = a_0 + a_1 x + \ldots + a_{k-1} x^{k-1}$$

- The $l+1$ breakpoints $\{\xi_j\}$ which divide the interval $I = [a, b]$ in l subintervals $I_j = [\xi_j, \xi_{j+1}]$ in a strict ascending order:

$$a = \xi_1 < \xi_2 < \ldots < \xi_{l+1} = b$$

- The class $\mathcal{C}^n$ which specify the maximum derivation degree n for which the derivative function f^n is still continuous over a specified interval.

- The intermediate breakpoints $\{\nu_j\}$, sequence of non-negative integers which defines the continuity condition $C^{\nu_j - 1}$ at the associated breakpoint ξ_j. They are defined from $j = 2, \cdots, l$ since continuity is not required at the box limit ($\nu_1 = \nu_{l+1} = 0$).

- The knots $\{t_i\}$, another sequence of points, defined as:

$$t_1 \leq t_2 \leq \ldots \leq t_m$$

  and associated with ξ_j and ν_j as follows:

$$\begin{aligned} t_1 = t_2 = \ldots = t_{\mu_1} &= \xi_1 \\ t_{\mu_1+1} = t_{\mu_1+2} = \ldots = t_{\mu_1+\mu_2} &= \xi_2 \\ &\vdots \\ t_{\mu_1+\mu_2+\ldots+\mu_{i-1}+1} = \ldots = t_{\mu_1+\ldots+\mu_i} &= \xi_i \\ &\vdots \\ t_{\mu_1+\ldots+\mu_i+\ldots+\mu_l+1} = \ldots = t_{\mu_1+\ldots+\mu_{l+1}} &= \xi_{l+1} \end{aligned}$$

  where μ_j is the multiplicity of the knots t_i at ξ_j and is given by the relation $\mu_j = k - \nu_j$ which implies that $\mu_1 = \mu_{l+1} = k$.

  The most common choice for knot multiplicity at inner breakpoints is unity. This choice ensures the maximum continuity C^{k-2} in the interval $I =]a, b[$ and is going to be adopted in the following. Then, the number of B-splines is given by:

$$n = l + k - 1 \tag{2.110}$$

These definitions introduced, we now can express any function f in a B-spline basis set over an interval $[a, b]$:

$$f(x) = \sum_{i=1}^{n} c_i B_i^k(x) \tag{2.111}$$

f is a linear combination of B-splines, made of l polynomial pieces of order k, one for each subinterval I_j. For this reason, such a function is conventionally called a *piecewise polynomial function* (pp-function).

The B-spline basis set Relying on the definition of those basic concepts, we now can better specify the basis set. A single B-spline $B_i^k(x)$ defined by the order $k > 0$ and a set of $k+1$ knots possesses the following properties:

- $B_i^k(x)$ is a pp-function of order k over $[t_i, t_{i+k}]$
- $B_i^k(x) > 0$ for $x \in]t_i, t_{i+k}[$
- $B_i^k(x) = 0$ for $x \notin [t_i, t_{i+k}]$
- $B_i^k(x) \in C^{k-1-\mu_j}$ for $x = \xi_j$
- $B_j^k(x) \neq 0$ over $]t_i, t_{i+k}[$ for $j = i-k+1, \ldots, i$ which implies that there are exactly k non-zero B-splines on each interval I_j and:

$$B_i^k(x) \cdot B_j^k(x) = 0 \qquad \text{for } |i-j| \geq k \tag{2.112}$$

- The previous property reduces the number of expansion terms to k:

$$f(x) = \sum_{j=1}^{n} c_j B_j^k(x) = \sum_{j=i-k+1}^{i} c_j B_j^k(x) \qquad \text{for } x \in [t_i, t_{i+1}] \tag{2.113}$$

- The B-splines are normalized:

$$\sum_i B_i^k(x) = 1 \qquad \text{over } [t_k, t_{n+1}] \tag{2.114}$$

- For simple equidistant knots, each $B_i^k(x)$ is just a translation by one interval of the previous one. If the knots are not equidistant there is a smooth change in the shape.
- The index i of each B-spline corresponds to the index of the left knot of the interval $I_j = [\xi_j, \xi_{j+1}] = [t_i, t_{i+1}]$
- Since the B-splines are defined positive and own a minimal support (i.e. an interval $]t_i, t_{i+1}[$ where $B_j^k(x) > 0$), the expansion coefficients of an arbitrary function f are close to the function values at the knot. The main consequence is that wild oscillations in the coefficients are avoided, cancellation errors are minimal and numerical stability maximal.
- The B-splines satisfy the recursion relation:

$$B_i^k(x) = \frac{x - t_i}{t_{i+k-1} - t_i} B_i^{k-1}(x) + \frac{t_{i+k} - x}{t_{i+k} - t_{i+1}} B_{i+1}^{k-1}(x) \tag{2.115}$$

From the last relation it is possible to construct recursively all of the k B-splines of order k from a former one of order $k = 1$ at a specific x. To illustrate this point, Figure 2.6 presents two consecutive applications of the formula (2.115) from a B-spline of order $k = 1$ to construct one of order $k = 3$.

The former B-spline of order $k = 1$ is defined by:

$$B_1^k(x) = \begin{cases} 1 & \text{for } t_i \leq x \leq t_{i+1} \\ 0 & \text{otherwise} \end{cases} \tag{2.116}$$

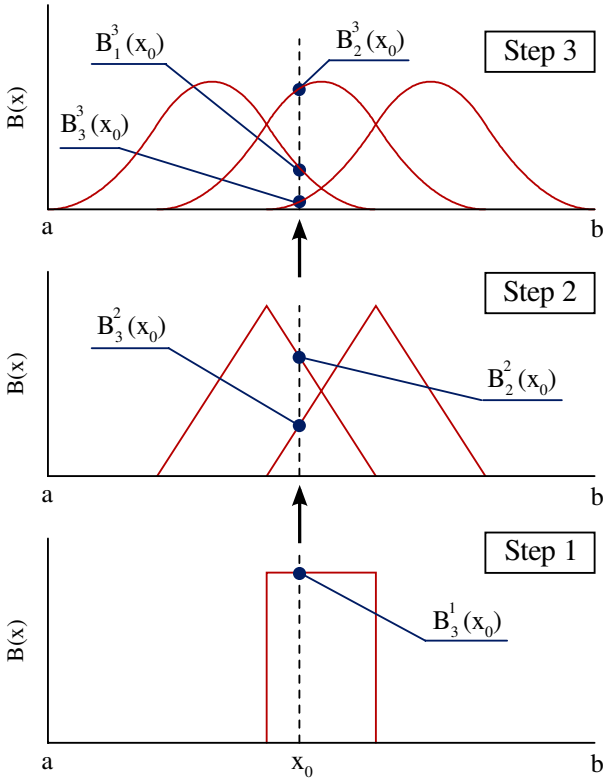

Figure 2.6: Construction of a B-spline of order 3 from a B-spline of order 1

It is worth recalling that for each x, we obtain k non-zero B-splines and their sum equal to 1. The choice of the first and the last k points is completely free but has to fulfill the increasing order condition:

$$t_1 \leq \ldots \leq t_k \leq \xi_1 \quad \text{and} \quad \xi_{l+1} \leq t_{n+1} \leq \ldots \leq t_{n+k} \tag{2.117}$$

Although it affects only the first and last k B-spline functions but it is generally adopted to use the following sequence:

$$t_1 = \ldots = t_k = \xi_1 \quad \text{and} \quad \xi_{l+1} = t_{n+1} = \ldots = t_{n+k} \tag{2.118}$$

This choice is very convenient because it imposes to all B-splines to cancel outside of the interval $I = [a, b]$. Furthermore, only the first $B_1(x)$ and the last B_n B-spline are respectively discontinuous at $x = a$ and $x = b$. In this context, the boundary conditions can be easily implemented removing B_1 and B_n to satisfy $f(a) = 0$ and $f(b) = 0$.

When approximating analytical functions, it is also useful to estimate the maximum error using the relation:

$$\varepsilon \sim \frac{h_j^k}{k!} \left| f^k(\eta_j) \right| \tag{2.119}$$

where h_j is the width of the interval I_j and $\eta_j \in I_j$.

Practically, the stable evaluation of splines is accomplished by the recursion algorithm (2.115) and is efficiently implemented in subroutine BSPLVP [77]. By giving as input values the spline order, the knot sequence, the value of the abscissa and the index of the "left knot" t_i, BSPLVP evaluates the k B-splines that are non-zero at x. Another subroutine, called BSPLVD, can also be used in order to obtain their derivatives (needed in most of the quantum mechanical applications).

To give a clearer idea of the B-spline basis set construction, an example is shown in Figures 2.7 and 2.8. In this particular case, an arbitrary function $f(x)$ is expanded on a B-spline basis set of order $k = 4$, with an inner breakpoint multiplicity $\xi_j = 1$ and $l = 9$. The number of B-splines is given by Equation (2.110): $n = 12$. However, Figures 2.7 and 2.8 shows only 10 B-splines. It is due to the fact that, as mentioned above, first and last B-splines are commonly removed in order to tackle the discontinuity at the edges of the box.

Figures 2.7 and 2.8 serve to illustrate the use of the basis and include few B-spline functions. But for complex systems, such as molecules, where electronic and nuclear wavefunctions require to be accurately described, the basis set can be very large and with high B-spline parameters. For instance, the parameters used to perform the calculations are presented in Section 4.5.

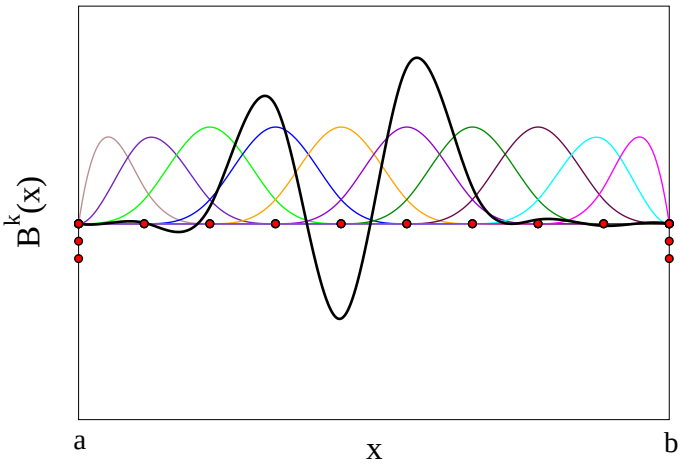

Figure 2.7: Set of B-splines used for the expansion of an ordinary function f (thick black curve). The colored curves correspond to each B-spline functions of the set and the red dots to the knot points located at each breakpoints.

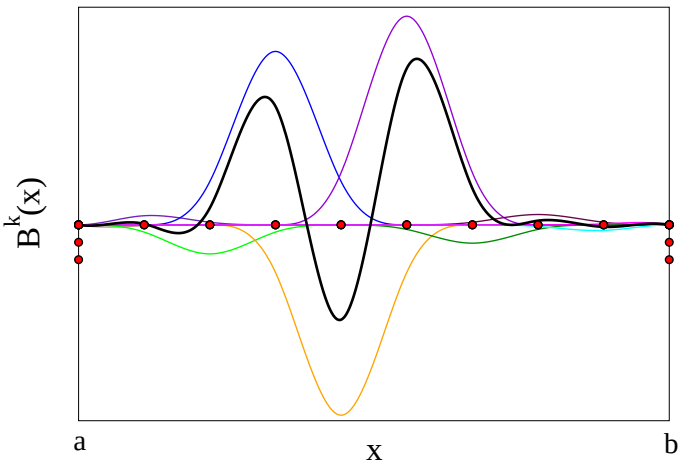

Figure 2.8: The same ordinary function f is expanded on the same B-splines basis set than in Figure 2.7, except that B-spline functions are shown here balanced by their respective coefficients. It appears that three B-splines contribute for more than 80 % to the description of the function. Other coefficients are very close to 0.

2.4 Electronic transition to the continuum

2.4.1 Review of the theoretical methods

So far, we have seen that many computational methods have been designed to solve numerically the Schrödinger equation. All of them are able to describe the ground state of molecules with a degree of accuracy that depends on their own approximations. All of them are nowadays commonly used in order to study many molecular properties since they have been implemented in commercial softwares (such as Molpro or ADF). However, the study of electronic transitions often requires to investigate excited states whose electronic configurations cannot be calculated by such programs (e.g., core hole states - see Section 3.2). Although most of the *ab initio* methods can be adapted to describe any electronic state, their implementation in commercial softwares which are designed for a general purpose complicates or prevents the investigation of more specific processes. This is the case of photoionization in which the final electronic state includes one or more electrons in the continuum. Orbitals that describe electrons in the continuum oscillate at large distances from the reaction center are generally poorly described by conventional basis and require more sophisticated treatment. For the molecular single photoionization, several theoretical methods have been developed in the last forty years. Most of these methods have been successfully used to obtain total photoionization cross sections within the fixed-nuclei approximation and/or the single-channel approximation.

Single-channel methods The most popular is probably the Continuum Multiple Scattering Method (CMSM) which has been used in conjunction with muffin-tin (MT) effective potentials, like the Xα local exchange-correlation potential, as in DFT (CO, N_2 [305, 92, 349, 74, 84, 83, 59]). This method was for a long time the only one capable to treat large systems with a reasonably low computational cost and is now a standard approach in core photoabsorption studies (NEXAFS). The MT approximation is appropriate for fast electrons but introduces some non-physical effects a low energies [127, 9]. Another single channel approach is the Stieltjes-Tchebycheff moment theory (STMT) (CO [275, 212] ; N_2 [433, 308, 304, 212]) which is able to describe shape resonances near the ionization threshold (see results below) but suffers from limited energy resolution and range. The Schwinger iterative approach that has been implemented at the frozen core (FCHF) [232, 230, 353] and relaxed core (RCHF) [447, 446, 325, 311, 237, 236] levels for polyatomic molecules can instead produce accurate solutions of the molecular electronic continuum. Another method that has been shown to provide accurate results for large systems is the present multicenter B-spline static-exchange DFT method [357, 359, 360, 356, 394], which makes use of the Kohn-Sham density functional

theory to describe the molecular ionic states and the Galerkin approach to evaluate the continuum electron wave function in the field of the corresponding Kohn-Sham density. One can also mention the logarithmic derivative version of the Kohn variational principle Lobatto technique (LDKL) [428, 429], which employs multicenter GTO functions and a one center Lobatto polynomials expansion, somewhat similar in spirit.

Multi-channel methods Approaches that include additional correlation and multi-channel interactions, which are particularly important near the ionization threshold, are more sparse. Most have been implemented only for diatomics or linear molecules. The multichannel Schwinger variational method (MCS) has been extended to close-coupling wavefunctions within a configuration interaction framework [372, 224, 225, 19, 235, 22] and is able to account for electronic correlations leading to sharp resonances at low photon energy as well as more complex electronic states. Another approach based on the close-coupling expansion of the wavefunction is the R-matrix method. The method has been recently used to study valence-shell photoionization of N_2 [378]. Also recently a one-center expansion method has been applied within the close-coupling approach [90]. Due to their high computational cost, the latter approaches have not been used beyond the fixed-nuclei approximation. One of the most successful approaches is based on the Random Phase Approximation (RPA), which makes use of the relaxed-core Hartree Fock (RCHF) approximation (N_2 [60, 179, 333, 226, 340, 339, 227, 329, 409, 342, 401] ; CO [170, 179]) in order to describe core-orbital relaxation effects that may play an important role, e.g., in K-shell photoionization. At higher energies the RCHF approximation has also been used (CO [341, 2, 335, 262, 57, 59, 176, 210, 1, 338, 178, 336], N_2 [60]). This is in contrast with the frozen core Hartree Fock (FCHF) approximation, which has widely been used in most earlier and some recent works (CO [353, 325, 236, 73, 295, 303, 33], N_2 [232, 236, 235, 73, 295, 337, 303]).

A very useful alternative to include multichannel couplings is provided by the multicenter B-spline time-dependent static-exchange DFT method within the linear response approximation [357, 14]. This method has been shown to provide accurate results for large systems. Earlier methods that are less employed nowadays are the multichannel quantum-defect theory (MQDT) (CO [218]), the many-body perturbation theory (MBPT) (N_2 [416, 310]) and the linear algebraic method (LA) (N_2 [69]).

2.4.2 Multicenter B-spline static-exchange DFT method

Only a few methods described in the previous section have been used to calculate vibrationally resolved molecular photoionization cross section. These have been applied mostly to diatomic molecules, such as CO [2, 279, 335, 58, 59, 1, 281, 338, 256, 218, 303, 45] or N_2 [409, 340, 58, 407, 339, 401, 226, 136, 304, 303, 22, 45], and almost none in the region of high photon energies. As far we know, none of these methods could be used to compute vibrationally resolved cross sections for polyatomic molecules. These limitations in the investigation scope is due to the inclusion of the nuclear motion which requires to evaluate electronic continuum wave functions and potential energy curves in a dense grid of internuclear distances. For most of these methods, it makes the calculation prohibitively expensive. In this context, DFT-like methods as those described in the previous section appear as a useful alternative, since they can accurately describe continuum states resulting from core and valence-shell photoionization at a relatively moderate computational cost. In their most sophisticated version, they can even include interchannel couplings and describe some autoionization processes. In this section, we will describe the DFT-like method that has been used to calculate vibrationally resolved cross section at high photon energies for diatomic molecules ([45]) as well as polyatomic molecules [11, 290].

DFT method is appropriate to calculate monoelectronic wavefunctions on large systems (at least, larger than H_2) because it offers a good compromise between accuracy and computational time. Although this method is rigorously a ground state theory, calculations on excited states can still be performed at the single-particle LDA (see Section 2.2.2 level and by using an appropriate exchange-correlation potential (see Section 2.2.2).

In this method, Kohn-Sham orbitals are used to compute the electronic transitions. Although, it is often reminded that such orbitals have no physical meaning, Figures 2.9, 2.10 and 2.11 show that at least they closely resemble to the Hartree-Fock molecular orbitals (in this example for the inner and valence shell of CO)[5].

[5] for a deeper analysis, see [371]

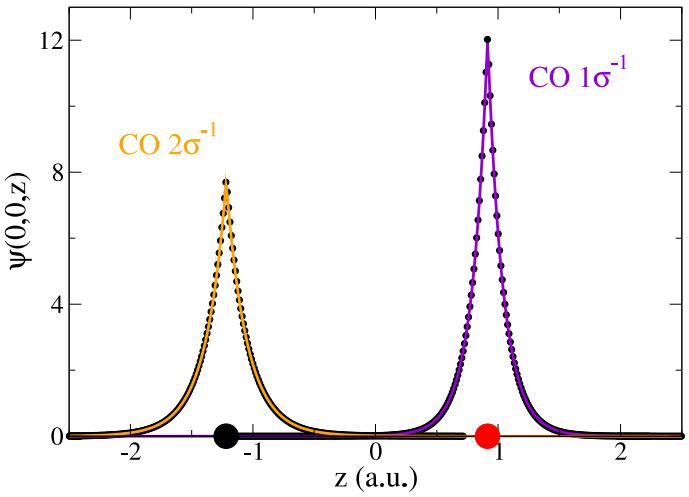

Figure 2.9: Comparison of the Hartree-Fock (black dots) and Kohn-Sham (colored solid lines) 1σ and 2σ orbitals of CO. Values of the wavefunction has been taken along the z axis when $x = 0$ and $y = 0$.

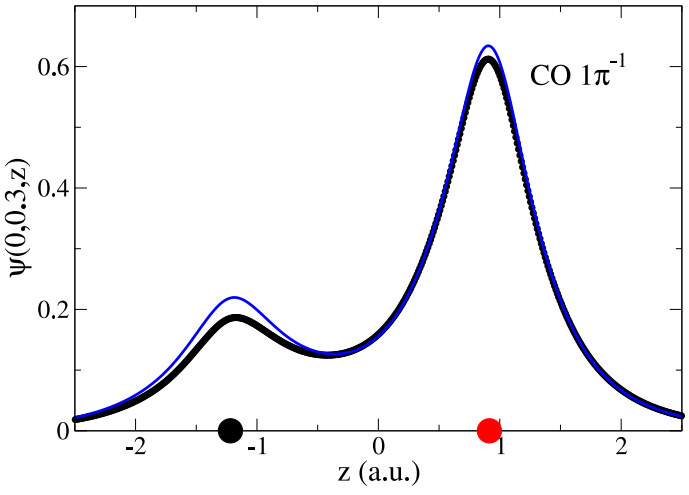

Figure 2.10: Same as Figure 2.9 for the 1π orbital of CO at $x = 0$ and $y = 0.3$.

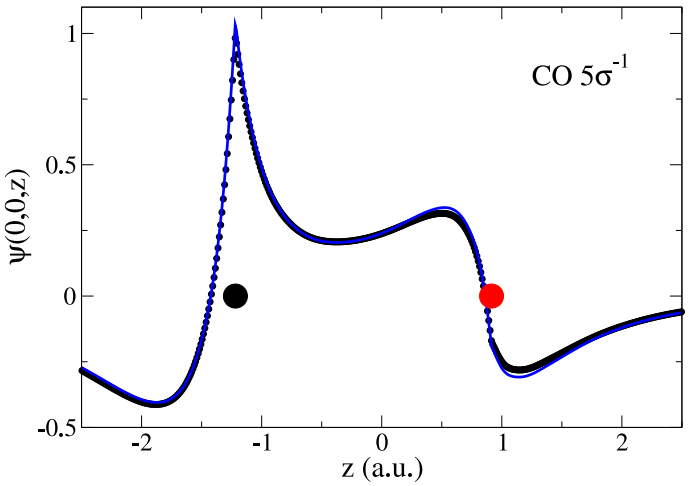

Figure 2.11: Same as Figure 2.11 for the 5σ orbital of CO.

The present approach can be simplified as presented in the following scheme:

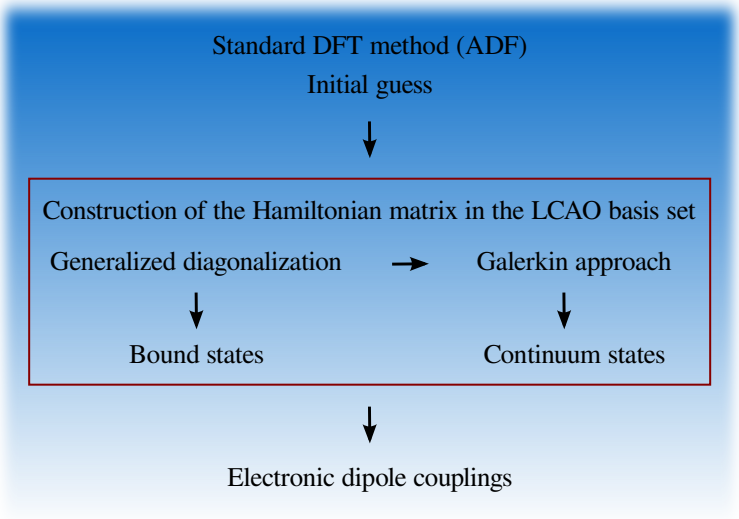

Following the order of this scheme, the next sections present the details of each steps of the method.

Initial guess

The first step consists in performing a standard LCAO-DFT calculation (LCAO stands for linear combination of atomic orbitals) for the ground state of the molecule by using the program ADF *(Amsterdam Density Functional)*. In these ADF calculations, we use a double zeta plus polarization (DZP) basis

set centered on each atom and a LB94 or LDA functional to describe exchange and correlation effects. This permits to generate the Kohn-Sham orbitals for the ground state as a linear combination of STOs (see Equation 2.106).

The ground state density is expressed in terms of calculated STOs:

$$\rho_0(\mathbf{r}) = \sum_{i=1}^{N} \varphi_i^*(\mathbf{r})\varphi_i(\mathbf{r}) \tag{2.120}$$

where the Kohn-Sham orbitals are defined as:

$$\varphi_i(\mathbf{r}) = \sum_{nlm} a_{nlm}\phi_{nlm\zeta}^{STO}(\mathbf{r}) \tag{2.121}$$

This density is then used as an initial guess to build the hamiltonian matrix in a new basis set.

Construction of the LCAO basis set

The present method expand the wavefunction in a B-spline basis set. Its first implementation was making use of a one center expansion (OCE) [357], located at the geometrical center of the molecule. However, it has been observed that introducing few off-center elements to the B-spline expansion improves dramatically the convergence of the calculation for most of the molecules [394] and permits to reduce the angular expansion. The multicenter approach supplements the original one-center expansion (OCE) with off-centers located at non-equivalent nuclei. In this sense, the employed basis set can be called LCAO. Traditional LCAO basis sets make use of GTOs or STOs functions. These provide fast convergence for the lowest bound states with a limited number of basis functions. However it appears difficult to increase the basis because numerical linear dependences rapidly come up, due to the large overlap between functions on different centers. Thanks to the local nature of the spherical B-spline functions, it is possible to control the overlap between functions, by retaining only a short-range expansion on each off-center and obtain a sufficient density of states in the continuum without running into numerical linear dependence problems [14].

The LCAO basis set consists in an expansion of B-splines multiplied by a symmetry adapted linear combination of real spherical harmonics:

$$\xi_{pqhlj}^{i}(r,\theta,\phi) = \sum_{k=1}^{N_a^i} \frac{1}{r_k} B_j^i(r_k) X_{pqhl}^k(\theta_k,\phi_k) \tag{2.122}$$

where:

$$X_{pqhl}^k(\theta_k,\phi_k) = \sum_{m=-l}^{l} b_{pqhlm}^k Y_{lm}^R(\theta_k,\phi_k) \tag{2.123}$$

and $\mathbf{r_k} = \mathbf{r} - \mathbf{R}$ and $(\theta_k, \phi_k) = \widehat{\mathbf{r} - \mathbf{R}}$. The $\{pqhl\}$ set of indexes define the symmetry of the expanded function. p denotes the irreducible representation (IR) of the molecular point group under consideration, q stands for a component of this representation if its dimensionality is greater than one, h distinguishes between different bases of the same IR corresponding to the same value of the angular momentum l. The index i distinguishes the shells of equivalent centers. $i \neq 0$ defines the off-centers for which N_a^i corresponds to the number of equivalent centers. $i = 0$ defines the one-center expansion for which $N_a^i = 1$.

The real spherical harmonics are defined as:

$$Y_{lm}^R(\theta_k, \phi_k) = \begin{cases} \sqrt{2}\,\Re\left(Y_{lm}\right) & m > 0 \\ Y_{l0} & m = 0 \\ \sqrt{2}\,\Im\left(Y_{lm}\right) & m < 0 \end{cases} \tag{2.124}$$

In order to describe correctly bound and continuum states, the radial and angular parts are expanded over several appropriate centers (see Figure 2.12 and 2.13):

- The center of the molecule (denoted by the superscript 0), which is associated with a large sphere of radius R_{max}^0 to correctly account for the long range behavior of the continuum wave functions.
- The position occupied by each nuclei (denoted by the superscript $i \neq 0$), which is associated with a small sphere of radius R_{max}^i to comply with the Kato cusp. The radius is generally quite small (≈ 1 *a.u.*) in order to avoid significant overlap with expansions performed on neighboring centers.

Thus, considering that the molecule comprises κ non-equivalent nuclei, the B-splines basis set is defined by the ensemble:

$$\{B_j^0(r_0)\} \cup \{B_j^1(r_1)\} \cup ... \cup \{B_j^\kappa(r_\kappa)\} \tag{2.125}$$

Since we want to treat both bound and continuum states, the B-splines are built over two different radial intervals: $\left[0; R_{max}^0\right]$ for the set $\left\{B_j^0\right\}$ and $\left[0; R_{max}^i\right]$ for the set $\left\{B_j^i\right\}$. As we mentioned, $R_{max}^0 \gg R_{max}^i$ (see Figure 2.12 and 2.13). Also, each shell i possesses a different number of B-splines N_b^i.

The B-splines are completely defined by their order k and by the grids of knots. For the calculations performed in this study, k has been fixed to 10 and the grids defined linearly with a specific density for each shell.

The LCAO basis set and consequently the cost/accuracy of the calculation is determined by:

- The point group symmetry of the molecule (for highly symmetric molecules such as CH_4 or SF_6, where all the off-centers are equivalent, the explicit use of symmetry leads to a significant reduction of the computational effort).
- The B-spline parameters k, R^0_{max}, R^i_{max} and N^i_b.
- The maximum value of the angular momentum l^i_{max} used in the expansion over each center i.

Actually, because of the large size of the one-center expansion with respect to the multicenter part, it is the size of the former which dominates the computational cost.

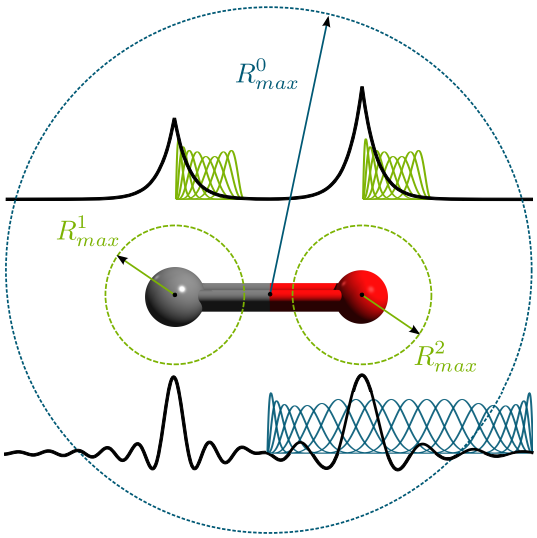

Figure 2.12: Schematic illustration of the B-spline expansion used to describe bound and continuum wavefunctions of heteronuclear diatomic molecules such as carbon monoxide.

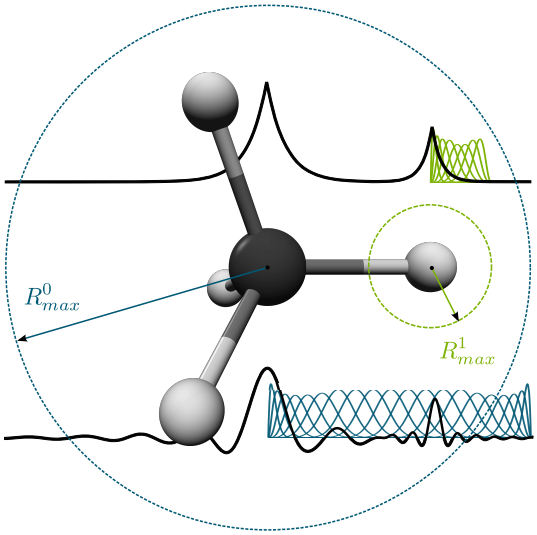

Figure 2.13: Same as Figure 2.12 for polyatomic molecules such as methane.

Construction of the Hamiltonian matrix

The Hamiltonian matrix is generated from the density functional provided by the ADF calculation and is used to get bound and continuum states. In that sense, the present method can be called "static-exchange DFT" (by reference to static-exchange in Hartree-Fock method). A better approximation would be to build a different matrix for the former and the ion molecule, but the static approximation has the advantage to provide directly orthogonal bound and continuum states.

In the LCAO basis, each elements of the matrix reads:

$$\mathbf{H}^{pq}_{ijmnhh'll'} = \int B^i_m(r_i)\, X^i_{pqhl}(\theta_i,\phi_i)\, \hat{h}_{KS} B^j_n(r_j)\, X^j_{pqh'l'}(\theta_j,\phi_j) \qquad (2.126)$$

The hamiltonian matrix $\mathbf{H}$ is by definition totally symmetric. Then it is block-diagonal with the quantum numbers p and q and can be partitioned into blocks for each (p,q) couple. Since the off-center spheres do not overlap, the only non-zero blocks are diagonal blocks $\mathbf{H}_{ii}$ connecting basis functions from the same set $\left\{\xi^i_{pqhl}\right\}$ and off-diagonal blocks $\mathbf{H}_{i0}$ and $\mathbf{H}_{0i}$ connecting basis

functions from two different sets $\left\{\xi^0_{pqhl}\right\}$ and $\left\{\xi^i_{pqhl}\right\}$.

$$\hat{H} = \begin{pmatrix} \hat{H}_{00} & \hat{H}_{01} & \dots & \hat{H}_{0i} & \dots & \hat{H}_{0\kappa} \\ \hat{H}_{10} & \hat{H}_{11} & \dots & 0 & \dots & 0 \\ \vdots & \vdots & \vdots & 0 & \vdots & \vdots \\ \hat{H}_{i0} & 0 & \dots & \hat{H}_{ii} & \dots & 0 \\ \vdots & \vdots & \vdots & 0 & \vdots & \vdots \\ \hat{H}_{\kappa 0} & 0 & \dots & 0 & \dots & \hat{H}_{\kappa\kappa} \end{pmatrix} \tag{2.127}$$

The largest computational effort corresponds to calculation of the non-diagonal block elements H_{i0} and H_{0i} because polycentric bielectronic integrals between B-splines are not analytical. To carry out the integration, a numerical three-dimensional Gauss-Legendre scheme is employed. Also, a rotation of the coordinate framework of the main center along the polar axis leads to significant improvement. It allows to reduce the integration to two variables (r and φ). Only the molecular potential has to be numerically integrated over the whole space. It is clear that the calculation takes a dramatic advantage of the equivalent nuclei consideration because integrals are calculated only once for each of the κ non-equivalent centers.

Solutions of the KS equations

Bound and continuum states are obtained by diagonalizing the Kohn-Sham Hamiltonian (2.127). Every term can be evaluated separately:

- the kinetic energy term and the Coulomb attraction potential do not present any technical difficulty for the integration.
- $V_H\left[\rho\left(\mathbf{r}_i\right)\right]$ (the classical electrostatic Hartree potential) is obtained as a solution of the Poisson equation: $\nabla^2 V_H = -4\pi\rho\left(\mathbf{r}\right)$ in the same basis.
- several semi-empirical exchange-correlation potentials $V_{XC}\left[\rho\left(\mathbf{r}_i\right)\right]$ are available (see Section 2.2.2). Depending on the molecular system and the properties to study, different choices can be made. In particular, for few-electron molecules, LB94 and LDA functionals appear to reproduce quite well the photoelectron spectra [363]. In some cases, LB94 is better because it has been designed to describe accurately the asymptotic behavior of the potential at large distances (see Section 2.2.2).

The diagonalization provides a set of eigenvalues which correspond to the bound states if the energy is lower than the ionization threshold and to discretized continuum states otherwise.

Bound and continuum states vary strongly close to the nuclei and require a dense knot grid around the nuclei. Despite this fact, both kind of states

do not have the same properties and require different considerations for the parametrization of the basis:

- the bound wavefunctions spread spatially as the principal quantum number increases: the description of higher bound states implies a bigger box size
- continuum states vary at large scales: a rather large box (bigger than for bound states) is needed
- the asymptotic period of radial oscillations of the continuum wavefunctions decreases linearly with the square root of the energy: the description of higher continuum states requires a denser knot grid
- the density of calculated continuum states is directly related to the size of the box: the bigger the size, the better the energy resolution is.

The KS equations (2.54) are solved using a generalized diagonalization of the Hamiltonian. The resulting Kohn-Sham orbitals are expanded on the basis set and over each center:

$$\varphi_{npq} = \sum_{j=1}^{N_b^0} \sum_{h} \sum_{l}^{L_{max}^0} c_{npqhlj}^0 \xi_{pqhlj}^0 + \sum_{i=1}^{\kappa} \sum_{j=1}^{N_b^i} \sum_{h} \sum_{l}^{L_{max}^i} c_{npqhlj}^i \xi_{pqhlj}^i \tag{2.128}$$

where N_b^i is the number of B-spline functions for each shell. Here, n distinguishes the eigenvectors resulting from the diagonalization. In the continuum case, they are related to the energy ε and a new set of quantum numbers $\{hl\}$.

The continuum

The spectrum of the static-exchange DFT Hamiltonian comprises a point spectrum (or bound eigenvalues) located below the energy of the parent ion, and an essential spectrum (or continuum eigenvalues) above. The latter correspond to generalized eigenstates that do not belong to a Hilbert space but which nevertheless can be normalized as. In the following are described two main approaches used to obtain these continuum states with a correct normalization: the diagonalization and the Galerkin (or least-squares) approach.

The diagonalization If the basis set is restricted to those functions which vanish at the box boundary then the Hamiltonian restricted to the box is self-adjoint and can be diagonalized. This procedure selects those generalized stationary eigenfunctions which vanish at R_{max} and thus discretizes the continuum. The quality of this discretization is related to the energy spacing, then to the density of states:

$$\rho\left(\varepsilon_i\right) = \left.\frac{\partial n}{\partial E_n}\right|_{n=i} \tag{2.129}$$

For R_{max} sufficiently large, the continuum wavefunction can be approximated by a plane wave. Thus, the discretized spectrum approaches that of a free particle in a box:

$$\varepsilon_n \sim \frac{n^2\pi^2}{2R_{max}^2} \tag{2.130}$$

and the density can be approximately evaluated by:

$$\rho(\varepsilon) = \frac{R_{max}}{\pi\sqrt{2}}\frac{1}{\sqrt{\epsilon}} \tag{2.131}$$

Thus, density of states depends linearly on the box size. In a single-channel picture, the continuum wavefunction can be obtained at a specific energy by simply varying the size of the box according to Equation (2.130).

The Galerkin approach In this work, we use a generalization of the Ritz-Galerkin method originally developed to extract bound states. One of the advantage of this approach is that the continuum states do not vanishes at R_{max}^0 and are obtained for specific energies in a fix basis set [41]. The traditional Galerkin equations lead to the algebraic eigenvalue problem $(\mathbf{H} - E\mathbf{S})\,\mathbf{c} = 0$. For the continuous spectrum, the energy ε of the photoelectron is fixed and such equation does not admit non-trivial solutions $\mathbf{c} \neq 0$ anymore. Then, we have:

$$\mathbf{A}(\varepsilon)\,\mathbf{c} = a\mathbf{c} \tag{2.132}$$

where $A(\varepsilon) = \mathbf{H} - \varepsilon\mathbf{S}$. A solution proposed by Fischer and Idrees [123] is to take as approximate solutions the values of $\mathbf{c}$ that correspond to the eigenvalues closest to zero. In fact, it has been observed that the minimum modulus eigenvalue a of $\mathbf{A}$ is well separated from the others when the basis set is sufficiently dense and flexible to provide accurate solutions. For n coupled partial waves, always n eigenvalues are found with moduli smaller than the others. Due to the lack of boundary conditions, the matrix $\mathbf{A}$ is not Hermitian and the eigenvalues a and eigenvectors c are generally complex. Nevertheless, $\mathbf{A}$ is real, and they necessarily occur by conjugate pairs (a, c) and (a^*, c^*). Therefore, if all these solutions are associated to the same energy ε, it is possible to avoid complex representations by taking $\Re(\mathbf{c})$ and $\Im(\mathbf{c})$ as independents solutions. Eigenvectors are efficiently obtained by block inverse iteration [140] when the eigenvalues are known.

The set of calculated eigenfunctions $\{\varphi_\varepsilon\}$ forms a complete and independent set of stationary solutions. From these states, it is possible to form continuum states that are normalized and which fulfill prescribed scattering boundary conditions. In the next section, we will detail the theory which gives the correct normalization to apply to the continuum wavefunctions.

The method of partial waves The complete set of continuum states $\varphi_\varepsilon(\mathbf{r})$ resulting from the diagonalization of the Hamiltonian matrix is perfectly defined on the whole interval $\left[0, R^0_{max}\right]$. Nevertheless, as a result of the finite normalization of the basis elements, these continuum states are normalized to unity and then have to be renormalized to some analytical solutions at large distances (where the potential can be considered as Coulombian).

The electronic wavefunctions expanded in the B-spline basis sets can be split into a radial and angular function:

$$\varphi_{\varepsilon pqh'l'}(\mathbf{r}) = \sum_{i=0}^{\kappa} \sum_{h} \sum_{l}^{L^i_{max}} \sum_{k}^{N^i_a} P^k_{\varepsilon pqhlh'l'}(r_k)\, X^k_{pqhl}(\theta_k, \varphi_k) \tag{2.133}$$

where:

$$P^k_{\varepsilon pqhlh'l'}(r_k) = \sum_{j=1}^{N^i_b} c^k_{npqhlh'l'j} \frac{1}{r_k} B_j(r_k) \tag{2.134}$$

Only the OCE expansion is non-zero at large distances. Then, for R^0_{max} sufficiently large:

$$\varphi^-_{\varepsilon pqh'l'}(\mathbf{r}) \sim \sum_{l} P^0_{\varepsilon pqhlh'l'}(r)\, X^0_{pqhl}(\theta, \varphi) \tag{2.135}$$

Beyond R^0_{max}, the radial part of the outgoing wavefunction is assumed to be an eigenfunction of the Coulomb Hamiltonian $\acute{H}_c$. Therefore, the solution for $r > R^0_{max}$ can be expressed in terms of linear combinations of the regular $F_{\varepsilon l}(r)$ and irregular $G_{\varepsilon l}(r)$ Coulomb functions (see Appendix A.3) and which asymptotic behavior is described analytically by:

$$f_{\varepsilon l}(r) \xrightarrow{\rho\to\infty} \sqrt{\frac{2}{\pi k}} \frac{1}{r} \sin\left(\theta_l(\rho)\right) \tag{2.136}$$

$$g_{\varepsilon l}(r) \xrightarrow{\rho\to\infty} \sqrt{\frac{2}{\pi k}} \frac{1}{r} \cos\left(\theta_l(\rho)\right) \tag{2.137}$$

where:

$$\theta_l(\rho) = \rho - l\frac{\pi}{2} - \eta \log 2\rho + \sigma_l \tag{2.138}$$

σ_l is the Coulomb phase shift defines as a function of the Euler's gamma function Γ:

$$\sigma_l = \arg\Gamma(l + 1 + i\eta) \tag{2.139}$$

and $\rho = kr$.

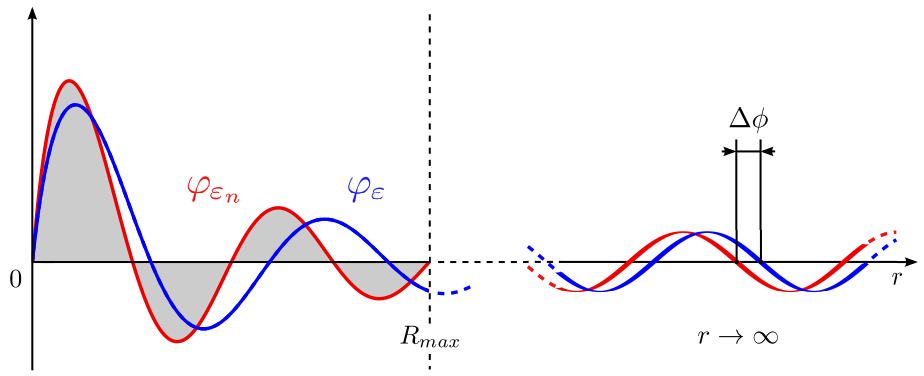

Figure 2.14: Schematic illustration of the phase shift $\Delta\phi$ at $r \to \infty$ between the Coulomb wavefunctions and the free ones.

$\Delta\phi = -\eta \log 2\rho + \sigma_l$ corresponds to the phase shift due to the Coulomb potential (see Figure 2.14).

The continuum states resulting from the diagonalization should then satisfy boundary conditions of the form:

$$\lim_{r\to\infty} P^0_{\varepsilon pqh'l'}(r) = \sum_{hl} a_{pqhlh'l'} f_{\varepsilon l}(r) + b_{pqhlh'l'} g_{\varepsilon l}(r) \tag{2.140}$$

where the coefficients $a_{npqhlh'l'}$ and $b_{npqhlh'l'}$ define two matrices $\mathbf{A}$ and $\mathbf{B}$ that can be determined by fitting the obtained solutions to linear combinations of the asymptotic regular and irregular functions.

We define the K-matrix as:

$$\mathbf{K} = \mathbf{B}\mathbf{A}^{-1} \tag{2.141}$$

The K-matrix is related to the usual scattering matrix S (see Appendix A.2) through the equation:

$$\mathbf{I} - i\mathbf{K} = (\mathbf{I} + i\mathbf{K})\,\mathbf{S} \tag{2.142}$$

and the K-matrix eigenvalues k_l to the phase shift δ_l due to the short-range potential:

$$k_l = \tan\delta_l \tag{2.143}$$

The continuum states are linear combinations of functions that depends on h and l. In other words, the continuum states are degenerate in energy and for each ε, specific couplings of $\{hl\}$ channels can be found in order to get the correct normalization. $f_{\varepsilon l}(r)$ and $g_{\varepsilon l}(r)$ are used to fit the calculated

continuum wavefunction through the K-matrix elements k_{npqhl}:

$$\varphi_{\varepsilon pqh'l'}\left(R^0_{max},\theta_0,\varphi_0\right)=\sum_{hl}\left[\delta_{pqhlh'l'}f_{\varepsilon l}\left(R^0_{max}\right)+k_{pqhlh'l'}g_{\varepsilon l}\left(R^0_{max}\right)\right]X^0_{pqhl}\left(\theta_0,\varphi_0\right) \tag{2.144}$$

$$\begin{aligned}&\left.\frac{\partial\varphi_{\varepsilon pqh'l'}\left(r,\theta_0,\varphi_0\right)}{\partial r}\right|_{r=R^0_{max}} \\ &=\left[\delta_{pqhlh'l'}\left.\frac{\partial f_{\varepsilon l}\left(r\right)}{\partial r}\right|_{r=R^0_{max}}+k_{pqhlh'l'}\left.\frac{\partial g_{\varepsilon l}\left(r\right)}{\partial r}\right|_{r=R^0_{max}}\right]X^0_{pqhl}\left(\theta_0,\varphi_0\right)\end{aligned} \tag{2.145}$$

The latter Equations correspond to the so-called K-normalization. Since the K-matrix is real, numerical implementation is easier. Finally, the computed continuum wavefunctions $\tilde{\varphi}_{\varepsilon hl}$ are renormalized to the correct boundary conditions by using the two following transformations:

$$\varphi_{\varepsilon l}\left(\mathbf{r}\right)=\tilde{\varphi}_{\varepsilon l}A^{-1} \tag{2.146}$$

$$\varphi^-_{\varepsilon l}\left(\mathbf{r}\right)=\varphi_{\varepsilon l}\left(\mathbf{r}\right)\left(\mathbf{I}-i\mathbf{K}\right)^{-1} \tag{2.147}$$

A necessary condition for the method to work is that the basis set must reproduce the asymptotic region. This condition can be easily satisfied with B-splines by choosing a box size large enough to contain a significant part of the asymptotic region. Dipole matrix elements are calculated from the solution of the SCF calculation for each angular momentum l, as a function of the photoelectron energy and the internuclear distance.

Time-dependent DFT

The DFT method described in the previous paragraphs may be inappropriate when the coupling between different ionization channels is important and/or when singly- or doubly-excited Feshbach resonances in which electron correlation have an important contribution. An alternative procedure (generally more accurate) is to use TDDFT at the first order of perturbation theory (i.e., as a linear response). The TDDFT approach makes use of many ingredients from the TIDFT method, and for this reason, we refer the reader to Section 2.2.3 or [358, 365] for a more complete theoretical overview.

Compared to TIDFT, the TDDFT approach permits to introduce couplings between the treated photoionization channels and some single excitation transitions. The electronic wavefunction is then described by a linear combination of determinants including single excitations:

$$\psi_{\varepsilon\alpha pqhl}\left(\mathbf{r},R\right)=\sum_{\alpha'}^{N_c}\Theta\left[\psi_\alpha\left(\mathbf{r_1},\mathbf{r_2},\cdots,\mathbf{r_{N-1}},R\right)\varphi_{\varepsilon pqhl}\left(\mathbf{r_N},R\right)\right] \tag{2.148}$$

where N_c corresponds to the number of open channels.

The interchannel mixing is visible in the cross section by the emergence of relatively sharp structures (compared to the shape resonance) appearing at photon energies corresponding to the coupled single-excitations. As illustrated in Figure 2.15, each photoionization channel can couple with single-excitation transitions from a state lower in energy. For this reason, core photoionization cross sections are much less affected by the inclusion of interchannel couplings and a TDDFT calculation of the lowest core orbital photoionization gives equivalent results than TIDFT.

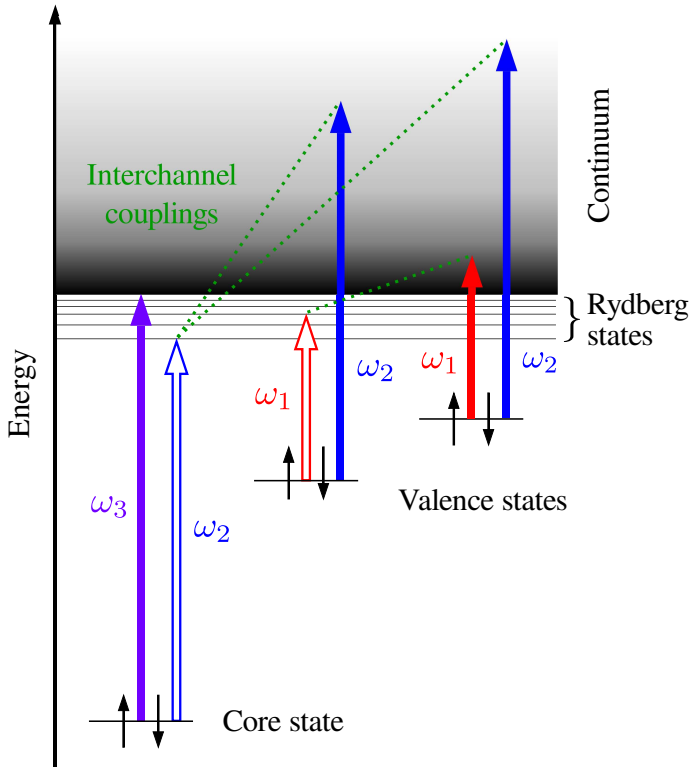

Figure 2.15: Illustrative scheme of the interchannel couplings between the different photoionization channels (filled arrows) and some single-excitation transitions (unfilled arrows).

A comparison of the relevant equations shows that sophisticated methods such as the random phase approximation (RPA) is formally equivalent to linear TDDFT, from which it can be obtained by replacing V_{xc} matrix elements by the exchange integrals used in RPA. In general, the v_{xc} potential provides a better description of electron correlation and, for this reason, TDDFT is sometimes a bit more accurate than RPA at a substantially lower computational

cost, and is often comparable to more sophisticated approaches. It must be stressed however that, although interchannel coupling and singly excited autoionizations are included, double or higher electron excitations are presently outside the scope of the approach. In many cases, the local density approximation is appropriate to treat photoabsorption processes in "small" systems (in atoms [444] as well as in molecules [45, 290, 11, 394, 361, 395, 365, 393]).

In spite of this, there is an important warning to make when slow-decaying Feshbach resonances come into play. In many cases, the autoionization lifetimes of these resonances are comparable or even larger than the time employed by the nuclei to move significantly. Under these circumstances, the use of the Born-Oppenheimer approximation is not justified and may lead to wrong results. This has been clearly shown in the case of the autoionization decay of H_2 [242], for which an accurate description of the experimental findings in the region of the autoionizing doubly-excited states requires going beyond the Born-Oppenheimer approximation. Therefore, although the TDDFT approach will always do a better job than the DFT one in describing correlations due to the coupling between different open ionization channels, it is not guaranteed that it will do so when slow decaying Feshbach resonances are involved.

3. Vibrational structure

3.1 General theory

3.1.1 Classical treatment

For polyatomic molecules, the classical kinetic energy of the nuclei in the cartesian coordinates is written:

$$T = \frac{1}{2}\sum_{i=1}^{M} m_i \dot{\mathbf{r}}_\mathbf{i}^2 \tag{3.1}$$

where $\dot{\mathbf{r}}_\mathbf{i}$ is the position of the nucleus i. The use of mass-weighted coordinates q_i makes the expression of the kinetic energy simpler:

$$T = \frac{1}{2}\sum_{i=1}^{3M} \left(\frac{dq_i}{dt}\right)^2 \tag{3.2}$$

where:

$$\begin{aligned} q_1 &= \sqrt{m_1}\,(x_1 - x_{1,e}) \\ q_2 &= \sqrt{m_1}\,(y_1 - y_{1,e}) \\ q_3 &= \sqrt{m_1}\,(y_1 - z_{1,e}) \\ q_4 &= \sqrt{m_2}\,(x_2 - x_{2,e}) \\ &\vdots \\ q_{3M} &= \sqrt{m_N}\,(z_N - z_{N,e}) \end{aligned} \tag{3.3}$$

The vibrational motion of the molecule is controlled by its potential energy surface $V(q_1, q_2, \cdots, q_{3M})$ which is obtained, in the Born-Oppenheimer approximation, by solving the electronic TISE in a grid of $3N$ nuclear coordinates.

This potential can be expanded as a Taylor series around the equilibrium values of the nuclear coordinates:

$$V\left(q_1, q_2, \cdots, q_{3M}\right) = V_e + \sum_{i=1}^{3M}\left(\frac{\partial V}{\partial q_i}\right)_e + \frac{1}{2}\sum_{i=1}^{3M}\sum_{j=1}^{3M}\left(\frac{\partial^2 V}{\partial q_i \partial q_j}\right)_e q_i q_j + \frac{1}{3!}\sum_{i=1}^{3M}\sum_{j=1}^{3M}\sum_{k=1}^{3M}\left(\frac{\partial^3 V}{\partial q_i \partial q_j \partial q_k}\right)_e q_i q_j q_k + \cdots \quad (3.4)$$

By convenience, we choose $V_e = 0$. Noticing that since V_e is a minimum, the first derivative is equal to zero, and truncating the Taylor expansion to the quadratic term, we can write:

$$V\left(q_1, q_2, \cdots, q_{3M}\right) = \frac{1}{2}\sum_{i=1}^{3M}\sum_{j=1}^{3M} u_{ij} q_i q_j \quad (3.5)$$

where u_{ij} correspond to the harmonic force constants:

$$u_{ij} = \left(\frac{\partial^2 V}{\partial q_i \partial q_j}\right)_e \quad (3.6)$$

The kinetic and potential energies can be expressed as a function of the mass-weighted coordinates matrix $\mathbf{q}$ and the square matrix of the force constants $\mathbf{U}$:

$$T = \frac{1}{2}\dot{\mathbf{q}}^T\dot{\mathbf{q}} \quad (3.7)$$

$$V = \frac{1}{2}\mathbf{q}^T\mathbf{U}\mathbf{q} \quad (3.8)$$

By using the second law of Newton, it is easily demonstrable that $\mathbf{U}$ satisfies the equation:

$$\ddot{\mathbf{q}} + \mathbf{U}\mathbf{q} = 0 \quad (3.9)$$

However, the set of differential equations in (3.9) is coupled, i.e. that the second derivative of each coordinate q_i depends on all the other coordinates. These couplings complicate the resolution of Equation (3.9), but they can be eliminated by choosing an appropriate change of variable.

By using the transformation $\mathbf{q} = \mathbf{L}\mathbf{Q}$, where $\mathbf{Q}$ is a vector containing a new set of variables and $\mathbf{L}$ is the transformation matrix, it is possible to rewrite Equation (3.10) as:

$$V = \frac{1}{2}\left(\mathbf{L}\mathbf{Q}\right)^T\mathbf{U}\mathbf{L}\mathbf{Q} = \frac{1}{2}\mathbf{Q}\mathbf{L}^T\mathbf{U}\mathbf{L}\mathbf{Q} \quad (3.10)$$

Then, the eigenvalues matrix equation of $\mathbf{U}$ is given by:

$$\mathbf{U}\mathbf{L} = \mathbf{L}\mathbf{\Lambda} \quad (3.11)$$

where Λ is the diagonal matrix of eigenvalues.

Since $\mathbf{U}$ is Hermitian, its eigenvectors matrix $\mathbf{L}$ is orthonormal and we have:

$$\mathbf{L}^T\mathbf{U}\mathbf{L} = \mathbf{\Lambda} \tag{3.12}$$

Then the potential energy becomes:

$$V = \frac{1}{2}\mathbf{Q}^T\mathbf{\Lambda}\mathbf{Q} \tag{3.13}$$

which can be developed as:

$$V = \frac{1}{2}\sum_{i=1}^{3M}\lambda_i Q_i^2 \tag{3.14}$$

where λ_i are the eigenvalues from the diagonal matrix $\mathbf{Q}$.

Equivalently, Equation (3.7) can be reformulated as a function of the matrix $\mathbf{Q}$:

$$\begin{aligned}\mathbf{T} &= \frac{1}{2}\dot{\mathbf{q}}^T\dot{\mathbf{q}} = \frac{1}{2}\left(\mathbf{L}\dot{\mathbf{Q}}\right)^T\mathbf{L}\dot{\mathbf{Q}} \\ &= \frac{1}{2}\dot{\mathbf{Q}}^T\mathbf{L}^T\mathbf{L}\dot{\mathbf{Q}} = \frac{1}{2}\dot{\mathbf{Q}}^T\mathbf{L}^{-1}\mathbf{L}\dot{\mathbf{Q}} \\ &= \frac{1}{2}\dot{\mathbf{Q}}^T\dot{\mathbf{Q}}\end{aligned} \tag{3.15}$$

which can be developed as:

$$T = \frac{1}{2}\sum_{i=1}^{3M}\left(\frac{dQ_i}{dt}\right)^2 \tag{3.16}$$

We know that $\mathbf{q} = \mathbf{L}\mathbf{Q}$ and according to Equation (3.11) $\mathbf{U} = \mathbf{L}\mathbf{\Lambda}\mathbf{L}^{-1}$. Introducing these two expressions in Equation (3.9), we obtain:

$$\mathbf{L}\left(\ddot{\mathbf{Q}} + \mathbf{\Lambda}\mathbf{Q}\right) = 0 \tag{3.17}$$

The eigenvalues λ_i are generally non-zero and Equation (3.18) cancels when:

$$\ddot{\mathbf{Q}} + \mathbf{\Lambda}\mathbf{Q} = 0 \tag{3.18}$$

The latter equation can be reformulated as:

$$\frac{d^2Q_i}{dt^2} + \lambda_i Q_i = 0 \quad i = 1, \cdots, 3M \tag{3.19}$$

The new set of equations is now completely decoupled, and each equation of (3.19) involve only one coordinate Q_i called normal coordinate. These equations describe the normal modes for any polyatomic systems. For molecules composed by more than three atoms, solutions are uneasy to obtain. However, many of their characteristics can be deduced by simple theoretical considerations based on group theory. Equation (3.3) and (3.7) teach us that the vibrational normal modes depend on the molecular symmetry, the nuclear masses and the force constants. As a consequence, the simple knowledge of the molecular formula gives already an idea of the relative nature of the molecular vibration:

- the heavier the atoms, the lower the vibrational frequency
- the stronger the force constants, the higher the vibrational frequency

The total number of active normal modes is in fact not $3M$ because some of them are equivalent to translational or rotational motions. Then, they have to be removed from the count of normal modes, and depending on the geometry of the molecules, the total number of normal modes can be:

- $3M-5$ for linear molecules (-3 translational modes, -2 rotational modes)
- $3M-6$ for non-linear molecules (-3 translational modes, -3 rotational modes)

Also, a deeper theoretical analysis of the different normal modes can be made by using group theory (see section 4.3).

3.1.2 Quantum treatment

In order to treat the nuclear motion in the quantum mechanics formalism, we first have to give a formulation to the vibrational Hamiltonian. It can be demonstrated (see for example [307]) that using the classical definitions (3.14) and (3.16), the vibrational Hamiltonian operator for a non-linear polyatomic molecule is given by:

$$\hat{H}_{vib} = \hat{T} + \hat{V} = \frac{1}{2}\sum_{i=1}^{3M-6}\left(\frac{d\hat{Q}_i}{dt}\right)^2 + \frac{1}{2}\sum_{i=1}^{3M-6}\lambda_i Q_i^2 \tag{3.20}$$

By using the transformation $\mathbf{q} = \mathbf{LQ}$, the kinetic energy operator can be rewritten as:

$$\frac{d\hat{Q}_i}{dt} = -i\hbar\sum_{j=1}^{3M} l_{ij}\frac{\partial}{\partial q_j} \tag{3.21}$$

According to the chain rule:

$$\frac{\partial}{\partial Q_i} = \sum_{j=1}^{3M}\frac{\partial}{\partial q_j}\frac{\partial q_j}{\partial Q_i} = \sum_{j=1}^{3M} l_{ij}\frac{\partial}{\partial q_j} \tag{3.22}$$

Then, the vibrational Hamiltonian operator reads:

$$\hat{H}_{vib} = -\frac{\hbar^2}{2}\sum_{i=1}^{3M-6}\frac{\partial^2}{\partial Q_i} + \frac{1}{2}\sum_{i=1}^{3M-6}\lambda_i Q_i^2 = \sum_{i=1}^{3M-6}\hat{h}_i \tag{3.23}$$

Equation (3.23) shows that the vibrational Hamiltonian can be split in terms of decoupled $\hat{h}_i$ in such way that the nuclear wavefunctions $\chi_{v_i}(Q_i)$ are eigenfunctions of the eigenvalues equation:

$$\hat{h}_i\chi_{v_i}(Q_i) = \varepsilon_{v_i}\chi_{v_i}(Q_i) \tag{3.24}$$

with:

$$\hat{h}_i = -\frac{\hbar^2}{2}\frac{\partial^2}{\partial Q_i} + \frac{1}{2}\lambda_i Q_i^2 \tag{3.25}$$

Due to the approximation used to develop the potential (3.5), the previous formulation of the Hamiltonian corresponds to the unidimensional harmonic oscillator whose eigenfunctions and eigenvalues are respectively:

$$\chi_{v_i}(Q_i) = \left(\frac{\alpha_i}{\pi}\right)^{\frac{1}{4}}(2^{v_i}v_i)^{-\frac{1}{2}}\,e^{-\alpha_i\frac{Q_i^2}{2}}H_{v_i}(\sqrt{\alpha_i}Q_i) \tag{3.26}$$

$$\varepsilon_{v_i} = \left(v_i + \frac{1}{2}\right)\hbar\omega_i \quad v_i = 0, 1, 2, \cdots \tag{3.27}$$

where the first Hermite polynomials are:

$$H_0(x) = 1 \tag{3.28}$$
$$H_1(x) = 2x \tag{3.29}$$
$$H_2(x) = 4x^2 - 1$$
$$H_3(x) = 8x^3 - 12$$

$$\text{and} \quad \alpha_i = \frac{\sqrt{\lambda_i}}{\hbar} = \frac{\omega_i}{\hbar} = \frac{2\pi\nu_i}{\hbar} \quad \text{since} \quad \omega_i = 2\pi\nu_i = \sqrt{\lambda_i} \tag{3.30}$$

v_i corresponds to the vibrational quantum number associated with the normal mode i and ω_i to its vibrational frequency.

The total vibrational wavefunction is given by:

$$\psi_{vib} = \prod_{i=1}^{3M-6}\chi_{v_i}(Q_i) \tag{3.31}$$

and the total vibrational energy:

$$E_{vib} = \sum_{i=1}^{3M-6} \varepsilon_{v_i} \tag{3.32}$$

In the harmonic approximation it is possible to decouple the Hamiltonian for each normal mode. Also, even though one of the vibrational mode is strongly anharmonic, it still can be decoupled from the others, assuming that the rest lays in the harmonic approximation. In the following, we will suppose that the studied processes occur in such regime and consider Equation (3.24) as a general formula for the vibrational problem.

The vibrational ground state (also called the zero-point energy) is defined by the set of quantum numbers $(v_1, v_2, \cdots, v_{3M-6}) = (0, 0, \cdots, 0)$. When two or several normal modes have the same symmetry and describe equivalent vibrational motions, then their frequencies v_i are equal and the molecule have degenerated vibrational energies. Quasi-degeneration can occurs when a vibrational frequency is accidentally the multiple of one or several other ones (e.g., the asymmetric stretching, the asymmetric bending and the symmetric stretching in CH_4^+ [209]).

Typical vibrational frequencies are of the order of 100 meV, which correspond to a temperature close to 290 K. At room temperature, therefore, the population of any state other than the ground state is entirely negligible. It can be shown using the Boltzmann distribution:

$$p_i = \frac{n_i}{N} = \frac{e^{-\beta E_i}}{\sum_j e^{-\beta E_j}} \tag{3.33}$$

where $\beta = (k_B T)^{-1}$ and k_B is the Boltzmann constant.

In the harmonic approximation, the vibrational energies progression is given by Equation (3.27). Then we have:

$$p_{v_i} = \frac{e^{-\beta\left(v_i + \frac{1}{2}\right)\hbar\omega_i}}{\sum_{v_i'} e^{-\beta\left(v_i' + \frac{1}{2}\right)\hbar\omega_i}} \tag{3.34}$$

This formula gives an idea of the statistical distribution of the molecules among the different vibrational levels at the standard experimental conditions. Table 3.1 shows the first values obtained for the highest and lowest vibrating molecules studied in this work (the distributions of all the other molecules varying as a function of their respective harmonic frequencies between these two limits). In both cases, the energetic distribution is widely dominated by the first vibrational level for every normal mode of vibrations and molecules

Molecule	Sym. i	Deg. μ	Frequency ν_i (cm^{-1})	Population per v_i (%)		
				0	1	2
H_2	Σ_g^+	1	4395	99.999	6.088×10^{-8}	3.706×10^{-17}
SF_6	A_{1g}	1	835.831	98.232	1.736	3.069×10^{-2}
	E_g	2	658.346	95.835	3.991	1.662×10^{-1}
	T_{1g}	3	702.391	96.633	3.253	1.095×10^{-1}
	T_{1u}	3	1051.865	99.377	6.190×10^{-1}	3.856×10^{-3}
	T_{2g}	3	563.563	93.418	6.148	4.046×10^{-1}
	T_{2u}	3	379.738	84.014	13.431	2.147

Table 3.1: Vibrational distribution of H_2 and SF_6. For SF_6, frequencies have been calculated at the Hartree-Fock *ab initio* level with a 6-311G(d)+p basis set. The internuclear distances have been set to 1.5867 Å according to [376] and the first vibrational frequency is in good agreement with the value reported in the same article.

can be assumed to be initially in their ground state $(0, 0, \cdots, 0)$ when photoionization occurs.

We have seen that it is reasonable to consider the former molecules in their ground states. For all the systems studied in this work, the totally symmetric stretching modes associated with the ionized molecules are predominantly populated. Then, by taking into account the effects of other possible processes such as the post-collision interaction (PCI)[1] or the recoil momentum of the photoelectron (see Section 5.3.1), it is possible to extract experimentally the spectrum that corresponds to the particular vibronic transition between the ground state and the cation in its totally symmetric stretching vibrational mode. From a theoretical point of view, excitation of a single vibrational mode reduces the nuclear motion to a one-dimensional problem: since the vibrational states are decoupled (in the harmonic approximation), the inactive vibrational modes can be treated separately and the nuclear motion is assumed to be described by the active vibrational mode which, in the case of the totally stretching mode, depends only on the internuclear coordinate R.

3.1.3 The nuclear motion Schrödinger equation in 1D

In the following section, we will treat the case of the diatomic molecule whose vibrational structure is formally equivalent to the uncoupled totally symmetric

[1]The PCI line shapes are observable at low photoelectron energies and are due to the interaction of the photoelectron with the subsequent Auger electron: when Auger electrons are emitted faster than photoelectrons, the latter feel a partially screened ionic field and decelerate. A kinetic energy transfer takes place and consequently induces an energetic shift in the fine structure, positive for the Auger spectrum and negative for the photoelectron spectrum. Also, a certain asymmetry of the vibrational peaks is reported.

stretching mode of polyatomic molecules. For a system whose nuclear motion depends on the coordinate $\mathbf{R}$, the nuclear Hamiltonian reads:

$$\hat{H}_{nuc}(\mathbf{R}) = -\frac{1}{2M}\nabla^2_{CM} - \underbrace{\frac{1}{2\mu}\nabla^2_{AB} + V(\mathbf{R})}_{\hat{H}_{int}} \tag{3.35}$$

where M is the total mass of the system and μ the reduced mass.

In this last formulation, we can clearly see that the kinetic energy is composed by a translational movement of the center of mass (CM) and an internuclear motion (AB). The translational part is not quantized and just contribute by adding a constant energy to the the eigenvalues of the nuclear time-independent Schrödinger equation. Let therefore concentrate on the secular equation for the internal Hamiltonian $\hat{H}_{int}$:

$$\hat{H}_{int}\psi_{int}(\mathbf{R}) = E_{int}\psi_{int}(\mathbf{R}) \tag{3.36}$$

The internal Hamiltonian can also be written in polar coordinates:

$$\left[-\frac{\hbar^2}{2\mu}\left(\frac{\partial^2}{\partial R^2} + \frac{2}{R}\frac{\partial}{\partial R}\right) + \frac{\hat{L}^2}{2\mu R^2} + V(R)\right]\psi_{int}(R,\theta,\phi) = E_{int}\psi_{int}(R,\theta,\phi) \tag{3.37}$$

where $\hat{L}^2$ is the square of the total angular momentum operator which commutes with the Hamiltonian $\hat{H}_{int}$.

Thus, the eigenfunctions $\psi_{int}(\mathbf{R})$ are also eigenfunctions of $\hat{L}^2$:

$$\hat{L}^2\psi_{int}(\mathbf{R}) = J(J+1)\hbar^2\psi_{int}(\mathbf{R}) \qquad J = 0, 1, 2, \ldots \tag{3.38}$$

and:

$$\hat{L}_z\psi_{int}(\mathbf{R}) = M\hbar\psi_{int}(\mathbf{R}) \qquad M = -J, -J+1, \ldots, J-1, J \tag{3.39}$$

where J and M are the quantum numbers associated to the angular momentum operators.

We can write without any approximations the eigenfunctions $\psi_{int}(\mathbf{R})$ as a product of a radial part $\chi(R)$ and spherical harmonics $Y^M_J(\theta,\phi)$:

$$\psi_{int}(R,\theta,\phi) = \chi(R)\, Y^M_J(\theta,\phi) \tag{3.40}$$

In the Eckart conditions [432], it is possible to separate the vibrational motion (dependence on R) from the rotational one (dependence on the angles). Rotational motion can be neglected since the order of the rotational

quantum is relatively small ($\sim 10^{-4} - 10^{-3}$eV). Then, the TISE associated to the vibrational motion is:

$$\hat{H}_{vib}(R)\,\chi(R) = E_{vib}\chi(R) \tag{3.41}$$

where:

$$\hat{H}_{vib}(R) = -\frac{\hbar^2}{2\mu}\left(\frac{d^2}{dR^2} + \frac{2}{R}\frac{d}{dR}\right) + V(R) \tag{3.42}$$

By rewriting:

$$\chi(R) = \frac{\zeta(R)}{R} \tag{3.43}$$

one can considerably simplify the TISE for the vibrational motion to:

$$\left[-\frac{\hbar^2}{2\mu}\frac{d^2}{dR^2} + V(R)\right]\zeta(R) = E_{vib}\zeta(R) \tag{3.44}$$

As mentioned previously, Equation (3.44) is also valid for polyatomic molecules when the vibrational motion can be reduced to a one-dimensional problem. The Lagrangian of a N-body system is given by:

$$L = \sum_{i=1}^{N} m_i \dot{\mathbf{r}}_i^2 - V(\mathbf{r}_1, \mathbf{r}_2, \cdots, \mathbf{r}_N) \tag{3.45}$$

We consider the particular case of high symmetry molecules such as CH_4, CF_4, BF_3 or SF_6 for which the central atom coincides with the center of mass. In such systems, the totally symmetric vibration corresponds to a displacement of the N_s equivalent surrounding atoms by a same quantity R with respect to the central atom. Then, the Lagrangian can be rewritten as:

$$L = \sum_{i=1}^{N_s} m_i \dot{R}_1^2 - V(R) \tag{3.46}$$

the reduced mass is then given by:

$$\mu = N_s m_s \tag{3.47}$$

where m_s is the mass of the equivalent surrounding atoms.

Except for acetylene which is a diatomic-like molecule when the C-H bond is considered as fixed, the reduced mass of all the mentioned polyatomic molecules in their breathing mode is given by Equation (3.47) (for a detailed description of the reduced mass used in this work, see Table B.2).

3.2 Vibrational eigenfunctions and eigenvalues

The B-splines method

A very efficient method to solve the Schrödinger equation for the vibrational motion, Equation (3.44), makes use of B-spline basis sets. The method, first implemented to study molecular vibrations by F. Martín *et al.* [242] has been successfully applied to several ionization problems in H_2 [318, 320, 125, 126, 243, 118, 276, 117, 119, 323, 181, 180].

In this method, the radial wavefunction is expanded on a B-spline basis set defined on the interval $I = [0, R_{max}]$:

$$\zeta(R) = \sum_{i}^{N} c_i B_i(R) \tag{3.48}$$

Substituting (3.48) in (3.42), we obtain the secular equation (written in its matrix form):

$$\mathbf{Hc} = E\mathbf{Sc} \tag{3.49}$$

where the matrix elements of the Hamiltonian are given by:

$$H_{ij} = \int_0^{R_{max}} B_i(R) H_{vib} B_j(R) dR \tag{3.50}$$

and those of the overlap matrix by:

$$S_{ij} = \int_0^{R_{max}} B_i(R) B_j(R) dR \tag{3.51}$$

B-splines are not orthogonal, yet the overlap matrix is band-diagonal and therefore well conditioned. All the integrals involved in the matrix can be computed exactly with a Gauss-Legendre integration method on a finite grid. The secular equation is solved using a standard matrix diagonalization which provides the eigenfunctions and the eigenvalues of Equation (3.38).

Its resolution requires knowing the effective potential energy term $V(R)$, which has to be calculated separately, by solving the electronic TISE. It can be done by using *ab initio* methods (see Section 2.1) or derived from spectroscopic parameters as for the Morse potential.

The Morse potential

Simple models have been widely used to approximate PECs. They are particularly useful when *ab initio* calculations are not feasible or do not properly describe the system. The Morse potential is an analytical function which can

model PECs in the region close to the equilibrium geometry.

As shown in Section 3.1.2, the PEC associated with an uncoupled vibrational mode can be described by a harmonic potential. However, it is clear that such approximation is too drastic to describe correctly the vibrational states that do not lie in the very bottom of the PEC.

Taking into account the general behavior of the diatomic PECs (boundary conditions, value at $R = R_e$, etc.), Philip M. Morse proposed in 1929 [261] a simple semi-empirical formula that goes beyond the harmonic approximation and which depend only on three parameters:

$$V_M(R) = V(R_e) + D_e \left[1 - e^{-\alpha(R-R_e)}\right]^2 \tag{3.52}$$

where the well depth D_e is given by the Birge-Spooner formula:

$$D_e = \frac{\omega_e^2}{4\omega_e X_e} - \frac{\omega_e X_e}{4} \simeq \frac{\omega_e^2}{4\omega_e X_e} \tag{3.53}$$

and:

$$\alpha = \sqrt{\frac{k_e}{2D_e}} = 2\pi\omega_e \sqrt{\frac{\mu}{2D_e}} \tag{3.54}$$

ω_e corresponds to the harmonic frequency and X_e an anharmonicity correction.

The eigenvalues of the Schrödinger equation can also be extracted analytically, developing the radial functions in term of Laguerre polynomials [261]. The final expression for the energy is:

$$\varepsilon_v \sim \omega_e \left(v + \frac{1}{2}\right) - \omega_e X_e \left(v + \frac{1}{2}\right)^2 \tag{3.55}$$

$$\sim \omega_e \left(v + \frac{1}{2}\right) \left[1 - X_e \left(v + \frac{1}{2}\right)\right] \tag{3.56}$$

In the Morse model the anharmonicity constant X_e is given by:

$$X_e = \frac{\omega_e}{4D_e} \tag{3.57}$$

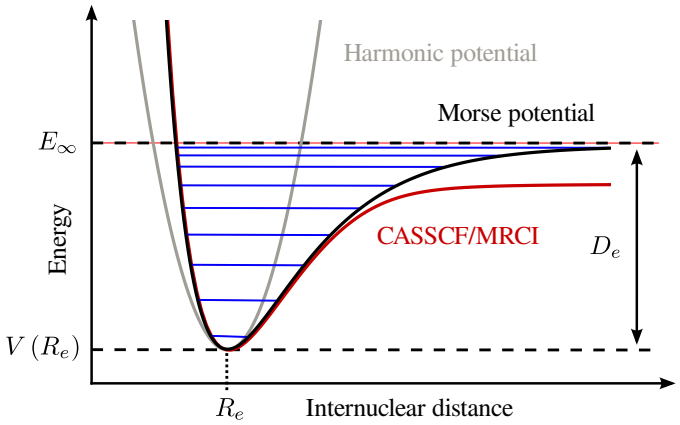

Figure 3.1: Comparison between harmonic, Morse and CASSCF/MRCI PECs.

In Figure 3.1, we present a comparison between a harmonic potential, a Morse potential and a PEC obtained at the CASSCF-MRCI theory level (the latter being considered as the correct reference). It is visible that the harmonic oscillator only accurately describes the bottom of the PEC at the internuclear equilibrium distance. The Morse potential has a much better agreement with the accurate CASSCF/MRCI calculation, although the two curves diverge for both small and large internuclear distances.

In practice, Morse potentials are built using experimental data. The typical spectroscopic parameters required to compute Morse potential are the harmonic vibrational frequency ω_e, the anharmonic term X_e and the internuclear distance at the equilibrium R_e. Morse potentials have been used to compute the vibrational wavefunctions for the ground and core ionized states of N_2, CO, CH_4, BF_3 and for the $4T_{1u}^{-1}$ inner-valence state of SF_6 (see PECs in Results Part). Some of the Morse parameters used to derive them are shown in Table B.3.

4. Calculation of the cross section

4.1 General definition

Once the vibrational wavefunctions and the dipole matrix elements are calculated, cross section is computed easily by using Equation (1.37). For randomly oriented diatomic molecule interacting with a linear polarized light, and in the Born-Oppenheimer approximation, the vibrationally resolved cross section in atomic units is given by:

$$\sigma_\alpha\left(v,v',\omega\right)=\frac{4\pi^2\omega}{3c}\left|\iint\chi^*_{i,v}\left(R\right)\psi^*_i\left(\mathbf{r},R\right)\hat{d}\psi_{f_\alpha+e^-(\varepsilon)}\left(\mathbf{r},R\right)\chi_{f_\alpha,v'}\left(R\right)dRd\mathbf{r}\right|^2 \tag{4.1}$$

i and f_α stand for the initial and final states respectively. α denotes the electronic state of he residual ion, χ is the vibrational wavefunction and ψ the electronic wavefunction. v and v' are respectively the initial and final vibrational quantum number. ω is still the photon energy and ε is the photoelectron energy.

The dipole moment operator $\hat{d}$ is in fact the sum of the electronic and the nuclear dipoles:

$$\hat{d}=\hat{d}_{el}+\hat{d}_{nuc} \tag{4.2}$$

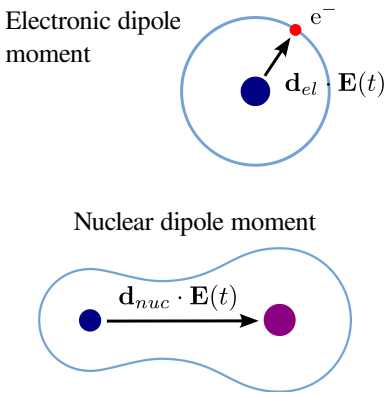

Figure 4.1: Schematic illustration of the electronic and nuclear dipole moment

Thus, Equation 4.1 becomes:

$$\begin{aligned}&\sigma_\alpha\left(v,v',\omega\right)\\&=\frac{4\pi^2\omega}{3c}\left|\int\chi_{i,v}^*\left(R\right)\chi_{f_\alpha,v'}\left(R\right)\left[\int\psi_i^*\left(\mathbf{r},R\right)\hat{d}_{el}\psi_{f_\alpha+e^-(\varepsilon)}\left(\mathbf{r},R\right)d\mathbf{r}\right]dR\right.\\&\left.+\int\chi_{i,v}^*\left(R\right)\hat{d}_{nuc}\chi_{f_\alpha,v'}\left(R\right)\left[\int\psi_i^*\left(\mathbf{r},R\right)\psi_{f_\alpha+e^-(\varepsilon)}\left(\mathbf{r},R\right)d\mathbf{r}\right]dR\right|^2\end{aligned}\tag{4.3}$$

For molecules without center of inversion, the nuclear dipole is non-zero (see Figure 4.1). Nevertheless, $\psi_i^*\left(\mathbf{r},R\right)$ and $\psi_{f_\alpha+e^-(\varepsilon)}\left(\mathbf{r},R\right)$ are eigenfunctions of the electronic Hamiltonian $\hat{H}_{el}$ with different eigenvalues. They are orthogonal and the second integral of the second term of the Equation (4.3) cancel out:

$$\int\psi_i^*\left(\mathbf{r},R\right)\psi_{f_\alpha+e^-(\varepsilon)}\left(\mathbf{r},R\right)d\mathbf{r}=0\tag{4.4}$$

Thus, the single photoionization cross section only depends on the electronic transition dipole moment d_{el}:

$$\sigma_\alpha\left(v,v',\omega\right)=\frac{4\pi^2\omega}{3c}\left|\int\chi_{i,v}^*\left(R\right)T_\alpha\left(\varepsilon,R\right)\chi_{f_\alpha,v'}\left(R\right)dR\right|^2\tag{4.5}$$

where $T_\alpha\left(\varepsilon,R\right)$ is a function of the internuclear distance R and the photoelectron energy ε:

$$T_\alpha\left(\varepsilon,R\right)=\int\psi_i^*\left(\mathbf{r},R\right)\hat{d}_{el}\psi_{f_\alpha+e^-(\varepsilon)}\left(\mathbf{r},R\right)d\mathbf{r}\tag{4.6}$$

4.2 Angular distribution

More insight on the photoionization process can be gained looking at the photoelectron angular distribution (PAD). Such spatial information is a sensitive probe of the structure and dynamics of electronic continua. It corresponds to an angular resolution of the cross sections that can be done in the laboratory frame or in the molecular frame (MFPAD). The laboratory frame angular distribution could have been resolved experimentally already in the 70's because measurement techniques are similar to the ones used in more traditional spectroscopy. It is generally express as a parameter β which characterizes the asymmetry of the angularly resolved cross section with respect to the polarization vector. On the other hand, MFPAD are harder to extract experimentally because it requires somehow to fix in space the molecules. Several techniques have been developed in the last two decades, but nowadays the most efficient in gas phase is without any doubt the COLTRIMS (for Cold Target Recoil Ion Momentum Spectrometer). As the name suggests, and as illustrated by the Figure 4.2, the basic idea of the technique consists in measuring in coincidence the momenta of the photoelectron and of the ion fragments resulting from a dissociative photoionization. Knowing the position of the molecule with respect to the detectors and the time of flight of the detected particles, it is then possible to recompose the classical trajectory and deduce the former momentum of the photoelectron at the time where the photoionization occurs. The optimal momentum resolution is obtained when the molecular target is at rest at the fragmentation time, situation that can be approached by cooling down the gas jet to sub-milli Kelvin temperatures. The original idea was conceptualized by Lew Cocke and Horst Schmidt-Böcking in 1978, but ten years were necessary to built up the machinery and perform the first successful measurements.

4.2.1 Molecular frame angular distribution

Theoretically, the derivation of a cross section formula that depends on the angles of the photoelectron in the molecular frame consists in rewriting the equations in a new frame of reference. Although the basic idea is straightforward, its setting up is not trivial and many years of investigation were needed to achieve this task. The first expressions for the theoretical MFPAD were given by Fano and Dill in 1972 [111] for the photoemission processes in $^1\Sigma_g$ electronic state of diatomic molecules. Many papers on this topic were published in the following decade, each one treating a different symmetry and lying on different assumptions. In 1986, Chandra demonstrated that it is possible to derive an MFPAD expression for the general case (for polyatomic molecules and any states of the polarization) by making use of group theory [51, 52, 53]. In this section, we will write down the essential steps that permit to obtain

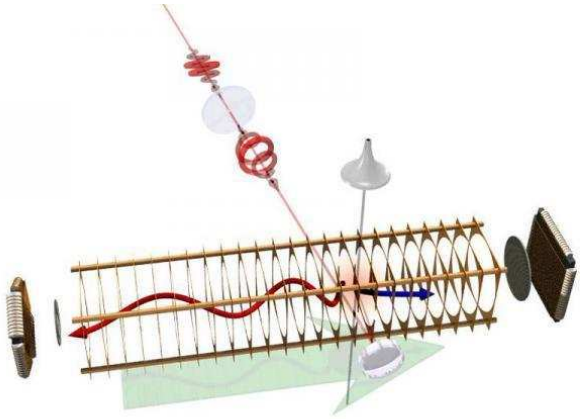

Figure 4.2: Schematic illustration of the COLTRIMS device (picture from the Ultrafast Laser Physics of ETH Zurich).

the general formulas.

The lifetime of the molecular core ionized states is generally much lower than the time of rotation of the molecule. Axis recoil approximation can be assumed and two coordinate systems whose origins coincide with the center of mass of the molecule are chosen: the photon frame of reference (which defines also the laboratory frame) and the molecular frame of reference. When light is linearly polarized, the first one is defined by the polarization vector which has a fixed position in the laboratory frame. The second frame of reference is attached to the molecular target in the equilibrium geometry (see Figure 4.3).

The two coordinate systems are related by the set of Euler's angles $\{\alpha, \beta, \gamma\}$ (see Figure 4.4) defined as:

$$\{\alpha, \beta, \gamma\} = \Omega_M \tag{4.7}$$

Molecular frame is brought into coincidence with the photon frame by a rotation of $(-\alpha, -\beta, -\gamma)$.

It is mathematically represented by the Wigner rotation matrix $\mathcal{D}^l_{mm'}(\Omega_M)$ which transforms any angular functions expressed in the laboratory frame into the molecular frame. For example, spherical harmonics are transformed as:

$$Y_l^{m'}\left(\theta', \phi'\right) = \sum_m \mathcal{D}^l_{mm'}(\Omega_M)\, Y_l^m(\theta, \phi) \tag{4.8}$$

where unprimed (primed) variables refer to the molecular (laboratory) frame of reference.

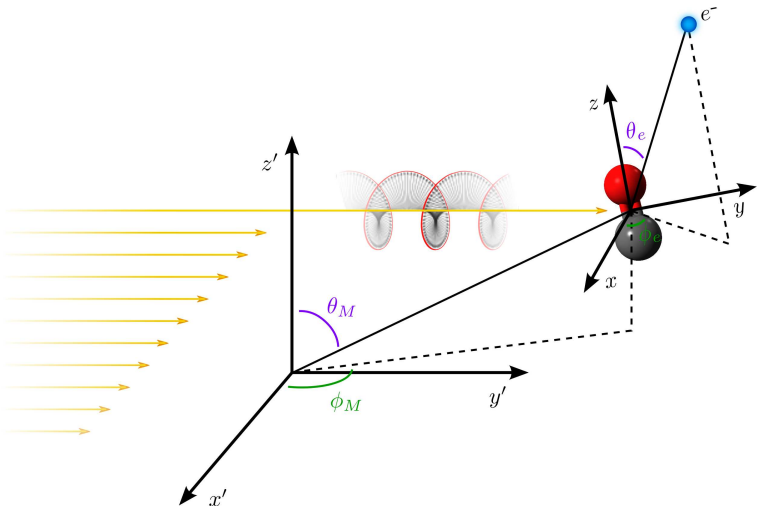

Figure 4.3: Photoionization process in the molecular and laboratory frames.

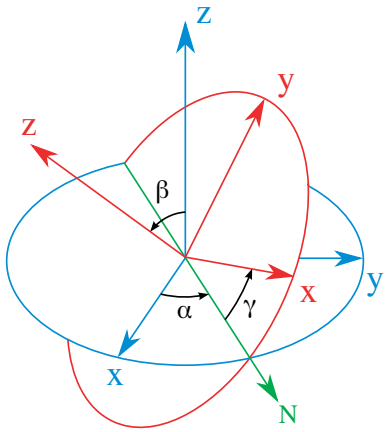

Figure 4.4: Euler angles characterizing the rotation between the rotated frame (red) with respect to the fixed one (blue). The line of nodes (N) is shown in green.

By indexing explicitly the symmetry of the final state and bringing out the coordinate dependences, the vibrationally resolved cross section formula (4.5) for a light polarization μ' can be written in the length gauge as:

$$\sigma_{\alpha}^{vv'}(\omega) = \frac{4\pi^2\omega}{3c} \sum_{p,q,h,l,\mu'} \left| T_{\alpha pqhl\mu'}^{vv'-}(\omega) \right|^2 \tag{4.9}$$

where:

$$T^{vv'-}_{\alpha pqhl\mu'}(\omega) = \left\langle \varphi^{-}_{\varepsilon pqhl}(\mathbf{r}, R)\, \chi_{f_\alpha,v'}(R) \left| \hat{\epsilon}_{\mu'} \cdot \mathbf{d}_{\mu'} \right| \varphi_\alpha(\mathbf{r}, R)\, \chi_{i,v}(R) \right\rangle \tag{4.10}$$

φ_α is the initial α molecular orbital from which is the electron is emitted, $\varphi_{\varepsilon pqhl}$ the final electronic continuum state of the photoelectron with energy ε in the $(pqhl)$-th channel. ω is the photon energy which is related to the photoelectron energy ε through the equation $\omega = IP_\alpha^{v,v'} + \varepsilon$, where $IP_\alpha^{v,v'}$ is the ionization energy required to create a hole in the α molecular orbital. p denotes the irreducible representation (IR) of the molecular point group under consideration, q stands for a component of this representation if its dimensionality is greater than one, h distinguishes between different bases of the same IR corresponding to the same value of the angular momentum of the escaping electron l, $\chi_{i,v}$ is the initial vibrational state, $\chi_{f_\alpha,v'}$ is the final vibrational state, $\mathbf{d}_{\mu'}$ represents one of the following spherical components of the electronic dipole operator:

$$d_{-1} = \frac{(d_x - i d_y)}{\sqrt{2}} = d \times \left(\frac{4\pi}{3}\right)^{1/2} Y_1^{-1}\left(\theta', \phi'\right) \tag{4.11}$$

$$d_0 = d_z = d \times \left(\frac{4\pi}{3}\right)^{1/2} Y_1^{0}\left(\theta', \phi'\right) \tag{4.12}$$

$$d_1 = -\frac{(d_x + i d_y)}{\sqrt{2}} = d \times \left(\frac{4\pi}{3}\right)^{1/2} Y_1^{1}\left(\theta', \phi'\right) \tag{4.13}$$

and $\epsilon_{\mu'}$ one of the spherical components of the polarization vector:

$$\epsilon_{-1} = \frac{(\epsilon_x - i\epsilon_y)}{\sqrt{2}} \tag{4.14}$$

$$\epsilon_0 = \epsilon_z \tag{4.15}$$

$$\epsilon_1 = -\frac{(\epsilon_x + i\epsilon_y)}{\sqrt{2}} \tag{4.16}$$

In the length gauge $\mathbf{d} = \mathbf{r}$ and, therefore, $d = r$.

We see that the cross section depends on the photoelectron coordinates in the molecular frame, while the dipole operator is defined in the laboratory frame. Using Equation (4.8), dipole components can be easily expressed into the molecular frame by expanding on the photon state μ:

$$d_{\mu'} = d \times \left(\frac{4\pi}{3}\right)^{1/2} Y_1^{\mu'}\left(\theta', \phi'\right) = d \times \left(\frac{4\pi}{3}\right)^{1/2} \sum_{\mu=-1}^{1} \mathcal{D}^1_{\mu\mu'}(\Omega_M)\, Y_1^{\mu}(\theta, \phi) \tag{4.17}$$

In order to derive the equation of the angularly resolved cross section, we have to use continuum wavefunction that depends explicitly on the photoelectron momentum $\mathbf{k}$. The geometrical transformation proposed in [51], permits to express them as function of the normalized continuum wavefunctions:

$$\varphi_k(\mathbf{r}) = \sum_{pqhl} i^l e^{-i\sigma_l(\omega)} X^*_{pqhl}(\theta,\phi)\, \varphi^-_{\varepsilon pqhl}(r,R) \tag{4.18}$$

where the continuum state $\varphi^-_{\varepsilon pqhl}(r,R)$ is called a partial wave and where we remind that $\sigma_l(\omega)$ corresponds to the Coulomb phase shift (see Equation (2.139)).

The scattered electron has a well defined angular momentum l that is given by the symmetry adaptation of real spherical harmonics defined at the geometric center of the molecule:

$$X_{pqhl}(\theta,\phi) = \sum_m b^{pqh}_{lm} Y^m_l(\theta,\phi) \tag{4.19}$$

Due to the non-spherical nature of the molecular potential, l is no more a good quantum number and the sum over l has to be infinite. Nevertheless, it has been observed that the partial-wave expansion converges rather rapidly and practically, it is a good approximation to truncate the sum to a limited number of terms.

Using Equation (4.17) and (4.18), the differential cross section in the molecular frame becomes:

$$\frac{d^2\sigma^{vv'}_{\alpha\mu'}(\omega)}{d\Omega_M d\Omega_e} = \frac{4\pi^2\omega}{3c}\left|\sum_{p,q,h,l,\mu}(-i)^l e^{i\sigma_l(\omega)} \mathcal{D}^1_{\mu\mu'}(\Omega_M)\, T^{vv'-}_{\alpha pqhl\mu}(\omega)\, X_{pqhl}(\Omega_e)\right|^2 \tag{4.20}$$

where $\Omega_e = (\theta,\phi)$ and:

$$T^{vv'-}_{\alpha pqhl\mu}(\omega) = \left\langle \varphi^-_{\varepsilon pqhl}(r,R)\, \chi_{f_\alpha,v'}(R)\, |rY^\mu_1(\theta,\phi)|\, \varphi_\alpha(r,R)\, \chi_{i,v}(R)\right\rangle \tag{4.21}$$

Then:

$$\begin{aligned}\frac{d^2\sigma^{vv'}_{\alpha\mu'}(\omega)}{d\Omega_M d\Omega_e} &= \frac{4\pi^2\omega}{3c}\sum_{\substack{p_1,q_1,h_1\\ l_1,m_1,\mu_1}}\sum_{\substack{p_2,q_2,h_2\\ l_2,m_2,\mu_2}}(-i)^{l_1-l_2}e^{i\left[\sigma_{l_1}(\omega)-\sigma_{l_2}(\omega)\right]} \\ &\times b^{p_1q_1h_1}_{l_1m_1}\left(b^{p_2q_2h_2}_{l_2m_2}\right)^* \mathcal{D}^1_{\mu_1\mu'}(\Omega_M)\,\mathcal{D}^{1*}_{\mu_2\mu'}(\Omega_M) \\ &\times T^{vv'-}_{\alpha p_1q_1h_1l_1\mu_1}(\omega)\, T^{vv'-*}_{\alpha p_2q_2h_2l_2\mu_2}(\omega)\, Y^{m_1}_{l_1}(\Omega_e)\, Y^{m_2*}_{l_2}(\Omega_e)\end{aligned} \tag{4.22}$$

The products of rotation matrices can be expressed in terms of Wigner $3-j$ symbols as:

$$\begin{aligned}&\mathcal{D}^{j_1}_{m_1 m_1'}(\alpha,\beta,\gamma)\,\mathcal{D}^{j_2}_{m_2 m_2'}(\alpha,\beta,\gamma) \\ &= \sum_{JMM'} \langle j_1 m_1 j_2 m_2 \mid JM\rangle \left\langle j_1 m_1' j_2 m_2' \mid JM'\right\rangle \mathcal{D}^{J}_{MM'}(\alpha,\beta,\gamma)\end{aligned} \tag{4.23}$$

where $M = m_1 + m_2$ and $M' = m_1' + m_2'$. The Wigner $3-j$ symbols are related to the Clebsch-Gordan coefficients by:

$$\langle j_1 m_1 j_2 m_2 \mid j_3 m_3\rangle = (-1)^{j_1 - j_2 + m_3}\sqrt{2j_3+1}\begin{pmatrix} j_1 & j_2 & j_3 \\ m_1 & m_2 & -m_3\end{pmatrix} \tag{4.24}$$

and have to fulfill the following selection rules to be non-zero:

$$\begin{pmatrix} j_1 & j_2 & j_3 \\ m_1 & m_2 & m_3\end{pmatrix} \neq 0 \quad \text{if} \quad \begin{cases} m_1 + m_2 + m_3 = 0 \\ j_1 + j_2 + j_3 \text{ is an integer} \\ |m_i| \leq j_i \\ |j_1 - j_2| \leq j_3 \leq j_1 + j_2 \end{cases} \tag{4.25}$$

Then, Equation (4.23) becomes:

$$\begin{aligned}\mathcal{D}^{j_1}_{m_1 m_1'}(\alpha,\beta,\gamma)\,\mathcal{D}^{j_2}_{m_2 m_2'}(\alpha,\beta,\gamma) &= \sum_{JMM'} (-1)^{M+M'}(2J+1) \\ &\times \begin{pmatrix} j_1 & j_2 & J \\ m_1 & m_2 & -M\end{pmatrix}\begin{pmatrix} j_1 & j_2 & J \\ m_1' & m_2' & -M'\end{pmatrix} \\ &\times \mathcal{D}^{J}_{MM'}(\alpha,\beta,\gamma)\end{aligned} \tag{4.26}$$

Considering that:

$$\mathcal{D}^{j*}_{mm'}(\alpha,\beta,\gamma) = (-1)^{m-m'}\,\mathcal{D}^{j}_{-m-m'}(\alpha,\beta,\gamma) \tag{4.27}$$

then the product of rotation matrices in Equation (4.22) becomes:

$$\begin{aligned}\mathcal{D}^{1}_{\mu_1\mu'}(\Omega_M)\,\mathcal{D}^{1*}_{\mu_2\mu'}(\Omega_M) &= (-1)^{\mu_2-\mu'}\,\mathcal{D}^{1}_{\mu_1\mu'}(\Omega_M)\,\mathcal{D}^{1}_{-\mu_2-\mu'}(\Omega_M) \\ &= (-1)^{\mu_1-\mu'}\sum_{\Lambda,\mu_1,\mu_2}(2\Lambda+1)\begin{pmatrix} 1 & 1 & \Lambda \\ \mu' & -\mu' & 0\end{pmatrix} \\ &\times \begin{pmatrix} 1 & 1 & \Lambda \\ \mu_1 & -\mu_2 & -(\mu_1-\mu_2)\end{pmatrix}\mathcal{D}^{\Lambda}_{\mu_1-\mu_2 0}(\Omega_M)\end{aligned} \tag{4.28}$$

and according to the transformation:

$$\begin{pmatrix} j_1 & j_2 & j_3 \\ m_1 & m_2 & m_3\end{pmatrix} = (-1)^{j_1+j_2+j_3}\begin{pmatrix} j_1 & j_2 & j_3 \\ -m_1 & -m_2 & -m_3\end{pmatrix} \tag{4.29}$$

we can rewrite (4.28) as follows:

$$\begin{aligned}\mathcal{D}^{1}_{\mu_1\mu'}(\Omega_M)\,\mathcal{D}^{1*}_{\mu_2\mu'}(\Omega_M) &= (-1)^{\mu_1-\mu'}\sum_{\Lambda,\mu_1,\mu_2}(2\Lambda+1)\begin{pmatrix}1 & 1 & \Lambda\\ -\mu' & \mu' & 0\end{pmatrix}\\ &\times\begin{pmatrix}1 & 1 & \Lambda\\ -\mu_1 & \mu_2 & \mu_1-\mu_2\end{pmatrix}\mathcal{D}^{\Lambda}_{\mu_1-\mu_20}(\Omega_M)\end{aligned} \quad (4.30)$$

The product of spherical harmonics can also be simplified by using their relation with the rotation matrix:

$$Y^{m}_{l}(\beta,\gamma)=\left(\frac{2l+1}{4\pi}\right)^{\frac{1}{2}}\mathcal{D}^{l}_{0m}(\alpha,\beta,\gamma) \quad (4.31)$$

and:

$$\begin{aligned}Y^{m_1}_{l_1}(\Omega_e)\,Y^{m_2*}_{l_2}(\Omega_e) &= (-1)^{m_1}\sum_{L=0}^{2l_{max}}\sum_{M=-L}^{L}\left(\frac{(2l_1+1)(2l_2+1)(2L+1)}{4\pi}\right)^{\frac{1}{2}}\\ &\times\begin{pmatrix}l_1 & l_2 & L\\ 0 & 0 & 0\end{pmatrix}\begin{pmatrix}l_1 & l_2 & L\\ -m_1 & m_2 & M\end{pmatrix}Y^{M}_{L}(\Omega_e)\end{aligned}$$

where l_{max} correspond to the maximum value of the ensemble $\{l_1,l_2\}$. Finally the Equation (4.22) can be put in the form:

$$\frac{d^2\sigma^{vv'}_{\alpha\mu'}(\omega)}{d\Omega_M d\Omega_e}=\frac{4\pi^2\omega}{3c}(-1)^{\mu'}\sum_{L=0}^{2l_{max}}\sum_{M=-L}^{L}A^{vv'}_{\alpha LM}(\Omega_M,\omega)\,Y^{M}_{L}(\Omega_e) \quad (4.32)$$

where the amplitudes are given by:

$$\begin{aligned}&A^{vv'}_{\alpha LM}(\Omega_M,\omega)\\ &=\sum_{\substack{p_1,q_1,h_1\\ l_1,m_1,\mu_1}}\sum_{\substack{p_2,q_2,h_2\\ l_2,m_2,\mu_2}} i^{l_2-l_1}e^{i\left[\sigma_{l_1}(\omega)-\sigma_{l_2}(\omega)\right]}(-1)^{m_1+\mu_1}\\ &\times\left(\frac{(2l_1+1)(2l_2+1)(2L+1)}{4\pi}\right)^{\frac{1}{2}}\begin{pmatrix}l_1 & l_2 & L\\ 0 & 0 & 0\end{pmatrix}\begin{pmatrix}l_1 & l_2 & L\\ -m_1 & m_2 & M\end{pmatrix}\\ &\times b^{p_1q_1h_1}_{l_1m_1}\left(b^{p_2q_2h_2}_{l_2m_2}\right)^{*}T^{vv'-}_{\alpha p_1q_1h_1l_1\mu_1}(\omega)\,T^{vv'-*}_{\alpha p_2q_2h_2l_2\mu_2}(\omega)\\ &\times\sum_{\Lambda}(2\Lambda+1)\begin{pmatrix}1 & 1 & \Lambda\\ -\mu' & \mu' & 0\end{pmatrix}\begin{pmatrix}1 & 1 & \Lambda\\ -\mu_1 & \mu_2 & \mu_1-\mu_2\end{pmatrix}\mathcal{D}^{\Lambda}_{\mu_1-\mu_20}(\Omega_M)\end{aligned} \quad (4.33)$$

These two last equations correspond to the general formula of the vibrationally resolved angular distribution for the single photoionization of fixed-in-space molecules. It can be applied to molecules of any point-group symmetry and it provides the maximum information that can be theoretically accessible.

4.2.2 Averaged molecular frame angular distribution

Different kinds of information can be extracted by integrating Equation (4.36) over different coordinates. For example, it can be useful to consider the MF-PADs averaged over all the possible orientations of the polarization vector. Remembering that the dipole components have been transformed into the MF thanks to the rotation matrices $\mathcal{D}^{1}_{\mu\mu'}(\Omega_M)$ (see Equation (4.18)), we can eliminate the dependence on the polarization angles by averaging the matrix product in Equation (4.30). Noticing that:

$$\frac{1}{8\pi^2}\int \mathcal{D}^{j_1}_{m_1 n_1}(\Omega_M)\,\mathcal{D}^{j_2 *}_{m_2 n_2}(\Omega_M)\,d\Omega_M = \frac{1}{2j_1+1}\delta_{m_1 m_2}\delta_{n_1 n_2}\delta_{j_1 j_2} \tag{4.34}$$

then Equation (4.30) simplifies as:

$$\frac{1}{8\pi^2}\int \mathcal{D}^{1}_{\mu_1\mu'}(\Omega_M)\,\mathcal{D}^{1*}_{\mu_2\mu'}(\Omega_M)\,d\Omega_M = \frac{1}{3}\delta_{\mu_1\mu_2} \tag{4.35}$$

and the averaged MFPAD reads:

$$\frac{d^2\sigma^{vv'}_{\alpha\mu'}(\omega)}{d\Omega_e} = \frac{4\pi^2\omega}{3c}(-1)^{\mu'}\sum_{L=0}^{2l_{max}}\sum_{M=-L}^{L} A^{vv'}_{\alpha LM}(\omega)\,Y^{M}_{L}(\Omega_e) \tag{4.36}$$

where the amplitudes are given by:

$$\begin{aligned} &A^{vv'}_{\alpha LM}(\omega) \\ &= \frac{1}{3}\sum_{\substack{p_1,q_1,h_1\\ l_1,m_1}}\sum_{\substack{p_2,q_2,h_2\\ l_2,m_2}}\sum_{\mu_1} i^{l_2-l_1}e^{i\left[\sigma_{l_1}(\omega)-\sigma_{l_2}(\omega)\right]}(-1)^{m_1+\mu_1} \qquad (4.37)\\ &\times\left(\frac{(2l_1+1)(2l_2+1)(2L+1)}{4\pi}\right)^{\frac{1}{2}}\begin{pmatrix} l_1 & l_2 & L\\ 0 & 0 & 0\end{pmatrix}\begin{pmatrix} l_1 & l_2 & L\\ -m_1 & m_2 & M\end{pmatrix} \\ &\times b^{p_1 q_1 h_1}_{l_1 m_1}\left(b^{p_2 q_2 h_2}_{l_2 m_2}\right)^{*} T^{vv'-}_{\alpha p_1 q_1 h_1 l_1 \mu_1}(\omega)\,T^{vv'-*}_{\alpha p_2 q_2 h_2 l_2 \mu_1}(\omega) \qquad (4.38)\end{aligned}$$

Such formula permits to obtain an angular distribution that only depends on the angles of the photoelectron. It is particularly useful in low symmetric polyatomic molecules where there is many nonequivalent particular orientations of the polarization vector.

Depending on the degree of information required, it can be convenient to carry out other integrations or transformations of Equation (4.36) and (4.33). In particular, it can be useful to express the angular distribution in the laboratory frame as a function of the angle θ'_e formed by the photoelectron momentum and the propagation vector of the light.

4.2.3 β asymmetry parameter

To transform Equation (4.36) into the laboratory frame, we first have to express the spherical harmonics as a function of the laboratory frame coordinates. Taking into account the usual orthogonality of the rotation matrices:

$$\sum_{m} \bar{\mathcal{D}}^{j}_{m'm}(\gamma,\beta,\alpha)\,\mathcal{D}^{j}_{m''m}(\alpha,\beta,\gamma) = \delta_{m'm''} \tag{4.39}$$

and by using Equation (4.8), we can write:

$$Y^{M}_{L}(\Omega_e) = \sum_{M'} \bar{\mathcal{D}}^{L}_{M'M}(\Omega_M)\,Y^{M'}_{L}\left(\Omega'_e\right) \tag{4.40}$$

and we now have to evaluate the product $\bar{\mathcal{D}}^{L}_{M'M}(\Omega_M)\,\mathcal{D}^{\Lambda}_{\mu_1-\mu_20}(\Omega_M)$. Noticing the following property of the rotation matrix:

$$\bar{\mathcal{D}}^{j}_{mm'}(\gamma,\beta,\alpha) = (-1)^{m-m'}\,\mathcal{D}^{j}_{m'm}(\alpha,\beta,\gamma) \tag{4.41}$$

then we can write:

$$\begin{aligned}\bar{\mathcal{D}}^{L}_{M'M}(\Omega_M)\,\mathcal{D}^{\Lambda}_{\mu_1-\mu_20}(\Omega_M) &= (-1)^{-\mu_1+\mu_2}\sum_{KQQ'}(2K+1)\begin{pmatrix} L & \Lambda & K \\ -M' & 0 & M'\end{pmatrix} \\ &\quad\times\begin{pmatrix} L & \Lambda & K \\ -M & \mu_1-\mu_2 & Q\end{pmatrix}\mathcal{D}^{K}_{QM'}(\Omega_M)\end{aligned} \tag{4.42}$$

and Equation (4.36) becomes:

$$\frac{d^2\sigma^{vv'}_{\alpha\mu'}(\omega)}{d\Omega_M d\Omega'_e} = \frac{4\pi^2\omega}{3c}(-1)^{\mu'}\sum_{L=0}^{2l_{max}}\sum_{M'=-L}^{L}\bar{A}^{vv'}_{\alpha LM'}(\Omega_M,\omega)\,Y^{M'}_{L}\left(\Omega'_e\right) \tag{4.43}$$

where the new amplitudes read:

$$\begin{aligned}&\bar{A}^{vv'}_{\alpha LM'}(\Omega_M,\omega) = \sum_{M} A^{vv'}_{\alpha LM}\bar{\mathcal{D}}^{L}_{M'M}(\Omega_M) \\ &= \sum_{\substack{p_1,q_1,h_1\\ l_1,m_1,\mu_1}}\sum_{\substack{p_2,q_2,h_2\\ l_2,m_2,\mu_2}} i^{l_2-l_1}e^{i\left[\sigma_{l_1}(\omega)-\sigma_{l_2}(\omega)\right]}(-1)^{m_1+\mu_1} \\ &\times\left(\frac{(2l_1+1)(2l_2+1)(2L+1)}{4\pi}\right)^{\frac{1}{2}}\sum_{M}\begin{pmatrix} l_1 & l_2 & L \\ 0 & 0 & 0\end{pmatrix}\begin{pmatrix} l_1 & l_2 & L \\ -m_1 & m_2 & M\end{pmatrix} \\ &\times b^{p_1q_1h_1}_{l_1m_1}\left(b^{p_2q_2h_2}_{l_2m_2}\right)^{*}T^{vv'-}_{\alpha p_1q_1h_1l_1\mu_1}(\omega)\,T^{vv'-*}_{\alpha p_2q_2h_2l_2\mu_2}(\omega) \\ &\times\sum_{\Lambda}(2\Lambda+1)\begin{pmatrix} 1 & 1 & \Lambda \\ -\mu' & \mu' & 0\end{pmatrix}\begin{pmatrix} 1 & 1 & \Lambda \\ -\mu_1 & \mu_2 & \mu_1-\mu_2\end{pmatrix} \\ &\times\sum_{KQ}(2K+1)\begin{pmatrix} L & \Lambda & K \\ -M' & 0 & M'\end{pmatrix}\begin{pmatrix} L & \Lambda & K \\ -M & \mu_1-\mu_2 & Q\end{pmatrix}\mathcal{D}^{K}_{QM'}(\Omega_M)\end{aligned} \tag{4.44}$$

Seeing that $Q = M + \mu_2 - \mu_1$ and $M = m_1 - m_2$, it is possible to take out the sum over Q and M:

$$\begin{aligned}
&\bar{A}^{vv'}_{\alpha LM'}(\Omega_M,\omega) \\
&= \sum_{\substack{p_1,q_1,h_1\\ l_1,m_1,\mu_1}} \sum_{\substack{p_2,q_2,h_2\\ l_2,m_2,\mu_2}} i^{l_2-l_1} e^{i\left[\sigma_{l_1}(\omega)-\sigma_{l_2}(\omega)\right]} (-1)^{m_1+\mu_1} \\
&\times \left(\frac{(2l_1+1)(2l_2+1)(2L+1)}{4\pi}\right)^{\frac{1}{2}} \begin{pmatrix} l_1 & l_2 & L \\ 0 & 0 & 0 \end{pmatrix} \begin{pmatrix} l_1 & l_2 & L \\ -m_1 & m_2 & m_1-m_2 \end{pmatrix} \\
&\times b^{p_1q_1h_1}_{l_1m_1} \left(b^{p_2q_2h_2}_{l_2m_2}\right)^* T^{vv'-}_{\alpha p_1q_1h_1l_1\mu_1}(\omega)\, T^{vv'-*}_{\alpha p_2q_2h_2l_2\mu_2}(\omega) \\
&\times \sum_{\Lambda} (2\Lambda+1) \begin{pmatrix} 1 & 1 & \Lambda \\ -\mu' & \mu' & 0 \end{pmatrix} \begin{pmatrix} 1 & 1 & \Lambda \\ -\mu_1 & \mu_2 & \mu_1-\mu_2 \end{pmatrix} \\
&\times \sum_{K} (2K+1) \begin{pmatrix} L & \Lambda & K \\ -M' & 0 & M' \end{pmatrix} \begin{pmatrix} L & \Lambda & K \\ m_2-m_1 & \mu_1-\mu_2 & Q \end{pmatrix} \mathcal{D}^K_{QM'}(\Omega_M)
\end{aligned} \tag{4.45}$$

In the laboratory frame, the molecules are randomly oriented with respect to the polarization vector. To reproduce experimental situations in which the fragment ions and the photoelectron cannot be measured in coincidence, the differential cross section has to be averaged over all the possible orientations of the molecules:

$$\frac{d\sigma^{vv'}_{\alpha\mu'}(\omega)}{d\theta'_e} = \int \frac{d^2\sigma^{vv'}_{\alpha\mu'}(\omega)}{d\Omega_M d\theta'_e} d\Omega_M \tag{4.46}$$

where Ω'_e has been reduced to θ'_e since emitted electrons for randomly oriented molecules present a cylindrical symmetry along the propagation vector.

The amplitudes $\bar{A}^{vv'}_{\alpha LM'}(\Omega_M,\omega)$ carry the dependence on the molecular coordinates. Considering that for averaged orientations of the molecules $M' = 0$, $Q = 0$, $K = 0$ and $\Lambda = L$, then the integrated amplitudes take the form:

$$\begin{aligned}
&\frac{1}{8\pi^2}\int \bar{A}^{vv'}_{\alpha LM'}(\Omega_M,\omega)\, d\Omega_M = \bar{A}^{vv'}_{\alpha L0}(\omega) \\
&= \sum_{\substack{p_1,q_1,h_1\\ l_1,m_1,\mu_1}} \sum_{\substack{p_2,q_2,h_2\\ l_2,m_2,\mu_2}} i^{l_2-l_1} e^{i\left[\sigma_{l_1}(\omega)-\sigma_{l_2}(\omega)\right]} (-1)^{m_1+\mu_2} \\
&\times \left(\frac{(2l_1+1)(2l_2+1)(2L+1)}{4\pi}\right)^{\frac{1}{2}} \begin{pmatrix} l_1 & l_2 & L \\ 0 & 0 & 0 \end{pmatrix} \begin{pmatrix} l_1 & l_2 & L \\ -m_1 & m_2 & m_1-m_2 \end{pmatrix} \\
&\times b^{p_1q_1h_1}_{l_1m_1} \left(b^{p_2q_2h_2}_{l_2m_2}\right)^* T^{vv'-}_{\alpha p_1q_1h_1l_1\mu_1}(\omega)\, T^{vv'-*}_{\alpha p_2q_2h_2l_2\mu_2}(\omega) \\
&\times (2L+1) \begin{pmatrix} 1 & 1 & L \\ -\mu' & \mu' & 0 \end{pmatrix} \begin{pmatrix} 1 & 1 & L \\ -\mu_1 & \mu_2 & \mu_1-\mu_2 \end{pmatrix} \\
&\times \begin{pmatrix} L & L & 0 \\ 0 & 0 & 0 \end{pmatrix} \begin{pmatrix} L & L & 0 \\ m_2-m_1 & \mu_1-\mu_2 & 0 \end{pmatrix} \mathcal{D}^0_{00}(\Omega_M)
\end{aligned} \tag{4.47}$$

where we see that $L \leq 2$ and $\mathcal{D}^0_{00}(\Omega_M) = 1$.

The Wigner $3-j$ symbols take a simpler form when $j_3 = 0$ and $m_3 = 0$:

$$\begin{pmatrix} j_1 & j_2 & 0 \\ -m_1 & m_2 & 0 \end{pmatrix} = (-1)^{j_2+m_2} \frac{\delta_{j_1 j_2}\delta_{-m_1 m_2}}{\sqrt{2j_2+1}} \tag{4.48}$$

and some of them can simplified in Equation (4.48):

$$\begin{pmatrix} L & L & 0 \\ 0 & 0 & 0 \end{pmatrix} = \frac{(-1)^L}{\sqrt{2L+1}} \tag{4.49}$$

$$\begin{pmatrix} L & L & 0 \\ m_2 - m_1 & \mu_1 - \mu_2 & 0 \end{pmatrix} = \frac{(-1)^{L+\mu_1-\mu_2}}{\sqrt{2L+1}} \tag{4.50}$$

Now, the integrated cross section is:

$$\frac{d\sigma^{vv'}_{\alpha\mu'}(\omega)}{d\theta'_e} = \frac{4\pi^2\omega}{3c}(-1)^{\mu'} \sum_{L=0}^{2} \bar{A}^{vv'}_{\alpha L0}(\omega) P_L\left(\cos\theta'_e\right) \tag{4.51}$$

where:

$$\begin{aligned} \bar{A}^{vv'}_{\alpha L0}(\omega) \;=\; & \left(\frac{2L+1}{4\pi}\right) \sum_{\substack{p_1,q_1,h_1 \\ l_1,m_1,\mu_1}} \sum_{\substack{p_2,q_2,h_2 \\ l_2,m_2,\mu_2}} i^{l_2-l_1} e^{i\left[\sigma_{l_1}(\omega)-\sigma_{l_2}(\omega)\right]} (-1)^{m_1+\mu_2} \\ & \times\sqrt{(2l_1+1)(2l_2+1)} \begin{pmatrix} l_1 & l_2 & L \\ 0 & 0 & 0 \end{pmatrix} \begin{pmatrix} l_1 & l_2 & L \\ -m_1 & m_2 & m_1-m_2 \end{pmatrix} \\ & \times b^{p_1q_1h_1}_{l_1m_1} \left(b^{p_2q_2h_2}_{l_2m_2}\right)^* T^{vv'-}_{\alpha p_1 q_1 h_1 l_1 \mu_1}(\omega) T^{vv'-*}_{\alpha p_2 q_2 h_2 l_2 \mu_2}(\omega) \\ & \times (2L+1) \begin{pmatrix} 1 & 1 & L \\ -\mu' & \mu' & 0 \end{pmatrix} \begin{pmatrix} 1 & 1 & L \\ -\mu_1 & \mu_2 & \mu_1-\mu_2 \end{pmatrix} \end{aligned} \tag{4.52}$$

and:

$$Y^0_L\left(\theta'_e\right) = \left(\frac{2L+1}{4\pi}\right)^{\frac{1}{2}} P_L\left(\cos\theta'_e\right) \tag{4.53}$$

The differential cross section can also be put in another form. Considering that an integration over Ω'_e would give:

$$\sigma^{vv'}_{\alpha\mu'}(\omega) = \frac{4\pi^2\omega}{3c}(-1)^{\mu'} 4\pi \bar{A}^{vv'}_{\alpha 00}(\omega) \tag{4.54}$$

the amplitude $\bar{A}^{vv'}_{\alpha 00}(\omega)$ can be factorized in Equation (4.51):

$$\frac{d\sigma^{vv'}_{\alpha\mu'}(\omega)}{d\theta'_e} = \frac{4\pi^2\omega}{3c}(-1)^{\mu'} \bar{A}^{vv'}_{\alpha 00}(\omega) \left[1 + \frac{\bar{A}^{vv'}_{\alpha 10}(\omega)}{\bar{A}^{vv'}_{\alpha 00}(\omega)} \cos\theta'_e + \frac{\bar{A}^{vv'}_{\alpha 20}(\omega)}{\bar{A}^{vv'}_{\alpha 00}(\omega)} P_2\left(\cos\theta'_e\right)\right] \tag{4.55}$$

where:

$$P_2(x) = \frac{1}{2}\left(3x^2 - 1\right) \tag{4.56}$$

The Wigner $3-j$ rules shows that $\mu' = 1$ for $\bar{A}^{vv'}_{\alpha 10}$ and $\mu' = 0$ for $\bar{A}^{vv'}_{\alpha 20}$. Finally, the differential cross section in the laboratory frame and for randomly oriented molecules is written:

$$\frac{d\sigma^{vv'}_{\alpha\mu'}(\omega)}{d\theta'_e} = \frac{\sigma^{vv'}_{\alpha\mu'}(\omega)}{4\pi}\left[1 + \mu'\beta^{v,v'}_{1,\alpha}(\omega)\cos\theta'_e + \left(-\frac{1}{2}\right)^{\mu'}\beta^{v,v'}_{\alpha}(\omega)\,P_2\left(\cos\theta'_e\right)\right] \tag{4.57}$$

where:

$$\beta^{v,v'}_{1,\alpha}(\omega) = \frac{\bar{A}^{vv'}_{\alpha 10}(\omega)}{\bar{A}^{vv'}_{\alpha 00}(\omega)} \tag{4.58}$$

and:

$$\beta^{v,v'}_{\alpha}(\omega) = \frac{\bar{A}^{vv'}_{\alpha 20}(\omega)}{\bar{A}^{vv'}_{\alpha 00}(\omega)} \tag{4.59}$$

For a linear polarized light, Equation (4.57) becomes:

$$\frac{d\sigma^{vv'}_{\alpha\mu'}(\omega)}{d\theta'_e} = \frac{\sigma^{vv'}_{\alpha\mu'}(\omega)}{4\pi}\left[1 + \beta^{v,v'}_{\alpha}(\omega)\,P_2\left(\cos\theta'_e\right)\right] \tag{4.60}$$

The asymmetry parameter β is a function that varies between -1 and 2 and depends only on the photon energy (all the angular dependence being contained in the second order Legendre polynomial). As presented in Figure 4.5, angular information can be retrieved from the asymmetry parameter β by considering the evolution of the function contained in the bracket of Equation (4.60).

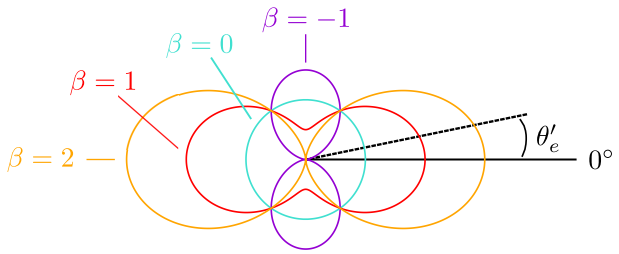

Figure 4.5: Polar plot of $[1 + \beta(\omega)\,P_2(\cos\theta'_e)]$ function for $\beta = -1, 0, 1, 2$.

4.2.4 Total cross section

It is possible to recover the formula of the total cross section given in Equation (4.9) by averaging over the angles of the photoelectron and all possible orientations of the molecules:

$$\sigma_{\alpha\mu'}^{vv'}(\omega) = \frac{1}{8\pi^2}\iint \frac{d^2\sigma_{\alpha\mu'}^{vv'}(\omega)}{d\Omega_M d\Omega_e} d\Omega_M d\Omega_e \tag{4.61}$$

Such integrals can be easily evaluated, by considering:

$$\int Y_L^M(\Omega_e)\, d\Omega_e = \delta_{L0}\delta_{M0}\sqrt{4\pi} \tag{4.62}$$

Then, integrating Equation (4.33):

$$\sigma_{\alpha\mu'}^{vv'}(\omega) = \frac{4\pi^2\omega}{3c}(-1)^{\mu'}\frac{\sqrt{4\pi}}{8\pi^2}A_{\alpha 00}^{vv'}(\omega) \tag{4.63}$$

According to the Equation (4.48), it is possible to simplify some terms in the expression of $A_{\alpha 00}^{vv'}(\omega)$:

$$\begin{aligned}&\sum_{l_2,m_2}\left(\frac{(2l_1+1)(2l_2+1)}{4\pi}\right)^{\frac{1}{2}}\begin{pmatrix} l_1 & l_2 & 0\\ 0 & 0 & 0\end{pmatrix}\begin{pmatrix} l_1 & l_2 & 0\\ -m_1 & m_2 & 0\end{pmatrix}\\ &= \frac{2l_1+1}{\sqrt{4\pi}}\frac{(-1)^{l_1}}{\sqrt{2l_1+1}}\frac{(-1)^{l_1-m_1}}{\sqrt{2l_1+1}} = \frac{(-1)^{m_1}}{\sqrt{4\pi}}\end{aligned} \tag{4.64}$$

And since:

$$\int \mathcal{D}_{\mu_1-\mu_2 0}^{\Lambda}(\Omega_M)\, d\Omega_M = 8\pi^2\delta_{\Lambda 0}\delta_{\mu_1-\mu_2 0} \tag{4.65}$$

then:

$$\sum_{\mu_2}\begin{pmatrix} 1 & 1 & 0\\ -\mu' & \mu' & 0\end{pmatrix}\begin{pmatrix} 1 & 1 & 0\\ -\mu_1 & \mu_2 & 0\end{pmatrix} = \frac{(-1)^{1-\mu'}}{\sqrt{3}}\frac{(-1)^{1-\mu_1}}{\sqrt{3}} = \frac{(-1)^{\mu_1+\mu'}}{3} \tag{4.66}$$

The irreducible representations characterized by the set $\{pqh\}$ are by definition orthogonal, and consequently, products of symmetry adapted spherical harmonics of same l and m vanishes for different symmetries:

$$\sum_{m_1} b_{l_1 m_1}^{p_1 q_1 h_1}\left(b_{l_1 m_1}^{p_2 q_2 h_2}\right)^* = \delta_{p_1 p_2}\delta_{q_1 q_2}\delta_{h_1 h_2} \tag{4.67}$$

Finally, we have:

$$A_{\alpha 00}^{vv'}(\omega) = (-1)^{\mu'}\frac{1}{3}\frac{8\pi^2}{\sqrt{4\pi}} \tag{4.68}$$

and Equation (4.63) becomes:

$$\sigma_{\alpha}^{vv'}(\omega) = \frac{4\pi^2\omega}{3c} \sum_{p_1,q_1,h_1,l_1} \sum_{\mu_1} \left| T^{vv'-}_{\alpha p_1 q_1 h_1 l_1 \mu_1}(\omega) \right|^2 \tag{4.69}$$

which can be reformulated as:

$$\sigma_{\alpha}^{vv'}(\omega) = \frac{4\pi^2\omega}{3c} \sum_{p,q,h,l} \sum_{\mu} \left| \int \chi^*_{i,v}(R)\, T^{-}_{\alpha pqhl\mu}(\omega, R)\, \chi_{f_\alpha,v'}(R)\, dR \right|^2 \tag{4.70}$$

where the electronic dipole couplings are:

$$T^{-}_{\alpha pqhl\mu}(\omega, R) = \left\langle \varphi^{-}_{\varepsilon pqhl}(r, R) \left| \hat{d}^{\mu} \right| \varphi_{\alpha}(r, R) \right\rangle \tag{4.71}$$

The vibrational cross section $\sigma_{\alpha}^{vv'}(\omega)$ depends on the α-channel, the active symmetry p_1, q_1, h_1, l_1, the initial and final vibrational states[1], the photon or photoelectron energy.

The calculation procedure can be summarized as illustrated in the Figure 4.6. Once the vibrational wavefunctions and the dipole matrix elements have been calculated, they have to be integrated according Equation (4.71). Integrating/summing the partial cross section over one or several differential magnitudes leads to partially differential or total cross sections, each one representing a specific experimental situation.

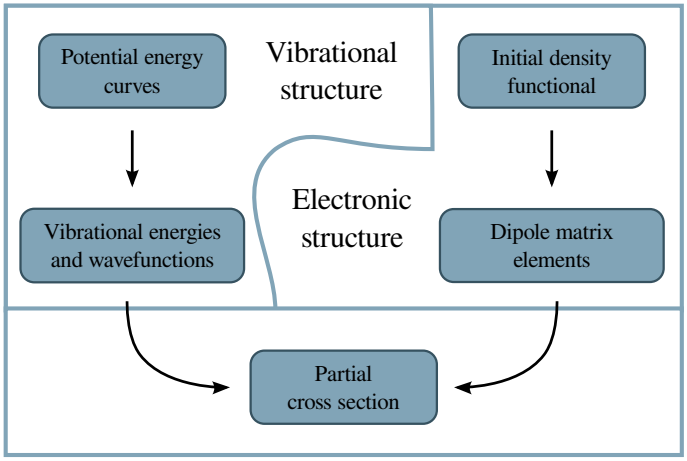

Figure 4.6: General procedure to calculate the single photoionization cross section.

[1]In this work, the initial vibrational state v is fixed and always chosen in the ground state ($v = 0$)

4.3 Group theory applied to spectroscopy

Group theory is a powerful theoretical tool to analyze and reduce the complexity of the photoionization process. From a computational point of view, it permits to save time of calculation by prescribing which transitions are allowed and which partial wave components contribute to both the initial and final states. This section summarizes and illustrates with an example, some major results of point-group theory that are used throughout the thesis. Part of the concepts used here refer to elements of group theory (notes can be found in Appendix A.1). For a complete account of the formalism of group theory, which is beyond the scope of this current work, we refer the reader to [71].

4.3.1 Selection rules

Group theory is used in spectroscopy to determine the possible transitions according to the initial and final symmetries. The results of this formal analysis give rise to the *selection rules*.

Electronic transitions

We have seen in Equation (4.5) that the transition probability between an initial state $|\psi_n\rangle$ and a finale state $|\psi_m\rangle$ is proportional to:

$$\sigma_{nm} \propto \left| \int \psi_m^* \hat{d}_i \psi_n \right|^2 \tag{4.72}$$

where $\hat{d}_i$ is a component of the dipole operator.

Depending on the symmetry of the functions ψ_n, ψ_m and $\hat{d}_i$ (if they have nodes, are odd or even, etc.), the integral in Equation (4.72) can vanishes or not. The group theory says that "an electric dipole transition is allowed if the direct product of the representations $\Gamma_n(R)$ and $\Gamma_m(R)$ contains the IR to which the dipole component $\hat{d}_i$ belongs". Then, knowing the point group symmetry of a molecule, it is possible (and generally straightforward) to determine if an electronic transition can occur.

Vibrational transitions

The fundamental vibrational transitions (i.e., the transitions between the vibrational ground state and an i-th excited one in any vibrational mode but in the same electronic state) are induced by IR absorption or Raman scattering and their amplitude is equivalently described by Equation (4.72). Then, fundamental vibrational transitions obey to selection rules given by group theory. In the harmonic oscillator approximation, the vibrational wavefunction is given by Equation (3.26) and since $H_0(x) = 1$, the vibrational ground state

is invariant under all symmetries and form a basis for the totally symmetric representation. As a consequence, the excited vibrational states have the symmetry of their Hermite polynomial, i.e. of their normal mode. According to the group theory selection rules, the allowed fundamental vibrational transitions are the ones for which the product of the dipole component and the vibrational excited state contains the totally symmetric IR (the vibrational ground state). In other words, only the normal modes of same symmetry as the Cartesian coordinates (for the IR absorption) or the quadratic function of the Cartesian coordinate (for the Raman scattering) are active for the fundamental vibrational transitions.

Vibronic transitions

The vibronic transitions is a more complicated case since it involves both the electronic and vibrational symmetries. In the Born-Oppenheimer approximation, the transition is proportional to:

$$\sigma_{nm}^{vv'} \propto \left| \int \chi_{m,\{v'\}}^{*} \psi_m^{*} \hat{d}_i \psi_n \chi_{n,\{v\}} \right|^2 \tag{4.73}$$

Then, according to the selection rules, the integral is zero unless the direct product $\Gamma_{m,\{v'\}} \otimes \Gamma_m \otimes \Gamma_{d_i} \otimes \Gamma_n \otimes \Gamma_{n,\{v\}}$ contains the totally symmetric representation Γ^1.

In the Franck-Condon approximation (see Section II), the electronic dipole couplings can be factorized out:

$$\sigma_{nm}^{vv'} = F_{nm}^{vv'} \sigma_{nm} \tag{4.74}$$

where:

$$\sigma_{nm} \propto \left| \int \psi_m^{*} \hat{d}_i \psi_n \right|^2 \tag{4.75}$$

Then, the cross section is proportional to the integral of the initial and final wavefunctions:

$$F_{nm}^{vv'} = \left| \int \chi_{m,\{v'\}}^{*} \chi_{n,\{v\}} \right|^2 = \prod_{k}^{3M-6} \int \left| \chi_{k,v'_k}^{*} \chi_{k,v_k} \right|^2 \tag{4.76}$$

Then, two selection rules for the vibrational states involved in the vibronic transition arise:

- for non totally symmetrical vibrational modes, the overlap of wavefunctions with different parity will gives 0. Then, the allowed vibronic transitions satisfy the condition: $\Delta v_k = 0, \pm 2, \pm 4, \cdots$

- for totally symmetric stretching modes, the geometry at the equilibrium is generally different for the final state. Then initial and final vibrational wavefunctions are shifted one with respect to the other and all the vibrational transitions are allowed: $\Delta v_k = 0, \pm 1, \pm 2, \pm 3, \cdots$

In this work, only the totally symmetric vibrational mode will be considered for both ground and ionized electronic states. Going back to the general vibronic selection rules, $\Gamma_{n,\{v\}} = \Gamma_{m,\{v'\}} = \Gamma_1$ and then, the vibronic transitions are governed by the selection rules applied to the electronic transitions $\Gamma_m \otimes \Gamma_n \supset \Gamma_{d_i}$.

4.3.2 Example: the core photoionization of methane

In order to illustrate the efficiency of group theory applied to spectroscopy, we will study the case of CH_4 molecule. The four C-H bonds are disposed along the vertices of a tetrahedron molecule and then methane is invariant under the symmetry operations of the T_d point group symmetry (see Table 4.1).

T_d	E	$8C_3$	$3C_2$	$6S_4$	$6\sigma_d$		
A_1	1	1	1	1	1		$x^2 + y^2 + z^2$
A_2	1	1	1	-1	-1		
E	2	-1	2	0	0		$(2z^2 - x^2 - y^2, x^2 - y^2)$
T_1	3	0	-1	1	-1	(R_x, R_y, Rz)	
T_2	3	0	-1	-1	1	(x, y, z)	(xy, xz, yz)

Table 4.1: Character table of the T_d point group symmetry.

A molecule has three types of internal energy, which are (in decreasing order of magnitude) electronic, vibrational and rotational. The rotational states are generally not resolved in photoionization experiment. Their role in the symmetry of transition matrix elements, therefore, can be neglected.

Vibrational states

We have seen in Section 3.1 that nuclear motion close to the equilibrium position can be separated in decoupled normal modes, consequently simplifying the analysis of the molecular vibrations. Group theory permits to operate such reduction by inferring the symmetries of the normal modes of vibrations. To do so, one has first to express the nuclear motion in the symmetry group

of the molecule. The displacement of each atom can be described in terms of three unitary vectors in the atomic frames of reference (see Figure 4.7). The transformation of these atomic displacements through the different symmetry operations is defined by the $3M \times 3M$ transformation matrix $\mathbf{M}$, where $M(R)$ is the number of atoms in the molecule.

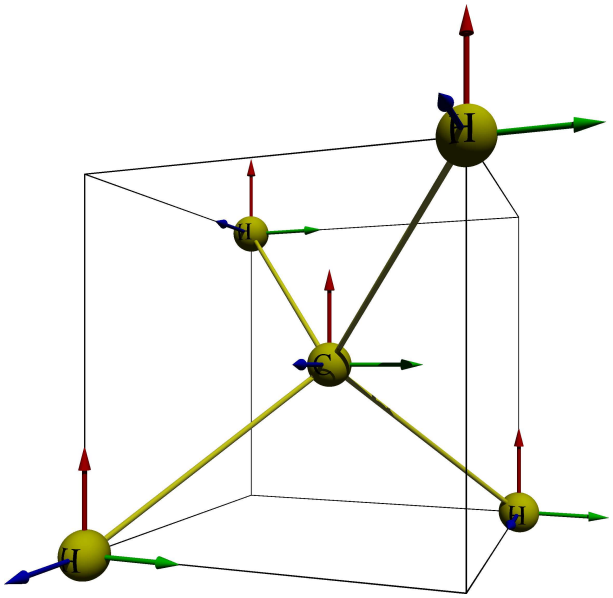

Figure 4.7: Geometrical representation of CH_4 molecule.

To determine how many normal modes there are for each IR, there is no need to evaluate this matrix for each operation symmetry, we only need the trace of it. Considering the transformations of all the 3M vectors:

- the identity E conserves of course all the vectors
- each C_3 axis passes through a different vertex of the cube and do not conserve any atomic vectors: $\chi(C_3) = 0$
- each C_2 axis is aligned with a different vector of the central C atom and then conserve one (1) and flip the two others: $\chi(C_2) = 1 - 1 - 1 = -1$
- each improper rotation S_4 rotates two vectors of the central C atom by $\pi/4$ and flip the third aligned one: $\chi(S_4) = -1$
- each diagonal plane σ_d is perpendicular to a different cube face and passes through two atoms. It conserves the aligned vector of each two atoms, as well as the one of the central C atom: $\chi(\sigma_d) = 1 + 1 + 1 = 3$.

T_d	E	$8C_3$	$3C_2$	$6S_4$	$6\sigma_d$
Γ_{nuc}	15	0	-1	-1	3

Table 4.2: Representation of the atomic displacements in the T_d point group symmetry.

Then, the representation Γ_{nuc} of the atomic displacements is expressed in the T_d point group symmetry as:

This representation can be decomposed in a basis of IR whose coefficients are given by Equation (A.4):

$$\Gamma_{nuc} = A_1 + E + T_1 + 3T_2 \tag{4.77}$$

According to Table 4.1, the T_1 IR corresponds to the rotations while the translations transform as T_2. Then, the vibration normal modes are represented by:

$$\Gamma_{vib} = A_1 + E + 2T_2 \tag{4.78}$$

where A_1 and E are Raman active and T_2 are both IR and Raman active.

If we now use the set of four C-H bond lengths and the set of six H-C-H interbond angles as bases, we obtain in a similar way the expression of the representation for the bond lengths displacements Γ_{str} and for the angles variations Γ_{ben} respectively:

T_d	E	$8C_3$	$3C_2$	$6S_4$	$6\sigma_d$
Γ_{str}	4	1	0	0	2
Γ_{ben}	6	0	2	0	2

Table 4.3: Representation of the C-H bond lengths and the H-C-H interbond angles in the T_d point group symmetry.

Using the great orthogonality theorem, it easily found that these representations reduce as:

$$\Gamma_{str} = A_1 + T_2 \tag{4.79}$$

$$\Gamma_{ben} = A_1 + E + T_2 \tag{4.80}$$

The sum of all the representations $\Gamma_{rot} + \Gamma_{tra} + \Gamma_{str} + \Gamma_{ben}$ should give in principle the representation Γ_{nuc}. But as seen, the sum is one in excess of the correct number for each symmetry operation, which means that there is an extra A_1 representation which corresponds to the impossible situation where all the angles are varying by the same quantity. This result is due to the fact that we treated the six angles as independent while in fact they are not. Then, we see that vibrational normal modes are composed by four stretching modes (one for the A_1 and three degenerated for the T_2) and five bending ones (two for the E and three degenerated for the T_2). The sum of all the modes is of course consistent with the simple formula $3M - 6 = 9$. The totally symmetric stretching mode is the most easy to identify since it implies a totally symmetric representation, i.e. A_1.

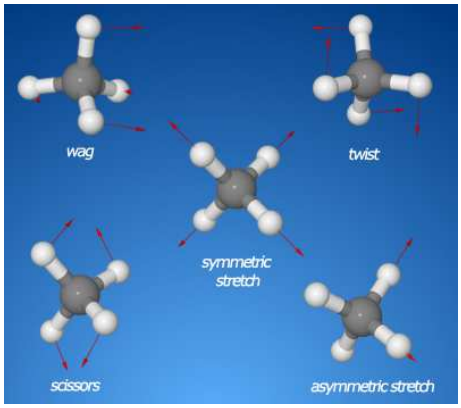

Figure 4.8: The CH_4 vibrational modes.

Electronic states

In a monodeterminantal picture, the total symmetry of the molecular electronic state is given by the direct product of each MO symmetry. For CH_4, we have the following configuration: $1A_1^2\ 2A_1^2\ 1T_2^6$. Since the direct product of two identical IR at least contains the totally symmetric representation and that each MO of the ground state is filled by two paired electrons, then we can deduce that the symmetry of CH_4 is A_1. In fact, this argument is quite general and holds for any closed shell molecule, atom or ion: any doubly occupied level contribute A_1. Therefore, for an ion, only the singly occupied levels will determined the total molecular symmetry. In CH_4, the lowest MO corresponds almost entirely to the C 1s AO. The carbon atom being central and the 1s AO totally symmetric, we know even without looking to the MO diagram that the core orbital is a basis for the A_1 representation. Then, the core ionized CH_4 molecule is also totally symmetric. As an example, and ac-

cording to Figure B.4, emission of a valence electron from the HOMO to the continuum state, would give instead a T_2 symmetry for the molecular ion. The total symmetry of the final state is the direct product of the symmetry of the residual molecule Γ_{ion} and of the electron in the continuum Γ_{e^-}. Because the ground state is totally symmetric, the selection rules predict that the direct product $\Gamma_{gs} \otimes \Gamma_{ion} \otimes \Gamma_{e^-}$ should be the same as the ones of the dipole components (the Cartesian coordinates in the character table). For the C1s photoionization of methane, we have seen that $\Gamma_{gs} = \Gamma_{ion} = A_1$ and then $\Gamma_{e^-} = T_2$ (all the dipole components lying into the T_2 IR).

Now we have to analyze the involved vibrational and electronic symmetries for the photoionization process of interest ; to do this we need to determine the partial wave contributions to the photoelectron symmetry in the T_d point group of symmetry. Such knowledge is particularly useful for theoretical calculations in order to avoid to evaluate vanishing integrals and gain computational time. To complete the example, we will study the contribution of the first three angular momenta to the T_2 photoelectron symmetry. In this case, the character table 4.1 provides directly the information needed to reduce their representation:

- the totally symmetric functions are defined by $x^2 + y^2 + z^2$, then the s AO is characterized by the A_1 IR (it is general for all the point group)
- the linear functions are defined by the Cartesian coordinates, then the p AO is characterized uniquely by the T_2 IR
- the quadratic functions are defined by $(2z^2 - x^2 - y^2, x^2 - y^2)$ and (xy, xz, yz), then the d AO is characterized by E and T_2 IR.

Since the $l = 0$ function only belong to A_1, it will show up only for a photoelectron having a A_1 symmetry. The same logic applies to the $l = 1$ functions but for the T_2 symmetry. The $l = 2$ functions are represented by the E and T_2 IR. They contribute partially to both symmetries and the coefficients of the symmetry adapted linear combination (SALC) can be deduce by constructing explicitly the Wigner operator:

$$P_{ij}^k = \frac{l_k}{g} \sum_R D_{ij}^{k*}(R)\hat{R} \tag{4.81}$$

where:

$$P_{ij}^k P_{lm}^n = \delta_{kn}\delta_{jl}P_{im}^k \tag{4.82}$$

i and j refer to the matrix index of the transformation matrix for the representation Γ^k of dimension l_k.

The construction of the projector operator requires the construction of the transformation matrices which can be a very tedious task. Then, it is convenient to define a projector operator that employs only the characters (accessible form the character tables). Summing over the diagonal elements of the matrix, we obtain the expression:

$$P^k = \sum_i P^k_{ii} = \frac{l_k}{g} \sum_R \chi^k(R)\hat{R} \tag{4.83}$$

Analyzing the transformation of a d AO under all the symmetry operations of th T_d point group and applying the incomplete operator, it is possible to evaluate the SALC coefficient for the $l = 2$ partial wave, in this case equal to 1. For more lower symmetric point groups (e.g., O_h for SF_6), the coefficients are generally real numbers and requires to be evaluated computationally. Table Page 286 summarizes the different allowed electronic transitions investigated in this work, as well as the partial waves contribution to each of the possible photoelectron symmetry in the point group of the molecule.

4.4 Studied molecular systems

The choice of the studied molecular systems for the present study came naturally:

- H_2 (dihydrogen, identified in 1766 by Henry Cavendish) is the simplest compound in the universe. Since it can be numerically solve with minor approximations, it is a natural good base step for any general molecular studies.

- N_2 (dinitrogen, identified in 1772 by Daniel Rutherford) is the main compound of earth's atmosphere (78.084%). As H_2, it is a homonuclear diatomic molecule but owns much more electrons (14 in total). Its treatment then requires the use of *ab initio* methods but its high symmetry $D_{\infty h}$ makes it affordable by the most accurate ones.

- CO (carbon monoxide, identified in 1800 by William Cumberland Cruikshank) is a toxic and short lived gas in earth's atmosphere. It is a heteronuclear diatomic molecule, isoelectronic with N_2 and has very localized core MOs on the oxygen and carbon atoms. Polarization of the electronic cloud is expect to have an influence on the photoionization cross section and can be directly compared with N_2

- C_2H_2 (acetylene, discovered in 1836 by Edmund Davy) is an unstable gas in pure form and the simplest alkyne. It is a polyatomic linear molecule, isoelectronic with N_2 and CO. It belongs to the same point group symmetry than H_2 and N_2 and since the core MOs result almost exclusively

from the linear combination of C 1s AOs, the core photoionization cross section of C_2H_2 is expected to present homonuclear diatomic-like features.

- CH_4 (methane, identified in 1777 by Alessandro Volta) is the simplest alkane and probably the most abundant organic compound on earth. It is an important greenhouse gases (much by its quantity in the atmosphere than by its potential which is about 25 GWP), mainly produced via natural routes (human-induced or not). It is a few electrons (10 in total) non-linear polyatomic molecule with a high symmetry and very localized core MO on the carbon atom (as in CO).

- CF_4 (tetrafluoromethane, discovered in 1926) is the simplest fluorocarbon and a very potent and stable greenhouse gas (6500 GWP, even though few abundant in the atmosphere). It is structurally equivalent to CH_4 where hydrogen atoms have been replaced by fluorines (the most electronegative element), which makes the bonds stronger and more polarized. Also, addition of fluorine atoms increase considerably the number of electrons of the system (42 in total) and reduces the use of high level *ab initio* methods.

- BF_3 (boron trifluoride, discovered in 1808 by Joseph Louis Gay-Lussac and Louis Jacques Thnard) is a toxic gas and a useful Lewis acid. It is a planar polyatomic molecule composed of 32 electrons, containing polar bonds with fluorine atoms (as for CF_4). The main interest of this molecular system is due to its very wide and well resolved vibrational progression in the photoelectron spectra and the expected strong influence of the fluorine atoms to the scattering of the photoelectron at low photon energies.

- SF_6 (sulfur hexafluoride, discovered in 1901 by Henri Moissan and Paul Lebeau) is a hypervalent molecule and the most potent greenhouse gas (22800 GWP). It is mainly used as a gaseous dielectric medium in the electrical industry. It is part of the series of fluorinated molecules and the biggest system studied in this work (although its complexity is reduced computationally by the high symmetry of the O_h point group). A particular outer-valence shell photoionization involving many open-channel transitions has been investigated, in order to prove the general character and the wide-range applicability of the theoretical method developed here.

Structural details and database are presented in Appendix B.2. The complete molecular diagrams for each of these systems are shown in section B.3.

4.5 Computational details

It is noteworthy to mentioned some technical details in the implementation of the present method:

- The vibrational wavefunctions calculated using the B-spline basis set form an orthogonal basis but have to be normalized to 1:

$$\int \chi_v^* (R) \chi_v (R) \, dR = 1 \tag{4.84}$$

- The PECs calculated in the CASSCF/MRCI theory level are generally obtained for a limited range of internuclear distances, depending on the ionized states. In order to calculate the bound and unbound vibrational states, the PECs need to be extrapolated at both extremities. By fitting with pieces of analytical functions at each side of the potentials, we are able to produce all the PECs on the interval $[0.0001, 20]$.

- For diatomic molecules, when the internuclear distance R is smaller than twice the maximum radial intervals R^i_{max} of the off-centers, we took $R^i_{max} = R/2$ in order to avoid overlap between the off-centers.

- In the off-centers, continuity of the wavefunction is ensured by removing the last three B-spline functions from the localized set.

- The grid of B-splines is linear but an additional knot point is chosen at the position of the off-centers in order to obtain a better description of the cusp in the wavefunction.

- Gauss-Legendre integrations are carried out in a set of radial and angular intervals with different density of points of integration. These intervals are defined according to the point-group symmetry of the molecule and to the electronic density. Because the electronic density is strongly concentrated around the atoms, the number of points of integration is usually increased close to the nuclei.

- In the resolution of the eigenvalues equation, the global phase of the wavefunctions is unpredictable. Thus, random signs appear in the dipole matrix elements values depending on the internuclear distances. They have to be changed afterward, taking care of the continuity of each coupling function (see Figure 4.10), in order to have a consistent phase of the calculated wavefunctions for all molecular geometries. Because the number of geometries, photoelectron energies and photoionization channels can be very large (as in the case of the $4T_{1u}^{-1}$ photoionization of SF_6), a program has been designed to reconstruct automatically the continuity of each electronic dipole couplings as a function of the normal coordinate.

- The dipole matrix elements depend on the angular momentum of the photoelectron, the internuclear distance and the photoelectron energy. The latter is defined in a grid which is generally chosen of quadratic form:

$$\varepsilon_k = \varepsilon_{min} + k^2 \frac{\varepsilon_{max} - \varepsilon_{min}}{N_{grid}^2} \tag{4.85}$$

  where N_{grid} is the number of energy values contained in the grid.

  In order to calculate the single photoionization cross section for specific values of the photon or the photoelectron energy, one has to interpolate the dipole matrix elements for each R, l and ε (see Figure 4.9). This interpolation in ε can be carried out by using B-splines and taking into account the simple relation: $\varepsilon = \omega - (E_{v'} - E_v)$.

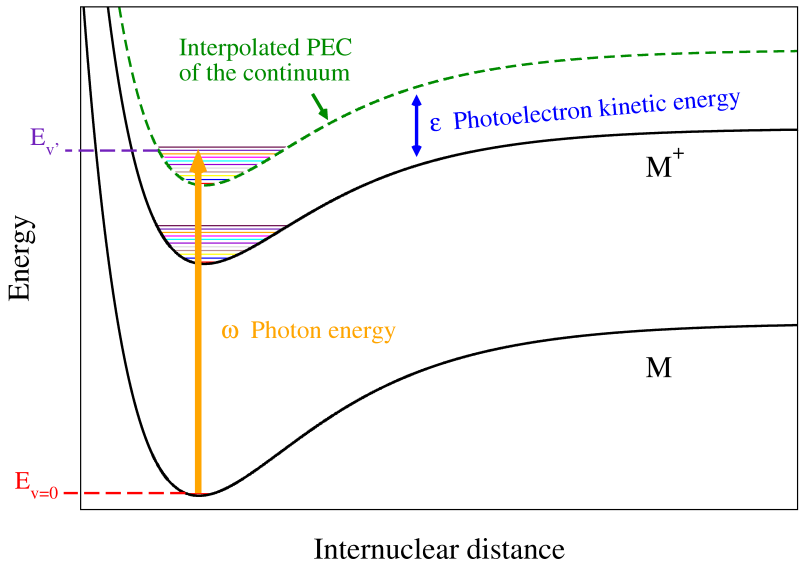

Figure 4.9: Interpolation process for an ordinary dipole matrix element.

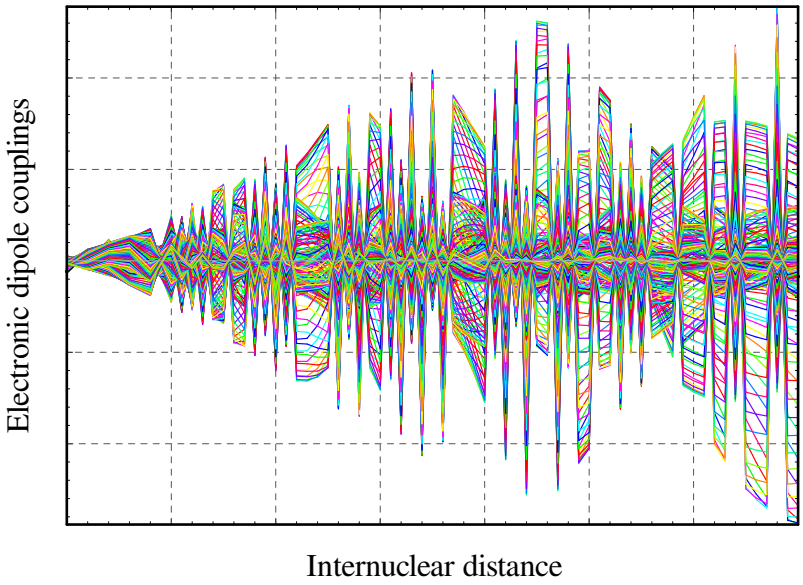

(a) Raw dipole matrix elements

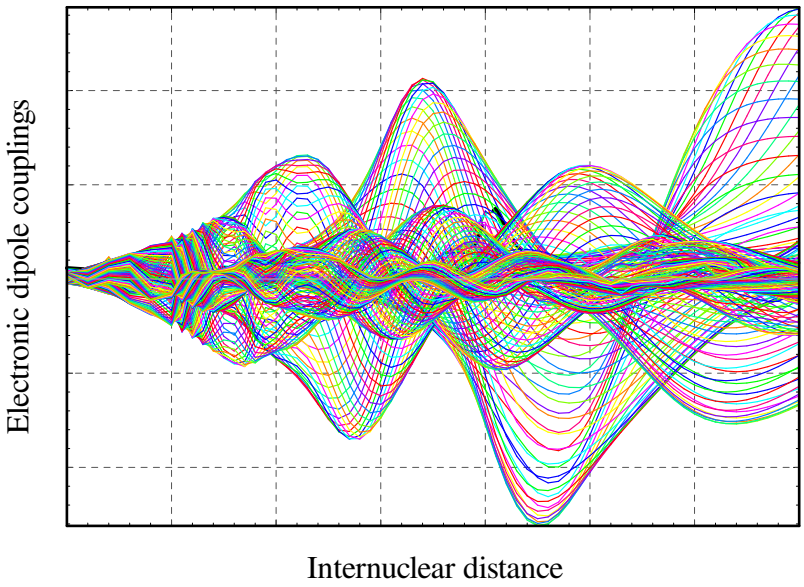

(b) Corrected dipole matrix elements

Figure 4.10: Sign changing operation on the real part of an ordinary set of dipole matrix elements, for a determined partial wave. Each curve corresponds to a specific energy ε of the photoelectron energy grid.

Some important parameters used in the calculation of the different molecular systems are presented in Table 4.4.

Mol.	κ	N_R	N_ε	R^0_{max} (a.u.)	R^i_{max} (a.u.)	N^0_b	N^i_b	L^0_{max}	L^i_{max}
N_2	1	56	200	25	1.0	200	10	10	1
CO	2	56	200	25	1.0	200	10	10	1
C_2H_2	2	88	200	40	0.5	400	10	20	1
CH_4	1	60	200	40	0.5	200	10	13	1
CF_4	1	69	200	40	1.0	400	14	14	2
BF_3	1	34	150	30	0.6	200	10	30	2
SF_6	1	34	200	25	0.8	200	12	30	2

Table 4.4: Computational parameters for the electronic structure calculation. The order of the B-splines is always set to $k = 10$ and the order of the Gauss-Legendre integration to 12.

All the calculations performed to obtained the vibrational structure of H_2, CO, C_2H_2, CH_4, CF_4, BF_3 and SF_6 made uses of 1000 B-splines of order $k = 8$ expanded linearly in a box of 10 a.u.

Computational times for the calculation of the electronic structure are compared in Table B.4 for most of the molecular systems studied in this work and in the case of core photoionization.

Part II

Results

Introduction

A very simple and usual approach for the description of the vibronic transitions is the Franck-Condon principle. The so-called Condon approximation states that the electronic dipole couplings are independent of the nuclear coordinates, at least in a spatial region close to the geometry equilibrium of both ground and ionized states (the Franck-Condon region). Then, Equation 4.70 can be factorized as:

$$\sigma_{\alpha}^{vv'}(\omega) = \frac{4\pi^2\omega}{3c} T_{\alpha}^{-}(\omega) \left| \int \chi_{i,v}^{*}(R)\, \chi_{f_\alpha,v'}(R)\, dR \right|^2 \tag{4.86}$$

This equation shows that the vibrationally resolved cross section is approximately proportional to the overlap between the initial and final wavefunctions. Then, during an electronic transition, a change from one vibrational energy level to another will be more likely to happen if the two vibrational wavefunctions overlap more significantly (see Figure 4.11).

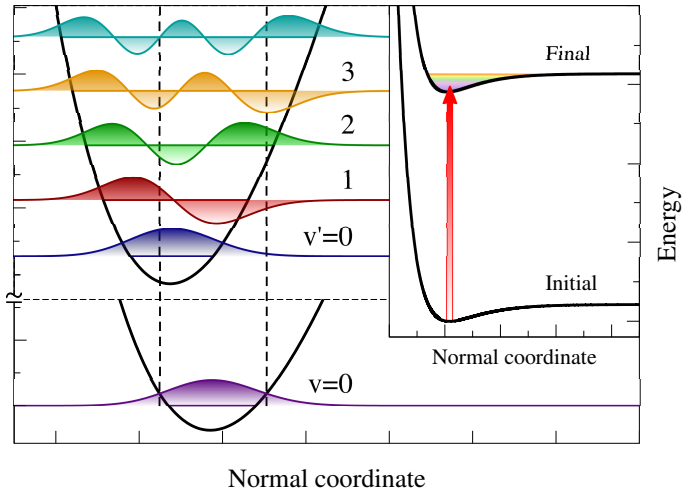

Figure 4.11: Schematic illustration of the potential energy curves and vibrational wavefunctions corresponding to the initial and final states. Dashed lines delimit the Franck-Condon region.

The Condon approximation can be justified classically by considering that the electronic transitions are essentially instantaneous compared with the time

scale of the nuclear motion. Then, the final vibrational level must be instantaneously compatible with the nuclear positions and momenta of the initial vibrational level.

The Franck-Condon principle is a simple and useful tool to predict the relative intensities of the vibrational peaks in the photoelectron spectra but is somehow too rudimentary. In fact, many deviations to the Franck-Condon principle have been observed close to the ionization threshold from the earlier synchrotron radiation experiments. Until the advent of third generation synchrotron radiation sources and despite few pioneer theoretical works [84, 73, 295, 423], information on the high energy region was inaccessible. But because the electronic correlation plays a minor role at high photoelectron energies, it was commonly assumed that the Franck-Condon was valid far from the ionization threshold (see for example [198]). Recent experiments using third generation synchrotron radiation (e.g., [209]) demonstrated the contrary by revealing the presence of deviations also in the high energy region.

The present work aims to study these Franck-Condon deviations in the photoelectron spectra of diatomic and polyatomic molecules at low and high energies. The molecules presented in this part (H_2, N_2, CO, C_2H_2, CH_4, CF_4, BF_3 and SF_6) have been widely studied experimentally from the early 60's. Some of them, such as N_2 and SF_6, have drawn very soon a particular scientific interest and have been used as prototypes for the study of structures in the photoelectron spectra at low energies. In fact, most of the articles treating the molecular photoionization aim to describe the behavior of the total cross section in the low energy region. It is only very recently that some experimental and theoretical investigations have addressed the features appearing at higher energy, mostly in core photoionization.

In particular, results for N_2 and CO obtained from theoretical methods have led to the observation of interesting interference phenomena that are often difficult to identify in total photoelectron spectra, especially at high photon energies [170, 73, 295, 385, 340, 84, 407, 226, 227, 45]. Two of these phenomena lie at the heart of quantum mechanics: (i) two-center coherent electron emission leading to Young's type double-slit interferences [75] and (ii) electron diffraction by the molecule's atomic centers. These processes are possible because, at high photon energy, the wavelength λ_e of the ejected electron is comparable to or smaller than the size of the molecule [118]; consequently, ejected electrons experience the same phenomena as normal wave do. As a result, oscillations in the photoelectron spectra are expected but they are barely observed in the total photoelectron spectra due to the rapid decrease of the corresponding cross section with photon energy [64].

Actually there is a growing interest in such interference and diffraction patterns at high electron kinetic energies, both because of fundamental under-

standing of the basic phenomenon, which has been hitherto barely explored due to limitations of the previous generation of synchrotron radiation sources, and because of its great potential as a means of (i) reconstructing molecular geometry and (ii) following the time evolution of the electronic cloud during chemical processes. The latter aspect has become a real possibility due to the advent of ultrashort, femto and sub-femtosecond radiation pulses produced by free-electron lasers or high-harmonic generation sources [435, 202]. While weak EXAFS oscillations in absorption cross sections due to diffraction are nowadays a standard tool for local structure determination in solid state, surface science and biological studies, comparable studies in photoelectron emission in the gas phase are just in their infancy. In fact up to now only two cases have been thoroughly explored: the diatomic homonuclear case, especially N_2 [340, 84, 73, 295, 407, 385, 226, 227], after the Cohen-Fano prediction [64], and the HOMO/HOMO-1 oscillations in C_{60} and related systems [221, 65, 81, 129, 436, 220, 201]. It is becoming clear, however, that such interference/diffraction patterns are an ubiquitous phenomenon, although more complex in non-symmetrical molecules and further complicated in the valence shell by mixing of different atomic orbitals (i.e. delocalized molecular orbitals), which on the other side offer an important source of information on electronic structure and chemical effects. Actually the main experimental difficulty is to extract the relatively small diffraction features from the rapidly decreasing cross section as a function of photoelectron energy. The latter difficulty can be easily overcome by taking the ratios between two related cross sections, the neatest examples being $1\sigma_g/1\sigma_u$ emission in N_2 or the HOMO/HOMO-1 in C_{60}. Alternatively, such oscillations become apparent in angular distribution parameters and in non-dipolar parameters [392], as well as in the ratios of vibrationally resolved photoelectron spectra [45]. It is this latter observable that will be preferentially explored in the present study.

It is clear from the foregoing discussion that, although the basic mechanism is clear, quantitative interpretation of the experimental results and inversion of the experimental data to reconstruct molecular parameters will require accurate computational modeling, able at the same time to deal seamlessly all the way from diatomics to large, non-symmetrical molecules.

Because it has been designed to treat accurately the photoionization process at high photoelectron energies and for any kind of molecules, the present method (described in Section 2.4.2) is particularly suitable to carry out such study. In this part we present the results obtained for different molecular systems. The first Chapter will be devoted to analyze the theoretical results obtained for core and valence shell photoionization of two diatomic molecules: N_2 and CO. In particular, we will analyze the interferences appearing in the v-ratios at high photon energies and give a simple model that permits to interpret the valence shell photoionization of both molecules. The second Chapter is devoted to the study of polyatomic molecules. To each section correspond

a particular molecular system. Because of its structural proximity with N_2, the polyatomic study starts with C_2H_2. In particular, we will show that the core shell photoionization of C_2H_2 indeed resemble the one of N_2 and observe for the first time two-center interferences in a polyatomic molecule. The three next cases concern the core photoionization of CH_4, CF_4 and BF_3 respectively. It will be shown in particular that diffraction patterns are observed at high photoelectron energies as in the core shell photoionization of CO. A simple model will be developed in order to get a better understanding of the mechanism. Finally, valence shell photoionization of SF_6 associated with the fifth band of the photoelectron spectra will be presented and discussed. In particular, complex features will be observed in the v-ratios at high energies.

5. Diatomic molecules

Photoionization of simple diatomic molecules has been extensively investigated both from the experimental and theoretical points of view. In particular, a wealth of experimental and theoretical data has been published for total cross sections corresponding to core as well as valence-shell photoionization of the prototype N_2 [134, 189, 60, 227, 293, 151, 434, 317, 333, 308, 84, 429, 58, 237, 83, 224, 356, 225, 326, 378, 379, 235, 437, 357, 372, 43, 337, 416, 69, 304, 260, 232, 359, 74, 22] and CO [134, 189, 398, 160, 200, 154, 316, 293, 151, 349, 325, 429, 58, 59, 336, 414, 230, 275, 353, 360, 74] molecules, from the ionization threshold up to a few tens of eV above it. More recently, the advent of high-brilliance 3rd-generation synchrotron radiation sources in combination with high energy-resolution detection techniques has opened the way for the determination of vibrationally resolved photoionization spectra of these molecules, both at low and high photon energies [2, 199, 335, 300, 200, 1, 256, 245, 154, 369, 303, 190, 409, 340, 158, 339, 226, 304, 22]. These experimental achievements have fostered the development of new theoretical methods that, in addition to accounting for electronic degrees of freedom, are also able to describe the molecule's vibrations [2, 279, 335, 58, 59, 1, 281, 338, 256, 218, 303, 409, 340, 407, 339, 401, 226, 136, 304, 22].

It is well known that, in general, reasonable values of total cross sections can be obtained by assuming that the nuclei are fixed at their equilibrium positions (the fixed-nuclei approximation). However, to evaluate the vibrationally resolved cross sections, one must also calculate the electronic wavefunctions in a grid of molecular geometries, since the nuclei move in the potential created by the electrons. This makes the calculations much more expensive.

A large number of pioneering theoretical studies have been performed by Poliakoff and coworkers, and McKoy and Lucchese. Reviews covering most early work can be found in reference [296], and in a recent paper [229] (see also references therein). However, most of these studies have focused on the valence low-energy region and on the effect of shape resonances in vibrational branching ratios. Only a few of these studies have been performed in the high energy region [73, 295, 303].

In this Chapter we present results obtained with the present method for two diatomic molecules: N_2 and CO. The study concerns the core and valence shell

photoionization. Vibrationally resolved cross sections have been calculated with DFT and TDDFT method using a LDA or a LB94 functional. Since a large number of theoretical methods often making use of the fixed-nuclei approximation have been used to evaluate total photoionization cross sections at lower energies, we will also discuss the performance of our method (DFT and TDDFT) for total core and valence-shell photoionization cross sections of N_2 and CO at low photon energies. The results obtained with the present method are systematically compared with the available experimental and theoretical data at low and high photon energies and for both core and valence-shell ionization.

5.1 Potential energy curves

In order to calculate the vibrational structure (see Chapter 3), we first need to evaluate the electronic energy term $V(R)$ in Equation (3.44). The eigenvalues of the electronic TISE have to be obtained in a sufficiently dense grid of internuclear distances which range should be at least large as the Franck-Condon region.

The potential energy curves used in these calculations are obtained from different methods. The ground state of the neutral molecule and the ground and excited states of the molecular cation have been evaluated by using a multi-reference configuration interaction (MRCI) method within the complete active space self-consistent field (CASSCF) approximation. For electronic states of the cation containing a hole in the core, we have used Morse potentials using accurate spectroscopic data taken from the literature. Figure 5.1 shows the potential energy curves used in the vibrational motion Schrödinger equation for the N_2 and CO molecules. In the case of the ground state of the neutral molecule, the figure illustrates a comparison between the Morse potential and calculated *ab initio* potential energy curve. As can be seen, both potentials are nearly identical in the vicinity of the energy minimum, thus suggesting that a Morse description of core-hole states for which standard CASSCF-MRCI calculations are not so easy to perform is accurate enough. For the ground state of the neutral and the cation, as well as for the lowest excited (valence) states of the cation, our calculated potential energy curves are in very good agreement with the ones previously reported in the literature [294, 135, 215, 342, 426, 219, 409, 10, 17, 133, 105, 104, 434, 265, 279, 18, 49, 107, 405, 178].

5.2 Total cross section

In this section we will present non vibrationally resolved photoionization cross sections for photon energies going from the ionization threshold up to several

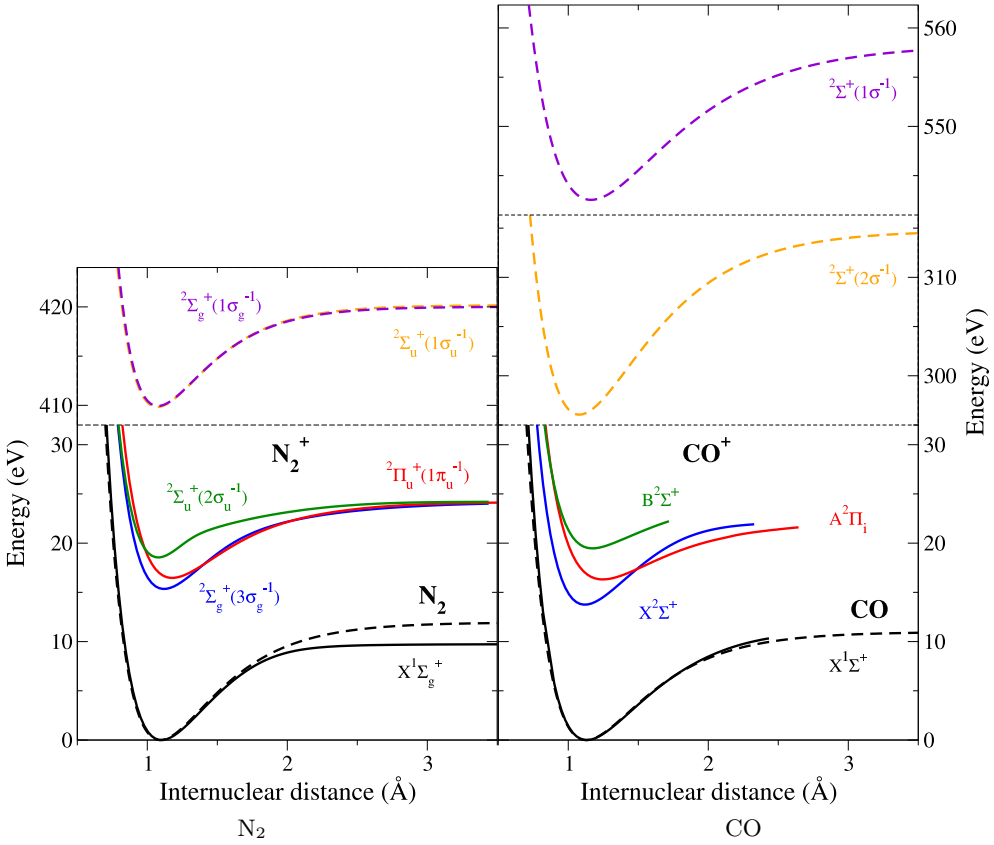

Figure 5.1: Potential energy curves for the ground state of N_2 and CO, the three first valence electronic states and the K-shell of N_2^+ and CO^+. Valence electronic states (solid lines) were obtained using CASSCF-MRCI *ab initio* method and core ionized electronic states (dashed lines) are Morse potentials taken from literature: [382] for N_2 ; [245] for the ground state of CO and [157] for the core ionized states.

hundreds eV above it. These cross sections have been obtained by summing over all the vibrationally resolved cross sections. In all transformations from photoelectron energies to photon energies and vice versa, we have used the values of the adiabatic ionization potentials given in Table B.3.

Before entering in the detailed analysis of each figure, it is important to remind a well-known deviation to the Franck-Condon factor that appears in the near threshold photoelectron spectra of many molecules: the shape resonance.

Shape resonance

Shape resonance is a phenomenon that results from the existence of a potential barrier. The name indicates by itself the dependence of the resonance on the "shape" of the barrier and the associated inner and outer wells. Shape resonances constitutes a category of resonances involving "centrifugal barriers" and which has been found to play a prominent role in a large variety of processes in molecular physics. In molecular photoionization, the mechanism is illustrated by Figure 5.2. It shows that at a certain energy, the photoelectron can be trapped by the potential barrier and may eventually tunnel and escape. This temporal trapping generates a quasi-bound state (green line) whose lifetime is short and produces a relatively sharp and strong resonance in the cross section. This resonance is as strong as the overlap with initial state. Below this energy and for higher energies, the inner well does not support a quasi bound state and the resulting wavefunction is essentially an eigenfunction of the outer well. As seen, the shape resonance phenomenon is a one-electron process in nature that can be treated at the present level of theory. However, formation of a quasi-bound state may amplify the many-electron effects. In general, the photoelectron has a such diffuse wavefunction that it barely couples with the residual electrons. But since the resonant wavefunction is enhanced in the core region, overlap with the residual bond states is higher and can give rises to amplified many-electron effects in the shape resonance energy range.

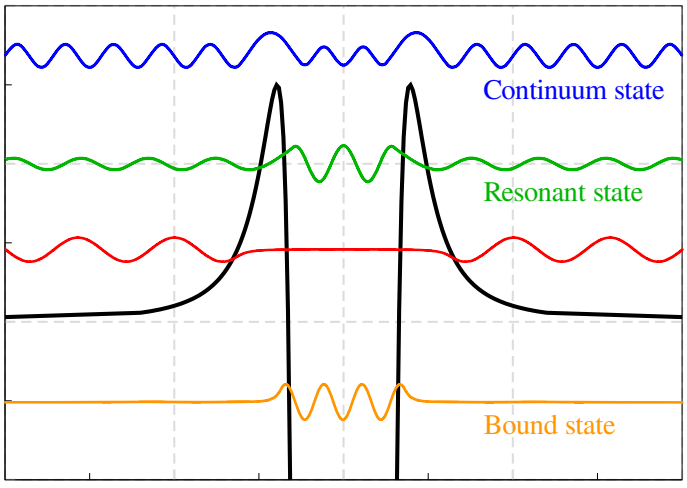

Figure 5.2: Schematic illustration of the formation of a resonant quasi-bound state in the inner well of a molecular potential.

The potential barriers that cause shape resonance derives from a competition between the attractive electrostatic forces and the repulsive centrifugal

forces and can be simplified as follows:

$$V_{eff} \propto V_c + \frac{l(l+1)}{r^2} \quad \text{for } l \geq 1 \tag{5.1}$$

Figure 5.3 presents an example of molecular electrostatic potential taken along the main axis of CO molecule and calculated at the CASSCF-MRCI *ab initio* level of theory. Because of the absence of inversion symmetry, the resulting two centrifugal barriers have different characteristics (height, width). As for most of the cases, the barriers resides on the perimeter of the charge distribution. As illustrated in Figure 5.3, an alternative but equivalent interpretation of shape resonances is to assign them to excitations to virtual anti-bonding MOs located above the ionization threshold. When looking at the molecular potential taken in a direction perpendicular to the main axis (see Figure 5.4), one can notice the absence of centrifugal barrier. Consequently, the shape resonance effects are not expected to manifest in all the ionization channels. As illustrated by Figure 5.4, for diatomic molecules with the barrier located along the main axis, shape resonances are observed only in the symmetry channel associated with the z dipole component (i.e. when the polarization vector is parallel to the main axis).

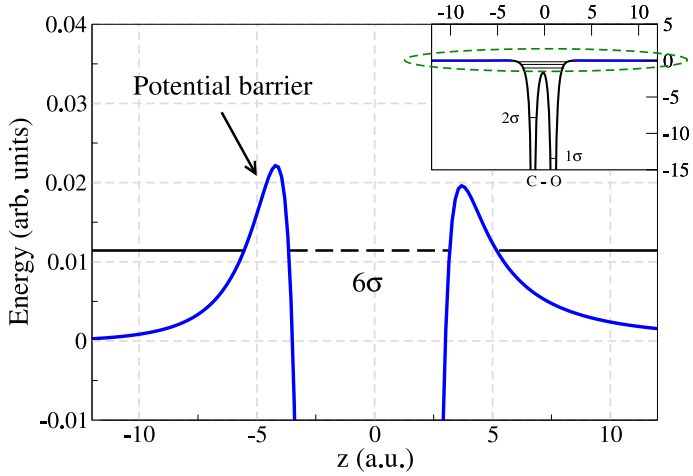

Figure 5.3: Molecular electrostatic potential (MEP) of ground state CO calculated using CASSCF-MRCI. The MEP has been taken along the main axis of the molecule.

The shape resonance is a molecular effect in origin because it results from the interaction between the photoelectron and an anisotropic potential. In an isotropic potential, the core photoionization process produces a p-wave photoelectron at infinity. But when considering the anisotropy of the molecular field, this electron is expected to scatter into the entire range of angular mo-

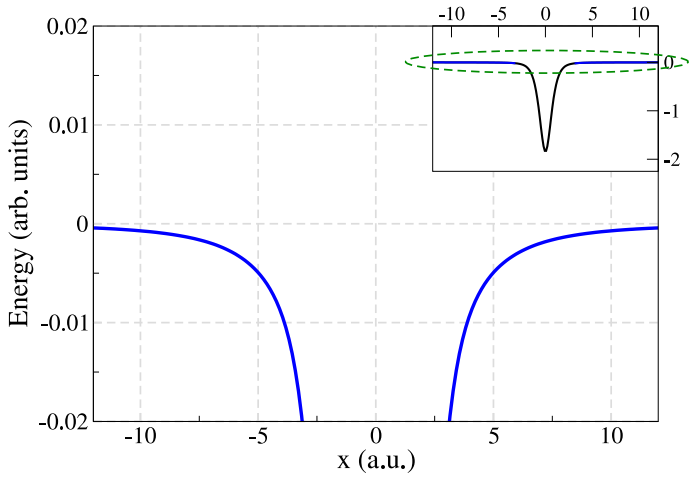

Figure 5.4: Same as Figure 5.3. The MEP has been taken along a direction perpendicular to the main axis of the molecule.

mentum states contributing to the allowed ionization channels. Depending on the distance between the centrifugal barriers, which is related to the spatial extent of the atoms, specific angular momentum components of the continuum states will be capable to penetrate the barrier. In other words, shape resonance affects only a few partial waves of the continuum wavefunction.

Among the earliest and strongest evidences of the shape resonant effects in molecules are the core photoabsorption spectra of SF_6 and the core photoionization of N_2. In 1975, J. L. Dehmer and Dan Dill published an article [83] in which they use nitrogen molecule as a prototype for the study of the shape resonance effects. The authors performed a calculation using the multiple scattering method (MSM) and described for the first time the shape resonance in the $1\sigma_g \rightarrow \varepsilon\sigma_u$ transition channel. More particularly, they could observe that this resonance is due to the trapping of the $l = 3$ component of the σ_u wavefunction. So far, shape resonances have been observed experimentally in many molecules, diatomics (e.g., N_2, O_2, CO, NO, $\cdots$) as polyatomics (CO_2, OCS, N_2O, SF_6, BF_3, SiF_4, NF_3, CF_4, $\cdots$). The shape resonance effects are also visible in the valence-shell photoionization and are expected to be stronger since the overlap between initial MO and quasi-bound state is higher.

Figures 5.5, 5.6 and 5.7 show the photoionization cross sections of N_2 and CO that correspond to electron removal from the highest-occupied molecular orbital (HOMO), the HOMO-1 and the HOMO-2 orbitals of both molecules. The photon energy range goes from the ionization threshold up to 60 eV. The available experimental data are compared with theoretical results previously

published in the literature and with those obtained by using the DFT and TDDFT methods described in the previous section. As can be seen, results from the TDDFT method are slightly in better agreement with experiment than those from the DFT method. This is not surprising because, electrons ejected in this range of photon energies are slow and, therefore, electron correlation is expected to play a significant role. This is especially important in the vicinity of shape and Feshbach resonances, which lead to the peaks observed just above the ionization threshold. Previous theoretical methods also lead to reasonable results, although they were obtained in the fixed nuclei approximation and, in some cases, they do not predict any structure near the ionization threshold. RPA results are very close to our TDDFT results and to experiment, and they also predict the existence of resonance near threshold, but one should notice that some of these RPA results were obtained by using effective charges chosen to minimize the differences with the experimental results. The many structures observed in the R-matrix results for N_2 are likely due to the presence of pseudo-resonances that are the consequence of using the fixed-nuclei approximation. These resonances are completely washed out by inclusion of the nuclear motion.

The magnitude and overall shape of the cross sections is very similar for N_2 and CO. However, resonance structures near the ionization threshold are different. For instance, while experiments exhibit a pronounced peak at around 23 eV in $N_2(1\pi_u^{-1})$ photoionization, such peak is barely visible in $CO(1\pi^{-1})$ photoionization. Interestingly, the present TDDFT results predict the existence of a peak in both cases (although less pronounced than that observed in $N_2(1\pi_u^{-1})$. Also, $N_2(2\sigma_u^{-1})$ and CO $(4\sigma^{-1})$ photoionization cross sections are significantly different near threshold. While experiments for the former predict the existence of a small maximum at around 35 eV, for the latter they predict a pronounced maximum at around 32 eV. The latter maximum is very well reproduced by most existing theories, but the former is only reproduced by the present TDDFT results although 5 eV lower in energy.

In the $1\pi_u^{-1}$ photoionization channel, a sharp structure is visible in all the experiments at around 23 eV and is only described by the R-matrix method (a little bit higher in energy). Then appears a very smooth bump described by the multichannel methods (MCFCHF, RPA and TDDFT). The energy position of this feature ($\sim$ 30 eV) indicates that it is due to the mixing with the $3\sigma_g \rightarrow \varepsilon\sigma_u$ channel.

It has been shown by multi-channel RPA calculations performed on valence photoionization of N_2 [337] that interchannel couplings are responsible for unexpected structures in the $2\sigma_u \rightarrow \varepsilon\sigma_g$ photoionization channel. Indeed, the contribution of the $1\pi_u \rightarrow \varepsilon\pi_g$ channel leads to an enhancement of the maximum close to the threshold, the $3\sigma_g \rightarrow \varepsilon\sigma_u$ affects predominantly the region around 30eV and the $2\sigma_g \rightarrow \varepsilon\sigma_u$ seems responsible for a bump at $\sim$ 50eV (see Figure 5.7).

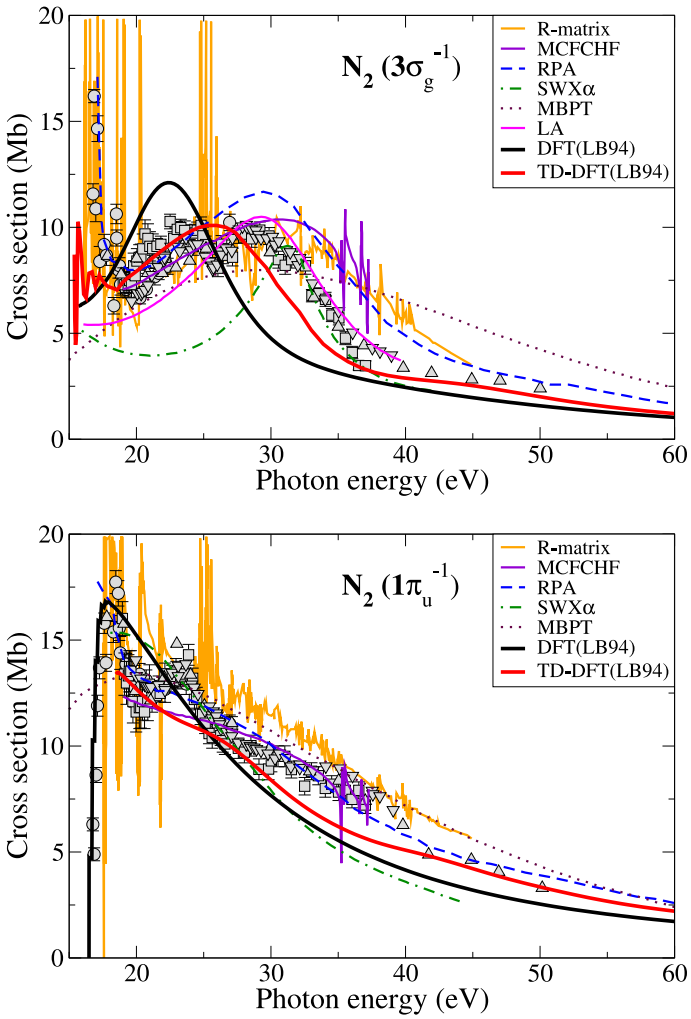

Figure 5.5: Total cross section for the $3\sigma_g^{-1}$ and $1\pi_u^{-1}$ photoionization of N_2 as a function of the photon energy. Symbols correspond to experiments - Circle: [317], Square: [434], Triangle-up: [151], Triangle-down: [293] ; Lines correspond to theory - Orange solid: R-matrix CASSCF [378], Violet solid: multichannel frozen-core Hartree-Fock (MCFCHF) four-channel length gauge [235], Blue dashed: random phase approximation (RPA) [337], Green dashed-dotted: scattered-wave (SW) Xα method [74], Maroon pointed: many-body perturbation theory (MBPT) [416], Magenta solid: Linear algebraic method (LA) [69], Black thick solid: multicenter B-splines time-independent DFT (DFT) method using a LB94 functional (this work), Red thick solid: multicenter B-splines time-dependent DFT (TDDFT) method using a LB94 functional (this work).

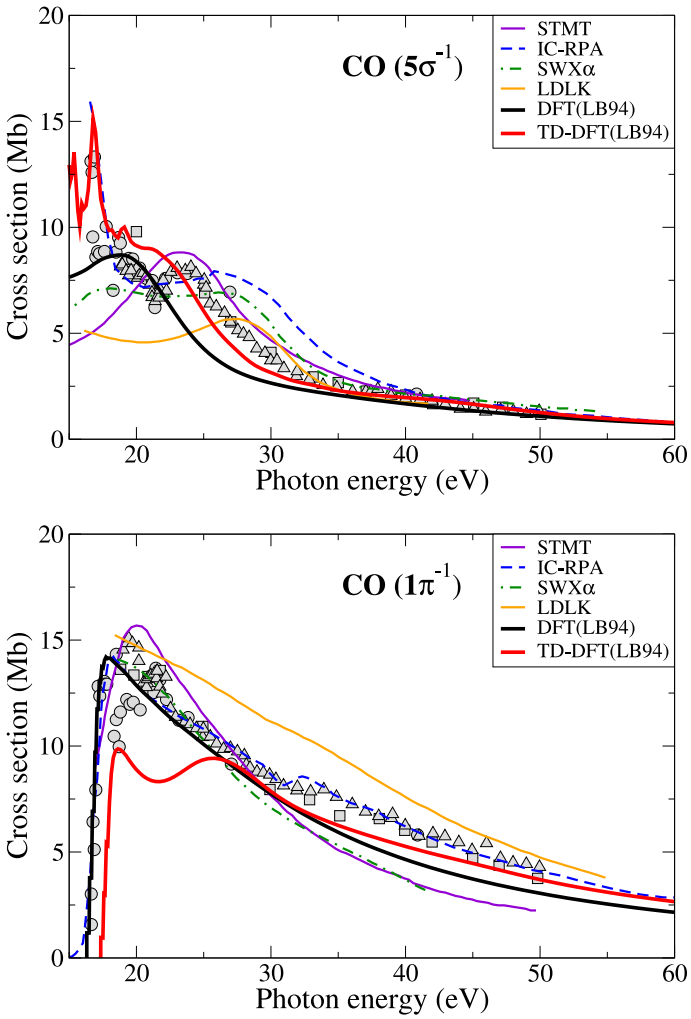

Figure 5.6: Total cross section for the 5σ and $1\pi^{-1}$ photoionization of CO as a function of the photon energy. Dots correspond to experiments - Circle: [316], Square: [151], Triangle-up: [293] ; Lines correspond to theory - Violet solid: Stieltjes-Tchebycheff moment theory (STMT) [275], Blue dashed: IC random phase approximation (RPA) in the mixed gauge [360], Green dashed-dotted: scattered-wave (SW) Xα method [74], Orange solid: logarithmic derivative version of the Kohn variational principle Lobatto technique (LDKL) [428], Black thick solid: multicenter B-splines time-independent DFT (DFT) method using a LB94 functional (this work), Red thick solid: multicenter B-splines time-dependent DFT (TDDFT) method using a LB94 functional (this work).

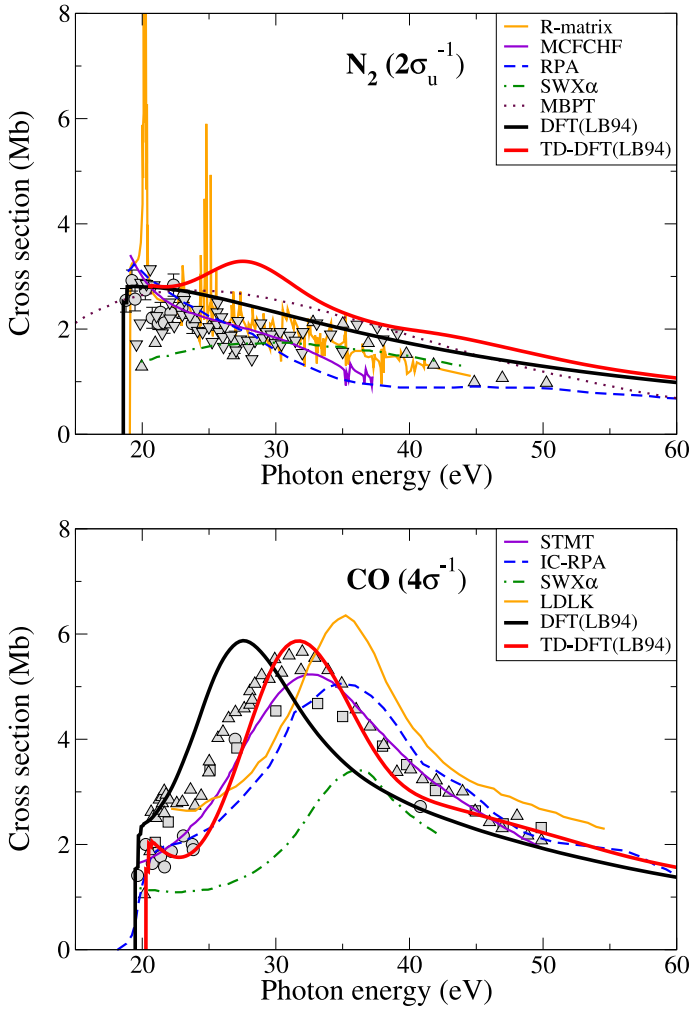

Figure 5.7: Same as Figure 5.5 and 5.6 for the $2\sigma_u$ photoionization of N_2 and the 4σ photoionization of CO respectively.

Figures 5.8 and 5.9 show photoionization cross sections of N_2 and CO from the K-shell orbitals for photon energies up to ∼35 eV above the ionization threshold. For N_2, the K-shell is formed by the $1s\sigma_g$ and $1s\sigma_u$ molecular orbitals, which are separated by only 101 meV (see Table B.3) and have a strongly delocalized character. For CO, this shell consists of the 1σ and 2σ orbitals, which are separated by almost 250 eV and are almost identical to the 1s orbitals of O and C, respectively. As for valence-shell photoionization, the best overall agreement with the existing experimental data corresponds to the TDDFT and fitted-RPA results. All cross sections exhibit a pronounced maximum in the interval lying between 5 and 10 eV above the ionization threshold. This is due to a wide shape resonance.

As seen, the shape resonance effects are stronger in the $2\sigma^{-1}$ photoionization of CO than in the $1\sigma^{-1}$ (see Figure 5.9). This due to the polarization of the anti-bonding 6σ MO which overlap more with the 2σ MO. Because N_2 is homonuclear, no such difference in the amplitude of the shape resonance is observable in the $1\sigma_u^{-1}$ and $2\sigma_u^{-1}$ photoionization of N_2 (see Figures 5.8a and 5.7a).

Apart from the shape resonances, no other structures are apparent in this low energy region, which is the consequence of the K-shell orbitals lying far away from the rest of the molecular orbitals, i.e., of the weak coupling with other ionization channels. The peaks resulting from the multichannel Schwinger configuration interaction (MCSCI) calculations are probably associated to pseudo-resonances that result from the use of the fixed nuclei approximation.

Figures 5.10 and 5.11 show the total cross section obtained with TDDFT method for all the previously considered photoionization channels of N_2 and CO. The results are plotted in a logarithmic scale and for an extended photon energy range (up to 600 eV) in order to observe the effect of the interchannel mixing. In both cases (for N_2 and CO), striking resonances show up close to the ionization threshold of each channel. It is the result of the mixing of the different photoionization channels with single excitations involving the transition of an electron from a deepest MOs to Rydberg orbitals. The most affected channel is the HOMO photoionization one since it can couple with low and high energetic single excitations. Because the core MO are the deepest, they are not affected by the interchannel mixing.

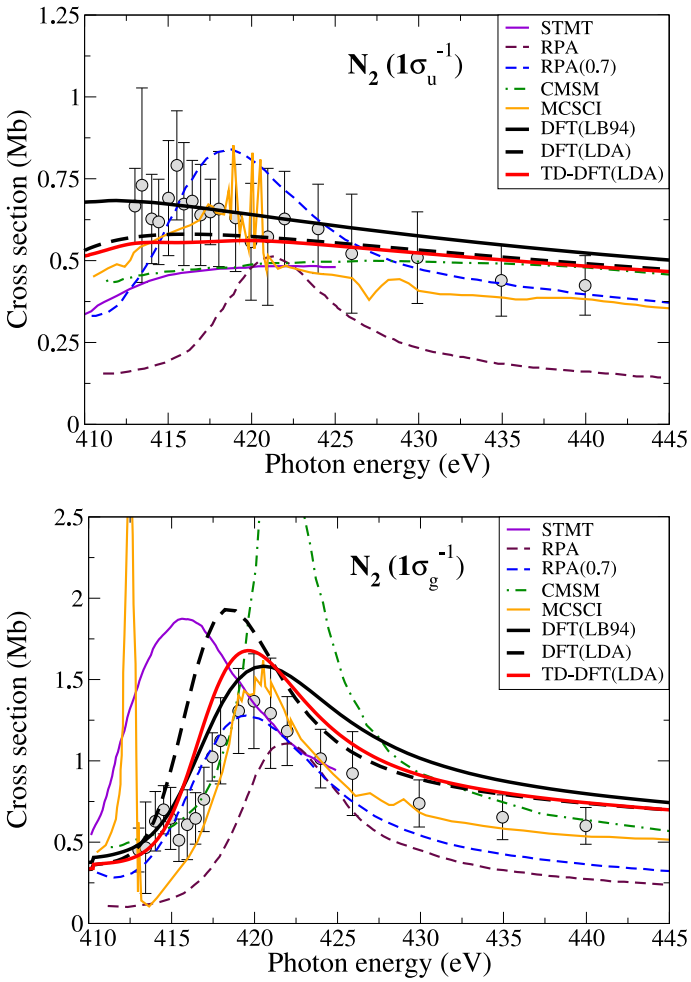

Figure 5.8: Total cross section for the $1\sigma_g^{-1}$ and $1\sigma_u^{-1}$ photoionization of N_2 as a function of the photon energy. Dots correspond to experiments - Circle: [339] ; Lines correspond to theory - Violet solid: Stieltjes-Tchebycheff moment theory (STMT) [308], Maroon dashed: random phase approximation (RPA) [60], Blue dashed: RPA with the fractional charge basis set RCHF(0.7) [339], Green dashed-dotted: continuum multiple scattering method (CMSM) [83], Orange solid: multichannel Schwinger configuration interaction (MCSCI) ten-channel [225], Black thick solid: DFT method using a LB94 functional (this work), Black dashed thick: DFT method using a LDA functional (this work), Red thick solid: TDDFT method using a LDA functional (this work).

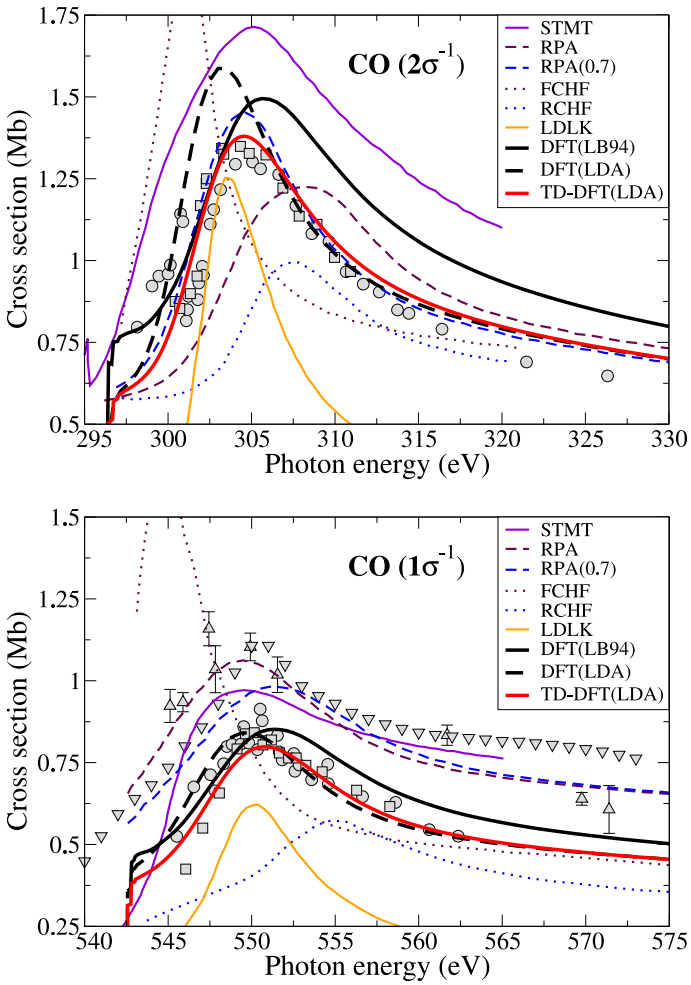

Figure 5.9: Total cross section for the $1\sigma^{-1}$ and $2\sigma^{-1}$ photoionization of CO as a function of the photon energy. Dots correspond to experiments - Circle: [157], Square: [256], Triangle-up: [398], Triangle-down: [21] ; Lines correspond to theory - Violet solid: Stieltjes-Tchebycheff moment theory (STMT) [275], Maroon dashed: random phase approximation (RPA) [336], Blue dashed: RPA with the fractional charge basis set RCHF(0.7) [336], Maroon points: frozen-core Hartree-Fock (FCHF) in the length gauge [325], Blue points: relaxed core Hartree-Fock (RCHF) in the length gauge [325], Orange solid: logarithmic derivative version of the Kohn vartiational principle Lobatto technique (LDKL) [429], Black thick solid: DFT method using a LB94 functional (this work), Black dashed thick: DFT method using a LDA functional (this work), Red thick solid: TDDFT method using a LDA functional (this work). (Experimental data [157] and [256] were renormalized to our theoretical ones).

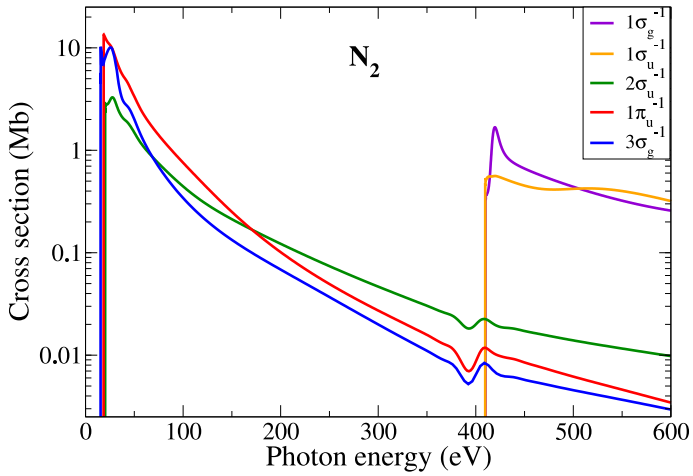

Figure 5.10: Total cross section for the core and valence photoionization of N_2. Each line corresponding to a different photoionization channel. All of the photoionization cross sections have been calculated with the multicenter B-splines time-dependent DFT (TDDFT) method using a LB94 functional for the valence shell and a LDA functional for the core shell.

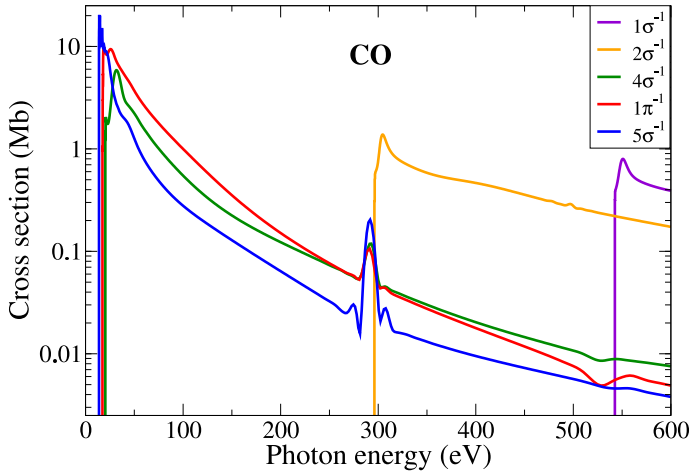

Figure 5.11: Same as Figure 5.10 for CO.

Very recently, there has been an increasing interest in evaluating photoionization cross sections at high photon energies. Figures 5.13, 5.12, 5.15 and 5.14 show the total cross section corresponding to the core photoionization of N_2 and CO for each symmetry channel of the photoelectron and for a large range

of photoelectron momentum [1]. Contribution from the different partial waves is also shown. Partial waves are associated with the different angular terms in the symmetry-adapted real-spherical-harmonics expansion that describes the photoelectron wave function. For example, in N_2, a p-wave represents a continuum electron wave function with outgoing $l = 1$ character. The total cross section is just the sum over all partial waves. In general, only the few first partial waves contribute significantly to the cross section. In the present calculations, we achieve convergence by including partial waves up to $l = 9$.

In the N_2 figures, we compare our results obtained by using the DFT method (including the nuclear motion) with recent theoretical calculations reported by Semenov *et al.* [340, 226] in the fixed nuclei approximation. The authors employed RPA within the relaxed-core Hartree Fock (RCHF) approximation at low photon energy in order to describe the strong electronic correlation in this region. RCHF is used for higher energies (> 3 a.u.). Since the authors claim that the standard RCHF method generally overestimates the influence of the relaxation effects for K-shells and give rise to a shift of the cross section toward higher energies, they make use of an adjustable parameter, the fractional charge z_e, which corresponds to some intermediate value of the charge of the hole state [340]. The value $z_e = 0.7$ has been empirically chosen to give the best agreement with the experimental data. For all partial waves, there is a reasonable agreement between the present DFT and the previous RPA/RCHF results, in particular at high photoelectron energies where DFT is more appropriate. Nevertheless, the RPA/RCHF methods lead somehow to sharper minima, which is the consequence of not including the nuclear motion in their calculations. A similar effect has been reported in H_2 photoionization [118, 117, 119].

The present DFT method succeeds in describing the so-called *shape resonance* for the $1\sigma_g \rightarrow \varepsilon\sigma_u$ transition at around $k_e \leq 1$ a.u. Some disagreement between RPA and DFT methods can be seen for $k_e \leq 3$ a.u. (the RPA region): for $l = 1$ (Figure 5.13a), $l = 3$ (Figure 5.13b), $l = 0, 2, 4$ (Figure 5.12a) and $l = 2, 4$ (Figure 5.12b). The difference comes from the fact that in RPA there is a significant interchannel coupling close to threshold, as can be clearly seen in the peak appearing in the $1\sigma_u^{-1}$ cross section. Evidence of this coupling has been claimed [60], but it is not apparent even in the TDDFT cross section, which formally includes this coupling, and produces an equally good agreement with the experimental data [356].

[1] According to the simple relation between the photoelectron momentum and the photoelectron energy $k_e = \sqrt{2\varepsilon}$, the energy range of Figures 5.13, 5.12, 5.15 and 5.14 is equivalent to a photoelectron energy that goes from 0 to 1200 eV.

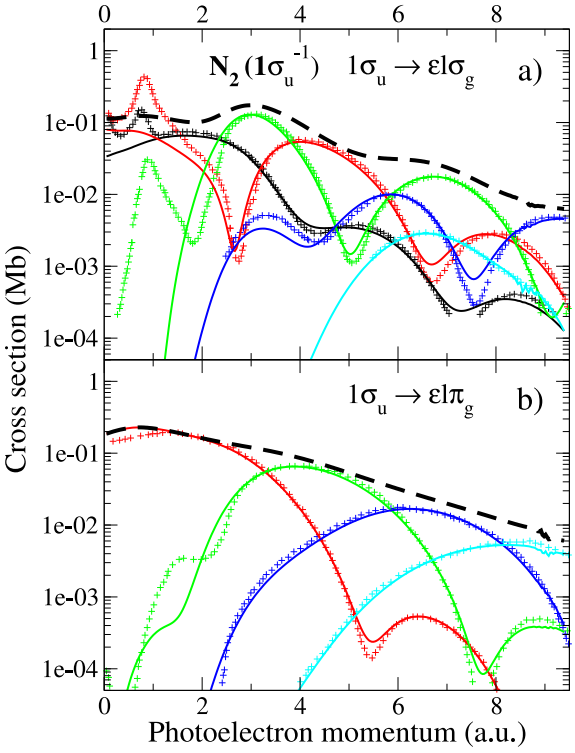

Figure 5.12: Contribution of the five first partial waves to the total cross section of the $1\sigma_u \rightarrow \varepsilon l\sigma_g$ (a) and $1\sigma_u \rightarrow \varepsilon l\pi_g$ (b) transitions of N_2 as a function of the photoelectron momentum. Crosses: RPA (at $k \leq 3a.u.$) and RCHF (at $k > 3a.u.$) from [226]. Solid lines: DFT method using a LDA functional (this work).

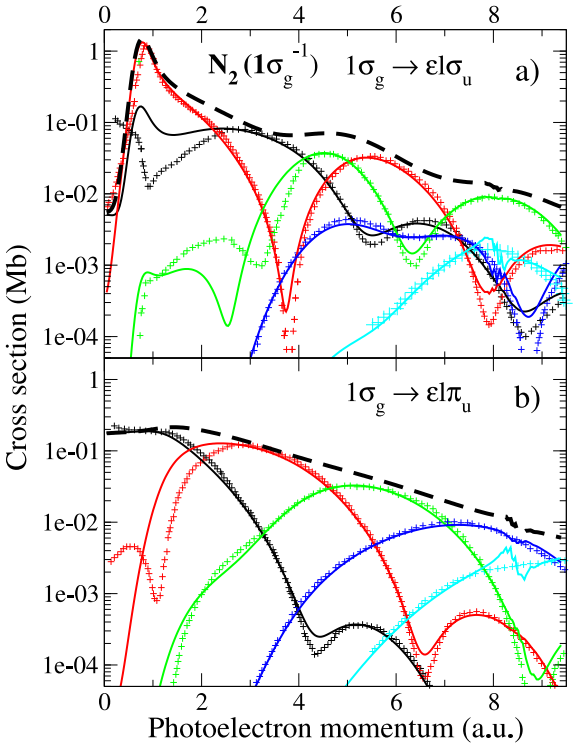

Figure 5.13: Contribution of the five first partial waves to the total cross section of the $1\sigma_g \rightarrow \varepsilon l\sigma_u$ (a) and $1\sigma_g \rightarrow \varepsilon l\pi_u$ (b) transitions of N_2 as a function of the photoelectron momentum. Crosses: RPA (at $k \leq 3a.u.$) and RCHF (at $k > 3a.u.$) from [340]. Solid lines: DFT method using a LDA functional (this work).

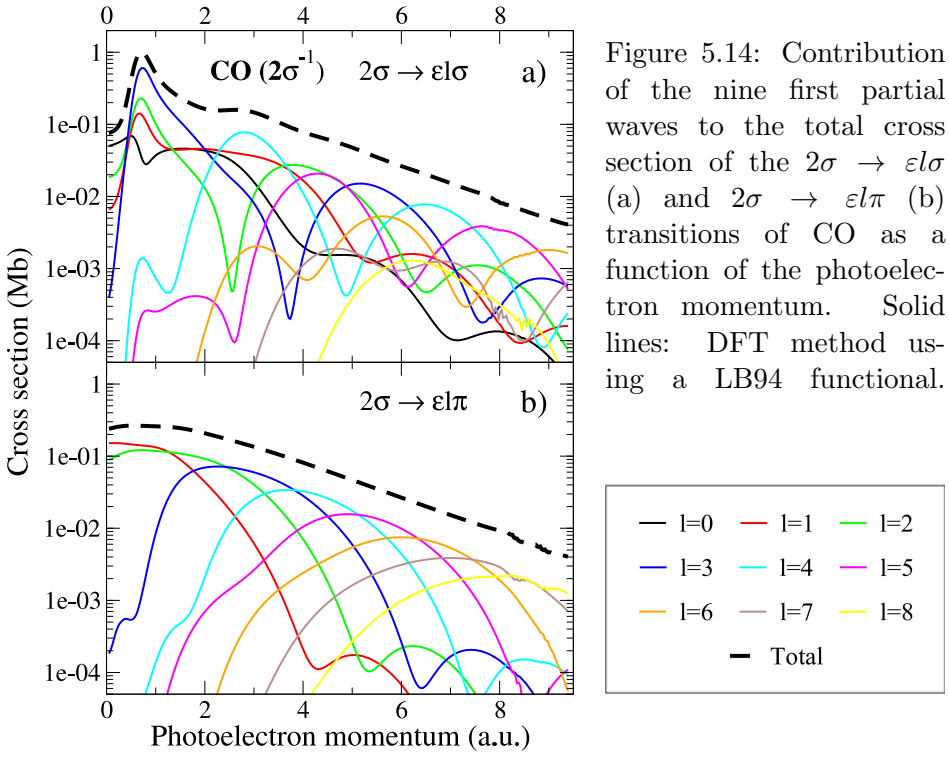

Figure 5.14: Contribution of the nine first partial waves to the total cross section of the $2\sigma \rightarrow \varepsilon l\sigma$ (a) and $2\sigma \rightarrow \varepsilon l\pi$ (b) transitions of CO as a function of the photoelectron momentum. Solid lines: DFT method using a LB94 functional.

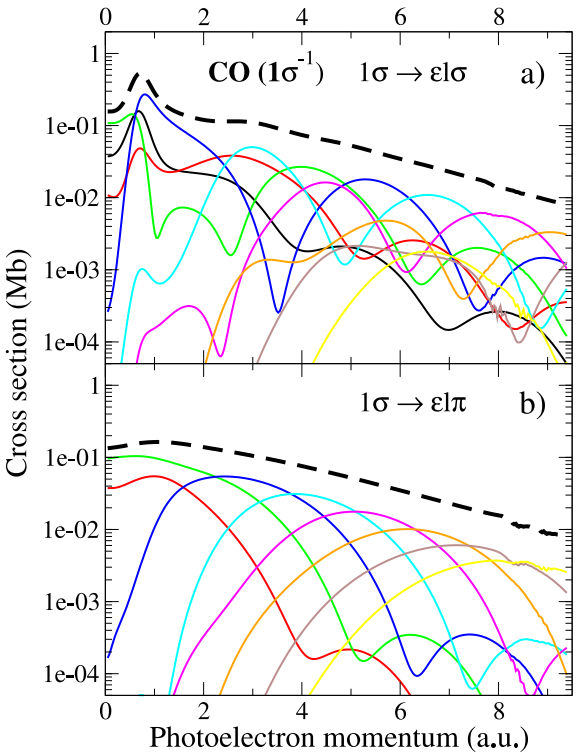

Figure 5.15: Contribution of the nine first partial waves to the total cross section of the $1\sigma \rightarrow \varepsilon l\sigma$ (a) and $1\sigma \rightarrow \varepsilon l\pi$ (b) transitions of CO as a function of the photoelectron momentum. Solid lines: DFT method using a LB94 functional.

Confinement model

The origin of the minima in the partial wave contributions can be explained in terms of electron confinement. It appears when the momentum of the ejected electron approximately satisfies the equation $k_e R_{eq} \sim l\pi$, where R_{eq} is the molecule's equilibrium distance. This is very similar to the quantization condition for a particle in a box and, therefore, reflects the fact that an integer multiple of half-wavelengths fits within the molecular dimensions. The formula is only expected to work qualitatively at high enough momentum of the photoelectron[2], i.e., when the potential felt by the escaping electron is small compared to its kinetic energy, and it should work better for $\sigma \to \sigma$ than for $\sigma \to \pi$ transitions because, in the former, electrons mainly escape along the direction of the molecular axis (see [118, 117, 119] for a more detailed description in the case of the H_2 molecule). The effect is less pronounced in the CO partial wave contributions (see Figures 5.15 and 5.14).

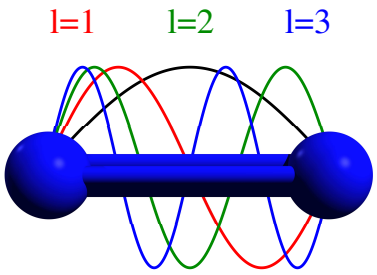

Figure 5.16: Schematic illustration of the analogy between nuclear confinement of the photoelectron and the model of the free particle in a box.

In some cases (when the radial part of the initial MO have nodes) an alternative but somehow equivalent interpretation is used to explain the existence of minima in the partial waves. This interpretation has been formulated by John W. Cooper in 1962.

Cooper's minima

In a famous article [70], Cooper analyzed the minima appearing in the atomic photoionization cross sections of Ne, Ar and Kr. The author explained the existence of energy dependent minima as due to the nodal structure of the ground and continuum states. Although such analysis was primarily designed for the atomic case, a qualitative generalization can be made for molecules.

[2] k_e should however not be too high neither, otherwise the photoelectron is not expected to feel any barrier at all.

According to the equation of the cross section (4.48) and considering that in the length gauge and for a linearly polarized light $\hat{d} = \hat{\epsilon} \cdot \mathbf{r}$, the electronic dipole matrix elements read:

$$T^{-}_{\alpha pqhl}(\omega, R) = \left\langle \varphi^{-}_{\varepsilon pqhl}(r, R) \left| \hat{\epsilon} \cdot \mathbf{r} \right| \varphi_{\alpha}(r, R) \right\rangle \tag{5.2}$$

Bound and continuum states can split into a radial and angular part. Then, by factorizing out the angular integration in (5.2), one can show that the electronic transition probability is proportional to the integral:

$$T^{-}_{\alpha pqhl}(\omega, R) \propto \int P^{-}_{\varepsilon pqhl}(r, R)\, r P_{\alpha}(r, R)\, dr \tag{5.3}$$

The latter equation shows clearly that the nodal structure defined by the α symmetry for the bound state and the angular momentum l for the continuum states will give rise to some possible integral vanishing. As an example, Figure 5.17 shows two situations where a σ_g bound state can overlap with a continuum state of ungerade symmetry, angular momentum l and energy ε_1 and the same continuum state at higher energy ε_2.

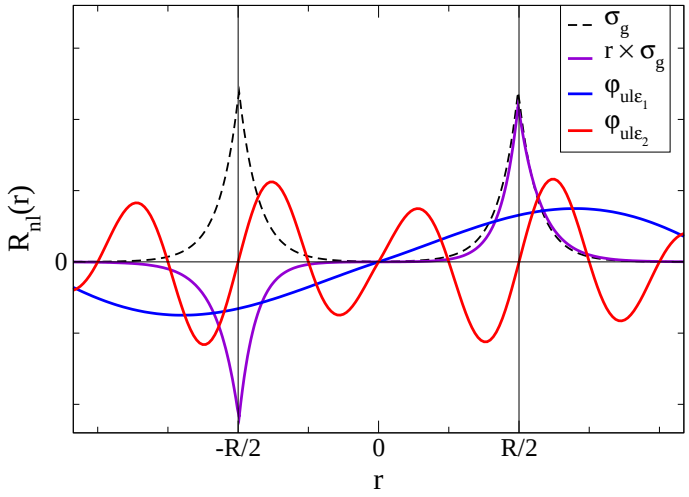

Figure 5.17: Schematic illustration of a vanishing electronic dipole transition moment at the origin of the Cooper's minima. Two overlapping situations are represented: a constructive one between the σ_g bound state (in violet) and a low photoelectron energy ε_1 continuum state (in blue); a destructive one between the bound state and a continuum state with a photoelectron energy ε_2 that corresponds to a Cooper's minimum.

As can be seen, the bound state overlaps with the former continuum state to give positive dipole matrix values. But as the photoelectron energy increases, the frequency of the continuum state increases as well. Then, the

dipole matrix pass through a maximum when bound and continuum wavefunction maxima coincide and start to decrease until vanishing and changing sign. The particular cases where the transition moment passes through zero are called Cooper's minima and are clearly visible when plotting the contribution of the partial wave to the cross section. Several Cooper minimum can occur since the vanishing condition is related to the period of oscillation of the continuum state. In Figure 5.17, the second continuum wavefunction correspond in fact to the second Cooper's minimum of the partial wave.

In the case of core photoionization of N_2 and CO, the minima appear at regular intervals in each partial waves (see Figures 5.13, 5.12, 5.15 and 5.14). In the case of N_2, they are described equivalently by DFT and RPA methods.

For the N_2 $\sigma_g \rightarrow \sigma_u$ transition (see Figure5.13a), both methods predict that the $l = 3$ partial wave is dominant ($\sim$ 1 Mb) in the low energy region (small photoelectron momentum k_e), followed by the $l = 1$ ($\sim 10^{-1} - 10^{-2}$ Mb) and the $l = 5$ ($\sim 10^{-3} - 10^{-4}$ Mb) partial waves. For the $\sigma_u \rightarrow \sigma_g$ transition shown in Figure5.12a, the situation is slightly different because the $l = 0$ and $l = 2$ partial waves are dominant and comparable in the region of small k_e. For the $\sigma_g \rightarrow \pi_u$ transition (see figure 5.13b), the $l = 1$ partial wave dominates for $k_e \leq 1$ a.u.. As k_e increases, partial waves with progressively higher l values become dominant: $l = 1$ dominates in the interval $[0, 1.5]$, $l = 3$ in $[1.5, 4.5]$, $l = 5$ in $]4.5, 7]$ and $l = 7$ in $[7, 9]$. This is very similar to what can be observed in Figures 5.12b for N_2 and Figures 5.15b and 5.14b for CO in the case of the $\sigma \rightarrow \pi$ transition. As we will discuss below, the increasing dominant role of higher partial waves is at the origin of coherent two-center electron emission in the case of N_2 and electron diffraction by the neighboring center in the case of CO.

For N_2 and to a lesser extent for CO, the total photoionization cross sections oscillate as functions of photon energy, especially for the $\sigma \rightarrow \sigma$ transitions. For CO, the oscillations are much less pronounced. For N_2, they have opposite phase in the $1s\sigma_g^{-1}$ and $1s\sigma_u^{-1}$ channels due to the different bonding character of the orbitals from which the electron is removed. The oscillations are barely visible in a linear scale (notice that we have used logarithmic scale in figures 5.13, 5.12, 5.15 and 5.14) because they are superimposed to a rapidly decreasing background. The rapid decrease is the consequence of the increasing oscillatory behavior of the continuum wave function with photoelectron energy, which leads to increasing cancellations in the integral given by Equation (4.71). Oscillations are more clearly visible in the ratio between the corresponding cross sections because the two rapidly decreasing backgrounds compensate each other. The results are shown in Figure 5.18a, where they are compared with experimental data taken from [226]. The agreement between theory and experiment is very good.

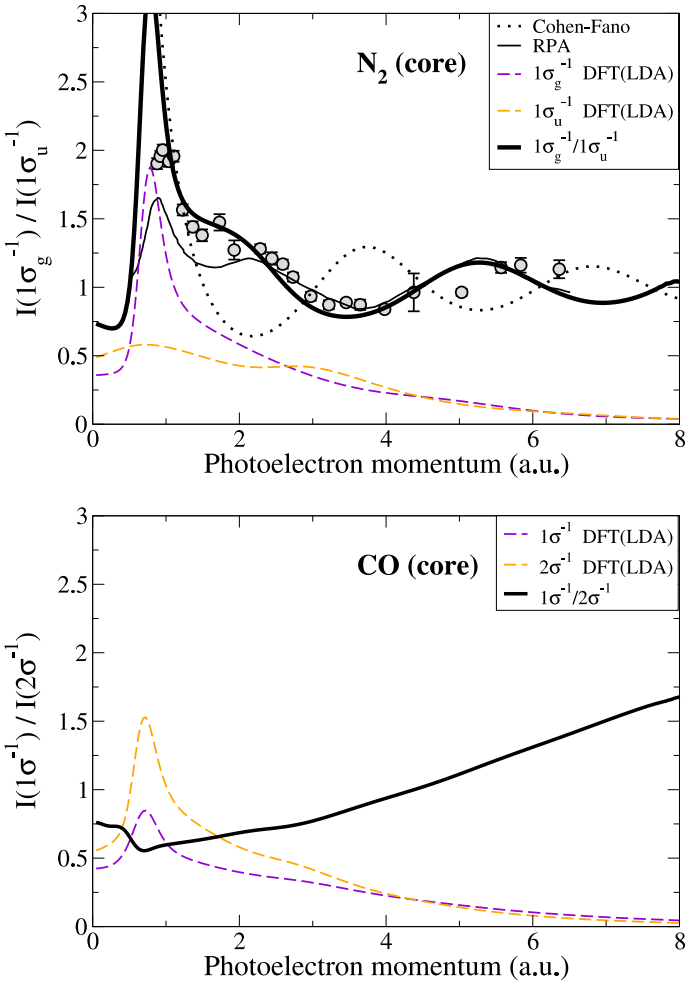

Figure 5.18: (Upper panel) Ratio of the $1\sigma_g^{-1}$ and $1\sigma_u^{-1}$ photoionization cross sections of N_2. DFT calculation: solid line. Experimental data from [226]: open circles. Total cross section (DFT) for $1\sigma_g^{-1}$ and $1\sigma_u^{-1}$ photoionization: dashed lines. (Lower panel) Same as above for the $1\sigma^{-1}$ and $2\sigma^{-1}$ photoionization cross sections of CO.

Cohen-Fano model

The oscillations observed in the N_2 photoionization cross sections as well as in other ionization processes involving homonuclear diatomic molecules [8, 203, 126, 119, 12, 370, 255, 185, 251, 125] are the fingerprint of coherent two-center electron emission. Cohen and Fano gave in 1966 [64] a physical interpretation of these oscillations in the case of H_2 photoionization.

Their original idea is to consider that when the polarization vector is perpendicular to the main axis of the molecule, the nuclei act as two-center emitters. The resulting waves interfere as a typical Young's double slit experiment and fingerprints of these interferences are expected in the photoionization cross section.

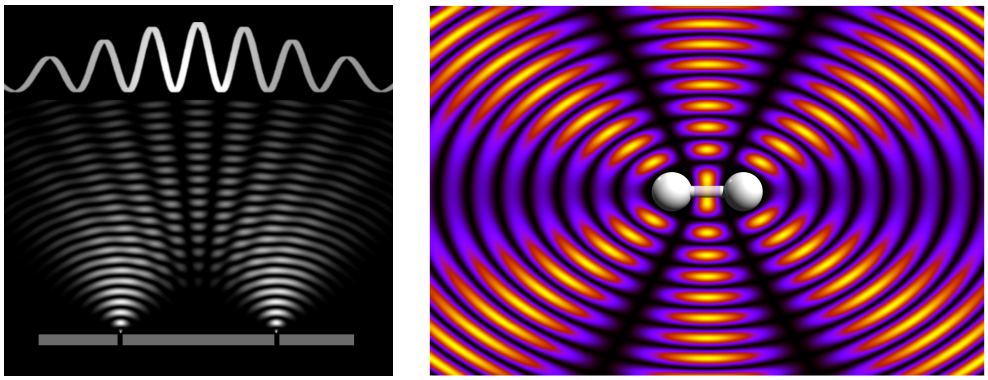

(a) Young's double slit interferences (b) Cohen-Fano's interferences

Figure 5.19: Interference patterns

In the case of homonuclear diatomic molecules, the $1s\sigma_g$ and $1s\sigma_u$ orbitals can be approximately written

$$1s\sigma_{g/u} = \frac{1}{\sqrt{2}}(1s_a \pm 1s_b), \tag{5.4}$$

where $1s_a$ and $1s_b$ are atomic $1s$ orbitals centered on the a and b protons, respectively.

In this simple picture, and when the wavelength is similar to the internuclear distance, the photoelectron is expected to be emitted coherently from the two atomic centers: $\|\mathbf{k}_A\| = \|\mathbf{k}_B\| = k_e$. This approximation makes sense for initial MOs that are partially localized, as it is often the case for core MOs of homonuclear molecules. But as we will see, such approximation can be reasonably applied to the case of valence shell photoionization for small molecular systems such as N_2 and CO.

For sufficiently high kinetic energy of the photoelectron, the total cross section can be approximated as the sum of two resulting plane waves[3]:

$$\tilde{\sigma}_{g/u}(\omega) \simeq \sigma^{(0)}_{g/u}(\omega) \langle \frac{1}{2} \left| e^{i\mathbf{k}_A \cdot \mathbf{r}_A} \pm e^{i\mathbf{k}_B \cdot \mathbf{r}_B} \right|^2 \rangle_{\hat{R}} \tag{5.5}$$

where $\sigma^{(0)}_{g/u}$ is the atomic photoionization cross section.

The two vectors $\mathbf{r}_A$ and $\mathbf{r}_B$ are related by:

$$\mathbf{r}_A = \mathbf{r} + \frac{\mathbf{R}}{2} = r\mathbf{n} + \frac{R}{2}\mathbf{e}_z \tag{5.6}$$

$$\mathbf{r}_B = \mathbf{r} - \frac{\mathbf{R}}{2} = r\mathbf{n} - \frac{R}{2}\mathbf{e}_z \tag{5.7}$$

and:

$$\tilde{\sigma}_{g/u}(\omega) \propto \frac{1}{2} \iint \left| e^{ik_e \mathbf{n}_A \cdot \left(r\mathbf{n} + \frac{R}{2}\mathbf{e}_z\right)} \pm e^{ik_e \mathbf{n}_B \cdot \left(r\mathbf{n} - \frac{R}{2}\mathbf{e}_z\right)} \right|^2 \sin\theta d\theta d\varphi \tag{5.8}$$

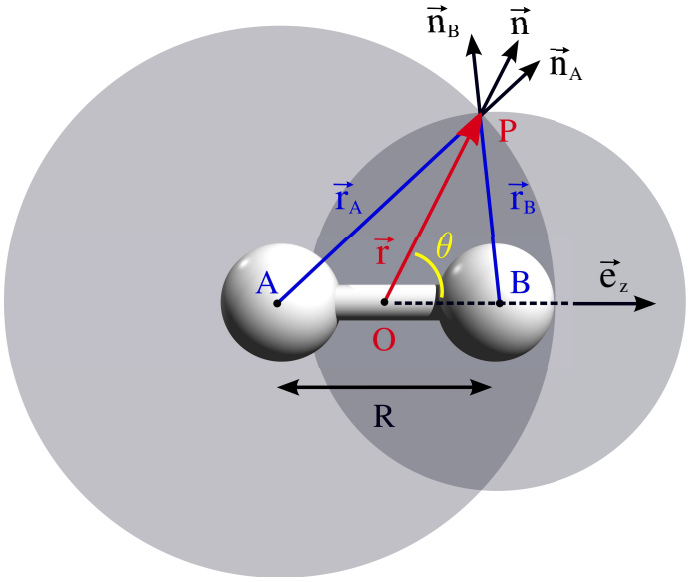

Figure 5.20: Schematic representation of two plane waves interfering in a point P, contained in the plane (xz) of the molecular frame of reference.

Assuming that $r \gg R$ (for fast electron emission, i.e. for high photon energies), one can write:

$$\mathbf{n}_A \sim \mathbf{n}_B \sim \mathbf{n} \tag{5.9}$$

[3]The model presented in the following corresponds to an alternative derivation of the Cohen-Fano's formula starting from two radiating dipole antenna interferences [117].

and:

$$\begin{aligned}\tilde{\sigma}_{g/u}(\omega) &\propto \frac{1}{2}\iint \left| e^{ik_e\mathbf{n}\cdot r\mathbf{n}} e^{ik_e\mathbf{n}\cdot\frac{R}{2}\mathbf{e}_z} \pm e^{ik_e\mathbf{n}\cdot r\mathbf{n}} e^{-ik_e\mathbf{n}\cdot\frac{R}{2}\mathbf{e}_z} \right|^2 \sin\theta d\theta d\varphi \\ &\propto \frac{1}{2}\iint e^{i2k_e r} \left| e^{ik_e\frac{R}{2}\mathbf{n}\cdot\mathbf{e}_z} \pm e^{-ik_e\frac{R}{2}\mathbf{n}\cdot\mathbf{e}_z} \right|^2 \sin\theta d\theta d\varphi \end{aligned} \tag{5.10}$$

Using the Moivre identity, we can simplify Equation 5.10 as:

$$\tilde{\sigma}_g(\omega) \propto \iint \cos^2\left(\frac{k_e R}{2}\cos\theta\right) \sin\theta d\theta d\varphi \tag{5.11}$$

and:

$$\tilde{\sigma}_u(\omega) \propto -\iint \sin^2\left(\frac{k_e R}{2}\cos\theta\right) \sin\theta d\theta d\varphi \tag{5.12}$$

Integrating the previous equations using trigonometric identities and integration by parts, we finally obtain the well known Cohen-Fano's formula:

$$\tilde{\sigma}_{g/u}(\omega) = \sigma^{(0)}_{g/u}(\omega)\left(1 \pm \frac{\sin k_e R}{k_e R}\right) \tag{5.13}$$

As it can be seen, the oscillations are described by a sinusoidal function that depends on the photoelectron momentum and the internuclear distance (chosen at the ground state equilibrium for fixed nuclei approximation). It varies from 0 to $\sigma^{(0)}_{g/u}$ which is a smooth decreasing background. The model predicts also that the σ_u cross section is exactly shifted by π with respect to theσ_g one, i.e., it oscillates in anti-phase as shown in Figure 5.18a.

As mentioned above, due to the rapid decrease of $\tilde{\sigma}$ with photon energy, i.e., with k_e, oscillations are usually hidden. Thus, very often, they must be uncovered by dividing the total cross section by a "reasonable" independent estimate of $\sigma^{(0)}_{g/u}$. This may lead to ambiguous interpretations. Instead, as shown in Figure 5.18, one can consider the ratio of two rapidly decreasing cross sections associated with different ionization channels. Within this model, the ratio between the σ_g and σ_u cross sections is independent of $\sigma^{(0)}_{g/u}$ and is given by:

$$\frac{\tilde{\sigma}_g(\omega)}{\tilde{\sigma}_u(\omega)} \simeq \frac{1+\Gamma(k_e)}{1-\Gamma(k_e)} \tag{5.14}$$

where:

$$\tag{5.15}$$

where

$$\Gamma(k_e) = \frac{\sin k_e R}{k_e R} \tag{5.16}$$

In the case of some heteronuclear diatomic molecules (such as CO), the lowest molecular orbitals, 1σ and 2σ, are practically identical to the 1s AOs

of each atoms ($1s_O$ and $1s_C$). Thus, electrons escape from a well localized area around one of the nuclei. Therefore, coherent two-center emission is not possible and the above oscillatory pattern is not observed in the corresponding $1\sigma/2\sigma$ ratio (see figure 5.18). Instead another interesting effect may be observed by choosing the appropriate observables: diffraction by the neighboring atomic centers. The latter effect has also been described in previous work [211, 446].

In [85], Dehmer *et al.* shows that in the core photoionization of N_2, the shape resonance energy position, width and amplitude is a sensitive function of R. In particular they observed that by increasing the internuclear distance, the resonance shifts to lower energies and become narrower and stronger. At the contrary, for $R > R_{eq}$ the resonance tends to shift to higher energies and disappear. According to the authors, "this indicates that nuclear motion exercises great leverage on the spectral behavior of shape resonances, since small variations in R can significantly shift the delicate balance between attractive (mainly Coulomb) and repulsive (mainly centrifugal) forces which combine to form the barrier."

Figure 5.21 shows the evolution of the shape resonance with the geometry change as a function of the photoelectron energy for the core and HOMO photoionization of N_2. The grid of R in both cases is linear and varies by step of 0.5 a.u.. The first evident that the shape resonance at the ground state equilibrium (around $R \sim 2.05$ a.u.) is located at different positions (~ 11 eV for $1\sigma_g^{-1}$ and ~ 9.5 eV for $3\sigma_g^{-1}$). This difference that was already observable in the total cross section (Figures 5.8 and 5.5) shows the dependence of the shape resonance on the electron hole. The two graphics show that the shape resonance evolves in a very similar way for both photoionization channel. As formerly described by Dehmer *et al.* for the core photoionization, the shape resonance becomes narrower and stronger with the increase of R until reaching a limit for $R \sim 2.50$ a.u. for $1\sigma_g^{-1}$ and $R \sim 2.45$ a.u. for $3\sigma_g^{-1}$.

The observation of this dependence on the geometry change proves the importance of the electronic-nuclear couplings in the photoionization process. Also, inclusion of the nuclear motion should gives rise to vibrational components of the cross section that reflect this dependence, i.e. that differ one to each other and breakdown the Franck-Condon principle.

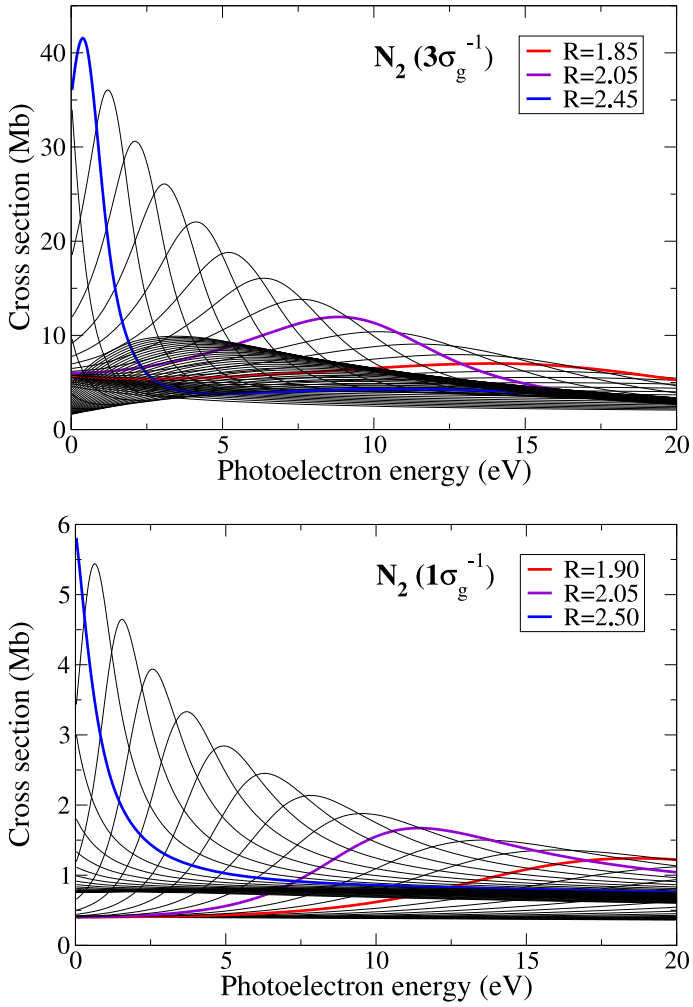

Figure 5.21: Cross sections in the fixed nuclei approximation for the $1\sigma_g^{-1}$ and $3\sigma_g^{-1}$ photoionization of N_2. Lines correspond to the cross section calculated for different internuclear distances with a DFT method using a LB94 functional. Thick red and blue curves are specific values of R and violet curve corresponds to the cross section calculated at the ground state equilibrium geometry.

5.3 Vibrationally resolved cross section

5.3.1 Core shell photoionization

In this section we consider photoionization from the $1\sigma_g$ and $1\sigma_u$ orbitals of N_2, and from the 1σ and 2σ orbitals of CO.

Figures 5.22 and 5.23 show the photoelectron spectra that correspond to the core photoionization of CO and N_2 respectively. Contributions from the different vibrational states are also shown. Compared to CO, the core photoionization study of N_2 presents an additional difficulty. As can be seen in the photoelectron spectrum, the two gerade and ungerade photoionization channels are quasi-degenerate with an energy splitting smaller than the vibrational energy spacing. Experimentally, improvements of the detection techniques has been necessary to resolve the two symmetries. For this reason and during a long time, no modulations were observed in the N1s photoionization cross section because as shown by the Cohen-Fano formula, the gerade and ungerade cross sections oscillate in anti-phase and their sum should lead to a flat distribution with the photon energy. According to the photoelectron spectrum of N_2, the two symmetries possess the same vibrational energy spacing. The vibrational progression is relatively limited (only the two first vibrational levels have been resolved) and resemble the one of the O1s photoionization of CO. The energy spacing between the two first vibrational peaks is however larger in the case of N_2 and very similar to the one observed in the C1s photoelectron spectrum of CO. The latter present a very well resolved vibrational structure which could have been fitted up to $v' = 2$ ($v' = 3$ is also visible at ∼202.95 eV in the measured points). This larger vibrational progression results from a larger geometry change in the case where an electron is emitted from the 2σ MO (-∼ 4.9 pm compared to averaged value of -∼ 1.9 pm for the core ionized states of N_2). It has to be noticed that compared to the other cases, emission of an electron from the 1σ MO of CO results in a bond length relaxation (∼ 3.9 pm).

From the fitting procedure, its is possible to evaluate the natural linewidth Γ of the vibrational peaks, which is related to the lifetime of the core hole through the relation $\tau = \hbar/\Gamma$. The most recent values reported in the literature are: $\Gamma_{1\sigma_g}$ =116 meV, $\Gamma_{1\sigma_u}$ =124 meV, $\Gamma_{1\sigma}$ =95 meV and $\Gamma_{2\sigma}$ =167 meV. The values for the $1\sigma_g^{-1}$ and the $1\sigma_u^{-1}$ are very closed and often assumed to be equals. The difference with CO is due to the localized nature of the core hole. In particular, since the O1s core hole is bonded to a more electronegative atom, the electron density in its vicinity is enhanced and the probability of Auger decay greater. Then, O1s core hole lifetime is small compared to N_2, while for opposite reasons, the C1s core hole lifetime is relatively long.

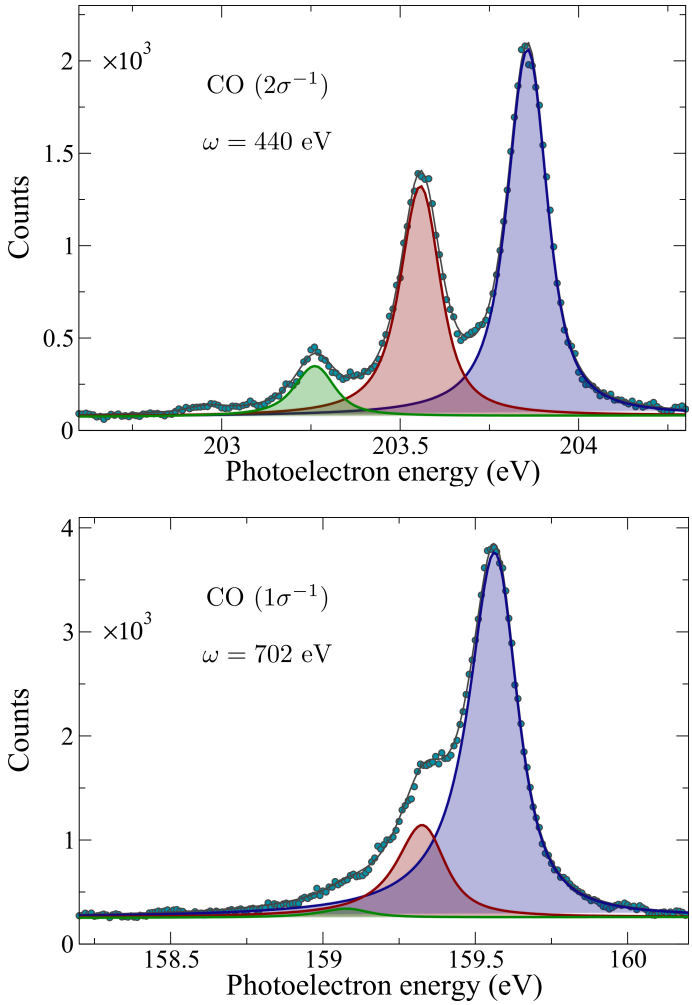

Figure 5.22: C1s (upper panel) and O1s (lower panel) photoelectron spectra of CO taken respectively at ω =440 and 702 eV. Dots correspond to the measured experimental data from [245]. Lines correspond to the fit of the experimental data - Solid blue, red and green: fitted vibrational peaks ($v' = 0$, 1 and 2 respectively), Solid black: sum of the fitted peaks.

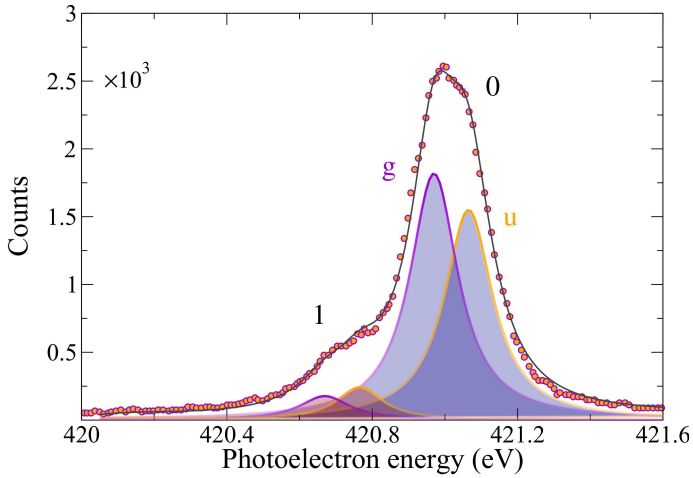

Figure 5.23: Core photoelectron spectrum of N_2 taken at ω =534 eV. Dots correspond to the measured experimental data from [227]. Lines correspond to the fit of the experimental data - Solid violet: fitted vibrational peaks for the $^2\Sigma_g^+$ final state, Solid orange: fitted vibrational peaks for the $^2\Sigma_u^+$ final state, Solid black: sum of the fitted peaks.(upper panel). Peak numbers indicate the vibrational quantum number v' of N_2^+.

Figures 5.24 and 5.25 show absolute photoelectron spectra as functions of photon energy for the lowest vibrational states of the remaining molecular cation. Comparison with the available experimental data [339, 157, 256, 200] is also shown. The comparison is made on absolute scale except for the $1\sigma^{-1}$ cross sections of CO, which were measured in arbitrary units (see the lower panel of Figure 5.25). In this case, the statistics and the resolution of the experimental data are poorer than in the other three cases.

Good agreement between the present theoretical results, the RPA ones and the experimental data is obtained in most cases. As already noticed when discussing Figures 5.8b and 5.12, the $N_2(1\sigma_g^{-1})$ photoelectron spectrum presents a shape resonance at $\omega \sim 420$ eV. The resonance is visible in all the vibrational channels. A similar structure can be seen in the $1\sigma^{-1}$ and $2\sigma^{-1}$ photoelectron spectra of CO (Figure 5.25b).

As has been previously mentioned, the present theoretical results do not predict the existence of pronounced shape resonances in the $N_2(1\sigma_u^{-1})$ photoelectron spectrum, in good agreement with the experimental data but in disagreement with the RPA spectra that exhibit pronounced maxima similar to those observed in the $N_2(1\sigma_g^{-1})$ case.

A closer inspection of the figures corresponding to N_2 $(1\sigma_g^{-1})$ and CO $(2\sigma^{-1})$ shows that the position of the resonance peak moves to lower photon energies as v' increases. The shift between two consecutive v' components is

approximately 2 eV in both cases. At the contrary, the shape resonance shifts to higher energies in the CO ($1\sigma^{-1}$) case.

As we have seen before, the characteristics of the shape resonance depend on the internuclear distance. Since the overlap between the initial and different final vibrational wavefunctions samples different spatial regions, the characteristics of the shape resonance is also sensitive to v'. In the case of the $1\sigma_g^{-1}$ photoionization of N_2, the bond length is contracted and then the higher the v' the larger R will contribute to the cross section. And as the shape resonance in the electronic dipole transition moments tends to be shifted to lower energies when the nuclear separation increases (see Figure 5.21b), then the energetic position of the shape resonance in the vibrationally resolved cross section tends also to be shifted to lower energies as v' increases. The same mechanism explains the shape resonance behavior in the CO ($2\sigma^{-1}$) cross section, as well as for CO ($1\sigma^{-1}$) in which the bond relaxation of the ionized state leads to an enhancement of the lower spatial region and a shift of the shape resonance toward higher energies with v'.

Feshbach resonances associated with doubly excited states are probably responsible for the small structures that can be seen in the experimental results shown in Figure 5.24 at $\sim$ 415 eV and Figure 5.25 at $\sim$ 300 eV. They are less apparent in the $1\sigma_u^{-1}$ photoionization of N_2 (Figure 5.24a, upper panel) probably due to the lower statistics in the experimental data. Their doubly excited nature is confirmed by the fact that neither the present TD-DFT results nor the RPA ones predict the existence of these structures.

Figure 5.26 shows the vibrationally resolved cross section corresponding to the first five vibrational levels of the two active symmetry channels of the $1\sigma_g^{-1}$ photoionization of N_2 and for an extended photon energy range (up to 1000 eV). Contribution of the different partial wave are also plotted and show the importance of the vibrational motion in the photoionization dynamics. Indeed, by looking to the $l = 1, 3, 7$ partial waves, and more particularly in the $1\sigma_g \rightarrow \varepsilon l\sigma_u$ transition channel, it appears that the different minima change drastically of positions as v' changes. From $v' = 0$ to $v' = 2$, the dip in the $l = 1$ component is shifted to lower energies by $\sim$70 eV while it is shifted by $\sim$40 eV in the same direction for the $l' = 3$ component. Following the Cooper's minima picture, this shift to lower energies can be explained as follow: when the distance between the two nuclei increases, the photoelectron energy required to vanishes the integral in (5.3) decreases. Since the bond length of the $1\sigma_g^{-1}$ state is contracted with respect to the ground state, the highest vibrational wavefunctions then probe larger internuclear distances for which the Cooper's minima appears at lower energies. For higher v', the pattern that corresponds to the evolution of the dips is less evident, although the $l' = 7$ and $l' = 9$ components seem to indicate a similar behavior.

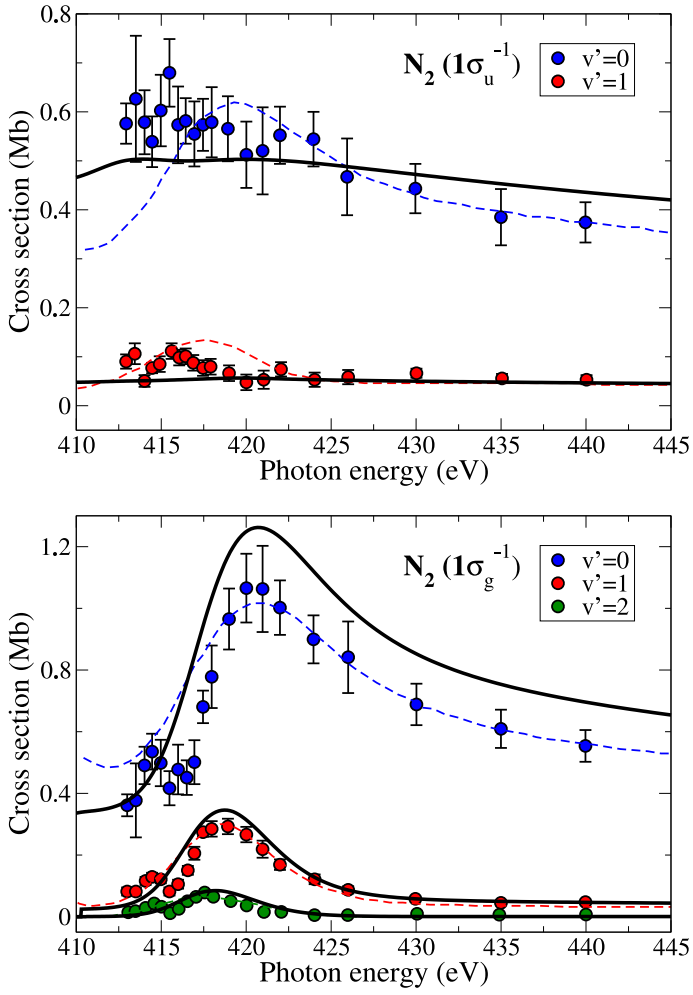

Figure 5.24: Vibrationally resolved cross section for the three first vibrational levels of the $1\sigma_g^{-1}$ and $1\sigma_u^{-1}$ photoionization of N_2 as a function of the photon energy. Circles: experimental data from [339]. Thin dashed lines: RPA with the fractional charge basis set RCHF(0.7) from [339]. Thick black line: TDDFT method using a LDA functional.

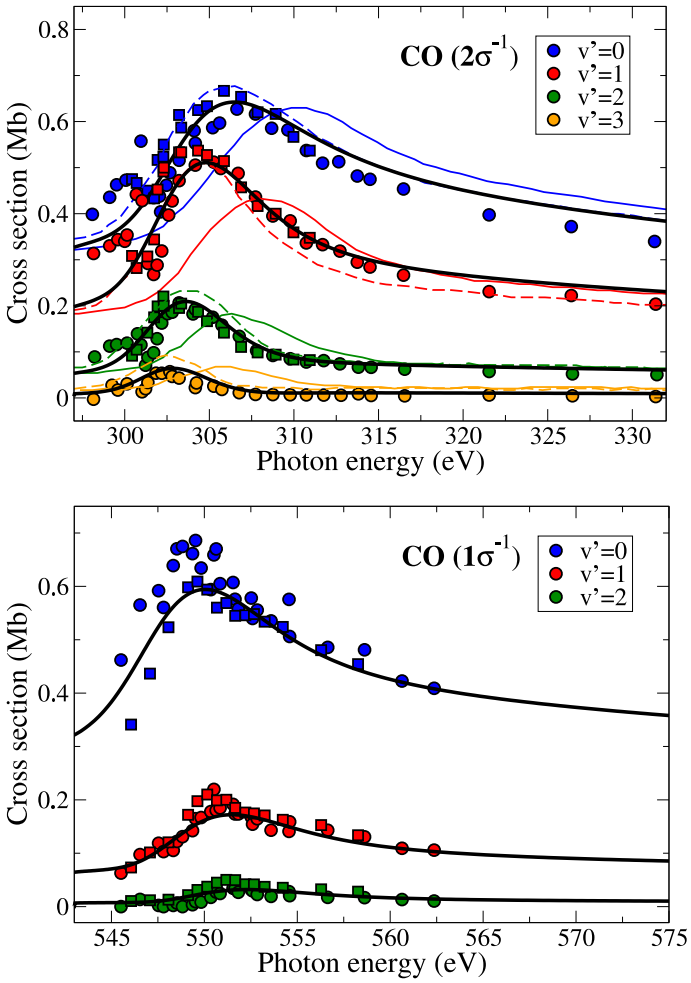

Figure 5.25: (Lower panel) Vibrationally resolved cross section for the three first vibrational levels of the $1\sigma^{-1}$ photoionization of CO as a function of the photon energy. Circles: experimental data from [157]. Squares: experimental data from [256]. Thick black line: TDDFT method using a LDA functional. (Experimental data were renormalized to the theoretical ones). (Upper panel) Vibrationally resolved cross section for the four first vibrational levels of the $2\sigma^{-1}$ photoionization of CO as a function of the photon energy. Circles: experimental data from [200]. Squares: experimental data from [256]. Thin solid lines: RCHF with the integer charge $z_e = 1$ from [338]. Thin dashed lines: RCHF with the fractional charge $z_e = 0.5$ from [338]. Thick black line: TDDFT method using a LDA functional.

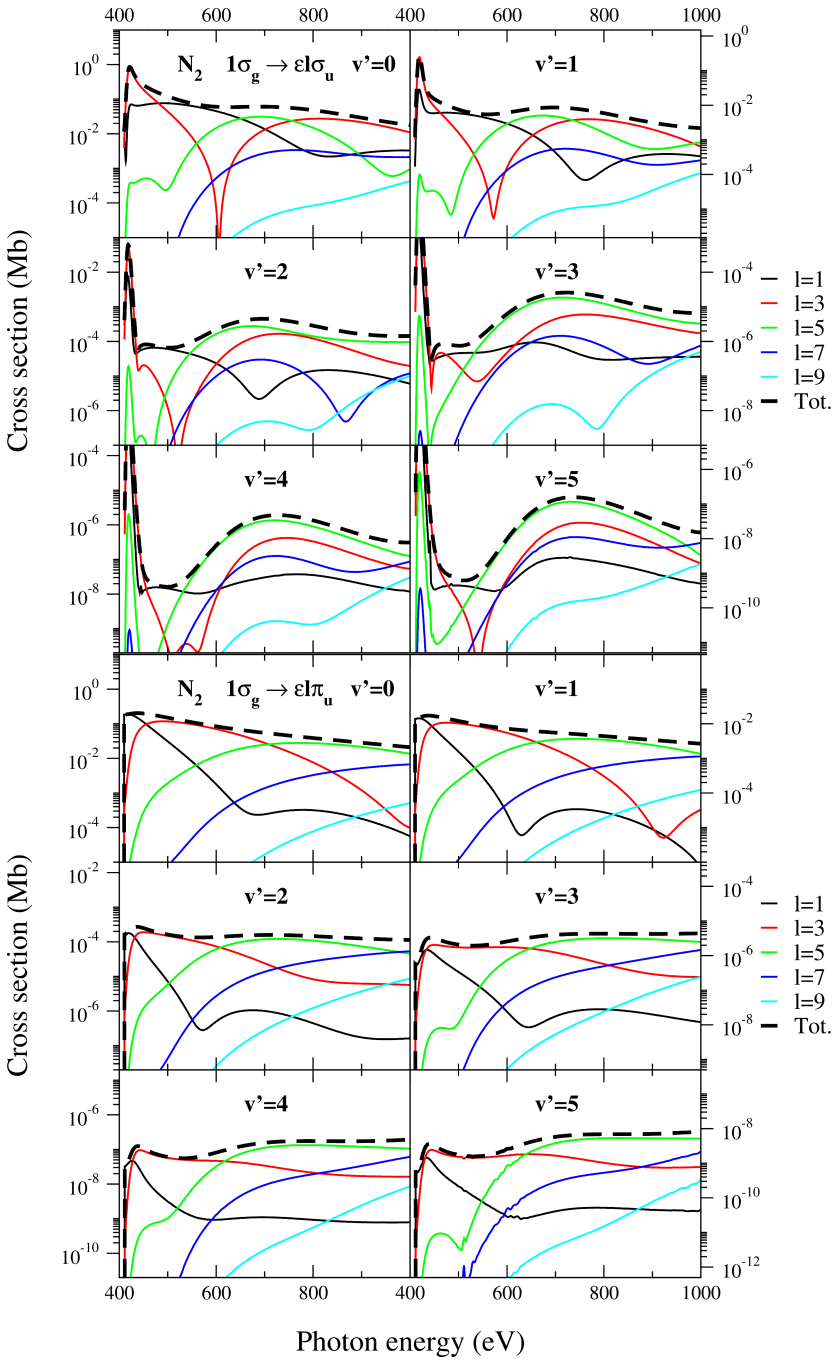

Figure 5.26: Contribution of the five first partial waves to the vibrationally resolved cross section of the $1\sigma_g \rightarrow \varepsilon l\sigma_u$ and $1\sigma_g \rightarrow \varepsilon l\pi_u$ transitions of N_2 as a function of the photoelectron momentum. Solid lines: DFT method using a LB94 functional.

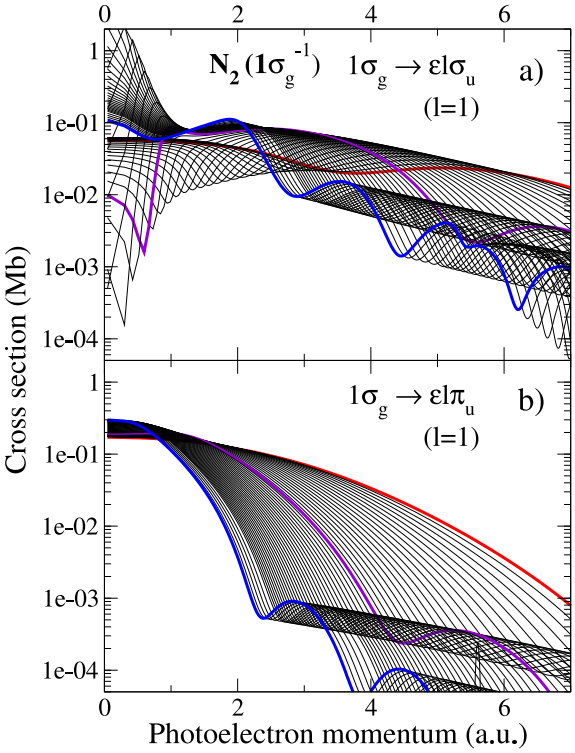

Figure 5.27: Cross sections associated with the $l = 1$ partial wave in the fixed nuclei approximation for the $1\sigma_g \rightarrow \varepsilon l\sigma_u$ and $1\sigma_g \rightarrow \varepsilon l\pi_u$ photoionization channels of N_2. Lines correspond to the cross section calculated for different internuclear distances with a DFT method using a LDA functional. Thick red and blue curves are respectively the smaller (1 a.u.) and bigger (4 a.u.) values of R in the grid and violet curve corresponds to the cross section calculated at the ground state equilibrium geometry.

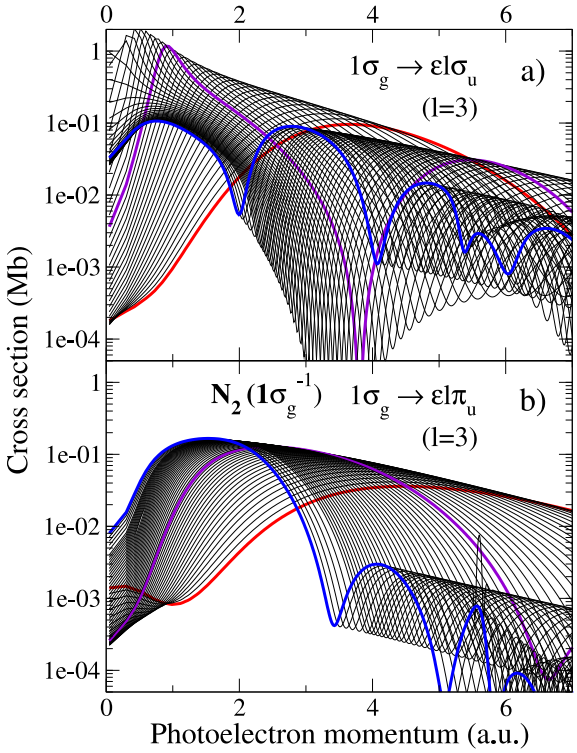

Figure 5.28: Same as Figure 5.27 for the $l = 3$ partial wave.

Figures 5.27 and 5.28 shows the evolution of the minima with the geometry change as a function of the photoelectron energy for the $l = 1$ and $l = 3$ partial waves. The shift of the dips toward lower energy values with R increasing can be clearly appreciated for both partial waves and in both channels ($1\sigma_g \rightarrow \varepsilon l\sigma_u$ and $1\sigma_g \rightarrow \varepsilon l\pi_u$). As for the shape resonance, the contraction of the bond length in the core ionized state explains the direction of the shift toward lower energies in the vibrationally resolved cross section presented in Figure 5.26. The evolution of the dips with R also shows the importance of the electronic-nuclear couplings, even at high photon energies.

Figure 5.29 shows the same results presented in Figure 5.24 for the $1\sigma_g^{-1}$ photoionization of N_2 but for an extended energy range (up to 1000 eV of the photon energy). This example illustrates the typical behavior of the cross section for high photon energies: above the shape resonance region, the cross section decrease as a polynomial function and seems to be structureless. However, we have seen in Figures 5.13, 5.12, 5.15 and 5.14 that small oscillations are observable when the cross section is plotted in a logarithmic scale. These figures seem to indicate that there exist Franck-Condon deviations even far from the threshold ionization energy but which are unfortunately covered by the rapid decay of the cross section. During long time, variations at high photon energies were observed by dividing the total cross section by the atomic cross section of the emitter atom (see upper panel in Figure 5.30) or by computing the ratio between two photoionization channels (see Figure 5.18). A more elegant method to uncover the possible structures consists in taking advantage of the vibrational resolution and compute ratios of vibrationally resolved cross sections. Since each vibrational component decays equivalently, ratios between each of these components and one of reference permits to remove this trend. An example of ratios between two vibrational cross sections, also called v-ratios is shown in Figure 5.30 for the O1s and C1s photoionization of CO (middle and lower panels respectively). The first v-ratio that corresponds to the $v' = 1$ over the $v' = 0$ component is compared for both photoionization channel to the Franck-Condon prediction which is constant with the energy. As seen, deviations to the Franck-Condon distribution are unequivocally unhidden by the use of this method. In the following, we will aim to find the origin of such deviations.

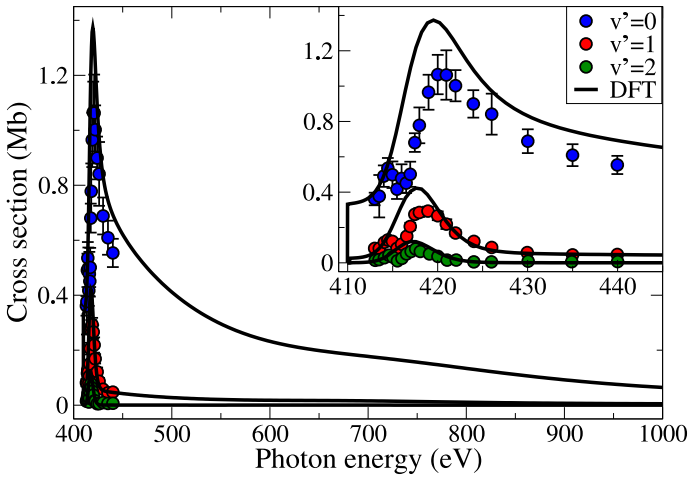

Figure 5.29: Vibrationally resolved cross section for the three first vibrational levels of the $1\sigma_g^{-1}$ photoionization of N_2 as a function of the photon energy. Circles: experimental data from [339]. Thick black line: TDDFT method using a LDA functional. Enclosed figure: same results in a reduced energy scale.

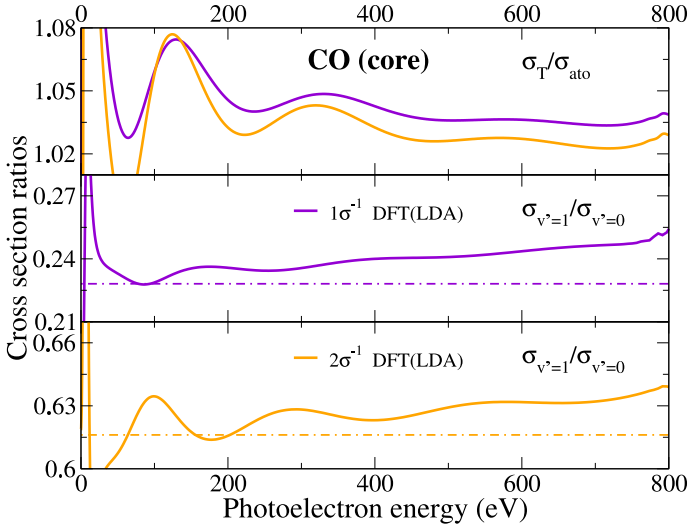

Figure 5.30: Ratios of cross sections for the O1s (violet solid line) and C1s (orange solid line) photoionization of CO. (Upper panel) Ratio between the total cross section and the atomic cross section that corresponds to the atom from which is emitted the electron. (Middle panel) Ratio between the $v' = 1$ and $v' = 0$ cross sections for the O1s photoionization cross section of CO. Dashed-dotted line: Franck-Condon factor ratio. (Lower panel) Same as the middle panel for the C1s photoionization of CO.

Figure 5.31 presents experimental and calculated v-ratios as functions of photon energy for the core ionization processes $N_2 \rightarrow N_2(1s\sigma_g^{-1})$ and $N_2 \rightarrow N_2(1s\sigma_u^{-1})$ (upper pannel), and $CO \rightarrow CO^+(1\sigma^{-1}, v')$ and $CO \rightarrow CO^+(2\sigma^{-1}, v')$ (lower panel). Oscillations are visible in all the photoionization channels.

In the upper panel of Figure 5.31, the DFT results are compared to an extension of the Cohen-Fano model in which the nuclear motion has been included by simple integration of the square root of the Cohen-Fano formula with the initial and final vibrational wavefunctions:

$$\tilde{\sigma}_{g/u}^{v,v'}(\omega) \propto \left| \int_0^\infty \chi_{i,v}^*(R) \left[1 \pm \frac{\sin k_e R}{k_e R} \right]^{\frac{1}{2}} \chi_{g/u,v'}(R) dR \right|^2 \tag{5.17}$$

The model describes pretty well the oscillations in the v-ratios for both the $N_2(1s\sigma_g^{-1})$ and $N_2(1s\sigma_u^{-1})$ channels. A blow up of the low energy region, also shows a very good agreement with the available experimental data.

In the case of CO (lower panel of Figure 5.31b), oscillations are quite apparent, also in the experimental data, but they cannot be explained by the model because the core 1σ and 2σ orbitals of CO are localized on the atomic centers. In this case, the origin of the oscillations is diffraction of the electron ejected from one of the atomic centers by the other atomic center. This particular point will be studied in detail in the case of polyatomic molecules.

A part from the oscillations, a linear increase with the photon energy is visible in the v-ratios. This additional deviation to the Franck-Condon prediction is due to the recoil of the photoelectron momentum on the emitter atom(s) of the molecule.

Recoil effect

The Franck-Condon principle states that the position and the momentum of the nuclei are not directly affected by the electronic transition. However, according to the conservation of the momentum, the residual ion is expected to differ from the neutral molecule also by a momentum equal but opposite to the one of the escaping electron: $\mathbf{p_M} = -\mathbf{p_e}$. It is important to understand that this recoil momentum is not exactly due to a momentum transfer from the photoelectron to the nuclei but to the unbalanced momentum remaining in the molecular ion after emission of the electron. Recoil momentum not only induces a translational motion but also vibrational and rotational excitations. The vibrational recoil has been observed several times experimentally for diatomic molecules (N_2 and CO [407, 136, 385]) as polyatomic molecules (CH_4 and CF_4 [209, 386, 207, 208]). Effect of the recoil generally comes out as an increasing deviation to the Franck-Condon factor ratio as a function of the photoelectron energy (see Figure 5.30). For this reason, the recoil effect has not been observed experimentally until the advent of third generation of synchrotron radiation sources which gave access to photon energies sufficient to

appreciate the resulting deviations. In the framework of this study whose purpose is to investigate the photoelectron spectra deep in the continuum, such effects have to be taken into account. Theoretically, it has been described for the first time by Domcke and Cederbaum in a quantum mechanical formalism [100] and reformulated by Gel' mukhanov [407]. In this paragraph, we will present a classical approach to the phenomenon. A proper quantum mechanical description of the recoil effects will be presented in the framework of a simple model in Section 6.1.2.

As we have said already, the recoil momentum is distributed among translational, rotational and vibrational motions. The first one has no incidence on the photoionization cross section and can be depreciated. Also, at the present level of description, we are not interested in resolving the rotational spectra and will not consider effects on the rotational motion. Then, we are left with the vibrational induced excitations. Beforehand, we need to postulate two assumptions: the momentum of the photon is so small that it is negligible ; the electron is considered (in a first approach) as uniquely bound to one atom, denoted A. If we consider a diatomic molecule AB initially at rest, departure of the photoelectron from A with a kinetic energy ε will leave the molecule with an energy equal to the recoil energy $E_A = M_A p_e^2/2$ already contained by the emitter atom. This energy is distributed between the translation energy $E_t = M p_e^2/2$ and the excitation energy Ee which takes the form:

$$E_e = E_A - E_t = \frac{M_B}{2(M_A M)} p_e^2 \tag{5.18}$$

where M_A, M_B and M are respectively the mass of atom A, B and of the molecule.

The situation described so far can be applied to the core photoionization case of an heteronuclear diatomic molecule where the electron can be considered as localized on an atom. The model can be easily extend to the case of valence photoemission since the valence wavefunction is partially localized on the individual atoms of the molecule. Treatment of the recoil effect in the valence photoionization requires nevertheless to estimate the localization probabilities n_A and n_B in the vicinity of each atoms:

$$E_e = n_A \frac{M_B}{2(M_A M)} p_e^2 + n_B \frac{M_A}{2(M_B M)} p_e^2 \tag{5.19}$$

In the general case of polyatomic molecules, it can be assumed that the recoil provoked by the fast photoelectron emission is elastic and that the whole molecule receives the momentum transfer rigidly. But when the emitted electron is initially localized around a specific atom, the momentum transfer happens in a time scale much faster than the vibrational motion and is not redistributed elastically on every atoms. The "kick" received by the emitter atom

generates a vibrational excitation of several normal modes and the recoil momentum $\mathbf{\Delta p}$ has to be distributed among all of them:

$$\mathbf{\Delta p} = \sum_i \Delta p_i \mathbf{p_i} \tag{5.20}$$

where Δp_i is a coefficient which represents the change in momentum for each normal mode. When the emitter atom A is at the center of mass of the molecule, no rotational excitations occur, $M_B = M_A$ in Equation (5.18) and the repartition of the excitation energy for each vibrational mode i is given by:

$$E_e^i = f_i E_e = f_i \frac{p_e^2}{2M_A} \tag{5.21}$$

where f_i defines the proportion of excitation energy E_e that ends up in the vibrational mode i.

For undefined orientation of the photoelectron emission, the previous formula has to be averaged over all the directions. For high symmetric molecules such as CH_4, CF_4, BF_3 and SF_6, the total excitation is independent of the angle of emission of the photoelectron and the integration gives rise to a factor $1/3$. For linear molecules such as C_2H_2, excitations have to be evaluated for two active symmetry channels (i.e., for emission parallel and perpendicular to the main axis of the molecule).

The recoil momentum affects differently the photoelectron spectra depending on the number of vibrational modes and on the initial MO. In the case of diatomic molecules, only the stretching vibrational mode exists and can consequently be excited. Then, recoil of the photoelectron emission only induces excitations of higher vibrational levels. In the case of polyatomic molecules where the photoelectron is emitted from a localized central MO, the departing electron causes an additional motion of the emitter atom that results in the excitation of the asymmetric stretching and bending modes (the vibrational modes involving the motion of the central atom).

It is possible to get an estimate of the Franck-Condon deviation by using a procedure exposed in [209]. In the harmonic oscillator approximation, the two first eigenfunctions of the Hamiltonian in the momentum space are given by:

$$\chi_0(p) = \frac{e^{-\frac{p^2}{2}}}{\sqrt[4]{\pi}} \quad \text{and} \quad \chi_1(p) = 2p\frac{e^{-\frac{p^2}{2}}}{\sqrt[4]{4\pi}} \tag{5.22}$$

where p is the momentum dimensionless coordinate.

Then, the Franck-Condon amplitudes including the excitation of the first vibrational quantum number are given by:

$$\langle \chi_0(p) \mid \chi_0(p+\Delta p) \rangle = e^{-\frac{\Delta p^2}{4}} \tag{5.23}$$

$$\langle \chi_1(p) \mid \chi_0(p+\Delta p) \rangle = \frac{\Delta p}{\sqrt{2}} e^{-\frac{\Delta p^2}{4}} \tag{5.24}$$

A more general form of these amplitudes for all v' is obtained recursively and the resulting intensity gives rise to a Poisson distribution:

$$\langle \chi_{v'}(p) \mid \chi_0(p+\Delta p) \rangle = \frac{S^{v'}}{v'} e^{-S} \tag{5.25}$$

where $S = \Delta p^2/2$. Considering the properties of the Poisson distribution, the value S_i for each vibrational mode can be written (in atomic units) as a function of the excitation energy E_e and the harmonic frequency ω_i:

$$S_i = f_i \frac{E_e}{\omega_i} \tag{5.26}$$

According to Equation (5.25), we have:

$$\frac{\langle \chi_1(p) \mid \chi_0(p+\Delta p) \rangle}{\langle \chi_0(p) \mid \chi_0(p+\Delta p) \rangle} = S \tag{5.27}$$

Then, the $v' = 1/v' = 0$ Franck-Condon ratio including corrections of the recoil effect is evaluated easily for the diatomic case:

$$\left(\frac{F_{v'=1}}{F_{v'=0}} \right)_{rec} = \frac{F_{v'=1}}{F_{v'=0}} + R_c \varepsilon \tag{5.28}$$

where:

$$R_c = \frac{1}{3\omega_e} \left[n_A \frac{M_B}{M_A M} + n_B \frac{M_A}{M_B M} \right] \tag{5.29}$$

Results of Equation (5.28) are shown in Figure 5.31 for the core photoionization of N_2 and CO. They are compared with theoretical results obtained with the DFT method. Although the present method is not dynamic (i.e. for each geometry calculation the nuclei can be considered as having an infinite mass with respect to the leaving electron), part of the recoil effect is adiabatic and then can be described by the DFT method. In the case of N_2, the photoelectron is emitted in the two considered photoionization channels from both atomic centers. Then, for the recoil model we have taken $n_A = n_B = 1/2$, $M_A = M_B = M_N$ and with a harmonic frequency $\omega_e = 294$ meV we obtained $R_c \sim 0.0222$ meV^{-1}. For the O1s photoionization of CO, $n_A = n_O \sim 1$,

$n_B = n_C \sim 0$ and $\omega_e = 269$ meV: R_c ∼0.0182 meV^{-1}. For the C1s photoionization of CO, $n_A = n_C \sim 1$ and $n_B = n_O \sim 0$: R_c ∼0.0323 meV^{-1}. As seen in Figure 5.31, results obtained with this simple model reproduce nicely the increasing trend visible in the DFT curves[4] As expected, the importance of the effect is inversely proportional to the mass of the emitter atom and deviations to the Franck-Condon factor ratios is stronger in C1s photoionization than in O1s photoionization of CO.

The deviations to the Franck-Condon prediction can also be observed by looking at the vibrational gerade/ungerade branching-ratio of N_2. It is shown in the upper panel of Figure 5.32. DFT method and experimental data are in very good agreement and, as expected, present striking oscillations. Earlier RPA results also agree, but they provide a poorer description at low photon energies. Prediction of the Cohen-Fano model including the nuclear motion is also shown. As for Figure 5.18, the model reproduces nicely the oscillating pattern but is out of phase. As a result of the many approximations made to obtain Cohen-Fano formula, the model does not account for the relative phase between the $N_2(1s\sigma_g^{-1})$ and $N_2(1s\sigma_u^{-1})$ channels. Vibrational branching ratios between the $1\sigma^{-1}$ and $2\sigma^{-1}$ photoionization cross section of CO is also shown (lower panel). No oscillations are visible.

[4]It has to be mentioned that the recoil effect is taken into account in the Born-Oppenheimer approximation by the DFT calculation but only for the symmetric stretching vibrational mode (that is the only vibrational mode in diatomic molecules).

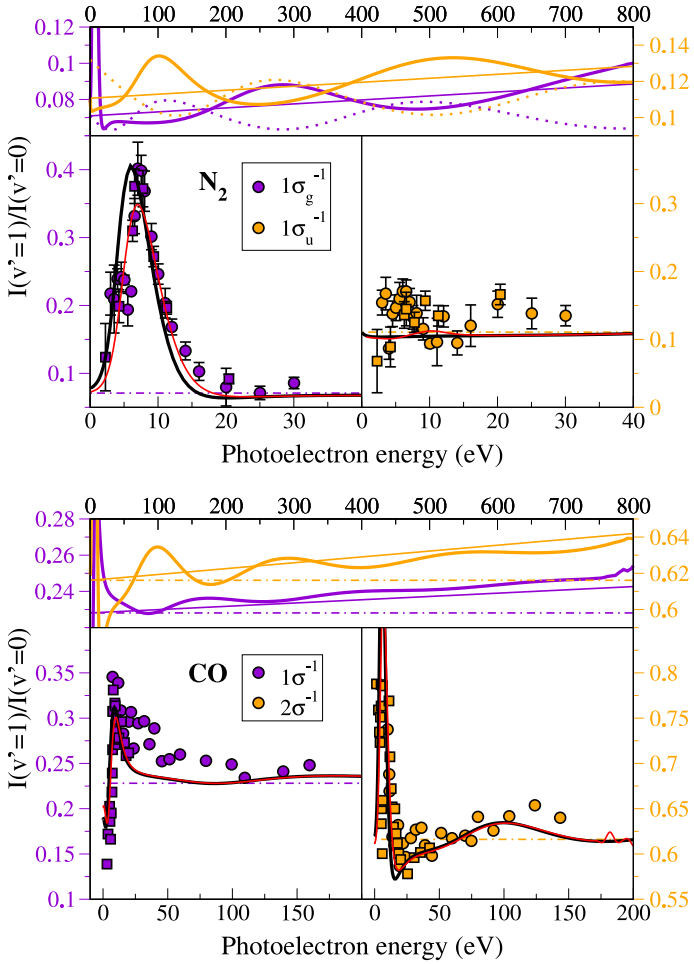

Figure 5.31: (Upper panel) $v' = 1/v' = 0$ cross section ratios for the $1\sigma_g^{-1}$ and $1\sigma_u^{-1}$ photoionization of N_2 as a function of the photoelectron energy (upper panel: large range ; lower panels: small range). Circles: experimental data from [339]. Squares: experimental data from [158]. Thick black and colored lines: DFT method using a LDA functional. Red thin lines: TDDFT method using a LDA functional. Dotted lines: vibrational Cohen-Fano calculations (see [45]). Thin colored lines: effect of the recoil predicted by Equation (5.28). (Lower panel) $v' = 1/v' = 0$ cross section ratios for the $1\sigma^{-1}$ and $2\sigma^{-1}$ photoionization of CO as a function of the photoelectron energy (upper panel: large range ; lower panels: small range). Circles: experimental data from [245]. Squares: experimental data from Kugeler *et al.* published in [245]. Thick black and colored lines: DFT method using a LDA functional. Red thin lines: TDDFT method using a LDA functional. Dashed- dotted lines: theoretical Franck-Condon values. Thin colored lines: effect of the recoil predicted by Equation (5.28)

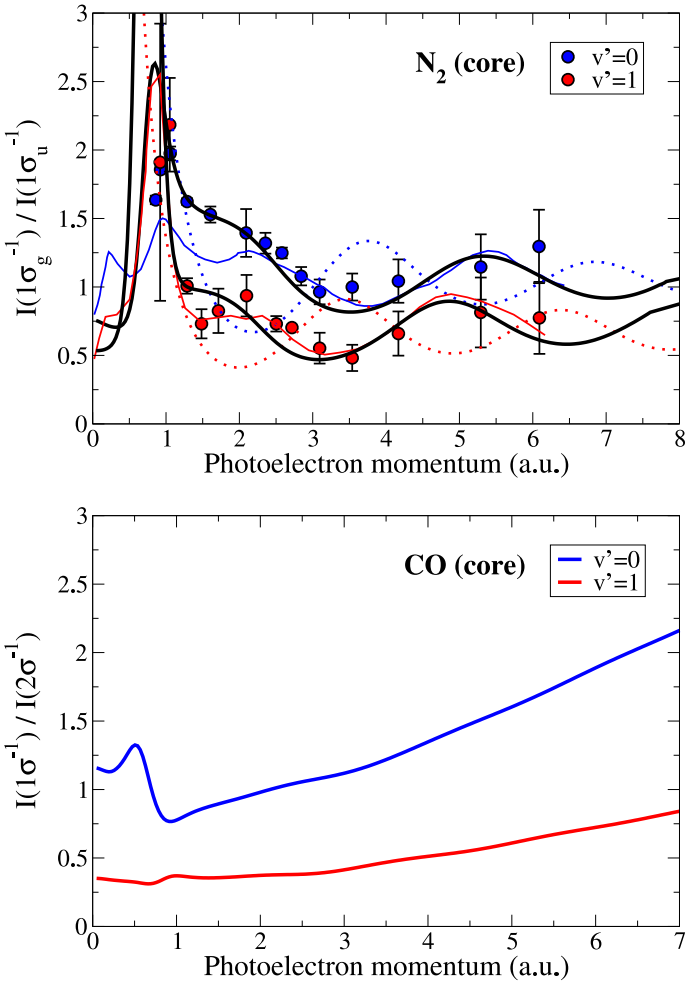

Figure 5.32: (Upper panel) $1\sigma_g/1\sigma_u$ cross section ratios for the photoionization of N_2 as a function of the photoelectron momentum. Circles: experimental data from [226]. Thin blue and red lines: RPA calculations from [226]. Thick black lines: DFT method using a LDA functional. Dotted lines: vibrational Cohen-Fano calculations (see [45]). (Lower panel) $1\sigma/2\sigma$ cross section ratios for the photoionization of CO as a function of the photoelectron momentum. Thick black lines: DFT method using a LDA functional.

5.3.2 Valence shell photoionization

In this section we present vibrationally-resolved photoionization cross sections for photon energies going from the ionization threshold up to several hundreds eV above it.

Figures 5.33 and 5.34 present ratios between vibrationally resolved photoelectron spectra (v-ratios for short) of N_2 and CO, respectively, calculated by using both the DFT and TD-DFT methods. Only v-ratios associated with ionization from the outer valence orbitals is shown: $3\sigma_g$, $1\pi_u$ and $2\sigma_u$ orbitals of N_2 and 5σ, 1π and 4σ orbitals of CO. The results are compared with very recent experimental data from [45]. For each molecule, the v-ratios have been extracted by normalizing the vibrationally resolved cross sections to that of the dominant v-channel. These ratios vary from $\sim$1 down to $\sim 10^{-3}$ for the two molecules. The agreement between the results of both theories and the experimental ones is reasonably good, especially for the TD-DFT ones, which reproduce most of the peaks appearing near the ionization threshold. The most important disagreement appears for the very sharp structures lying just above the threshold. There are also some deviations for the largest v values and photon energies, which is not surprising because the corresponding vibrationally resolved cross sections are very small and, therefore, the measured v-ratios might be affected by large systematic errors.

The structures observed just above the ionization threshold are due to shape resonances and are correctly described by theory for the largest v-ratios. The structures appearing at slightly higher photon energies are likely due to interchannel coupling or to resonances associated with singly-excited autoionizing states. As mentioned above, description of these effects is not possible within the DFT approach, but is pretty well achieved within the TD-DFT method.

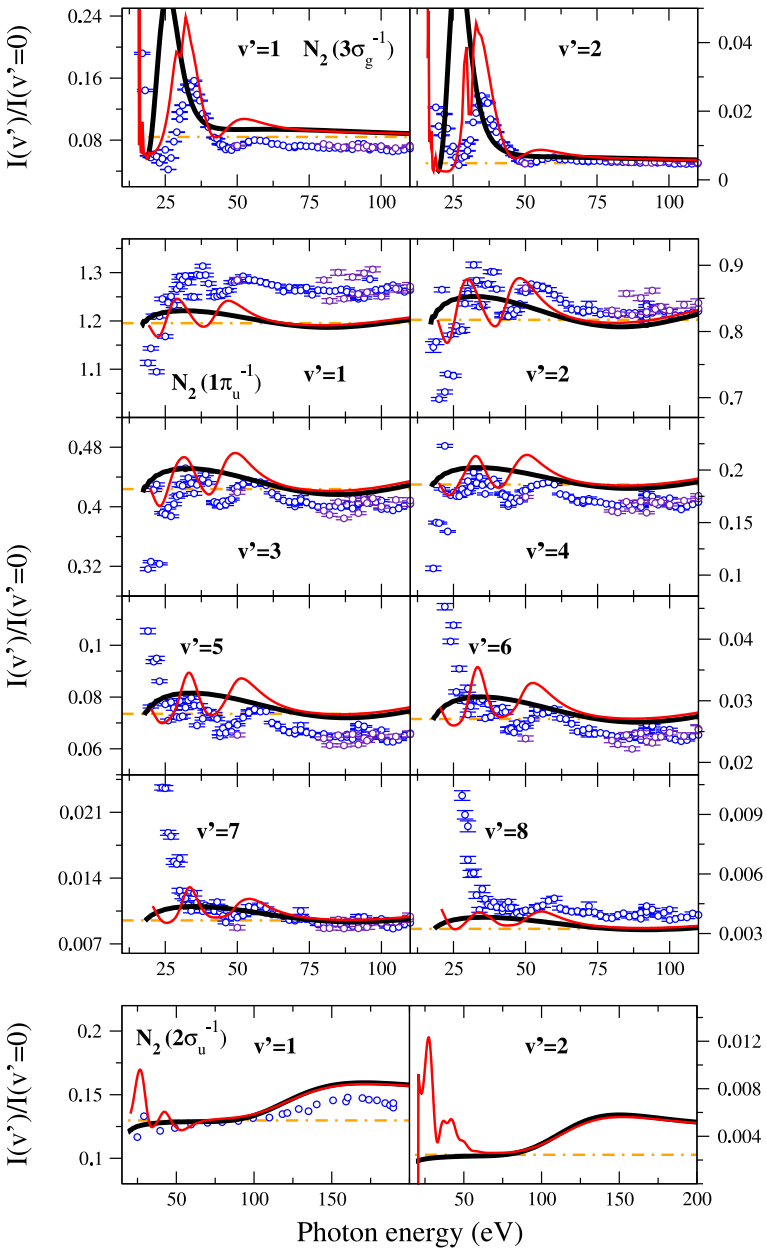

Figure 5.33: Ratios of the vibrationally resolved photoionization spectra to the $v' = 0$ cross section as a function of the photon energy for the $3\sigma_g^{-1}$, $1\pi_u^{-1}$ and $2\sigma_u^{-1}$ photoionization of N_2. Circles: experimental data from [45] (the differents colors indicate different runs). Thick black solid line: DFT method using a LB94 functional. Thin red solid line: TDDFT method using a LB94 functional. Dashed-dotted orange line: Theoretical Franck-Condon value.

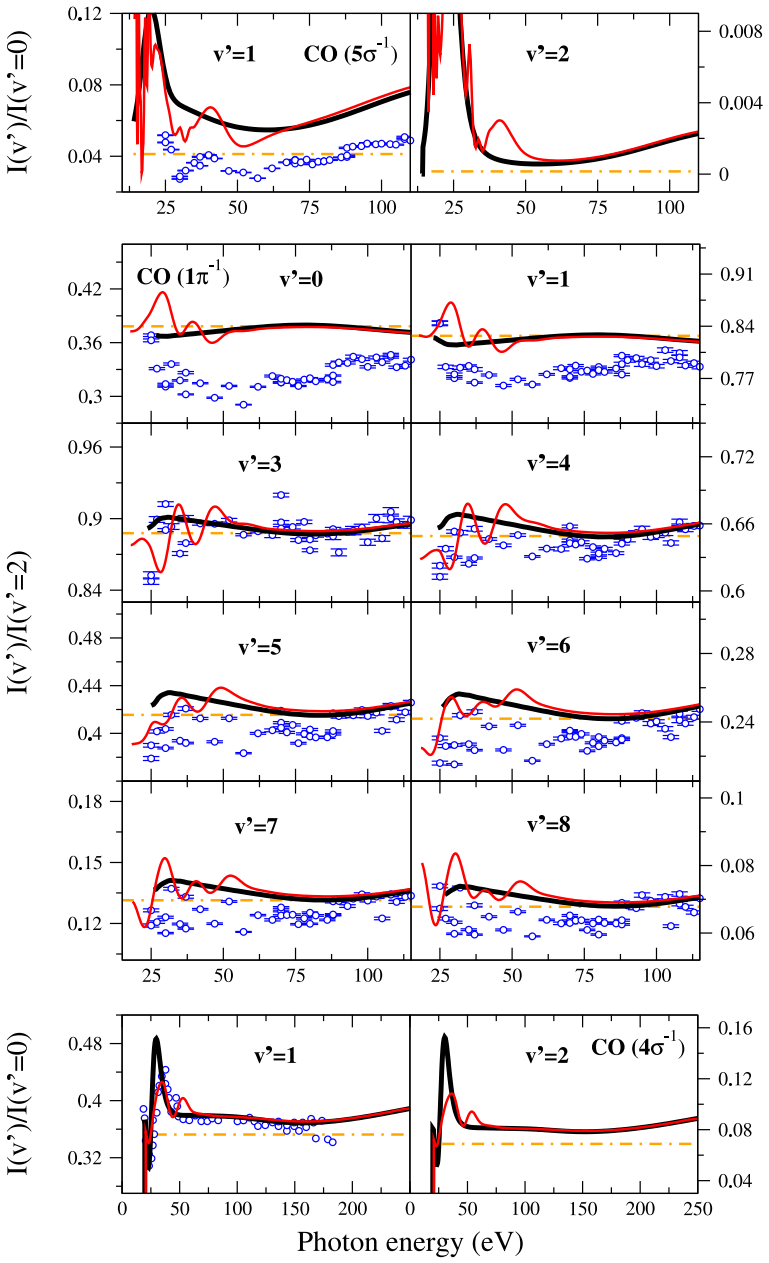

Figure 5.34: Same as Figure 5.33 for the $5\sigma^{-1}$, $1\pi^{-1}$ and $4\sigma^{-1}$ photoionization of CO.

Extended Cohen-Fano model

A common feature to all the v-ratios is the presence of pronounced oscillations around the value predicted by the Franck-Condon (FC) approximation. These oscillations are less visible for CO than for N_2. As shown in [45], they can also be explained as resulting from coherent two-center electron emission since valence MOs of both molecules have contributions on both atomic centers. Indeed, by generalizing Cohen-Fano ideas to the case of vibrationally resolved photoelectron spectra for both homonuclear and heteronuclear diatomic molecules and by using the LCAO expansion $\varphi_\alpha = c_A\varphi_A + c_B\varphi_B$, one can write a first extension of the Cohen-Fano formula:

$$\tilde{\sigma}\left(\omega\right) = \sigma^{(0)}\left(\omega\right)\left(1 + 2c_A c_B \frac{\sin k_e R}{k_e R}\right)(R) \tag{5.30}$$

where $c_A^2 + c_B^2 = 1$. For the valence orbitals of N_2, $|c_A| = |c_B|$ due to the inversion symmetry of the molecule, while for the valence orbitals of CO, these coefficients are different.

A reasonable choice for CO is $c_A^2 = 0.32$ and $c_B^2 = 0.68$, which correspond to the normalized electron occupancy of the C and O valence orbitals, respectively, resulting from a simple Hartree-Fock calculation performed with a minimal basis of atomic orbitals. Photoelectron spectra corresponding to different final v' states of the remaining molecular cation probe different regions of R. Thus one can gives an approximation of the v-ratios by replacing the variable R by the characteristic value $R_{v'}$ associated with the v' vibrational state, then performing a first-order expansion of $\tilde{\sigma}^{v'}/\tilde{\sigma}^{v'_{ref}}$ in terms of $\delta R_{v'} = R_{v'} - R_{v'_{ref}}$, and finally taking the limit to large values of the electron momentum k_e. Hence one obtains:

$$\frac{\tilde{\sigma}^{v'}\left(\omega\right)}{\tilde{\sigma}^{v'_{ref}}\left(\omega\right)} = \frac{|\left\langle \chi_{i,v}|\chi_{f_\alpha,v'}\right\rangle|^2}{|\left\langle \chi_{i,v}|\chi_{f_\alpha,v'_{ref}}\right\rangle|^2}\left[1 + 2c_A c_B \frac{\delta R_{v'}}{R_{v'_{ref}}}\cos(k_e R_{v'_{ref}})\right] \tag{5.31}$$

The formula predicts that the $\tilde{\sigma}^{v'}/\tilde{\sigma}^{v'_{ref}}$ ratio should approximately oscillate around the Franck-Condon ratio value:

$$\frac{FC_{v'}}{FC_{v_{ref}}} = \frac{|\left\langle \chi_{i,v}|\chi_{f_\alpha,v'}\right\rangle|^2}{|\left\langle \chi_{i,v}|\chi_{f_\alpha,v'_{ref}}\right\rangle|^2} \tag{5.32}$$

with a $\cos(k_e R_{v'_{ref}})$ dependence and amplitude proportional to $\delta R_{v'}/R_{v'_{ref}}$. This is precisely the qualitative behavior observed in all the ratios depicted in Figures 5.33 and 5.34. Notice that, when $R_{v'}$ is smaller than $R_{v'_{ref}}$, the ratio $\delta R_{v'}/R_{v'_{ref}}$ is negative and, therefore, the oscillations have opposite phase.

This can be clearly seen in figure 5.36, when comparing the $v' = 0/v' = 2$ and $v' = 1/v' = 2$ ratios with the $v' = 3/v' = 2$, $v' = 4/v' = 2$, etc, ones.

The nuclear motion can also be explicitly included by integrated the square root of the Cohen-Fano formula in (5.30) with the initial and final vibrational wavefunctions:

$$\tilde{\sigma}_{\alpha}^{v,v'}(\omega) \propto \left| \int_0^{\infty} \chi_{i,v}^{*}(R) \left[1 + 2c_A c_B \frac{\sin k_e R}{k_e R} \right]^{\frac{1}{2}} \chi_{f_\alpha,v'}(R) dR \right|^2 \tag{5.33}$$

The last formula corresponds to an extended version of the Cohen-Fano formula that takes into account the nuclear motion and can be applied to both homonuclear and heteronuclear molecules. Results obtained using this simple model is presented together with the previous experimental data and the TIDFT calculation for the valence photoionization of N_2 and CO in Figures 5.33 and 5.34. Good agreement between model, theory and experiment is observed. In particular, results presented in the HOMO photoionization of N_2 and CO agree remarkably well, probably because these particular photoionization channels involves less electronic correlation (not included in the simple model). Also, it has to be mentioned that the phase matching between the extended Cohen-Fano v-ratios and the experimental data is a coincidence since the model is not expected to reproduce the correct phase shift.

Figures 5.35 and 5.36 show a comparison between the previous DFT results, the experimental data and the extended Cohen-Fano model.

For $N_2(1\pi_u^{-1})$ and $CO(1\pi^{-1})$, the agreement with the model is less satisfactory and essentially qualitative. This is not surprising because equation (5.33) was derived with a superposition of 1s orbitals centered on each nuclei, i.e., $1\sigma_g \sim 1s_A + 1s_B$ as initial molecular orbital. However, the initial molecular orbitals in N_2 $1\pi_u^{-1}$ and CO $1\pi^{-1}$ photoionization are, at least, a superposition of $2p_{+1}$ (or $2p_{-1}$) orbitals, i.e., $1\pi \sim 2p_{+1,A} + 2p_{+1,B}$ (in reality, they involve even more AOs). In the original paper by Cohen and Fano [64], it was suggested that photoionization from a π orbital should exhibit twice as many maxima as from σ orbitals [i.e., the dependence should be $\sin(2k_eR)$ as opposed to $\sin(k_eR)$ in equation (5.33)]. Checking for this possibility leads to an even poorer agreement, so it can be concluded that the original model captures the essential features of the ratios. For completeness, an equivalent study has been carried out for the original molecular prototype H_2. Extended Cohen-Fano model, experimental data and results obtained using a more accurate numerical method[5] are compared in Figure 5.37. As can be seen, the model reproduces almost perfectly the oscillations in H_2, apart from a global

[5]The theoretical method to obtain the electronic and vibrational wave functions of H_2 makes use of B-spline functions and has been successfully applied to study a variety of ionization problems in H_2, such as resonant dissociative photoionization [320, 243] and ion impact ionization [214] in the dipole approximation. We refer the reader to those works and,

scaling factor, which is likely due to the assumption of identical σ_0 for the two vibrational channels involved in the ratio and to the fact that, as previously mentioned, such a simple model does not include any electron correlation or "molecular" distortion of the initial and final electronic wave functions. Interestingly, the period of the oscillations is larger in H_2 than in N_2 and CO, reflecting the fact that H_2 have an equilibrium internuclear distance significantly smaller than N_2 and CO (1.4 a.u. compared to 2.07 a.u. and 2.13 a.u. respectively).

for more details, to the reviews of references [242, 14]. Electron correlation and interferences between the different ionization and dissociative channels are accounted for. As in [117], we have not included doubly excited states in the basis of states since we are only interested in the region of high photon energies.

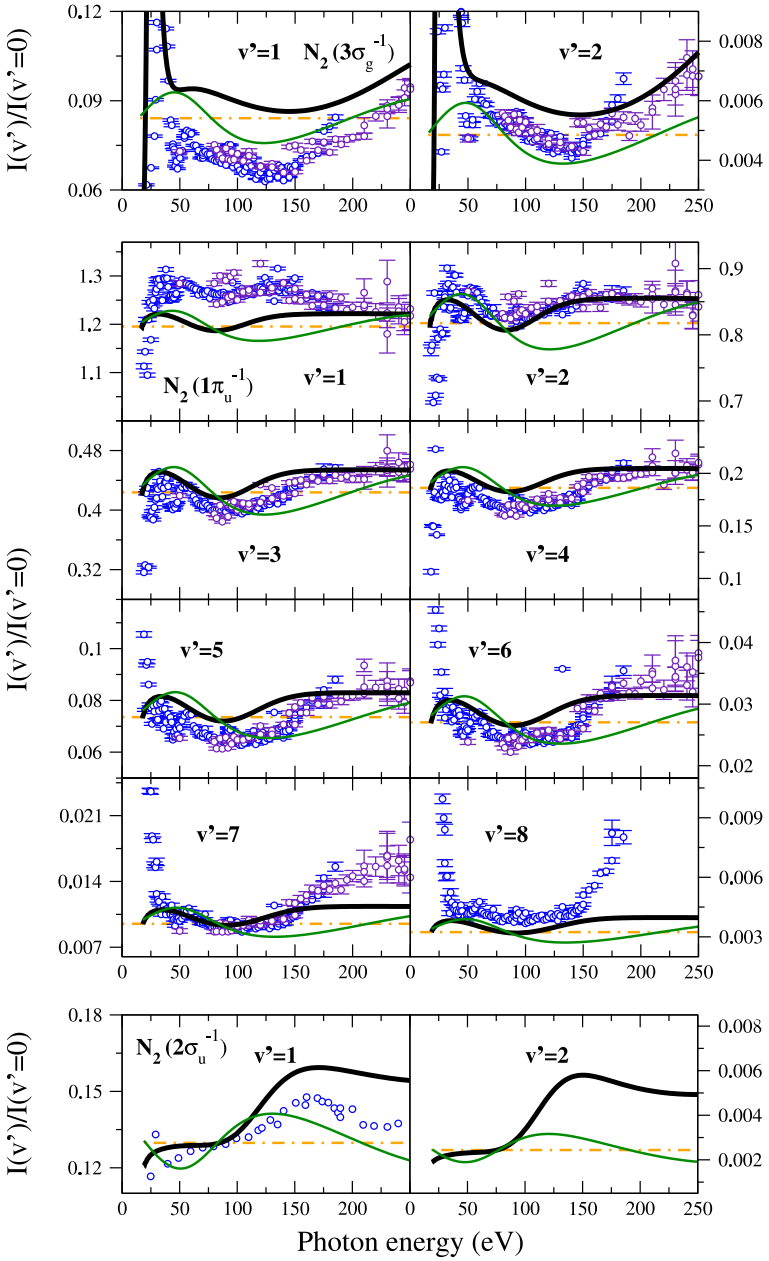

Figure 5.35: Ratios of the vibrationally resolved photoionization spectra to the $v' = 0$ cross section as a function of the photon energy for the $3\sigma_g^{-1}$, $1\pi_u^{-1}$ and $2\sigma_u^{-1}$ photoionization of N_2. Circles: experimental data from [45] (the different colors indicate different runs). Thick black solid line: DFT method using a LB94 functional. Thin green solid line: vibrationally resolved Cohen-Fano results obtained from equation (5.33). Dashed-dotted orange line: Theoretical Franck-Condon value.

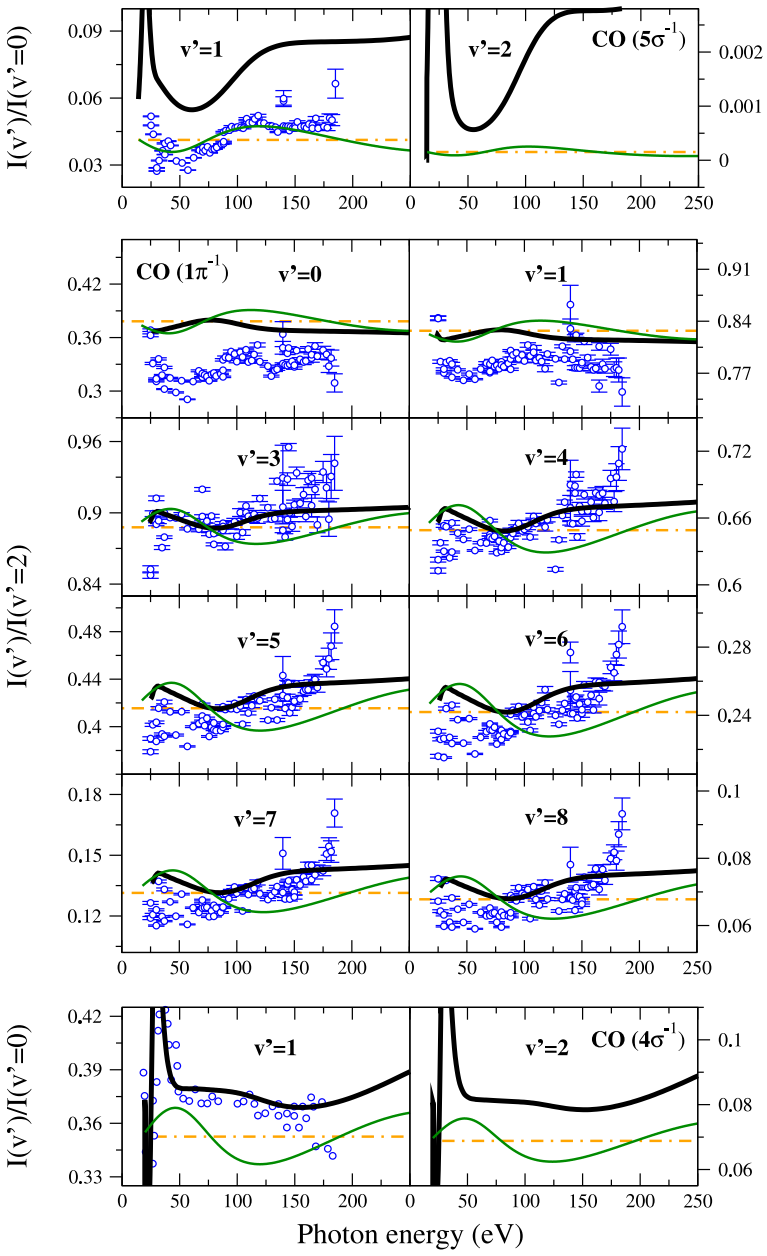

Figure 5.36: Same as Figure 5.35 for the $5\sigma^{-1}$, $1\pi^{-1}$ and $4\sigma^{-1}$ photoionization of CO.

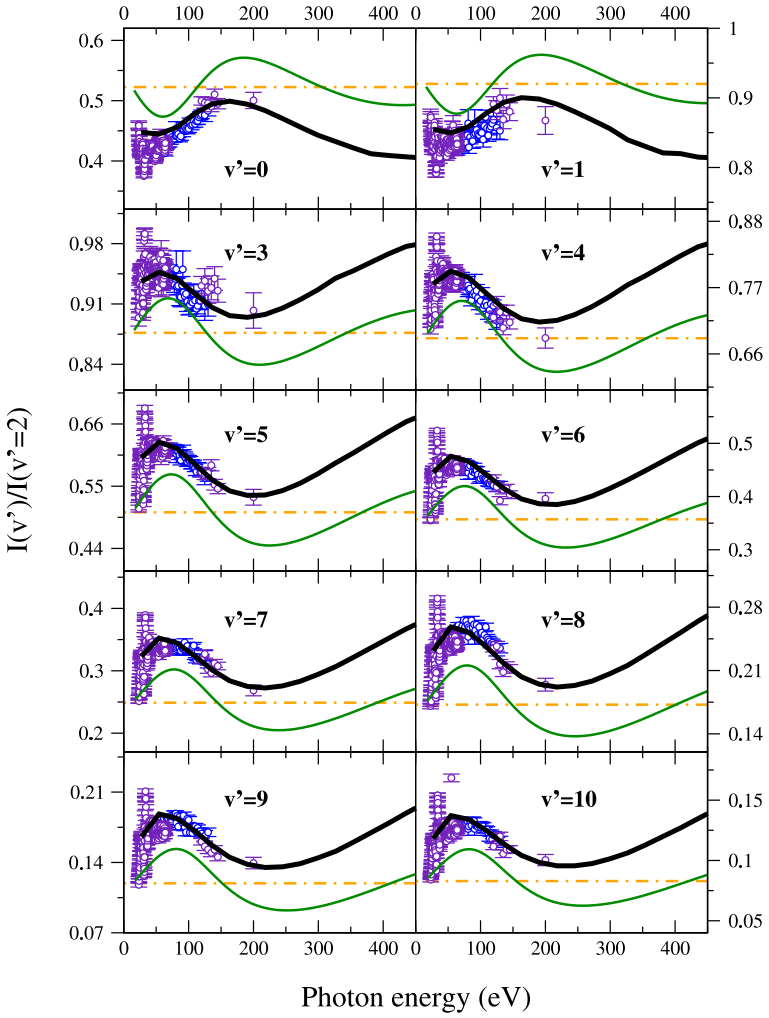

Figure 5.37: Ratios of the vibrationally resolved photoionization spectra to the $v' = 2$ cross section as a function of the photon energy for the photoionization of H_2. Circles: experimental data from [45] (the different colors indicate different runs). Thick black solid line: Theoretical results obtained using the B-splines method described in [242]. Thin green solid line: vibrationally resolved Cohen-Fano results obtained from equation (5.33). Dashed-dotted orange line: Theoretical Franck-Condon value.

5.4 Angularly resolved cross section

There are very few experimental data for vibrationally resolved angular distributions and most of them have been obtained for randomly oriented molecules. Thus, to gauge the quality of the present calculations, we first present results for randomly oriented molecules and then for fixed-in-space molecules for which there are no experimental data.

5.4.1 β asymmetry parameter

In this section, we present the calculated vibrationally resolved electron asymmetry parameters for K-shell and valence-shell photoionization of N_2 (Figures 5.38 and 5.40) and CO (Figures 5.39 and 5.41). The results are compared with the available experimental data [200, 339, 336, 241] for photoelectron energies smaller than 60 eV. In the case of valence-shell photoionization, the direct comparison over a wide range of photon energies (right panels) can only be carried out with vibrationally averaged β parameters. Nevertheless, for the sake of completeness, in the last case we have also included in the figures our vibrationally resolved results.

As expected, for both N_2 and CO, the β parameter tends to a value close to 2 as the photon energy increases. A β value of 2 is associated to a perfect p-like electron angular distribution, which is what one would expect for an electron moving in the field of a perfectly spherical potential. Indeed, at very high energies, the escaping electron does not see the details of the two-center potential and, consequently, the resulting angular distribution should have an almost perfect atomic character. This is so unless the electron wavelength coincides or is of the order of the internuclear distance, where two-center interferences and diffraction effects are expected to occur (see next section). The latter effects are responsible for the oscillations that are observed in the β parameter as it approaches the value of 2 (see right panels in Figures 5.40 and 5.41).

Figures 5.38, 5.40, 5.39 and 5.41 show a very good agreement between the present results and the available experimental data. They are also in reasonable agreement with previous theoretical results obtained within the random-phase approximation [339, 336], although the latter are obtained by using a free parameter in the theory. As can be seen, the β parameters associated with different vibrational levels v' of the residual molecular cation are very similar. The largest variations with v' are observed for photoionization from the highest-occupied molecular orbital (HOMO), namely $N_2(3\sigma_g^{-1})$ and $CO(5\sigma^{-1})$. These are the orbitals where electron delocalization is more important. They also have several nodes along the internuclear axis. Consequently,

one can reasonably expect that the electron angular distribution should be more sensitive to the particular range of internuclear distances probed by the different vibrational levels of the molecular cation. In particular, it can be seen that the larger v' the smaller the value of β, i.e., the less atom-like the angular distribution. This is due to the fact that, as v' increases, photoionization probes regions of increasingly larger values of R, hence the angular distribution has a less pronounced atomic character (i.e., β is far lower than 2).

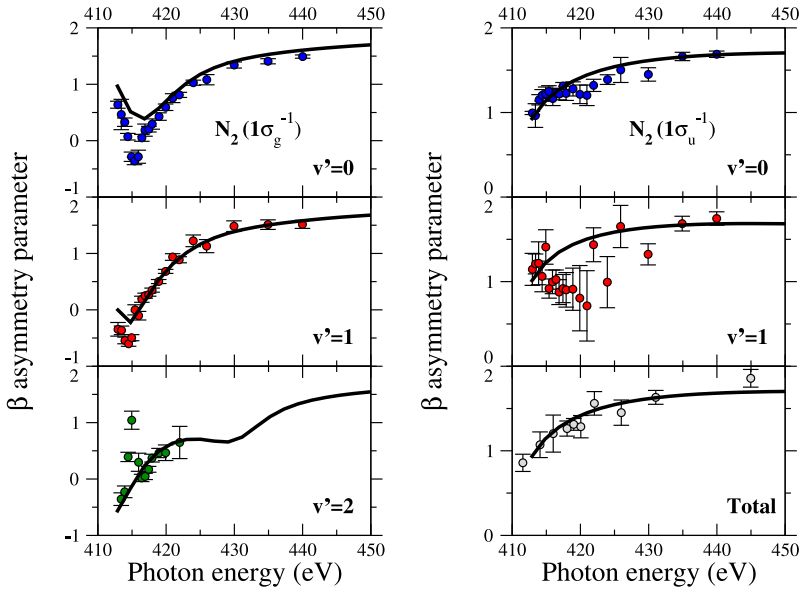

Figure 5.38: Vibrationally resolved electron β asymmetry parameter for the $1\sigma_g^{-1}$ and $1\sigma_u^{-1}$ photoionization of N_2. Circles: experimental data from [339] (left and right panels). Thick black solid line: DFT method using a LB94 functional.

The closeness between the averaged β asymmetry parameter and the $v' = 0$ component in the HOMO photoionization of N_2 and CO, as well for the $2\sigma_u$ photoionization of N_2 is explained by the dominance of the $v = 0 \rightarrow v' = 0$ transition. Indeed, according to the Franck-Condon principle, the fundamental vibronic transition composed more than 85% of the photoelectron spectrum in these channels. In the case of the 4σ photoionization of CO, the vibrational peaks are of comparable intensities and the averaged β asymmetry parameter deviates from a single vibrational component. This behavior is more apparent when looking at larger energy range (Figure 5.41).

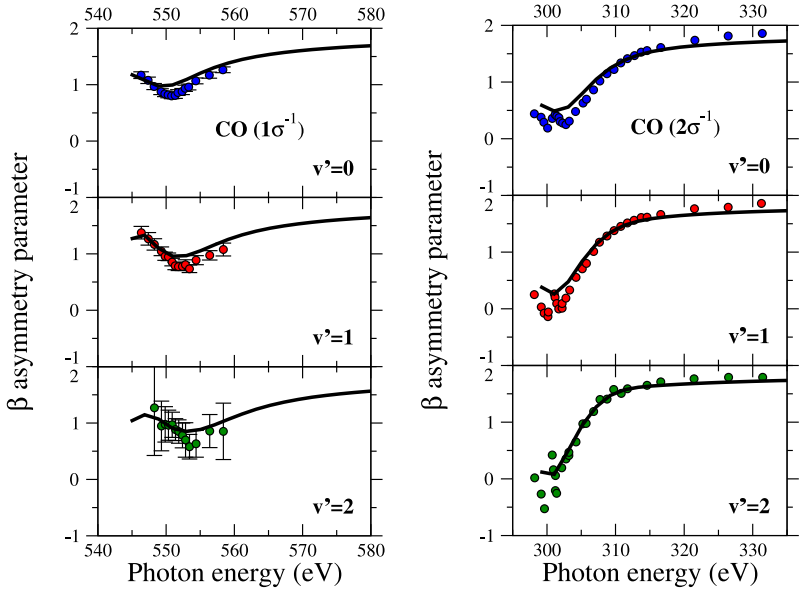

Figure 5.39: Vibrationally resolved electron β asymmetry parameter for the $1\sigma^{-1}$ and $2\sigma^{-1}$ photoionization of CO. Circles: experimental data from [336] (left panel) and [200] (right panel). Thick black solid line: DFT method using a LB94 functional.

Shape resonances associated with the f-wave photoelectron are observed in β asymmetry parameter associated with the $3\sigma_g^{-1}$ photoionization of N_2 and $5\sigma^{-1}$ and $4\sigma^{-1}$ photoionization of CO. The absence of shape resonances in the σ_u and π_u photoionization channel of N_2 is consistent with the usual interpretation which states that only the $3\sigma_u$ virtual MO lays in the shape resonance region. Then, owing to selection rules, only transition from gerade states are allowed. In the case of $1\pi^{-1}$ photoionization of CO, the shape resonance effect is barely visible. As illustrated by the comparison between $5\sigma^{-1}$ and $1\pi^{-1}$ photoionizations in Figure 5.42, it results from the dominance of the non-resonant $1\pi \rightarrow \varepsilon\delta$ component over the resonant $1\pi \rightarrow \varepsilon\sigma$ component in the $1\pi^{-1}$ channel.

Autoionization is responsible for some structures visible at low energies in the HOMO photoionization β asymmetry parameter of N_2 and CO. In the $3\sigma_g^{-1}$ photoionization of N_2, it leads to the $C^2\Sigma_u^+$ state and shows up at $\sim$ 22eV [372]. The excitation energy of the fourth band has been evaluated by Stratmann *et al.* at the CASCI level of theory to 10.58 eV. This state correspond to the promotion of a bonding σ_g electron to an anti-bonding π_g MO, i.e. to the configuration $(1\sigma_g^2)$ $(1\sigma_u^2)$ $(2\sigma_g^2)$ $(2\sigma_u^2)$ $(1\pi_u^3)$ $(3\sigma_g^1)$ $(1\pi_g^1)$. According to their calculation, the highest-lying open channel corresponds to the $B^2\Sigma_u^+$. Most of the theoretical calculation performed in the fixed nuclei

approximation conclude that better agreement would be obtained by including the nuclear motion and averaging on the vibrational components.

As shown in Section 5.2, interchannel couplings play a non-negligible role in the $2\sigma_u^{-1}$ photoionization channel of N_2. As shown by the discrepancy between the DFT and the experimental β asymmetry parameter (see Figure 5.40), such effects are even more visible in the angular distribution. In order to take into account the interchannel couplings, we performed a TDDFT calculation in the fixed nuclei approximation (dashed black line). The TDDFT results reproduce nicely the dips at ~ 30 eV and ~ 50 eV and previously associated to couplings with the $3\sigma_g \rightarrow \varepsilon\sigma_u$ and $2\sigma_g \rightarrow \varepsilon\sigma_u$ transition channels. Because deviations between DFT and TDDFT are concentrated in the shape resonance region of the $3\sigma_g^{-1}$ and $2\sigma_g^{-1}$ photoionization channel, we refer to them as shape resonance enhancement mediated by continuum-continuum coupling. Similar mediated resonances have been observed many times in atomic photoionization and studied in some molecular cases, such as N_2 [366] and SF_6 [87]. In the case of the $2\sigma_u^{-1}$ photoionization of N_2, it corresponds to the following mechanism: when a electron is emitted from the $3\sigma_g$ (or $2\sigma_g$) MO and trapped into a σ_u quasi-bound state, electronic collision may occur and leads to the ejection of an electron from the $2\sigma_u$ MO by simultaneous de-excitation of the σ_u wave electron into its initial MO.

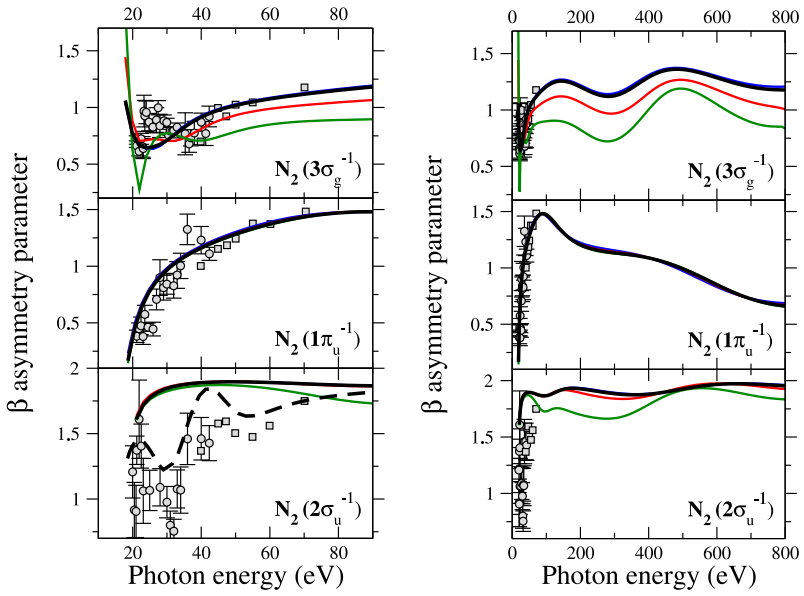

Figure 5.40: Same as Figure 5.38 for the valence shell. Circle: [241], Squares: [143]. Black dashed line correspond to the vibrational average theoretical result obtained with the TDDFT method using a LB94 functional.

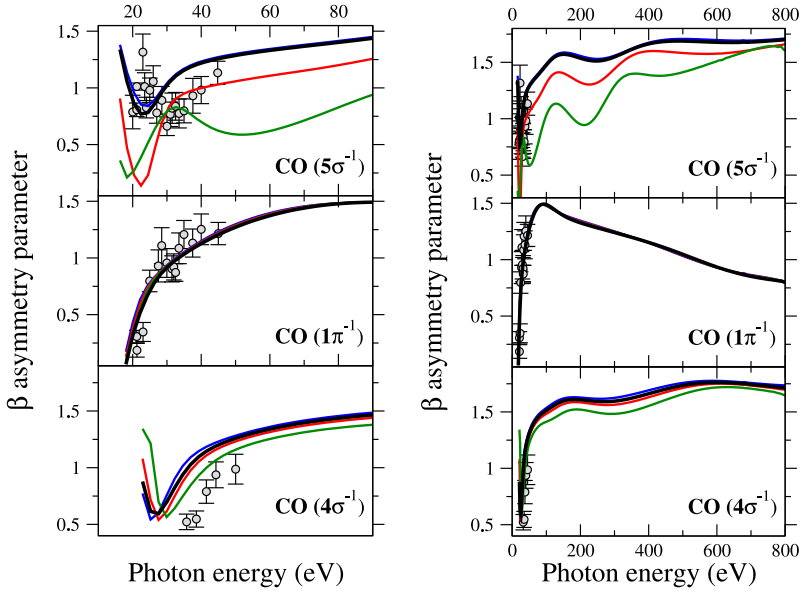

Figure 5.41: Same as Figure 5.38 for the valence shell. Circles: [241].

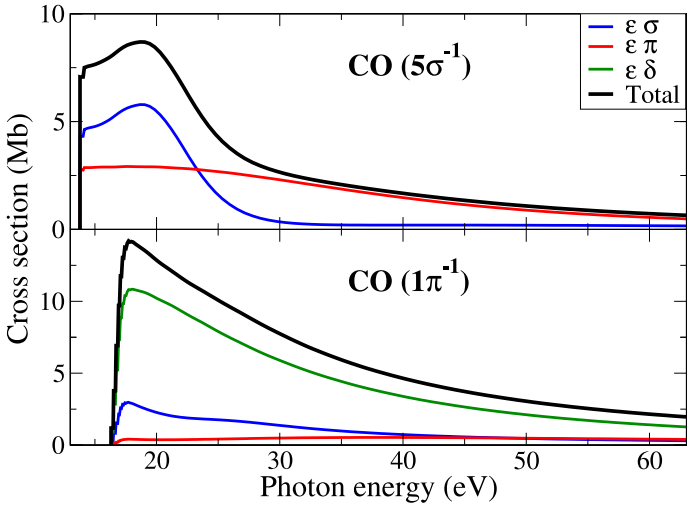

Figure 5.42: Symmetry resolved cross section for the $5\sigma^{-1}$ (upper panel) and $1\pi^{-1}$ (lower panel) photoionizations of CO as a function of the photon energy. Lines correspond to the DFT method using a LB94 functional - Colored lines: symmetry components, Black line: total cross section.

5.4.2 MFPADs

In this section we present non-vibrationally and vibrationally resolved MFPADs of N_2 and CO for two particular molecular orientations: parallel and

perpendicular to the polarization direction of the incident light. These two orientations provide information for molecular states of Σ and Π symmetries, respectively. The first series of figures (5.43, 5.44 and 5.45) shows a comparison between the DFT method using a LB94 functional and experimental data taken from the literature.

Figures 5.43 and 5.44 present results for the O1s and C1s photoionization of CO respectively. Each figure contains four polar MFPADs taken at different photon energies for each orientation of the polarization vector. For the O1s photoionization channel (Figure 5.43), best agreement between experiment and theory is found for the smallest photon energy ($\omega = 545$ eV). It is surprising since DFT is expected to be less accurate close to the threshold. For higher energies, there is a qualitative agreement but almost always a discrepancy on one particular side of the polar plot. In the parallel case, there is an overestimation in the experimental MFPADs by a constant factor on the side of the oxygen atom. This constant discrepancy seems to indicate a systematic error that is angular dependent. For the perpendicular case, the disagreement is less regular. In all the cases, the the three first components of the MFPADs present the same shape. As indicated by the photoelectron spectrum (see Figure 5.22b), $v' = 0$ (blue line) is the dominant contribution, followed by $v' = 1$ (red) and $v' = 2$ (green)[6]. For the C1s photoionization channel (Figure 5.44), a good agreement between theory and experiment is found for all the photon energies in the parallel case. The first photon energy ($\omega = 301$ eV) corresponds to the beginning of the shape resonance in the total cross section, the second one ($\omega = 304.5$ eV) corresponds approximately to the energy position of the shape resonance and the third and fourth ones ($\omega = 310$ eV and $\omega = 317$ eV) to the end of the shape resonance. Then, Figure 5.44a shows the evolution of the MFPADs from one side of the shape resonance to the other. It can be seen how the MFPAD undergoes a drastic change of symmetry passing through the shape resonance. From a f-like orbital with a strong forward-backward asymmetry ($\omega = 301$ eV), the MFPAD becomes p-like and more symmetric at $\omega = 310$ eV, and gain an asymmetry in the opposite direction at $\omega = 317$ eV. In the perpendicular case, the agreement is only qualitative. For the two lowest photon energies ($\omega = 299$ and 301 eV), there is an important discrepancy between theoretical results and experimental data on the side of the carbon atom. Since the C1s photoelectron spectrum of CO has a larger vibrational progression, contribution of the three first vibrational components is better appreciated in the parallel as in the perpendicular case.

[6]For the sake of clarity, the other vibrational components have not been plotted.

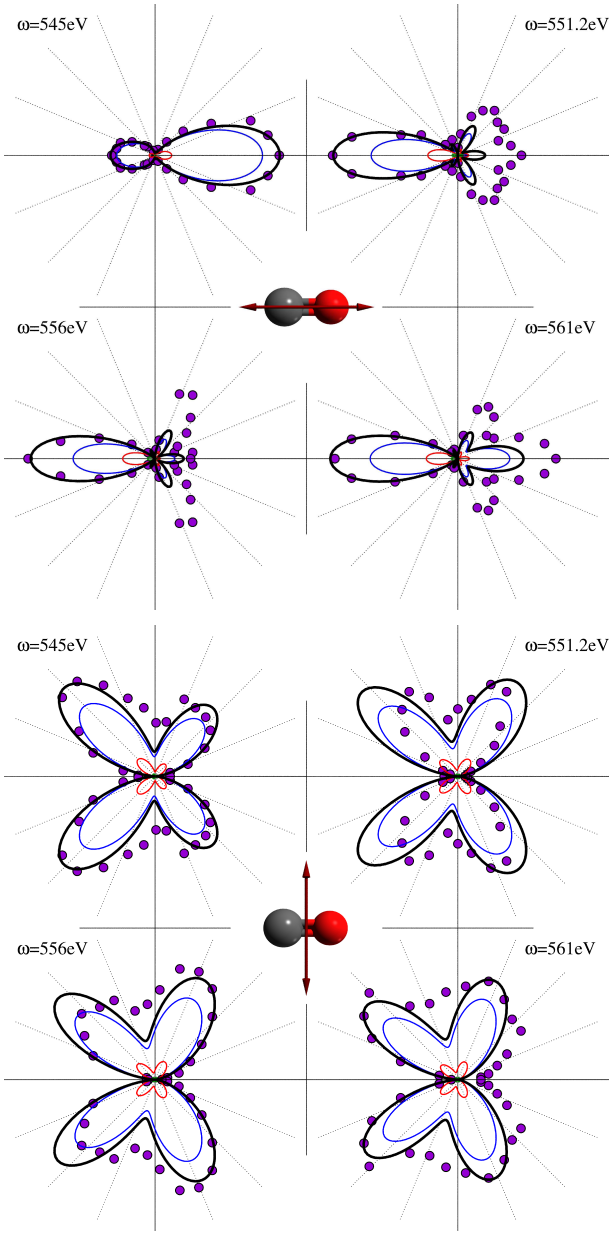

Figure 5.43: Vibrationally resolved MFPADs for the CO($1\sigma^{-1}$) photoionization. Molecules are parallel (perpendicular) to the polarization vector in the upper (lower) panel. The MFPADs are taken in a plane containing the main axis of the molecule for photon energies equals to 545, 551.2, 556 and 561 eV. Circles correspond to non-vibrationally resolved experimental data from [262], normalized to the theoretical results. Solid lines correspond to vibrationally resolved theoretical results obtained with the DFT method using a LB94 functional - Colored solid lines: vibrational components (only v' =0, 1 and 2), Thick black solid line: sum over all the vibrational components.

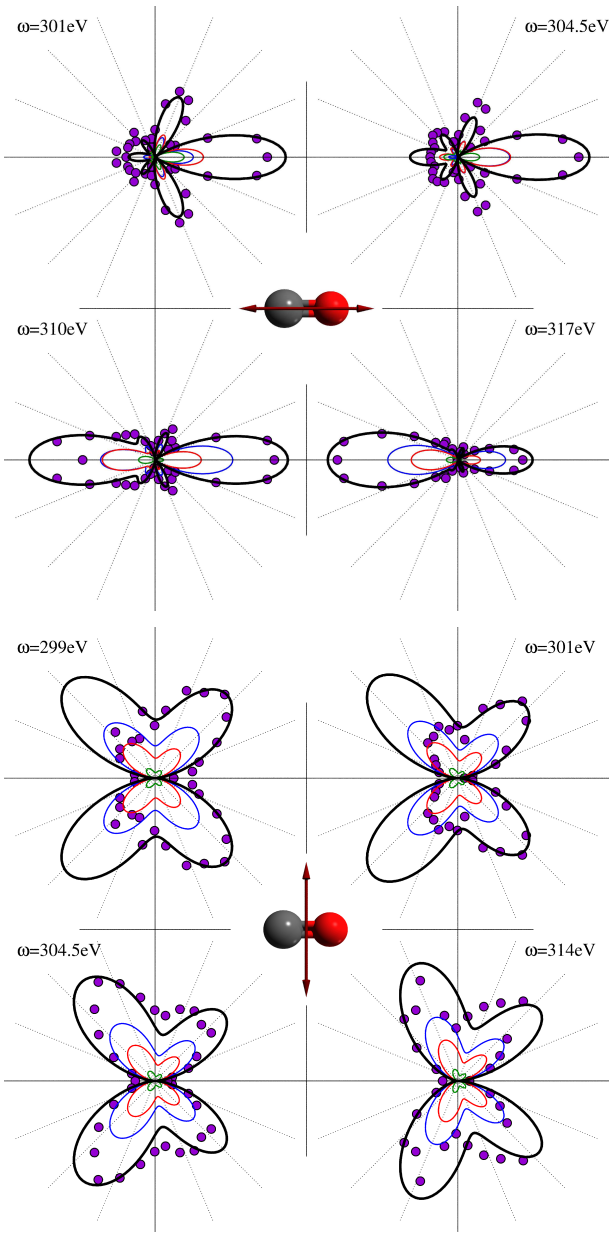

Figure 5.44: Same as Figure 5.43 for the CO($2\sigma^{-1}$) photoionization and for photon energies equals to 301, 304.5, 310 and 317 eV (upper panel) and 299, 301, 304.5 and 314 eV (lower panel).

Recent improvement of synchrotron radiation sources and detection techniques have enabled the measurements of the photoelectron angular distribution for several final vibrational levels and for photon energies covering valence and core shell photoionization. Figure 5.45a shows vibrationally resolved experimental data for the C1s photoionization cross section of CO. It is compared for three different photon energies with the DFT method. The chosen photon energies correspond more or less to the position of the shape resonance in each vibrational component: $\omega \sim 303.2$ eV corresponds to the shape resonance in $v' = 2$, $\omega \sim 305.1$ eV in $v' = 1$ and $\omega \sim 310.1$ eV in $v' = 0$. For this reason, the $v' = 2$ component at $\omega = 305.1$ is similar to $v' = 0$ at $\omega = 310.1$. The agreement between theory and experiment is good, except for an important discrepancy in the experimental $v' = 0$ MFPAD at $\omega \sim 310.1$ eV on the side of the carbon atom. Similarly to the non- vibrational case (see Figure 5.44a), it is possible to observe the transformation of the vibrational MFPADs, from an asymmetric f-like orbital at $\omega = 303.2$ eV to a less asymmetric p-like orbital at $\omega = 310.1$ eV. Since the shape resonance in the $v' = 1$ component is closer to $\omega = 310.1$ eV than in the $v' = 2$, the resulting vibrational MFPAD is less deported in the direction of the carbon atom. For the same reason, the $v' = 0$ presents an asymmetry in the opposite direction.

The new energy resolution capabilities also enabled to resolved the gerade and ungerade states in the core photoionization of N_2. Figure 5.45b shows a comparison between non-vibrationally resolved experimental MFPADs and vibrationally resolved MFPADs obtained with DFT for the $1\sigma_g^{-1}$ and $1\sigma_u^{-1}$ photoionization of N_2. The chosen photon energy corresponds to the energy of the shape resonance in the $1\sigma_g^{-1}$ photoionization channel. For this reason, and because the $l = 3$ partial wave is trapped by the potential barrier, the angular distribution is almost an f orbital in the gerade-parallel case. Because the potential barrier is along the z direction, the angular distribution is aligned perpendicularly in the gerade-perpendicular case. Since the $1\sigma_u^{-1}$ photoionization channel do not present any shape resonances, the angular distribution resembles a p-wave in the parallel case and has a characteristic "butterfly shape in the perpendicular case.

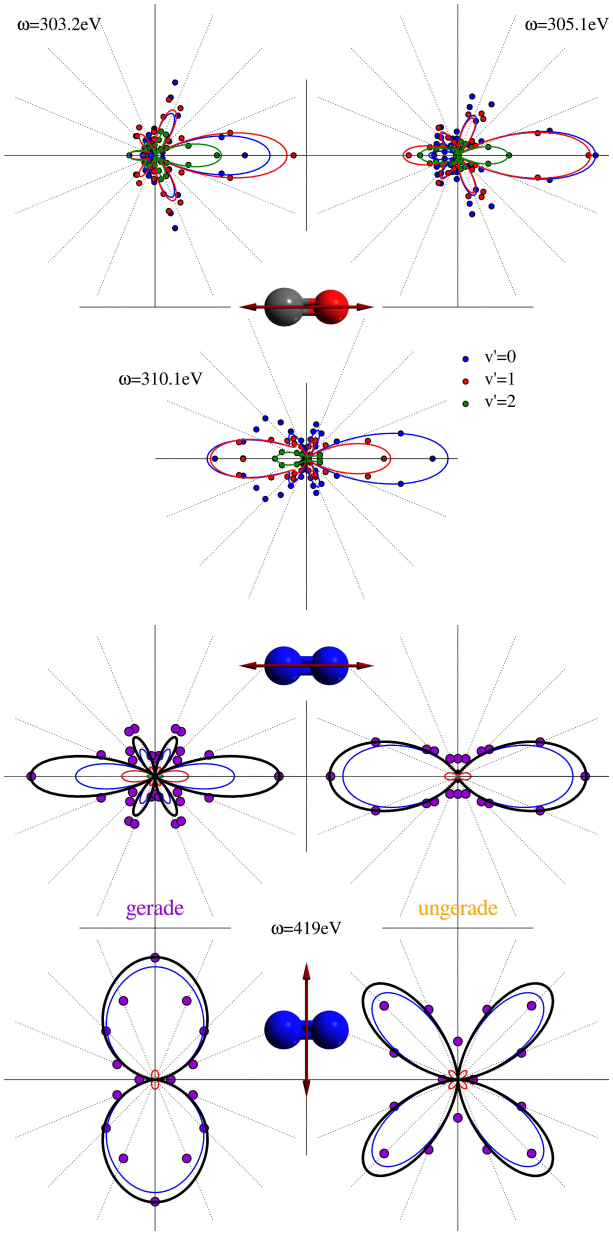

Figure 5.45: Same as Figure 5.43 for the CO($1\sigma^{-1}$) photoionization (upper panel) and the $N_2(1\sigma_g^{-1})$ and $N_2(1\sigma_u^{-1})$ photoionizations (lower panel). Molecules are parallel (parallel and perpendicular) to the polarization vector in the upper (lower) panel. The MFPADs are taken in a plane containing the main axis of the molecule for photon energies equals to 303.2, 305.1 and 310.1 eV (upper panel) and 419 eV (lower panel). Circles correspond to vibrationally resolved experimental results from [1] (upper panel) and to non vibrationally resolved experimental results from [311] (lower panel).

So far, we have analyzed non-vibrationally and vibrationally resolved MFPADs in the shape resonance region. The present DFT method can also be used to discuss the evolution of these MFPADS at higher energies. The second series of figures (5.46, 5.47, 5.48 and 5.49) shows purely theoretical vibrationally resolved three-dimensional MFPADs calculated with DFT using a LB94 functional.

Figures 5.46 and 5.47 present our results for K-shell ionization of N_2 with parallel and perpendicular orientations, respectively, at five photon energies: 420, 550, 605, 699 and 750 eV. Only results for the final vibrational levels $v' = 0$ and $v' = 2$ are shown. To better understand the origin of the different structures observed in the MFPAD, the figures also include the total cross sections and partial-wave contributions as functions of photon energy. Due to symmetry considerations, only partial waves associated with odd values of the angular momentum lead to non zero contributions. In the parallel case (see Figure 5.46), the $l = 3$ partial-wave contribution presents a pronounced minimum at around 600 eV for $v' = 0$ and at around 520 eV for $v' = 2$. The position of this minimum progressively shifts to lower energies at v' increases. Other partial waves also exhibit minima, although they are less pronounced and, in some cases, they lie very close to the ionization threshold. The origin of these minima has been explained in Ref. [118, 117] in the context of H_2 photoionization as resulting from electron confinement in between the two nuclei. This is possible when the electron momentum k_e approximately satisfies the equation $k_e R = l\pi$, which is nothing else than the particle-in-a-box formula. Indeed, when the molecule is parallel to the polarization direction, the electron is forced to move along the internuclear axis and, when its wavelength coincides or is approximately equal to the internuclear separation, it is transiently trapped and, consequently, does not follow the internuclear axis. This behavior can be clearly seen in the MFPAD for photon energies in the vicinity of the minimum of the $l = 3$ partial wave. In contrast, at lower and higher energies, the calculated MFPADs indicate that the electron escapes preferentially along the internuclear axis. For N_2, the equilibrium internuclear distance is $R_e = 2.07$ a.u. and the previous formula predicts that the lowest energy at which the minima should appear is approximately 30 eV above threshold for the $l = 1$ partial wave and 280 eV for the $l = 3$ one. The first one is so close to threshold that it is barely seen. Furthermore, at such low energy, the escaping electron is strongly perturbed by the remaining ionic core, which cannot be described by the above simple formula because it is only valid for a free electron.

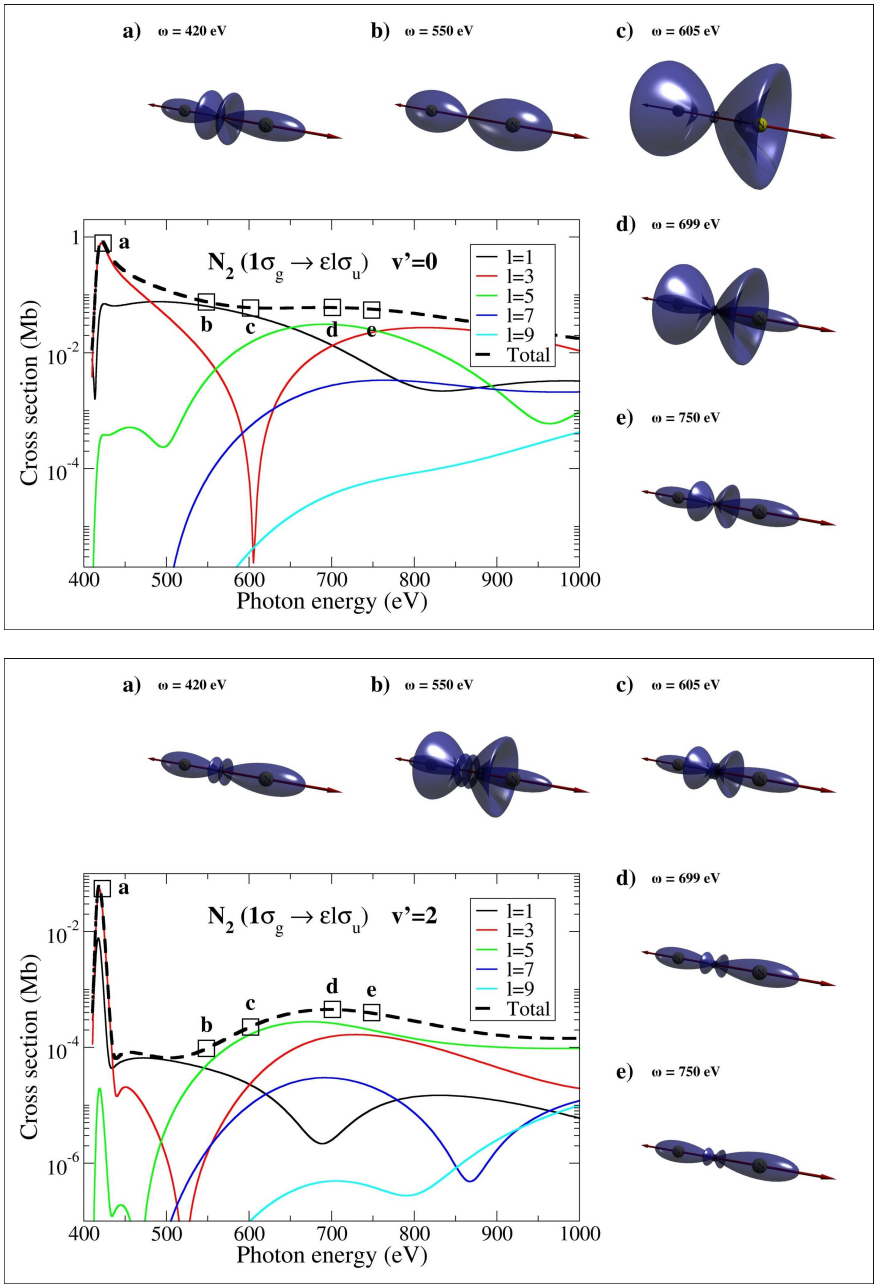

Figure 5.46: Vibrationally resolved molecular-frame photoelectron angular distributions (MFPADs) for the $N_2(1\sigma_g^{-1})$ photoionization. Molecules are parallel to the polarization vector (indicated by a double arrow). The MFPADs are represented in the form of 3D polar plots for photon energies equal to 420, 550, 605, 699 and 750 eV. Integrated total and partial photoionization cross sections as functions of photon energy are shown in a 2D box. Upper panel: $v' = 0$. Lower panel: $v' = 2$.

Confinement is actually observed in the range of photoelectron energies between 200 and 300 eV, i.e., in the vicinity of the $l = 3$ minimum. It can be seen that, for $v' = 2$, confinement appears at lower photon energies than for $v' = 0$. This is because the actual internuclear distance that the escaping electron sees is intermediate between R_e and that of the remaining $N_2^+(v')$ cation, R'. As v' increases, the mean value of R' also increases due to the anharmonicity of the potential energy curves. Therefore, the electron momentum and energy at which confinement should be observed are smaller. This is similar to what has been observed in H_2 [118, 117]. It is worth stressing here that the minima observed in the different partial waves should not be called Cooper minima because the latter arise from cancellations in the dipole transition matrix elements that involve wave functions with one or several radial nodes. Since the $1\sigma_g$ orbital from which the electron escapes has no radial node, it is clear that this concept does not apply here.

In the perpendicular case (see Figure 5.47b) and at very low photon energy, the MFPADs are almost perfect dipole-like, which is the consequence of the dominance of the $l = 1$ partial wave and is what one would expect for a pure atomic system. In other words, the electron mainly follows the direction imposed by the electric field. As the photon energy increases, one can see the appearance of smaller satellite lobes whose magnitude progressively increases. The position of these lobes is approximately given by the simple formula $\sin\theta_e = n\lambda_e/R$, where θ_e is the angle between the main lobe perpendicular to the internuclear axis and the satellite lobes. This formula is identical to that used to explain the position of the interference peaks observed in the famous Young's double-slit experiment. A behavior similar to that observed in Figure 5.47b has been reported in [118, 117] for the H_2 molecule. One can thus conclude that the observed angular patterns are due to the coherent emission of the electron from the two atomic centers in a direction perpendicular to the molecular axis. The above formula predicts that, as the photon energy increases, i.e., as λ_e decreases, there is an increasing number of n values compatible with the constraint $|\sin\theta_e| \leq 1$. This explains the appearance of more and more satellite lobes as the photon energy increases. The appearance thresholds for these satellite lobes as well as the angle they form with the dominant central lobe is also reasonably explained by this formula. As can be seen in Figure 5.47b, the appearance thresholds depend on the final value of v'. Indeed, for $v' = 2$, the threshold energies associated with the different n values are lower than for $v' = 0$: for $v' = 2$, satellite lobes associated with $n = 2$ can be clearly seen at 700 eV, while, for $v' = 0$ they are absent at this energy. The explanation for the v' dependence is the same as that given in the previous paragraph: as v' increases, the mean value of R' also increases and the minimum energy (electron wavelength) required to open a new channel n is smaller (larger).

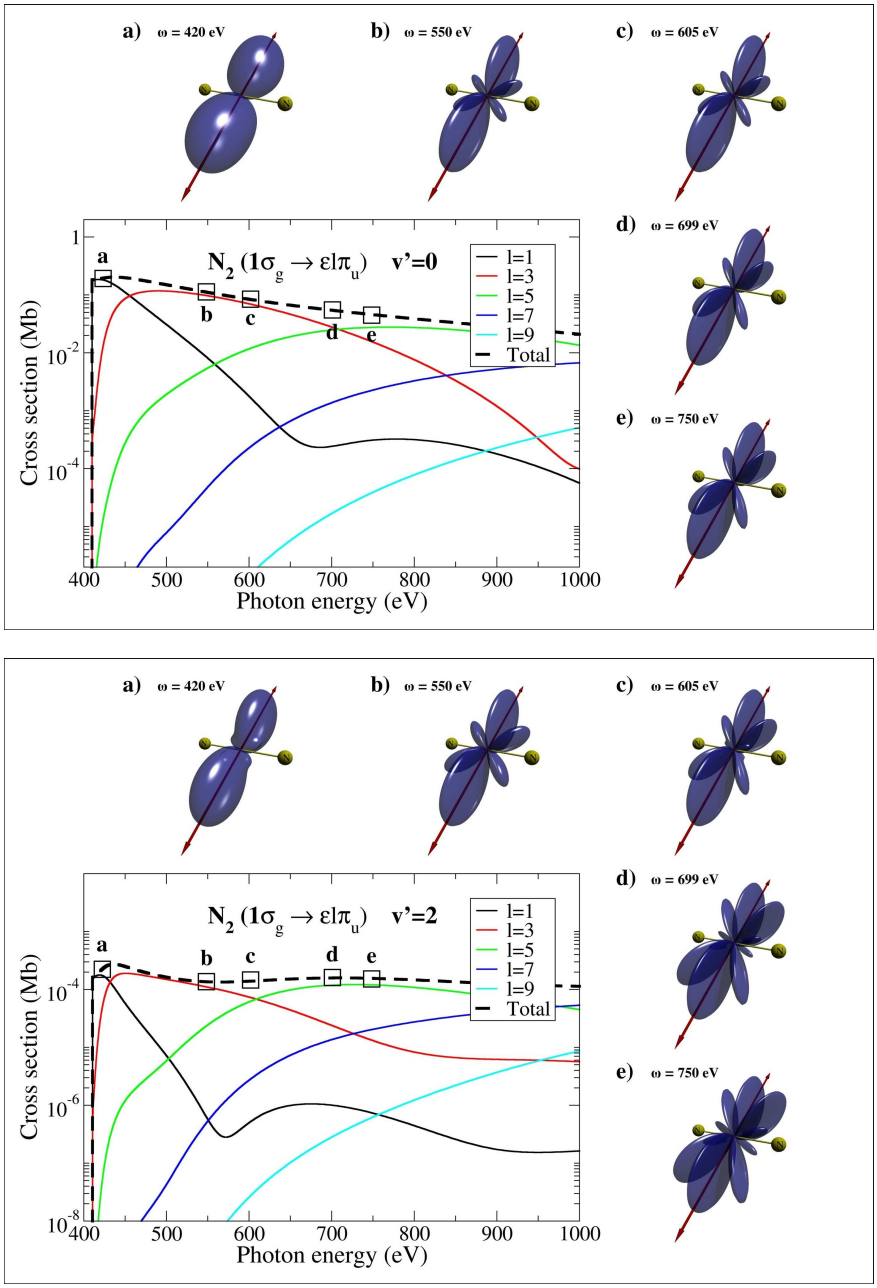

Figure 5.47: Same as Figure 5.46 for molecules perpendicular to the polarization vector.

Figures 5.48 and 5.49 present our results for O($1s^{-1}$) ionization of CO with parallel and perpendicular orientations, respectively, at five photon energies: 549, 579, 620, 720 and 850 eV. The figures also include the total cross sections and partial-wave contributions as functions of photon energy. In this case no selection rule limits the number of contributing partial waves. The partial-wave contributions exhibit a very complex behavior, with maxima and minima that do not follow a simple pattern. The main difference with the N_2 case is that the initial orbital from which the electron is ejected is almost perfectly localized on the oxygen atom. Therefore, one cannot expect angular patterns associated with coherent emission from the two atomic centers as those observed for N_2. Instead, diffraction of the ejected electron by the neighboring carbon atom should leave its trace in the MFPADs. This should occur when the electron wavelength is comparable to the CO equilibrium internuclear distance, which is $R_e = 2.13$ a.u. and corresponds to a photoelectron energy of approximately 120 eV (i.e., a photon energy of 662 eV). So, according to this formula, one should observe scattering by the neighboring C atom at around this energy. In both the parallel and perpendicular cases, one can see that, around this photoelectron energy, the MFPAD is complex and exhibits lobes that point to both the C and O atoms, indicating that the electron coming from the O center is efficiently diffracted by the C center. In the parallel case the lobes are oriented along the molecular axis, while in the perpendicular case they are preferentially oriented in the normal direction. As the photon energy increases in the parallel case (Figure 5.48), the MFPAD is more and more localized around the O atom, which reflects the fact that there is less and less diffraction by the neighboring C atom. In the perpendicular case (Figure 5.49), the MFPAD becomes more and more dipole-like, as if it was a purely atomic angular distribution, and the additional satellite lobes progressively disappear. This is the opposite behavior to that observed in N_2 (see Figure 5.47b). The transition from the diffraction zone to the atom-like one occurs earlier for $v' = 2$ than for $v' = 0$, which is again the consequence of the effective internuclear distance increasing with v'.

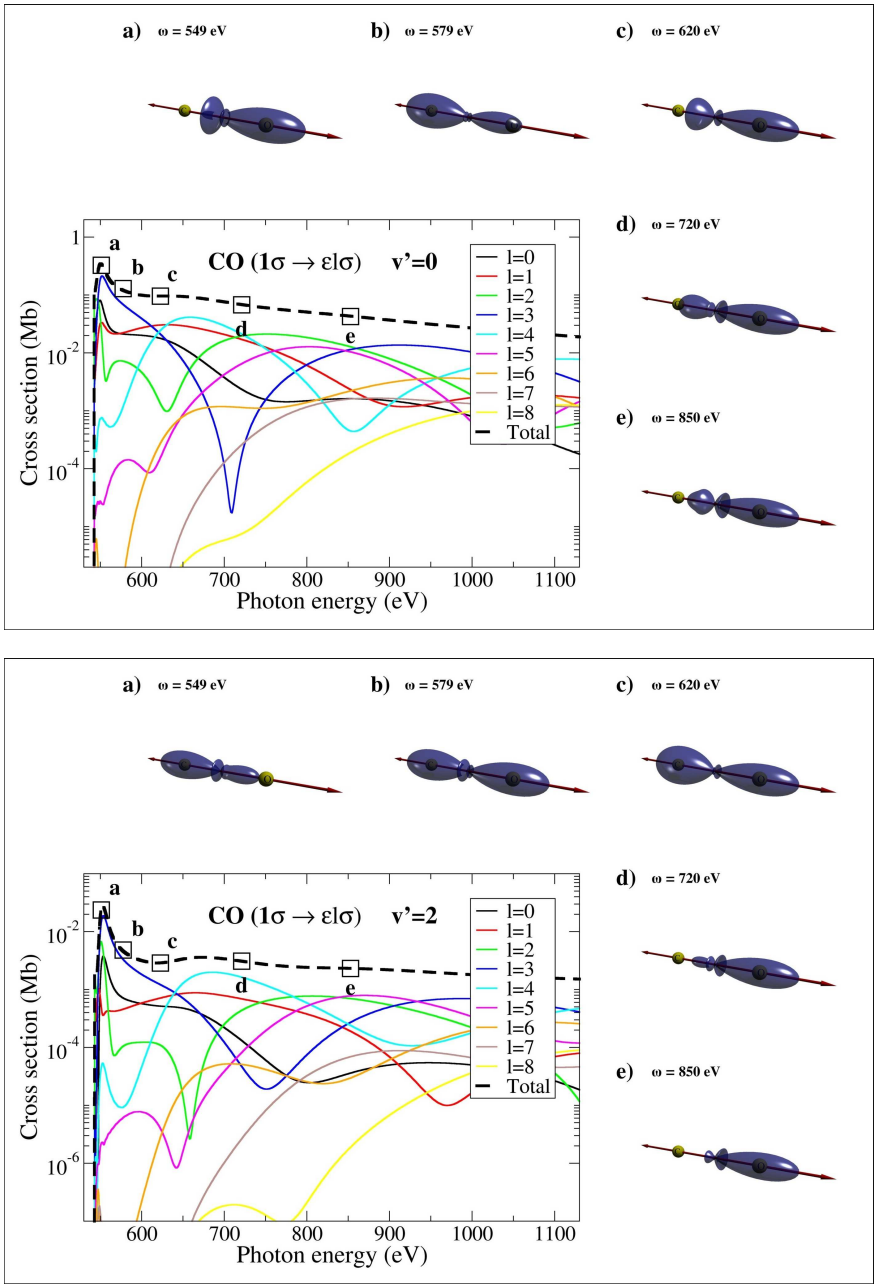

Figure 5.48: Vibrationally resolved molecular-frame photoelectron angular distributions (MFPADs) for the CO($1\sigma^{-1}$) photoionization. Molecules are parallel to the polarization vector (indicated by a double arrow). The MFPADs are represented in the form of 3D polar plots for photon energies equal to 549, 579, 620, 720 and 850 eV. Integrated total and partial photoionization cross sections as functions of photon energy are shown in a 2D box. Upper panel: $v' = 0$. Lower panel: $v' = 2$.

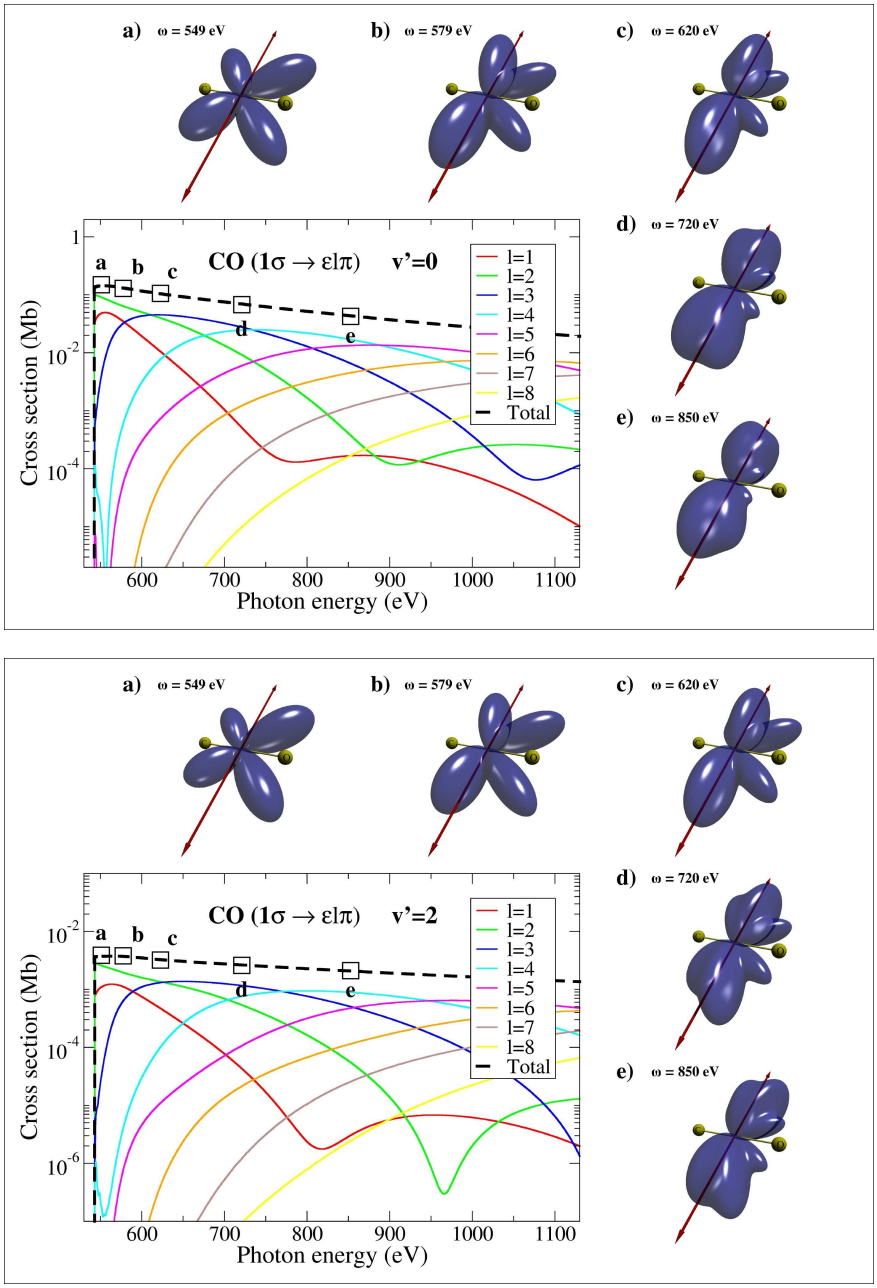

Figure 5.49: Same as Figure 5.48 for molecules perpendicular to the polarization vector.

6. Polyatomic molecules

In this Chapter, we present results obtained with the present method for a series of polyatomic molecules: C_2H_2, CH_4, CF_4, BF_3 and SF_6. The study concerns the core shell photoionization of the four first molecules and the HOMO-5 photoionization of SF_6. Vibrationally resolved cross sections have been calculated with DFT method using a LDA functional in all the cases except for SF_6 for which we employed a LB94 functional. TDDFT results are also shown in the case of CF_4 and BF_3. The results obtained with the present method are systematically compared with the available experimental and theoretical data at low and high photon energies.

6.1 Acetylene

Given the wealth of evidence for double-slit interferences in nitrogen [340, 311, 329, 446, 401, 328], the question arises as to whether a similar phenomenology can be observed also in systems larger than diatomics. The answer is not obvious, since polyatomic molecules feature several vibrational modes, some of which are not totally symmetric. As a result, degenerate electronic levels may be unstable and split, through vibronic coupling (Renner-Teller effect in linear molecules [252]), by spontaneously breaking the molecular symmetry. For closely-spaced core-holes, the symmetry break results in a localization of the core-hole [132]. The idea that core-holes in polyatomic molecules should be regarded as being always localized altogether has been around for quite some time (e.g. [99]).

For example, data available for C_2H_6 (ethane) and C_2H_4 (ethene) show that the energy separation between the σ_g and the σ_u core holes is too small ($\leq$ 50 meV [192, 187]) to be compatible with delocalized core holes.

Acetylene differs distinctively from ethane and ethene, because its C-C bond length is smaller, 1.203 Å [222] versus 1.536 Å and 1.337 Å, respectively, and comparable to that of nitrogen, 1.112 Å. Thus, one could reasonably expect that double-slit interferences associated with delocalized core holes, i.e., large core-hole σ_u/σ_g energy splittings, should also exist for acetylene. However, this splitting [192] is comparable to the frequency of the stretching modes of the molecule and, as a result, the $^2\Sigma_u^+(v'=1)$ state of the antisymmetric carbon-hydrogen stretching mode is partly mixed with the $^2\Sigma_g^+(v'=0)$ state [31]. Still, the most prominent signal corresponds to the excitation of

the totally symmetric C-C normal mode, which suggests that this is the normal mode that one should ideally choose to observe double-slit interference effects. Nevertheless, the issue of core-hole localization versus delocalization in acetylene is still far from being settled. Indeed, measurements of the σ_u/σ_g ratio reported by Thomas *et al.* [384] and Hoshino *et al.* [172] have shown no indications of double-slit interferences, likely due to the fact that the photon energy only extended up to 50-60 eV from the threshold. Furthermore, in the context of asymmetric molecular fragmentation, evidences of core-hole localization have been reported [3] and similar considerations have also been expressed by Osipov [274].

6.1.1 Total cross section

Figure 6.1 shows the core photoionization cross section of C_2H_2 for photon energies up to ∼360 eV. The broad structure at ∼ 310eV, assigned to a shape resonance in earlier papers (see [191, 384]), is confirmed by the DFT calculation which gives the correct width and position. However, the it clearly overestimates the cross section for all the photoionization channels. The structure is also reproduced by a CI calculation performed at the fixed nuclei approximation [223]. This calculation includes shake-up states to the interchannel couplings which appear to compose the dominant feature at the shape resonance energy. Then, it is reasonable to admit that part of the discrepancy between the DFT calculation and the experiment is due to a poor description of the shake-up processes. One-channel CI calculation shows also the importance an accurate description of the electronic correlation which is expected to be strong in acetylene. Despite the global improvement obtained using a six-channel SCI calculation, the sharp structures do not show up in the experiment and the shape resonance appears too narrow. This is a typical artifact of the fixed nuclei approximation. Indeed, one of the effects of the inclusion of the nuclear motion is to broaden the structures. As a consequence, relatively smooth variations such as shape resonances are broaden, while many sharp peaks appearing in the fixed nuclei total cross section are just washed out. Resonances due to autoionization and shake-up satellites are visible but are not taken into account at the DFT level of theory. TDDFT method includes interchannel couplings but calculation performed at the fixed nuclei approximation for core photoionization of C_2H_2 [130] shows very small improvements of the cross section in the shape resonance region.

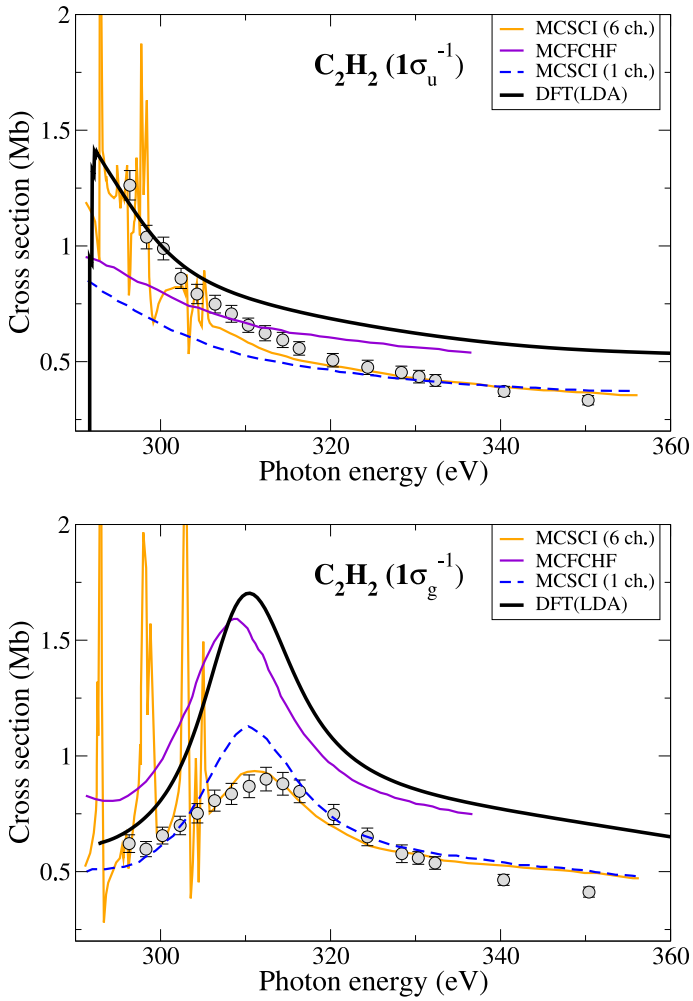

Figure 6.1: Total cross section for the $1\sigma_g^{-1}$ and $1\sigma_u^{-1}$ photoionization of C_2H_2 as a function of the photon energy. Circles correspond to experimental data from [172] ; Lines correspond to theory - Violet solid: multichannel Schwinger method with frozen-core Hartree-Fock approximation (MCFCHF) [223], Blue dashed: multichannel Schwinger configuration interaction (MCSCI) [223] one-channel, Orange solid: multichannel Schwinger configuration interaction (MCSCI) six-channel [223], Black thick solid: DFT method using a LDA functional (this work).

As for N_2, the shape resonance is present in the $1\sigma_g^{-1}$ photoionization cross section and more specifically in the $1\sigma_g^{-1} \rightarrow \varepsilon l\sigma_u$ channel, but not in the $1\sigma_u^{-1}$ (see Figures 6.3 and 6.2). The origin and the behavior of the shape resonance in the $1\sigma_g^{-1}$ photoionization of acetylene is essentially the same as the one predicted by Dehmer for N_2 [83]. We can observe that, as for N_2, the resonant continuum wavefunction is predominantly of f-wave character. It is however trapped by the potential barrier at a higher resonant energy ($\sim$ 10 eV above ionization threshold). Considering that the potential barrier generally grows with the nuclear separation, this difference can be attributed to the larger C-C distance ($R_{\text{C-C}}$ =1.2 Å compared to $R_{\text{N-N}}$ =1.1 Å). Comparison between Figures 6.3 and 6.2 for C_2H_2 and Figures 5.13 and 5.12 for N_2 reveals a very similar behavior. In particular, minima are found to be located at the same energy positions.

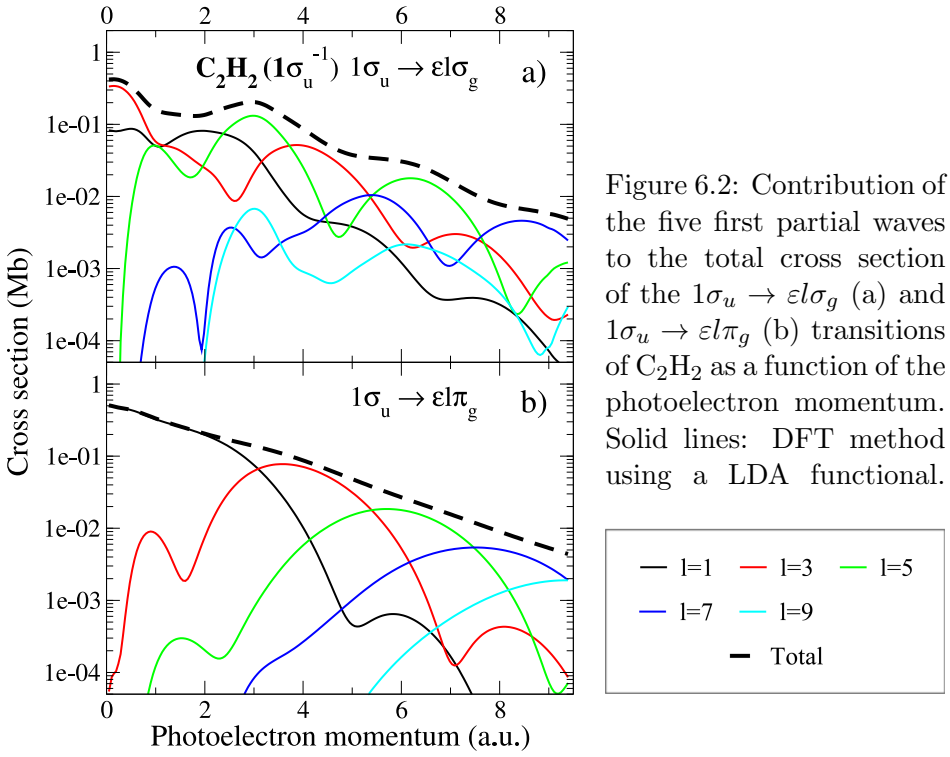

Figure 6.2: Contribution of the five first partial waves to the total cross section of the $1\sigma_u \rightarrow \varepsilon l\sigma_g$ (a) and $1\sigma_u \rightarrow \varepsilon l\pi_g$ (b) transitions of C_2H_2 as a function of the photoelectron momentum. Solid lines: DFT method using a LDA functional.

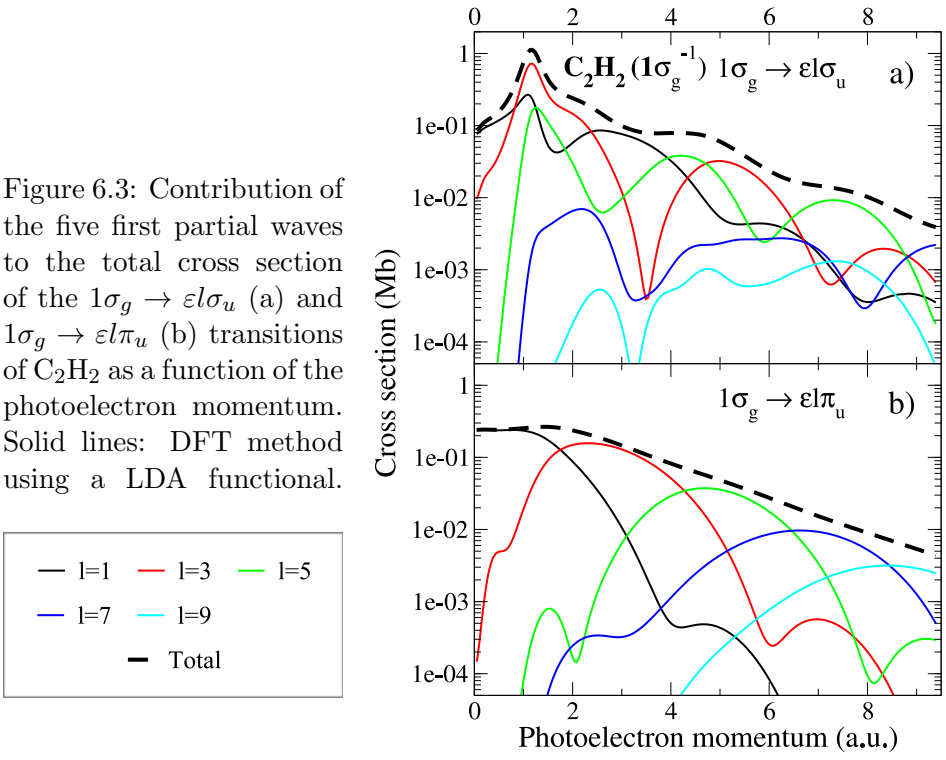

Figure 6.3: Contribution of the five first partial waves to the total cross section of the $1\sigma_g \rightarrow \varepsilon l\sigma_u$ (a) and $1\sigma_g \rightarrow \varepsilon l\pi_u$ (b) transitions of C_2H_2 as a function of the photoelectron momentum. Solid lines: DFT method using a LDA functional.

6.1.2 Vibrationally resolved cross section

Figure 6.4 shows the photoelectron spectrum at a photon energy of 534 eV. As can be seen, C 1s photoionization mainly leads to $C_2H_2^+$ ions in the ground vibrational state $v' = 0$ of the C-C symmetric stretching mode. This is because the equilibrium geometries of C_2H_2 and $C_2H_2^+$ are very similar for this core-ionized electronic state. In other words, a vertical one-photon transition from the ground state of C_2H_2 necessarily leads to core ionized $C_2H_2^+$ with a geometry close to that of the ground state, so that the maximum Franck-Condon overlap corresponds to the $v = 0 \rightarrow v' = 0$ transition. Consequently, the intensity of the observed peaks decreases rapidly with the degree of vibrational excitation of the remaining $C_2H_2^+$ ion and, for all practical purposes, it is negligible beyond $v' = 3$. Each v' peak is formed by two components, which correspond to C 1s ionization from the $1\sigma_g$ and $1\sigma_u$ molecular orbitals. The energy separation between these two components is 102.7 meV, in good agreement with the value of the $1\sigma_g$-$1\sigma_u$ splitting reported in previous work. As can be inferred from Figure 6.4, the high energy resolution of the spectra allows us to clearly separate the two components.

A photoelectron spectrum measured at 313 eV and reproduced theoretically in [68] shows that these first vibrational peaks are almost exclusively due to excitation of the C-C stretching mode. Contribution of the C-H stretching mode start to be significant at lower photoelectron kinetic energy and is responsible for the small hump in the place of the third peak. Calculations performed by Thomas *et al.* in [388] also concluded to the weak excitation of the C-H stretching in the lower vibrational part of the band. Then, by limiting the study to the first two vibrational peaks of the photoelectron spectra, vibrational wavefunctions can be obtained by using a projection of the potential energy surface along the C-C symmetric stretching coordinate. It is important to stress here that the present description of the C-C symmetric stretching vibrational mode is rather rudimentary, because in assuming that the C-H distance remains fixed during the vibration for both the parent molecule and the remaining ion, we neglect the possible mixing between the two symmetric stretching modes associated with the electronic excitation (Dushinsky effect).

Figure 6.5 shows the vibrationally resolved cross sections for photon energies up to ∼360 eV. As observed by Mistrov *et al.* in [256], the energy position of the shape resonance in the $1\sigma_g^{-1}$ photoionization of C_2H_2 is decreasing with the vibrational level. It is due to the same mechanism as for N_2 ($1\sigma_g^{-1}$). To the disagreement already observed in the total cross section, the vibrationally resolved DFT results present an additional discrepancy in the relative values of the vibrational components. This is mainly due to the nuclear structure, i.e. to the choice of the potential energy curves. Two calculations have been performed, using LDA and harmonic potential energy curves but led to an

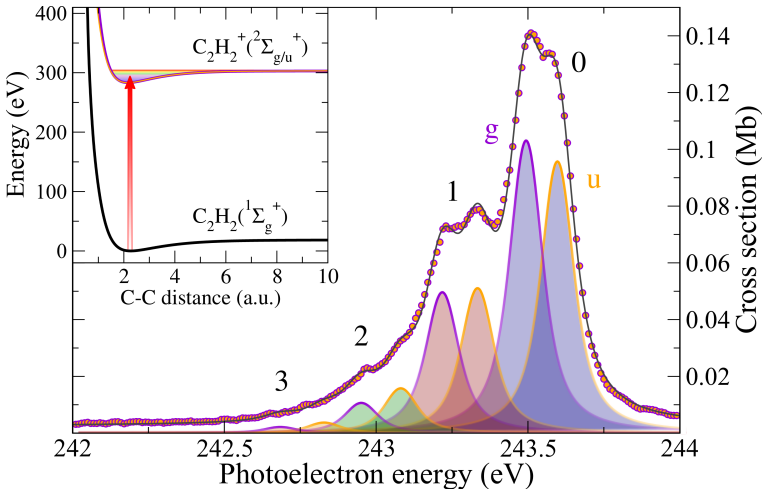

Figure 6.4: Photoelectron spectrum of C_2H_2 taken at $\omega = 534$ eV. Circles: experimental data from [11]. Solid lines: fit of the experimental data. Peak numbers indicate the vibrational quantum number v' of $C_2H_2^+$. The spectrum has been normalized to the value predicted by theory for the $^2\Sigma_u^+(1s\sigma_u, v' = 0)$ peak. Inset: Potential energy curves of the ground state of C_2H_2 ($^1\Sigma_g^+$) (black line) and the $^2\Sigma_g^+(1s\sigma_g)$ (purple line) and $^2\Sigma_u^+(1s\sigma_u)$ (orange line) states of core-ionized $C_2H_2^+$ along the C-C symmetric-stretching normal coordinate. The red arrow indicates a vertical one-photon transition. The horizontal line in the upper potential energy curves indicates the dissociation limit and the shaded area below it the vibrational states in the $^2\Sigma_g^+(1s\sigma_g)$ and $^2\Sigma_u^+(1s\sigma_u)$ states.

equivalent result. An accurate treatment of the vibrational structure would require an *ab initio* calculation of the potential energy curves at a higher level of theory (e.g. a CI calculation). The discrepancies observed so far in the core photoionization of C_2H_2 are expected to manifest only in the shape resonance energy region where the electronic correlation plays an important role. In the following, we will then concentrate on the study at higher photon energies.

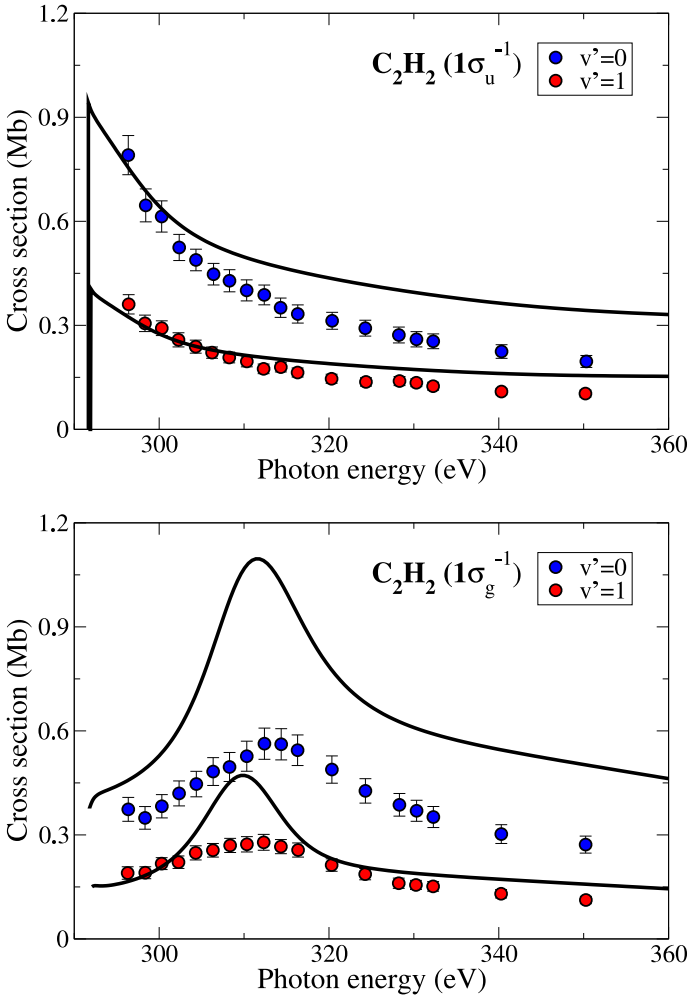

Figure 6.5: Vibrationally resolved cross section for the two first vibrational levels of the $1\sigma_g^{-1}$ and $1\sigma_u^{-1}$ photoionization of C_2H_2 as a function of the photon energy. Circles correspond to experimental data from [172]. Solid lines correspond to the DFT method using harmonic potential energy curves taken from literature (see Table B.3).

Figures 6.6 and 6.7 show the measured and calculated $1\sigma_g/1\sigma_u$ and $v' = 1/v' = 0$ ratios as functions of photon energy. As can be seen, both ratios exhibit pronounced oscillations superimposed on a slowly increasing background. The agreement between theory and experiment is excellent. In particular, the theory reproduces quite well the differences between $1\sigma_g/1\sigma_u$ ratios associated with different vibrational states of the remaining $C_2H_2^+$ ion, as well as the phase opposition of the v-ratios in the $1\sigma_g$ and $1\sigma_u$ channels. Similar oscillations have been observed in non vibrationally resolved $1\sigma_g/1\sigma_u$ ratios resulting from N 1s photoionization of N_2 [340]. In that work, the oscillations in the $1\sigma_g/1\sigma_u$ ratios have been interpreted as resulting from Cohen-Fano interferences. These interferences reflect a different phase in the $1\sigma_g$ and $1\sigma_u$ channels due to the difference in sign in the corresponding linear combinations of 1s orbitals.

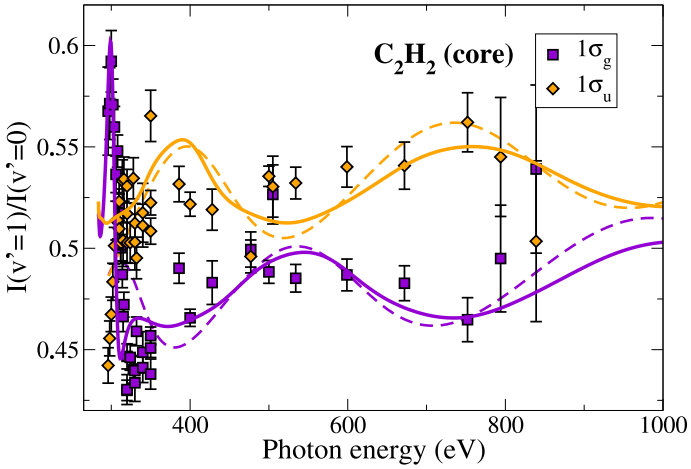

Figure 6.6: $v' = 1/v' = 0$ ratios between vibrationally resolved photoionization cross sections in C 1s photoionization of C_2H_2 for the C-C symmetric stretching mode of $C_2H_2^+$ in the σ_g and σ_u channels. Squares and diamonds: experimental data from [11]. The error bars include both statistical and systematic contributions. Dashed lines: results from the simple model discussed in the text. Solid lines: DFT method using a LDA functional. Theoretical results have been shifted so that, at high photon energy, they tend to the value of the Franck-Condon factor ratios determined experimentally.

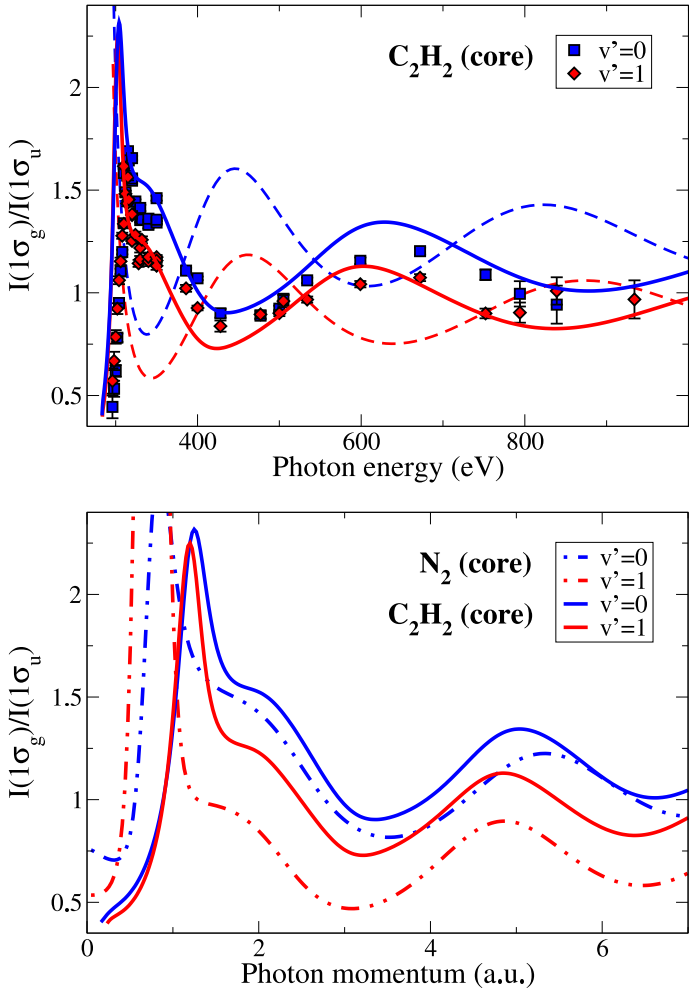

Figure 6.7: Vibrationally resolved $1\sigma_g/1\sigma_u$ ratios in C 1s photoionization of C_2H_2 for the C-C symmetric stretching mode of $C_2H_2^+$. Solid lines: DFT method using a LDA functional. (Upper panel) Squares and diamonds: experimental data from [11]. The error bars include both statistical and systematic contributions. Dashed lines: results from the simple model discussed in the text. (Lower panel) Dotted dashed lines: results from the DFT method using a LDA functional for the core photoionization of N_2 (see Figure 5.18a).

Scattering model

The similarity of the present $1\sigma_g/1\sigma_u$ ratios with those found in N 1s photoionization of N_2 suggests that the origin of the oscillations is the same. In order to ascertain that the observed features are indeed to be interpreted as genuine Cohen-Fano oscillations, Luca Argenti developed in [11] a simple model in which, in addition to two-center interference effects, we also account for intramolecular scattering. As we will see for the C1s photoionization of CH_4, the latter effect can lead to diffraction of the ejected electron and, therefore, to visible structures in the vibrationally resolved cross section ratios.

In the model, the integral vibrationally-resolved photoionization cross section $\sigma_{g/u}^{v'}$ for a randomly oriented acetylene molecule is estimated within the single-active-electron approximation as:

$$\sigma_{g/u}^{v'} = \frac{1}{4\pi}\int d\Omega_R \int d\Omega_k \; 2\,\frac{4\pi^2 k}{c\omega}\,\left|\,\langle\,\psi_{\mathbf{k}}\,\chi_{g/u,v'}\,|\,\hat{\epsilon}\cdot\mathbf{p}\,|\sigma_{g/u}\,\chi_0\rangle\,\right|^2 \tag{6.1}$$

Here χ_0 is the wave function of the initial ground vibrational state of the neutral molecule and $\chi_{g/u,v'}$ is the vibrational wave function for the final ionized state (either g or u) in either the $v'=0$ or $v'=1$ state of the C-C stretching vibrational mode. The initial core molecular orbital is approximated with a symmetry-adapted combination of the $1s$ core orbitals of the two carbon atoms as shown in Equation (5.4). In momentum coordinates, this expression can be reformulated as:

$$\sigma_{g/u}(\mathbf{p}) = e^{-i\mathbf{p}\cdot\mathbf{R}_{\rm CC}}\,\frac{e^{i\mathbf{p}\cdot\mathbf{R}/2}\pm e^{-i\mathbf{p}\cdot\mathbf{R}/2}}{\sqrt{2(1\pm S(R))}}\;1s(p) \tag{6.2}$$

where the $1s$ orbital now is centered on the origin; $\mathbf{R}_{\rm CC} = (\mathbf{R}_{\rm C_1} + \mathbf{R}_{\rm C_2})/2$ indicates the center of mass of the two carbons and $\mathbf{R} = \mathbf{R}_{\rm C_2} - \mathbf{R}_{\rm C_1}$ is their relative position. The overlap $S(R)$ turns out to be very small and will be neglected. The final electronic state is approximated with a plane wave:

$$\langle\,\mathbf{r}\,|\,\psi_{\mathbf{k}}\,\rangle = (2\pi)^{-3/2}\,\exp(i\mathbf{k}\cdot\mathbf{r}) \tag{6.3}$$

therefore, the transition amplitude in (6.21) becomes:

$$\mathcal{A}_{g/u}^{v'} = \langle\,\psi_{\mathbf{k}}\,\chi_{g/u,v'}|\,\hat{\epsilon}\cdot\mathbf{p}\,|\sigma_{g/u}\,\chi_0\rangle = \frac{\hat{\epsilon}\cdot\mathbf{k}}{\sqrt{2}}\,1s(k)\,\langle\,\chi_{g/u,v'}\,|\,e^{i\mathbf{k}\cdot\mathbf{R}/2}\pm e^{-i\mathbf{k}\cdot\mathbf{R}/2}\,|\,\chi_0\,\rangle \tag{6.4}$$

(In this last expression we dropped the term $\exp[-i\mathbf{p}\cdot\mathbf{R}_{\rm CC}]$, related to the conservation of the total momentum of the CC moiety). Based on these and other additional assumptions, several authors have already commented on the effect of the vibrational motion on Cohen-Fano oscillations [136, 407]. As we will see below, the present model includes effects not considered in those works, but, when truncated to zeroth order, it leads to similar results.

As in the first-principle calculations, we will consider only the C-C symmetric stretching vibrational mode in which the C-H distance is kept constant:

$$\mathbf{R}_{\mathrm{C}_1} = -\mathbf{R}/2, \qquad \mathbf{R}_{\mathrm{C}_2} = \mathbf{R}/2, \tag{6.5}$$

$$\mathbf{R}_{\mathrm{H}_1} = -(R/2 + R_{\mathrm{CH}})\hat{R}, \qquad \mathbf{R}_{\mathrm{H}_2} = (R/2 + R_{\mathrm{CH}})\hat{R} \tag{6.6}$$

To evaluate the vibrational transition amplitude in (6.4) we assume the harmonic approximation and that the vibrational frequency in both final parent ions is the same as in the initial neutral molecule. In this context, we can express the internuclear distance in terms of the dimensionless vibrational normal coordinate of the neutral molecule:

$$R = R^0 \, + \, (\mu\omega)^{-1/2} \, Q \tag{6.7}$$

while the final vibrational state $\chi_{g/u,v'}$ can be written as the translation by a quantity equal to the shift in the equilibrium position, $\Delta R^0_{g/u} = R^0_{g/u} - R^0$, of the vibrational function $\chi_{g/u,v'}$ of the neutral molecule:

$$\chi_{g/u,v'} \, = \, e^{-i\,\sqrt{\mu\omega}\,\Delta R^0_{g/u}\,\hat{P}} \; \chi_{g/u,v'} \, = \, D\left(\sqrt{\frac{\mu\omega}{2}}\,\Delta R^0_{g/u}\right) \; \chi_{g/u,v'} \tag{6.8}$$

In this last expression, $\hat{P}$ is the dimensionless momentum of the harmonic oscillator canonically conjugated to Q, $[Q, P] = i$, while the displacement operator $D(\alpha)$ is the generator of vibrational coherent states:

$$D(\alpha) = e^{\alpha\hat{a}^\dagger - \alpha^*\hat{a}}, \qquad |\alpha\rangle = D(\alpha)|0\rangle \, = \, \sum_{v'} \, |v'\rangle \, e^{-|\alpha|^2/2} \frac{\alpha^{v'}}{\sqrt{v'!}} \tag{6.9}$$

$$D^\dagger(\alpha) = D(-\alpha), \qquad D(\alpha)D(\beta) = D(\alpha+\beta)\, e^{(\alpha\beta^* - \beta\alpha^*)/2} \tag{6.10}$$

In a similar way, the action of any exponential operator whose argument is linear in the normal coordinate Q can also be expressed in terms of displacement operators:

$$e^{iKQ} = D\left(i\,\frac{K}{\sqrt{2}}\right) \tag{6.11}$$

By applying the relations listed above, after some passages, we are led to the expression:

$$\begin{aligned} \langle\, \chi_{g/u,v'} \,|\, e^{ip\,R} \,|\, \chi_0 \,\rangle \;\; &= \;\; e^{ip\,\bar{R}^0_{g/u}} \left\langle v' \left| -\sqrt{\frac{\mu\omega}{2}}\,\Delta R^0_{g/u} + i\frac{p}{\sqrt{2\mu\omega}} \right\rangle = \\ &= \;\; e^{-\frac{p^2}{4\mu\omega}}\, e^{ip\,\bar{R}^0_{g/u}}\, e^{-\frac{\mu\omega}{4}(\Delta R^0_{g/u})^2} \;\times \\ &\times \;\; \frac{1}{\sqrt{v'!}} \left(-\sqrt{\frac{\mu\omega}{2}}\,\Delta R^0_{g/u} \, + \, i\,\frac{p}{\sqrt{2\mu\omega}}\right)^{v'} \end{aligned} \tag{6.12}$$

where $\bar{R}^0_{g/u} = (R^0 + R^0_{g/u})/2$. For $p = 0$, we recover the familiar Franck-Condon amplitude:

$$\langle \chi_{g/u,v'} | \chi_0 \rangle = e^{-\frac{\mu\omega}{4}(\Delta R^0_{g/u})^2} \frac{1}{\sqrt{v'!}} \left(-\sqrt{\frac{\mu\omega}{2}}\, \Delta R^0_{g/u} \right)^{v'} \tag{6.13}$$

For the vibrational mode under consideration, the factor $\mu\omega$ is very large: $\mu \simeq 6.5$ a.m.u.$\simeq$12,000 a.u., $\omega \simeq$270 meV$\simeq$0.01 a.u., hence $\mu\omega \simeq 120$. The momentum factor p can be assumed to be of the same order of magnitude of the final momentum k of the photoelectron. For photoelectron energies up to ~ 600 eV, the factor $\exp(-p^2/4\mu\omega)$ is thus very close to 1, so we will ignore it altogether. To be consistent with this approximation, we need also to drop all those terms arising from the expansion of the last power in Equation (6.12) which are not linear in $p/\sqrt{2\mu\omega}$. To conclude, as long as $k^2/4\mu\omega \ll 1$, the following approximate expression can be used:

$$\langle\, \chi_{g/u,v'} \,|\, e^{ip\,R} \,|\, \chi_0 \,\rangle \simeq \langle \chi_{g/u,v'} | \chi_0 \rangle\, e^{ip\,\bar{R}^0_{g/u}} \left(1 - i \frac{v'\,p}{\mu\omega\, \Delta R^0_{g/u}} \right) \tag{6.14}$$

In this latter linearized form, this expression is essentially equivalent to Equation (18) in [407], where no assumptions on the form of the vibrational functions was made.

By using the relations (6.14) in (6.4) we finally obtain the expression of the differential photoionization amplitudes for an oriented molecule:

$$\begin{aligned}
\mathcal{A}^{v'}_g &\simeq \frac{\hat{\epsilon}\cdot\mathbf{k}}{\sqrt{2}}\, 1s(k)\, \langle\, \chi_{f_g,v'} \,|\, \chi_0 \,\rangle \left[2\, \cos(\mathbf{k}\cdot\bar{\mathbf{R}}^{\mathbf{0}}_{\mathbf{g}}/2) + v'\, \frac{\mathbf{k}\cdot\hat{\bar{R}}^0_g}{\mu\omega\Delta R^0_g}\, \sin(\mathbf{k}\cdot\bar{\mathbf{R}}^{\mathbf{0}}_{\mathbf{g}}/2) \right] \\
\mathcal{A}^{v'}_u &\simeq \frac{\hat{\epsilon}\cdot\mathbf{k}}{\sqrt{2}}\, 1s(k)\, \langle\, \chi_{f_u,v'} \,|\, \chi_0 \,\rangle \left[2i\, \sin(\mathbf{k}\cdot\bar{\mathbf{R}}^{\mathbf{0}}_{\mathbf{u}}/2) - iv'\, \frac{\mathbf{k}\cdot\hat{\bar{R}}^0_u}{\mu\omega\Delta R^0_u}\, \cos(\mathbf{k}\cdot\bar{\mathbf{R}}^{\mathbf{0}}_{\mathbf{u}}/2) \right]
\end{aligned}$$

We can recover the familiar Cohen-Fano model from these latter expressions by retaining only the first term within parenthesis. Notice that in the present treatment the internuclear distance that appears in the final formula is intermediate between that in the neutral and that in the parent ion. As the second term in the parenthesis shows, the model accounts for the sensitivity of the interference amplitudes to the nuclear motion. This effect, which at this level is not visible in the amplitude for the transition to the ground vibrational state, is a manifestation of the nuclear recoil. Indeed, the factor $\exp(i\mathbf{k}\cdot\mathbf{R}_i)$ can be seen as a boost by a momentum $\mathbf{k}$ on nucleus i. Nuclear recoil is therefore one of the mechanisms which mirror double-slit interferences to non-Franck-Condon vibrational excitations and which thus permits to monitor the latter by looking at the $\sigma^1_{g/u}/\sigma^0_{g/u}$ ratios.

After taking the square module and carrying out the angular integrations,

$$\sigma_{g/u}^{v'} = \frac{1}{4\pi} \int d\Omega_R \int d\Omega_k \, 2 \, \frac{4\pi^2 k}{c\omega} \, \left| \mathcal{A}_{g/u}^{v'} \right|^2 \tag{6.15}$$

the cross sections in plane wave approximation is finally obtained

$$\begin{aligned} \sigma_{g/u}^{v'} &= 2 \, \frac{4\pi^2 k^3}{3c\omega} \, 1s^2(k) \, \left| \langle \chi_{g/u,1} | \chi_0 \rangle \right|^2 \times \\ &\times \left[1 \pm \frac{\sin k\bar{R}_{g/u}^0}{k\bar{R}_{g/u}^0} \mp \frac{v' \, k}{\mu\omega \Delta R_{g/u}^0} \, \frac{\cos(k\bar{R}_{g/u}^0)}{k\bar{R}_{g/u}^0} \pm \frac{v'}{\mu\omega \, \bar{R}_{g/u}^0 \Delta R_{g/u}^0} \, \frac{\sin(k\bar{R}_{g/u}^0)}{k\bar{R}_{g/u}^0} \right] \end{aligned} \tag{6.16}$$

In agreement with the previous approximations, in this last expression we dropped the terms quadratic in v'. The last term in parenthesis amounts to a correction to the amplitude of the Cohen-Fano oscillations. This term has not been considered in previous models. By neglecting this term, we end up with an equation similar to Equation (20) of Ueda *et al.* [407]. Indeed, by borrowing part of their notation, one obtains an expression formally identical to Equations (22-23) in [407]:

$$\sigma_{g/u}^{v'} = 2 \, \frac{4\pi^2 k^3}{3c\omega} \, 1s^2(k) \, \left| \langle \chi_{g/u,1} | \chi_0 \rangle \right|^2 \, \left[1 \pm \chi_{v'}^{g,u}(k) \right] \tag{6.17}$$

$$\chi_{g/u,v'}(k) = \frac{\sin\left(k\bar{R}_{g/u}^0 + \psi_{g/u}^{v'}(k) \right)}{\cos\left(\psi_{g/u}^{v'}(k) \;\; k\bar{R}_{g/u}^0 \right)}, \quad \tan\psi_{g/u}^{v'} = -\frac{v'k}{\mu\omega\Delta\bar{R}_{g/u}^0} \tag{6.18}$$

The recoil thus induces an energy-dependent phaseshift $\psi_{g/u}^{v'}(k)$ in the Cohen-Fano oscillations. Within the harmonic approximation adopted here, this phase shift is known analytically. Comparison with Equation (23) in [407] leads to the following correspondence with the parametrization chosen by Ueda *et al.*:

$$\Delta R^{v'} = -\frac{v'}{\mu\omega\Delta\bar{R}_{g/u}^0} \tag{6.19}$$

What is indicated in [407] as an effective displacement $\Delta R^{v'}$ of the carbon-carbon internuclear distance appears, within the harmonic approximation, to be related in a simple way to the parameters of the vibrational mode. On the basis of Equation (6.7), we can in fact recognize in $1/\sqrt{\mu\omega}$ the characteristic length R_ω of the oscillator, and write the formula:

$$\frac{\Delta R^{v'}}{R_\omega} = -v' \, \frac{R_\omega}{\Delta\bar{R}_{g/u}^0} \tag{6.20}$$

The internuclear distances in the neutral are $R^0 = 2.273$ a.u., $R_{\mathrm{CH}} = 2.002$ a.u. Theoretical estimate of the C-C internuclear distance exist and have

been published in [31]: $R_g^0 = 2.198$ a.u., $R_u^0 = 2.185$ a.u. With these values, $\bar{R}_g^0 = 2.236$ a.u., $\bar{R}_u^0 = 2.230$ a.u., $\Delta R_g^0 = -0.075$ a.u., and $\Delta R_u^0 = -0.088$ a.u. In Figure 6.6, the dashed lines show the $v' = 1/v' = 0$ intensity ratios computed with the complete formula (6.16). As can be seen from the figure, the model reproduces quite nicely the experimental and theoretical results. In particular, the model accounts for the phase opposition of the oscillations in the gerade and ungerade cases. The oscillation periods are some $2-3\%$ larger than the $\Delta k \sim 2\pi/R_{g/u}^0$ value which are expected on the basis of simple dimensional considerations. A closer inspection of these results show that the two ratios feature small oscillations around baselines which start at the corresponding Franck-Condon ratios and increase with the photoelectron energy. This is due to the momentum transfered to either nuclei as the photoelectron is ejected (recoil). Since the amplitudes for the photoelectron ejection from the two nuclei add coherently, the momentum transfer, and therefore the vibrational excitation, is affected by the same interference features observed in the total cross section. The largest discrepancy between the plane-wave prediction and the experiment is in the position of the baselines, i.e. in the Franck-Condon ratios $|\langle\chi_{g/u,1}|\chi_0\rangle/\langle\chi_{g/u,0}|\chi_0\rangle|^2$. The latter, however, depend strongly on the precise value of the contractions $\Delta R_{g/u}^0$ of the C-C bond length. It is possible that the theoretical estimates for the equilibrium positions in the parent ions given in [31] are not accurate enough. In fact, small adjustments to $R_{g/u}^0$ are sufficient to bring the theoretical curves on top of the experimental ones. A similar discrepancy between theory and experiment is observed also in the case of the first-principle DFT calculations.

In contrast to the good agreement found for the vibrational ratios, the σ_g/σ_u ratios computed in plane wave approximation turn out to be almost in phase opposition with respect to the measurements. The prediction of the model is shown in Figure 6.7a. In the case of the excited final vibrational state $v' = 1$, the nuclear recoil induces a phase shift in the σ_g/σ_u ratio that partly reduces the distance with the experimental points. This effect, however, is still too small to compensate the error of the Cohen-Fano prediction. Moreover, at the preset level of approximation, the recoil does not have any effect on the $v' = 0$ cross section. The major cause for the observed discrepancy must therefore be sought in a different mechanism. The phase shift difference between the $v' = 0$ and the $v' = 1$ cases predicted by the recoil should presumably show up in the experiment as well. Unfortunately, the present experimental accuracy does not allow to draw any conclusion in this sense.

We have extended the present model beyond the plane-wave approximation [290] by including the contributions from the carbon and hydrogen Coulomb potentials in the first Born approximation. The corresponding results barely differ from those shown in Figures 6.7a and 6.6, thus leading further support to our interpretation of the observed oscillations as resulting from two-center Cohen-Fano interferences.

6.2 Methane

The study of CH_4 is motivated by the successful previous results and by recent works published on diatomic molecules. In all molecules, inner-shell molecular orbitals are localized on the atomic centers, so that electrons can be effectively ejected from a very localized region of space and can be subsequently scattered by the neighboring atomic centers thus leading to diffraction. K-shell photoionization experiments on isolated fixed-in-space CO molecules have shown evidence of such scattering processes in photoelectron angular distributions [211, 446]. Also, recently observed diffraction of laser-induced tunneling electrons produced by intense infrared femtosecond pulses on N_2 and O_2 [248, 272]. In these experiments, the oscillating electric field of the laser forces a fraction of the tunneled electron to go back to the parent ion where it can diffract.

The specific example we consider here is vibrationally resolved C(1s) photoionization of CH_4, a molecule for which there is a vast literature [47, 157, 209, 208], but no evidence of diffraction has been reported so far. This is partly due to the need for high kinetic-energy resolution in combination with high photon energy (that of X-rays) but also to the fact that emission of a fast electron is accompanied by recoil of the residual cation [209], thus leading to a redistribution of the available energy even on symmetry-forbidden vibrational modes. As shown by Kukk *et al.* [209], the recoil of CH_4^+ ions leads to excitation of the asymmetric stretching and bending vibrations, which superimpose to the dominant symmetric stretching vibrational components. As a result, the apparent v-ratios increase almost linearly with photon energy, thus hiding the underlying diffraction.

In this section, we present the results obtained using the multicenter B-spline static-exchange DFT method. As before, the case of the total cross section will be treated first. Then, the theoretical v-ratios will be compared to a new set of experimental data obtained using the SOLEIL synchrotron (France). Theoretical results obtained for the vibrationally resolved angular distribution in the laboratory and molecular frames will be discussed at the end of the section.

6.2.1 Total cross section

Figure 6.8 shows the core photoionization cross section of CH_4 for photon energies up to ∼368 eV. Agreement between DFT model and experimental data is very good and much better than for Schwinger variational method reported in [267]. Although rather broad, the experimental structure at ∼ 300 eV can be attributed to doubly excited states resonances. This assumption is coherent with the fact that theoretical calculations does not yield to such variation in the cross section. According to [198], these doubly excited states are associated with the configurations $1a_1^1\ 2a_1^2\ 1t_2^5\ 3a_1^2$ and $1a_1^1\ 2a_1^2\ 1t_2^5\ 3a_1^1\ 2t_2^1$. At

higher energies, the discrepancy between experiment and theory is probably due to systematic errors in the experimental measurements. Contrary to all the previous studied cross sections, CH_4 does not present any shape resonance because hydrogen atoms cannot compete against the attractive potential created by the central carbon atom.

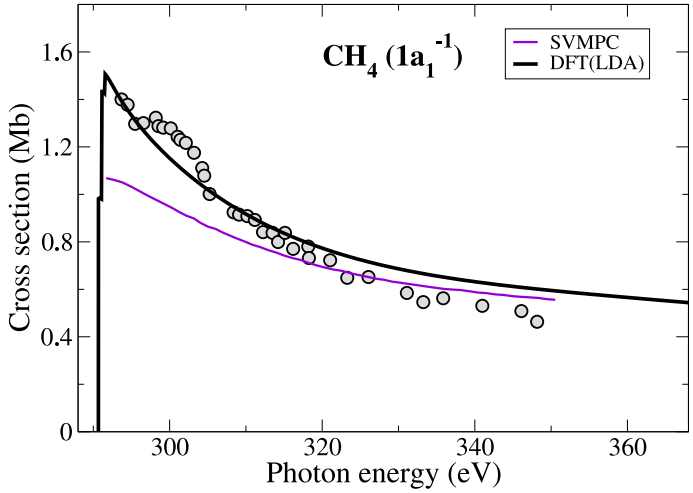

Figure 6.8: Total cross section for the C1s photoionization of CH_4 as a function of the photon energy. Circles correspond to experimental data from [198] ; Lines correspond to theory - Violet solid: Schwinger variational method with Padé correction (SVMPC) [267], Black thick solid: DFT method using a LDA functional (this work).

Figure 6.9 shows the total cross section and the contribution of the different partial waves for an extended range of photon energy. Compared to the previous cases, partial waves in C1s photoionization of CH_4 are less structured and do not present deep minima. Also, it has to be noticed that the $l = 1$ partial wave is dominant in the whole photon energy range, reflecting the atomic character of the initial MO and the relatively isotropic molecular potential.

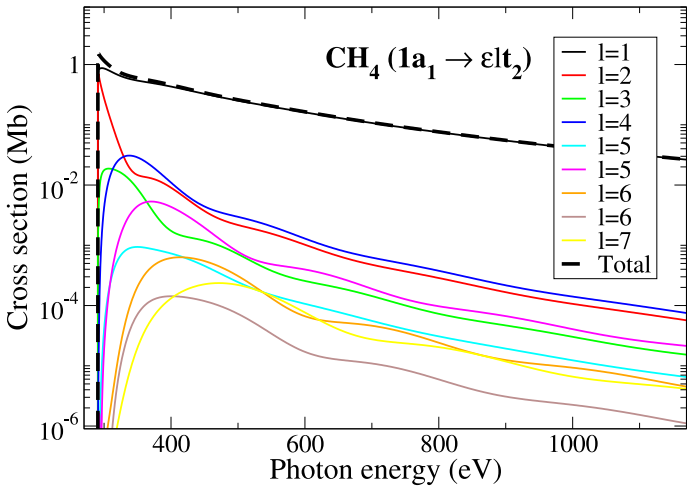

Figure 6.9: Contribution of the nine first partial waves to the total cross section of the $1a_1 \rightarrow \varepsilon l t_2$ transition of CH_4 as a function of the photoelectron momentum. Solid lines: DFT method using a LDA functional.

6.2.2 Vibrationally resolved cross section

Figure 6.10a (upper panel) shows the photoelectron spectrum for the symmetric stretching mode at a photon energy of 330 eV. The experimental data have been renormalized to the theoretical results, which are shown by vertical bars. As can be seen, CH_4 photoionization mainly leads to CH_4^+ ions in the ground vibrational state $v' = 0$ of its stretching mode. This is because the equilibrium geometries of CH_4 and CH_4^+ are very similar. Indeed, as illustrated in the lower panel, a vertical one-photon transition from the ground state of CH_4 necessarily leads to CH_4^+ ions with a geometry close to that of the minimum of the potential energy surface (PES), so that the maximum Franck-Condon overlap corresponds to the $v = 0 \rightarrow v' = 0$ transition. Consequently, the intensity of the observed peaks decreases rapidly with the degree of vibrational excitation of the remaining CH_4^+ ion and, for all practical purposes, it is negligible beyond $v' = 2$.

Theoretically, a good description of the geometry of the neutral and core-ionized state of methane is primordial since the the vibrational progression present a strong dependency on the geometry change. As for core photoionizations of N_2 and CO, the real computational challenge lays in the description of the core-ionized state which is higher in energy than many other electronic states of the cation. Then, one has to avoid the mixing of such states in the variational procedure by defining macro-iterations where valence and core MOs are optimized separately, keeping the core and the valence shell frozen respectively [186]. In the case of methane, Karlsen *et al.* computed the geometrical

and vibrational parameters at the valence-correlated level of theory. Values obtained in this work for ground state CH_4 ($\omega_e = 3059.9$ cm^{-1}, $X_{11} = -13.7$ cm^{-1}) and core ionized state CH_4^+ ($\omega_e = 3383.5$ cm^{-1}, $X_{11} = -15.8$ cm^{-1}) have been used to derive the Morse potentials.

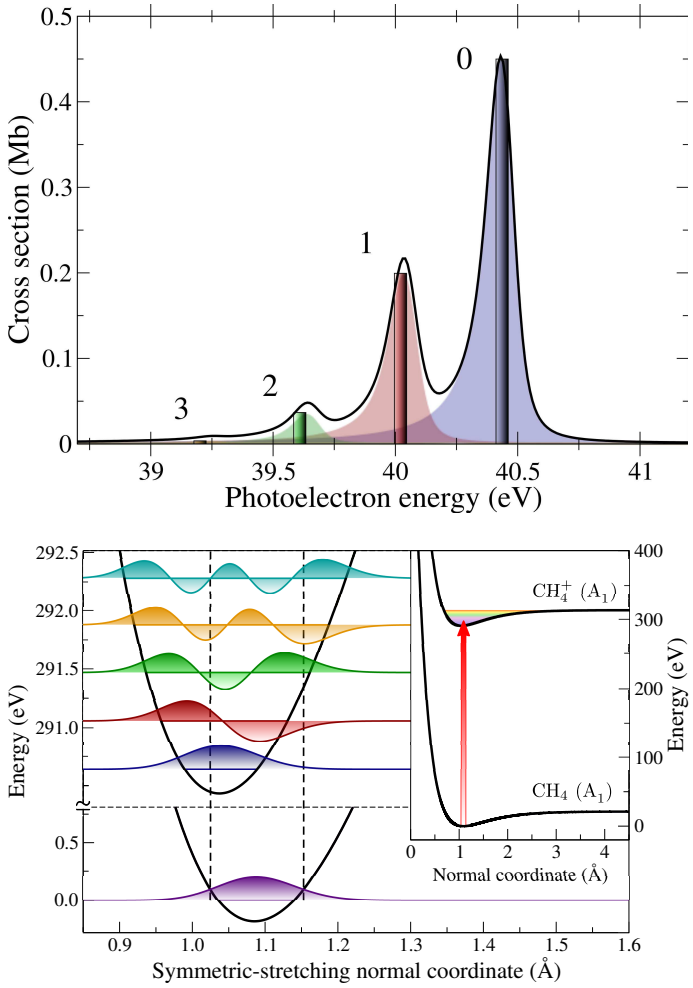

Figure 6.10: (Upper panel) Photoelectron spectrum of CH_4 taken at $\omega = 330$ eV. Solid lines: fit of the experimental data [290]. Bars: DFT method using a LDA functional. Peak numbers indicate the vibrational quantum number v' of CH_4^+. (Lower panel) Potential energy curves of the ground states of CH_4 (A_1) and CH_4^+ (A_1) along the symmetric-stretching normal coordinate. The vibrational wave functions associated with the relevant vibrational states are also shown. The vertical red arrow indicates a vertical one-photon transition. The vertical dashed lines enclose the Franck-Condon region.

Figure 6.11 shows the vibrationally resolved cross sections for photon energies up to ∼368 eV. Agreement between theory and experiment is very good and shows that the vibrational structure has been calculated correctly. Because CH_4 does not present shape resonances, it is not possible to observe any relative variations of the vibrational components in the vibrationally resolved absolute cross section. Then, it is very useful to compute the so-called v-ratios in order to unravel the possible variations between the vibrational components.

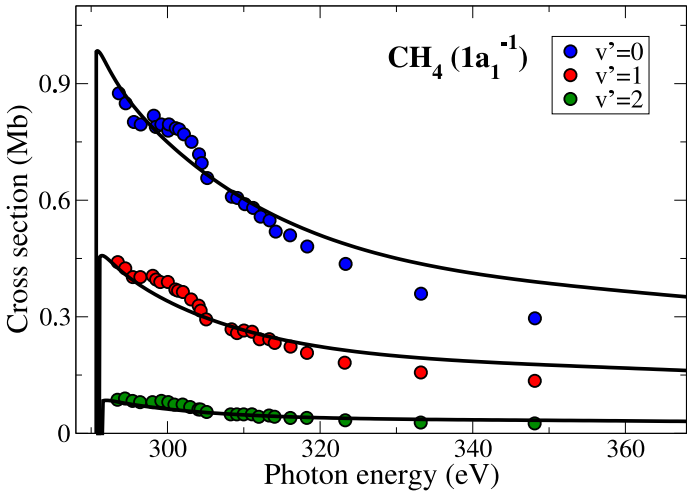

Figure 6.11: Vibrationally resolved cross section for the three first vibrational levels of the C1s photoionization of CH_4 as a function of the photon energy. Circles correspond to experimental data from [198]. Solid lines correspond to the DFT method using a LDA functional.

Figure 6.12 shows the measured and calculated v-ratios as functions of photon energy. As can be seen, the v-ratios exhibit pronounced oscillations superimposed to a nearly flat background. The agreement between theory and the results of the SOLEIL experiment is excellent, even for the very small $v' = 2/v' = 0$ ratio (notice that experimental statistical errors are significantly smaller than in previously reported measurements). The oscillations are also visible, although with larger error bars, in the experiment performed a few years ago at the Spring-8 synchrotron (Japan) after removing from the v-ratios the contribution of the asymmetric modes due to recoil (data shown in Figure 6.12).

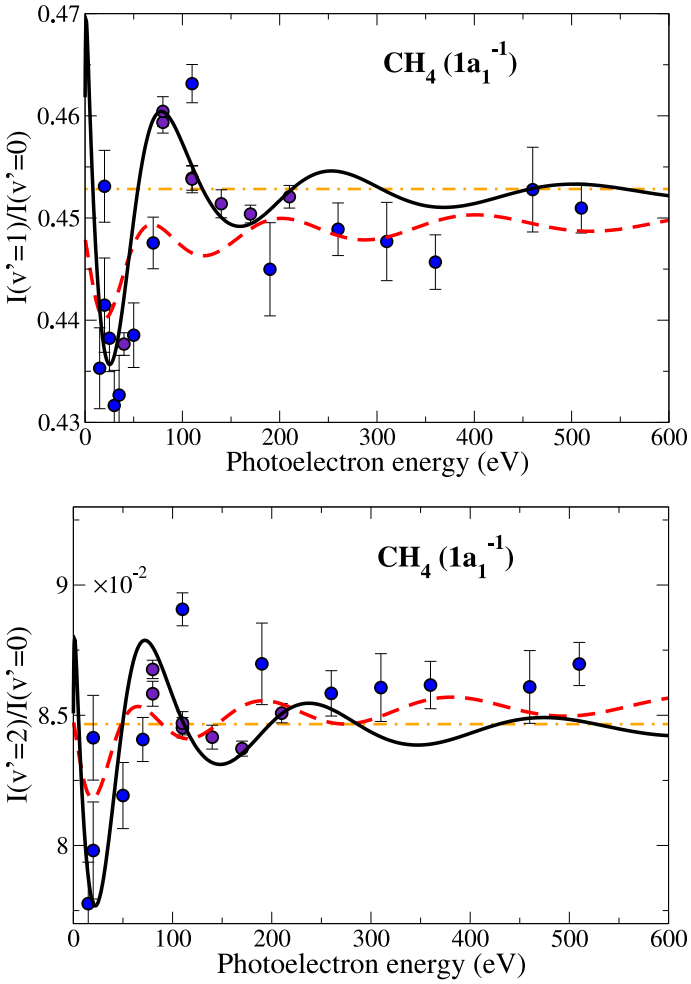

Figure 6.12: Ratios between vibrationally resolved photoionization cross sections in C 1s photoionization of CH_4 for the CH_4^+ symmetric stretching mode. (Upper panel) $v' = 1/v' = 0$ ratio. (Lower panel) $v' = 2/v' = 0$ ratio. Blue circles: experimental data from [209] obtained at Spring-8 after removing the recoil contributions. Violet circles: present experimental data. Both data sets include the statistical and systematic errors. Black solid lines: results of the DFT method using a LDA functional. Red dashed lines: results of the simple model explained in the text. Dashed-dotted lines: ratios predicted by the Franck-Condon approximation.

Scattering model

To provide more physical insight into these results, we have performed one-electron calculations using the model developed by Luca Argenti in [290]. The initial electronic state of CH_4 is represented by the 1s orbital of the C atom, ϕ_{1s_C}, and the final continuum state of the ionized electron by a plane wave plus a first order correction representing the scattering from the central C atom and the four H atoms, $\psi^-_{\vec{k}}(\vec{r}) = \exp(i\vec{k}\cdot\vec{r}) + \psi^-_{C,\vec{k}}(\vec{r}) + \psi^-_{H,\vec{k}}(\vec{r})$. Within this model, the transition dipole matrix elements have been evaluated as functions of the symmetric stretching normal coordinate and then used to obtain vibrationally resolved photoionization cross sections.

In more detail, the vibrationally-resolved photoionization cross section $\sigma_{v'}$ from the carbon $1s$ core orbital, $\phi_{1s_{\rm C}}$, of methane in the ground vibrational state is estimated within the single-active-electron approximation:

$$\sigma_{v'} = 2\,\frac{4\pi^2 k}{c\omega}\int d\Omega_k \left|\,\langle\,\psi^-_{\vec{k}}\,\chi_{f,v'}|\,\hat{\epsilon}\cdot\vec{p}\,|\phi_{1s_{\rm C}}\,\chi_{i,0}\rangle\,\right|^2 \tag{6.21}$$

In the final state, the CH_4^+ parent ion in the (possibly excited) vibrational state $\chi_{f,v'}$ is coupled to an electron state in the continuum $\psi^-_{\vec{k}}$ with asymptotic momentum $\vec{k}$. The latter is computed at the level of the first-order Born approximation,:

$$|\psi^-_{\vec{k}}\rangle = |\vec{k}\rangle + G_0^- V|\vec{k}\rangle, \qquad V = V_{\rm C} + \sum_{i=1}^{4} V_{{\rm H}_i} \tag{6.22}$$

where the interaction between the photoelectron and the parent ion is represented with an effective potential given by a sum of screened atomic charges:

$$V_{\rm C} = \frac{1-(Z^*_{1s,{\rm C}}-1)\,e^{-|\vec{r}-\vec{R}_{\rm C}|}}{|\vec{r}-\vec{R}_{\rm C}|}, \quad V_{{\rm H}_i} = \frac{e^{-|\vec{r}-\vec{R}_{{\rm H}_i}|}}{|\vec{r}-\vec{R}_{{\rm H}_i}|} \tag{6.23}$$

According to Slater's prescription, the nuclear effective charge felt by the electron in the C(1s) orbital is $Z^*_{1s,{\rm C}} = 5.7$. At large distances, V reduces to the Coulomb potential of the parent ion's single residual charge. In momentum coordinates, the expression for the electronic part of the final wave function reads:

$$\psi^-_{\vec{k}}(\vec{p}) \simeq \delta(\vec{p}-\vec{k}) + \psi^-_{{\rm C},\vec{k}}(\vec{p}) + \psi^-_{{\rm H},\vec{k}}(\vec{p}) \tag{6.24}$$

where:

$$\psi^-_{{\rm C},\vec{k}}(\vec{p}) = -\frac{1}{\pi^2}\frac{e^{-i(\vec{p}-\vec{k})\cdot\vec{R}_{\rm C}}}{(k+p)(k-p-i0^+)}\left(\frac{1}{|\vec{p}-\vec{k}|^2} + \frac{Z^*_{1s,{\rm C}}-1}{|\vec{p}-\vec{k}|^2+\lambda^2_{\rm C}}\right) \tag{6.25}$$

$$\psi^-_{{\rm H},\vec{k}}(\vec{p}) = -\frac{1}{\pi^2}\frac{1}{(k+p)(k-p-i0^+)}\sum_i \frac{e^{-i(\vec{p}-\vec{k})\cdot\vec{R}_{{\rm H}_i}}}{|\vec{p}-\vec{k}|^2+\lambda^2_{\rm H}} \tag{6.26}$$

In principle, the factors $e^{-i\Delta\vec{k}\cdot\vec{R}}$ in the scattering components $\psi^-_{\mathrm{C},\vec{k}}$ and $\psi^-_{\mathrm{H},\vec{k}}$ couple the photoelectron to all the degrees of freedom of the nuclei. In practice, the dominant monopolar term $\sin(\Delta kR)/\Delta kR$ affects just the totally-symmetric stretching mode; hence, we will focus on the excitation of the latter, assuming $v' = 0$ for all the other vibrational modes. When computing the square module of the transition amplitude, Coulomb corrections are retained to first order only:

$$\left| \langle\, \psi^-_{\vec{k}}\, \chi_{f,v'} \,|\, \hat{\epsilon}\cdot\vec{p}|\phi_{1s_\mathrm{C}}\, \chi_{i,0}\rangle \right|^2 \simeq \left| \langle\, \chi_{f,v'} \,|\, \chi_{i,0} \,\rangle \right|^2 \phi^2_{1s_\mathrm{C}}(k)(\vec{k}\cdot\hat{\epsilon})^2 \tag{6.27}$$
$$+2\phi_{1s_\mathrm{C}}(k)(\vec{k}\cdot\hat{\epsilon})\langle\, \chi_{f,v'} \,|\, \chi_{i,0} \,\rangle\, \langle \chi_{i,0}|\, \Re\left(\langle \phi_{1s_\mathrm{C}}|\hat{\epsilon}\cdot\vec{p}|\psi^-_{\mathrm{H},\vec{k}}\rangle \,+\, \langle \phi_{1s_\mathrm{C}}|\hat{\epsilon}\cdot\vec{p}|\psi^-_{\mathrm{C},\vec{k}}\rangle \right) |\, \chi_{f,v'} \,\rangle$$

In this picture, the violation of the Franck-Condon principle is caused by the scattering of the photoelectron by the hydrogen atoms incorporated in the second term on the right-hand side of (6.27).

The total cross section is thus given by:

$$\begin{aligned} \sigma_{v'} \;&\simeq\; \frac{32\pi^3 k}{3c\omega}\phi^2_{1s_\mathrm{C}}(k)\, \left| \langle\, \chi_{f,v'} \,|\, \chi_{i,0} \,\rangle \right|^2 \\ &+\; \frac{16\pi^2 k}{c\omega}\phi_{1s_\mathrm{C}}(k)\, \langle\, \chi_{f,v'} \,|\, \chi_{i,0} \,\rangle\, \langle\, \chi_{i,0} \,|\, F(k;\lambda,R) \,|\, \chi_{f,v'} \,\rangle \end{aligned} \tag{6.28}$$

The function $F(k;\lambda,R)$ accounts for the scattering of the photoelectron by the hydrogen atoms, which leads to oscillations in the photoionization cross section, as well as for the non-Franck-Condon character of the excitation of the symmetric stretching mode. $F(k;\lambda,R)$ has the following expression:

$$\begin{aligned} &F(k;\lambda,R) \\ &= -\frac{8}{3}\sum_i Z_i \int p^2 dp\, \phi_{1s_\mathrm{C}}(p)\, \frac{\mathcal{P}}{k^2-p^2} \int_{-1}^{1} d\cos\theta \frac{p\,k\,\cos\theta}{|\vec{p}-\vec{k}|^2+\lambda_i^2} \frac{\sin|\vec{p}-\vec{k}|d_{CA_i}}{|\vec{p}-\vec{k}|d_{\mathrm{CA}_i}} \end{aligned} \tag{6.29}$$

where d_{CA_i} is the distance between the central carbon atom and the $i-th$ atom in the effective potential. Notice that, within the present approximations, the two terms corresponding to the carbon atom do not give rise to any vibronic coupling. The angular integral has a closed solution in terms of the exponential integral $E_1(z)$, a well known special function. The integral over the momentum p, as well as that between symmetric vibrational wave functions must instead be carried out numerically.

The above formula have been evaluated by using the same vibrational wave functions as in the *ab initio* calculations described in section II. The results of the model are shown by dotted lines in Figure 6.12. For photoelectron energies larger than 50-100 eV, where the first-order correction to the plane wave description of the continuum electron is a reasonable approximation, the model reproduces quite nicely the amplitude and approximate periodicity

π/R_{CH} (where R_{CH} is the C-H distance at the equilibrium geometry) of the oscillations. The phase is not well described because electron delocalization and correlation effects, not included in the model, are responsible for additional phase shifts in the scattering wave function. The relative importance of the different terms contributing to the continuum wave function $\psi^-_{\vec{k}}(\vec{r})$ is illustrated in Figure 6.14. This figure shows that neglect of the $\psi^-_{C,\vec{k}}(\vec{r})$ term, i.e., of the scattering from the central C atom, has a negligible effect in the v-ratios beyond 300 eV. In contrast, neglect of the $\psi^-_{H,\vec{k}}(\vec{r})$ term, i.e., of the scattering by the four H atoms, leads to no oscillations at all. Therefore, the amplitude and frequency of the oscillations is entirely explained by scattering from the surrounding H atoms (as illustrated in Figure 6.13). Scattering from the C atom plays some role below 300 eV by decreasing the amplitude of the oscillations due to scattering by the H atoms.

In order to fit the measured v-ratios, it is much more useful to use a further simplification of the above expression, which leads to the following analytical formula:

$$\frac{\sigma_1}{\sigma_0} \simeq A + B\, e^{-k^2/26} \left[0.42 \cdot \cos(2k\bar{R}_{\rm CH} + \phi) - \sin(2k\bar{R}_{\rm CH} + \phi)/k\right] \qquad (6.30)$$

This expression contains four free parameters: A is an adjusted Franck-Condon ratio, B controls the oscillation amplitude, $\bar{R}_{\rm CH}$ is the average C-H distance, and ϕ is a phase shift. Although, strictly speaking, ϕ is a function of photoelectron energy, we have assumed that it is a constant since the largest variation with photoelectron energy comes from the $2k\bar{R}_{\rm CH}$ term. We have fitted the experimental data in the range 40-600 eV (in this way, we exclude the low-energy region in which electron correlation is important). The result of the fit is $\bar{R}^0$=1.1±0.1Å, $A = 0.452 \pm 0.01$, $B = 0.020 \pm 0.004$, and $\phi = (0.5 \pm 0.4)\pi$. The value of the C-H bond distance is in good agreement with that obtained from spectroscopic data [137].

It is worth noticing here that, as shown in [45] for the case of coherent two-center photoelectron emission from diatomic molecules, the oscillatory structures observed in the v-ratios carry structural information associated with both the initial neutral molecule and the final molecular cation. This is because the photoelectron probes regions of internuclear distances that are different for each final vibrational state of the cation. The geometries of CH_4 and CH_4^+ are so similar that the model used here assumes that both species have identical geometries. However, disentangling the structure of the neutral molecule and the resulting molecular cation when their geometries are significantly different requires a more elaborate treatment along the lines described in [45].

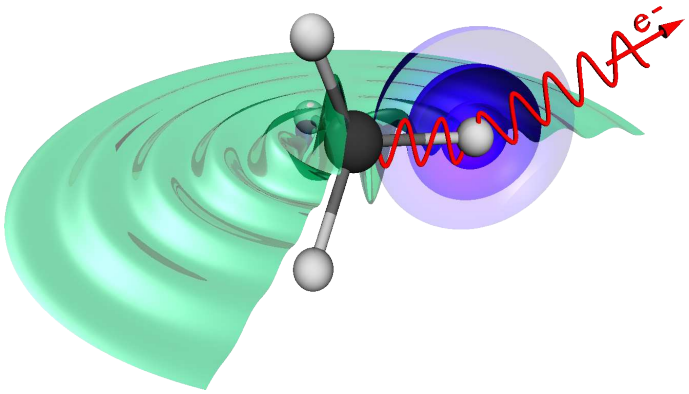

Figure 6.13: Schematic illustration of the photoelectron scattering by the peripheral H atoms.

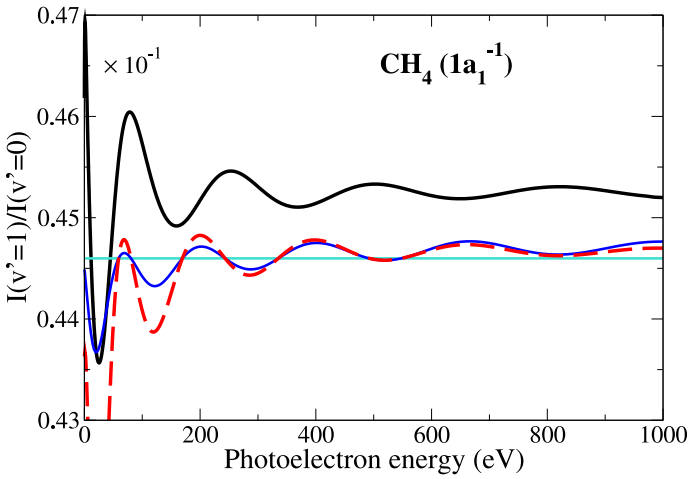

Figure 6.14: Origin of the oscillations in the v-ratios (here $v' = 1/v' = 0$). Black solid line: result of the DFT method using a LDA functional. Red dashed line: result of the simple model explained in the text. Blue thin line: results of the simple model obtained by excluding the scattering of the ejected electron by the central C atom. Turquoise thin line: results of the simple model obtained by excluding the scattering of the ejected electron by the peripheral H atoms. The latter curve simply corresponds to the ratio between the Franck-Condon factors for the two final vibrational states of the CH_4^+ ion.

6.3 Angularly resolved cross section

We have seen that in the case of N_2 and CO (see Section 5.4), the two-center interferences leave their signatures in the β asymmetry parameter and the MFPAD at high energies. Interferences due to intramolecular scattering are also expected to be observable in the angular distribution. In this section are shown angular distributions corresponding to the C1s photoionization of methane in both laboratory and molecular frame. The vibrationally resolved DFT results are compared with vibrationally and non-vibrationally resolved experimental data taken from the literature.

6.3.1 β asymmetry parameter

Figure 6.15 shows the vibrationally resolved β asymmetry parameter for two different photon energy ranges: up to 380 eV (left panel) and up to 1080 eV (right panel). It is notable that compared to N_2 and CO, the different vibrational components have a very similar behavior. In all cases, the DFT results agree qualitatively with the vibrationally resolved experimental data.

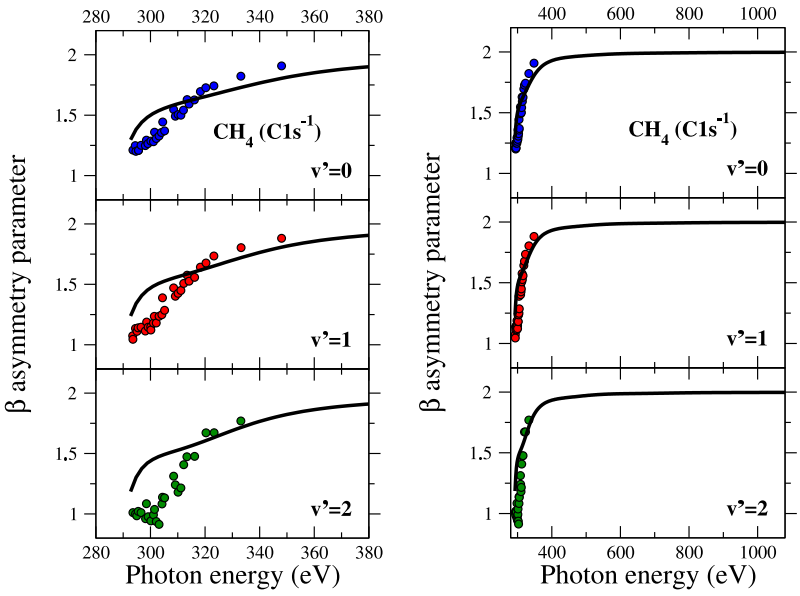

Figure 6.15: Vibrationally resolved electron β asymmetry parameter for the C1s photoionization of CH_4. Circles correspond to experimental data from [198]. Solid lines correspond to vibrationally resolved theoretical results obtained with the DFT method using a LDA functional.

The theoretical results do not reproduce the inflection that is observed experimentally at ~ 310 eV. TDDFT calculation performed at the fixed nuclei approximation and published in [361] does not lead to a better agreement in this energy region. This seems to confirm that the non-monotonous behavior of the β values at ~ 310 eV is probably due to doubly excited states. The values of β are close to 1 near threshold and tend rapidly to 2 with the increase of the photon energy. Then, in the laboratory frame, the angular distribution does not present any traces of the diffraction effects. Moreover, above $\omega \sim 400$ eV, the β asymmetry parameter has an almost perfect atomic character.

6.3.2 MFPADs

As shown by the simple model, the outgoing electron is essentially scattered by the H atoms at high photon energies. Because it contains information on the interplay of the different angular momentum of the photoelectron wavefunction in the molecular frame, MFPADs are expected to be sensitive probes of the intramolecular scattering effects. Figure 6.16 show non-vibrationally and vibrationally resolved MFPADs taken a photoelectron energy of 4.35 eV. The experimental MFPADs have been obtained by measuring in coincidence the initial momentum vectors of the photoelectron and the ionic fragments resulting from the dissociation by simultaneous double Auger decay. Theoretical results published in [430] and obtained using the complex Kohn variational method (CKVM) are also shown. The calculations have been performed at the same level of theory than the present DFT method but in the fixed nuclei approximation. As it can be seen, the dominant vibrational MFPAD component ($v' = 0$) obtained with the DFT method is in very good agreement for all orientations of the polarization vector as well as for the averaged case. The MFPADs corresponding to different orientations of the polarization vector show that the shape of the MFPADs emerge essentially from the competition between two effects: one is the propensity of the photoelectron to follow the bonds because of the scattering by the molecular potential ; the other one is the propensity of the photoelectron to follow the polarization vector because of the acceleration by the electric field. Because they are averaged over all possible orientations of the polarization vector, the MFPADs presented in the last column does not present evidences of such competition. In fact, in such situation the electron is accelerated by the electric field in all the directions and is expected to lead to an isotropic contribution to the MFPAD. The effect that remains is the intramolecular scattering which arises when the photoelectron escapes along the bonds.

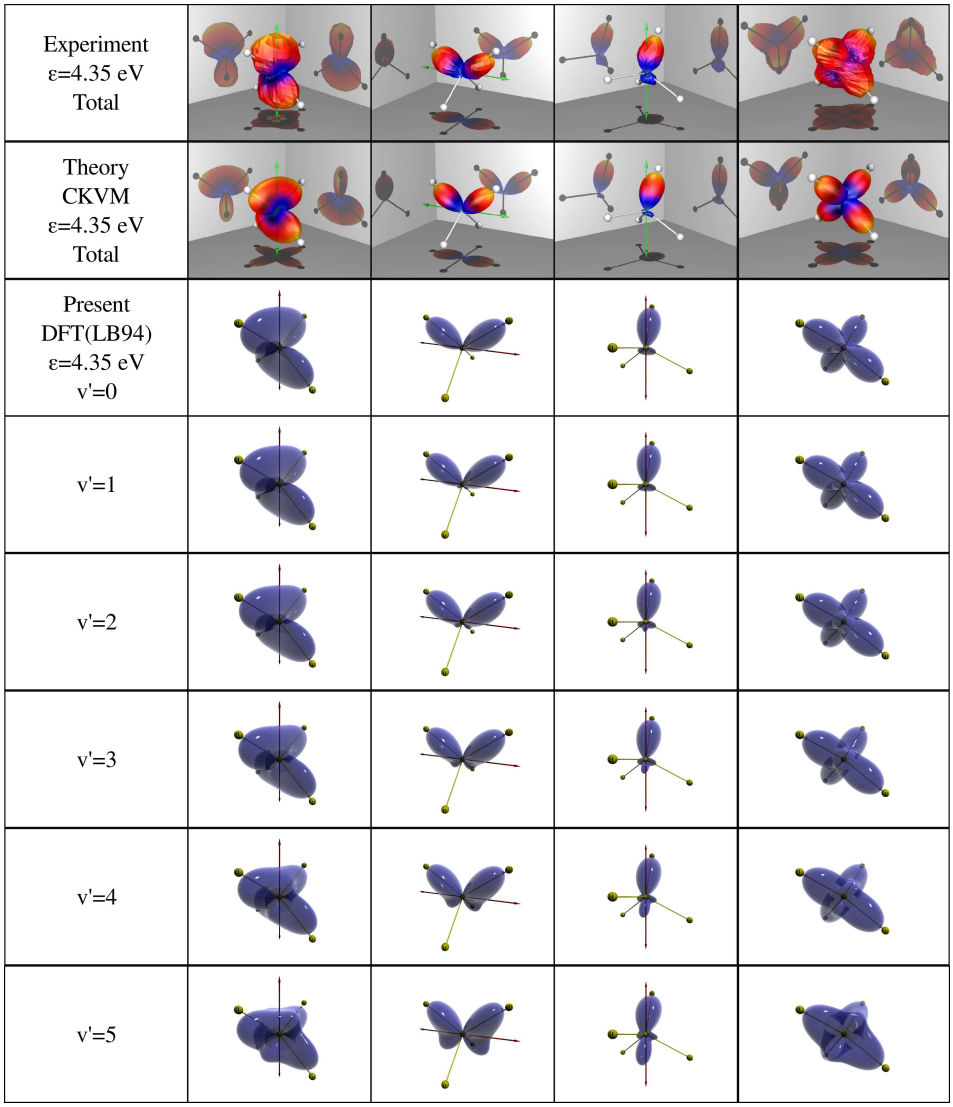

Figure 6.16: MFPADs for the C1s photoionization of CH_4 at a photoelectron energy of 4.35 eV. The MFPADs are shown for different orientations of the polarization vector (indicated by a double arrow) - Second column: polarization vector aligned to a C_2 symmetry axis, Third column: polarization vector perpendicular to a C_2 axis and in the plane of two hydrogen bonds, Fourth column: polarization vector perpendicular to a C_3 axis along one bond and in a plane with another bond. The fifth column correspond to the averaged MFPADs. First row: non-vibrationally resolved experimental results from [430]. Second row: theoretical results obtained using the complex Kohn variational method (CKVM) in the fixed nuclei approximation [430]. Last four rows: vibrationally resolved MFPADs calculated with the present DFT method using a LDA functional for the v' =0, 1, 3 and 5 vibrational quantum number.

Indeed, at the considered photoelectron energy (∼4.35 eV), the angular distribution nicely image the molecular geometry of CH_4. However, this molecular geometry mapping is rapidly lost with the increase of the energy. As shown experimentally and theoretically in Figure 6.17, the averaged MFPAD becomes much more spherical for slightly higher photoelectron energies. This radical change of the MFPAD shape indicates a destructive interference due to the diffraction of the photoelectron by the surrounding H atoms. This interpretation is corroborated by the fact that most spherical angular distribution is found at ε ∼23 eV, a photoelectron energy which corresponds to the deepest minima in the v-ratios presented in Figure 6.12. The DFT calculation of the averaged MFPAD at 80 eV shows that the molecular geometry mapping is recovered at higher energies. This alternation between isotropic and molecular geometric distributions in the molecular frame is as a direct consequence of the energy dependence of the diffraction effects.

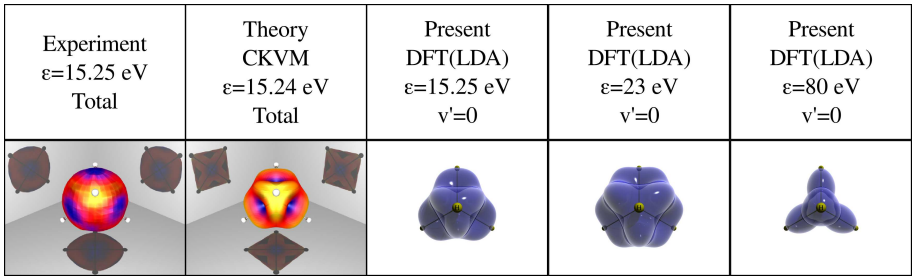

Figure 6.17: Averaged MFPADs for the C1s photoionization of CH_4 at photoelectron energies equal to ∼15.25, 23 and 80 eV. First column: non-vibrationally resolved experimental results from [431]. Second row: theoretical results obtained using the complex Kohn variational method (CKVM) in the fixed nuclei approximation [431]. Last three columns: vibrationally resolved MFPADs calculated with the present DFT method using a LDA functional for photoelectron energies equal to 15.24, 23 and 80 eV.

6.4 Tetrafluoromethane

As seen with the study on CH_4, diffraction occurring in the core photoionization process leads to oscillating pattern which contains information about the molecular structure. More particularly, it has been demonstrated that the interferences arise essentially from the diffraction of the C1s photoelectron by the surrounding H atoms. Although this study revealed the mechanism at the origin of the observed oscillations, it did not discussed the role of the nature of the peripheral atoms in this process. In fact, the simple model elaborated to describe the diffraction pattern shows a dependence on some atomic parameters such as the nuclear effective charges Z_i and the screening factors λ_i (see Equation 6.29). Then, replacement of the H atoms by another set of atoms is expected to affect the diffraction as much as the new element is different from hydrogen. Fluorine being the most electronegative element, it should yield to significant changes in the oscillating pattern.

Several works [410, 267, 263, 208] have carried out comparative studies of the K-shell photoabsorption/photoionization spectra of CH_4 and CF_4. In [410], Ueda et al. made a systematic investigation by substituting one by one the hydrogen atoms of CH_4 by fluorine atoms. Comparison of the photoabsorption spectra of CH_4, CH_3F, CH_2F_2, CHF_3 and CF_4 clearly shows a gradual chemical shift as well as an increasing dominance of the valence-like transitions on the Rydberg-like transitions as the number of F atoms increases. As we will see in the photoionization of BF_3 and SF_6, this behavior is commonly observed in fluorine compounds and is related to the strong electronegativity of the F atom. Another difference pointed out in [267] is the existence of a near-threshold resonant peak in the C1s photoionization cross section of CF_4 that does not exist in CH_4. Such resonant structure is also found in another halogenated methane compound: CCl_4. Although the structure is more intense and narrower in the photoionization of CCl_4, it seems to proceed through a similar mechanism. Then, it can be concluded that some characteristics of the peripheral atoms (such as the electronegativity and the atomic number) has a strong incidence on the molecular potential and consequently on the photoionization cross section at low energies. A key question is then to understand how such substitution would affect the photoelectron spectra at high photon energies, i.e. when the photoelectron is escaping so fast that the details of the molecular potential has a minor influence on it. In the following, we will present an analysis of the high energy region of the C1s photoelectron spectra of CF_4. Comparison with the previous study of CH_4 will be made in order to draw conclusions with respect to the above formulated key question.

6.4.1 Electronic structure

Compared to methane, CF_4 is a rather complex molecule since it possesses 42 electrons in total. As for CH_4, the C1s AO is very localized on the central atom but, in contrast, it does not correspond to the lowest core MO. The electronic configuration of CF_4 is shown in Table 6.1. Experimental and theoretical vertical ionization energies are also reported. It shows a systematic disagreement of ∼1 eV between DFT results and experimental values in the outer valence shell and with increasing discrepancy as the compared MOs get lower in energy. The DFT energy corresponding to the C1s AO (the $2a_1$ MO) is about 3.5 eV smaller than the experimental value. This relatively large difference is not a relevant criterion to evaluate the accuracy of the Kohn-Sham orbitals but argue in favor of using a potential energy curve obtained with different ab initio methods or derived from experiment.

Inner shell	$1a_1^2$ (F1s)	$1t_2^6$ (F1s)	$2a_1^2$ (C1s)
Exp. [184]	-695.0	-695.0	-301.8
DFT (LDA)	-663.61	-663.61	-305.33

Inner valence	$3a_1^2$	$2t_2^6$
Exp. [167]	∼-43.81	∼-40.30
DFT (LDA)	-40.55	-36.97

Outer valence	$4a_1^2$	$3t_2^6$	$1e^4$	$4t_2^6$	$1t_1^6$
Exp. [20]	-25.11	-22.04	-18.54	-17.51	-16.29
DFT (LDA)	-23.87	-21.67	-17.06	-16.57	-15.14

Table 6.1: Comparison between experimental and theoretical vertical ionization energies (in eV) for CF_4. Theoretical results are obtained using a LDA exchange-correlation functional and a DZP basis set at C-F∼ 1.316 Å (no geometry optimization).

6.4.2 Vibrational structure

In the case of CF_4, we made use of two harmonic potentials essentially derived from theoretical results (see Table B.3). It has to be mentioned that the wells of the PECs for the ground and ionized states of CF_4 are very deep. Therefore, the vibrational wavefunctions are localized in a narrow spatial region and a small geometry change can induce very different overlapping contributions. For instance, in the present calculation, a change of 0.1 pm of the core-ionized state bond length has been found to lead to a 44% variation of the Franck-Condon factor ratio. This point shows the remarkable sensitivity

of the Franck-Condon factor to the bond lengths.

Ab initio calculations have been carried out at the CCSD(T) level of theory using a cc-pVTZ adjusted basis in [420] and gave the following values for the harmonic frequencies of the four normal modes of vibration of CF_4 ground state: the symmetric stretching $\omega_1(a_1) = 921.57$ cm^{-1}, the bending $\omega_2(e) = 439.91$ cm^{-1}, the asymmetric stretching $\omega_3(t_2) = 1303.01$ cm^{-1} and another bending $\omega_4(t_2) = 637.89$ cm^{-1}. The corresponding anharmonic constants have been obtained by using a six-order Canonical Van Vleck Perturbation Theory (CVPT) method: $X_{11} = -1.109$ cm^{-1}, $X_{12} = -0.911$ cm^{-1}, $X_{13} = -6.253$ cm^{-1} and $X_{14} = -0.675$ cm^{-1}.

6.4.3 Total cross section

Figure 6.18 shows the C1s photoionization cross section of CF_4 for photon energies up to ∼580 eV. The large peak appearing in the low energy region is the signature of a shape resonance. As we will see in the next sections, similar structures are visible in the photoionization cross section of BF_3 and SF_6. The presence of strong shape resonances in these molecules arise from the competition between the attractive coulomb potential and the repulsive centrifugal forces due to the strongly electronegative surrounding atoms. However, it has been pointed out in [267] that in the case of CF_4, the anti-bonding $\sigma*(t_2)$ unoccupied valence state is believed to exist below the C1s ionization threshold. Then, it should not be observable in the photoionization cross section and any possibles resonances are expected to be due to non-valence states. First evidences of a shape resonance in the C1s photoionization cross section of CF_4 has been found experimentally in [427] and [398]. A calculation using the multiple scattering method [368] confirmed the presence of a resonance near threshold but did not investigate a higher energy region. A deeper characterization of the shape resonance has been carried out in [267] by analyzing the eigenphase sum which gave an energetic position of 308.3 eV and a width of $\Gamma \sim 14$ eV. In Figure 6.18 the peak corresponding to the shape resonance appears at ~ 315 eV and is much broader than the ones observed in N_2, CO and C_2H_2.

Contrary to the F1s photoionization cross section of CF_4 which is expected to show two peaks close to the ionization threshold (due to shape resonance in the t_2 and a_1 symmetries), the C1s photoionization should lead only to a single peak because the continuum state has a unique t_2 symmetry. However, as can be seen in Figure 6.18, an extended energy range study reveals the presence of a second peak at ∼370 eV. It has been observed for first time by Hitchcock *et al.* [161] using electron energy loss spectroscopy. This second peak has similar characteristics (amplitude and width) with the former one but is located at such high photoelectron energy that it cannot be associated

with a shape resonance. Even for fluorine compounds, the centrifugal barrier cannot support resonant states of more than few tens of eV above ionization threshold (see the pioneer articles by Dehmer *et al.* on SF_6 and BF_3 [82, 44]). Another unexpected feature hardly related to shape resonance is the very broad and smooth structure shown by the DFT calculation at ~ 500 eV.

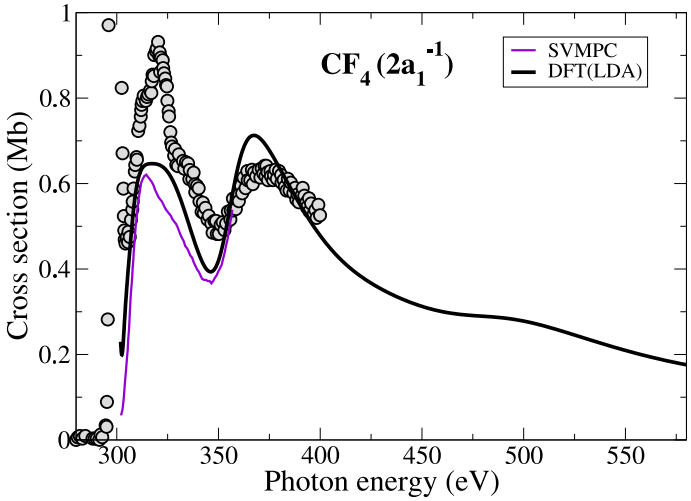

Figure 6.18: Total cross section for the C1s photoionization of CF_4 as a function of the photon energy. Circles correspond to experimental data from [161] ; Lines correspond to theory - Violet solid: Schwinger variational method with Padé correction (SVMPC) [267], Black thick solid: DFT method using a LDA functional (this work).

Figure 6.19 shows the total cross section and the contribution of the different partial waves for an extended range of photon energy. As observed in CH_4, the $l = 1$ partial wave is dominant. This similarity between the C1s photoionization of CH_4 and CF_4 confirms the importance of the molecular symmetry as the localized character of the initial MO in the photoionization process. The molecular potential of CF_4 being more anisotropic, the higher partial waves have a greater contribution to the total cross section than in CH_4. Also, minima due to the confinement of the photoelectron and broadened by the nuclear motion are visible in all the partial waves while it was not observed in the case of CH_4.

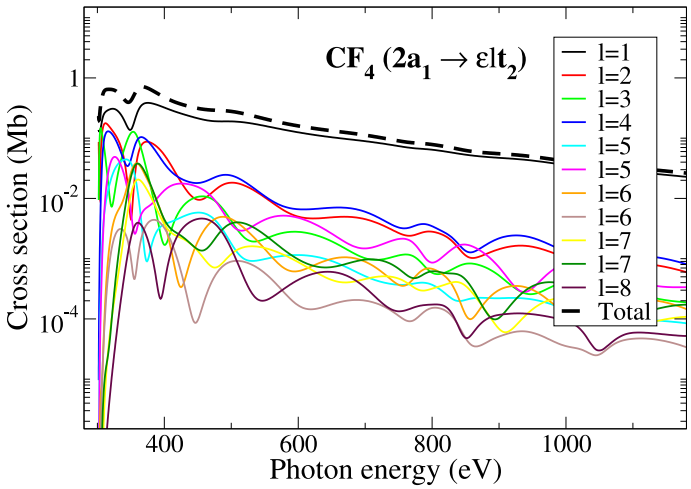

Figure 6.19: Contribution of the eleven first partial waves to the total cross section of the $2a_1 \rightarrow \varepsilon l t_2$ transition of CF_4 as a function of the photoelectron momentum. Solid lines: DFT method using a LDA functional.

6.4.4 Vibrationally resolved cross section

The C1s photoionization spectra of CF_4 and CO are often compared in the literature (see for example [398, 263, 48, 400]). Comparison with CH_4 is less abundant: [263, 267]. Figure 6.20a shows a comparison between experimental C1s photoionization photoelectron spectra of CH_4, CO and CF_4 as a function of the photon energy. It can be seen that compared to CH_4 and CO, the vibrational progression of the CF_4 spectra is quite limited and presents almost no other structure than the main photoionization line ($v = 0 \rightarrow v' = 0$). It is due to the very small change in the equilibrium bond length (-0.61 pm compared to -4.9 pm for CO and -4.8 pm for CH_4). In general, removal of a 1s electron from a central atom is expected to lead to a bond contraction. However, in molecules such as CF_4 where the peripheral atoms are halogen elements, repulsions compete with the former process. Analysis of the natural linewidths of each photoelectron spectrum reveals further peculiarities in the photoelectron spectra of CF_4. The natural linewidth of CO is about 95±5 meV for a photon energy of 330eV [48]. Very similar values are obtained at the same photon energy for CH_4 (95.4 meV [47]) and C_2H_2 (106 meV [31]). However, the natural linewidth of CF_4 is much smaller ($\sim$ 67±2 meV [386]). This decrease is related to the Auger decay rate which depends on the density of the valence electrons that couples with the localized core hole. Thus, when the hydrogen atoms of CH_4 are replaced by strongly electronegative atoms such as fluorine, electronic cloud is expected to be denser on the peripheral atoms and then core hole lifetime to be lower. In principle, the Auger decay

rate should also depend on the number of valence electrons: the higher this number, the more possible Auger decay routes, and consequently the faster the decay. However, as seen with the present examples, the total number of valence electrons is not relevant to understand the evolution of the natural linewidth because screening of the core-hole has to be taken into account.

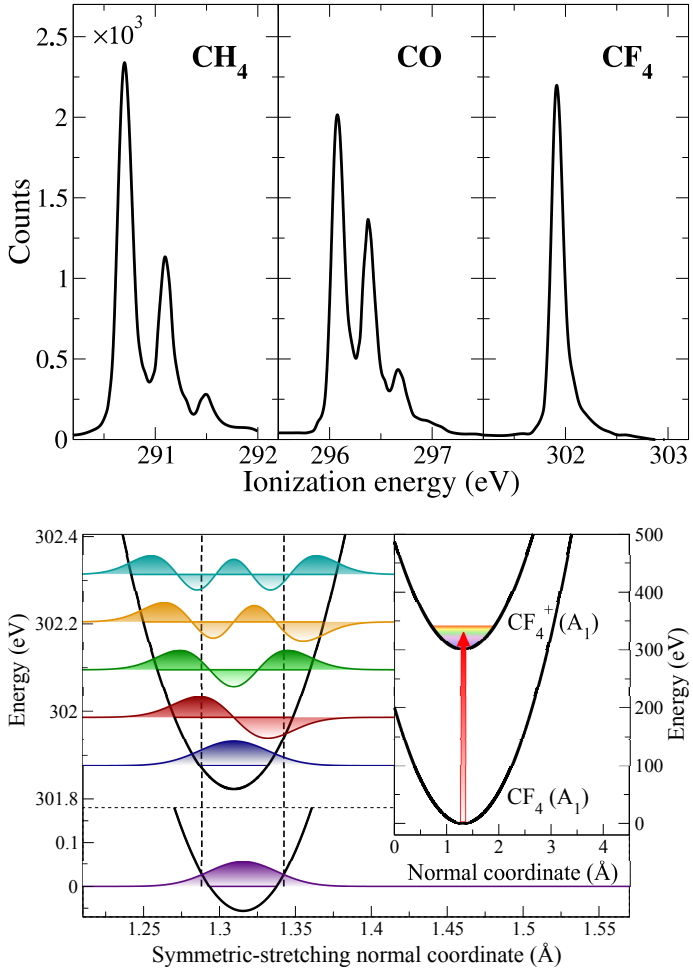

Figure 6.20: (Upper panel) C1s photoelectron spectra of CH_4, CO and CF_4 (left, middle and right panel respectively). Solid lines correspond to experimental data from [263]. (Lower panel) Potential energy curves of the ground states of CF_4 (A_1) and CF_4^+ (A_1) along the symmetric-stretching normal coordinate. The vibrational wave functions associated with the relevant vibrational states are also shown. The vertical red arrow indicates a vertical one-photon transition. The vertical dashed lines enclose the Franck-Condon region.

Figure 6.21 shows two photoelectron spectra measured at a photon energy of 360 and 383 eV. Deconvolution of the vibrational peaks is also shown. Non-symmetric vibrational peaks (the magenta lines) are observed in both spectra and account for another breakdown of the Franck-Condon principle. In some cases, it can occur that normal modes forbidden by selection rules are excited due to non-Born-Oppenheimer effects. However, as in the case of C1s photoionization of CH_4, excitations of the non-symmetric vibrational modes are nicely explained by the recoil momentum effect of the emitted electron on the central carbon atom. This interpretation is supported by the fact that the non-symmetric contributions to the photoelectron spectra is increasing with the photon energy (see Figure 6.21). In particular, a recent study by Thomas *et al.* [386] for photon energies up to 1500 eV shows that the increase of the non-symmetric contributions is linear with the energy and can be qualitatively explained by the simple model described in Section 5.3.1. CF_4 is of T_d point group symmetry and, as for C1s photoionization of methane, only the T_2 vibrational modes are excited by the recoil momentum: the asymmetric stretching v_3 and asymmetric bending v_4. However, theoretical predictions in [386] shows that contrary to CH_4, the momentum transfer affects more the asymmetric stretching than the asymmetric bending and that the vibrational excitations are more important than the momentum transfer to the translation of the molecule. These differences between CH_4 and CF_4 arise from the different masses of the ligand atoms and more particularly to the fact that the heavier fluorine atoms tends to mix the stretching and bending modes that were almost pure in the case of methane. For an equivalent reason, recoil vibrational excitations are expected to be stronger than the recoil translational excitation and to play a predominant role at high photon energies. In fact, CF_4 is a much better prototype than CH_4 for the study of recoil effects: the atomic mass of the central atom being much more different than the molecular mass, stronger internal excitations are generated. The study of the photoelectron spectra for a photon energy up to 1500 eV [386] revealed how the $v' = 0, 1, 2$ components of the asymmetric stretching mode and the $v' = 0, 1$ components of the asymmetric bending mode show up, one after the other, as the photon energy increases. At a photon energy of 1500 eV, the $v' = 2$ component of the antisymmetric stretching mode and the $v' = 1$ component of the antisymmetric bending mode are as intense as the ground state peak. Above this energy, the recoil excitations become the dominant source in the photoelectron spectra.

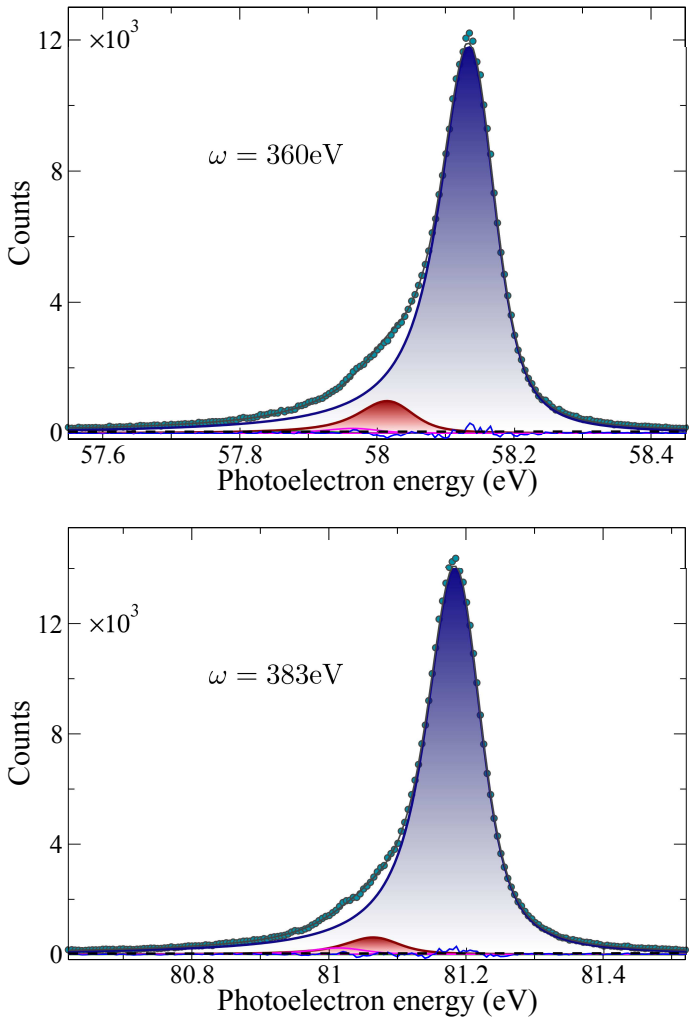

Figure 6.21: C1s photoelectron spectra of CF_4 taken at $\omega = 360$ eV (upper panel) and $\omega = 383$ eV (lower panel). Dots correspond to the measured experimental data [406]. Lines correspond to the fit of the experimental data - Solid dark blue and dark red: deconvoluted symmetric stretching vibrational peaks ($v' = 0$ and 1 respectively), Solid magenta: deconvoluted recoil excited asymmetric vibrational peaks, Dashed black: subtracted background, Solid black: sum of the deconvoluted peaks, Solid blue: residue (difference between the total fitted spectrum and the measured experimental data).

Figure 6.22 shows the vibrationally resolved cross section for photon energies up to ∼580 eV. The previously discussed resonant structures appear in both vibrational components and are shifted to lower photon energies for higher v'. As for N_2 and CO, it indicates that the increase of the nuclear separation induces a shift of the shape resonance towards lower energies.

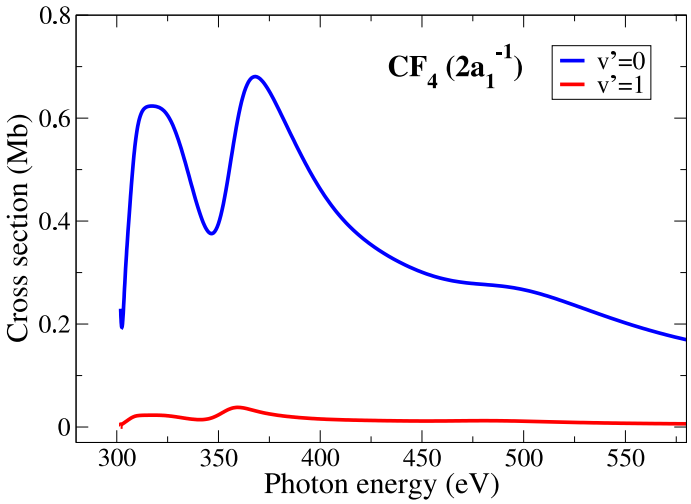

Figure 6.22: Vibrationally resolved cross section for the two first vibrational levels of the C1s photoionization of CF_4 as a function of the photon energy. Solid lines correspond to the DFT method using a LDA functional.

Given the small value of the $v' = 1$ component and the rapid decrease of the cross section with photon energy, it is more convenient to look at the v-ratio. Figure 6.23 shows the $(v' = 1)/(v' = 0)$ v-ratio for an extended photon energy range (up to 720 eV). The DFT method is compared to experimental data [406] where the effect of the recoil has been removed. Results of the simple model discussed in Section 6.2.2 is also shown. As it can be observed, both experimental and theoretical results oscillate around the theoretical Franck-Condon factor ratio (∼ 0.037). There is a very good agreement between the experiment and the DFT method, particularly in the lowest photon energy region. Both present a sharp peak around 355 eV. This structure is the result of the energy shifting of the shape resonance (discussed above) that brought the maximum of the $v' = 1$ cross section close to the inter-peaks minimum of the $v' = 0$ cross section located at ∼ 350 eV. The smooth bump observed at ∼ 500 eV in the theoretical total cross section is confirmed here by the experiment and appears logically at slightly smaller energies. For higher photon energies, the photoelectron is less sensitive to the details of the molecular potential and effects of the diffraction by the surrounding atoms are expected to be predominant in the cross section. This argument is confirmed by the good

agreement between the DFT method and the simple model above 450 eV. In particular, the simple model indicates that the structure at $\sim$ 500 eV is partly due to intramolecular scattering. As for CH_4, scattering contributions from the different atoms have been computed separately and shows that the photoelectron is mainly scattered by the surrounding atoms. Above 500 eV, only three experimental points have been measured. The points at highest energies are in good agreement with both DFT method and simple model. However, the discrepancy with the point at $\sim$ 570 eV prevent us to confirm the characteristics (period and amplitude) of the theoretical oscillations.

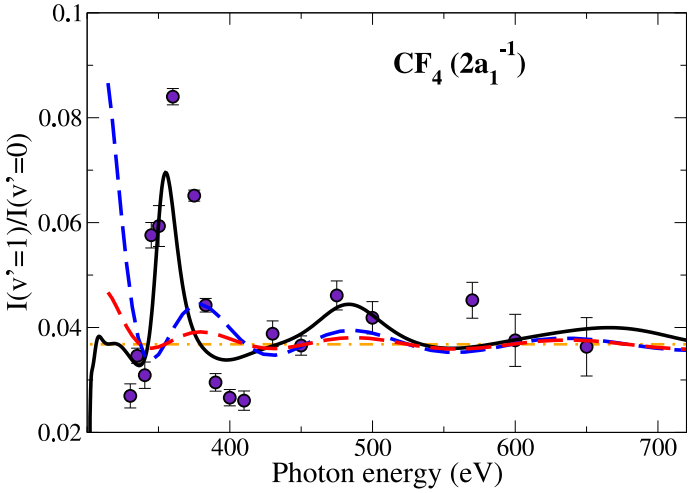

Figure 6.23: Ratio between the two first vibrationally resolved photoionization cross sections in C 1s photoionization of CF_4 for the CF_4^+ symmetric stretching mode. Violet circles: experimental data from [406] including the statistical and systematic errors. Black solid line: results of the DFT method using a LDA functional. Red dashed line: results of the simple mode. Blue dashed line: results of the simple model obtained by excluding the scattering of the ejected electron by the central C atom. Dashed-dotted line: ratios predicted by the Franck-Condon approximation.

6.5 Boron trifluoride

The reduced vibrational progression of the C1s photoelectron spectrum of CF_4 has two major disadvantages: a relatively important systematic error in the experimental measurements due to the low intensity of the second vibrational peak ; the fact that the observation of the diffraction effects is limited to a single v-ratio. The choice of a similar molecular system (such as BF_3) in which the core photoionization leads to a larger vibrational progression should permit to overcome these drawbacks and should give a better understanding of the effect of the nuclear motion on the diffraction phenomenon. BF_3 in the ground state has almost the same bond length at the equilibrium than CF_4 (about $\sim$1.31 Å). However, as shown in [387], the bond shrinkage resulting from the B1s ionization is much larger (~ -5.8 pm) than after removal of the C1s electron in CF_4 (~ -0.61 pm). Consequently, the vibrational progression associated with the B1s photoionization band is richer. It is also richer than CO ($2\sigma^{-1}$) which yet has an equivalent bond shrinkage. The reduced mass of BF_3 being larger than the one of CO, the vibrational spectrum is denser and the Franck-Condon region selects more vibronic transitions (see Figure 6.26).

Most of the studies dedicated to the photoelectron spectra of BF_3 concerns the valence shell photoionization [374, 149, 150, 86, 148, 166, 442, 238, 231] and the B1s photoionization [374, 175, 402, 403, 348, 399, 387]. As for CF_4, the influence of the surrounding atoms have been analyzed by comparing BF_3 and some halogenated compounds such as BF_3, BCl_3 and BBr_3 [141, 175, 238].

6.5.1 Electronic structure

Table 6.2 reports the experimental and theoretical vertical ionization energies that corresponds to BF_3. The agreement between DFT results and experimental values in the outer valence shell is better with energy differences lower than 0.8 eV. In the inner shell, the same disagreement is sensibly the same, particularly for the MO that corresponds to the B1s AO (the $2a'_1$) which is about 3.4 eV below the experimental value. For the ground and ionized states of BF_3, we made use of Morse potentials derived from experimental measurements [387].

According to *ab initio* calculations [141], MOs with a'_1, a''_2 and e' symmetries are mainly responsible for the B-F bonding while the ones with a'_2 and e" symmetries are responsible for the F-F bonding.

6.5.2 Vibrational structure

The vibrational structure has been calculated using Morse potentials. For the ground state, we used accurate parameters obtained by coherent Raman spectroscopy [195]. For the core ionized state, we used parameters obtained from the analysis of the experimental B1s photoelectron spectrum [387].

Inner shell	$1a'^2_1$ (F1s)	$1e'^4_1$ (F1s)	$2a'^2_1$ (B1s)
Exp. [146]	∼-694.8	∼-694.8	∼-202.8
DFT (LDA)	-663.2	-663.2	-206.2

Inner valence	$3a'^2_1$	$2e'^4_1$
Exp.	-	-
DFT (LDA)	-37.57	-36.38

Outer valence	$4a'^2_1$	$3e'^4_1$	$1a''^2_2$	$4e'^4_1$	$1e''^4_1$	$1a'^2_2$ (F2p)
Exp. [442]	-21.528	∼-20.12	-19.17	-17.11	∼-16.63	-15.91
DFT (LDA)	-20.76	-19.75	-18.58	-16.34	-16.12	-15.11

Table 6.2: Comparison between experimental and theoretical vertical ionization energies (in eV) for BF_3. Theoretical results are obtained using a LDA exchange-correlation functional and a DZP basis set at B-F∼ 1.313 Å (no geometry optimization).

BF_3 has four normal modes of vibration: the totally symmetric stretching υ_1 (a'$_1$), the out of plane bending υ_2 (a"$_2$), the asymmetric stretching υ_3 (e') and the asymmetric bending υ_4 (e'). Their values in the ground state are respectively: ω_1(a'$_1$) = 886.20 cm^{-1}, ω_2(a"$_2$) =692.85 cm^{-1}, ω_3(e') =1458.20 cm^{-1} and ω_4(e') =483.38 cm^{-1} [166]. The two last have been found to be Jahn-Teller active modes [442].

6.5.3 Total cross section

The core photoabsorption spectrum of BF_3 is known to present a strong feature near threshold which was very early attributed to a shape resonance in the e' symmetry channel [82, 374]. This shape resonance has been observed also in photoionization channels from valence MOs [166]. The influence of the fluorine atoms on the formation of the potential barrier and thus on the shape resonance has been studied in various articles by comparing the photoionization spectra of BF_3, BCl_3 and BBr_3 [175, 238]. The LUMO has been assigned to the 2a"$_2$ non-bonding MO while the lowest unoccupied anti-bonding MO corresponds to the 5e' and is believed to reside above the ionization threshold.

Figure 6.24 shows the total cross section for the B1s photoionization of BF_3. Its two active symmetry channel contributions are also shown. Results of the DFT method are compared to symmetry-resolved experimental data. Since (x, y) dipole components are associated with the e' symmetry and z with the a"$_2$, the experimental β asymmetry parameter can be used to resolve the

symmetry channels. Even though both experiment and theory present the shape resonance at the same energy position ($\sim$ 205 eV), there is a dramatic discrepancy in the width and amplitude. Also, the experimental data seems to reveal a weak maximum in the a"$_2$ channel at the same energy position. However, only the e' shape resonance is dipole-allowed. This unexpected structure in the experimental a"$_2$ channel could be due to shape resonance enhancement by interchannel coupling (as in the $2\sigma_u^{-1}$ photoionization of N_2). However, the experimentalists themselves [348] suggest a possible failure of the axial recoil approximation.

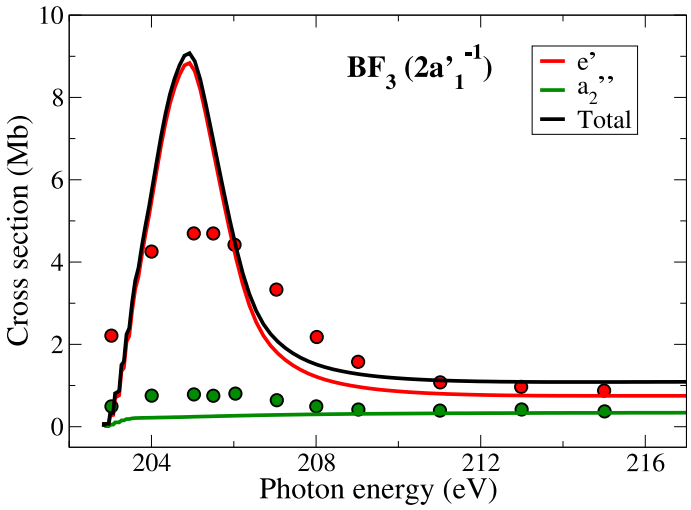

Figure 6.24: Contribution of the two photoionization channels 2a'$_1 \rightarrow \varepsilon l$e' and 2a'$_1 \rightarrow \varepsilon l$a"$_2$ to the total cross section for B1s photoionization of BF_3. Circles: experimental data from [348]. (Experimental data were renormalized to the theoretical ones). Solid lines: DFT method using a LDA functional.

The total cross section for an extended range of photon energy is plotted in Figure 6.25. Contribution of the different partial waves for the two active symmetry channels are also shown. As for CH_4 and CF_4, the $l = 1$ partial wave is dominant, particularly in the 2a'$_1 \rightarrow \varepsilon l$a"$_2$ channel. The shape resonance results from an increase of the $l = 1$ and $l = 2$ components. There is a clear dip in the total cross section about $k_e \sim 1.9$ a.u. which is due to the superimposition of several minima appearing in the $l = 2$, $l = 4(1)$, $l = 4(2)$ and $l = 5(2)$. It can be seen that the minima become broader with the increase of the photoelectron momentum. This behavior was already observable in the case of CF_4 and is the signature of the confinement of the photoelectron. The absence of minima in the high energy region of the 2a'$_1 \rightarrow \varepsilon l$a"$_2$ is probably due to the propensity of the photoelectron to follow the direction of the polarization vector perpendicular to the molecular plane. A notable fact is that far from

the ionization threshold, all the partial waves are oscillating with the same period which looks sensibly different from the one predicted by the simple formula $T_{k_e} \sim \pi/R_{eq}$. This behavior will be discussed in the following section.

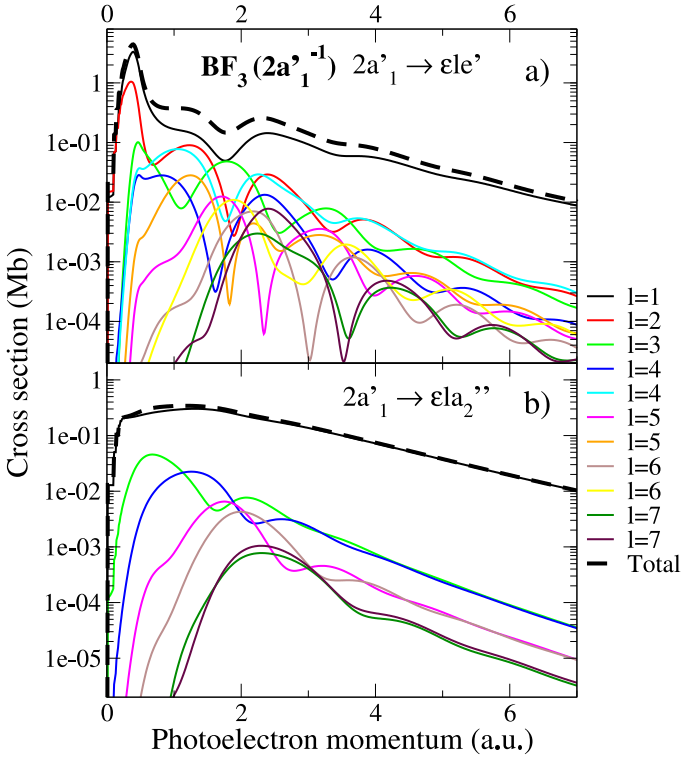

Figure 6.25: Contribution of the eleven first partial waves to the total cross section of the 2a'$_1$ $\rightarrow$ εle' (a) and 2a'$_1$ $\rightarrow$ εla"$_2$ (b) transitions of BF_3 as a function of the photoelectron momentum. Solid lines: DFT method using a LDA functional.

6.5.4 Vibrationally resolved cross section

Figure 6.26 shows the photoelectron spectrum of BF_3 at a photon energy of 518 eV. As for CF_4, decomposition of the vibrational peaks is also shown, revealing mainly the excitation of symmetric stretching vibrational modes but also a few of non-symmetric ones.

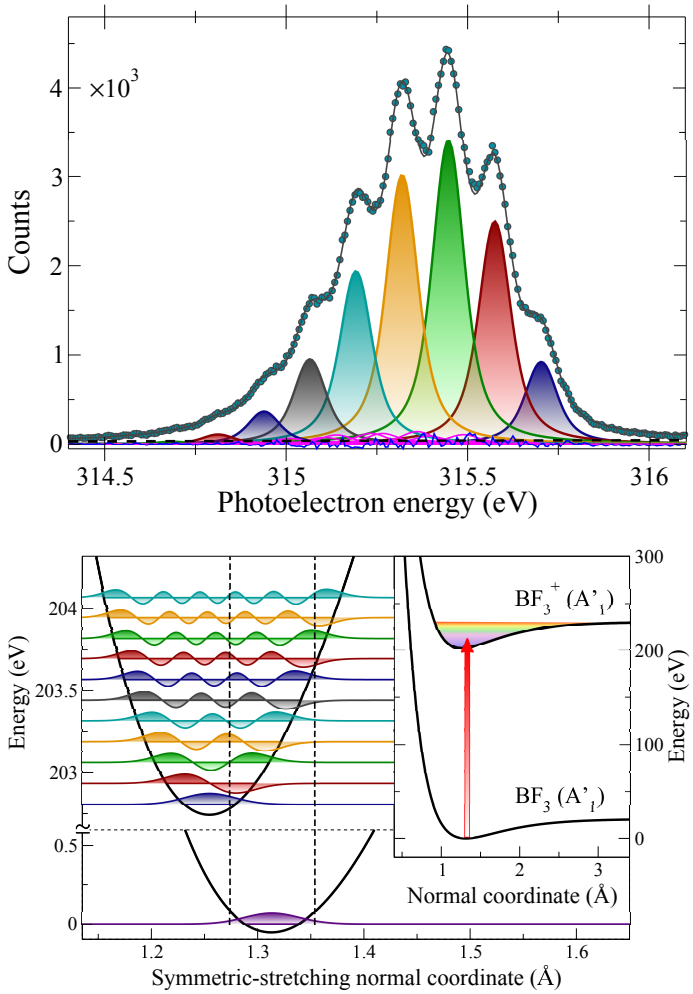

Figure 6.26: (Upper panel) B1s photoelectron spectrum of BF_3 taken at $\omega = 518$ eV. Dots correspond to the measured experimental data [253]. Lines correspond to the fit of the experimental data - Solid dark blue and dark red: deconvoluted symmetric stretching vibrational peaks ($v' = 0$ and 1 respectively), Solid magenta: deconvoluted recoil excited asymmetric vibrational peaks, Dashed black: subtracted background, Solid black: sum of the deconvoluted peaks, Solid blue: residue (difference between the total fitted spectrum and the measured experimental data). (Lower panel) Potential energy curves of the ground states of BF_3 (A'_1) and BF_3^+ (A'_1) along the symmetric-stretching normal coordinate. The vibrational wave functions associated with the relevant vibrational states are also shown. The vertical red arrow indicates a vertical one-photon transition. The vertical dashed lines enclose the Franck-Condon region.

The high vibrational resolution allows the identification of nine vibrational peaks. The most intense one corresponds to the $v = 0 \rightarrow v' = 2$ transition, as predicted by the Franck-Condon principle. The Franck-Condon overlaps can be seen in the lower panel of Figure 6.26. However, the Franck-Condon prediction fails at other energies, such as in the shape resonance energy region (see Figure 6.27). Indeed, at $\omega = 205$ eV, the most populated vibrational state is not $v' = 2$ but $v' = 3$. This Franck-Condon breakdown mediated by the shape resonance shows that the dipole couplings vary significantly with the bond distance.

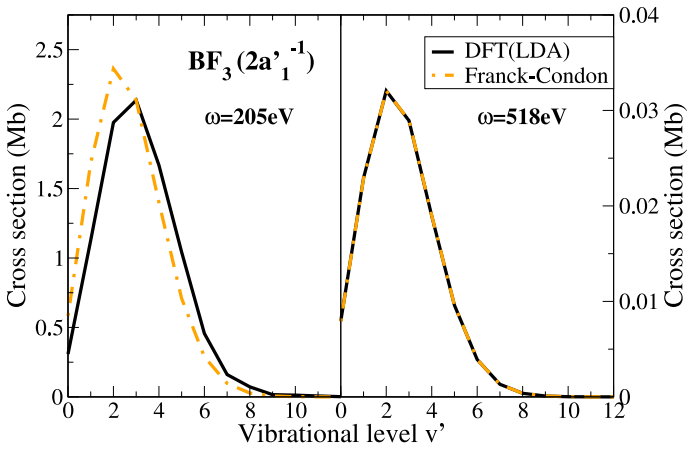

Figure 6.27: B1s photoionization cross section of BF_3 as a function of the vibrational quantum number v' taken at $\omega = 205$ eV (left panel) and $\omega = 518$ eV (right panel). Solid black line: DFT method using a LDA functional. Dashed-dotted orange line: Franck-Condon distribution renormalized to the theoretical maximum.

The redistribution of the vibrational peak intensities in the shape resonance energy region is better seen in Figure 6.28 which shows the vibrationally resolved cross sections for photon energies up to 227 eV (upper panel) and up to 347 eV (lower panel). The shape resonance, located at $\omega = 205$ eV, is very narrow and intense. As expected, it is shifted to lower energies as the vibrational quantum number v' increases. At 205 eV, the Franck-Condon principle is clearly violated because the cross section is not enhanced with the same intensity for the different vibrational components. Above 212 eV, the spectral distribution becomes Franck-Condon's like.

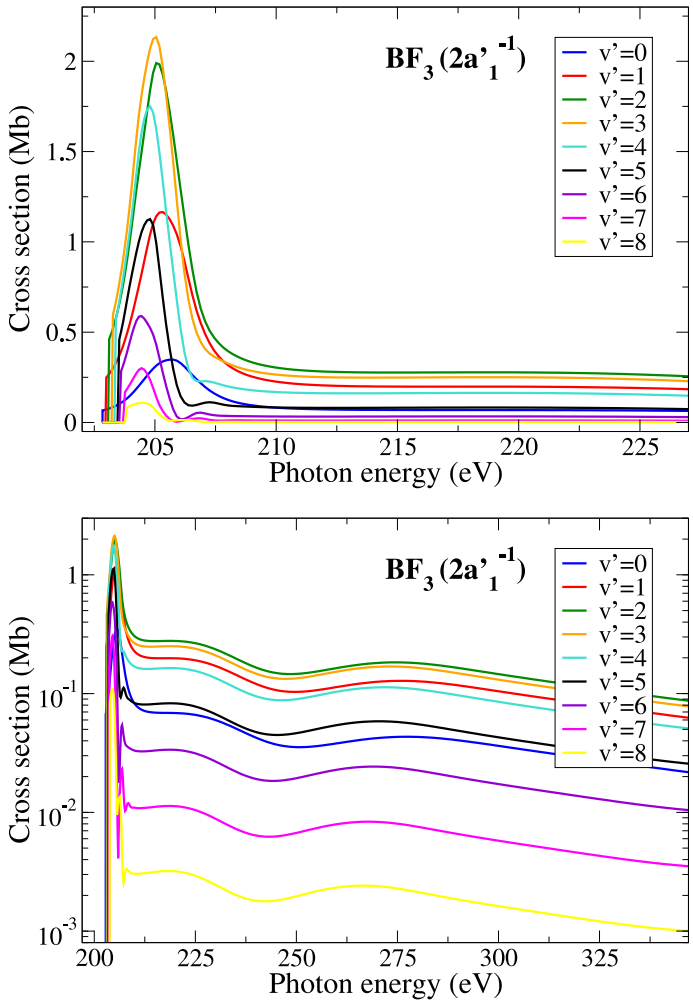

Figure 6.28: Vibrationally resolved cross section for the nine first vibrational levels of the B1s photoionization of BF_3 as a function of the photon energy. Solid lines correspond to the DFT method using a LDA functional.

The first eight theoretical v-ratios (respect to the $v' = 2$) are plotted in Figure 6.29. DFT and TDDFT give equivalent results for the low energy region. This region corresponds to photon energies up to $\sim$ 350eV where the cross section present resonant structures (see Figure 6.28). Above $k_e \sim 3$ a.u. (i.e., $\omega \geq 325$ eV), strong oscillations around the Franck-Condon values are observed. Because the period of oscillation is shorter (T_{k_e} $\sim$1.5 a.u.) than in the case of CF_4 (T_{k_e} $\sim$3.4 a.u.), the oscillations are better characterized. As observed for CH_4, there is a damping of the diffraction effects with the photoelectron momentum. This is due to the fact that high kinetic photoelectrons are escaping so fast that they are hardly diffracted by the fluorine atoms.

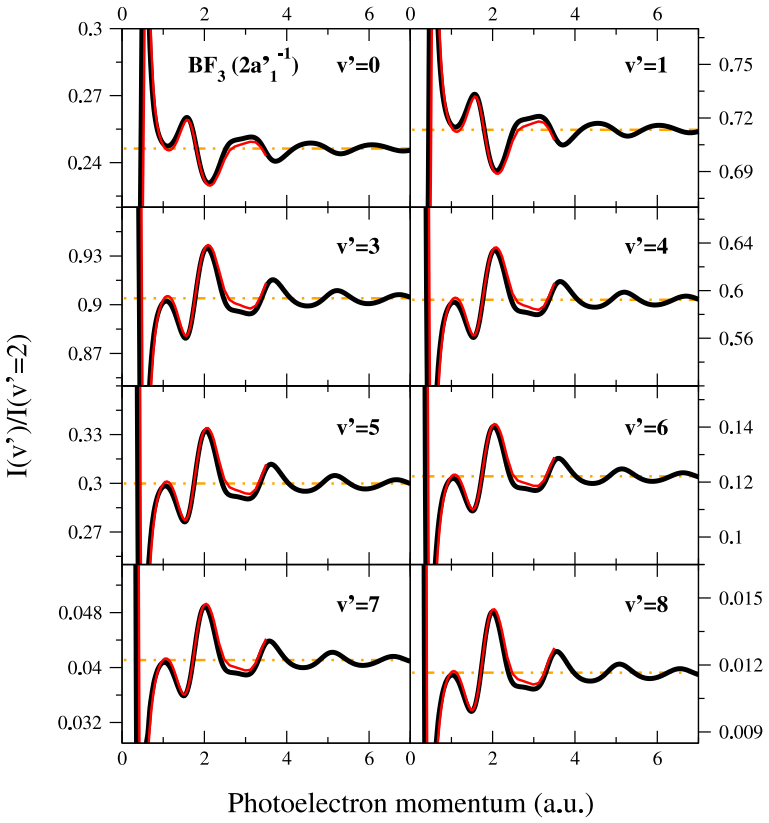

Figure 6.29: Ratios of the vibrationally resolved photoionization spectra to the $v' = 2$ cross section as a function of the photon energy for the B1s photoionization of BF_3. Thick black solid line: DFT method using a LDA functional. Thin red solid line: TDDFT method using a LDA functional. Dashed-dotted orange line: Theoretical Franck-Condon value.

It is remarkable that the v-ratios are all very similar (even for the two first which are just "flipped" compared to the others). It seems that the non-Franck-Condon behavior is the same for all the vibrational transitions, i.e. that the relative vibrational intensities are changing similarly as the photon energy varies. In other words, the envelope of the vibrational spectrum is conserved but is shifted toward higher or lower v', depending on the photon energy (see Figure 6.30). This feature can be used to define a quantity (the *Generalized factor* or "G-factor") that permits to emphasize the general character of the deviation from the Franck-Condon distribution in the photoelectron vibrational spectra.

G-factor

Within the Franck-Condon approximation, the vibrationally-resolved photoionization cross section is related to the total cross section by:

$$\sigma_{v'}(\omega) = \sigma_{Tot}(\omega) F_{v'} \tag{6.31}$$

where $F_{v'}$ is the Franck-Condon factor. Stated, otherwise:

$$\frac{\sigma_{v'}(\omega)}{\sigma_{Tot}(\omega) F_{v'}} = 1 \tag{6.32}$$

If the Franck-Condon approximation breaks down, the right hand side of Equation 6.32 will generally be a function of the vibrational quantum number v' (see Figure 6.30):

$$\frac{\sigma_{v'}(\omega)}{\sigma_{Tot}(\omega) F_{v'}} = 1 + f(v', \omega) \tag{6.33}$$

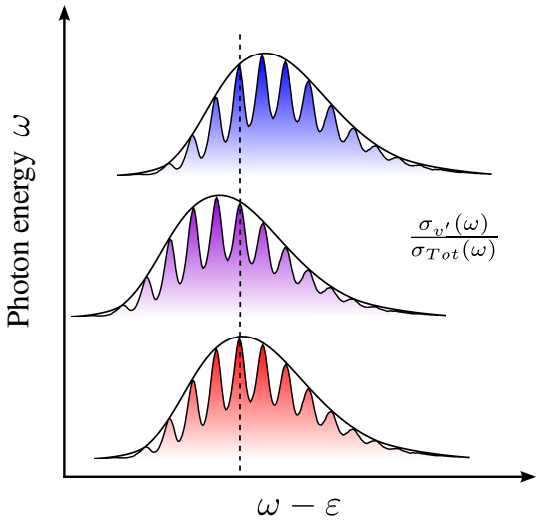

Figure 6.30: Schematic illustration of the evolution of the vibrational envelope with the photon energy.

In the presence of only small deviations, we can conveniently expand the function f in a Taylor series around the averaged vibrational quantum number $\bar{v}' = \sum_{v'} F_{v'} v'$:

$$\frac{\sigma_{v'}(\omega)}{\sigma_{Tot}(\omega) F_{v'}} = 1 + G(\omega) \cdot (v' - \bar{v}') + O[(v' - \bar{v}')^2] \tag{6.34}$$

Truncating the expansion to the first two terms, then the deviation of the vibrationally-resolved branching rations from the Franck-Condon prediction

can be expressed in terms of the single additional parameter $G_{v'}(\omega)$:

$$\frac{\sigma_{v'}(\omega)}{\sigma_{Tot}(\omega)} \simeq F_{v'}\left[1 + (v' - \bar{v}')G_{v'}(\omega)\right] \tag{6.35}$$

One can check the validity of this linearization procedure by verifying the independence from the vibrational number of the residual functions $G_{v'}$, defined as:

$$G_{v'}(\omega) \equiv \frac{f(v',\omega)}{(v' - \bar{v}')} = \frac{1}{v' - \bar{v}'}\left[\frac{1}{F_{v'}}\frac{\sigma_{v'}(\omega)/\sigma_{v'_{ref}}(\omega)}{\sum_{v'}\sigma_{v'}(\omega)/\sigma_{v'_{ref}}(\omega)} - 1\right] \tag{6.36}$$

where v'_{ref} is the final vibrational quantum number of reference in the $\sigma_{v'}(\omega)/\sigma_{v'_{ref}}$ v-ratio.

In the cases that have been examined so far (CH_4, CF_4 and BF_3), $G_{v'}$ is practically independent of v'. This circumstance gives the opportunity of reducing significantly the number of free parameters employed in the fitting of the experimental data, thus improving the statistical significance of the parameters that are extracted. This aspect is particularly crucial for those cases where the breakdown of the Franck-Condon approximation manifests at high photoelectron energies, since the total cross section is very small.

As long as the linear assumption is valid, it is convenient to refer to an averaged G factor, defined as:

$$\bar{G}(\omega) = \sum_{v'} F_{v'}G_{v'}(\omega) \tag{6.37}$$

The averaged factor $\bar{G}(\omega)$ can also be expressed in the suggestive form:

$$\bar{G} = \sum_{v'}\frac{1}{v' - \bar{v}'}\left[\frac{\sigma_{v'}(\omega)/\sigma_{v'_{ref}}(\omega)}{\sum_{v'}\sigma_{v'}(\omega)/\sigma_{v'_{ref}}(\omega)} - \frac{F_{v'}/F_{v'_{ref}}}{\sum_{v'}F_{v'}/F_{v'_{ref}}}\right] \tag{6.38}$$

where we used $\sum_{v'} F_{v'} = 1$.

The averaged G-factor of BF_3 is plotted in Figure 6.31 for photoelectron momenta up to 5.2 a.u.. The agreement between experiment and theory is very good. Compared to CF_4, the statistics of the experimental measurement is sufficient to observe the oscillating pattern. These oscillations have the same modulated period and amplitude than the DFT curve. However, the peculiar plateau described by the DFT calculation at $\sim$ 2.8 a.u. is not reproduced. The experimental $\bar{G}$ values are higher than the theoretical ones for $k_e \geq 3$. Although the recoil effect has been in principle removed from the experimental measurement, there may be a small contamination for the highest symmetric

vibrational peaks. The simple model is in very good agreement with the full *ab initio* method and the experimental results above $k_e \sim 3$ a.u. (in the energy region where it is expected to work). It confirms that the period of oscillation is approximately 1.5 a.u. in this energy region and shows that the predominant non-Franck-Condon effect at high photon energies is due to the diffraction of the photoelectron by the fluorine atoms.

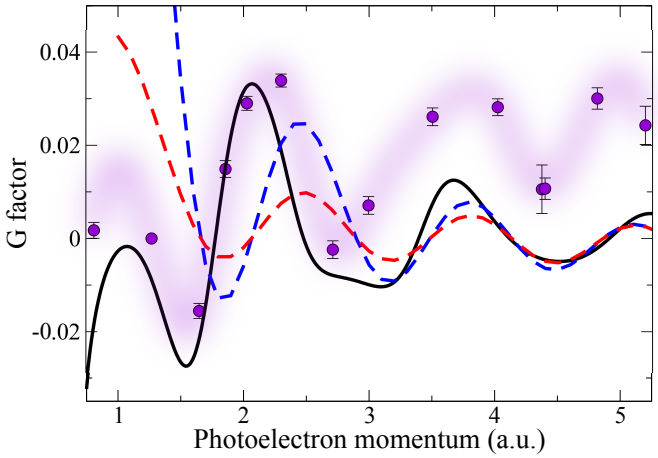

Figure 6.31: G-factor for the B1s photoionization of BF_3 as a function of the photoelectron momentum. Violet circles: experimental data from [253] including the statistical and systematic errors. Black solid line: results of the DFT method using a LDA functional. Red dashed line: results of the simple mode. Blue dashed line: results of the simple model obtained by excluding the scattering of the ejected electron by the central B atom.

The G-factor can also be used to compare the Franck-Condon deviations in the photoionization of different molecular targets. Figure 6.32 shows the G-factors associated with the C1s photoionization of CF_4 (results presented in Section 6.4.4), the B1s photoionization of BF_3 (present results) and the S1s photoionization of SF_6 (results not detailed in this work). As discussed previously, shape resonances are responsible for most of the structures observed in the low energy region (for photoelectron momenta below 1.2 a.u.). Above, it can be noticed that the resonant structures in the CF_4 and SF_6 G-factor are much stronger than in CH_4 of BF_3 and appear in the same momentum region (between 1.85 and 2 a.u., i.e. for photoelectron energies $46.5 \leq \varepsilon \leq 54.5$ eV). Above this energy, the CF_4 and SF_6 G-factors seem to oscillate in phase. The CH_4 and BF_3 G-factors have shorter periods of oscillation. It was expected that the CH_4 G-factor has a larger period of oscillation since the bond length (that governs the diffraction pattern) is the smallest one. However, the phase match between CF_4 and SF_6 as well as the mismatch with BF_3 contradicts

this simple picture. Indeed, while the bond length of CF_4 and BF_3 are almost the same ($\sim$ 1.31Å), the SF_6 bond length is much larger ($\sim$ 1.58Å). Explanation to this apparent contradiction can be found in the different geometry changes upon ejection of the core electron. Since the equilibrium geometry of the CF_4 ground and core ionized states are very close, the nuclear wavepacket probes a region of the space that is centered on the equilibrium bond length of the ground state. As a consequence, the period of the oscillations in the CF_4 G-factor is approximately $T_{k_e} \sim \pi/R_{eq} \sim 1.27$ a.u. (R_{eq} being the bond length of the ground state at the equilibrium). However, due to an important contraction of the core ionized bond length in BF_3 and to the relaxation of the core ionized bond length in SF_6, the other G-factors present oscillations whose period is slightly different from the one predicted using the equilibrium bond length of the ground state. Finally, it can be noticed that contrary to all the other G-factors, SF_6 presents a more complex oscillating pattern at high energies. The oscillations are not totally regular and seems to result from the superimposition of two oscillating patterns.

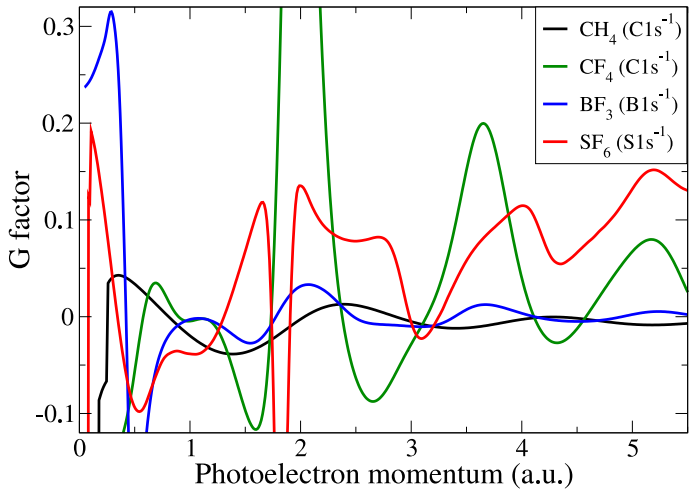

Figure 6.32: Theoretical G-factors as a function of the photoelectron momentum for the core photoionization of several molecules. Lines correspond to results of the DFT method using a LDA functional, except for the $SF_6(1a_{1g}^{-1})$ which made use of the LB94 functional. The latter result is not detailed in this work but has been compared successfully with experimental data at low photon energy.

6.6 Sulfur hexafluoride

So far in this work, we have studied the photoionization of polyatomic molecules only from the core. As shown, the photoemission of an electron from a localized orbital around the central atom can lead to complex structures even at high photoelectron energies, especially when the molecule possesses peripheral fluorine atoms. However, core shell photoionization is somehow a simpler process compared to valence shell photoionization. As shown in the present study for the valence shell photoionization of N_2 and CO (see Section 5.3.2), the delocalized character of the initial orbital reflects in the photoionization cross section. Also, and contrary to the core photoionization, possible mixing with other photoionization channels can occur. From a theoretical point of view, treating the valence shell photoionization of polyatomic molecules represents an additional difficulty as it makes harder the development of simple models such as the one presented all along this study. For a complex molecule as SF_6, the difficulty is such that very few theoretical methods can be used to describe the valence shell photoelectron spectra: the multiple scattering method [87], the Stieltjes imaging technique method in the static-exchange approach [439] and the present method [365, 364, 390]. All these calculations have been performed in the fixed nuclei approximation because inclusion of the nuclear motion represents a considerable computational effort. In fact, the numerous resulting theoretical works published on the core shell photoionization spectra [82, 429, 268, 365, 80] illustrates this difficulty to treat theoretically the valence photoionization process. Experimentally, it is the other way around since the study of the core shell photoionization require higher photon energies and better energetic resolution than for the valence shell photoionization.

There exist interesting applications that uses SF_6. In most of the cases, this molecule is employed as an electron trapper in ionization experiments because it readily forms the negative ion SF_6^-. Since the fluorine atoms are very electronegative, an electron can be easily caught to form a stable anion against autodetachment and photodetachment. Photoionization of neutral SF_6 is interesting because the outer valence photoelectron spectra exhibit pronounced structures. By outer valence shell we refer to the generally accepted series of MOs: $(5a_{1g}^2)$ $(4t_{1u}^6)$ $(1t_{2g}^6)$ $(3e_g^4)$ $(1t_{2u}^6)$ $(5t_{1u}^6)$ $(1t_{1g}^6)$. Photoionization from each of these MO yields to seven spectroscopic bands. The six first are presented in the photoelectron spectrum in Figure 6.34. As observed, the $1T_{2u}$ and $5T_{1u}$ MOs are nearly degenerate and the three first bands are structureless even under high resolution experimental conditions. The C^2E_g band presents a complex vibrational structure whose progression (flat on the top) seems to indicate a splitting of the doubly degenerate state by Jahn-Teller interactions. The fine structure of the D^2T_{2g} and E^2T_{1u} bands are well resolved, although the former one is structured only in the low energy part. In both cases, the totally symmetric stretching mode is responsible for the vibrational progres-

sion. The peaks of the E^2T_{1u} band are possibly broadened by predisociation since threshold for SF_3^{3+} formation has been measured at the adiabatic IP of the E^2T_{1u} state.

6.6.1 Electronic structure

Table 6.3 reports the experimental and theoretical vertical ionization energies for SF_6. Although the DFT calculation inverts the order of the $1t_{2u}$ and $5t_{1u}$ MOs which are quasi-degenerated, the sequence of MOs is correctly described. With the LB94 exchange-correlation functional and the DZP basis set employed for the calculation, some energy differences are notable, from a typical overestimation of ~ 1.5 eV for the outer valence MOs to an underestimation of 33 eV for the deepest orbital. For the MO of concern in the present study (the $4t_{1u}$), the DFT calculation is in a rather good agreement with the experimental value.

Inner shell	$1a_{1g}^2$ (S1s)	$2a_{1g}^2$ (F1s)	$1t_{1u}^6$ (F1s)	$1e_g^4$ (F1s)
Exp. [184]	-2490.10	-695.04	-695.04	-695.04
DFT (LB94)	-2457.10	-692.33	-692.33	-692.33

Inner shell	$3a_{1g}^2$ (S2s)	$2t_{1u}^6$ (S1p)
Exp. [184]	-244.7	-180.67
DFT (LB94)	-235.78	182.09

Inner valence	$4a_{1g}^2$	$3t_{1u}^6$	$2e_g^4$
Exp. [184]	-44.1	-40.9	-39.8
DFT (LB94)	-42.11	-39.13	-37.92

Outer valence	$5a_{1g}^2$	$4t_{1u}^6$	$1t_{2g}^6$
Exp. [164]	-26.8	-22.5	-19.7
DFT (LB94)	-27.43	-23.52	-20.60

Outer valence	$3e_g^4$	$1t_{2u}^6$	$5t_{1u}^6$	$1t_{1g}^6$
Exp. [164]	-18.3	-16.9	-17.2	-15.7
DFT (LB94)	-20.31	-18.36	-18.52	-17.40

Table 6.3: Comparison between experimental and theoretical vertical ionization energies (in eV) for SF_6. Theoretical results are obtained using a LB94 exchange-correlation functional and a DZP basis set at S-F$\sim$ 1.586 Å (no geometry optimization).

6.6.2 Vibrational structure

The potential energy curve chosen for the ground state is an harmonic potential taken from the literature. The one used for the $4t_{1u}^{-1}$ ionized state has been obtained using experimental values [164] for the harmonic and anharmonic Morse parameters. The geometry change has been taken from the DFT calculation using a LB94 functional. The fundamental vibrational frequencies of the different normal modes have been calculated at the Hartree-Fock *ab initio* level with a 6-311G(d)+p basis set: $\omega_1(a_{1g}) = 835.831$ cm^{-1}, $\omega_2(e_g) = 658.346$ cm^{-1}, $\omega_3(t_{1g}) = 702.391$ cm^{-1}, $\omega_4(t_{1u}) = 1051.865$ cm^{-1}, $\omega_5(t_{2g}) = 563.563$ cm^{-1}, and $\omega_6(t_{2u}) = 379.738$ cm^{-1}.

6.6.3 Total cross section

Many investigations (mostly experimental) have been carried out for inner [82, 120, 174, 429, 268, 269, 365, 297, 80], inner-valence [439, 441, 196] and valence [87, 134, 7, 168, 164, 443, 439, 365, 364, 390] photoabsorption/photoionization of SF_6. This particular interest stems from the existence of strong resonant features dominating the Rydberg transitions. Dehmer *et al.* [82, 87] interpreted this unexpected intensity distribution through the cage-like property of SF_6, in which the molecular potential partitions the states into either inner-well or outer-well states near the electronegative ligands. The Rydberg orbitals are believed to reside in the outer-well, relatively far from the atomic centers while virtual orbitals are located in the inner-well and can efficiently overlap with the initial state. This former interpretation in SF_6 has been in fact a pioneer work which led, two years later, to a more general description of shape resonances in molecules [94]. Some of the inner-well virtual states can lie above the ionization threshold and form quasi-bound resonant states. It has been pointed out in [257] that four unoccupied MOs exist below the upper limit of the potential barrier. They have been identified and assigned to the following energy values: $6a_{1g}^0$ at $\sim -5.55 \pm 0.15$ eV, $6t_{1u}^0$ at $\sim -4.1 \pm 0.3$ eV, $2t_{2g}^0$ at $\sim +5.4 \pm 0.2$ eV (or +5.2 eV in [164]) and $4e_g^0$ at $\sim +15.8 \pm 1.8$ eV (or +15.5 eV in [164]). The energies of the two highest MOs coincide with the resonant structure observed in the total $4t_{1u}^{-1}$ photoionization cross section plotted in Figure 6.33. Although the DFT calculation poorly describe the ionization threshold, a comparison with experimental data permits to assign the sharp structures at 29 eV and 40 eV to shape resonances involving intravalence transitions to the $2t_{2g}$ and $4e_g$ MOs respectively. These resonant structures appear in each photoionization channel at around the same photoelectron kinetic energy positions, but their shape vary according to the final molecular symmetry. The sharpest shape resonant structures appear in the T_{1u} and T_{2u} bands, i.e. the A, B and particularly the E (the one studied in this Section). The sharpness of the shape resonances indicates that trapping of the d-wave electron inside the cage is very effective but only on a limited region of the

photoelectron kinetic energy. This can be seen in Figure 6.33 which shows the total cross section associated with the $4t_{1u}^{-1}$ photoionization of SF_6 for photon energies up to 130 eV. Experiment, DFT and multiple scattering methods describe two resonant structures below 60 eV. The second, associated with the $4e_g$ MO, is weaker but consequently broader than the first one. The TDDFT result is also presented and gives rise to additional structures around 40 eV that are however not resolved experimentally.

In 1995, Holland *et al.* [164] measured the outer valence spectra of SF_6 with high accuracy. By comparing the total photoionization cross sections, the branching ratios and the asymmetry parameters for the six first outer valence bands ($^2T_{1u}$ and $^2T_{2u}$ are not resolved), this work showed that shape resonances associated with $2t_{2g}$ and $4e_g$ virtual MOs are visible in all the photoionization channels and leave their signature in the asymmetry parameter plots. It confirmed previous experimental observations in [87, 7] where shape resonances were also found in the $1t_{2g}^{-1}$ and $3e_g^{-1}$ photoionization channels. However, according to the dipole selection rules within the single particle approximation, only the MOs whose symmetry is ungerade should overlap constructively with the $2t_{2g}$ and $4e_g$ unoccupied valence states. Existence of shape resonances in the gerade photoionization channels historically found three explanations: i) In [124], Fock *et al.* suggested for the first time that the t_{1u} shape resonance could lie above the ionization threshold in the case of valence shell excitation. Since the valence shell ionized potentials are slightly different from the core ionized ones, it may globally shift the inner well virtual MOs of a few eV towards higher energies. Then, the structures observed near threshold in the gerade symmetry state photoionizations could be attributed to shape resonance associated with the $6t_{1u}$ MO. This resonance has been estimated theoretically at ~ 2.05 eV above the threshold in [7]. ii) Another interpretation, supported by [87], consider that interchannel couplings are responsible for the resonant structure. A possible mechanism [366] is that continuum-continuum couplings, normally weak compared to ground-state-continuum couplings, transfer the shape resonant behavior into the gerade symmetries. Hence, shape resonances appearing in the $1t_{1g}^{-1}$, $1t_{2g}^{-1}$ and $3e_g^{-1}$ photoionization channels could still be associated with the $2t_{2g}$ and $4e_g$ MOs. iii) Interchannel couplings involving discrete-continuum states transitions can also enhance shape resonances by coupling the gerade $\rightarrow 6t_{1u}$, $6a_{1g}$ transitions with the ungerade $\rightarrow 2t_{2g}$, $4e_g$ ones. Whatever the interpretation is, observation of shape resonances in all the valence photoionization channels shows the complexity of the process compared to the core shell photoionization. This complexity is such that most of the articles published on the topic conclude on the necessity of a "theoretical guidance" that can be achieved by performing accurate calculations (including interchannel couplings) for an extended energy range. The experiment of Holland *et al.* [164] also revealed an unexpected broad variation in the overall photoionization cross section around

60 eV photoelectron kinetic energy. The energy position of such structure is much higher than the predicted shape resonance region. This smooth variation is observed in all the outer-valence photoionization channels and is particularly strong in the $4t_{1u}^{-1}$ photoionization cross section (see Figure 6.33). Such feature is reproduced by both DFT and multiple-scattering method, proving that it is indeed due to a potential effect. This feature originates from the $4t_{1u} \rightarrow \varepsilon t_{1g}$ channel. In [365], Stener *et al.* ascribed it to a strong centrifugal barrier generated by the high angular momentum of the photoelectron ($l = 4$ at this kinetic energy). The same study present a comparison between the β asymmetry parameters obtained from TIDFT and TDDFT calculations using a LB94 in the fixed nuclei approximation and experimental data. The three above mentioned resonances are clearly observed in the $4t_{1u}^{-1}$ photoionization channel. The TDDFT gives rise to additional peaks (also observed in the total cross section - see Figure 6.33) which are not resolved experimentally. In general, comparison between TIDFT and TDDFT results confirms that inclusion of the response effects improves significantly the agreement with the experiment only for the C^2E_g band where interchannel couplings and autoionization plays an important role.

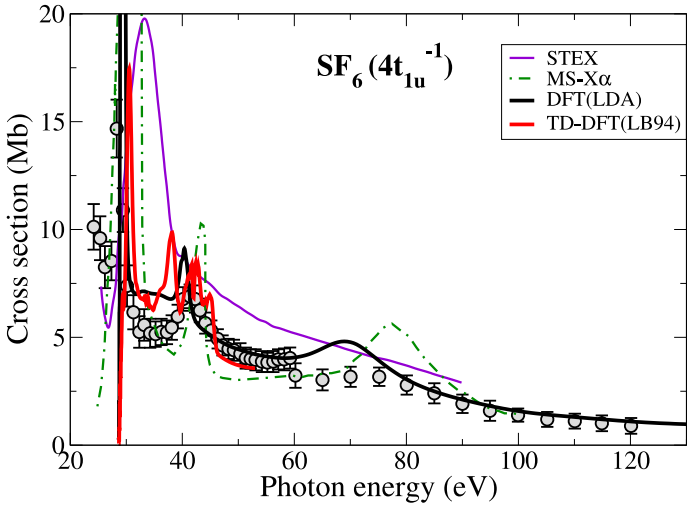

Figure 6.33: Total cross section for the $4t_{1u}^{-1}$ photoionization of SF_6 as a function of the photon energy. Circles correspond to experimental data from [164] ; Lines correspond to theory - Violet solid: direct static exchange technique (STEX) [439], Green dashed: multiple scattering Xα method (MS-Xα) [7], Black thick solid: DFT method using a LDA functional (this work), Red Thick line: TDDFT method using a LDA functional (this work).

6.6.4 Vibrationally resolved cross section

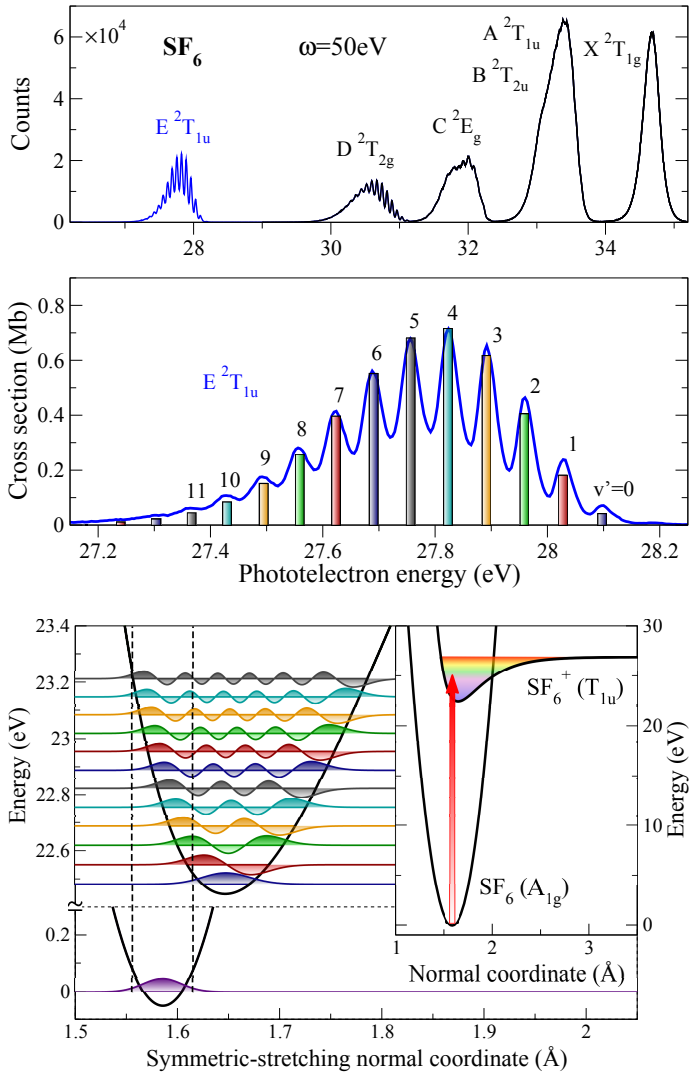

Figure 6.34: (Upper panel) Valence photoelectron spectrum of SF_6 taken at $\omega = 50$ eV. Lines: measured experimental data [46]. (Middle panel) Enlargement of the fifth band ($4t_{1u}^{-1}$ photoionization channel). Bars: theoretical results obtained with the DFT method using a LB94 functional. Peak numbers indicate the vibrational quantum number v' of SF_6^+. (Lower panel) PECs of the ground states of SF_6 (A_{1g}) and SF_6^+ (T_{1u}) along the symmetric-stretching normal coordinate. The vibrational wavefunctions associated with the relevant states are also shown. The vertical red arrow indicates a vertical one-photon transition. The vertical dashed lines enclose the Franck-Condon region.

Because the electron is emitted from a bonding valence MO, the S-F bond length elongates upon photoionization. The geometry change ($\sim$ 6.1 pm) is approximately the same (in absolute value) than for BF_3. For this reason, the $4t_{1u}^{-1}$ photoelectron spectrum of SF_6 presents also an extended vibrational progression, even a bit larger since the reduced mass of SF_6 is bigger. The middle panel of Figure 6.34 shows the experimental photoelectron spectrum of the E $^2T_{1u}$ band taken at a photon energy of 50 eV. One can distinguish a very weak peak at 28.18 eV, attributed to an initial excitation of the Jahn-Teller active mode E_g. The first symmetric vibrational peak $v' = 0$ is located $\sim$ 85 meV lower in energy. The energy difference with the following peak $v' = 1$ is about 67 meV, i.e. $\sim$540 cm^{-1} which is in good agreement with the harmonic frequency of 562.5 cm^{-1} given by [164]. In [164], Holland *et al.* also performed a least-square fitting of the vibrational energies and give an estimate of 2.2583 cm^{-1} for the first order anharmonic term. As expected, it is a rather small value compared to the above mentioned harmonic frequency. Theoretical intensities (the bars) obtained with the DFT method using a LB94 functional are also reported in the figure and present a very good agreement with the experiment. Both experiment and theory agree with the Franck-Condon principle (illustrated in the lower panel) which predicts that the maximum intensity is associated with the $v = 0 \rightarrow v' = 4$ vibrational transition. But as for BF_3, this agreement is local and observation of the vibrational intensity distribution at different photon energies (as shown in Figure 6.35) shows breakdown of the Franck-Condon principle.

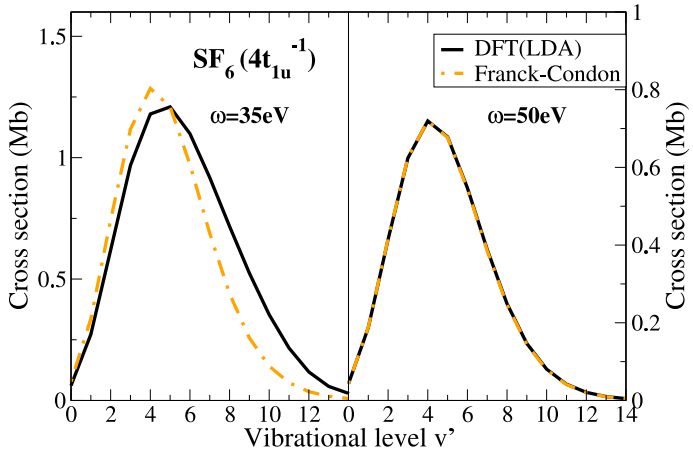

Figure 6.35: $4t_{1u}^{-1}$ photoionization cross section of SF_6 as a function of the vibrational quantum number v' taken at ω = 35 eV (left panel) and ω = 50 eV (right panel). Solid black line: DFT method using a LB94 functional. Dashed-dotted orange line: Franck-Condon distribution renormalized to the theoretical maximum.

Figure 6.36 shows the vibrationally resolved cross section for two photon energy ranges: up to ∼47 eV (upper panel) and up to ∼89 eV (lower panel). In Figure 6.36a, the two shape resonances are clearly visible for all the vibrational components. Many crossings between each vibrational component occur in these energy regions ($23 \leq \omega \leq\sim 25$ eV and $32.8 \leq \omega \leq\sim 36.6$ eV). It shows a strong dependence on the vibronic couplings and a general breakdown of the Franck-Condon principle.

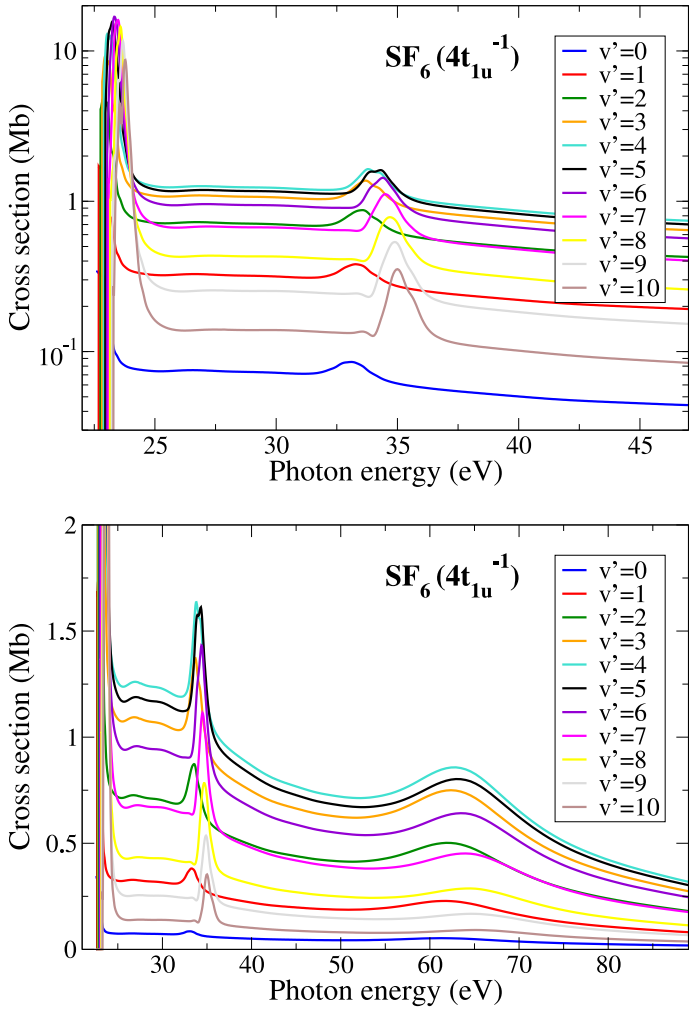

Figure 6.36: Vibrationally resolved cross section for the eleven first vibrational levels of the $4t_{1u}^{-1}$ photoionization of SF_6 as a function of the photon energy. Solid lines correspond to the DFT method using a LB94 functional.

The two above mentioned resonant structures appear in both vibrational components and are shifted to higher photon energies when v' increases. It reflects the relaxation of the bond length associated with the ionization of a valence bonding MO. The bump observed at $\sim$ 65 eV in the total cross section is also present in all the vibrational components and induces a Franck-Condon violation visible in the overlap between $v' = 2$ and $v' = 7$ components.

As for BF_3, it is convenient to analyze the deviations to the Franck-Condon behavior by looking at the G-factor. Figure 6.37 shows the averaged G-factor corresponding to the $4t_{1u}^{-1}$ photoionization of SF_6 for photon energies up to 100 eV. Strong deviations to the Franck-Condon prediction are observed in this energy range. The two structures previously attributed to shape resonances are neatly observed in both experiment and theory at $\sim$ 29 eV and $\sim$ 40 eV. The smooth variation at $\sim$ 65 eV is well observed in the theoretical G-factor (even better than in the absolute cross section). It agrees with a similar variation of the experimental G-factor at the same energy. Unfortunately, the experimental statistic is too spread in this energy region to unambiguously identify it.

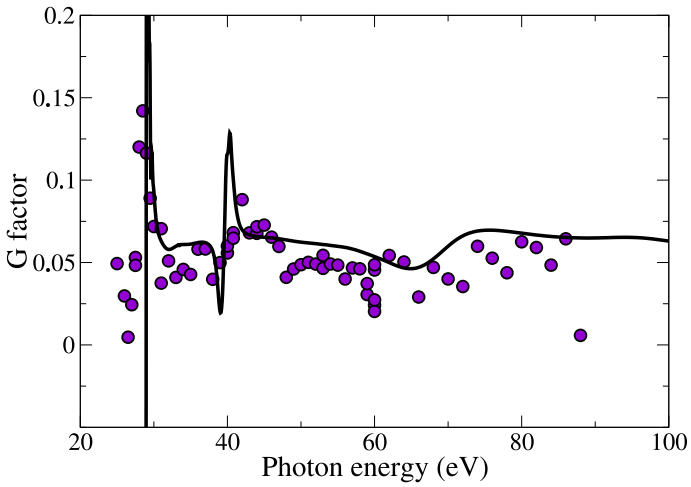

Figure 6.37: G-factor for the $4t_{1u}^{-1}$ photoionization of SF_6 as a function of the photoelectron momentum. Violet circles: experimental data from [46]. Black solid line: results of the DFT method using a LB94 functional.

Figure 6.38 shows the theoretical averaged G-factor presented in Figure 6.37 as a function of the photoelectron momentum. It is plotted for an extended momentum range, up to 9 a.u. (i.e., for photon energies up to ∼3590 eV). Important deviations to the Franck-Condon prediction are observed at high momenta. These deviations seem to result from the superposition of different oscillating patterns. In this photoionization channel, the electron is emitted from a bonding valence MO which is rather delocalized (see Figure 6.39). If the presence of fluorine atoms do not alter too much the process, multi-center interferences are then expected to show up at high photon energies and could be responsible for some oscillations. In Figure 6.38, it is possible to identify two different period of oscillations. One is shown in the enclosed graphic which correspond to an enlargement of the main figure in the $1.5 \leq k_e \leq 3$ a.u. region. The period is very short ($T_{k_e} \sim 0.335$ a.u.) which could correspond to interferences between centers separated by ($\sim 2\pi/T_{k_e} \sim 18.76$ a.u. ~ 9.92 Å). This separation is more than three times the maximum F-F distance (= 3.172 Å). It is then difficult to attribute these short oscillations to two-center's like interferences. However, there is another identifiable oscillating pattern whose period is about ~ 1.3 a.u.. It would corresponds to a distance of ~ 4.84 a.u. ~ 2.56 Å, much closer to the F-S-F distance.

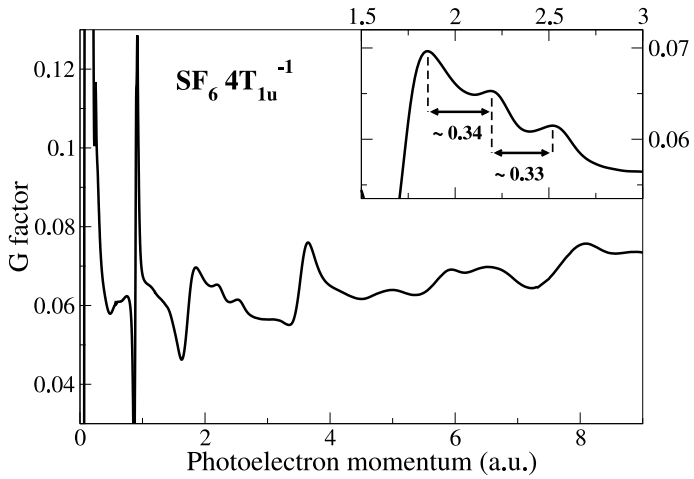

Figure 6.38: Same as Figure 6.37.

Emitter centers that could be responsible for interferences in the photoionization process are presented in Figure 6.39. The two centers separated by ∼ 4.4 a.u. could be at the origin of the second oscillating pattern. Although we discuss the interferences in terms of two-center interferences, these interferences obviously involve all possible centers. A better description would be obtained by extending the model developed in Section 6.1.2 for six centers

(the ones that correspond to the two external lobes on each F-S-F direction).

As shown in Figure 6.39, the electronic distribution is concentrated around four centers in each component of the degenerated $4t_{1u}$ MO. This four lobes have an alternative negative (blue) and positive (red) contribution to the wave-function.

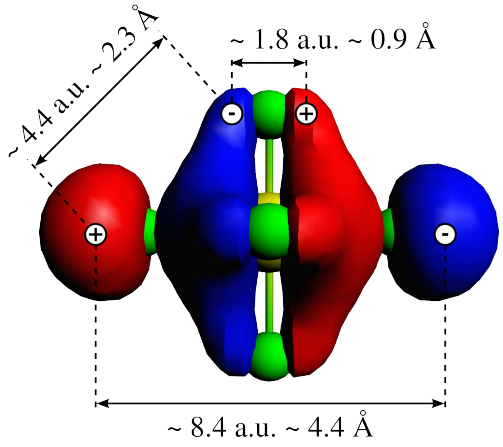

Figure 6.39: Representation of the $4t_{1u}$ molecular orbital of SF_6.

Conclusions

In this work, we have presented a detailed description of a theoretical method based on density functional theory specially designed to obtain vibrationally resolved photoionization cross sections of simple molecules within the Born-Oppenheimer approximation. The method has been successfully applied to N_2, CO, C_2H_2, CH_4, CF_4, BF_3 and SF_6 in a wide range of photon energies. All along the study, comparison with experimental data permits to observe several deviations from the Franck-Condon principle at low and high energies. The origin of these deviations have been attributed to:

- doubly excited states
- shake-up satellites
- autoionization of singly excited states
- shape resonances
- recoil effects
- two-center interferences
- intramolecular scattering

Apart from the doubly excited states and the shake-up satellites, all the effects have been taken into account at the present level of theory. Moreover, the use of simple models have permitted us to understand and characterize the deviations appearing at high energies: the recoil effect, the two-center interferences and the intramolecular scattering.

The first part of the results have been essentially devoted to discuss the efficiency of the multicenter B-spline static-exchange DFT method by studying N_2 and CO, two prototype molecules for which there exists an abundant literature. This discussion has been carried out by comparing systematically the results obtained with the present method with available theoretical results and experimental data.

At high photon energies, static-exchange-DFT and TDDFT lead to almost identical results in good agreement with experiment for both vibrationally and

non-vibrationally resolved photoelectron spectra, while, at low photon energies, TDDFT is able to describe features observed near the ionization threshold but not arising from static-exchange-DFT, such as singly-excited Feshbach resonances and structures resulting from interchannel coupling. TDDFT also provides a better description of shape resonances. Very often, this description is of similar quality as that obtained from more elaborate multireference or close coupling methods, which are prohibitively expensive to obtain vibrationally resolved photoelectron spectra in complex molecules. It is also a bit more accurate than that provided by RPA methods, whose computational cost is similar but whose accuracy often relies on the introduction of fitting parameters.

We have paid a particular attention to the region of high photon energies, where the electron wavelength is comparable to the bond length and, therefore, two-center interferences and diffraction are expected to occur. In this region, the main experimental difficulty is to extract the relatively small interference and diffraction features from the rapidly decreasing cross section as a function of photon energy. However, this difficulty can be easily overcome by determining ratios of vibrationally resolved photoelectron spectra. The results unambiguously demonstrate the existence of Cohen-Fano interferences in vibrationally-resolved valence-shell photoionization of homo- and heteronuclear diatomic molecules. They lead to marked oscillations in the ratios between vibrationally resolved cross sections. The oscillations are well reproduced by a straightforward extension of the original Cohen-Fano formula and by state-of-the-art calculations. Based on these combined experimental and theoretical results, several aspects of the CF interferences have been uncovered and clarified for the first time.

Vibrationally resolved photoelectron angular distributions from randomly oriented and fixed-in-space N_2 and CO molecules has also been evaluated. Both K-shell and valence-shell photoionization have been considered. The results for randomly oriented molecules are in excellent agreement with experiment, while the absence of experimental data for fixed-in-space molecules at high photon energies gives our results a predictive value. Vibrationally resolved β parameters do not depend very much on the chosen vibrational level, except for the HOMO ionization channel, for which the higher the final vibrational state the lower the value of β. For fixed-in-space N_2 molecules, the MFPADs exhibit the signature of electron confinement and coherent two-center interferences, similar to what has been found in H_2 photoionization [118, 117]. For fixed-in-space CO, they exhibit diffraction patterns resulting from the intramolecular scattering of an electron arising from a very localized area of the molecule. The conclusions reported in this work suggest that vibrationally resolved photoelectron angular distributions can also be used to determine the structure of these simple molecules.

The study has been extended to the case of polyatomic molecules, starting with C_2H_2. We have seen that vibrationally resolved C 1s photoelectron spectra of acetylene obtained with 3rd generation synchrotron radiation exhibit Cohen-Fano interferences similar to those previously reported in diatomic molecules. The oscillations are unambiguously observed in both the v and g/u ratios, for which no correction/adjustment for the rapidly decreasing cross section is required. Results obtained with the present method are in excellent agreement with the experimental measurements. The predictions of experiment and theory are further supported by a simple model that basically follows the premises of the original Cohen-Fano model developed for H_2^+. Although no quantitative agreement with either the experiment or the first-principles calculations is found, the qualitative features of the oscillations are correctly described: the overall period of the oscillations, the fact that the v'=1/v'=0 ratio for the gerade and ungerade case are in phase opposition, and the fact that there is no discernible influence by the nearby hydrogen atoms. These results constitute the first evidence of Cohen-Fano interferences ever observed in a polyatomic molecule. It confirms also the delocalized character of the core-hole created in the primary photoionization event and demonstrate that intramolecular core-hole coherence can survive the decoherent influence associated to the asymmetric nuclear degrees of freedom that are characteristic of polyatomic molecules.

As shown in the study of N_2, CO and C_2H_2, two competing processes can lead to interferences during photoionization. One is the simultaneous emergence of the electron wave from the two centers of the molecule. The other, is the scattering of the electron by the other atomic center. We have seen that, according to the extended Cohen-Fano formula, coherent emission from two atomic centers is no longer possible in the absence of electron delocalization. This occurs in K-shell photoionization of CO since the inner 1σ and 2σ molecular orbitals are almost entirely localized on the O and C atoms, respectively, and resemble the corresponding 1s atomic orbitals. A similar situation occurs in some polyatomic molecules such as CH_4, CF_4 and BF_3, where the 1s orbital of the central atom is well localized. The present study of the high-energy photoionization of CH_4, CF_4 and BF_3 from the 1s orbital of the central atom gave unambiguous experimental and theoretical evidence of intramolecular photoelectron scattering in the collective vibrational excitation. We have shown that the v-ratios exhibit pronounced oscillations as a function of photon energy, which is the fingerprint of electron diffraction by the surrounding atomic centers. This interpretation is supported by the excellent agreement between first-principles static-exchange and time-dependent density functional theory calculations and high-energy resolution measurements, as well as by qualitative agreement at high energies with a first-Born approximation model. The latter model allowed us to rationalize the results for all the v-ratios in terms

of a G-factor which contains the imprint of the molecular geometry.

In the case of CH_4, vibrationally resolved angular distributions in the laboratory and molecular frames have also been presented. Due to the small electronic density of the hydrogen atoms, intramolecular scattering effects are barely observed in the β asymmetry parameter which has essentially an atomic character for all the vibrational components. The MFPADs are more sensitive to such effects and showed very clearly the resulting constructive and destructive interferences at different energies.

The last case presented in this work concerned the photoionization of SF_6 from an outer valence orbital. Both experimental and theoretical results showed very strong deviations to the Franck-Condon distribution at low energies. The study of the theoretical G-factor at high energies reveals a very complex pattern which seems to result from the superimposition of different interference fingerprints. One of the identified oscillation pattern possibly arises from the interferences between the coherent emission from two or more centers.

In a more general aspect, from all the presented results, it can be concluded that vibrationally resolved photoelectron spectroscopy can be used to determine the structure of molecules. In this respect, an approach that is worth to explore is to extract structure parameters by fitting the experimental data to theoretical results by varying the shape of the Morse potentials.

Some improvements of the present theoretical methods are also necessary to fully account for the experimental observations in polyatomic molecules. Indeed, experimental observation of excitations to forbidden vibrational modes have been ascribed to non-Born-Oppenheimer effects and implies going beyond the Born-Oppenheimer approximation. In addition, it would be desirable to extend the present formalism to the time domain by solving, e.g., the time-dependent Schrödinger equation in a basis of Kohn-Sham orbitals. This would allows one to study the electron dynamics during the photoionization process. One interesting application would be the investigation of the ultrafast migration of core-holes, which has attracted considerable interest in the recent years. Future theoretical developments should focus on solving these problems in order to improve the performance of present DFT-like methods since these are currently the only ones able to provide vibrationally resolved information all the way from diatomics to large, symmetric molecules.

A. Theory

A.1 Elements of group theory

All molecules can be categorized according to their spatial symmetry group, i.e., the set of isometries that map equivalent nuclei onto each other. These may comprise, beyond the identity E: rotations of order n C_n, reflections σ, and rotoreflections S_n. The most common point groups for molecules are listed in Table A.1.

Nonaxial	C_n	C_{nv}	C_{nh}	D_n	D_{nh}	D_{nd}	S_n	Higher	Linear
C_1	C_2	C_{2v}	C_{2h}	D_2	D_{2h}	D_{2d}	S_4	T_d	$C_{\infty v}$
C_s	C_3	C_{3v}	C_{3h}	D_3	D_{3h}	D_{3d}	S_6	O_h	$D_{\infty h}$
C_i	C_4	C_{4v}	C_{4h}	D_4	D_{4h}	D_{4d}	S_8	I_h	
	C_5	C_{5v}	C_{5h}	D_5	D_{5h}	D_{5d}	S_{10}		
	C_6	C_{6v}	C_{6h}	D_6	D_{6h}	D_{6d}			

Table A.1: Ordered point group symmetries.

The use of group theory permits to greatly reduce the complexity of the secular problem on the basis of purely geometrical considerations. In fact, many quantum numbers familiar from basic quantum mechanics are nothing else than the indexes of irreducible representations (IR) of the Hamiltonian's invariance group. For example, the linear momentum $\mathbf{k}$ of a plane waves identifies an IR of the translation group and, indeed, it is a constant of motion if the system is translationally invariant.

In the physical application of group theory, a prominent role is occupied by group representations. In general, a representation Γ is a group homomorphism between $\mathcal{G}$ and a group of linear maps of a vector space V onto itself, which can be represented with matrices. A basic result of finite-group theory ensures that any representation of $\mathcal{G}$ can be decomposed into the direct sum of IRs. IRs are those representations which do not admit proper invariant subspaces: there is no similarity transformation that brings all the matrices of the representation to a same block-diagonal form. Point groups, in particular, have only a finite number of similarity-inequivalent IRs, all of them with finite

dimension.

The Hilbert space $\mathcal{H}$ of molecular states is closed under the action of the symmetry group $\mathcal{G}$ of the molecule, therefore, a basis for $\mathcal{H}$ is also a basis for a *unitary representation* of the group. The state space $\mathcal{H}$ can thus be written as a finite direct sum of subspaces $\mathcal{H}_\Gamma$ in each of which only one IR Γ is represented (possibly multiple times): $\mathcal{H} = \bigoplus_\Gamma \mathcal{H}_\Gamma$. The importance of this decomposition relies on the fact that the operations R of the molecular point-group commute with the Hamiltonian H: $[R, H] = 0$. This implies that states corresponding to different IRs Γ and Γ' are decoupled: $\langle \psi^\Gamma | H | \psi^{\Gamma'} \rangle = 0$; stated otherwise, Γ is a constant of motion. Thus, the problem of finding the spectrum and the corresponding eigenfunctions of the Hamiltonian breaks up in several smaller problems defined on symmetry-adapted configuration spaces.

The IRs of a group, formulated in terms of matrices $D^\alpha_{ij}(R)$, satisfy the so-called great orthogonality theorem

$$\sum_{R\in\mathcal{G}} D^{\alpha *}_{ij}(R) D^\beta_{lm}(R) = \frac{g}{n_\alpha n_\beta} \delta_{\alpha\beta}\delta_{il}\delta_{jm}, \quad \forall\, \alpha,\, \beta,\; i,\, j \,<n_\alpha,\; l,\, m \,<n_\beta \tag{A.1}$$

where g is the order of the group and n_α, n_β are the dimensions of the IRs α and β.

A simplification consists in expressing this relation as a function of the trace of the transformation matrices:

$$\sum_R \chi^*_\alpha(R)\chi_\beta(R) = g\delta_{\alpha\beta} \tag{A.2}$$

where $\chi_\alpha(R) = \sum_m D^\alpha_{mm}$ is called the character of the matrix $D^\alpha(R)$.

The vector of IR traces form a basis set which can be used to express the trace of any reducible representation Γ:

$$\chi_\Gamma(R) = \sum_\alpha a_\alpha \chi_\alpha(R) \tag{A.3}$$

Using Equation (A.2) and (A.3), the expansion coefficients are given by:

$$a_\alpha = \frac{1}{g}\sum_R \chi^*_\alpha(R)\chi_\Gamma(R) \tag{A.4}$$

Another important theorem states that:

$$\chi_{\Gamma\otimes\Gamma'}(R) = \chi_\Gamma(R)\chi_{\Gamma'}(R) \tag{A.5}$$

A.2 Elements of scattering theory

Continuum states result from the interaction of a free electron with the molecular electrostatic potential. In the molecular case, the electrostatic potential is not spherical and leads to a complicated change in the wavefunction. Classically, the scattering process can be separated in three different paths (see Figure 1.1): the incident path, in which the electron is approaching the target along an almost straight trajectory ; the interacting path, in which the electron interacts with the potential; the scattered path, in which the electron is leaving along an approximately straight trajectory. Due to the complexity of the process in the interaction region, only the asymptotic behavior of the particle can be described analytically. However, it is a relevant information since photoelectrons are measured experimentally at large distances (when they reach the detector).

In the quantum picture, the description of the scattering process can be done resolving the TDSE using the time-dependent scattering theory (see for example [380]).

$$i\hbar\frac{\partial}{\partial t}\psi\left(\mathbf{r},t\right)=\hat{H}\left(\mathbf{r},t\right)\psi\left(\mathbf{r}\right) \tag{A.6}$$

If the potential tends fast enough to zero as $r\rightarrow\infty$, the scattered electron can be reasonably considered in the asymptotic region as a free particle. This particular case is considered firstly in the following as an illustrative example.

The Hamiltonian can be written as:

$$\hat{H}\left(\mathbf{r},t\right)=\hat{H}_{0}\left(\mathbf{r}\right)+V\left(\mathbf{r}\right) \tag{A.7}$$

where $\hat{H}_{0}\left(\mathbf{r}\right)=-\frac{1}{2}\nabla^{2}$ is the Hamiltonian of a free particle and $V\left(\mathbf{r},t\right)$ is the interaction potential with the residual ion.

The general solution of this equation has the form:

$$\psi\left(\mathbf{r},t\right)=\hat{U}\left(t\right)\psi\left(\mathbf{r}\right)=e^{-i\hat{H}t}\psi\left(\mathbf{r}\right) \tag{A.8}$$

where $\hat{U}\left(t\right)$ is the so-called evolution operator.

Then, assuming that the time of radiation by the electromagnetic is sufficiently long that molecules can cross the interaction region and that the time of flight of the electron is much higher than the interaction time, steady-state conditions can apply and the asymptotic scattered wavefunction $\varphi^{\pm}$ of a non-relativistic electron is then a solution of the free particle TISE:

$$\left(\nabla^{2}+k^{2}\right)\varphi^{\pm}\left(\mathbf{r}\right)=0 \tag{A.9}$$

where + and − refer to the in and out asymptotic conditions:

$$\hat{U}(t)\,\psi_{+}(\mathbf{r}) \xrightarrow{t\to-\infty} \hat{U}'(t)\,\varphi^{+}(\mathbf{r}) \qquad \text{(incoming)} \tag{A.10}$$

$$\hat{U}(t)\,\psi_{-}(\mathbf{r}) \xrightarrow{t\to+\infty} \hat{U}'(t)\,\varphi^{-}(\mathbf{r}) \qquad \text{(outgoing)} \tag{A.11}$$

and $U'(t)$ to the free particle evolution operator:

$$\hat{U}'(t) = e^{-i\hat{H}_0 t} \tag{A.12}$$

Such approximation is demonstrated to be valid when the potential is less singular than r^{-2} at the origin, tends to 0 faster than r^{-3} at infinity and is reasonably smooth in between. Nevertheless, Coulomb potential does not satisfies the second condition since it tends to $1/r$ as $r \to \infty$. Then, the scattered wavefunction cannot be anymore considered asymptotically as a free particle but as a Coulomb wavefunction, solution of the following equation:

$$\hat{H}_c(\mathbf{r})\,\varphi^{\pm}(\mathbf{r}) = \varepsilon\varphi^{\pm}(\mathbf{r}) \tag{A.13}$$

where the Coulomb Hamiltonian $\hat{H}_c(\mathbf{r})$ is:

$$\hat{H}_c(\mathbf{r}) \sim -\frac{1}{2}\nabla^2 - \frac{1}{r} \tag{A.14}$$

Then, the asymptotic evolution operator becomes:

$$\hat{U}'(t) = e^{-i\hat{H}_c t} \tag{A.15}$$

Considering that every $\hat{U}'(t)\,\varphi^{\pm}(\mathbf{r})$ is the asymptote of a vector $\hat{U}(t)\,\psi_{\pm}(\mathbf{r})$ belonging to the Hilbert space, then:

$$\hat{U}(t)\,\psi_{\pm}(\mathbf{r}) - \hat{U}'(t)\,\varphi^{\pm}(\mathbf{r}) \xrightarrow{t\to\mp\infty} 0 \tag{A.16}$$

Multiplying this equation by the unitary operator $\hat{U}^{\dagger}(t)$:

$$\psi_{\pm}(\mathbf{r}) - \hat{U}^{\dagger}(t)\,\hat{U}'(t)\,\varphi^{\pm}(\mathbf{r}) \xrightarrow{t\to\mp\infty} 0 \tag{A.17}$$

The latter equation can be rewritten as follow:

$$\psi_{\pm}(\mathbf{r}) = \hat{\Omega}_{\pm}\varphi^{\pm}(\mathbf{r}) \tag{A.18}$$

where the so-called Møller operator $\hat{\Omega}_{\pm}$ is defined by:

$$\hat{\Omega}_{\pm} = \lim_{t\to\mp\infty} \hat{U}^{\dagger}(t)\,\hat{U}'(t) \tag{A.19}$$

The action of the Møller operator is easily understandable: it transforms any asymptotic vector of the Hilbert space to the scattering eigenstates of the

Hamiltonian that fulfills some boundary conditions at $t \to \mp\infty$.

It is assumed that the Hilbert space $\mathcal{H}$ spanned by the eigenvectors $\psi(\mathbf{r})$ is the sum of two orthogonal vector subspaces: the bound states subspace $\mathcal{B}$ that contains all the states of $\mathcal{H}$ which do not have in or out asymptotes ; the scattering states subspace $\mathcal{R}_\pm$ that contains all the states of $\mathcal{H}$ which do have the in/out asymptotes.[1] For some potentials (as molecular ones), the scattering theory is said "asymptotically complete". It means that every state with "in" asymptote also has unique "out" asymptote (and vice versa), and then $\mathcal{R}_+ = \mathcal{R}_- = \mathcal{R}$. Subspaces spanned by the bound and scattering states are orthogonal, so $\mathcal{H} = \mathcal{B} \oplus \mathcal{R}$. In such condition:

$$\psi(\mathbf{r}) = \hat{\Omega}_+ \varphi^+(\mathbf{r}) = \hat{\Omega}_- \varphi^-(\mathbf{r}) \tag{A.20}$$

Since $\hat{\Omega}_\pm^\dagger \hat{\Omega}_\pm = 1$, asymptotic wavefunctions can be expressed in terms of actual states:

$$\varphi^\pm(\mathbf{r}) = \hat{\Omega}_\pm^\dagger \varphi(\mathbf{r}) = \hat{\Omega}_\pm^\dagger \hat{\Omega}_\mp \varphi^\mp(\mathbf{r}) \tag{A.21}$$

Finally, outcoming scattering wavefunctions are connected to their corresponding incoming ones through the scattering operator $\hat{S}$:

$$\varphi^+(\mathbf{r}) = \hat{S} \varphi^-(\mathbf{r}) \tag{A.22}$$

where:

$$\hat{S} = \hat{\Omega}_+^\dagger \hat{\Omega}_- \tag{A.23}$$

The single $\hat{S}$ operator contains all the information relative to the scattering process. In particular, it provides the probability that an incident particle with in asymptote $\varphi^+(\mathbf{r})$ will be observed with out asymptote $\varphi^-(\mathbf{r})$. Let's consider the actual states arising from the Møller transformation of the asymptote states:

$$\psi_-(\mathbf{r}) = \hat{\Omega}_- \varphi^-(\mathbf{r}) \tag{A.24}$$

$$\psi_+(\mathbf{r}) = \hat{\Omega}_+ \varphi^+(\mathbf{r}) \tag{A.25}$$

The probability amplitude for the scattering process $\psi_i(\mathbf{r}) \to \psi_j(\mathbf{r})$ is then given by:

$$\begin{aligned} |\langle \psi_+(\mathbf{r}) \mid \psi_-(\mathbf{r}) \rangle|^2 &= \left| \left\langle \varphi^+(\mathbf{r}) \left| \hat{\Omega}_+^\dagger \hat{\Omega}_- \right| \varphi^-(\mathbf{r}) \right\rangle \right|^2 \\ &= \left| \left\langle \varphi^+(\mathbf{r}) \left| \hat{S} \right| \varphi^-(\mathbf{r}) \right\rangle \right|^2 \end{aligned} \tag{A.26}$$

It is possible to give a formulation of the differential cross section in terms of the S-matrix elements $\left\langle \varphi^+(\mathbf{r}) \left| \hat{S} \right| \varphi^-(\mathbf{r}) \right\rangle$.

[1] Note that $\mathcal{R}_+ = \mathcal{R}_-$.

Reminding that the spatial projection of the momentum eigenvector $|\mathbf{k}\rangle$ is the plane wave:

$$\langle \mathbf{r}|\ \mathbf{k}\rangle = (2\pi)^{-\frac{3}{2}}\, e^{i\mathbf{k}\cdot\mathbf{r}} \tag{A.27}$$

it is convenient to expand the asymptotic wavefunctions in a basis of plane-waves:

$$\varphi^{\pm}(\mathbf{r}) = \int \varphi^{\pm}(\mathbf{k})\,|\mathbf{k}\rangle\, d^3k \tag{A.28}$$

According to Equation (A.22) we can write:

$$\varphi^{+}(\mathbf{k}) = \int \langle \mathbf{k}|\,\hat{S}\,|\mathbf{k}'\rangle\,\varphi^{-}\left(\mathbf{k}'\right)|\mathbf{k}\rangle\, d^3k' \tag{A.29}$$

where $\langle \mathbf{k}|\,\hat{S}\,|\mathbf{k}'\rangle$ is the S-matrix in the momentum space. It is easily demonstrable that $\hat{S}$ commutes with $\hat{H}_0$ (see [380]).

Using this property, we can write:

$$\langle \mathbf{k}|\left[\hat{H}_0, \hat{S}\right]\left|\mathbf{k}'\right\rangle = (\varepsilon_k - \varepsilon_{k'})\,\langle \mathbf{k}|\,\hat{S}\,\left|\mathbf{k}'\right\rangle = 0 \tag{A.30}$$

The momentum-space matrix is then different from zero only when $\varepsilon_k = \varepsilon_{k'}$, which is nothing more than the energy conservation rule for elastic scattering. The S-matrix can be decomposed into an unscattered and a scattered part. The latter is represented by the $\hat{R}$ operator which is defined by the relation:

$$\hat{S} = 1 - \hat{R} \tag{A.31}$$

The R-matrix should obviously includes the energy conservation which is expressed by the Dirac function $\delta(\varepsilon_k - \varepsilon_{k'})$. The S-matrix then takes the form:

$$\langle \mathbf{k}|\,\hat{S}\,\left|\mathbf{k}'\right\rangle = \delta_3\left(\mathbf{k} - \mathbf{k}'\right) + i\frac{1}{2\pi}\delta(\varepsilon_k - \varepsilon_{k'})\, f\left(\mathbf{k}, \mathbf{k}'\right) \tag{A.32}$$

where $f(\mathbf{k}, \mathbf{k})$ is the so-called scattering amplitude and is defined only for $\varepsilon_k = \varepsilon_{k'}$. The meaning of the two terms in Equation (A.32) emerges easily: the first one corresponds to the unscattered electron for which no momentum change occur ; the second term arises when the electron is elastically scattered, i.e. when $\varepsilon_k = \varepsilon_{k'}$ and $\mathbf{k} \neq \mathbf{k}'$.

This formulation is valid for the single-channel case but can be formulated also for the multi-channel case (see [183]).

A.3 Analytical solutions to the Coulomb radial TISE

Analytical solutions can be found by solving the radial Schrödinger equation in the spherical polar coordinates:

$$\left[-\frac{1}{2}\left(\frac{1}{r}\frac{d^2}{dr^2}r - \frac{l\left(l+1\right)}{r^2}\right) + \frac{Z_1 Z_2}{r}\right] P_{\varepsilon l}\left(r\right) = \varepsilon P_{\varepsilon l}\left(r\right) \tag{A.33}$$

$$\left[\frac{1}{r}\frac{d^2}{dr^2}r - \frac{l\left(l+1\right)}{r^2} - \frac{2Z_1 Z_2}{r} + 2\varepsilon\right] P_{\varepsilon l}\left(r\right) = 0 \tag{A.34}$$

We define $\rho = kr$. Derivatives then transform in:

$$\frac{d}{dr} = \frac{d}{d\rho}\frac{d\rho}{dr} = k\frac{d}{d\rho} \tag{A.35}$$

$$\frac{d^2}{dr^2} = k^2\frac{d^2}{d\rho^2} \tag{A.36}$$

and the Equation (A.34) becomes:

$$\left[\frac{k^3}{\rho}\frac{d^2}{d\rho^2}\frac{\rho}{k} - \frac{k^2 l\left(l+1\right)}{\rho^2} - \frac{2kZ_1 Z_2}{\rho} + 2\varepsilon\right] P_{\varepsilon l}\left(\rho\right) = 0 \tag{A.37}$$

Since $\varepsilon = k^2/2$:

$$\left[\frac{1}{\rho}\frac{d^2}{d\rho^2}\rho - \frac{l\left(l+1\right)}{\rho^2} - \frac{2Z_1 Z_2}{k\rho} + 1\right] P_{\varepsilon l}\left(\rho\right) = 0 \tag{A.38}$$

Defining $\eta = Z_1 Z_2/k$ and $u_{\varepsilon l}\left(\rho\right) = \rho P_{\varepsilon l}\left(\rho\right)$:

$$\left[\frac{1}{\rho}\frac{d^2}{d\rho^2} - \frac{l\left(l+1\right)}{\rho^2} - \frac{2\eta}{\rho} + 1\right] u_{\varepsilon l}\left(\rho\right) = 0 \tag{A.39}$$

We notice immediately that if $\eta = 0$, the latter equation reduces to the free particle Schrödinger equation. In our case, the photoelectron of charge $z_1 = -1$ is scattered by the residual ion. Its effective charge Z_∞ depends on the distance, but when $r \to \infty$ the potential created by the $N-1$ electrons and N protons on can considered $Z_\infty \sim 1$.

It can be proved (see [249]) that such equation have two independent solutions $f_l\left(\rho\right)$ and $g_l\left(\rho\right)$, respectively called regular and irregular continuum functions. They are characterized by their asymptotic behaviors:

$$f_{\varepsilon l}\left(r\right) \xrightarrow{\rho\to\infty} \sqrt{\frac{2}{\pi k}}\frac{1}{r}\sin\left(\theta_l\left(\rho\right)\right) \tag{A.40}$$

$$g_{\varepsilon l}\left(r\right) \xrightarrow{\rho\to\infty} \sqrt{\frac{2}{\pi k}}\frac{1}{r}\cos\left(\theta_l\left(\rho\right)\right) \tag{A.41}$$

where:

$$\theta_l(\rho) = \rho - \eta \log 2\rho - l\frac{\pi}{2} + \sigma_l \tag{A.42}$$

and σ_l is the Coulomb phase shift defines as a function of the Euler's gamma function Γ:

$$\sigma_l = \arg \Gamma(l + 1 + i\eta) \tag{A.43}$$

B. Data

B.1 Constants and units

Quantity	Value (SI and non-SI)	Value (a.u.)
Bohr radius	$0.529\ 177\ 208\ 59(36)\times10^{-10}$ m	1
Hartree energy	27.211 383 86(68) eV	1
atomic unit of time	$2.418\ 884\ 326\ 505(16)\times10^{-17}$ s	1
electron charge	$1.602\ 176\ 487(40)\times10^{-19}$ C	1
electron mass	$9.109\ 382\ 15(45)\times10^{-31}$ kg	1
proton mass	$1.672\ 621\ 637(82)\times10^{-27}$ kg	1836.152 672 47(80)
neutron mass	$1.674\ 927\ 211(84)\times10^{-27}$ kg	1836.683 6605(11)
atomic mass unit	$1.660\ 538\ 921(73)\times10^{-27}$ kg	1822.888 39
fine-structure	$7.297\ 352\ 5376(50)\times10^{-3}$	0.007 297 352
reduced Planck constant	$1.054\ 571\ 628(53)\times10^{-34}$ Js	1
Boltzmann constant	$1.380\ 648\ 8(13)\times10^{-23}$ $J.K^{-1}$	3.166811 4(29)
speed of light in vacuum	299 792 458 $m.s^{-1}$	137.035 999 679(44)

B.2 Atomic and molecular database

Atom	Isotope	Composition	amu	amu (a.u.)
H	1	0.999 885(70)	1.007 825 032 07(10)	1837.152 6
B	11	0.801(7)	11.009 305 4(4)	20068.735
C	12	0.9893(8)	12.000 000 0(0)	21874.661
N	14	0.996 36(20)	14.003 074 004 8(6)	25526.041
O	16	0.997 57(16)	15.994 914 619 56(16)	29156.944
F	19	1.0000	18.998 403 22(7)	34631.969
S	32	0.922 23(19)	31.972 071 00(15)	58281.517

Table B.1: Atomic database for H, B, C, N, O, F.

Molecule		Angle	Bond	Reduced mass (a.u.)	
H_2			H−H	$m_H/2$	918.5763
N_2			N≡N	$m_N/2$	12763.021
CO			C≡O	$\frac{m_C m_O}{m_C + m_O}$	12498.103
C_2H_2		C-C-H 180°	C−H C=C	$\frac{m_C + m_H}{2}$	11855.907
CH_4		X-C-X 109.5°	sp^3	$4m_H$	7348.6104
CF_4				$4m_F$	138527.88
BF_3		F-B-F 120°	sp^2	$3m_F$	103895.91
SF_6		F-S-F 90°	sp^3d^2	$6m_F$	207791.81

Table B.2: Bond characteristics and reduced masses of H_2, N_2, CO, C_2H_2, CH_4, CF_4, BF_3 and SF_6.

Photoionization		R_e	ΔR_e	ω_e	IP
H_2	ground	0.742 Å [37]		4395 cm^{-1} [37]	
	$1\sigma_g^{-1}$	1.06 Å [37]	0.318 Å	2297 cm^{-1} [37]	15.603 eV [37]
N_2	Ground	1.101 Å or 1.093 Å [382]		2372 cm^{-1} [382]	
	$1\sigma_g^{-1}$	1.076 Å [382]	-0.017 Å	2440 cm^{-1} [382]	409.94 eV [55] or 413.45eV [382]
	$1\sigma_u^{-1}$	1.072 Å [382]	-0.021 Å	2437 cm^{-1} [382]	(g/u splitting: 101meV [382])
	$2\sigma_u^{-1}$	1.077 Å [291]	-0.024 Å	2419.1 cm^{-1} [294]	18.558 eV [291]
	$1\pi_u^{-1}$	1.177 Å [291]	0.076 Å	1448.0 cm^{-1} [294]	16.490 eV [291]
	$3\sigma_g^{-1}$	1.119 Å [291]	0.018 Å	2194.7 cm^{-1} [294]	15.347 eV [291]
CO	Ground	1.132 Å or 1.128 Å [193]		2169.8 cm^{-1} [245]	
	$1\sigma^{-1}$	1.167 Å [193]	0.039 Å	1887 cm^{-1} [157]	542.54 eV [299] or 541.99eV [382]
	$2\sigma^{-1}$	1.079 Å [193]	-0.049 Å	2457 cm^{-1} [157]	296.07 eV [263] or 300.00eV [382]
	$4\sigma^{-1}$	1.172 Å [291]	0.04 Å	1734.1 cm^{-1} [271]	19.483 eV [291]
	$1\pi^{-1}$	1.247 Å [291]	0.115 Å	1562.0 cm^{-1} [271]	16.326 eV [291]
	$5\sigma^{-1}$	1.118 Å [291]	-0.014 Å	2214.2 cm^{-1} [271]	13.768 eV [291]
C_2H_2	Ground	R_{C-H}: 1.061 Å [31]		3222.55 cm^{-1} [192]	
		R_{C-C}: 1.204 Å [31]		1997.98 cm^{-1} [192]	
	$1\sigma_g^{-1}$	R_{C-C}: 1.163 Å [31]	-0.041 Å	2231.62 cm^{-1} [172]	291.728 eV [378]
	$1\sigma_u^{-1}$	R_{C-C}: 1.156 Å [31]	-0.048 Å	2151.05 cm^{-1} [172]	291.634 eV [378]
CH_4	Ground	1.0853 Å [186]		3059.9 cm^{-1} [186]	
	$1A_1^{-1}$	1.0371 Å [186]	-0.0482 Å	3383.5 cm^{-1} [186]	290.689 eV [263]
CF_4	Ground	1.3166 Å [48]		907.31 cm^{-1} [386]	
	$2A_1^{-1}$	1.3105 Å [386]	-0.0061 Å	879.75 cm^{-1} [386]	301.898 eV [263]
BF_3	Ground	1.313 Å [205]		888 cm^{-1} [387]	
	$2A_1'^{-1}$	1.255 Å [387]	-0.058 Å	1032.024 cm^{-1} [387]	202.8 eV [402]
SF_6	Ground	1.5867 Å [376]		833 cm^{-1} [376]	
	$1A_{1g}^{-1}$	1.597Å *	0.010Å	665.27 cm^{-1} *	2490.1 eV [184]
	$4T_{1u}^{-1}$	1.647 Å *	0.061 Å	562.5 cm^{-1} [164]	22.5 eV [365]

Table B.3: Energetic and structural database for H_2, N_2, CO, C_2H_2, CH_4, CF_4, BF_3 and SF_6.
(* values calculated in this work with DFT using a LDA functional).

B.3 Molecular orbital diagrams

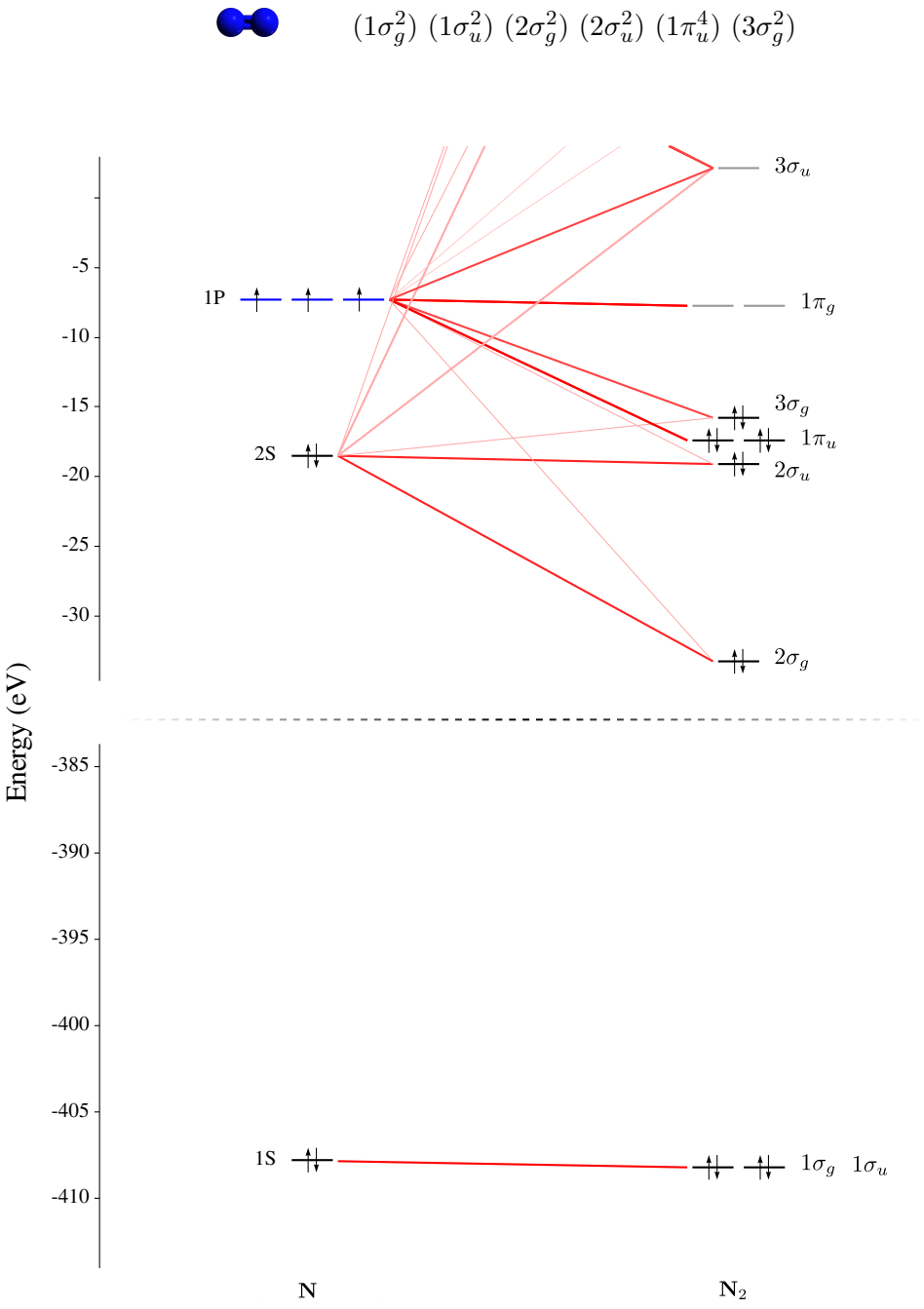

Figure B.1: Molecular orbital diagram for N_2.

$(1\sigma^2)\ (2\sigma^2)\ (3\sigma^2)\ (4\sigma^2)\ (1\pi^4)\ (5\sigma^2)$

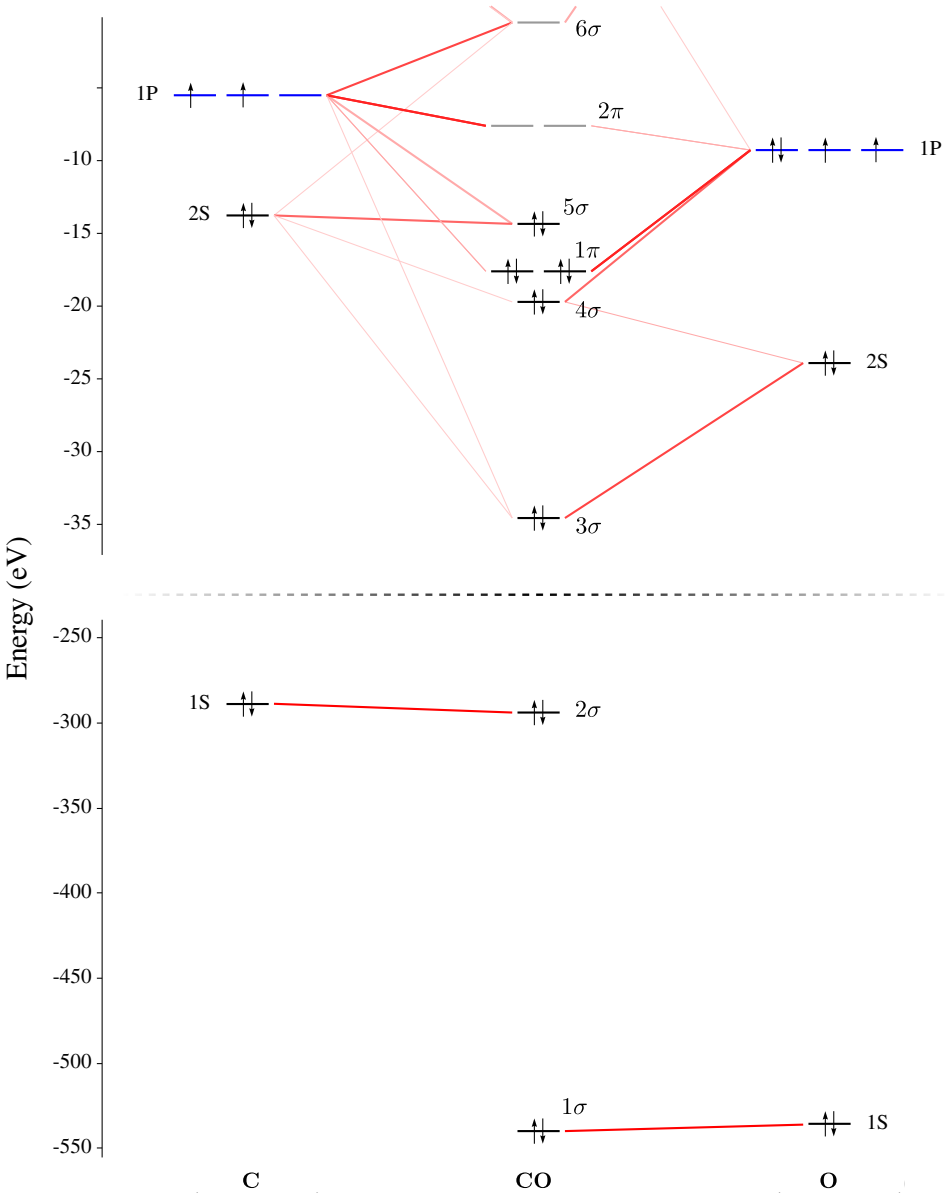

Figure B.2: Molecular orbital diagram for CO.

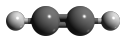

$(1\sigma_g^2)\ (1\sigma_u^2)\ (2\sigma_g^2)\ (2\sigma_u^2)\ (3\sigma_g^2)\ (1\pi_u^4)$

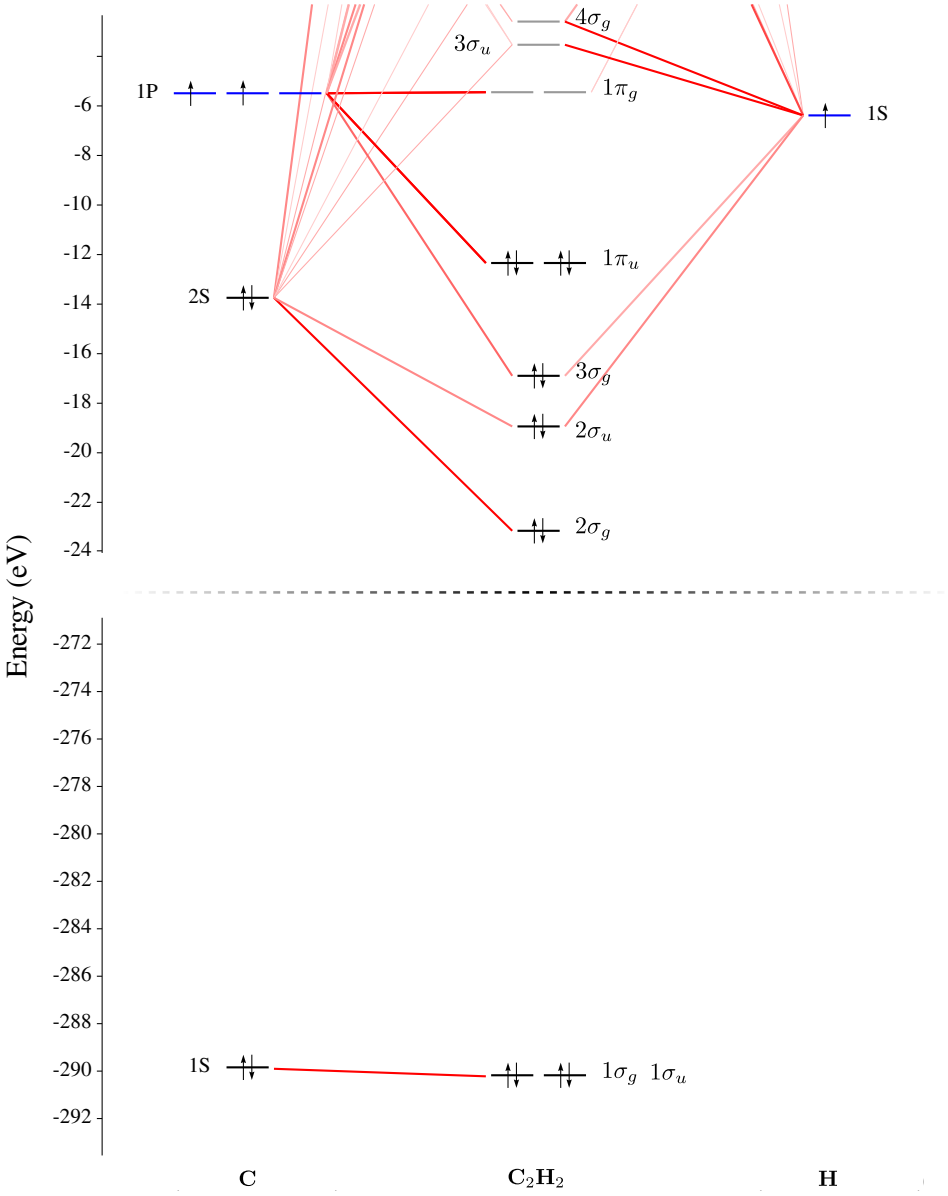

Figure B.3: Molecular orbital diagram for C_2H_2.

$(1a_1^2)\ (2a_1^2)\ (1t_2^6)$

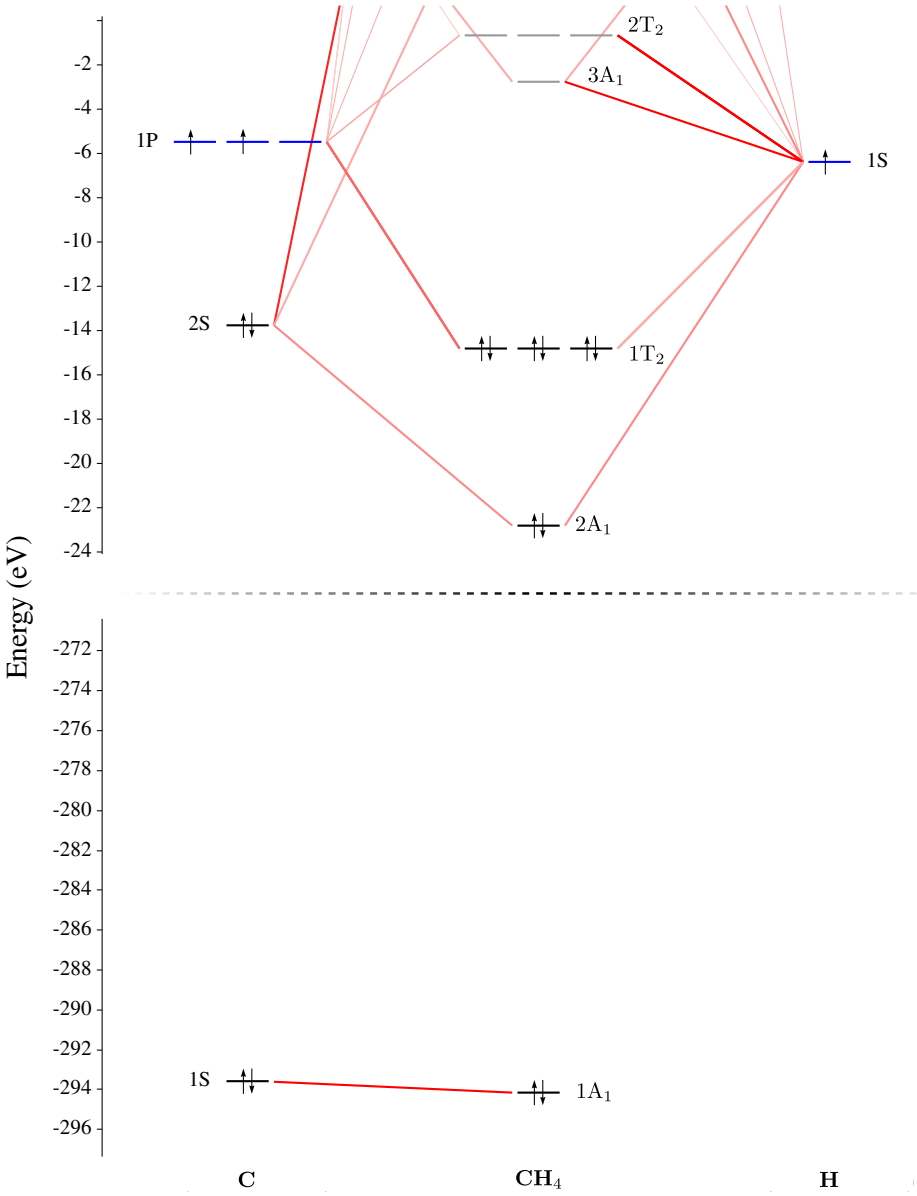

Figure B.4: Molecular orbital diagram for CH_4.

$(1a_1^2)\ (1t_2^6)\ (2a_1^2)\ (3a_1^2)\ (2t_2^6)\ (4a_1^2)\ (3t_2^6)\ (1e^4)\ (4t_2^6)\ (1t_1^6)$

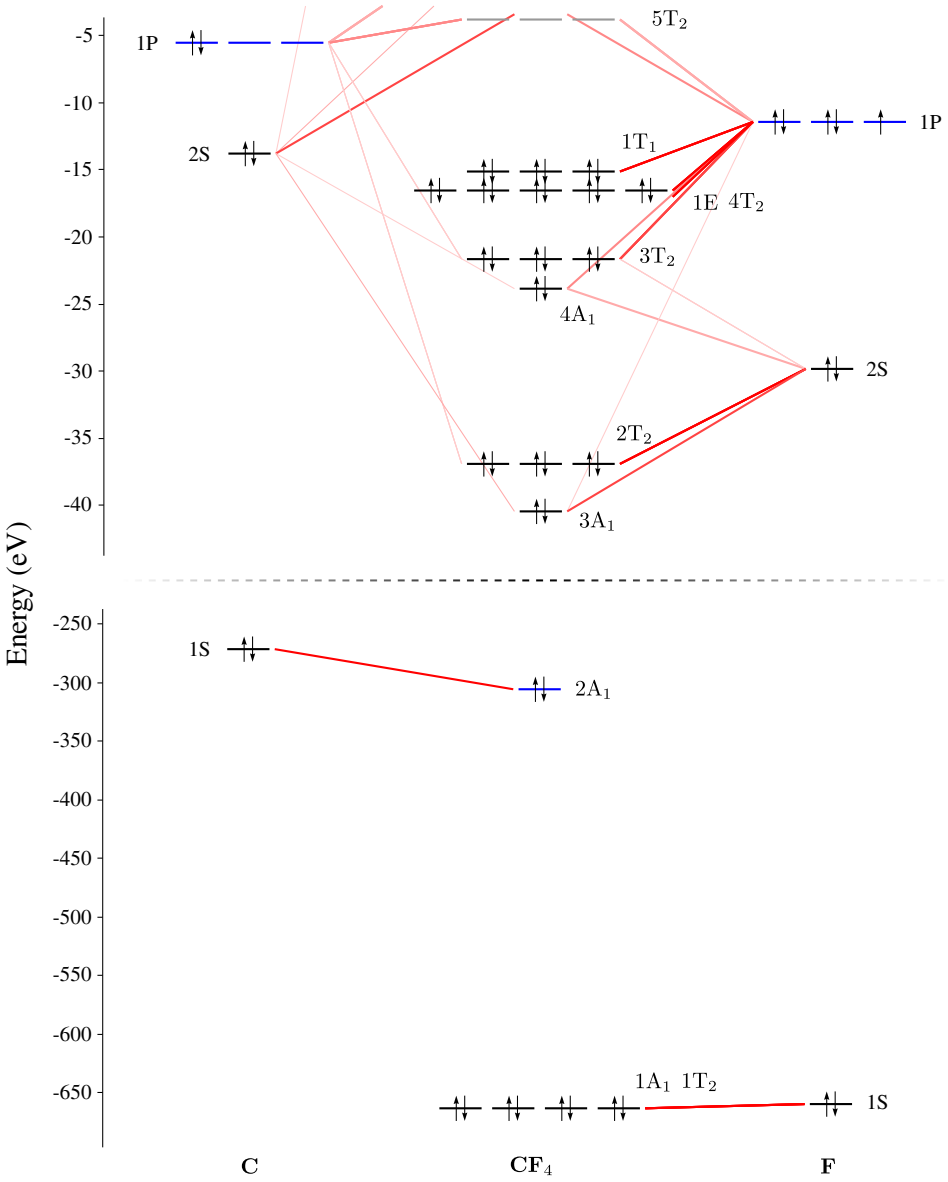

Figure B.5: Molecular orbital diagram for CF_4.

$(1a'^2_1)\ (1e'^4_1)\ (2a'^2_1)\ (3a'^2_1)\ (2e'^4)\ (4a'^2_1)\ (3e'^4)\ (1a''^2_2)\ (4e'^4)$
$(1e''^4)\ (1a'^2_2)$

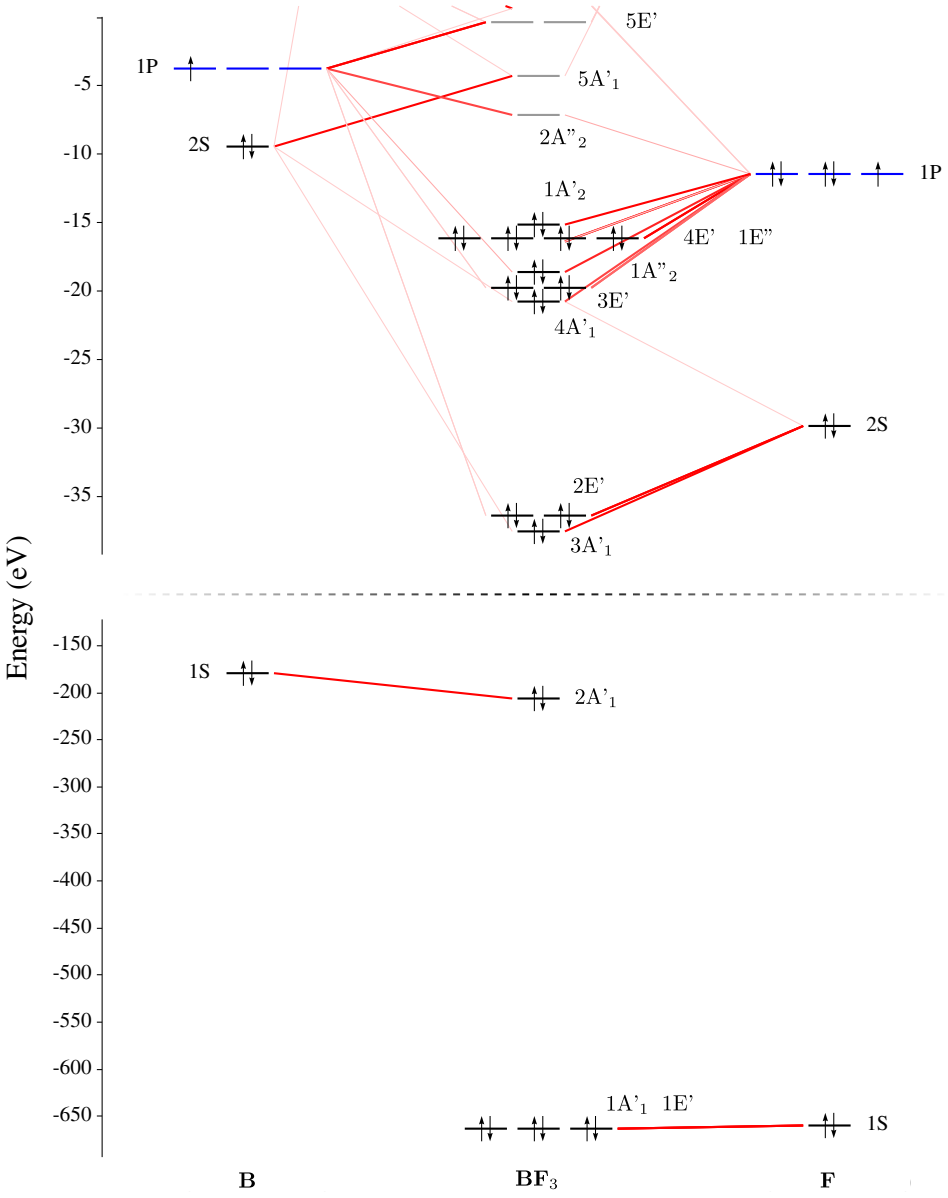

Figure B.6: Molecular orbital diagram for BF_3.

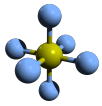

$(1a_{1g}^2)\ (2a_{1g}^2)\ (1t_{1u}^6)\ (1e_g^4)\ (3a_{1g}^2)\ (2t_{1u}^6)\ (4a_{1g}^2)\ (3t_{1u}^6)\ (2e_g^4)$
$(5a_{1g}^2)\ (4t_{1u}^6)\ (1t_{2g}^6)\ (3e_g^4)\ (1t_{2u}^6)\ (5t_{1u}^6)\ (1t_{1g}^6)$

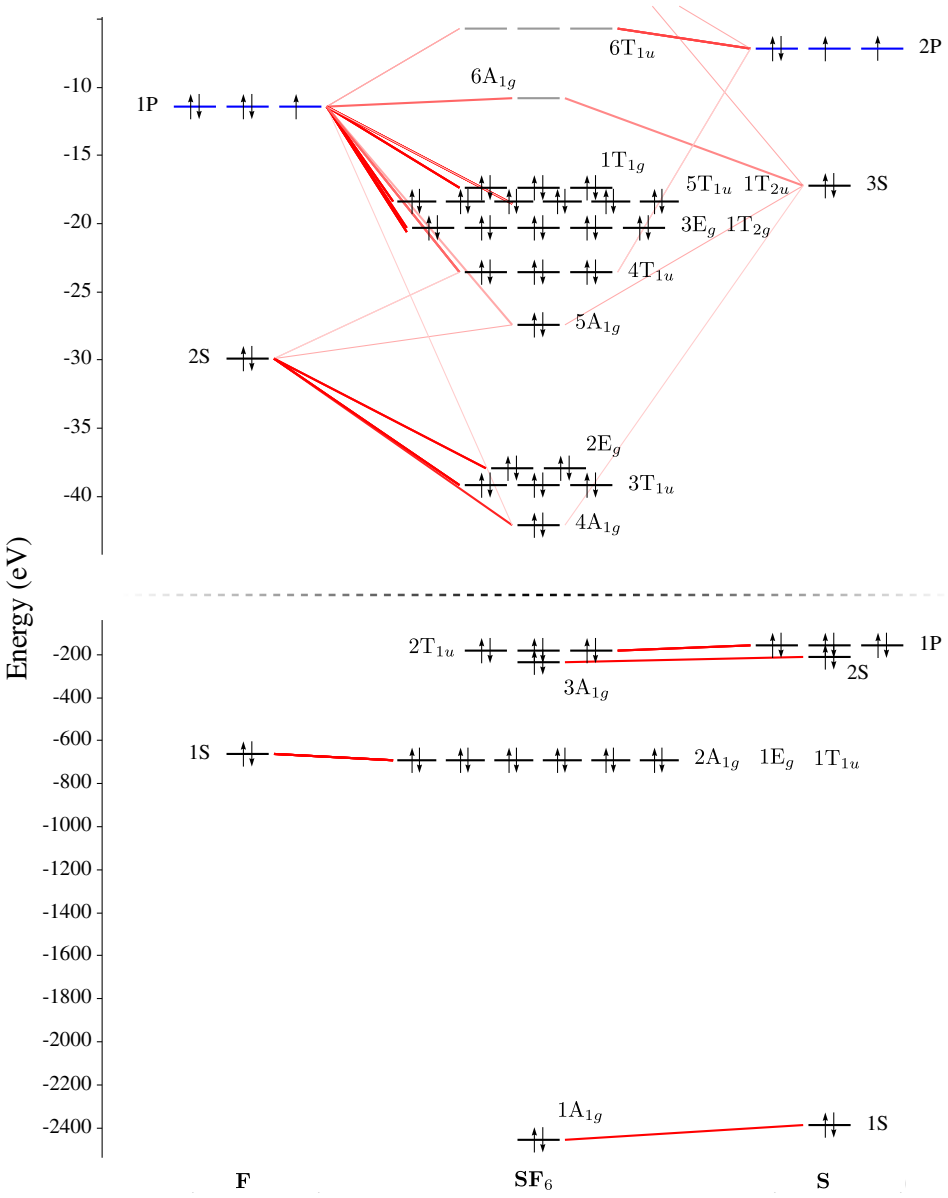

Figure B.7: Molecular orbital diagram for SF_6.

B.4 Molecular symmetries

See Table Page 286.

B.5 Computational times

See Table B.4 Page 287.

B.6 Overview of the calculated cross sections

See Figures B.8 and B.9 Pages 288 and 289.

Sym.	Mol.	$\lvert\psi_0\rangle$	$\langle\psi_\alpha\rvert$		$\langle\varphi_{l\varepsilon}\rvert$	**r**	Partial waves $l =$
$D_{\infty h}$	H_2 N_2 C_2H_2	$^1\Sigma_g^+$ ↗ → ↘	$^2\Sigma_g^+$	⊗	σ_u	z	$1(1), 3(1), 5(1), 7(1), 9(1), 11(1), \cdots$
					$\pi_{u:1}$	x	$1(1), 3(1), 5(1), 7(1), 9(1), 11(1), \cdots$
					$\pi_{u:2}$	y	
			$^2\Sigma_u^+$	⊗	σ_g	z	$0(1), 2(1), 4(1), 6(1), 8(1), 10(1), \cdots$
					$\pi_{g:1}$	x	$2(1), 4(1), 6(1), 8(1), 10(1), 12(1), \cdots$
					$\pi_{g:2}$	y	
			$^2\Pi_{u:1}^+$	⊗	σ_g	x	$0(1), 2(1), 4(1), 6(1), 8(1), 10(1), \cdots$
					$\pi_{g:1}$	z	$2(1), 4(1), 6(1), 8(1), 10(1), 12(1), \cdots$
					$\delta_{g:1}$	x	$2(1), 4(1), 6(1), 8(1), 10(1), 12(1), \cdots$
					$\delta_{g:2}$	y	
			$^2\Pi_{u:2}^+$	⊗	σ_g	y	$0(1), 2(1), 4(1), 6(1), 8(1), 10(1), \cdots$
					$\pi_{g:2}$	z	$2(1), 4(1), 6(1), 8(1), 10(1), 12(1), \cdots$
					$\delta_{g:1}$	y	$2(1), 4(1), 6(1), 8(1), 10(1), 12(1), \cdots$
					$\delta_{g:2}$	x	
$C_{\infty v}$	CO	$^1\Sigma^+$ ↗ ↘	$^2\Sigma^+$	⊗	σ	z	$0(1), 1(1), 2(1), 3(1), 4(1), 5(1), \cdots$
					$\pi_{:1}$	x	$1(1), 2(1), 3(1), 4(1), 5(1), 6(1), \cdots$
					$\pi_{:2}$	y	
			$^2\Pi_{:1}^+$	⊗	σ	x	$0(1), 1(1), 2(1), 3(1), 4(1), 5(1), \cdots$
					$\pi_{:1}$	z	$1(1), 2(1), 3(1), 4(1), 5(1), 6(1), \cdots$
					$\delta_{:1}$	x	$2(1), 3(1), 4(1), 5(1), 6(1), 7(1), \cdots$
					$\delta_{:2}$	y	
			$^2\Pi_{:2}^+$	⊗	σ	y	$0(1), 1(1), 2(1), 3(1), 4(1), 5(1), \cdots$
					$\pi_{:2}$	z	$1(1), 2(1), 3(1), 4(1), 5(1), 6(1), \cdots$
					$\delta_{:1}$	y	$2(1), 3(1), 4(1), 5(1), 6(1), 7(1), \cdots$
					$\delta_{:2}$	x	
T_d	CH_4 CF_4	$^1A_1$ →	$^2A_1$	⊗	$T_{2:1}$	z	$1(1), 2(1), 3(1), 4(1), 5(1), 5(2), \cdots$
					$T_{2:2}$	x	
					$T_{2:3}$	y	
D_{3h}	BF_3	$^1A'_1$ →	$^2A'_1$	⊗	$E'_{:1}$	x	$1(1), 2(1), 3(1), 4(1), 4(2), 5(1), \cdots$
					$E'_{:2}$	y	
					A''_2	z	$1(1), 3(1), 4(1), 5(1), 6(1), 7(1), \cdots$
O_h	SF_6	$^1A_{1g}$ →	$^2A_{1g}$	⊗	$T_{1u:1}$	z	$1(1), 3(1), 5(1), 5(2), 7(1), 7(2), \cdots$
					$T_{1u:2}$	x	
					$T_{1u:3}$	y	
			$^2T_{1u:1}$	⊗	A_{1g}	z	$0(1), 4(1), 6(1), 8(1), 10(1), 12(1), \cdots$
					$E_{g:1}$	z	$2(1), 4(1), 6(1), 8(1), 8(2), 10(1), \cdots$
					$T_{1g:2}$	x	$4(1), 6(1), 8(1), 8(2), 10(1), 10(2), \cdots$
					$T_{1g:3}$	y	
					$T_{2g:1}$	x	$2(1), 4(1), 6(1), 6(2), 8(1), 8(2), \cdots$
					$T_{2g:2}$	y	
			$^2T_{1u:2}$	⊗	A_{1g}	x	$0(1), 4(1), 6(1), 8(1), 10(1), 12(1), \cdots$
					$E_{g:1}$	x	$2(1), 4(1), 6(1), 8(1), 8(2), 10(1), \cdots$
					$E_{g:2}$	x	
					$T_{1g:1}$	y	$4(1), 6(1), 8(1), 8(2), 10(1), 10(2), \cdots$
					$T_{1g:2}$	z	
					$T_{2g:1}$	z	$2(1), 4(1), 6(1), 6(2), 8(1), 8(2), \cdots$
					$T_{2g:3}$	y	
			$^2T_{1u:3}$	⊗	A_{1g}	y	$0(1), 4(1), 6(1), 8(1), 10(1), 12(1), \cdots$
					$E_{g:1}$	y	$2(1), 4(1), 6(1), 8(1), 8(2), 10(1), \cdots$
					$E_{g:2}$	y	
					$T_{1g:1}$	x	$4(1), 6(1), 8(1), 8(2), 10(1), 10(2), \cdots$
					$T_{1g:3}$	z	
					$T_{2g:2}$	z	$2(1), 4(1), 6(1), 6(2), 8(1), 8(2), \cdots$
					$T_{2g:3}$	x	

Mol.	H diag.	Continuum states diagonalization						Time per geometry	
	t_{BS}	Sym.	R	t_{ε_1}	$t_{\varepsilon_{N_e}}$	$\sum_i t_{\varepsilon_i}$	$\langle t_{\varepsilon_i} \rangle$	$t_{BS}+t_{CS}$	Total
N_2	Σ_g^+ 1.2+0.7	σ_u	1.000	0.11	0.10	21.1	0.11	43.03	202.36
			2.050	0.10	0.10	21.3	0.11		
			4.000	0.10	0.97	20.3	0.10		
		π_u	1.000	0.10	0.10	20.8	0.10		
			2.050	0.11	0.97	20.1	0.10		
			4.000	0.10	0.97	19.8	0.10		
CO	Σ^+ 1.9+1.8	σ	1.000	0.43	0.28	64.5	0.32	114.00	287.923
			2.150	0.34	0.28	60.3	0.30		
			4.000	0.31	0.28	57.5	0.29		
		π	1.000	0.28	0.24	50.4	0.25		
			2.150	0.24	0.24	48.9	0.24		
			4.000	0.26	0.24	49.3	0.25		
C_2H_2	Σ_g^+ 5.1+7.2	σ_u	0.500	0.74	0.72	146.9	0.73	302.63	526.25
			2.250	0.73	0.72	146.0	0.73		
			7.000	0.74	0.70	146.3	0.73		
		π_u	0.500	0.71	0.71	144.0	0.72		
			2.250	0.72	0.72	144.1	0.72		
			7.000	0.70	0.72	143.7	0.72		
CH_4	A_1 11+10.4	T_2	1.300	7.05	7.07	1410.4	7.05	1477.23	6792.91
			2.050	7.84	7.86	1568.4	7.84		
			5.000	6.93	7.02	1388.7	6.94		
BF_3	A'_1 58.4+31.0	E'	1.000	11.78	11.83	1884.1	12.56	2327.90	7981.55
			2.500	11.32	11.17	1875.4	12.50		
			4.000	11.32	11.13	1778.1	11.85		
		A''_2	1.000	2.47	2.44	392.2	2.61		
			2.500	2.45	2.45	400.3	2.67		
			4.000	2.47	2.42	385.4	2.57		
SF_6	A_{1g} 258+158.2	A_{1g}	2.000	1.72	1.72	388.2	1.94	8327.07	12810.3
			3.000	2.81	2.26	506.0	2.53		
			6.000	1.51	1.50	326.1	1.63		
		E_g	2.000	6.26	6.26	1427.8	7.14		
			3.000	9.71	10.72	2160.3	10.80		
			6.000	5.57	4.80	1021.3	5.11		
		T_{1g}	2.000	7.85	7.85	1661.3	8.31		
			3.000	17.99	18.82	3808.9	19.04		
			6.000	7.97	7.98	1696.3	8.48		
		T_{2g}	2.000	11.75	11.75	2507.8	12.54		
			3.000	26.72	27.53	5717.8	28.59		
			6.000	11.74	11.76	2510.8	12.55		

Table B.4: Detailed computational times (s) obtained on the same machine using 16 processors (except for BF_3 for which 32 processors have been used).

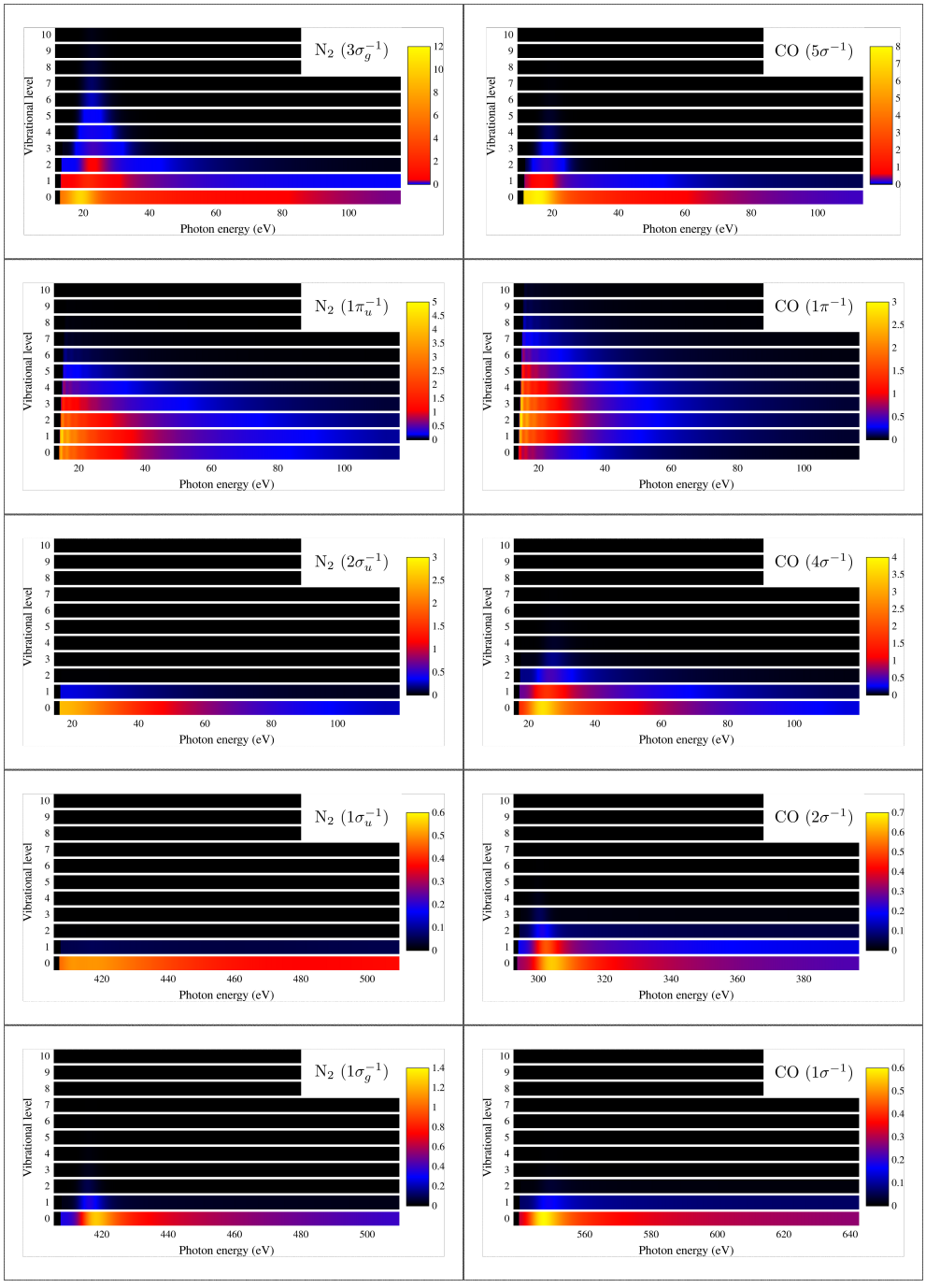

Figure B.8: Vibrationally resolved cross sections for the valence and core shells photoionization of N_2 and CO.

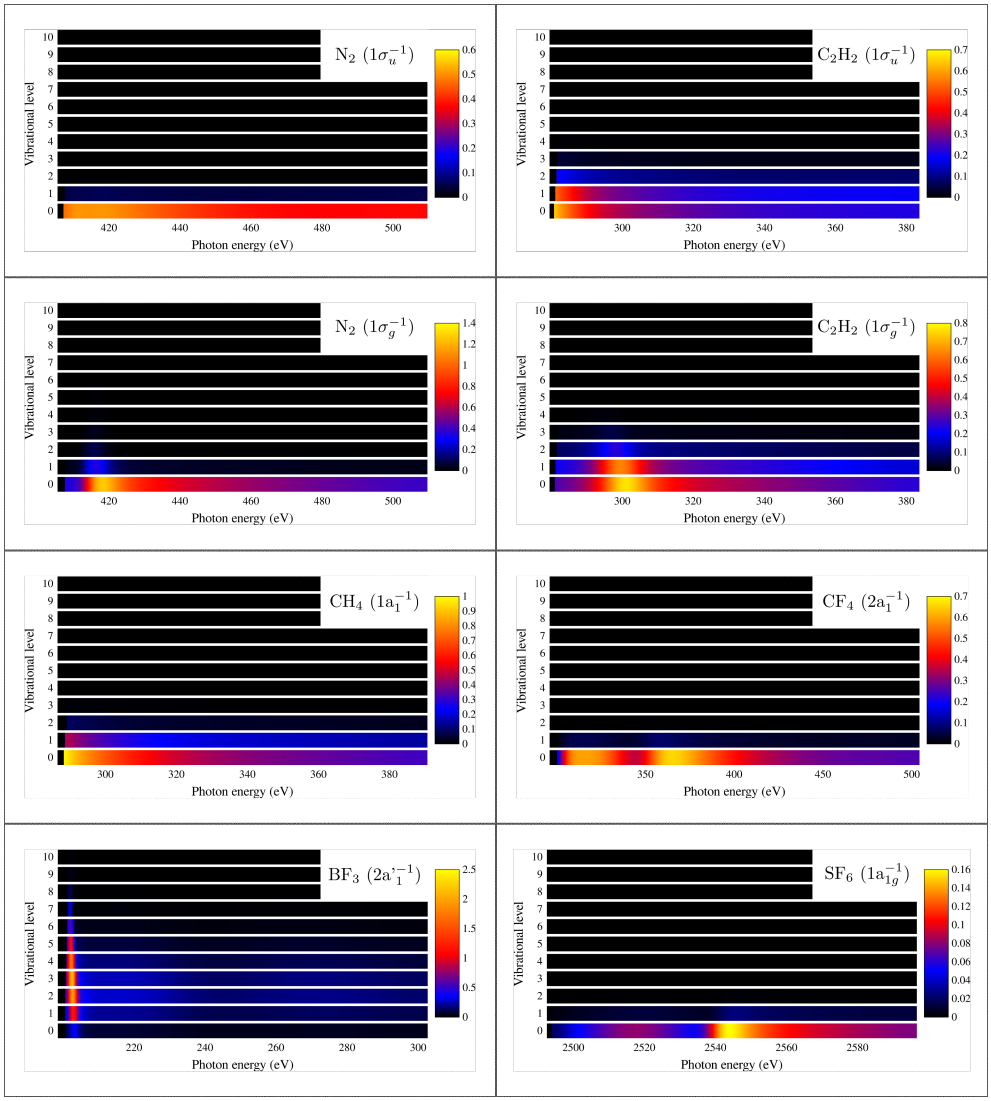

Figure B.9: Vibrationally resolved cross sections for the core shell photoionization of N_2, C_2H_2, CH_4, CF_4, BF_3 and SF_6.

Publications

- Sophie E. Canton, Etienne Plésiat, John D. Bozek, Bruce S. Rude, Piero Decleva, and Fernando Martín. Direct observation of Young's double-slit interferences in vibrationally resolved photoionization of diatomic molecules. *Proc. Natl. Acad. Sci.*, 108(18):7302–7306, May 2011

- Etienne Plésiat, Luca Argenti, Edwin Kukk, Catalin Miron, Kiyoshi Ueda, Piero Decleva, and Fernando Martín. Intramolecular electron diffraction in vibrationally resolved K-shell photoionization of methane. *Phys. Rev. A*, 85(2):023409, 2012

- Luca Argenti, T. Darrah Thomas, Etienne Plésiat, X.-J. Liu, Catalin Miron, Toralf Lischke, Georg Prümper, K. Sakai, T. Ouchi, Ralph Püttner, V. Sekushin, Takahiro Tanaka, Masamitsu Hoshino, Hiroshi Tanaka, Piero Decleva, Kiyoshi Ueda, and Fernando Martín. Double-slit experiment with a polyatomic molecule: vibrationally resolved C 1s photoelectron spectra of acetylene. *New J. Phys.*, 14:033012, 2012

- Etienne Plésiat, Piero Decleva, and Fernando Martín. Vibrational branching ratios in the photoelectron spectra of N_2 and CO: interference and diffraction effects. *Phys. Chem. Chem. Phys.*, 14(31):10853–71, August 2012

- Etienne Plésiat, Piero Decleva, and Fernando Martín. Vibrationally resolved photoelectron angular distributions from randomly oriented and fixed-in-space N_2 and CO molecules. *J. Phys. B: At. Mol. Opt. Phys.*, 45(19):194008, October 2012

Bibliography

[1] Jun-ichi Adachi, K. Hosaka, S. Furuya, K. Soejima, Masahiko Takahashi, Akira Yagishita, S. K. Semenov, and N. A. Cherepkov. Shape-Resonance-Enhanced Vibrational Effects in the Angular Distributions of C 1s Photoelectrons from Fixed-in-Space CO Molecules. *Phys. Rev. Lett.*, 91(16):163001, October 2003.

[2] Jun-ichi Adachi, K. Hosaka, S. Furuya, K. Soejima, Masahiko Takahashi, Akira Yagishita, S. K. Semenov, and N. A. Cherepkov. Angular distributions of vibrationally-resolved C 1s photoelectrons from fixed-in-space CO molecules: vibrational effect in the shape-resonant C 1s photoionization of CO. *J. Electron Spectrosc. Relat. Phenom.*, 137-140:243–248, July 2004.

[3] Jun-ichi Adachi, K. Hosaka, Takahiro Teramoto, Masakazu Yamazaki, Noboru Watanabe, Masahiko Takahashi, and Akira Yagishita. Photoelectronphotoionphotoion momentum spectroscopy as a direct probe of the core-hole localization in C 1s photoionization of C_2H_2. *J. Phys. B: At. Mol. Opt. Phys.*, 40:F285–F291, October 2007.

[4] Jun-ichi Adachi, Nobuhiro Kosugi, and Akira Yagishita. Symmetry-resolved soft x-ray absorption spectroscopy: its application to simple molecules. *J. Phys. B: At. Mol. Opt. Phys.*, 38(11):R127–R152, June 2005.

[5] Carlo Adamo and Vincenzo Barone. Exchange functionals with improved long-range behavior and adiabatic connection methods without adjustable parameters: The mPW and mPW1PW. *J. Chem. Phys.*, 108(2):664, 1998.

[6] Carlo Adamo and Vincenzo Barone. Implementation and validation of the Lacks-Gordon exchange functional in conventional density functional and adiabatic connection methods. *J. Comput. Chem.*, 19(4):418–429, 1998.

[7] B. M. Addison-Jones, K. H. Tan, B. W. Yates, J. N. Cutler, G. M. Bancroft, and J. S. Tse. A comparison of valence level photoelectron cross sections for SF_6, SeF_6 and "F_6" from 21eV to 100eV photon energy. *J. Electron Spectrosc. Relat. Phenom.*, 48:155–178, 1989.

[8] D. Akoury, K. Kreidi, T. Jahnke, Th. Weber, A. Staudte, M. S. Schöffler, N. Neumann, J. Titze, L. Ph. H. Schmidt, A. Czasch, O. Jagutzki, R. A. Costa Fraga, R. E. Grisenti, R. Díez Muiño, N. A. Cherepkov, S. K. Semenov, P. Ranitovic, C. L. Cocke, T. Osipov, H. Adaniya, J. C. Thompson, M. H. Prior, A. Belkacem, A. L. Landers, H. Schmidt-Böcking, and Reinhard Dörner. The simplest double slit: interference and entanglement in double photoionization of H_2. *Science*, 318:949–952, November 2007.

[9] Miron Ya. Amusia and Arkadiy S. Baltenkov. Non-physical consequences of the muffin-tin-type intra-molecular potential. *Cent. Eur. J. Phys.*, 8(5):825–832, December 2010.

[10] Tomohiro Aoto, Kenji Ito, Yasumasa Hikosaka, Akihiro Shibasaki, Ryo Hirayama, Norifumi Yamamono, and Eisaku Miyoshi. Inner-valence states of N_2^+ and the dissociation dynamics studied by threshold photoelectron spectroscopy and configuration interaction calculation. *J. Chem. Phys.*, 124(23):234306, June 2006.

[11] Luca Argenti, T. Darrah Thomas, Etienne Plésiat, X.-J. Liu, Catalin Miron, Toralf Lischke, Georg Prümper, K. Sakai, T. Ouchi, Ralph Püttner, V. Sekushin, Takahiro Tanaka, Masamitsu Hoshino, Hiroshi Tanaka, Piero Decleva, Kiyoshi Ueda, and Fernando Martín. Double-slit experiment with a polyatomic molecule: vibrationally resolved C 1s photoelectron spectra of acetylene. *New J. Phys.*, 14:033012, 2012.

[12] Markus Arndt, Olaf Nairz, Julian Vos-Andreae, Claudia Keller, Gerbrand van der Zouw, and Anton Zeilinger. Wave-particle duality of C_{60} molecules. *Nature*, 401:680, October 1999.

[13] D. Arvanitis, N. Haack, G. Ceballos, H. Wende, K. Baberschke, A. L. Ankudinov, and J.J. Rehr. Shape resonances of oriented molecules. *J. Electron Spectrosc. Relat. Phenom.*, 113:57–65, January 2000.

[14] Henri Bachau, E. Cormier, Piero Decleva, J. E. Hansen, and Fernando Martín. Applications of B-splines in atomic and molecular physics. *Rep. Prog. Phys.*, 64:1815–1942, 2001.

[15] Christian Baerlocher, Fabian Gramm, Lars Massüger, Lynne B. McCusker, Zhanbing He, Sven Hovmöller, and Xiaodong Zou. Structure of the polycrystalline zeolite catalyst IM-5 solved by enhanced charge flipping. *Science*, 315(5815):1113–6, February 2007.

[16] Arkadiy S. Baltenkov, Valery K. Dolmatov, and Steven Trent Manson. Theory of inner-shell photoionization of fixed-in-space molecules. *Phys. Rev. A*, 64(6):062707, November 2001.

[17] P. Baltzer, M. Larsson, Leif Karlsson, Björn Wannberg, and M. Carlsson Göthe. Inner-valence states of N_2^+ studied by uv photoelectron spectroscopy and configuration-interaction calculations. *Phys. Rev. A*, 46(9):5545, 1992.

[18] P. Baltzer, M. Lundqvist, Björn Wannberg, Leif Karlsson, M. Larsson, M. A. Hayes, J. B. West, M. R. F. Siggel, A. C. Parr, and J. L. Dehmer. Inner-valence states of CO^+ between 22 eV and 46 eV studied by high resolution photoelectron spectroscopy and ab initio CI calculations. *J. Phys. B: At. Mol. Opt. Phys.*, 27:4915–4932, 1994.

[19] Gunadya Bandarage and Robert R. Lucchese. Multiconfiguration multichannel Schwinger study of the C(1s) photoionization of CO including shake-up satellites. *Phys. Rev. A*, 47(3):1989, 1993.

[20] M. S. Banna, B. E. Mills, D. W. Davis, and D. A. Shirley. X-ray photoemission molecular orbitals of hydrogen fluoride and the fluorinated methanes. *J. Chem. Phys.*, 61:4780, 1974.

[21] D. M. Barrus, R. L. Blake, A. J. Burek, K. C. Chambers, and A. L. Pregenzer. K-shell photoabsorption coefficients of O_2, CO_2, CO, and N_2O. *Phys. Rev. A*, 20(3):1045–1061, 1979.

[22] Bryan Basden and Robert R. Lucchese. Vibrationally resolved cross sections and asymmetry parameters for the photoionization of N_2 with coupling between the $(3\sigma_g)^{-1}$ and the $(2\sigma_u)^{-1}$ channels. *Phys. Rev. A*, 37(1):89, 1988.

[23] C. F. Batten, J. Ashley Taylor, Bilin P. Tsai, and G. G. Meisels. Photoionization processes at threshold. II. Threshold photoelectron, photoionization, and coincidence ion-threshold photoelectron spectra of BF_3. *J. Chem. Phys.*, 69(6):2547, 1978.

[24] Axel D. Becke. Density-functional exchange-energy approximation with correct asymptotic behavior. *Phys. Rev. A*, 38(6):3098–3100, 1988.

[25] Axel D. Becke. A new mixing of Hartree-Fock and local density-functional theories. *J. Chem. Phys.*, 98:1372, 1993.

[26] Axel D. Becke. Density-functional thermochemistry. III. the role of the exact exchange. *J. Chem. Phys.*, 98:5648, 1993.

[27] Axel D. Becke. Density-functional thermochemistry. IV. A new dynamical correlation functional and implications for exact-exchange mixing. *J. Chem. Phys.*, 104(3):1040, 1996.

[28] Uwe Becker. Angle-resolved electron - electron and electron - ion coincidence spectroscopy : new tools for photoionization studies. *J. Electron Spectrosc. Relat. Phenom.*, 112:47–65, 2000.

[29] Uwe Becker. Matter-wave interference made clear. *Nature*, 474:586–587, October 2011.

[30] Donald H. Bilderback, Pascal Elleaume, and Edgar Weckert. Review of third and next generation synchrotron light sources. *J. Phys. B: At. Mol. Opt. Phys.*, 38(9):S773–S797, May 2005.

[31] Knut J. Bø rve, Leif J. Sæ thre, T. Darrah Thomas, Thomas X. Carroll, N. Berrah, John D. Bozek, and Edwin Kukk. Vibronic structure in the carbon 1s photoelectron spectra of HCCH and DCCD. *Phys. Rev. A*, 63(1):012506, December 2000.

[32] P. Bolognesi, G. Alberti, D. B. Thompson, L. Avaldi, and G. C. King. A study of the partial photoionization cross sections of the N_2 valence-shell states. *J. Phys. B: At. Mol. Opt. Phys.*, 37(23):4575–4588, December 2004.

[33] P. Bolognesi, V. Feyer, A. Lahmam-Bennani, M. E. Staicu Casagrande, L. Avaldi, S. K. Semenov, V. V. Kuznetsov, and N. A. Cherepkov. Inner shell ionization and relaxation of CO molecule studied by coincidence spectroscopies. *J. Electron Spectrosc. Relat. Phenom.*, 161:90–94, October 2007.

[34] Max Born and J. Robert Oppenheimer. On the quantum theory of molecules. *Ann. der Physik*, 84(457):1–32, 1927.

[35] J. E. Bowcock and Hugh Burkhardt. Principles and problems of phase-shift analysis. *Rep. Prog. Phys.*, 38:1099–1141, 1975.

[36] John D. Bozek, N. Berrah, Edwin Kukk, T. Darrah Thomas, Thomas X. Carroll, Leif J. Sæ thre, J. A. Sheehy, and P. W. Langhoff. High-resolution molecular inner-shell electron spectroscopies. In *X-Ray and Inner-Shell Processes*, volume 506, pages 188–204. Aip, 2000.

[37] B. H. Bransden and C. J. Joachain. *Physics of atoms and molecules*. Pearson Education, second edition, 2003.

[38] M. Braun, S. Barsotti, S. Marienfeld, E. Leber, J. M. Weber, M.-W. Ruf, and H. Hotop. High resolution study of anion formation in low-energy electron attachment to SF_6 molecules in a seeded supersonic beam. *Eur. Phys. J. D*, 35(2):177–191, August 2005.

[39] Svend Brodersen. The cubic potential function of CF4 fitted directly to the experimental frequencies. *J. Mol. Spectrosc.*, 145(2):331–351, February 1991.

[40] M. Brosolo and Piero Decleva. Variational approach to continuum orbitals in a spline basis: An application to H_2^+ photoionization. *Chem. Phys.*, 159(2):185–196, 1992.

[41] M. Brosolo, Piero Decleva, and A. Lisini. LCAO expansion in a spline basis for accurate variational determination of continuum wavefunctions. Applications to H_2^+ and HeH_2^+. *Chem. Phys.*, 181:85–95, 1994.

[42] Kieron Burke. Perspective on density functional theory. *J. Chem. Phys.*, 136(15):150901, 2012.

[43] Ivo Cacelli, Roberto Moccia, and Antonio Rizzo. Gaussian-type-orbital basis sets for the calculation of continuum properties in molecules: The differential photoionization cross section of molecular nitrogen. *Phys. Rev. A*, 57(3):1895–1905, 1998.

[44] B. Cadioli, U. Pincelli, E. Tosatti, U. Fano, and J. L. Dehmer. Barrier to electron passage through electronegative atoms in BF_3. *Chem. Phys. Lett.*, 17(1):15–18, 1972.

[45] Sophie E. Canton, Etienne Plésiat, John D. Bozek, Bruce S. Rude, Piero Decleva, and Fernando Martín. Direct observation of Young's double-slit interferences in vibrationally resolved photoionization of diatomic molecules. *Proc. Natl. Acad. Sci.*, 108(18):7302–7306, May 2011.

[46] Sophie E. Canton, Etienne Plésiat, Piero Decleva, and Fernando Martín. To be published.

[47] Thomas X. Carroll, N. Berrah, J. Bozek, J. Hahne, Edwin Kukk, Leif J. Sæ thre, and T. Darrah Thomas. Carbon 1s photoelectron spectrum of methane: Vibrational excitation and core-hole lifetime. *Physical Review A*, 59(5):3386–3393, May 1999.

[48] Thomas X. Carroll, Knut J. Bø rve, Leif J. Sæ thre, John D. Bozek, Edwin Kukk, Jeffrey A. Hahne, and T. Darrah Thomas. Carbon 1s photoelectron spectroscopy of CF_4 and CO: Search for chemical effects on the carbon 1s hole-state lifetime. *J. Chem. Phys.*, 116(23):10221, 2002.

[49] K. Chakrabarti and Jonathan Tennyson. R -matrix calculation of the continuum states of carbon monoxide. *J. Phys. B: At. Mol. Opt. Phys.*, 40(11):2135–2145, June 2007.

[50] Scott A. Chambers. Epitaxial film crystallography by high-energy Auger and X-ray photoelectron diffraction. *Adv. Phys.*, 40(4):357–415, 1991.

[51] N. Chandra. On the theories of photoemission processes in diatomic molecules. *Chem. Phys.*, 108:301–315, 1986.

[52] N. Chandra. Photoelectron spectroscopic studies of polyatomic molecules: I. Theory. *J. Phys. B: At. Mol. Opt. Phys.*, 20:3405–3415, January 1987.

[53] N. Chandra. Photoelectron spectroscopic studies of polyatomic molecules: II. Ionisation in the a_1 orbital of a T_d molecule. *J. Phys. B: At. Mol. Opt. Phys.*, 20:3417–3426, 1987.

[54] Henry N. Chapman, Petra Fromme, Anton Barty, Thomas A. White, Richard A. Kirian, Andrew Aquila, Mark S. Hunter, Joachim Schulz, Daniel P. DePonte, Uwe Weierstall, R. Bruce Doak, Filipe R. N. C. Maia, Andrew V. Martin, Ilme Schlichting, Lukas Lomb, Nicola Coppola, Robert L. Shoeman, Sascha W. Epp, Robert Hartmann, Daniel Rolles, Artem Rudenko, Lutz Foucar, Nils Kimmel, Georg Weidenspointner, Peter Holl, Mengning Liang, Miriam Barthelmess, Carl Caleman, Sébastien Boutet, Michael J. Bogan, Jacek Krzywinski, Christoph Bostedt, Saša Bajt, Lars Gumprecht, Benedikt Rudek, Benjamin Erk, Carlo Schmidt, André Hömke, Christian Reich, Daniel Pietschner, Lothar Strüder, Günter Hauser, Hubert Gorke, Joachim Ullrich, Sven Herrmann, Gerhard Schaller, Florian Schopper, Heike Soltau, Kai-Uwe Kühnel, Marc Messerschmidt, John D. Bozek, Stefan P. Hau-Riege, Matthias Frank, Christina Y. Hampton, Raymond G. Sierra, Dmitri Starodub, Garth J. Williams, Janos Hajdu, Nicusor Timneanu, M. Marvin Seibert, Jakob Andreasson, Andrea Rocker, Olof Jönsson, Martin Svenda, Stephan Stern, Karol Nass, Robert Andritschke, Claus-Dieter Schröter, Faton Krasniqi, Mario Bott, Kevin E. Schmidt, Xiaoyu Wang, Ingo Grotjohann, James M. Holton, Thomas R. M. Barends, Richard Neutze, Stefano Marchesini, Raimund Fromme, Sebastian Schorb, Daniela Rupp, Marcus Adolph, Tais Gorkhover, Inger Andersson, Helmut Hirsemann, Guillaume Potdevin, Heinz Graafsma, Björn Nilsson, and John C. H. Spence. Femtosecond X-ray protein nanocrystallography. *Nature*, 470(7332):73–7, February 2011.

[55] C. T. Chen, Y. Ma, and F. Sette. K-shell photoabsorption of the N_2 molecule. *Phys. Rev. A*, 40(11):6737–6740, 1989.

[56] N. A. Cherepkov and G. Raeev. Photoionization of oriented CO molecule: Linear dichroism in the angular distribution of photoelectrons. *J. Chem. Phys.*, 103(18):8238–8246, 1995.

[57] N. A. Cherepkov, G. Raeev, Jun-ichi Adachi, Yasumasa Hikosaka, Kenji Ito, S. Motoki, M. Sano, K. Soejima, and Akira Yagishita. K-shell photoionization of CO: II. Determination of dipole matrix elements and phase differences. *J. Phys. B: At. Mol. Opt. Phys.*, 33:4213–4236, 2000.

[58] N. A. Cherepkov and S. K. Semenov. New Developments in the Theory of Molecular K-Shell Photoionization. *Int. J. Quantum Chem.*, 107:2889–2901, 2007.

[59] N. A. Cherepkov, S. K. Semenov, A. V. Golovin, Jun-ichi Adachi, and Akira Yagishita. O K-shell photoemission of the CO molecule: comparison between theory and experiment. *J. Phys. B: At. Mol. Opt. Phys.*, 37:4803–4815, December 2004.

[60] N. A. Cherepkov, S. K. Semenov, Yasumasa Hikosaka, Kenji Ito, S. Motoki, and Akira Yagishita. Manifestation of many-electron correlations in photoionization of the K shell of N_2. *Phys. Rev. Lett.*, 84(2):250–253, January 2000.

[61] N. A. Cherepkov, S. K. Semenov, M. S. Schöffler, J. Titze, N. Petridis, T. Jahnke, K. Cole, L. Ph. H. Schmidt, A. Czasch, D. Akoury, O. Jagutzki, J. B. Williams, T. Osipov, S. Lee, M. H. Prior, A. Belkacem, A. L. Landers, H. Schmidt-Böcking, Reinhard Dörner, and Th. Weber. Auger decay of $1\sigma_g$ and $1\sigma_u$ hole states of the N_2 molecule. II. Young-type interference of Auger electrons and its dependence on internuclear distance. *Phys. Rev. A*, 82(2):023420, August 2010.

[62] Adrian Cho. What Shall We Do With the X-ray Laser? *Science*, 330:1470, 2010.

[63] L. G. Christophorou and J. K. Olthoff. Electron interactions with SF_6. *J. Phys. Chem. Ref. Data*, 29(3):267, 2000.

[64] Howard D. Cohen and U. Fano. Interference in the photo-ionization of molecules. *Phys. Rev.*, 150(1):30–33, 1966.

[65] P. Colavita, G. De Alti, G. Fronzoni, Mauro Stener, and Piero Decleva. Theoretical study of the valence and core photoemission spectra of C_{60}. *Phys. Chem. Chem. Phys.*, 3:4481–4487, 2001.

[66] B. E. Cole, D. L. Ederer, Roger Stockbauer, Keith Codling, Albert C. Parr, J. B. West, E. D. Poliakoff, and J. L. Dehmer. Wavelength and vibrational-state dependence of photoelectron angular distributions. Resonance effects in 5σ photoionization of CO. *J. Chem. Phys.*, 72(11):6308, 1980.

[67] Lee A. Cole and John P. Perdew. Calculated electron affinities of the elements. *Phys. Rev. A*, 25(3):1265–1271, 1982.

[68] R. Colle, D. Embriaco, M. Massini, S. Simonucci, and S. Taioli. Ab initio calculation of the C1s photoelectron spectrum of C_2H_2. *Nucl. Instrum. Meth. B*, 213:65–70, January 2004.

[69] L. A. Collins and B. I. Schneider. Molecular photoionization in the linear algebraic approach: H_2, N_2, NO, and CO_2. *Phys. Rev. A*, 29(4):1695, 1984.

[70] John W. Cooper. Photoionization from Outer Atomic Subshells. A Model Study. *Phys. Rev.*, 128(2):681–693, October 1962.

[71] F. Albert Cotton. *Chemical applications of group theory.* John Wiley and sons, third edition, 1963.

[72] Aloke Das, J. Scott Miller, E. D. Poliakoff, Robert R. Lucchese, and John D. Bozek. Vibrationally resolved photoionization dynamics of CF_4 in the D^2A_1 state. *J. Chem. Phys.*, 127(4):044312, July 2007.

[73] Romith Das, Chuanyong Wu, A. G. Mihill, E. D. Poliakoff, Kwanghsi Wang, and Vincent McKoy. Photoion Alignment: Chemical Signatures 200 eV above Threshold. *J. Phys. Chem.*, 99(6):1741–1747, February 1995.

[74] James W. Davenport. Ultraviolet Photoionization Cross Sections for N_2 and CO. *Phys. Rev. Lett.*, 36(16):945–949, 1976.

[75] Clinton J. Davisson. The discovery of electron waves. *Nobel Lecture*, page 387, 1937.

[76] M. Davister and R. Locht. The dissociative ionization of C_2H_2 and C_2D_2. The $[CH(CD)]^+$ dissociation channel. The H(D)C≡C(D)H binding energy. *Chem. Phys.*, 191:333–346, February 1995.

[77] Carl de Boor. *A practical guide to splines.* Springer, 1978.

[78] A. De Fanis, N. Saito, M. Machida, K. Okada, H. Chiba, A. Cassimi, R. Dörner, I. Koyano, and Kiyoshi Ueda. Asymmetric nuclear motion of the F 1s-ionized state in BF_3 probed by quadruple-ion-coincidence momentum imaging. *Phys. Rev. A*, 69(2):022506, February 2004.

[79] G. L. C. de Souza, A. S. dos Santos, Robert R. Lucchese, L. E. Machado, L. M. Brescansin, H. V. Manini, I. Iga, and M.-T. Lee. Theoretical investigation on electron scattering by benzene in the intermediate-energy range. *Chem. Phys.*, 393(1):19–24, January 2012.

[80] Piero Decleva, G. Fronzoni, A. Kivimäki, J. Álvarez Ruiz, and Svante Svensson. Shake-up transitions in S 2p, S 2s and F 1s photoionization of the SF_6 molecule. *J. Phys. B: At. Mol. Opt. Phys.*, 42(5):055102, March 2009.

[81] Piero Decleva, S. Furlan, G. Fronzoni, and Mauro Stener. High energy oscillations in the valence photoionization partial cross-section of C_60. *Chem. Phys. Lett.*, 348:363–367, 2001.

[82] J. L. Dehmer. Evidence of Effective Potential Barriers in the X-Ray Absorption Spectra of Molecules. *J. Chem. Phys.*, 56(9):4496, 1972.

[83] J. L. Dehmer and Dan Dill. Shape resonances in K-shell photoionization of diatomic molecules. *Phys. Rev. Lett.*, 35(4):213–215, 1975.

[84] J. L. Dehmer and Dan Dill. Molecular effects on inner-shell photoabsorption. K-shell spectrum of N_2. *J. Chem. Phys.*, 65(12):5327, 1976.

[85] J. L. Dehmer, Dan Dill, and Scott Wallace. Shape-Resonance-Enhanced Nuclear-Motion Effects in Molecular Photoionization. *Phys. Rev. Lett.*, 43(14):1005–1008, 1979.

[86] J. L. Dehmer, Albert C. Parr, S. H. Southworth, and D. M. P. Holland. Angle-resolved photoelectron study of the valence levels of BF_3 in the range $17 \leq h\nu \leq 28$ eV. *Phys. Rev. A*, 30(4):1783–1790, 1984.

[87] J. L. Dehmer, Albert C. Parr, Scott Wallace, and Dan Dill. Photoelectron branching ratios and angular distributions for the valence levels of SF_6 in the range $16 \leq h\nu \leq 30$eV. *Phys. Rev. A*, 26(6):3283, 1982.

[88] R. Della Picca, P. D. Fainstein, and A. Dubois. Cooper minima and Young-type interferences in the photoionization of H_2^+. *Phys. Rev. A*, 84(3):033405, September 2011.

[89] R. Della Picca, P. D. Fainstein, M. L. Martiarena, N. Sisourat, and A. Dubois. Cooper minima and Young-type interferences in photoionization of one-electron molecular ions. *Phys. Rev. A*, 79(3):032702, March 2009.

[90] Ph. V. Demekhin, A. Ehresmann, and V. L. Sukhorukov. Single center method: a computational tool for ionization and electronic excitation studies of molecules. *J. Chem. Phys.*, 134(2):024113, January 2011.

[91] Ph. V. Demekhin, I. D. Petrov, Takahiro Tanaka, Masamitsu Hoshino, Hiroshi Tanaka, Kiyoshi Ueda, W. Kielich, and A. Ehresmann. Large impact of the weak direct photoionization on the angularly resolved CO^+ ($A^2\Pi$) de-excitation spectra of the CO^* ($1\sigma^{-1}2\pi$) resonance. *J. Phys. B: At. Mol. Opt. Phys.*, 43(6):065102, March 2010.

[92] R. Díez Muiño, Daniel Rolles, F. J. García De Abajo, C. S. Fadley, and M. A. Van Hove. Multiple scattering theory of photoelectron angular distributions from oriented diatomic molecules. *Surf. Rev. Lett.*, 9(2):1213–1217, 2002.

[93] Dan Dill. Angular Distributions of Photoelectrons from H_2: Effects of Rotational Autoionization. *Phys. Rev. A*, 6(1):160–172, 1972.

[94] Dan Dill and J. L. Dehmer. Electron-molecule scattering and molecular photoionization using the multiple-scattering method. *J. Chem. Phys.*, 61(2):692, 1974.

[95] Dan Dill, Jon Siegel, and J. L. Dehmer. Spectral variation of fixed-molecule photoelectron angular distributions. *J. Chem. Phys.*, 65(8):3158–3160, 1976.

[96] Dan Dill, John R. Swanson, Scott Wallace, and J. L. Dehmer. Angular Distribution of Molecular K-Shell Auger Electrons: Spectroscopy of Photoabsorption Anisotropy. *Phys. Rev. Lett.*, 45(17):1393–1396, 1980.

[97] Dan Dill, Scott Wallace, Jon Siegel, and J. L. Dehmer. Molecular-photoelectron angular distributions as a probe of dynamic symmetry breaking. *Phys. Rev. Lett.*, 41(18):1230–1233, 1978.

[98] Dan Dill, Scott Wallace, Jon Siegel, and J. L. Dehmer. Molecular-photoelectron angular distributions as a probe of dynamic symmetry breaking (erratum). *Phys. Rev. Lett.*, 42(6):411, 1979.

[99] W. Domcke and Lorenz S. Cederbaum. Vibronic coupling and symmetry breaking in core electron ionization. *Chem. Phys.*, 25(2):189–196, 1977.

[100] W. Domcke and Lorenz S. Cederbaum. Electronic recoil effects in high-energy photoelectron spectroscopy. *J. Electron Spectrosc. Relat. Phenom.*, 13(3):161–173, 1978.

[101] Reinhard Dörner, V. Mergel, O. Jagutzki, L. Spielberger, J. Ullrich, R. Moshammer, and H. Schmidt-Böcking. Cold Target Recoil Ion Momentum Spectroscopy : a 'momentum microscope' to view atomic collision dynamics. *Phys. Rep.*, 330:95–192, 2000.

[102] Thom H. Jr. Dunning. Gaussian basis sets for use in correlated molecular calculations. I. The atoms boron through neon and hydrogen. *J. Chem. Phys.*, 90(2):1007, 1989.

[103] Carolyn Duzy and R. Stephen Berry. Photoionization and Rydberg states of N_2. *J. Chem. Phys.*, 64(6):2421, 1976.

[104] Masahiro Ehara, K. Kuramoto, H. Nakatsuji, Masamitsu Hoshino, Takahiro Tanaka, M. Kitajima, Hiroshi Tanaka, A. De Fanis, Yusuke Tamenori, and Kiyoshi Ueda. C1s and O1s photoelectron satellite spectra of CO with symmetry-dependent vibrational excitations. *J. Chem. Phys.*, 125(11):114304, September 2006.

[105] Masahiro Ehara, H. Nakatsuji, M. Matsumoto, T. Hatamoto, X.-J. Liu, Toralf Lischke, Georg Prümper, Takahiro Tanaka, C. Makochekanwa, Masamitsu Hoshino, Hiroshi Tanaka, James R. Harries, Yusuke Tamenori, and Kiyoshi Ueda. Symmetry-dependent vibrational excitation in N 1s photoionization of N_2: Experiment and theory. *J. Chem. Phys.*, 124(12):124311, March 2006.

[106] Maximilian Eichberger, Hanjo Schäfer, Marina Krumova, Markus Beyer, Jure Demsar, Helmuth Berger, Gustavo Moriena, Germán Sciaini, and R. J. Dwayne Miller. Snapshots of cooperative atomic motions in the optical suppression of charge density waves. *Nature*, 468(7325):799–802, December 2010.

[107] Michèle Eidelsberg, Françoise Launay, Kenji Ito, Takashi Matsui, Paul C. Hinnen, Elmar Reinhold, Wim Ubachs, and Klaus P. Huber. Rydberg-valence interactions of CO, and spectroscopic evidence characterizing the C' $1\Sigma^+$ valence state. *J. Chem. Phys.*, 121(1):292–308, July 2004.

[108] F. R. Elder, A. M. Gurewitsch, R. V. Langmuir, and H. C. Pollock. Radiation from electrons in a synchrotron. *Phys. Rev.*, 71:829–830, 1947.

[109] Peter Esherick, Adelbert Owyoung, and Chris W. Patterson. Inverse Raman Spectrum of the v_1-Fundamental of CF_4*. *J. Mol. Spectrosc.*, 86:250–257, 1981.

[110] M. Evans and C. Y. Ng. Rotationally resolved pulsed field ionization photoelectron study of CO^+ $(X^2\Sigma^+, v^+ = 0 - 42)$ inthe energy range of 13.9821.92 eV. *J. Chem. Phys.*, 111(19):8879–8892, 1999.

[111] U. Fano and Dan Dill. Angular momentum Transfer in the Theory of Angular Distributions. *Phys. Rev. A*, 6(1):185, 1972.

[112] George R. Farquar, J. Scott Miller, E. D. Poliakoff, Kwanghsi Wang, and Vincent McKoy. Rotationally resolved photoionization: Influence of the $4\sigma \rightarrow k\sigma$ shape resonance on $CO^+(B\ ^2\Sigma^+)$ rotational distributions. *J. Chem. Phys.*, 115(21):9764, 2001.

[113] D. G. Fedorov, M. Evans, Y. Song, M. S. Gordon, and C. Y. Ng. An experimental and theoretical study of the spinorbit interaction for

$CO^+(A^2\Pi_{3/2,1/2}, v^+ = 0 - 41)$ and $O_2^+(X^2\Pi_{3/2,1/2g}, v^+ = 0 - 38)$. *J. Chem. Phys.*, 111(14):6413–6421, 1999.

[114] R. Feifel, John H. D. Eland, L. Storchi, and F. Tarantelli. Complete valence double photoionization of SF_6. *J. Chem. Phys.*, 122(14):144309, April 2005.

[115] R. Feifel, Takahiro Tanaka, Masamitsu Hoshino, Hiroshi Tanaka, Yusuke Tamenori, Vincenzo Carravetta, and Kiyoshi Ueda. Quenching and restoring of the $A^2\Pi$ cationic state in resonant Auger electron spectra of CO in the vicinity of the O 1s$\rightarrow 2\pi$ resonance. *Phys. Rev. A*, 74(6):062717, December 2006.

[116] V. Felicíssimo, F. F. Guimarães, and Faris Gelmukhanov. Enhancement of the recoil effect in x-ray photoelectron spectra of molecules driven by a strong ir field. *Phys. Rev. A*, 72(2):023414, August 2005.

[117] J. Fernández, O. Fojón, and Fernando Martín. Double-slit, confinement, and non-Franck-Condon effects in photoionization of H_2 at high photon energy. *Phys. Rev. A*, 79(2):023420, February 2009.

[118] J. Fernández, O. Fojón, Alicia Palacios, and Fernando Martín. Interferences from Fast Electron Emission in Molecular Photoionization. *Phys. Rev. Lett.*, 98(4):043005, January 2007.

[119] J. Fernández, F. L. Yip, T. N. Rescigno, C. W. McCurdy, and Fernando Martín. Two-center effects in one-photon single ionization of H_2^+, H_2, and Li_2^+ with circularly polarized light. *Phys. Rev. A*, 79(4):043409, April 2009.

[120] T. A. Ferrett, Dennis W. Lindle, P. A. Heimann, H. G. Kerkhoff, Uwe Becker, and D. A. Shirley. Sulfur 1s core-level photoionization of SF_6. *Phys. Rev. A*, 34(3):1916–1930, September 1986.

[121] V. Feyer, P. Bolognesi, M. Coreno, K. C. Prince, L. Avaldi, L. Storchi, and F. Tarantelli. Effects of nuclear dynamics in the low-kinetic-energy Auger spectra of CO and CO_2. *J. Chem. Phys.*, 123(22):224306, December 2005.

[122] R. F. Fink, M. N. Piancastelli, A. N. Grum-Grzhimailo, and Kiyoshi Ueda. Angular distribution of Auger electrons from fixed-in-space and rotating C 1s–¿2π photoexcited CO: theory. *J. Chem. Phys.*, 130(1):014306, January 2009.

[123] Charlotte Froese Fischer and M. Idrees. Spline methods for resonances in photoionisation cross sections. *J. Phys. B: At. Mol. Opt. Phys.*, 23:679–691, 1990.

[124] J.-H. Fock and E. E. Koch. Shape resonances and partial photoemission cross sections of solid SF_6 and CCl_4. *Chem. Phys.*, 96:125–143, 1985.

[125] O. Fojón, J. Fernández, Alicia Palacios, R. D. Rivarola, and Fernando Martín. Interference effects in H_2 photoionization at high energies. *J. Phys. B: At. Mol. Opt. Phys.*, 37(15):3035–3042, August 2004.

[126] O. Fojón, Alicia Palacios, J. Fernández, R. D. Rivarola, and Fernando Martín. Interferences in the photoelectron spectrum of H_2^+ molecules at high energy. *Phys. Lett. A*, 350:371–374, February 2006.

[127] D. L. Foulis, R. F. Pettifer, and P. Sherwood. Removal of the muffin-tin approximation and use of self-consistent-field electron densities for calculating the K-edge X-ray absorption near-edge structure of chlorine. *Europhys. Lett.*, 29(8):647, 1995.

[128] James T. Francis, Cássia C. Turci, Tolek Tyliszczak, G. Gerson B. de Souza, Nobuhiro Kosugi, and Adam P. Hitchcock. Electron-impact core excitation of SF_6. I. S 2p, S 2s, and F 1s spectroscopy. *Phys. Rev. A*, 52(6):4665, 1995.

[129] Olaf Frank and Jan-michael Rost. Diffraction effects in the photoionization of clusters. *Chem. Phys. Lett.*, 271:367–371, 1997.

[130] G. Fronzoni, Mauro Stener, and Piero Decleva. Valence and core photoionization dynamics of acetylene by TD-DFT continuum approach. *Chem. Phys.*, 298:141–153, March 2004.

[131] Hironobu Fukuzawa, X.-J. Liu, T. Teranishi, K. Sakai, Georg Prümper, Kiyoshi Ueda, Y. Morishita, N. Saito, Mauro Stener, and Piero Decleva. Fluorine K-shell photoelectron angular distribution from CF_4 molecules in the molecular frame. *Chem. Phys. Lett.*, 451:182–185, January 2008.

[132] F. X. Gadea, Horst Köppel, Jochen Schirmer, Lorenz S. Cederbaum, K. J. Randall, A. M. Bradshaw, F. Sette, and C. T. Chen. Vibronic coupling and core-hole localization in K-shell excitations of ethylene. *Phys. Rev. Lett.*, 66(7):883–886, 1991.

[133] Etienne Gagnon, Predrag Ranitovic, Xiao-Min Tong, C. L. Cocke, Margaret M. Murnane, Henry C. Kapteyn, and Arvinder S. Sandhu. Soft X-ray-driven femtosecond molecular dynamics. *Science*, 317:1374, September 2007.

[134] J. W. Gallagher, C. E. Brion, James A. R. Samson, and P. W. Langhoff. Absolute Cross Sections for Molecular Photoabsorption, Partial Photoionization, and Ionic Photofragmentation Processes. *J. Phys. Chem. Ref. Data*, 17(1):9–153, 1988.

[135] Robert J. Gdanitz. Accurately solving the electronic Schrödinger equation of atoms and molecules using explicitly correlated (r_{12-}) MR-CI: the ground state potential energy curve of N_2. *Chem. Phys. Lett.*, 283:253–261, 1998.

[136] Faris Gelmukhanov, Victor Kimberg, X.-J. Liu, Georg Prümper, Takahiro Tanaka, Masamitsu Hoshino, Hiroshi Tanaka, and Kiyoshi Ueda. Youngs double-slit experiment using two-center core-level photoemission: Photoelectron recoil effects. *J. Electron Spectrosc. Relat. Phenom.*, 156-158:265–269, May 2007.

[137] Robert Georges, Michel Herman, Jean-Claude Hilico, and Olivier Robert. High-Resolution FTIR Spectroscopy Using a Jet: Sampling the Rovibrational Spectrum of $^1 2CH_4$. *J. Mol. Spectrosc.*, 187(1):13–20, January 1998.

[138] L. G. Gerchikov and G. F. Gribakin. Electron attachment to SF_6 and lifetimes of SF_6^- negative ions. *Phys. Rev. A*, 77(4):042724, April 2008.

[139] F. A. Gianturco, C. Guidotti, and U. Lamanna. Electronic Properties of Sulphur Hexafluoride. II. Molecular Orbital Interpretation of Its X-Ray Absorption Spectra. *J. Chem. Phys.*, 57(2):840, 1972.

[140] Gene H. Golub and Charles F. van Van Loan. *Matrix computations*. The Johns Hopkins University Press, third edition, 1996.

[141] D. Goutier and L. A. Burnelle. Ab initio calculation on BF_3 and BCl_3. *Chem. Phys. Lett.*, 18(3):460, 1973.

[142] W. J. Griffiths, S. Svensson, A. Naves de Brito, N. Correia, C. J. Reid, M. L. Langford, F. M. Harris, C. M. Liegener, and H. Å gren. Doubly ionized states of carbon tetrafhoride. *Chem. Phys.*, 173:109–121, 1993.

[143] Frederick A. Grimm and Thomas A. Carlson. Angular distribution for the major photoelectron bands of nitrogen below 45eV binding energy. *Chem. Phys.*, 80:389–394, 1983.

[144] C. Fonseca Guerra, J. G. Snijders, G. te Velde, and E. J. Baerends. Regular article Towards an order-N DFT method. *Theor. Chem. Acc.*, 99:391–403, 1998.

[145] Renaud Guillemin, Wayne C. Stolte, Maria Novella Piancastelli, and Dennis W. Lindle. Jahn-Teller coupling and fragmentation after core-shell excitation in CF_4 investigated by partial-ion-yield spectroscopy. *Phys. Rev. A*, 82(4):1–7, October 2010.

[146] Renaud Guillemin, Wayne C. Stolte, Maria Novella Piancastelli, and Dennis W. Lindle. Photofragmentation of BF_3 on B and F K-shell excitation by partial ion yield spectroscopy. *J. Phys. B: At. Mol. Opt. Phys.*, 43(21):215205, November 2010.

[147] T. Gustafsson. Partial photoionization cross sections of SF_6 between 20 and 54 eV: An interpretation of the photoelectron spectrum. *Phys. Rev. A*, 18(4):1481, 1978.

[148] G. Hagenow, K. Hottmann, and H. Baumgärtel. Vibronic coupling effects observed in the high-resolution He(I) photoelectron spectra of BF_3. *Chem. Phys. Lett.*, 164(4):395, 1989.

[149] E. Haller and Lorenz S. Cederbaum. Excitation of degenerate vibrations in non-degenerate electronic bands. *Chem. Phys. Lett.*, 85(1):12, 1982.

[150] E. Haller, Horst Köppel, Lorenz S. Cederbaum, W. von Niessen, and G. Bieri. Multimode Jahn-Teller and pseudo-Jahn-Teller effects in BF_3^+. *J. Chem. Phys.*, 78(3):1359, 1983.

[151] A. Hamnett, W. Stoll, and C. E. Brion. Photoelectron branching ratios and partial ionization cross-sections for CO and N_2 in the energy range 18-50 eV. *J. Electron Spectrosc. Relat. Phenom.*, 8:367–376, 1976.

[152] W. H. Hancock and James A. R. Samson. Angular distribution of photoelectrons at 584Å using polarized radiation. *J. Electron Spectrosc. Relat. Phenom.*, 9:211–216, 1976.

[153] Nicholas C. Handy and Aron J. Cohen. Left-right correlation energy. *Mol. Phys.*, 99(5):403–412, March 2001.

[154] J. E. Hardis, T. A. Ferrett, S. H. Southworth, A. C. Parr, P. Roy, J. L. Dehmer, P. M. Dehmer, and W. A. Chupka. Autoionization dynamics in the valence-shell photoionization spectrum of CO. *J. Chem. Phys.*, 89(2):812, 1988.

[155] Franz Heiser, Oliver Geß ner, Jens Viefhaus, K. Wieliczek, Rainer Hentges, and Uwe Becker. Demonstration of Strong Forward-Backward Asymmetry in the C1s Photoelectron Angular Distribution from Oriented CO Molecules. *Phys. Rev. Lett.*, 79(13):2435–2437, 1997.

[156] M. Hentschel, R. Kienberger, C. Spielmann, G. A. Reider, N. Milosevic, T. Brabec, P. Corkum, U. Heinzmann, M. Drescher, and F. Krausz. Attosecond metrology. *Nature*, 414(6863):509–13, November 2001.

[157] Uwe Hergenhahn. Vibrational structure in inner shell photoionization of molecules. *J. Phys. B: At. Mol. Opt. Phys.*, 37:R89–R135, June 2004.

[158] Uwe Hergenhahn, O. Kugeler, A. Rüdel, E. E. Rennie, and A. M. Bradshaw. Symmetry-Selective Observation of the N 1s Shape Resonance in N_2. *J. Phys. Chem. A*, 105:5704–5708, June 2001.

[159] Yasumasa Hikosaka and John H. D. Eland. Molecular frame photoelectron angular distributions in inner-valence photoionization of N_2. *J. Phys. B: At. Mol. Opt. Phys.*, 33:3137–3147, 2000.

[160] Adam P. Hitchcock, P. Lablanquie, Paul Morin, E. Lizon, A. Lugrin, M. Simon, P. Thiry, and I. Nenner. Ionic fragmentation of K-shell excited and ionized CO. *Phys. Rev. A*, 37(7):2448, 1988.

[161] Adam P. Hitchcock and D. C. Mancini. Bibliography and database of inner shell excitation spectra of gas phase atoms and molecules. *J. Electron Spectrosc. Relat. Phenom.*, 67:132, 1994.

[162] Ph. Hofmann, K. M. Schindler, S. Bao, A. M. Bradshaw, and D. P. Woodruff. Direct identification of atomic and molecular adsorption sites using photoelectron diffraction. *Nature*, 368:131, 1994.

[163] Pierre Hohenberg and Walter Kohn. Inhomogeneous electron gas. *Phys. Rev.*, 136(3B):B864, 1964.

[164] D. M. P. Holland, M. A. MacDonald, P. Baltzer, Leif Karlsson, M. Lundqvist, Björn Wannberg, and W. von Niessen. An experimental and theoretical study of the valence shell photoelectron spectrum of sulphur hexafluoride. *Chem. Phys.*, 192:333–353, March 1995.

[165] D. M. P. Holland, M. A. MacDonald, M. A. Hayes, Leif Karlsson, and Björn Wannberg. A photoelectron spectroscopy study of the valence shell photoionization dynamics of acetylene. *J. Electron Spectrosc. Relat. Phenom.*, 97:253–263, December 1998.

[166] D. M. P. Holland, M. A. MacDonald, M. A. Hayes, Leif Karlsson, and Björn Wannberg. The influence of non-adiabatic effects on the outer valence shell photoionisation dynamics of boron trifluoride. *Chem. Phys.*, 226(3):351–360, January 1998.

[167] D. M. P. Holland, A. W. Potts, A. B. Trofimov, J. Breidbach, J. Schirmer, R. Feifel, T. Richter, K. Godehusen, M. Martins, A. Tutay, M. Yalcinkaya, M. Al-Hada, S. Eriksson, and Leif Karlsson. An experimental and theoretical study of the valence shell photoelectron spectrum of tetrafluoromethane. *Chem. Phys.*, 308(1-2):43–57, January 2005.

[168] D. M. P. Holland, D. A. Shaw, A. Hopkirk, M. A. MacDonald, and S. M. McSweeney. A study of the absolute photoabsorption cross section and the photoionization quantum efficiency of sulphur hexafluoride from the

ionization threshold to 420 Å. *J. Phys. B: At. Mol. Opt. Phys.*, 25:4823–4834, 1992.

[169] R. M. Holmes and G. V. Marr. The angular distribution of photoelectrons from N_2 , O_2 and CO as a function of photon energy. *J. Phys. B: At. Mol. Opt. Phys.*, 13:945–950, 1980.

[170] K. Hosaka, Jun-ichi Adachi, A. V. Golovin, Masahiko Takahashi, Takahiro Teramoto, Noboru Watanabe, T. Jahnke, Th. Weber, M. S. Schöffler, L. Ph. H. Schmidt, T. Osipov, O. Jagutzki, A. L. Landers, M. H. Prior, H. Schmidt-Böcking, Reinhard Dörner, Akira Yagishita, S. K. Semenov, and N. A. Cherepkov. Nondipole effects in the angular distribution of photoelectrons from the C K shell of the CO molecule. *Phys. Rev. A*, 73(2):022716, February 2006.

[171] Masamitsu Hoshino, Raffaele Montuoro, Robert R. Lucchese, A. De Fanis, Uwe Hergenhahn, Georg Prümper, Takahiro Tanaka, Hiroshi Tanaka, and Kiyoshi Ueda. Vibrationally resolved partial cross sections and asymmetry parameters for nitrogen K-shell photoionization of the NO molecule. *J. Phys. B: At. Mol. Opt. Phys.*, 41:085105, April 2008.

[172] Masamitsu Hoshino, K. Nakagawa, C. Makochekanwa, Takahiro Tanaka, N. Kuze, M. Matsumoto, K. Fujiwara, A. De Fanis, Yusuke Tamenori, M. Kitajima, Hiroshi Tanaka, and Kiyoshi Ueda. Symmetry- and vibrationally-resolved C K-shell photoionization studies of C_2H_2. *Chem. Phys. Lett.*, 421:256–260, April 2006.

[173] Jan-Tsyu J. Huang and Frank O. Ellison. Angular asymmetry parameters of photoelectrons from H_2, N_2 and CH_4; an extended orthogonalized plane-wave calculation. *Chem. Phys. Lett.*, 29(4):565–568, 1974.

[174] E. Hudson, D. A. Shirley, M. Domke, G. Remmers, A. Puschmann, T. Mandel, C. Xue, and G. Kaindl. High-resolution measurements of near-edge resonances in the core-level photoionization spectra of SF_6. *Phys. Rev. A*, 47(1):361, 1993.

[175] Eiji Ishiguro, Iwata Suehiro, Yoshio Suzuki, Akira Mikuni, and Taizo Sasaki. The boron K photoabsorption spectra of BF_3, BCl_3, and BBr_3. *J. Phys. B: At. Mol. Opt. Phys.*, 15:1841–1854, 1982.

[176] Kenji Ito, Jun-ichi Adachi, Yasumasa Hikosaka, S. Motoki, K. Soejima, Akira Yagishita, G. Raeev, and N. A. Cherepkov. Photoelectron angular distributions from O K shell of oriented CO molecules: A critical comparison between theory and experiment. *Phys. Rev. Lett.*, 85(1):46, July 2000.

[177] Shin-ichi Itoh, Satoshi Tanaka, and Yosuke Kayanuma. Vibronic theory for the x-ray absorption spectrum of CF_4 molecules. *Phys. Rev. A*, 60(6):4488–4493, 1999.

[178] T. Jahnke, L. Foucar, J. Titze, R. Wallauer, T. Osipov, E. P. Benis, A. Alnaser, O. Jagutzki, W. Arnold, S. K. Semenov, N. A. Cherepkov, L. Ph. H. Schmidt, A. Czasch, A. Staudte, M. S. Schöffler, C. L. Cocke, M. H. Prior, H. Schmidt-Böcking, and Reinhard Dörner. Vibrationally Resolved K-shell Photoionization of CO with Circularly Polarized Light. *Phys. Rev. Lett.*, 93(8):083002, August 2004.

[179] T. Jahnke, Th. Weber, A. L. Landers, A. Knapp, S. Schössler, J. Nickles, S. Kammer, O. Jagutzki, L. Ph. H. Schmidt, A. Czasch, T. Osipov, E. Arenholz, A. Young, R. Díez Muiño, Daniel Rolles, F. J. García De Abajo, C. S. Fadley, M. A. Van Hove, S. K. Semenov, N. A. Cherepkov, J. Rösch, M. H. Prior, H. Schmidt-Böcking, C. L. Cocke, and Reinhard Dörner. Circular Dichroism in K-Shell Ionization from Fixed-in-Space CO and N_2 Molecules. *Phys. Rev. Lett.*, 88(7):073002, February 2002.

[180] Y. H. Jiang, A. Rudenko, Jhon Freddy Pérez-Torres, O. Herrwerth, L. Foucar, M. Kurka, K. U. Kühnel, M. Toppin, Etienne Plésiat, Felipe Morales, Fernando Martín, M. Lezius, M. F. Kling, T. Jahnke, Reinhard Dörner, Jose Luis Sanz-Vicario, J. van Tilborg, A. Belkacem, M. Schulz, Kiyoshi Ueda, T. J. M. Zouros, S. Düsterer, R. Treusch, C. D. Schröter, R. Moshammer, and J. Ullrich. Investigating two-photon double ionization of D_2 by XUV-pumpXUV-probe experiments. *Phys. Rev. A*, 81(5):051402, May 2010.

[181] Y. H. Jiang, A. Rudenko, Etienne Plésiat, L. Foucar, M. Kurka, K. U. Kühnel, Th. Ergler, Jhon Freddy Pérez-Torres, Fernando Martín, O. Herrwerth, M. Lezius, M. F. Kling, J. Titze, T. Jahnke, Reinhard Dörner, Jose Luis Sanz-Vicario, M. S. Schöffler, J. van Tilborg, A. Belkacem, Kiyoshi Ueda, T. J. M. Zouros, S. Düsterer, R. Treusch, C. D. Schröter, R. Moshammer, and J. Ullrich. Tracing direct and sequential two-photon double ionization of D_2 in femtosecond extreme-ultraviolet laser pulses. *Phys. Rev. A*, 81(2):021401, February 2010.

[182] Cheng Jin, Anh-Thu Le, Song-Feng Zhao, Robert R. Lucchese, and C. D. Lin. Theoretical study of photoelectron angular distributions in single-photon ionization of aligned N_2 and CO_2. *Phys. Rev. A*, 81(3):033421, March 2010.

[183] Charles J. Joachain. *Quantum collision theory.* Elsevier Science Ltd, 1984.

[184] W. L. Jolly, K. D. Bomben, and C. J. Eyermann. Core-electron binding energies for gaseous atoms and molecules. *At. Data Nucl. Data Tables*, 31(3):433–493, 1984.

[185] O. Kamalou, J.-Y. Chesnel, D. Martina, J. Hanssen, C. R. Stia, O. Fojón, R. D. Rivarola, and F. Frémont. Evidence for interference effects in both slow and fast electron emission from D_2 by energetic electron impact. *Phys. Rev. A*, 71(1):010702, January 2005.

[186] Tor Karlsen and Knut J. Bø rve. Accurate and approximate calculations of FranckCondon intensities in the carbon 1s photoelectron spectrum of methane. *J. Chem. Phys.*, 112(18):7979–7985, 2000.

[187] Tor Karlsen, Leif J. Sæ thre, Knut J. Bø rve, Nora Berrah, Edwin Kukk, John D. Bozek, Thomas X. Carroll, and T. Darrah Thomas. Vibrational Structure and Vibronic Coupling in the Carbon 1s Photoelectron Spectra of Ethane and Deuteroethane. *J. Phys. Chem. A*, 105:7700–7706, 2001.

[188] Hideki Katayanagi, Yoshiteru Matsumoto, Cornelis A. de Lange, Masaaki Tsubouchi, and Toshinori Suzuki. One- and two-color photoelectron imaging of the CO molecule via the $B^1\Sigma^+$ state. *J. Chem. Phys.*, 119(7):3737, 2003.

[189] R. B. Kay, Ph. E. Van der Leeuw, and M. J. Van der Wiel. Absolute oscillator strengths for the shape resonances near the K edges of N2 and CO. *J. Phys. B: At. Mol. Opt. Phys.*, 10(12):2513–2519, 1977.

[190] B. Kempgens, A. Kivimäki, M. Neeb, H. M. Köppe, A. M. Bradshaw, and J. Feldhaus. A high-resolution N 1s photoionization study of the N_2 molecule in the near-threshold region. *J. Phys. B: At. Mol. Opt. Phys.*, 29:5389–5402, 1996.

[191] B. Kempgens, H. M. Köppe, A. Kivimäki, M. Neeb, K. Maier, Uwe Hergenhahn, and A. M. Bradshaw. Reappraisal of the Existence of Shape Resonances in the Series C_2H_2, C_2H_4, and C_2H_6. *Phys. Rev. Lett.*, 79(1):35–38, July 1997.

[192] B. Kempgens, Horst Köppel, A. Kivimäki, M. Neeb, Lorenz S. Cederbaum, and A. M. Bradshaw. Core Level Energy Splitting in the C 1s Photoelectron Spectrum of C_2H_2. *Phys. Rev. Lett.*, 79(19):3617–3620, November 1997.

[193] B. Kempgens, K. Maier, A. Kivimäki, H. M. Köppe, M. Neeb, M. N. Piancastelli, Uwe Hergenhahn, and A. M. Bradshaw. Vibrational excitation in C 1s and O 1s photoionization of CO. *J. Phys. B: At. Mol. Opt. Phys.*, 30:L741–L747, 1997.

[194] Simon J. King and Stephen D. Price. Electron ionization of acetylene. *J. Chem. Phys.*, 127(17):174307, November 2007.

[195] Robynne Kirkpatrick, Tony Masiello, Alfons Weber, and Joseph W. Nibler. Coherent Raman spectra of the ν_1 mode of $^{10}BF_3$ and $^{1}1BF_3$. *J. Mol. Spectrosc.*, 237(1):97–103, May 2006.

[196] A. Kivimäki, J. Álvarez Ruiz, M. Coreno, M. Stankiewicz, G. Fronzoni, Mauro Stener, and Piero Decleva. S 2p photoabsorption of the SF_5CF_3 molecule: Experiment, theory and comparison with SF_6. *Chem. Phys.*, 375:101–109, September 2010.

[197] W. Kohn and L. J. Sham. Self-consistent equations including exchange and correlation effects. *Phys. Rev.*, 140(4A):1133, 1965.

[198] H. M. Köppe, B. S. Itchkawitz, A. L. D. Kilcoyne, J. Feldhaus, B. Kempgens, A. Kivimäki, M. Neeb, and A. M. Bradshaw. High-resolution C 1s photoelectron spectra of methane. *Phys. Rev. A*, 53(6):4120–4126, June 1996.

[199] H. M. Köppe, B. Kempgens, A. L. D. Kilcoyne, J. Feldhaus, and A. M. Bradshaw. Autoionisation of doubly excited states in the C 1s photoexcitation of CO. *Chem. Phys. Lett.*, 260:223–228, 1996.

[200] H. M. Köppe, A. L. D. Kilcoyne, J. Feldhaus, and A. M. Bradshaw. Relaxation effects in C1s photoionisation of CO: a high resolution photoelectron study in the near-threshold region. *J. Electron Spectrosc. Relat. Phenom.*, 75:97–108, 1995.

[201] S. Korica, A. Reinköster, M. Braune, Jens Viefhaus, Daniel Rolles, B. Langer, G. Fronzoni, Daniele Toffoli, Mauro Stener, Piero Decleva, O. M. Al-Dossary, and Uwe Becker. Partial photoionization cross sections of C_{60} and C_{70}: A gas versus adsorbed phase comparison. *Surface Science*, 604(21-22):1940–1944, October 2010.

[202] F. Krasniqi, B. Najjari, L. Strüder, Daniel Rolles, A. Voitkiv, and Joachim Ullrich. Imaging molecules from within: Ultrafast angström-scale structure determination of molecules via photoelectron holography using free-electron lasers. *Phys. Rev. A*, 81(3):033411, March 2010.

[203] K. Kreidi, D. Akoury, T. Jahnke, Th. Weber, A. Staudte, M. S. Schöffler, N. Neumann, J. Titze, L. Ph. H. Schmidt, A. Czasch, O. Jagutzki, R. A. Costa Fraga, R. E. Grisenti, M. Smolarski, P. Ranitovic, C. L. Cocke, T. Osipov, H. Adaniya, J. C. Thompson, M. H. Prior, A. Belkacem, A. L. Landers, H. Schmidt-Böcking, and Reinhard Dörner. Interference in the Collective Electron Momentum in Double Photoionization of H2. *Phys. Rev. Lett.*, 100(13):13305, April 2008.

[204] Yu. S. Krivosenko and A. A. Pavlychev. The influence of valence excitations on spectral distribution of vibrational excitations associated with C 1s photoionization in the CO molecule. *Chem. Phys. Lett.*, 500:14–17, November 2010.

[205] Kozo Kuchitsu and Shigehiro Konaka. B-F Bond Distance of Boron Trifluoride Determined by Gas Electron Diffraction. *J. Chem. Phys.*, 45:4342, 1966.

[206] O. Kugeler, E. E. Rennie, A. Rüdel, M. Meyer, A. Marquette, and Uwe Hergenhahn. N_2 valence photoionization below and above the $1s^1$ core ionization threshold. *J. Phys. B: At. Mol. Opt. Phys.*, 37(6):1353–1367, March 2004.

[207] Edwin Kukk, T. Darrah Thomas, and Kiyoshi Ueda. Photoelectron recoil effects in free molecules. *J. Phys.: Conf. Ser.*, 194:012007, November 2009.

[208] Edwin Kukk, T. Darrah Thomas, and Kiyoshi Ueda. Recoil effects in molecular photoemission. *J. Electron Spectrosc. Relat. Phenom.*, 183:53–58, January 2011.

[209] Edwin Kukk, Kiyoshi Ueda, Uwe Hergenhahn, X.-J. Liu, Georg Prümper, H. Yoshida, Yusuke Tamenori, C. Makochekanwa, Takahiro Tanaka, M. Kitajima, and Hiroshi Tanaka. Violation of the Franck-Condon Principle due to Recoil Effects in High Energy Molecular Core-Level Photoionization. *Phys. Rev. Lett.*, 95(13):133001, September 2005.

[210] V. V. Kuznetsov, S. K. Semenov, and N. A. Cherepkov. Photoionization of fixed-in-space molecules by partially polarized light. *J. Chem. Phys.*, 134(13):134301, April 2011.

[211] A. L. Landers, Th. Weber, I. Ali, A. Cassimi, M. Hattass, O. Jagutzki, A. Nauert, T. Osipov, A. Staudte, M. H. Prior, H. Schmidt-Böcking, C. L. Cocke, and Reinhard Dörner. Photoelectron Diffraction Mapping: Molecules Illuminated from Within. *Phys. Rev. Lett.*, 87(1):013002, June 2001.

[212] P. W. Langhoff, S. R. Langhoff, T. N. Rescigno, Jochen Schirmer, Lorenz S. Cederbaum, W. Domcke, and W. von Niessen. Theoretical studies of inner-valence-shell photoionization cross sections in N_2 and CO. *Chem. Phys.*, 58:71–91, 1981.

[213] C. J. Latimer, R. A. Mackie, A. M. Sands, N. Kouchi, and K. F. Dunn. The dissociative photoionization of methane in the VUV. *J. Phys. B: At. Mol. Opt. Phys.*, 32:2667–2676, 1999.

[214] G. Laurent, J. Fernández, S. Legendre, M. Tarisien, L. Adoui, A. Cassimi, X. Fléchard, F. Frémont, B. Gervais, E. Giglio, J. Grandin, and Fernando Martín. Kinematically Complete Study of Dissociative Ionization of D_2 by Ion Impact. *Phys. Rev. Lett*, 96(17):173201, May 2006.

[215] Robert J. Le Roy, Yiye Huang, and Calvin Jary. An accurate analytic potential function for ground-state N_2 from a direct-potential-fit analysis of spectroscopic data. *J. Chem. Phys.*, 125(16):164310, October 2006.

[216] Chengteh Lee, Weitao Yang, and Robert G. Parr. Development of the Colle-Salvetti correlation-energy formula into a functional of the electron density. *Phys. Rev. B*, 37(2):785, 1988.

[217] Timothy J. Lee, Jan M. L. Martin, and Peter R. Taylor. An accurate ab initio quartic force field and vibrational frequencies for CH_4 and isotopomers. *J. Chem. Phys.*, 102(1):254–261, 1995.

[218] B. Leyh and G. Raeev. Theoretical study of electronic autoionization in CO: Vibrationally resolved results between 17 and 18.3 eV. *Phys. Rev. A*, 34(4):2920, 1986.

[219] Xiangzhu Li and Josef Paldus. Full potential energy curve for N_2 by the reduced multireference coupled-cluster method. *J. Chem. Phys.*, 129(5):054104, August 2008.

[220] T. Liebsch, Rainer Hentges, A. Rüdel, Jens Viefhaus, Uwe Becker, and R. Schlögl. Evidence for oscillations in the C_{70} valence photoionization cross sections. *Chem. Phys. Lett.*, 279:197–202, 1997.

[221] T. Liebsch, O. Plotzke, Franz Heiser, Uwe Hergenhahn, O. Hemmers, R. Wehlitz, Jens Viefhaus, Burkhard Langer, S. B. Whitfield, and Uwe Becker. Angle-resolved photoelectron spectroscopy of C_{60}. *Phys. Rev. A*, 52(1):457, 1995.

[222] J. Liévin, J. Demaison, M. Herman, A. Fayt, and C. Puzzarini. Comparison of the experimental, semi-experimental and ab initio equilibrium structures of acetylene: influence of relativisitic effects and of the diagonal Born-Oppenheimer corrections. *J. Chem. Phys.*, 134(6):064119, February 2011.

[223] Ping Lin and Robert R. Lucchese. Multichannel Schwinger study of C 1s photoionization of acetylene. *J. Chem. Phys.*, 113(5):1843, 2000.

[224] Ping Lin and Robert R. Lucchese. Theoretical studies of core excitation and ionization in molecular systems. *J. Synchrotron Radiat.*, 8:150–153, 2001.

[225] Ping Lin and Robert R. Lucchese. Total cross sections and molecular frame photoelectron angular distributions in the N 1s photoionization of N_2: An investigation of electron correlation effects. *J. Chem. Phys.*, 117(9):4348, 2002.

[226] X.-J. Liu, N. A. Cherepkov, S. K. Semenov, Victor Kimberg, Faris Gelmukhanov, Georg Prümper, Toralf Lischke, Takahiro Tanaka, Masamitsu Hoshino, Hiroshi Tanaka, and Kiyoshi Ueda. Young's double-slit experiment using core-level photoemission from N_2: revisiting CohenFano's two-centre interference phenomenon. *J. Phys. B: At. Mol. Opt. Phys.*, 39:4801–4817, December 2006.

[227] X.-J. Liu, Georg Prümper, Faris Gelmukhanov, N. A. Cherepkov, Hiroshi Tanaka, and Kiyoshi Ueda. Youngs double-slit experiment using two-center core-level photoemission: Photoelectron scattering effects. *J. Electron Spectrosc. Relat. Phenom.*, 156-158:73–77, May 2007.

[228] J. A. López-Domínguez, David Hardy, Aloke Das, E. D. Poliakoff, Alex Aguilar, and Robert R. Lucchese. Mechanisms of FranckCondon breakdown over a broad energy range in the valence photoionization of N_2 and CO. *J. Electron Spectrosc. Relat. Phenom.*, 185(8-9):211–218, September 2012.

[229] Robert R. Lucchese, John D. Bozek, Aloke Das, and E. D. Poliakoff. Vibrational branching ratios in the $(b_{2u})^{-1}$ photoionization of C_6F_6. *J. Chem. Phys.*, 131(4):044311, July 2009.

[230] Robert R. Lucchese and Vincent McKoy. Padé-approximant corrections to general variational expressions of scattering theory: Application to 5σ photoionization of carbon monoxide. *Phys. Rev. A*, 28(3):1382, 1983.

[231] Robert R. Lucchese, Raffaele Montuoro, Konstantinos Kotsis, Motomichi Tashiro, Masahiro Ehara, John D. Bozek, Aloke Das, April Landry, Jeff Rathbone, and E. D. Poliakoff. The effect of vibrational motion on the dynamics of shape resonant photoionization of BF_3 leading to the $E^2A'_1$ state of BF_3^+. *Molecular Physics*, 108(7-9):1055–1067, April 2010.

[232] Robert R. Lucchese, Georges Raeev, and Vincent McKoy. Studies of differential and total photoionization cross sections of molecular nitrogen. *Phys. Rev. A*, 25(5):2572–2587, 1982.

[233] Robert R. Lucchese, J. Söderström, Takahiro Tanaka, Masamitsu Hoshino, M. Kitajima, Hiroshi Tanaka, A. De Fanis, J.-E. Rubensson, and Kiyoshi Ueda. Vibrationally resolved partial cross sections and asymmetry parameters for nitrogen K-shell photoionization of the N_2O molecule. *Phys. Rev. A*, 76(1):012506, July 2007.

[234] Robert R. Lucchese and Albert Stolow. Molecular-frame photoelectron angular distributions. *J. Phys. B: At. Mol. Opt. Phys.*, 45(19):190201, October 2012.

[235] Robert R. Lucchese and Robert W. Zurales. Comparison of the random-phase approximation with the multichannel frozen-core Hartree-Fock approximation for the photoionization of N_2. *Phys. Rev. A*, 44(1):291, 1991.

[236] Diane L. Lynch. Molecular orientation following K-shell photoionization. *Phys. Rev. A*, 43(9):5176, 1991.

[237] Diane L. Lynch and Vincent McKoy. Relaxation effects in molecular K-shell photoionization. *Phys. Rev. A*, 30(3):1561–1564, 1984.

[238] R. A. Mackie, L. G. Shpinkova, D. M. P. Holland, and D. A. Shaw. A study of the threshold photoelectron spectra and the photoionisation yield curves of the boron trihalides. *Chem. Phys.*, 288:211–240, March 2003.

[239] G. D. Mahan. Modified Sternheimer equation for polarizability. *Phys. Rev. A*, 22(5):1780, 1980.

[240] G. V. Marr and R. M. Holmes. The angular distribution of photoelectrons from CH_4 as a function of photon energy from near threshold to 30 eV. *J. Phys. B: At. Mol. Opt. Phys.*, 13:939–943, 1980.

[241] G. V. Marr, J. M. Morton, R. M. Holmes, and D. G. McCoy. Angular distribution of photoelectrons from free molecules of N_2 and CO as a function of photon energy. *J. Phys. B: At. Mol. Opt. Phys.*, 12:43–52, 1979.

[242] Fernando Martín. Ionization and dissociation using B-splines : photoionization of the hydrogen molecule. *J. Phys. B: At. Mol. Opt. Phys.*, 197:R197–R231, 1999.

[243] Fernando Martín, J. Fernández, T. Havermeier, L. Foucar, Th. Weber, K. Kreidi, M. S. Schöffler, L. Schmidt, T. Jahnke, O. Jagutzki, A. Czasch, E. P. Benis, T. Osipov, A. L. Landers, A. Belkacem, M. H. Prior, H. Schmidt-Böcking, C. L. Cocke, and Reinhard Dörner. Single photon-induced symmetry breaking of H_2 dissociation. *Science*, 315(5812):629–33, February 2007.

[244] Toshio Masuoka and Eiken Nakamura. Single-, double-, and triple-photoionization cross sections of carbon monoxide (CO) and ionic fragmentation of CO^+, CO^{2+}, and CO^{3+}. *Phys. Rev. A*, 48(6):4379, 1993.

[245] M. Matsumoto, Kiyoshi Ueda, Edwin Kukk, H. Yoshida, Takahiro Tanaka, M. Kitajima, Hiroshi Tanaka, Yusuke Tamenori, K. Kuramoto, Masahiro Ehara, and H. Nakatsuji. Vibrationally resolved C and O 1s photoelectron spectra of carbon monoxides. *Chem. Phys. Lett.*, 417:89–93, January 2006.

[246] Robin S. Mcdowell and Burton J. Krohn. Vibrational levels and anharmonicity in SF_6 - II. Anharmonic and potential constants. *Spectrochim. Acta*, 42A:371–385, 1986.

[247] Robin S. Mcdowell, Burton J. Krohn, Herbert Flicker, and Mariena C. Vasquez. Vibrational levels and anharmonicity in SF_6 - I. Vibrational band analysis. *Spectrochim. Acta*, 42A:351–369, 1986.

[248] M. Meckel, D. Comtois, D. Zeidler, A. Staudte, D. Pavicic, H. C. Bandulet, H. Pépin, J. C. Kieffer, Reinhard Dörner, D. M. Villeneuve, and P. B. Corkum. Laser-induced electron tunneling and diffraction. *Science*, 320(5882):1478–82, June 2008.

[249] Albert Messiah. *Quantum Mechanics*. Dover Publications, 1999.

[250] Y. R. Miao, C. G. Ning, and J. K. Deng. Calculation of Dyson orbitals using a symmetry-adapted-cluster configuration-interaction method for electron momentum spectroscopy: N_2 and H_2O. *Phys. Rev. A*, 83(6):062706, June 2011.

[251] D. S. Milne-Brownlie, M. Foster, Junfang Gao, B. Lohmann, and D. H. Madison. Young-Type Interference in (e,2e) Ionization of H_2. *Phys. Rev. Lett.*, 96(23):233201, June 2006.

[252] Catalin Miron, Victor Kimberg, Paul Morin, Christophe Nicolas, Nobuhiro Kosugi, Sergey Gavrilyuk, and Faris Gelmukhanov. Vibrational Scattering Anisotropy Generated by Multichannel Quantum Interference. *Phys. Rev. Lett.*, 105(9):093002, August 2010.

[253] Catalin Miron, Edwin Kukk, Etienne Plésiat, Luca Argenti, Minna Patanen, David Ayuso, Alicia Palacios, Piero Decleva, Fernando Martín, and Kiyoshi Ueda. To be published.

[254] Catalin Miron and Paul Morin. High-resolution Inner-shell Photoionization, Photoelectron and Coincidence Spectroscopy. In *Handbook of High-resolution Spectroscopy*, number 1, pages 1655–1689. 2011.

[255] Deepankar Misra, U. Kadhane, Y. P. Singh, L. C. Tribedi, P. D. Fainstein, and P. Richard. Interference Effect in Electron Emission in Heavy Ion Collisions with H_2 Detected by Comparison with the Measured Electron Spectrum from Atomic Hydrogen. *Phys. Rev. Lett.*, 92(15):153201, April 2004.

[256] D. A. Mistrov, A. De Fanis, M. Kitajima, Masamitsu Hoshino, H. Shindo, Takahiro Tanaka, Yusuke Tamenori, Hiroshi Tanaka, A. A. Pavlychev, and Kiyoshi Ueda. Vibrational effects on the shape resonance energy in the K-shell photoionization spectra of CO. *Phys. Rev. A*, 68(2):022508, August 2003.

[257] Koichiro Mitsuke, Shinzo Suzuki, Takashi Imamura, and Inosuke Koyano. Negative-ion mass spectrometric study of ion-pair formation in the vacuum ultraviolet. III. $SF_6 \rightarrow F+SF_5^+$. *J. Chem. Phys.*, 93(12):8717, 1990.

[258] T. Mizuno, Jun-ichi Adachi, N. Miyauchi, M. Kazama, Mauro Stener, Piero Decleva, and Akira Yagishita. Recoil frame photoelectron angular distributions of BF_3: A sensitive probe of the shape resonance in the F 1s continuum. *J. Chem. Phys.*, 136(7):074305, February 2012.

[259] Raffaele Montuoro, Robert R. Lucchese, John D. Bozek, Aloke Das, and E. D. Poliakoff. Quasibound continuum states in SiF_4 (D^2A_1) photoionization: photoelectron-vibrational coupling. *J. Chem. Phys.*, 126(24):244309, June 2007.

[260] Raffaele Montuoro and R. Moccia. Photoionization cross sections calculation with mixed L^2 basis set: STOs plus B-Splines. Results for N_2 and C_2H_2 by KM-RPA method. *Chem. Phys.*, 293:281–308, September 2003.

[261] Philip M. Morse. Diatomic molecules according to the wave mechanics. II. Vibrational levels. *Phys. Rev.*, 34:57, 1929.

[262] S. Motoki, Jun-ichi Adachi, Yasumasa Hikosaka, Kenji Ito, M. Sano, K. Soejima, Akira Yagishita, G. Raeev, and N. A. Cherepkov. K-shell photoionization of CO: I. Angular distributions of photoelectrons from fixed-in-space molecules. *J. Phys. B: At. Mol. Opt. Phys.*, 33:4193–4212, 2000.

[263] V. Myrseth, John D. Bozek, Edwin Kukk, Leif J. Sæ thre, and T. Darrah Thomas. Adiabatic and vertical carbon 1s ionization energies in representative small molecules. *J. Electron Spectrosc. Relat. Phenom.*, 122:57–63, 2002.

[264] A. M. Nadolinskii, V. A. Yavna, A. N. Khoperskii, and D. V. Dzyuba. Theoretical study of the K-photoabsorption cross section of carbon in the acetylene molecule. *Opt. Spectrosc.*, 97(6):854–859, 2004.

[265] O. Nagy, C. P. Ballance, K. A. Berrington, P. G. Burke, and B. M. McLaughlin. Vibrational excitation of the N_2^+ first negative (0,0), (1,0)

and (2,0) bands by electron impact: a theoretical study using the R-matrix approach. *J. Phys. B: At. Mol. Opt. Phys.*, 32:L469–L477, 1999.

[266] A. Naja, M. E. Staicu Casagrande, A. Lahmam-Bennani, M. Nekkab, F. Mezdari, B. Joulakian, O. Chuluunbaatar, and D. H. Madison. Triply differential (e,2e) cross sections for ionization of the nitrogen molecule at large energy transfer. *J. Phys. B: At. Mol. Opt. Phys.*, 40:3775–3783, September 2007.

[267] Alexandra P. P. Natalense, Luiz M. Brescansin, and Robert R. Lucchese. Cross section and asymmetry parameter calculations for the C 1s photoionization of CH_4, CF_4, and CCl_4. *Phys. Rev. A*, 68(3):032701, September 2003.

[268] Alexandra P. P. Natalense and Robert R. Lucchese. Cross section and asymmetry parameter calculation for sulfur 1s photoionization of SF_6. *J. Chem. Phys.*, 111(12):5344, 1999.

[269] Alexandra P. P. Natalense and Robert R. Lucchese. Erratum: Cross section and asymmetry parameter calculation for sulfur 1s photoionization of SF[sub 6] [J. Chem. Phys. 111, 5344 (1999)]. *J. Chem. Phys.*, 112(1):501, 2000.

[270] M. Neeb, A. Kivimäki, B. Kempgens, H. M. Köppe, and A. M. Bradshaw. The C 1s Auger decay spectrum of CF_4 : an analysis of the core-excited states. *J. Phys. B: At. Mol. Opt. Phys.*, 30:93–100, 1997.

[271] NIST. CO^+: Constants of diatomic molecules (http://webbook.nist.gov).

[272] Misaki Okunishi, Hiromichi Niikura, Robert R. Lucchese, Toru Morishita, and Kiyoshi Ueda. Extracting Electron-Ion Differential Scattering Cross Sections for Partially Aligned Molecules by Laser-Induced Rescattering Photoelectron Spectroscopy. *Phys. Rev. Lett.*, 106(6):3–6, February 2011.

[273] S. J. Osborne, A. Ausmees, Svante Svensson, A. Kivimäki, O.-P. Sairanen, A. Naves de Brito, H. Aksela, and S. Aksela. The vibrationally resolved participator Auger spectra of selectively excited C $1s(2\sigma)^{-1}2\pi^1$ vibrational states in carbon monoxide. *J. Chem. Phys.*, 102(19):7317–7324, 1995.

[274] T. Osipov, T. N. Rescigno, T. Weber, S. Miyabe, T. Jahnke, A. S. Alnaser, M. P. Hertlein, O. Jagutzki, L. Ph. H. Schmidt, M. S. Schöffler, L. Foucar, S. Schössler, T. Havermeier, M. Odenweller, S. Voss, B. Feinberg, A. L. Landers, M. H. Prior, Reinhard Dörner, C. L. Cocke, and

A. Belkacem. Fragmentation pathways for selected electronic states of the acetylene dication. *J. Phys. B: At. Mol. Opt. Phys.*, 41(9):091001, May 2008.

[275] N. Padial, G. Csanak, Vincent McKoy, and P. W. Langhoff. Photoabsorption in carbon monoxide: StieltjesTchebycheff calculations in the separated-channel static-exchange approximation. *J. Chem. Phys.*, 69(7):2992, 1978.

[276] Alicia Palacios, T. N. Rescigno, and C. W. McCurdy. Cross sections for short-pulse single and double ionization of helium. *Phys. Rev. A*, 77(3):032716, March 2008.

[277] Robert G. Parr and Weitao Yang. *Density-functional theory of atoms and molecules*. Oxford University Press, 1989.

[278] Robert G. Parr and Weitao Yang. Density-functional theory of the electronic structure of molecules. *Annu. Rev. Phys. Chem.*, 46:701, 1995.

[279] A. A. Pavlychev. C K-shell absorption and single-hole ionization in the CO molecule in the vicinity of the shape resonance. *J. Phys. B: At. Mol. Opt. Phys.*, 32:2077–2088, 1999.

[280] A. A. Pavlychev, N. G. Fominykh, Noboru Watanabe, K. Soejima, E. Shigemasa, and Akira Yagishita. Dynamic Properties of N and O $1s^{-1}$ σ_u^* Shape Resonances in N_2 and CO_2 Molecules. *Phys. Rev. Lett.*, 81(17):3623–3626, 1998.

[281] A. A. Pavlychev and D. A. Mistrov. Spectral distributions of vibrational excitations accompanying 1s shell photoionization in small molecules. *J. Phys. B: At. Mol. Opt. Phys.*, 42(5):055103, March 2009.

[282] John P. Perdew. Density-functional approximation for the correlation energy of the inhomogeneous electron gas. *Phys. Rev. B*, 33(12):8822, 1986.

[283] John P. Perdew, Kieron Burke, and Matthias Ernzerhof. Generalized Gradient Approximation Made Simple. *Phys. Rev. Lett.*, 77(18):3865–3868, October 1996.

[284] John P. Perdew, Kieron Burke, and Yue Wang. Generalized gradient approximation for the exchange-correlation hole of a many-electron system. *Phys. Rev. B*, 54(23):533–539, 1996.

[285] John P. Perdew, J. A. Chevary, S. H. Vosko, Koblar A. Jackson, Mark R. Pederson, D. J. Singh, and Carlos Fiolhais. Atoms, molecules, solids, and surfaces: Applications of the generalized gradient approximation for exchange and correlation. *Phys. Rev. B*, 46(11):6671, 1992.

[286] John P. Perdew and Yue Wang. Accurate and simple analytical representation of the electron-gas correlation energy. *Phys. Rev. B*, 45(23):244–249, 1992.

[287] John P. Perdew and Alex Zunger. Self-interaction correction to the density-functional approximations for many-electron systems. *Phys. Rev. B*, 23(10):5048, 1981.

[288] M. Perić and B. Engels. Ab initio study of the electronic spectrum of $C_2H_2^+$. II. Stretching potential energy surfaces for low-lying doublet electronic states. *Chem. Phys.*, 238(1):47–57, November 1998.

[289] M. Perić, B. Engels, and M. Hanrath. Ab initio study of the electronic spectrum of $C_2H_2^+$. I. Vertical spectrum and angular potential curves. *Chem. Phys.*, 238(1):33–46, November 1998.

[290] Etienne Plésiat, Luca Argenti, Edwin Kukk, Catalin Miron, Kiyoshi Ueda, Piero Decleva, and Fernando Martín. Intramolecular electron diffraction in vibrationally resolved K-shell photoionization of methane. *Phys. Rev. A*, 85(2):023409, 2012.

[291] Etienne Plésiat, Piero Decleva, and Fernando Martín. Vibrational branching ratios in the photoelectron spectra of N_2 and CO: interference and diffraction effects. *Phys. Chem. Chem. Phys.*, 14(31):10853–71, August 2012.

[292] Etienne Plésiat, Piero Decleva, and Fernando Martín. Vibrationally resolved photoelectron angular distributions from randomly oriented and fixed-in-space N_2 and CO molecules. *J. Phys. B: At. Mol. Opt. Phys.*, 45(19):194008, October 2012.

[293] E. W. Plummer, T. Gustafsson, W. Gudat, and D. E. Eastman. Partial photoionization cross sections of N_2 and CO using synchrotron radiation. *Phys. Rev. A*, 15(6):2339–2355, 1977.

[294] R. Polák and J. Fišer. A CASSCF/icMRCI study of the electric field gradient in low-lying electronic states of N_2^+/N_2. *Chem. Phys.*, 290:177–188, May 2003.

[295] E. D. Poliakoff, Heung Cheun Choi, R. M. Rao, A. G. Mihill, Sandeep Kakar, Kwanghsi Wang, and Vincent McKoy. Photoion rotational distributions from near-threshold to deep in the continuum. *J. Chem. Phys.*, 103(5):1773–1787, 1995.

[296] E. D. Poliakoff and Robert R. Lucchese. Evolution of photoelectronvibrational coupling with molecular complexity. *Phys. Scr.*, 74(5):C71–C79, November 2006.

[297] Georg Prümper, X.-J. Liu, Kiyoshi Ueda, and Yusuke Tamenori. Comparison of the nuclear motion in the ultrafast fragmentation of SF_6, CF_4 and CH_3F. *Radiat. Phys. Chem.*, 75(11):2019–2023, November 2006.

[298] Péter Pulay. Convergence acceleration of iterative sequences. The case of SCF iteration. *Chem. Phys. Lett.*, 73(2):393, 1980.

[299] Ralph Püttner, I. Dominguez, T. J. Morgan, C. Cisneros, R. F. Fink, E. Rotenberg, T. Warwick, M. Domke, G. Kaindl, and A. S. Schlachter. Vibrationally resolved O 1s core-excitation spectra of CO and NO. *Phys. Rev. A*, 59(5):3415, 1999.

[300] K. J. Randall, A. L. D. Kilcoyne, H. M. Köppe, J. Feldhaus, A. M. Bradshaw, J.-E. Rubensson, W. Eberhardt, Z. Xu, P. D. Johnson, and Y. Ma. Photon energy dependence of the high resolution C 1s photoelectron spectrum of CO in the threshold region. *Phys. Rev. Lett.*, 71(8):1156–1159, 1993.

[301] R. M. Rao and E. D. Poliakoff. Global Franck-Condon Breakdown Resulting from Cooper Minima. *Phys. Rev. Lett.*, 76(15):2666, 1996.

[302] M. Raoult, H. Le Rouzo, Georges Raseev, and H. Lefebvre-Brion. Ab initio approach to the multichannel quantum defect calculation of the electronic autoionisation in the Hopfield series of N_2. *J. Phys. B: At. Mol. Opt. Phys.*, 16:4601–4617, 1983.

[303] G. J. Rathbone, R. M. Rao, E. D. Poliakoff, Kwanghsi Wang, and Vincent McKoy. Vibrational branching ratios in photoionization of CO and N2. *J. Chem. Phys.*, 120(2):778–780, January 2004.

[304] G. Raeev, H. Le Rouzo, and H. Lefebvre-Brion. Partial photoionization cross section and photoelectron angular distribution for the $X^2\Sigma_g^+$ state of N_2^+ in the static-exchange approximation. *J. Chem. Phys.*, 72(10):5701, 1980.

[305] J.J. Rehr, W. Schattke, F. J. García de Abajo, R. Diez Muiño, and M. A. Van Hove. Development of the scattering theory of X-ray absorption and core level photoemission. *J. Electron Spectrosc. Relat. Phenom.*, 126:67–76, 2002.

[306] A. Reimer, Jochen Schirmer, J. Feldhaus, A. M. Bradshaw, Uwe Becker, H. G. Kerkhoff, Burkhard Langer, D. Szostak, R. Wehlitz, and W. Braun. Near-threshold measurements of the C 1s satellites in the photoelectron spectrum of CO. *Phys. Rev. Lett.*, 57(14):1707–1710, 1986.

[307] Alberto Requena Rodríguez and Jose Zuñiga Román. *Espectroscopia*. Pearson education, 2003.

[308] T. N. Rescigno and P. W. Langhoff. K-shell photoionization in molecular nitrogen. *Chem. Phys. Lett.*, 51(1):65–70, 1977.

[309] S. Rioual, G. Nguyen Vien, and A. Pochat. Ionization in coplanar symmetric (e,2e) experiments of N_2 and CO at intermediate energies. *Phys. Rev. A*, 54(6):4968–4977, December 1996.

[310] Jaume Rius i Riu, A. Karawajczyk, M. Stankiewicz, K. Yoshiki Franzén, P. Winiarczyk, and L. Veseth. Non FranckCondon effects in the photoionization of molecular nitrogen to the N_2^+ A $^2\Pi_u$ state in the 1934 eV photon energy region. *Chem. Phys. Lett.*, 338:285–290, April 2001.

[311] Daniel Rolles, Markus Braune, Slobodan Cvejanović, Oliver Gessner, Rainer Hentges, Sanja Korica, Burkhard Langer, Toralf Lischke, Georg Prümper, Axel Reinköster, Jens Viefhaus, Björn Zimmermann, Vincent McKoy, and Uwe Becker. Isotope-induced partial localization of core electrons in the homonuclear molecule N2. *Nature*, 437:711–715, September 2005.

[312] M.-W. Ruf, M. Braun, S. Marienfeld, I. I. Fabrikant, and H. Hotop. High resolution studies of dissociative electron attachment to molecules: dependence on electron and vibrational energy. In *J. Phys.: Conf. Ser.*, volume 88, page 012013, November 2007.

[313] Erich Runge and E. K. U. Gross. Density-functional thery for time-dependent systems. *Phys. Rev. Lett.*, 52(12):997, 1984.

[314] James A. R. Samson. Angular Distributions of Photoelectrons and Partial Photoionization Cross-Sections. *Phil. Trans. Roy. Soc. Lond. A*, 268:141–146, November 1970.

[315] James A. R. Samson, Y. Chung, and E.-M. Lee. Excited ionic and neutral fragments produced by dissociation of the N_2^{+*} H band. *J. Chem. Phys.*, 95:717–719, 1991.

[316] James A. R. Samson and J. L. Gardner. Partial photoionization cross-sections and branching ratios of CO from 750 to 304 Å. *J. Electron Spectrosc. Relat. Phenom.*, 8(1):35–44, 1976.

[317] James A. R. Samson, G. N. Haddad, and J. L. Gardner. Total and partial photoionization cross sections of N_2 from threshold to 100 AA. *J. Phys. B: At. Mol. Opt. Phys.*, 10(9):1749–1759, 1977.

[318] I. Sánchez and Fernando Martín. Origin of Unidentified Structures in Resonant Dissociative Photoionization of H_2. *Phys. Rev. Lett.*, 79(9):1654, 1997.

[319] I. Sánchez and Fernando Martín. Representation of the electronic continuum of H_2 with B-spline basis. *J. Phys. B: At. Mol. Opt. Phys.*, 30:679, 1997.

[320] I. Sánchez and Fernando Martín. Multichannel Dissociation in Resonant Photoionization of H_2. *Phys. Rev. Lett.*, 82(19):3775–3778, 1999.

[321] G Sansone, F Kelkensberg, J F Pérez-Torres, F Morales, M F Kling, W Siu, O Ghafur, P Johnsson, M Swoboda, E Benedetti, F Ferrari, F Lépine, J L Sanz-Vicario, S Zherebtsov, I Znakovskaya, A L'huillier, M Yu Ivanov, M Nisoli, Fernando Martín, and M J J Vrakking. Electron localization following attosecond molecular photoionization. *Nature*, 465(7299):763–6, June 2010.

[322] Jose Luis Sanz-Vicario, Jhon Freddy Pérez-Torres, Felipe Morales, Etienne Plésiat, and Fernando Martín. Probing H_2 autoionizing states with femto- and attosecond laser pulses. In *J. Phys.: Conf. Ser.*, volume 194, page 012013, November 2009.

[323] Jose Luis Sanz-Vicario, Jhon Freddy Pérez-Torres, Felipe Morales, Etienne Plésiat, and Fernando Martín. Molecular frame photoelectron angular distributions for H_2 ionization by single and trains of attosecond XUV laser pulses. *Int. J. Quantum Chem.*, 110:2462–2471, 2010.

[324] Dale E. Sayers, Edward A. Sterntf, and Farrel W. Lytle. New technique for investigating noncrystalline strctures: Fourier analysis of the extended X-ray-absorption fine structure. *Phys. Rev. Lett*, 27(18):1204, 1971.

[325] Jochen Schirmer, M. Braunstein, and Vincent McKoy. Molecular K-shell photoionization cross sections in the relaxed-core Hertree-Fock approximation. *Phys. Rev. A*, 41(1):283, 1990.

[326] Jochen Schirmer and F. Mertins. A new approach to the random phase approximation. *J. Phys. B: At. Mol. Opt. Phys.*, 29:3559–3580, 1996.

[327] M. Schmidbauer, A. L. D. Kilcoyne, H. M. Köppe, J. Feldhaus, and A. M. Bradshaw. Strong multi-electron excitations in the C 1s photoionization of CO and CO_2. *Chem. Phys. Lett.*, 199(1):119–123, 1992.

[328] M. S. Schöffler, T. Jahnke, J. Titze, N. Petridis, K. Cole, L. Ph. H. Schmidt, A. Czasch, O. Jagutzki, J. B. Williams, C. L. Cocke, T. Osipov, S. Lee, M. H. Prior, A. Belkacem, A. L. Landers, H. Schmidt-Böcking, Reinhard Dörner, and Th. Weber. Matter wave optics perspective at molecular photoionization: K-shell photoionization and Auger decay of N_2. *New J. Phys.*, 13(9):095013, September 2011.

[329] M. S. Schöffler, J. Titze, N. Petridis, T. Jahnke, K. Cole, L. Ph. H. Schmidt, A. Czasch, D. Akoury, O. Jagutzki, J. B. Williams, N. A. Cherepkov, S. K. Semenov, C. W. McCurdy, T. N. Rescigno, C. L. Cocke, T. Osipov, S. Lee, M. H. Prior, A. Belkacem, A. L. Landers, H. Schmidt-Böcking, Th. Weber, and Reinhard Dörner. Ultrafast probing of core hole localization in N_2. *Science*, 320:920–923, May 2008.

[330] S. W. J. Scully, R. A. Mackie, R. Browning, K. F. Dunn, and C. J. Latimer. Negative photoion spectroscopy of SF_6 in the inner valence and S 2p energy regions. *J. Phys. B: At. Mol. Opt. Phys.*, 35:2703–2711, 2002.

[331] M. Marvin Seibert, Tomas Ekeberg, Filipe R. N. C. Maia, Martin Svenda, Jakob Andreasson, Olof Jönsson, Duško Odić, Bianca Iwan, Andrea Rocker, Daniel Westphal, Max Hantke, Daniel P. DePonte, Anton Barty, Joachim Schulz, Lars Gumprecht, Nicola Coppola, Andrew Aquila, Mengning Liang, Thomas A. White, Andrew Martin, Carl Caleman, Stephan Stern, Chantal Abergel, Virginie Seltzer, Jean-Michel Claverie, Christoph Bostedt, John D. Bozek, Sébastien Boutet, A. Alan Miahnahri, Marc Messerschmidt, Jacek Krzywinski, Garth Williams, Keith O. Hodgson, Michael J. Bogan, Christina Y. Hampton, Raymond G. Sierra, Dmitri Starodub, Inger Andersson, Saša Bajt, Miriam Barthelmess, John C. H. Spence, Petra Fromme, Uwe Weierstall, Richard Kirian, Mark Hunter, R. Bruce Doak, Stefano Marchesini, Stefan P Hau-Riege, Matthias Frank, Robert L. Shoeman, Lukas Lomb, Sascha W. Epp, Robert Hartmann, Daniel Rolles, Artem Rudenko, Carlo Schmidt, Lutz Foucar, Nils Kimmel, Peter Holl, Benedikt Rudek, Benjamin Erk, André Hömke, Christian Reich, Daniel Pietschner, Georg Weidenspointner, Lothar Strüder, Günter Hauser, Hubert Gorke, Joachim Ullrich, Ilme Schlichting, Sven Herrmann, Gerhard Schaller, Florian Schopper, Heike Soltau, Kai-Uwe Kühnel, Robert Andritschke, Claus-Dieter Schröter, Faton Krasniqi, Mario Bott, Sebastian Schorb, Daniela Rupp, Marcus Adolph, Tais Gorkhover, Helmut Hirsemann, Guillaume Potdevin, Heinz Graafsma, Björn Nilsson, Henry N. Chapman, and Janos Hajdu. Single mimivirus particles intercepted and imaged with an X-ray laser. *Nature*, 470(7332):78–81, February 2011.

[332] S. K. Semenov and N. A. Cherepkov. Generalization of the atomic RPA method for diatomic molecules: H_2 photoionization cross-section calculation. *Chem. Phys. Lett.*, 291:375–380, 1998.

[333] S. K. Semenov and N. A. Cherepkov. Generalization of atomic random-phase-approximation method for diatomic molecules. II. N_2 K-shell photoionization. *Phys. Rev. A*, 66:022708, August 2002.

[334] S. K. Semenov and N. A. Cherepkov. Photoionization of the H_2 molecule in the random phase approximation. *J. Phys. B: At. Mol. Opt. Phys.*, 36(7):1409–1422, April 2003.

[335] S. K. Semenov, N. A. Cherepkov, A. De Fanis, Yusuke Tamenori, M. Kitajima, Hiroshi Tanaka, and Kiyoshi Ueda. Interplay of different partial waves on vibrationally resolved photoionization of the O K shell of the CO molecule. *Phys. Rev. A*, 70(5):052504, November 2004.

[336] S. K. Semenov, N. A. Cherepkov, A. De Fanis, Yusuke Tamenori, M. Kitajima, Hiroshi Tanaka, and Kiyoshi Ueda. Vibrationally resolved photoionization of the O K-shell of CO molecule. *J. Electron Spectrosc. Relat. Phenom.*, 144-147:211–214, June 2005.

[337] S. K. Semenov, N. A. Cherepkov, G. Fecher, and G. Schönhense. Generalization of the atomic random-phase-approximation method for diatomic molecules: N_2 photoionization cross-section calculations. *Phys. Rev. A*, 61(3):032704, February 2000.

[338] S. K. Semenov, N. A. Cherepkov, T. Jahnke, and Reinhard Dörner. Theoretical study of vibrationally resolved photoionization for the C K-shell of the CO molecule. *J. Phys. B: At. Mol. Opt. Phys.*, 37:1331–1342, March 2004.

[339] S. K. Semenov, N. A. Cherepkov, M. Matsumoto, K. Fujiwara, Kiyoshi Ueda, Edwin Kukk, F. Tahara, T. Sunami, H. Yoshida, Takahiro Tanaka, K. Nakagawa, M. Kitajima, Hiroshi Tanaka, and A. De Fanis. Vibrationally resolved photoionization of the $1\sigma_g$ and $1\sigma_u$ shells of N_2 molecule. *J. Phys. B: At. Mol. Opt. Phys.*, 39:375–386, January 2006.

[340] S. K. Semenov, N. A. Cherepkov, M. Matsumoto, T. Hatamoto, X.-J. Liu, Georg Prümper, Takahiro Tanaka, M. Hoashino, Hiroshi Tanaka, Faris Gelmukhanov, and Kiyoshi Ueda. Interference modulation in the vibrationally resolved photoionization of the $1\sigma_g$ and $1\sigma_u$ core levels of the N_2 molecule. *J. Phys. B: At. Mol. Opt. Phys.*, 39:L261–L267, June 2006.

[341] S. K. Semenov, V. V. Kuznetsov, N. A. Cherepkov, P. Bolognesi, V. Feyer, A. Lahmam-Bennani, M. E. Staicu Casagrande, and L. Avaldi. Angular distributions of molecular Auger electrons: The case of C 1s Auger emission in CO. *Phys. Rev. A*, 75(3):032707, March 2007.

[342] S. K. Semenov, M. S. Schöffler, J. Titze, N. Petridis, T. Jahnke, K. Cole, L. Ph. H. Schmidt, A. Czasch, D. Akoury, O. Jagutzki, J. B. Williams, T. Osipov, S. Lee, M. H. Prior, A. Belkacem, A. L. Landers, H. Schmidt-Böcking, Th. Weber, N. A. Cherepkov, and Reinhard Dörner. Auger

decay of $1\sigma_g$ and $1\sigma_u$ hole states of the N_2 molecule: Disentangling decay routes from coincidence measurements. *Phys. Rev. A*, 81:043426, April 2010.

[343] E. Shigemasa, Jun-ichi Adachi, M. Oura, and Akira Yagishita. N_2, Angular Distributions of $1s\sigma$ Photoelectrons from Fixed-in-Space Molecules. *Phys. Rev. Lett.*, 74(3):359–362, 1995.

[344] E. Shigemasa, Jun-ichi Adachi, K. Soejima, Noboru Watanabe, Akira Yagishita, and N. A. Cherepkov. Direct Determination of Partial Wave Contributions in the σ^* Shape Resonance of CO Molecules. *Phys. Rev. Lett.*, 80(8):1622, 1998.

[345] E. Shigemasa, T. Gejo, M. Nagasono, T. Hatsui, and Nobuhiro Kosugi. Double and triple excitations near the K-shell ionization threshold of N_2 revealed by symmetry-resolved spectroscopy. *Phys. Rev. A*, 66(2):022508, August 2002.

[346] E. Shigemasa, T. Hayaishi, T. Sasaki, and Akira Yagishita. Symmetry-resolved C and O K-shell photoabsorption spectra of free CO molecules. *Phys. Rev. A*, 47(3):1824–1829, 1993.

[347] E. Shigemasa, Kiyoshi Ueda, Y. Sato, T. Sasaki, and Akira Yagishita. Symmetry-resolved K-shell photoabsorption spectra of free N2 molecules. *Phys. Rev. A*, 45(5):2915–2921, 1992.

[348] Y. Shimizu, Kiyoshi Ueda, H. Chiba, Misaki Okunishi, K. Ohmori, J. B. West, Y. Sato, and T. Hayaishi. Symmetries and dissociation dynamics of F 1s core excited states of BF_3. *J. Chem. Phys.*, 107(7):2419, 1997.

[349] M. R. F. Siggel, M. A. Hayes, M. A. MacDonald, J. B. West, J. L. Dehmer, A. C. Parr, J. E. Hardis, I. Iga, and V. Tiit. Resonance effects in the $5\sigma^{-1}$ photoionization channel of CO. *J. Chem. Phys.*, 96(10):7433, 1992.

[350] Mutasem Omar Sinnokrot and C. David Sherrill. Density functional theory predictions of anharmonicity and spectroscopic constants for diatomic molecules. *J. Chem. Phys.*, 115(6):2439, 2001.

[351] Per Skytt, Peter Glans, Kerstin Gunnelin, Jinghua Guo, Joseph Nordgren, Yi Luo, and Hans Å gren. Role of screening and angular distributions in resonant x-ray emission of CO. *Phys. Rev. A*, 55(1):134–145, 1997.

[352] Ashley G. Smart. Simple molecules mimic double slits. *Physics today*, page 18, 2011.

[353] Maile E. Smith, Diane L. Lynch, and Vincent McKoy. Resonance effects in the 5σ photoionization of CO. *J. Chem. Phys.*, 85(11):6455–6459, 1986.

[354] Sérgio Filipe Sousa, Pedro Alexandrino Fernandes, and Maria João Ramos. General performance of density functionals. *J. Phys. Chem. A*, 111(42):10439–52, October 2007.

[355] S. H. Southworth, A. C. Parr, J. E. Hardis, and J. L. Dehmer. Channel coupling and shape resonance effects in the photoelectron angular distributions of the $3\sigma_g^{-1}$ and $2\sigma_u^{-1}$ channels of N_2. *Phys. Rev. A*, 33(2):1020–1023, 1986.

[356] Mauro Stener. Photoionization of oriented molecules: a time dependent density functional approach. *Chem. Phys. Lett.*, 356:153–160, 2002.

[357] Mauro Stener, G. De Alti, and Piero Decleva. Convergence of the density functional one-centre expansion for the molecular continuum : N_2 and $(CH_3)_3N$. *Theor. Chem. Acc.*, 101:247–256, 1999.

[358] Mauro Stener and Piero Decleva. Photoionization of zinc by TDLDA calculations. *J. Phys. B: At. Mol. Opt. Phys.*, 30:4481–4487, 1997.

[359] Mauro Stener and Piero Decleva. Time-dependent density functional calculations of molecular photoionization cross sections: N_2 and PH_3. *J. Chem. Phys.*, 112(24):10871, 2000.

[360] Mauro Stener, Piero Decleva, Ivo Cacelli, R. Moccia, and Raffaele Montuoro. Response function study of CO photoionization: ab initio SCF and density functional results. *Chem. Phys.*, 272(1):15–25, October 2001.

[361] Mauro Stener, G. Fronzoni, Daniele Toffoli, and Piero Decleva. Time dependent density functional photoionization of CH_4, NH_3, H_2O and HF. *Chem. Phys.*, 282:337–351, September 2002.

[362] Mauro Stener, S. Furlan, and Piero Decleva. Density functional calculations of photoionization with an exchange-correlation potential with the correct asymptotic behaviour. *J. Phys. B: At. Mol. Opt. Phys.*, 33:1081, 2000.

[363] Mauro Stener, A. Lisini, and Piero Decleva. Accurate Local Density Photoionization Cross Sections by LCAO Stieltjes Imaging Approach*. *Int. J. Quantum Chem.*, 53(2):229–244, 1995.

[364] Mauro Stener, Daniele Toffoli, G. Fronzoni, and Piero Decleva. Recent advances in molecular photoionization by density functional theory based approaches. *Theor. Chem. Acc.*, 117:943–956, December 2006.

[365] Mauro Stener, Daniele Toffoli, G. Fronzoni, and Piero Decleva. Time dependent density functional study of the photoionization dynamics of SF_6. *J. Chem. Phys.*, 124(11):114306, March 2006.

[366] J. A. Stephens and Dan Dill. Shape-resonance effects mediated by channel interaction: Angular distributions of N_2 $2\sigma_u$ photoelectrons. *Phys. Rev. A*, 31(3):1968, 1985.

[367] J. A. Stephens, Dan Dill, and J. L. Dehmer. Vibrational branching ratios and photoelectron angular distributions in 5σ photoionisation of CO. *J. Phys. B: At. Mol. Opt. Phys.*, 14:3911–3918, 1981.

[368] J. A. Stephens, Dan Dill, and J. L. Dehmer. Shape resonances in the photoionization of CF_4. *J. Chem. Phys.*, 84(7):3638, 1986.

[369] Roger Stockbauer, B. E. Cole, and D. L. Ederer. Effects of Shape resonances on Vibrational Intensity Distributions in Molecular Photoionization. *Phys. Rev. Lett.*, 43(11):757, 1979.

[370] N. Stolterfoht, B. Sulik, V. Hoffmann, B. Skogvall, J. Y. Chesnel, J. Rangama, F. Frémont, D. Hennecart, A. Cassimi, X. Husson, A. L. Landers, J. A. Tanis, M. E. Galassi, and R. D. Rivarola. Evidence for Interference Effects in Electron Emission from H_2 Colliding with 60 MeV/u Kr^{34+} Ions. *Phys. Rev. Lett.*, 87(2):023201, June 2001.

[371] Ralf Stowasser and Roald Hoffmann. What Do the Kohn-Sham Orbitals and Eigenvalues Mean ? *J. Am. Chem. Soc.*, 121(20):3414–3420, 1999.

[372] R. E. Stratmann, Gunadya Bandarage, and Robert R. Lucchese. Electron-correlation effects in the photoionization of N_2. *Phys. Rev. A*, 51(5):3756, 1995.

[373] Svante Svensson, A. Naves de Brito, M. P. Keane, N. Correia, Leif Karlsson, C.-M. Legener, and Hans Å gren. The N 1s core electron shake-up and the shake-up Auger satellite spectrum of the N , molecule. *J. Phys. B: At. Mol. Opt. Phys.*, 25:135–144, 1992.

[374] John R. Swanson, Dan Dill, and J. L. Dehmer. Shape resonance effects in the photoabsorption spectra of BF_3. *J. Chem. Phys.*, 75(2):619, 1981.

[375] Hiroto Tachikawa. Ab initio MO calculations of structures and electronic states of SF_6 and SF_6^-. *J. Phys. B: At. Mol. Opt. Phys.*, 35:55–60, 2002.

[376] Hiroto Tachikawa and Tadaomi Yamano. A full dimensional direct ab initio dynamics study of the electron capture by SF_6. *Chem. Phys.*, 264:81–89, 2001.

[377] Takahiro Tanaka, H. Shindo, C. Makochekanwa, M. Kitajima, Hiroshi Tanaka, A. De Fanis, Yusuke Tamenori, K. Okada, R. Feifel, S. Sorensen, Edwin Kukk, and Kiyoshi Ueda. Interference effects in Auger resonant Raman spectra of CO via selective vibrational excitations across the O $1s \rightarrow 2\pi$ resonance. *Phys. Rev. A*, 72(2):022507, August 2005.

[378] Motomichi Tashiro. Application of the R-matrix method to photoionization of molecules. *J. Chem. Phys.*, 132(13):134306–1, April 2010.

[379] Motomichi Tashiro, Masahiro Ehara, Hironobu Fukuzawa, Kiyoshi Ueda, Christian Buth, Nikolai V. Kryzhevoi, and Lorenz S. Cederbaum. Molecular double core hole electron spectroscopy for chemical analysis. *J. Chem. Phys.*, 132(18):184302, 2010.

[380] John R. Taylor. *The quantum theory of nonrelativistic collisions*. Dover Publications, 2006.

[381] Takahiro Teramoto, Jun-ichi Adachi, K. Hosaka, Masakazu Yamazaki, K. Yamanouchi, N. A. Cherepkov, Mauro Stener, Piero Decleva, and Akira Yagishita. New approach for a complete experiment: C1s photoionization in CO_2 molecules. *J. Phys. B: At. Mol. Opt. Phys.*, 40:F241–F250, August 2007.

[382] Alexander Thiel, Jochen Schirmer, and Horst Köppel. An intermediate state representation approach to K-shell ionization in molecules. II. Computational tests. *J. Chem. Phys.*, 119(4):2088–2101, 2003.

[383] Isabell Thomann, Robynne Lock, Vandana Sharma, Etienne Gagnon, Stephen T. Pratt, Henry C. Kapteyn, Margaret M. Murnane, and Wen Li. Direct measurement of the angular dependence of the single-photon ionization of aligned N_2 and CO_2. *J. Phys. Chem. A*, 112(39):9382–9386, October 2008.

[384] T. Darrah Thomas, N. Berrah, John D. Bozek, Thomas X. Carroll, Jeffrey A. Hahne, Tor Karlsen, Edwin Kukk, and Leif J. Sæ thre. Photon Energy Dependence of the $1\sigma_u/1\sigma_g$ Intensity Ratio in Carbon 1s Photoelectron Spectroscopy of Ethyne. *Phys. Rev. Lett*, 82(6):1120, 1999.

[385] T. Darrah Thomas, Edwin Kukk, T. Ouchi, A. Yamada, Hironobu Fukuzawa, Kiyoshi Ueda, Ralph Püttner, I. Higuchi, Yusuke Tamenori, T. Asahina, N. Kuze, H. Kato, Masamitsu Hoshino, Hiroshi Tanaka, A. Lindblad, and Leif J. Sæ thre. Valence photoelectron spectroscopy of N_2 and CO: Recoil-induced rotational excitation, relative intensities, and atomic orbital composition of molecular orbitals. *J. Chem. Phys.*, 133(17):174312, 2010.

[386] T. Darrah Thomas, Edwin Kukk, Rami Sankari, Hironobu Fukuzawa, Georg Prümper, Kiyoshi Ueda, Ralph Püttner, James R. Harries, Yusuke Tamenori, Takahiro Tanaka, Masamitsu Hoshino, and Hiroshi Tanaka. Recoil excitation of vibrational structure in the carbon 1s photoelectron spectrum of CF_4. *J. Chem. Phys.*, 128(14):144311, April 2008.

[387] T. Darrah Thomas, Ralph Püttner, Hironobu Fukuzawa, Georg Prümper, Kiyoshi Ueda, Edwin Kukk, Rami Sankari, James Harries, Yusuke Tamenori, Takahiro Tanaka, Masamitsu Hoshino, and Hiroshi Tanaka. Boron 1s photoelectron spectrum of $^{11}BF_3$: vibrational structure and linewidth. *J. Chem. Phys.*, 127(24):244309, December 2007.

[388] T. Darrah Thomas, Leif J. Saethre, Stacey L. Sorensen, and Svante Svensson. Vibrational structure in the carbon 1s ionization of hydrocarbons: Calculation using electronic structure theory and the equivalent-cores approximation. *J. Chem. Phys.*, 109(3):1041, 1998.

[389] T. Darrah Thomas and Robert W. Jr. Shaw. Accurate core ionization potentials and photoelectron kinetic energies for light elements. *J. Electron Spectrosc. Relat. Phenom.*, 5:1081–1094, 1974.

[390] Daniele Toffoli and Piero Decleva. A multicentric approach to the calculation of nondipolar effects in molecular photoemission. *J. Chem. Phys.*, 128(23):234101, June 2008.

[391] Daniele Toffoli and Piero Decleva. Nondipolar effects in the photoionization dynamics of carbon tetrafluoride. *Phys. Rev. A*, 78(6):063402, December 2008.

[392] Daniele Toffoli and Piero Decleva. Strong oscillations in the nondipole corrections to the photoelectron angular distributions from C_{60}. *Phys. Rev. A*, 81(6):061201, June 2010.

[393] Daniele Toffoli, Piero Decleva, F. A. Gianturco, and Robert R. Lucchese. Density functional theory for the photoionization dynamics of uracil. *J. Chem. Phys.*, 127(23):234317, December 2007.

[394] Daniele Toffoli, Mauro Stener, G. Fronzoni, and Piero Decleva. Convergence of the multicenter B-spline DFT approach for the continuum. *Chem. Phys.*, 276:25–43, January 2002.

[395] Daniele Toffoli, Mauro Stener, G. Fronzoni, and Piero Decleva. Photoionization cross section and angular distribution calculations of carbon tetrafluoride. *J. Chem. Phys.*, 124(21):214313, June 2006.

[396] David J. Tozer and Nicholas C. Handy. Improving virtual KohnSham orbitals and eigenvalues: Application to excitation energies and static polarizabilities. *J. Chem. Phys.*, 109(23):10180, 1998.

[397] C. S. Trevisan, C. W. McCurdy, and T. N. Rescigno. Imaging molecular shapes with molecular-frame photoelectron angular distributions from core hole ionization. *J. Phys. B: At. Mol. Opt. Phys.*, 45(19):194002, October 2012.

[398] C. M. Truesdale, D. W. Lindle, P. H. Kobrin, Uwe Becker, H. G. Kerkhoff, P. A. Heimann, T. A. Ferrett, and D. A. Shirley. Core-level photoelectron and Auger shape-resonance phenomena in CO, CO_2, CF_4, and OCS. *J. Chem. Phys.*, 80(6):2319, 1984.

[399] Kiyoshi Ueda. High-resolution inner-shell spectroscopies of free atoms and molecules using soft-x-ray beamlines at the third-generation synchrotron radiation sources. *J. Phys. B: At. Mol. Opt. Phys.*, 36:R1–R47, 2003.

[400] Kiyoshi Ueda. Core Excitation and De-excitation Spectroscopies of Free Atoms and Molecules. *J. Phys. Soc. Jpn*, 75(3):032001, March 2006.

[401] Kiyoshi Ueda. Which-pass information in the double-slit experiment of diatomic molecules. *J. Phys.: Conf. Ser.*, 212:012033, February 2010.

[402] Kiyoshi Ueda, H. Chiba, Y. Sato, T. Hayaishi, E. Shigemasa, and Akira Yagishita. Resonance-Auger-electron-photoion coincidence studies on state-to-state dissociation dynamics of inner-shell-excited BF_3. *Phys. Rev. A*, 46(1):R5–R8, July 1992.

[403] Kiyoshi Ueda, H. Chiba, Y. Sato, T. Hayaishi, E. Shigemasa, and Akira Yagishita. Electronic decay processes following the resonance excitation of the B 1s core electron in BF_3. *J. Chem. Phys.*, 101(5):3520, 1994.

[404] Kiyoshi Ueda and John H. D. Eland. Molecular photodissociation studied by VUV and soft x-ray radiation. *J. Phys. B: At. Mol. Opt. Phys.*, 38(9):S839–S859, May 2005.

[405] Kiyoshi Ueda, Masamitsu Hoshino, Takahiro Tanaka, M. Kitajima, Hiroshi Tanaka, A. De Fanis, Yusuke Tamenori, Masahiro Ehara, F. Oyagi, K. Kuramoto, and H. Nakatsuji. Symmetry-Resolved Vibrational Spectra of Carbon K-Shell Photoelectron Satellites in Carbon Monoxides: Experiment and Theory. *Phys. Rev. Lett.*, 94(24):243004, June 2005.

[406] Kiyoshi Ueda, Edwin Kukk, Catalin Miron, Etienne Plésiat, Luca Argenti, Minna Patanen, David Ayuso, Alicia Palacios, Piero Decleva, and Fernando Martín. To be published.

[407] Kiyoshi Ueda, X.-J. Liu, Georg Prümper, Toralf Lischke, Takahiro Tanaka, Masamitsu Hoshino, Hiroshi Tanaka, I. Minkov, Victor Kimberg, and Faris Gelmukhanov. Role of the recoil effect in two-center

interference in X-ray photoionization. *Chem. Phys.*, 329:329–337, October 2006.

[408] Kiyoshi Ueda, A. A. Pavlychev, Edwin Kukk, Uwe Hergenhahn, H. Yoshida, T. Sunami, F. Tahara, Takahiro Tanaka, M. Kitajima, Hiroshi Tanaka, A. De Fanis, and Yusuke Tamenori. Non-FranckCondon behavior in the C 1s photoelectron spectrum of the methane molecule. *Chem. Phys. Lett.*, 411:33–36, August 2005.

[409] Kiyoshi Ueda, Ralph Püttner, N. A. Cherepkov, Faris Gelmukhanov, and Masahiro Ehara. High resolution X-ray photoelectron spectroscopy on nitrogen molecules. *Eur. Phys. J. Special Topics*, 169:95–107, May 2009.

[410] Kiyoshi Ueda, Y. Shimizu, H. Chiba, Misaki Okunishi, K. Ohmori, Y. Sato, E. Shigemasa, and N. Kosugi. C 1s and F 1s photoabsorption and subsequent electronic decay of CH_4, CH_3F, CH_2F_2, CHF_3, and CF_4. *J. Electron Spectrosc. Relat. Phenom.*, 79:441–444, 1996.

[411] Kiyoshi Ueda, M. Simon, Catalin Miron, N. Leclercq, Renaud Guillemin, Paul Morin, and Satoshi Tanaka. Correlation between Nuclear Motion in the Core-Excited CF_4 Molecule and Molecular Dissociation after Resonant Auger Decay. *Phys. Rev. Lett*, 83(19):3800, 1999.

[412] L. Ungier and T. Darrah Thomas. Resonance-Enhanced Shakeup in Near-Threshold Core Excitation of CO and N_2. *Phys. Rev. Lett.*, 53(5):435–438, 1984.

[413] R. van Leeuwen and E. J. Baerends. Exchange-correlation potential with correct symptotic behavior. *Phys. Rev. A*, 49(4):2421, 1994.

[414] A. M. Velasco, I. Martín, and C. Lavín. MQDO study of photoionization cross-sections for carbon monoxide. *Int. J. Quantum Chem.*, 104(4):517–521, September 2005.

[415] M. Venuti, Mauro Stener, and Piero Decleva. Valence photoionization of C_6H_6 by the B-spline one-centre expansion density functional method. *Chem. Phys.*, 234:95–109, 1998.

[416] L. Veseth. Many-body calculation of total and partial photoabsorption cross sections in N2. *J. Phys. B: At. Mol. Opt. Phys.*, 27:481–496, 1994.

[417] S. H. Vosko, L. Wilk, and M. Nusair. Accurate spin-dependent electron liquid correlation energies for local spin density calculations: A critical analysis. *Can. J. Phys.*, 58:1200–11, 1980.

[418] Scott Wallace, Dan Dill, and J. L. Dehmer. Fixed-molecule photoelectron angular distributions: K-shell cross sections of CO at fixed detection angles. *Phys. Rev. B*, 17(4):2004, 1978.

[419] Scott Wallace, Dan Dill, and J. L. Dehmer. Spectral variation of molecular photoelectron angular distributions: valence shells of N_2 and CO. *J. Phys. B: At. Mol. Opt. Phys.*, 12(14):L417, 1979.

[420] Xiao-Gang Wang, Edwin L. Sibert III, and Jan M. L. Martin. Anharmonic force field and vibrational frequencies of tetrafluoromethane (CF_4) and tetrafluorosilane (SiF_4). *J. Chem. Phys.*, 112(3):1353–1366, 2000.

[421] N. Watanabe and M. Takahashi. Carbon 1s electron momentum spectroscopy of CF_4. *J. Phys. B: At. Mol. Opt. Phys.*, 44(10):105201, May 2011.

[422] Th. Weber, O. Jagutzki, M. Hattass, A. Staudte, A. Nauert, L. Ph. H. Schmidt, M. H. Prior, A. L. Landers, A. Bräuning-Demian, H. Bräuning, C. L. Cocke, T. Osipov, I. Ali, R. Díez Muiño, Daniel Rolles, F. J. García De Abajo, C. S. Fadley, M. A. Van Hove, A. Cassimi, H. Schmidt-Böcking, and Reinhard Dörner. K-shell photoionization of CO and N_2: is there a link between the photoelectron angular distribution and the molecular decay dynamics? *J. Phys. B: At. Mol. Opt. Phys.*, 34:3669–3678, September 2001.

[423] M. C. Wells and Robert R. Lucchese. The inner valence photoionization of acetylene. *J. Chem. Phys.*, 110(13):6365, 1999.

[424] M. C. Wells and Robert R. Lucchese. The outer valence photoionization of acetylene. *J. Chem. Phys.*, 111(14):6290, 1999.

[425] Hans-Joachim Werner and Peter J. Knowles. Accurate multireference configuration interaction calculations of the potential energy function and the dissociation energy of N_2. *J. Chem. Phys.*, 94(2):1264–1270, 1991.

[426] J. B. West, K. Codling, A. C. Parr, D. L. Ederer, B. E. Cole, Roger Stockbauer, and J. L. Dehmer. Branching ratios and photoelectron angular distributions through the Hopfield bands in N_2 between 650 and 730 Å. *J. Phys. B: At. Mol. Opt. Phys.*, 14:1791–1801, 1981.

[427] G. R. Wight and C. E. Brion. K-shell and valence shell excitations in CF_4 by 2.5 keV electron impact. *J. Electron Spectrosc. Relat. Phenom.*, 4:327–333, 1974.

[428] Immanuel Wilhelmy, Lutz Ackermann, Andreas Görling, and Notker Rösch. Molecular photoionization cross sections by the Lobatto technique I . Valence photoionization. *J. Chem. Phys.*, 100(4):2808, 1994.

[429] Immanuel Wilhelmy and Notker Rösch. Molecular photoionization cross sections by the Lobatto technique. II. Core level photionization. *Chem. Phys.*, 185:317–332, 1994.

[430] J. B. Williams, C. S. Trevisan, M. S. Schöffler, T. Jahnke, I. Bocharova, H. Kim, B. Ulrich, R. Wallauer, F. Sturm, T. N. Rescigno, A. Belkacem, Reinhard Dörner, Th. Weber, C. W. McCurdy, and A. L. Landers. Imaging Polyatomic Molecules in Three Dimensions Using Molecular Frame Photoelectron Angular Distributions. *Phys. Rev. Lett.*, 108(23):233002, June 2012.

[431] J. B. Williams, C. S. Trevisan, M. S. Schöffler, T. Jahnke, I. Bocharova, H. Kim, B. Ulrich, R. Wallauer, F. Sturm, T. N. Rescigno, A. Belkacem, Reinhard Dörner, Th. Weber, C. W. McCurdy, and A. L. Landers. Probing the dynamics of dissociation of methane following core ionization using three-dimensional molecular-frame photoelectron angular distributions. *J. Phys. B: At. Mol. Opt. Phys.*, 45(19):194003, October 2012.

[432] E. Bright Jr. Wilson, J. C. Decius, and Paul C: Cross. *Molecular vibrations. The theory of infrared and Raman vibrational spectroscopy.* Dover Publications, 1955.

[433] C. Winstead and P. W. Langhoff. Feshbach-Fano formalism in Hilbert space: Application to shape resonances in molecular photoionization. *J. Chem. Phys.*, 95(5):3107–3118, 1991.

[434] Pamela R. Woodruff and G. V. Marr. The Photoelectron Spectrum of N_2, and Partial Cross Sections as a Function of Photon Energy from 16 to 40 eV. *Proc. R. Soc. Lond. A*, 358(1692):87–103, 1977.

[435] H. J. Wörner, J. B. Bertrand, D. V. Kartashov, P. B. Corkum, and D. M. Villeneuve. Following a chemical reaction using high-harmonic interferometry. *Nature*, 466(7306):604–7, July 2010.

[436] Y. B. Xu, M. Q. Tan, and Uwe Becker. Oscillations in the photoionization cross section of C_{60}. *Phys. Rev. Lett.*, 76(19):3538–3541, May 1996.

[437] Satoshi Yabushita, C. W. McCurdy, and T. N. Rescigno. Complex-basis-function treatment of photoionization in the random-phase approximation. *Phys. Rev. A*, 36(7):3146–3151, 1987.

[438] Satoshi Yamamoto, Rika Kuwabara, Michio Takami, and Kozo Kuchitsu. Infrared Diode Laser Spectroscopy of the v_2 Band of BF_3. *J. Mol. Spectrosc.*, 115:333–352, 1986.

[439] Li Yang, Hans Å gren, Vincenzo Carravetta, Olav Vahtras, Leif Karlsson, Björn Wannberg, D. M. P. Holland, and M. A. MacDonald. Energy-dependent valence photoelectron spectra of SF_6. Ab initio calculations and measurements. *J. Electron Spectrosc. Relat. Phenom.*, 94:163–179, June 1998.

[440] Tomokazu Yasuike and Satoshi Yabushita. Valence photoionization and autoionizing states of acetylene studied by the complex basis function method in the random phase approximation. *Chem. Phys. Lett.*, 316:257–265, January 2000.

[441] Andrew J. Yencha, M. C. A. Lopes, D. B. Thompson, and G. C. King. Threshold photoelectron spectroscopy in the inner-valence ionization region and photo-double ionization of SF_6. *J. Phys. B: At. Mol. Opt. Phys.*, 33:945–954, 2000.

[442] Andrew J. Yencha, M.Cristina A. Lopes, and George C. King. Threshold photoelectron spectroscopy of boron trifluoride. *Chem. Phys.*, 279(1):55–69, May 2002.

[443] Andrew J. Yencha, D. B. Thompson, A. J. Cormack, D. R. Cooper, M. Zubek, P. Bolognesi, and G. C. King. Threshold photoelectron spectroscopy of SF_6. *Chem. Phys.*, 216:227–241, 1997.

[444] A. Zangwill and Paul Soven. Density-functional approach to local-field effects in finite systems: Photoabsorption in the rare gases. *Phys. Rev. A*, 21(5):1561, 1980.

[445] Ping Zhu, Tang Jingchang, and Cao Song. New insight on CH resonances in the simple hydrocarbons. *J. Electron Spectrosc. Relat. Phenom.*, 129:27–33, March 2003.

[446] Björn Zimmermann, Daniel Rolles, Burkhard Langer, Rainer Hentges, Markus Braune, Slobodan Cvejanović, Oliver Geß ner, Franz Heiser, Sanja Korica, Toralf Lischke, Axel Reinköster, Jens Viefhaus, Reinhard Dörner, Vincent McKoy, and Uwe Becker. Localization and loss of coherence in molecular double-slit experiments. *Nature Physics*, 4:649–655, June 2008.

[447] Björn Zimmermann, Kwanghsi Wang, and Vincent McKoy. Circular dichroism in K-shell ionization from fixed-in-space CO and N_2. *Phys. Rev. A*, 67(4):042711, April 2003.